



Vehicular Traffic: A Review of Continuum Mathematical Models

BENEDETTO PICCOLI, ANDREA TOSIN
Istituto per le Applicazioni del Calcolo “Mauro Picone”,
Consiglio Nazionale delle Ricerche,
Rome, Italy

Article Outline

Glossary
Definition of the Subject
Introduction
Macroscopic Modeling
Kinetic Modeling
Road Networks
Future Directions
Bibliography

Glossary

- Mathematical model** Simplified description of a real world system in mathematical terms, e. g., by means of differential equations or other suitable mathematical structures.
- Scale of observation/representation** Level of detail at which a system is observed and mathematically modeled.
- Macroscopic scale** Scale of observation focusing on the evolution in time and space of some *macroscopic quantities* of the system at hand; that is, quantities that can be experimentally observed and measured.
- Kinetic scale** Scale of representation focusing on a statistical description of the evolution of the microscopic states of the system at hand.
- Vehicular traffic** The overall dynamics produced by cars or other transports in motion along a road.
- Road network** A set of roads connected to one another by junctions.

Definition of the Subject

Vehicular traffic is attracting a growing scientific interest because of its connections with other important problems, like, e. g., environmental pollution and congestion of cities. Rational planning and management of vehicle fluxes are key topics in modern societies under both economical and social points of view, as the increasing number of projects aimed at monitoring the quality of the road traffic demonstrates. In spite of their importance, however, these issues cannot be effectively handled by simple experimental approaches. On the one hand, observation and data recording may provide useful information on the physics of traffic, highlighting some typical features like, e. g., clustering of the vehicles, the appearance of stop-and-go waves, the phase transition between the regimes of free and congested flow, the trend of the traffic in uniform flow conditions. The books by Kerner [48] and Leutzbach [54] extensively report about traffic phenomena, real traffic data, and their phenomenological interpretation. On the other hand, processing and organization of (usually huge amounts of) experimental measurements hardly allow one to catch the real unsteady traffic dynamics, which definitely makes this approach scarcely predictive. Therefore vehicular traffic is not only an engineering matter but also a challenging mathematical problem.

This paper reviews some of the major macroscopic and kinetic mathematical models of vehicular traffic available in the specialized literature. Application to road networks is also discussed, and an extensive list of references is provided to both the original works presented here and other sources for further details. Microscopic models are only briefly recalled in the introduction for the sake of thoroughness, as they are actually beyond the scope of the review. However, suitable references are included for the interested readers.

Introduction

The mathematical modeling of vehicular traffic requires, first of all, the choice of the scale of representation. The

relevant literature offers many examples of models at any scale, from the microscopic to the macroscopic through the kinetic one. Each of them implies some technical approximations, and suffers therefore from related drawbacks, either analytical or computational.

The microscopic scale is like a magnifying glass focused on each single vehicle, whose dynamics is described by a system of ordinary second-order differential equations of the form

$$\ddot{x}_i = a_i \left[t, \{x_k\}_{k=1}^N, \{\dot{x}_k\}_{k=1}^N \right], \quad i = 1, \dots, N, \quad (1)$$

where t is time, $x_i = x_i(t)$ the scalar position of the i th vehicle along the road, $\dot{x}_i = \dot{x}_i(t)$ its velocity, and $N \in \mathbb{N}$ the total number of vehicles. The function a_i describes the acceleration of the i th vehicle, which in principle might be influenced by the positions and velocities of all other vehicles simultaneously present on the road. As a matter of fact, each vehicle is commonly assumed to be influenced by its heading vehicle only (*follow-the-leader models*), so that the acceleration a_i depends at most on x_i , x_{i+1} and on \dot{x}_i , \dot{x}_{i+1} . It is immediately seen that the size of system (1) rapidly increases with the number N of vehicles considered, which frequently makes the microscopic approach not competitive for computational purposes. Furthermore, from the analytical point of view it is often difficult to investigate the relevant global features of the system, also in connection with control and optimization problems. In this paper we will not be concerned specifically with microscopic modeling of vehicular traffic. The interested reader can find further details on the subject in Aw et al. [4], Chakroborty et al. [20], Gazis et al. [36], Helbing [41,42], Kerner and Klenov [49], Nagel et al. [56] Treiber et al. [66,67,68] and in the main references listed therein, as well as in the review by Hoogendoorn and Bovy [46].

Macroscopic and kinetic models aim at describing the big picture without looking specifically at each single subject of the system, hence they are computationally more efficient: Few partial differential equations, that can be solved numerically in a feasible time, are normally involved, and the global characteristics of the system are readily accessible. Nevertheless, now the modeling is, in a sense, less accurate than in the microscopic case, due to the fact that both approaches rely on the *continuum hypothesis*, clearly not physically satisfied by cars along a road: The number of vehicles should be large enough so that it makes sense to introduce concepts like macroscopic density, average speed, or kinetic distribution function as continuous functions of space and, in the latter case, also

velocity. However, the continuum hypothesis can be profitably accepted as a technical approximation of the physical reality, regarding macroscopic quantities globally as measures of traffic features and as tools to depict the spatial and temporal evolution of traffic waves.

Macroscopic modeling is based on the idea, originally due in the fifties to Lighthill and Whitham, and independently, to Richards, that the classical Euler and Navier-Stokes equations of fluid dynamics describing the flow of fluids could also describe the motion of cars along a road, provided a large-scale point of view is adopted so as to consider cars as small particles and their density as the main quantity at which one looks. This analogy remains nowadays in all macroscopic models of vehicular traffic, as terms like traffic pressure, traffic flow, traffic waves demonstrate.

Kinetic modeling, first used by Prigogine in the sixties, relies instead on the principles of statistical mechanics introduced by Boltzmann to describe the unsteady evolution of a gas. The kinetic approach as well requires in principle a large number of particles in the system but, unlike the macroscopic approach, it is based on a microscopic modeling of their mutual interactions. The evolution of the system is described by means of a distribution function over the microscopic state of the particles, whence the interesting macroscopic quantities are obtained via suitable microscopic average procedures.

In this review we present and discuss some of the main continuum mathematical models of vehicular traffic available in the literature (see also Bellomo et al. [10]). Specifically, the paper is organized in four more sections that follow this Introduction. Section “[Macroscopic Modeling](#)” is devoted to macroscopic models of both first and second order, which describe the gross evolution of traffic via either the sole mass conservation equation supplemented by suitable closure relations or a coupled system of mass conservation and momentum balance equations. Section “[Kinetic Modeling](#)” reports about traffic modeling by methods of the kinetic theory, from the very first attempts recalled above to the more recent contributions in the field based on the discrete kinetic theory. These two sections account mainly for traffic models on single one-way roads, whereas Sect. “[Road Networks](#)” finally deals with traffic problems on road networks. Such topic provides, in the present context, a strong link between mathematical modeling and real world applications, as most prediction, control, and optimization problems concern precisely the management of car fluxes over complex systems of interconnected roads, e.g., urban networks or some specific sub-networks. In addition, it poses nontrivial theoretical questions, which motivate the de-

velopment of innovative mathematical methods and tools susceptible of application also to different fields. These sections of the paper are conceived so as to give first the general mathematical framework, which is then detailed to obtain particular models. Section “Future Directions” finally sketches some research perspectives in the field.

Macroscopic Modeling

In the macroscopic approach to the modeling of vehicular traffic the flow of cars along a road is assimilated to the flow of fluid particles, for which suitable balance or conservation laws can be written. For this reason, macroscopic models are often called in the present context *hydrodynamic models*.

In the macroscopic approach, cars are not followed individually. The point of view is rather that of the classical continuum mechanics, i.e., one looks at the evolution in time and space of some average quantities of interest such as the mass density or the mean velocity, referred to an infinitesimal reference volume individuated by a point in the geometrical space. In more detail, since the motion of cars along a road is usually modeled as one-dimensional, the spatial coordinate x is a scalar independent variable of the problem which ranges in an appropriate subset of \mathbb{R} , possibly in the whole real axis.

The main dependent variables introduced to describe the problem mathematically are the density of cars $\rho = \rho(t, x)$ and their average velocity $u = u(t, x)$ at time t in the point x . From these quantities another important variable is derived, namely the flux $q = q(t, x)$ given by $q = \rho u$, which is of great interest for both theoretical and experimental purposes. Indeed, many real data, used to construct and to validate macroscopic models, refer precisely to flux measurements, because these can be performed with higher precision than measurements of other variables.

Since, as said before, macroscopic models of vehicular traffic are inspired to the continuum equations of fluid dynamics, the Eulerian point of view is normally adopted, meaning that the above dependent variables evaluated at (t, x) yield the evolution at time t of the vehicles flowing through the fixed in space position x . In other words, the spatial coordinate is not linked to any reference configuration but rather to the actual geometrical space, hence at different times the values of the state variables computed in the point x refer in general to different continuum particles flowing through x . Of course, all models can in principle be converted in Lagrangian form, up to a proper change of variable.

The basic evolution equation translates the principle of conservation of the vehicles:

$$\frac{\partial \rho}{\partial t} + \frac{\partial}{\partial x}(\rho u) = 0. \quad (2)$$

According to this equation, the time variation in the amount of cars within any stretch of road comprised between two locations $x_1 < x_2$ is only due to the difference between the incoming flux at x_1 and the outgoing flux at x_2 . Integration of Eq. (2) over the interval $[x_1, x_2]$ produces indeed

$$\frac{d}{dt} \int_{x_1}^{x_2} \rho(t, x) dx = q(t, x_1) - q(t, x_2),$$

where the integral at the left-hand side defines precisely the mass of cars contained in $[x_1, x_2]$ at time t .

It can be questioned that Eq. (2) does not give rise by itself to a self-consistent mathematical model, as it involves simultaneously two variables, ρ and u . To overcome this difficulty, one possibility is to devise suitable closures which allow one to express the velocity u , or equivalently the flux q , as a function of the density ρ . This way Eq. (2) becomes an evolution equation for the sole density ρ :

$$\frac{\partial \rho}{\partial t} + \frac{\partial}{\partial x} f(\rho) = 0, \quad (3)$$

where $q = f(\rho)$ is the closure relation. Macroscopic models based on Eq. (3) are usually called *first order models*.

We briefly recall here that a diffusion term is sometimes added to the right-hand side of Eq. (3) in order to smooth the resulting density field ρ , which, from the theory of nonlinear conservation laws (see e.g., Bressan [18], Dafermos [27], Serre [63,64]), is known to possibly develop discontinuities in finite time even for smooth initial data. The resulting equation reads

$$\frac{\partial \rho}{\partial t} + \frac{\partial}{\partial x} f(\rho) = \epsilon \frac{\partial}{\partial x} \left(\kappa(\rho) \frac{\partial \rho}{\partial x} \right), \quad (4)$$

where $\epsilon > 0$ is a parameter accounting for the strength of the diffusion with respect to the other terms of the equation, and $\kappa(\rho)$ is the (possibly nonlinear) diffusion coefficient. Notice that if κ is a positive constant then Eq. (4) reduces formally to the linear heat equation with nonlinear advection. However, unlike Eq. (3), models based on Eq. (4) do not preserve in general the total amount of vehicles.

A second possibility consists instead in joining Eq. (2) to an evolution equation for the flux q inspired by the momentum balance of a continuum:

$$\frac{\partial q}{\partial t} + \frac{\partial}{\partial x} (qu) = A[\rho, u, D\rho, Du], \quad (5)$$

where A is some material model for the generalized forces acting on the system and responsible for momentum variations. These forces express the macroscopic outcome of the microscopic interactions among the vehicles; as we will see later, in most models they are assumed to be determined by either the local density ρ or the local velocity u of the cars, as well as by their respective variations in time and/or space which in the above equation are denoted by the operator D . Using $q = \rho u$ and taking Eq. (2) into account, Eq. (5) can be further manipulated to obtain

$$\frac{\partial u}{\partial t} + u \frac{\partial u}{\partial x} = a[\rho, u, D\rho, Du], \quad (6)$$

where $a := A/\rho$ is a material model for the acceleration of the vehicles to be specified. Finally, the set of equations resulting from this second approach is

$$\begin{cases} \frac{\partial \rho}{\partial t} + \frac{\partial}{\partial x}(\rho u) = 0 \\ \frac{\partial u}{\partial t} + u \frac{\partial u}{\partial x} = a[\rho, u, D\rho, Du] \end{cases} \quad (7)$$

which is self-consistent in the unknowns ρ, u once the acceleration a has been conveniently designed. Mathematical models based on the system (7) are commonly termed in the literature *second order models* or, less frequently, *two-equations models*.

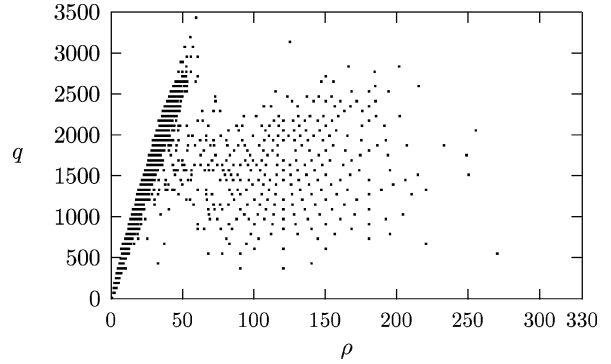
Lighthill–Whitham–Richards and Other First Order Models

First order models are obtained from the conservation law (3) by resorting to a suitable closure relation which expresses the flow of cars q as a function of the density ρ . A relation of the form $q = f(\rho)$ is named in this context *fundamental diagram*.

If $\rho_{\max} > 0$ denotes the maximum vehicle density allowed along the road according, for instance, to the capacity, i. e., the maximum sustainable occupancy of the latter, the function f is often required

1. to be monotonically increasing from $\rho = 0$ up to a certain density value $\sigma \in (0, \rho_{\max})$;
2. to be decreasing for $\sigma \leq \rho \leq \rho_{\max}$;
3. to have $\rho = \sigma$ as unique maximum point in $[0, \rho_{\max}]$;
4. to be concave in the interval $[0, \rho_{\max}]$.

These assumptions aim mainly at reproducing the typical behavior of experimentally computed fundamental diagrams (see Fig. 1 and, e. g., Bonzani and Mussone [16,17], Kerner [47,48,49]). In addition, some of them, for instance



Vehicular Traffic: A Review of Continuum Mathematical Models, Figure 1

Fundamental diagram based on experimental data referring to one-week traffic flow in viale del Muro Torto, Rome, Italy. Measures kindly provided by ATAC S.p.A.

assumptions (3) and (4), are stated for theoretical purposes linked to the qualitative properties of the conservation law (3). We observe that sometimes assumption (4) is relaxed, allowing the function f to possibly change concavity in the decreasing branch.

By prescribing the flux f one implicitly assigns also the relation between the average velocity u and the density ρ (*velocity diagram*), indeed using $q = \rho u$ one has

$$u(\rho) = \frac{f(\rho)}{\rho}.$$

Since the function f often vanishes for $\rho = 0$, this formula commonly determines a finite value for u in the limit $\rho \rightarrow 0^+$.

The prototype of all fluxes complying with the above assumptions is the parabolic profile firstly proposed by Lighthill and Whitham [55,71] and then, independently, by Richards [62], which gives rise to the so-called LWR model:

$$f(\rho) = u_{\max} \rho \left(1 - \frac{\rho}{\rho_{\max}} \right), \quad (8)$$

from which the following velocity diagram is obtained:

$$u(\rho) = u_{\max} \left(1 - \frac{\rho}{\rho_{\max}} \right) \quad (9)$$

(see Fig. 2a). The parameter $u_{\max} > 0$ identifies the maximum velocity of the cars in a situation of completely free road ($\rho = 0$). Notice that Eq. (8) assumes zero flux of vehicles when both $\rho = 0$ and $\rho = \rho_{\max}$; correspondingly, the average velocity given by Eq. (9) is maximum in the first case and vanishes in the second case.

A generalization of Eqs. (8), (9) is provided by the Greenshield model (Fig. 2b):

$$\begin{aligned} f(\rho) &= u_{\max} \rho \left[1 - \left(\frac{\rho}{\rho_{\max}} \right)^n \right], \\ u(\rho) &= u_{\max} \left[1 - \left(\frac{\rho}{\rho_{\max}} \right)^n \right] \quad (n \in \mathbb{N}), \end{aligned}$$

while an example of fundamental diagram satisfying all the previous assumptions but which generates an unbounded velocity diagram for $\rho \rightarrow 0^+$ is due to Greenberg (Fig. 2c):

$$\begin{aligned} f(\rho) &= u_0 \rho \log \left(\frac{\rho_{\max}}{\rho} \right), \\ u(\rho) &= u_0 \log \left(\frac{\rho_{\max}}{\rho} \right), \end{aligned}$$

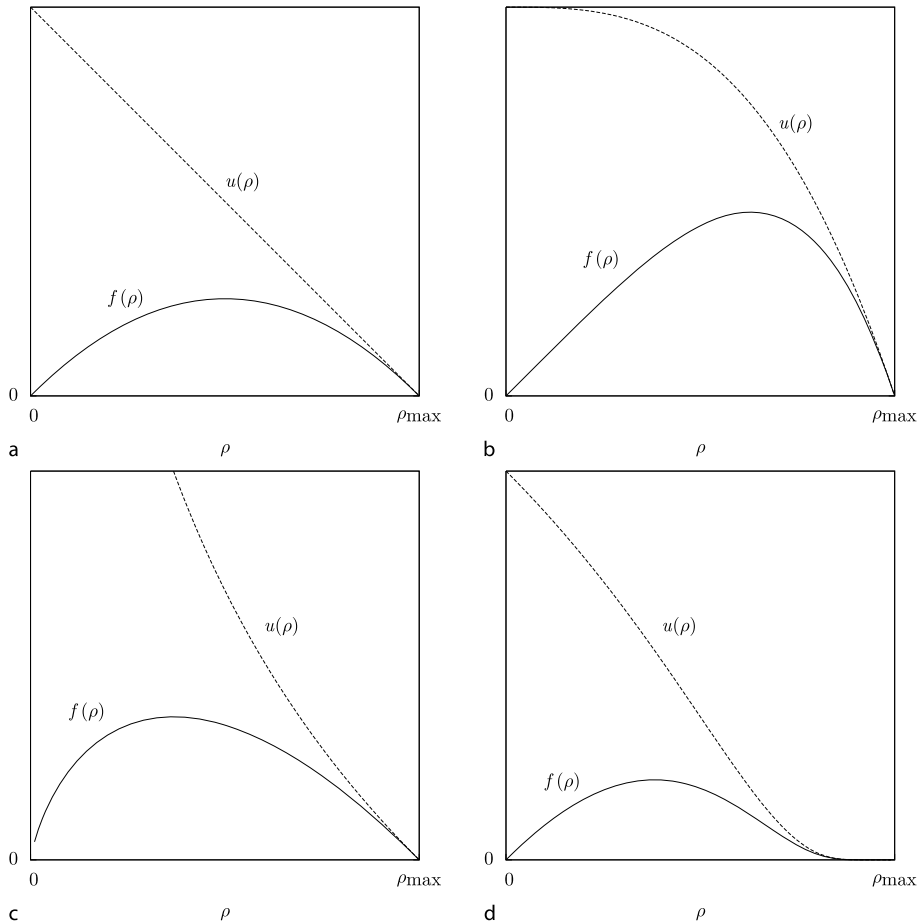
where $u_0 > 0$ is a tuning parameter. These formulas were

specifically conceived to fit some experimental data on the traffic flow in the Lincoln tunnel in New York.

Additional fundamental and velocity diagrams, for which some of the above discussed assumptions fail, are reported in the book by Garavello and Piccoli [34]. Moreover, other closure relations of the mass conservation equation for first order models are discussed in Bellomo and Coscia [8]. Here we simply mention a further diagram due to Bonzani and Mussone [17] (Fig. 2d):

$$\begin{aligned} f(\rho) &= u_{\max} \rho e^{-\alpha \frac{\rho}{\rho_{\max} - \rho}}, \\ u(\rho) &= u_{\max} e^{-\alpha \frac{\rho}{\rho_{\max} - \rho}} \end{aligned} \quad (10)$$

which depends on a phenomenological parameter $\alpha > 0$ linked to road and environmental conditions. In particular, the lower the α , the more the flow of vehicles is favored; according to the authors, comparisons with suit-



Vehicular Traffic: A Review of Continuum Mathematical Models, Figure 2

Fundamental diagrams (solid lines) and velocity diagrams (dashed lines) for **a** LWR model, **b** Greenshield's model, **c** Greenberg's model, and **d** Bonzani-Mussone's model

able sets of experimental data suggest the interval $[1, 2.5]$ as a standard range for α . Notice that in this case the function f may have an inflection point in the interval (σ, ρ_{\max}) , hence the hypothesis (4) is potentially violated.

Fictitious Density Model

In view of the analogy with the flow of fluid particles, the macroscopic modeling framework accounts for a fully mechanical evolution of the traffic. On the other hand, it can be argued that cars are actually not completely mechanical subjects, for the presence of the drivers is likely to affect their behavior in an essentially unconventional ‘human-like’ fashion.

Still in the context of first order hydrodynamic models, De Angelis [32] tries to explicitly account for the action of the drivers on the evolution of the traffic by introducing the concept of *fictitious density*. The fictitious density ρ^* represents the density of cars along the road as perceived by the drivers, hence it expresses the personal feelings of the latter about the local conditions of traffic. This new variable, which is in general different from the actual density ρ , is used to model the instantaneous reactions of the drivers.

Specifically, the fictitious density is linked to the actual density and to its spatial gradient in such a way that if ρ is increasing (respectively, decreasing) then ρ^* increases (respectively, decreases) in turn but more quickly than ρ , while for ρ approaching the limit threshold ρ_{\max} also ρ^* tends to saturate to ρ_{\max} . In other words, the sensitivity of the drivers should consist in feeling a fictitious congestion state of the road higher or lower than the real one, and by consequence in anticipating certain behaviors that a purely mechanical agent would exhibit only in presence of the appropriate external conditions.

The dependence of ρ^* on ρ and $\partial_x \rho$ proposed by De Angelis is

$$\rho^*[\rho, \partial_x \rho] = \rho + \eta \left(1 - \frac{\rho}{\rho_{\max}} \right) \frac{\partial \rho}{\partial x}, \quad (11)$$

where $\eta > 0$ is a parameter related to the sensitivity of the drivers, which weights the effect of the spatial variations of the density ρ . It can be observed that for increasing actual density, that is $\partial_x \rho > 0$, the fictitious density is larger than ρ , thus suggesting a more careful attitude of the system car-driver with respect to the purely mechanical case. Conversely, for decreasing actual density, namely $\partial_x \rho < 0$, the fictitious density is lower than ρ , which implies a more aggressive behavior induced by the presence of the driver.

Specific models are obtained by plugging Eq. (11) into the expression of the velocity diagram. This amounts es-

entially to devising a closure relation of the mass conservation equation (2) of the form $u = u(\rho^*)$, so that the evolution equation finally reads

$$\frac{\partial \rho}{\partial t} + \frac{\partial}{\partial x}(\rho u(\rho^*)) = 0.$$

In view of the dependence of ρ^* on $\partial_x \rho$, this class of models often specializes in nonlinear, possibly degenerate, parabolic equations in the unknown ρ . For instance, technical calculations with the Lighthill–Whitham–Richards diagram (9) give rise to

$$\frac{\partial \rho}{\partial t} + h(\rho) \frac{\partial \rho}{\partial x} = \frac{\eta}{\rho_{\max}} \left[f(\rho) \frac{\partial^2 \rho}{\partial x^2} + h(\rho) \left(\frac{\partial \rho}{\partial x} \right)^2 \right]$$

where the function h is defined by

$$h(\rho) = u_{\max} \left(1 - \frac{2\rho}{\rho_{\max}} \right)$$

while the flux f is given by Eq. (8).

Different models of fictitious density, as well as their correlations with diffusion models based on Eq. (4), are considered by Bonzani [15].

The Payne–Whitham Model

Payne [58] and Whitham’s [71] model is a second order model in which the acceleration a (cf. Eq. (6)) is constructed as the sum of two terms:

$$a[\rho, u, D\rho, Du] = a_r[\rho, u] + a_a[\rho, \partial_x \rho]. \quad (12)$$

The former, a_r , is called *relaxation* and models the tendency of each driver to travel at a certain desired speed depending on the level of congestion of the road:

$$a_r[\rho, u] = \frac{V_e(\rho) - u}{\tau}, \quad (13)$$

where u is the actual speed and $V_e(\rho)$ the desired one, while $\tau > 0$ is a parameter representing the relaxation time or, in other words, the reaction time of the drivers in adjusting their actual speed to $V_e(\rho)$. The desired speed in Eq. (13) may be thought of as the speed possibly observed in stationary homogeneous traffic conditions for a specific value of the density ρ . As a matter of fact, the function $V_e(\rho)$ can be one of the velocity diagrams used in first order models (see Subsect. “Lighthill–Whitham–Richards and Other First Order Models”).

The second term forming the acceleration, a_a , is named *anticipation* and accounts for the reaction of the drivers to the variations in the traffic conditions ahead of

them. In more detail, it models the tendency to accelerate or to decelerate in response to a decrease or an increase, respectively, of the density of cars, therefore it is linked to the density ρ and to its spatial gradient $\partial_x \rho$ as

$$a_a[\rho, \partial_x \rho] = -\frac{1}{\rho} \frac{\partial}{\partial x} p(\rho), \quad (14)$$

where the function $p = p(\rho)$ is the analogous to the *pressure* in the fluid dynamics equations. A common hypothesis on this traffic pressure is that it is a nondecreasing function of the density; assuming moreover differentiability of p with respect to ρ , the anticipation term can be formally rewritten in the equivalent form

$$a_a[\rho, \partial_x \rho] = -\frac{p'(\rho)}{\rho} \frac{\partial \rho}{\partial x}, \quad (15)$$

whence one sees that the ratio $p'(\rho)/\rho$ is a kind of weight on the gradient $\partial_x \rho$, which amplifies or reduces the effect of the latter on the basis of the local density of cars along the road.

In view of Eqs. (13)–(15), the final form of Payne–Whitham’s model is as follows:

$$\begin{cases} \frac{\partial \rho}{\partial t} + \frac{\partial}{\partial x}(\rho u) = 0 \\ \frac{\partial u}{\partial t} + u \frac{\partial u}{\partial x} = \frac{V_e(\rho) - u}{\tau} - \frac{p'(\rho)}{\rho} \frac{\partial \rho}{\partial x}. \end{cases} \quad (16)$$

According to the derivation of these equations proposed by Whitham himself in the book [71] as continuous approximation of a microscopic car-following model, one has the following representation of the traffic pressure:

$$p'(\rho) = \frac{1}{2\tau} |V_e'(\rho)|.$$

More in general, the relation between p and ρ can be expressed in the form (see e. g., Günther et al. [39], Klar and Wegener [50])

$$p(\rho) = \rho \Theta_e(\rho),$$

where Θ_e denotes the equilibrium value in homogeneous traffic conditions of the variance of the microscopic velocity of cars (cf. Eq. (25)).

For the sake of thoroughness, we recall that sometimes a diffusive acceleration term of the form

$$a_d[\partial_x^2 u] = \frac{\mu}{\rho} \frac{\partial^2 u}{\partial x^2}$$

is introduced in the decomposition (12), the parameter $\mu > 0$ representing a sort of viscosity by analogy with the theory of Newtonian fluids.

The Aw–Rascle Model

The hydrodynamic model by Payne and Whitham suffers from some severe drawbacks which led Daganzo [28] to write a celebrated ‘requiem’ for this kind of second order approximation of traffic flow. Flaws of the model include the possible onset of negative speeds of the vehicles as well as the violation of the so-called *anisotropy principle*, i. e., the fact that a car should be influenced only by the traffic dynamics ahead of it, being practically insensitive to what happens behind. By computing the characteristic speeds λ_1, λ_2 of the hyperbolic system (16) in the variables ρ, u one finds indeed $\lambda_{1,2} = u \pm \sqrt{p'(\rho)}$, meaning that some information generated by the motion of the vehicles travels faster than the vehicles themselves, hence affects the forward traffic dynamics.

Aw and Rascle [3] suggest that all of these inconsistencies are caused by a too direct application to cars of the analogy with fluid particles, to which, on the other hand, the principles of nonnegativity of the velocity and of anisotropy do not apply. In particular, they observe that the anticipation term a_a should not be regarded as an Eulerian quantity, as it is specifically linked to the perception of the traffic conditions by the drivers while in motion within the flow of vehicles. An external (Eulerian) observer might see an increasing vehicle density in a certain fixed spatial position x while, at the same time, a driver, i. e., an internal (Lagrangian) observer, flowing through x sees a decreasing density in front of her/him if, for example, cars ahead move faster. In such a situation, the behavior predicted by the Payne–Whitham’s anticipation term, that is a deceleration, is obviously inconsistent with the presumable reaction of the driver, who is instead expected to maintain the current speed if not to accelerate.

The problem is solved by Aw and Rascle by making the pressure p a material (i. e., Lagrangian) variable of the model, which technically amounts to expressing the anticipation term via the material derivative $D_t := \partial_t + u \partial_x$ of p :

$$\begin{aligned} a_a[\rho, u, \partial_t \rho, \partial_x \rho] \\ = -D_t p(\rho) = -\partial_t p(\rho) - u \partial_x p(\rho). \end{aligned} \quad (17)$$

The original Aw–Rascle’s (AR) model assumes in addition no relaxation term in the acceleration, thus it writes

$$\begin{cases} \frac{\partial \rho}{\partial t} + \frac{\partial}{\partial x}(\rho u) = 0 \\ \frac{\partial}{\partial t}(u + p(\rho)) + u \frac{\partial}{\partial x}(u + p(\rho)) = 0 \end{cases} \quad (18)$$

for a smooth and increasing function p of the density ρ , e. g.

$$p(\rho) = \rho^\gamma, \quad \gamma > 0.$$

Notice that, owing to the conservation of the vehicle mass, the second equation in (18) can be regarded as the non-conservative form of a conservation equation for the generalized flux ρw , with $w := u + p(\rho)$. For this reason, this equation is frequently encountered in the literature as

$$\frac{\partial}{\partial t}(\rho w) + \frac{\partial}{\partial x}(\rho w u) = 0. \quad (19)$$

Computing the characteristic speeds of the hyperbolic system (18) in the variables ρ, u gives $\lambda_1 = u, \lambda_2 = u - \rho p'(\rho)$, whence, in view of the assumption of nondecreasing pressure, one sees that no information can now be advected faster than cars.

Further extensions of the AR model involve the introduction of a relaxation term (Greenberg [38], Rascle [61]) to let drivers travel at some maximum desired speed when the traffic conditions allow. In particular, Greenberg's relaxation term takes the form

$$a_r[\rho, u] = \frac{V_m - (u + p(\rho))}{\tau},$$

where $V_m > 0$ is a constant value representing the maximum possible speed along the road and $\tau > 0$ is the relaxation time, while Rascle's relaxation term is more similar to the corresponding Payne-Whitham's term (cf. Eq. (13)):

$$a_r[\rho, u] = \frac{V(\rho) - u}{\tau},$$

though here the function $V(\rho)$ need not represent an equilibrium velocity.

The Phase Transition Model

Numerous experimental observations (see e.g., Kerner [47,48,49]) report about strongly different qualitative and quantitative features of the flow of vehicles in *free* and *congested* regimes, corresponding respectively to low and high density of cars, far from or close to the road capacity. In particular, from experimentally computed fundamental diagrams it can be inferred that the assumption that the average speed be a one-to-one function of the density applies well to free traffic, while being completely inadequate to describe congested flows. Indeed, in the latter case the density ρ no longer determines univocally the velocity u , or equivalently the flux q , of the vehicles, for relevant fluctuations are recorded so that the admissible pairs

(ρ, q) are scattered over a two-dimensional region of the state space. In the specialized literature, this phenomenon is called a *phase transition*.

Starting from these experimental facts, Colombo [23, 24] proposed a mathematical model in which the existence of the phase transition is postulated and accounted for by splitting the state space (ρ, q) in two regions, Ω_f and Ω_c , corresponding to the regimes of free and congested flow, respectively. In Ω_f a classical relation of the form $u = u(\rho)$ is imposed, and the model simply consists in the conservation law (3) with $f(\rho) = \rho u(\rho)$. In particular, the LWR velocity diagram (9) is chosen. Conversely, in Ω_c the density ρ and the flux q are regarded as two independent state variables, and the model is similar to a second order model in which the mass conservation equation (2) is joined to an evolution equation for the flux of the form

$$\frac{\partial q}{\partial t} + \frac{\partial}{\partial x}((q - q_*)u) = 0. \quad (20)$$

Furthermore, the average velocity is specified as a function of both ρ and q which, in a way, generalizes the LWR velocity diagram:

$$u(\rho, q) = \frac{q}{\rho} \left(1 - \frac{\rho}{\rho_{\max}} \right). \quad (21)$$

Notice that Eq. (20) closely recalls the momentum balance (5) of second order models with zero external force A . The parameter $q_* > 0$ is introduced to obtain that at high car density and high car speed breaking produces shocks and accelerating produces rarefaction waves, while at low car density and speed the opposite occurs (see [23] for further details).

Finally, Colombo's phase transition model writes:

Free flow: $(\rho, q) \in \Omega_f$

$$\begin{cases} \frac{\partial \rho}{\partial t} + \frac{\partial}{\partial x}(\rho u) = 0 \\ u = u(\rho), \end{cases}$$

Congested flow: $(\rho, q) \in \Omega_c$

$$\begin{cases} \frac{\partial \rho}{\partial t} + \frac{\partial}{\partial x}(\rho u) = 0 \\ \frac{\partial q}{\partial t} + \frac{\partial}{\partial x}((q - q_*)u) = 0 \\ u = u(\rho, q). \end{cases}$$

The regions Ω_f, Ω_c are defined so as to be positively invariant with respect to their corresponding systems of equations: If the initial datum is entirely contained in

one of the two regions, then the solution will remain in that region at all successive times of existence. In other words, if the traffic is initially free (respectively, congested), then it will remain free (respectively, congested) during the whole subsequent evolution. Technically, letting $\Omega = [0, \rho_{\max}] \times [0, +\infty) \ni (\rho, q)$ denote the state space:

$$\begin{aligned} \Omega_f &= \{(\rho, q) \in \Omega : u(\rho) \geq \hat{V}_f, q = u_{\max}\rho\}, \\ \Omega_c &= \left\{(\rho, q) \in \Omega : u(\rho, q) \leq \hat{V}_c, \frac{Q_1 - q_*}{\rho_{\max}} \leq \frac{q - q_*}{\rho} \right. \\ &\quad \left. \leq \frac{Q_2 - q_*}{\rho_{\max}} \right\}, \end{aligned}$$

where \hat{V}_f, \hat{V}_c are two fixed speed thresholds such that above the former the flow is free while below the latter the flow is congested, with furthermore $\hat{V}_c < \hat{V}_f \leq u_{\max}$ in order for the two phases not to overlap, and $Q_1 \in (0, q_*)$, $Q_2 \in (q_*, +\infty)$ are tuning parameters related to various environmental conditions.

Kinetic Modeling

The kinetic approach to the modeling of vehicular traffic is based on the choice of an intermediate representation scale between the macroscopic and the microscopic ones, technically called *mesoscopic*. Rather than looking at each single car of the system, like in the microscopic approach, a *distribution function*, usually denoted by f , is introduced over the microscopic state (x, v) of the vehicles, x standing for position and v for velocity assumed one-dimensional with moreover $v \geq 0$. The distribution function is such that the quantity

$$f(t, x, v) dx dv$$

represents a measure of the number of vehicles whose position at time t is comprised between x and $x + dx$, with a velocity comprised between v and $v + dv$. Consequently, under suitable integrability assumptions on f , if $D_x \subseteq \mathbb{R}$, $D_v \subseteq \mathbb{R}_+$ denote the spatial domain and the velocity domain, respectively, the quantity

$$N(t) = \int_{D_v} \int_{D_x} f(t, x, v) dx dv \quad (22)$$

gives the total amount of vehicles present in the system at time t . It is worth pointing out that f is in general not a probability distribution function over (x, v) , as the integral in Eq. (22) may not equal 1 at all times. However, if the total mass of cars is preserved then $N(t)$ is constant in t , hence it is possible to rescale the distribution function

so that it have a unit integral on $D_x \times D_v$ for all times t of existence.

The knowledge of the distribution function enables one to recover the usual macroscopic variables of interest as local averages over the microscopic states of the vehicles. For instance, the density ρ of cars at time t in the point x is given by

$$\rho(t, x) = \int_{D_v} f(t, x, v) dv, \quad (23)$$

while the flux q and the average velocity u are obtained from the first momentum of f with respect to v as

$$q(t, x) = \int_{D_v} v f(t, x, v) dv, \quad u(t, x) = \frac{q(t, x)}{\rho(t, x)}. \quad (24)$$

Higher order momenta are related to other macroscopic variables, such as the average kinetic energy and the variance of the velocity. In particular, the latter is given by

$$\Theta(t, x) = \frac{1}{\rho(t, x)} \int_{D_v} (v - u(t, x))^2 f(t, x, v) dv \quad (25)$$

and is often linked, at a macroscopic level, to the traffic pressure responsible for the anticipation terms in the hydrodynamic equations of traffic (see e.g., the Payne–Whitham’s model, Subsect. “[The Payne–Whitham Model](#)”, and Günther et al. [39] or Klar and Wegener [50] for further details).

Modeling of the system is obtained by stating an evolution equation in time and space for the distribution function f . Unlike the macroscopic approach, such an equation is written considering the influence of microscopic interactions among the vehicles on the microscopic states. Concerning this, it is useful to introduce a specific terminology to distinguish in an interaction the vehicle which is likely to change its state from the one which potentially causes such a change. The former is technically called the *candidate vehicle*, while the latter is called the *field vehicle*. Practically all kinetic models of vehicular traffic present in the literature describe the interactions by appealing to the following general guidelines:

1. Cars are regarded as points, their dimensions being negligible.
2. Interactions are binary, in the sense that those involving simultaneously more than two vehicles are disregarded.
3. Interactions modify by themselves only the velocity of the vehicles, not their positions. More specifically, in an interaction the sole velocity of the candidate vehicle may vary, but that of the field vehicle remains instead unchanged.

4. Vehicles are anisotropic particles which react mainly to frontal than to rear stimuli (see Daganzo [28]), therefore candidate vehicles only interact with field vehicles located ahead of them.
5. There exists a *probability of passing* P such that when a candidate vehicle encounters a slower field vehicle it may overtake it instantaneously with probability P without modifying its own velocity.
6. Interactions are conservative, in the sense that they preserve the total number of vehicles of the system.

The evolution equation for the distribution function is obtained from a balance principle which states that the time variation in the number of vehicles belonging to any subset of the state space $D_x \times D_v$ is determined by the state transitions due to the interactions of the vehicles with each other. Therefore, in the absence of external actions on the system it writes

$$\frac{\partial f}{\partial t} + v \frac{\partial f}{\partial x} = J[f], \quad (26)$$

where $J[f] = J[f](t, x, v)$ is an operator acting on the distribution function f , charged to describe the interactions and their effects on the states of the vehicles. Following the classical terminology coming from the collisional kinetic theory of the gas dynamics (see e.g., Villani [69]), J is frequently termed the *collisional operator*, though in the present context this is a slight abuse of speech because interactions among vehicles are not like collisions among mechanical particles.

In view of the assumption (6) above, the operator J is required to satisfy

$$\int_{D_v} J[f](t, x, v) dv = 0, \quad \forall x \in D_x, \quad \forall t \geq 0$$

so that integrating Eq. (26) with respect to v and recalling Eqs. (23), (24) yields the macroscopic mass conservation equation (2).

Specific models are obtained from Eq. (26) by detailing the form of the collisional operator.

The Prigogine Model

In his pioneering work on the mathematical modeling of vehicular traffic by methods of the kinetic theory, Prigogine [59,60] constructs the collisional operator through the contribution of two terms:

$$J[f] = J_r[f] + J_i[f_2]. \quad (27)$$

The first one, $J_r[f]$, is called *relaxation term* and models the tendency of each driver to adapt the state of her/his

vehicle to a desired standard state. The latter is described by the *desired distribution function* $f_0 = f_0(t, x, v)$, which in essence corresponds to the driving program each driver aims at. In Prigogine's model, the function f_0 is expressed as

$$f_0(t, x, v) = \rho(t, x) \tilde{f}_0(v), \quad (28)$$

where \tilde{f}_0 is a prescribed probability distribution over the variable v , independent of x and t . The factorization (28) translates the hypothesis that the desired distribution of the velocity is, for each driver, unaffected by the local vehicle density. The relaxation term is then taken to be

$$J_r[f] = -\frac{f - f_0}{T},$$

where T is the relaxation time which depends on the probability of passing P as

$$T = \tau \frac{1 - P}{P} \quad \text{for} \quad P = 1 - \frac{\rho}{\rho_{\max}}. \quad (29)$$

In these formulas, τ is a positive parameter of the model and ρ_{\max} denotes the maximum vehicle density locally allowed along the road according to the road capacity.

The second term appearing in the decomposition (27), $J_i[f_2]$, is called *interaction term* and is represented by an operator which models the interactions among candidate and field vehicles. As usual in the kinetic framework, it is further split into two more operators:

$$J_i[f_2] = G[f_2] - L[f_2].$$

The *gain operator* $G[f_2]$ accounts for the interactions of candidate vehicles having velocity $v_* > v$ with field vehicles with velocity v , which force the former to slow down to v if they cannot overtake the latter, causing this way a gain of cars with velocity state v :

$$G[f_2] = (1 - P) \int_v^{+\infty} (v_* - v) f_2(t, x, v_*, x, v) dv_*. \quad (30)$$

The *loss operator* $L[f_2]$ accounts instead for the interactions of candidate vehicles having velocity v with field vehicles with velocity $v_* < v$, which force the former to slow down to v_* if they cannot overtake the latter, thus giving rise to a loss of cars with velocity state v :

$$L[f_2] = (1 - P) \int_0^v (v - v_*) f_2(t, x, v, x, v_*) dv_*. \quad (31)$$

In Eq. (30) it is assumed $D_v = \mathbb{R}_+$, that is no upper limitation is imposed on the velocity of the cars.

The function f_2 appearing in Eqs. (30), (31) is the joint distribution function of candidate and field vehicles, such that $f_2(t, x, v, x_*, v_*)$ gives a measure of the joint probability to find a candidate vehicle in the state (x, v) and simultaneously a field vehicle in the state (x_*, v_*) . Introducing the hypothesis of *vehicular chaos* (see e. g., Hoogendoorn and Bovy [46]), which states that vehicles are actually uncorrelated due to the mixing caused by overtaking, one can express the function f_2 in terms of f as

$$f_2(t, x, v, x_*, v_*) = f(t, x, v)f(t, x_*, v_*),$$

so that J_i takes the form of a bilinear operator acting on f :

$$J_i[f, f] = (1 - P)f(t, x, v) \int_0^{+\infty} (v_* - v)f(t, x, v_*)dv_*$$

and Prigogine's model finally reads

$$\begin{aligned} \frac{\partial f}{\partial t} + v \frac{\partial f}{\partial x} = & -\frac{f(t, x, v) - f_0(t, x, v)}{T} \\ & + (1 - P)f(t, x, v) \int_0^{+\infty} (v_* - v)f(t, x, v_*)dv_* . \end{aligned} \quad (32)$$

Notice that the forms of G and L in Eqs. (30), (31) implicitly assume localized interactions ($x = x_*$) like in the classical Boltzmann collisional kinetic theory.

The Paveri Fontana Model

One of the main criticisms to Prigogine's model is that the desired speed distribution function \tilde{f}_0 in Eq. (28) is prescribed *a priori*, and is thus independent of the evolution of the system. In order to correct this drawback, Paveri Fontana [57] conceived a model in which the desired speed is taken into account as a further state variable w ranging in the same domain D_v of the true speed v . At the same time, a *generalized distribution function* $g = g(t, x, v, w)$ is introduced such that

$$g(t, x, v, w)dx dv dw$$

gives a measure of the number of vehicles that at time t have a position comprised between x and $x + dx$, a true speed comprised between v and $v + dv$, and a desired speed comprised between w and $w + dw$. Notice that the distribution function f and the desired distribution function f_0 are readily recovered by integrating out w and v ,

respectively, from g :

$$\begin{aligned} f(t, x, v) &= \int_{D_v} g(t, x, v, w)dw, \\ f_0(t, x, w) &= \int_{D_v} g(t, x, v, w)dv. \end{aligned} \quad (33)$$

Using these relations, an evolution equation for g is straightforwardly derived from the corresponding equation (26) for f :

$$\frac{\partial g}{\partial t} + v \frac{\partial g}{\partial x} = I[g], \quad (34)$$

where I is a new collisional operator acting on the generalized distribution function.

Analogously to Eq. (27), Paveri Fontana's choice consists in splitting I in a twofold contribution:

$$I[g] = I_r[g] + I_i[g, g],$$

where the first term is again a relaxation toward the desired speed having now the form

$$I_r[g] = -\frac{\partial}{\partial v} \left(\frac{w - v}{T} g \right), \quad (35)$$

while the second one describes the interactions among the vehicles. Specifically, in the same spirit as Prigogine's model (cf. Eqs. (30), (31)), gain and loss terms can be identified such that

$$I_i[g, g] = G[g, g] - L[g, g]$$

with

$$G[g, g] = (1 - P) \int_v^{+\infty} (v_* - v)f(t, x, v)g(t, x, v_*, w)dv_*, \quad (36)$$

$$L[g, g] = (1 - P) \int_0^v (v - v_*)f(t, x, v_*)g(t, x, v, w)dv_*, \quad (37)$$

the probability of passing P being defined as

$$P = \left(1 - \frac{\rho}{\rho_{\max}} \right) H \left(1 - \frac{\rho}{\rho_c} \right)$$

where $H(\cdot)$ is the Heaviside function and $\rho_c \in (0, \rho_{\max})$ a critical density threshold above which overtaking is inhibited. Notice in particular that candidate vehicles are described via the generalized distribution function g in order to take their desired speed into account, while field

vehicles are described by means of the distribution function f , in which the dependence on w has been integrated out, to focus rather on their actual speed. Moreover, Eqs. (36), (37) still assume localized interactions as confirmed by the fact that both f and g are evaluated at the same spatial position x .

Putting Eqs. (34)–(37) together we deduce the final form of Pavri Fontana's model:

$$\begin{aligned} \frac{\partial g}{\partial t} + v \frac{\partial g}{\partial x} = & -\frac{\partial}{\partial v} \left(\frac{w-v}{T} g \right) \\ & + (1-P) \left[f(t, x, v) \int_v^{+\infty} (v_* - v) g(t, x, v_*, w) dv_* \right. \\ & \left. - g(t, x, v, w) \int_0^v (v - v_*) f(t, x, v_*) dv_* \right]. \end{aligned} \quad (38)$$

Integrating Eq. (38) over w and using the first of Eqs. (33) gives an evolution equation for the distribution function f :

$$\begin{aligned} \frac{\partial f}{\partial t} + v \frac{\partial f}{\partial x} = & -\frac{\partial}{\partial v} \left[\frac{1}{T} \int_0^{+\infty} w g(t, x, v, w) dw - \frac{v f(t, x, v)}{T} \right] \\ & + (1-P) f(t, x, v) \int_0^{+\infty} (v_* - v) f(t, x, v_*) dv_*. \end{aligned}$$

This equation differs from the corresponding Eq. (32) of Prigogine's model only for the relaxation term at the right-hand side, which here maintains the explicit dependence on the generalized distribution function g .

Similarly, integration of Eq. (38) with respect to v , along with the second of Eqs. (33), yields the following evolution equation for the desired distribution function f_0 :

$$\frac{\partial f_0}{\partial t} + \frac{\partial}{\partial x} \left[\int_0^{+\infty} v g(t, x, v, w) dv \right] = 0$$

which definitely confirms that f_0 depends now on the overall evolution of the system.

Enskog-Like Models

As noticed by some authors (see e.g., Klar and Wegener [50]), the localized interactions framework used in classical kinetic models of traffic (like Prigogine's and Pavri Fontana's ones) prevents backward propagation

of the perturbations in the negative x direction. This is essentially due to the fact that the flow of vehicles is unidirectional, given the positivity constraint on the velocity v . On the other hand, the localized interactions assumption is a heritage of the Boltzmann collisional kinetic theory, where however the aforementioned drawback is not present because the flow of gas particles need not be unidirectional.

To obviate this difficulty of the theory, Klar and coworkers suggest, in a series of papers [39,40,50,51,70] focusing among other things on this topic, see also the review by Klar and Wegener [52], to describe the collisional operator J of the kinetic equation (26) as:

$$J[f] = G[f, f] - fL[f]$$

where the gain operator $G[f, f]$ is given by

$$\begin{aligned} G[f, f] = & \sum_{j=1}^M \iint_{\Omega_j} |v_1 - v_2| \sigma_j(v; v_1, v_2, \rho) \\ & \cdot f(t, x, v_1) f(t, x + h_j, v_2) k(h_j, \rho) dv_1 dv_2 \end{aligned} \quad (39)$$

and the loss operator by

$$L[f] = \sum_{j=1}^M \int_{\omega_j} |v - v_2| f(t, x + h_j, v_2) k(h_j, \rho) dv_2. \quad (40)$$

Notice that the interacting pairs are not supposed to occupy the same spatial position; in particular, the field vehicle is assumed to be located at $x + h_j$, x being the position of the candidate vehicle. The thresholds $h_j > 0$, $j = 1, \dots, M$, are introduced to delocalize the interactions, similar to an Enskog-like kinetic setting, and to trigger different behaviors of the candidate vehicle (acceleration, deceleration) on the basis of the distance separating it from its leading field cars. Integration is performed over subsets of the velocity domain, $\Omega_j \subseteq D_v^2$, $\omega_j \subseteq D_v$, associated with each of the thresholds h_j . Finally, the function k weights the interactions according to the distance of the interacting pairs and the local congestion of the road. Its presence in the collisional operator can be formally justified by referring to the Enskog kinetic equations of a dense gas. The interested reader might want to consult the book by Bellomo et al. [9] and the paper by Cercignani and Lampis [19] for further details on this part of the theory.

In the simplest case, two constant thresholds h_1, h_2 are considered to model, respectively, a deceleration of the candidate vehicle when the distance from the field vehicle falls below h_1 , and an acceleration when it grows instead

above h_2 . Correspondingly, the deceleration domains in G and L are given by

$$\begin{aligned}\Omega_1 &= \{(v_1, v_2) \in D_v^2 : v_1 > v_2\}, \\ \omega_1 &= \{v_2 \in D_v : v_2 > v\},\end{aligned}$$

while the acceleration domains are

$$\begin{aligned}\Omega_2 &= \{(v_1, v_2) \in D_v^2 : v_1 < v_2\}, \\ \omega_2 &= \{v_2 \in D_v : v_2 < v\}.\end{aligned}$$

Specifically, in the case of a deceleration it is assumed that the post-interaction velocity v of the candidate vehicle either remains unchanged, thus equal to the initial velocity v_1 , if an overtaking of the field vehicle is possible, or stochastically reduces to a certain fraction of the velocity v_2 of the field vehicle, if the candidate is forced to queue. This is expressed by the following form of the *transition probability* σ_1 :

$$\sigma_1(v; v_1, v_2, \rho) = P\delta(v-v_1) + (1-P)\frac{1}{(1-\beta)v_2}\chi_{[\beta v_2, v_2]}(v),$$

where P is the probability of passing defined like in Eq. (29), which carries the dependence of σ_1 on ρ , $\beta \in [0, 1]$ is a parameter, and χ_I is the indicator function of the set I .

Conversely, in the case of an acceleration the post-interaction velocity v of the candidate vehicle is assumed to be uniformly distributed between the values v_1 and $v_1 + \alpha(v_{\max} - v_1)$, where α depends on ρ through P as $\alpha = \alpha_0 P$ for a suitable parameter $\alpha_0 > 0$, and v_{\max} is the maximum allowed velocity on the road. Therefore, the transition probability associated to this second threshold takes the form

$$\sigma_2(v; v_1, v_2, \rho) = \frac{1}{\alpha(v_{\max} - v)}\chi_{[v_1, v_1 + \alpha(v_{\max} - v)]}(v).$$

The final form of Klar and coworkers' model with two equal interaction thresholds ($h_1 = h_2 \equiv h$) writes:

$$\begin{aligned}\frac{\partial f}{\partial t} + v \frac{\partial f}{\partial x} &= \sum_{j=1}^2 \iint_{\Omega_j} |v_1 - v_2| \sigma_j(v; v_1, v_2, \rho) \\ &\quad \cdot f(t, x, v_1) f(t, x + h, v_2) k(h, \rho) dv_1 dv_2 \\ &\quad - f(t, x, v) \sum_{j=1}^2 \int_{\omega_j} |v - v_2| f(t, x + h, v_2) k(h, \rho) dv_2.\end{aligned}$$

We observe that the spirit in which the collisional operator is constructed in model (42) somehow differs from Prigogine's and Paveri Fontana's models in that interactions are now defined by detailing the short-range reactions of each driver to the dynamics of the neighboring vehicles rather than by interpreting her/his overall behavior.

Discrete Velocity Models

Recently new mathematical models of vehicular traffic, based on the discrete kinetic theory, have been proposed in the literature, with the aim of taking into account, still at a mesoscopic level of description, some aspects of the strong granular nature of the flow of vehicles. Indeed, as reported by several authors (see e.g., Ben-Naim and Krapivsky [11,12], Berthelin et al. [13]), cars along a road tend to cluster, which gives granularity in space, with a nearly constant speed within each cluster, which makes also the velocity a discretely distributed variable.

Referring to Delitala and Tosin [33], the main idea is to make the velocity variable v discrete by introducing in the domain D_v a grid $I_v = \{v_i\}_{i=1}^n$ of the form

$$0 = v_1 < v_2 < \dots < v_n = 1$$

and letting then $v \in I_v$, while time and space are left continuous. Each v_i is interpreted as a *velocity class*, encompassing a certain range of velocities v which are not individually distinguished. Correspondingly, the distribution function f is expressed as a linear combination of Dirac functions in the variable v , with coefficients depending on time and space:

$$f(t, x, v) = \sum_{i=1}^n f_i(t, x) \delta(v - v_i), \quad (41)$$

where $f_i(t, x)$ gives the distribution of cars in the point x having at time t a velocity comprised in the i th velocity class. Using this representation, the following expressions for the macroscopic variables of interest are easily derived from Eqs. (23)–(24):

$$\begin{aligned}\rho(t, x) &= \sum_{i=1}^n f_i(t, x), \\ q(t, x) &= \sum_{i=1}^n v_i f_i(t, x), \\ u(t, x) &= \frac{\sum_{i=1}^n v_i^2 f_i(t, x)}{\sum_{i=1}^n v_i f_i(t, x)}.\end{aligned}$$

Moreover, plugging Eq. (41) into Eq. (26) yields the following system of evolution equations for the distribution functions f_i :

$$\frac{\partial f_i}{\partial t} + v_i \frac{\partial f_i}{\partial x} = J_i[\mathbf{f}], \quad i = 1, \dots, n, \quad (42)$$

where $\mathbf{f} = (f_1, \dots, f_n)$ and $J_i[\mathbf{f}]$ is the i th collisional operator. Modeling of $J_i[\mathbf{f}]$ is performed by appealing to

a discrete stochastic game theory (see Bertotti and Delitala [14]), after identifying gain and loss contributions:

$$J_i[\mathbf{f}] = G_i[\mathbf{f}, \mathbf{f}] - f_i L_i[\mathbf{f}]$$

with

$$G_i[\mathbf{f}, \mathbf{f}](t, x) = \sum_{h,k=1}^n \int_x^{x+\xi} \eta[\rho](t, x_*) A_{hk}^i[\rho](t, x_*) \cdot f_h(t, x) f_k(t, x_*) w(x_* - x) dx_* \quad (43)$$

and

$$L_i[\mathbf{f}](t, x) = \sum_{k=1}^n \int_x^{x+\xi} \eta[\rho](t, x_*) f_k(t, x_*) w(x_* - x) dx_*. \quad (44)$$

One of the main features of Delitala–Tosin’s model is that interactions are not local, but are distributed over a characteristic length $\xi > 0$, which can be interpreted as the *visibility length* of the drivers: A candidate vehicle located in x is supposed to be affected, in average, by all field vehicles comprised in the *visibility zone* $[x, x + \xi]$ ahead of it. One can therefore speak of *averaged binary interactions*. Averaging is carried out by the weight function w , which is nonnegative and supported in the above visibility zone, with unit integral there.

Acceleration and deceleration of the vehicles are described, like in Klar and coworkers’ model, as short-range reactions of the drivers to the traffic dynamics in terms of velocity class transitions. Specifically, a *table of games* A_{hk}^i is introduced, which gives the probability that a candidate vehicle in the h th velocity class adjusts its speed to the i th class after an interaction with a field vehicle in the k th class. These probabilities are parameterized by the density of cars ρ , so as to account for a dependence of the interactions on the local traffic congestion, and are subject to the additional requirements

$$A_{hk}^i[\rho] \geq 0, \quad \sum_{i=1}^n A_{hk}^i[\rho] = 1, \quad \forall i, h, k \in \{1, \dots, n\},$$

$$\forall \rho \in [0, \rho_{\max}],$$

where ρ_{\max} is the road capacity.

Finally, interactions are assumed to happen with more or less frequency according to the local degree of occupancy of the road, which is expressed in Eqs. (43), (44) by the *interaction rate* $\eta[\rho] > 0$. In particular, the latter can be thought of as a measure of the reactivity of the drivers to the evolution of the traffic in their visibility zone.

The framework depicted by Eqs. (42)–(44) can be formally derived from very general kinetic structures (see Ar-

lotti et al. [1], Bellomo [7]) as shown by Tosin [65]. Specific models are then obtained by detailing the table of games and the interaction rate as functions of the macroscopic density of cars ρ . In [33] the following form of $\eta[\rho]$ is proposed:

$$\eta[\rho] = \frac{1}{1 - \rho/\rho_{\max}}$$

which models an increasing reactivity of the drivers as the road becomes more and more congested, while the table of games is constructed by distinguishing three main cases:

- (i) If the candidate vehicle interacts with a faster field vehicle then it either maintains its current speed or possibly accelerates of one velocity class (follow-the-leader strategy), depending on the available surrounding free space.
- (ii) If the candidate vehicle interacts with a slower field vehicle then it either maintains its current speed, provided it can overtake the leader, or slows down to the velocity class of the latter and queues.
- (iii) If the candidate vehicle interacts with an equally fast field vehicle then a mix of the two previous situations arises, according to the current evolution of the system.

Technically, the expressions of the coefficients A_{hk}^i , where h, k denote the pre-interaction velocity classes of the candidate and the field vehicle, respectively, are as follows:

- (i) for $h < k$

$$A_{hk}^i[\rho] = \begin{cases} 1 - \alpha(1 - \rho/\rho_{\max}) & \text{if } i = h \\ \alpha(1 - \rho/\rho_{\max}) & \text{if } i = h + 1 \\ 0 & \text{otherwise;} \end{cases}$$

- (ii) for $h > k$

$$A_{hk}^i[\rho] = \begin{cases} 1 - \alpha(1 - \rho/\rho_{\max}) & \text{if } i = k \\ \alpha(1 - \rho/\rho_{\max}) & \text{if } i = h \\ 0 & \text{otherwise;} \end{cases}$$

- (iii) for $h = k$

$$A_{hk}^i[\rho] = \begin{cases} \alpha\rho/\rho_{\max} & \text{if } i = h - 1 \\ 1 - \alpha & \text{if } i = h \\ \alpha(1 - \rho/\rho_{\max}) & \text{if } i = h + 1 \\ 0 & \text{otherwise,} \end{cases}$$

where $\alpha \in [0, 1]$ is a parameter related to the quality of the road ($\alpha = 0$ stands for bad road, $\alpha = 1$ for good road). Notice that in case (ii) the coefficient $A_{hk}^h[\rho]$, linked to the possibility for the candidate vehicle to maintain its speed

because it can overtake the heading field vehicle, defines in practice a probability of passing

$$P = \alpha \left(1 - \frac{\rho}{\rho_{\max}} \right)$$

which closely recalls that of Prigogine's model (cf. Eq. (29)). Finally, in case (iii) a modification of the table of games is needed for $h = 1$ or $h = n$, for in these cases the candidate vehicle cannot brake or accelerate, respectively, due to the lack of further lower or higher velocity classes. The deceleration or the acceleration are then simply merged into the tendency of the drivers to preserve the current speed.

Figure 3 shows the dimensionless equilibrium diagrams for the flux q (fundamental diagram) and the average speed u vs. the vehicle density ρ , obtained as stationary solutions to Delitala–Tosin's discrete velocity model for two different values of the parameter α appearing in the table of games. Notice the almost linear growth of q , with a corresponding nearly constant u close to the maximum dimensionless allowed value $u_{\max} = 1$, for low density, and their subsequent strongly nonlinear decrease to zero for high density. This behavior, in good agreement with the experimental results, suggests that the model is able to capture in average the phase transition between free and congested flow occurring in traffic (see Subsect. “The Phase Transition Model” and also Kerner [47,48,49]). Further, we observe that when the quality of the road decreases the phase transition is correspondingly anticipated at lower values of ρ .

In the discrete velocity model by Coscia et al. [26] the velocity grid I_v is conceived so as to have a variable step, which tends to zero for high vehicle concentrations. Specifically, the discretization consists of $2n - 1$ points given by

$$v_i(\rho) = \frac{i-1}{n-1} V_e(\rho), \quad i = 1, \dots, 2n-1,$$

where $V_e(\rho)$ is an average equilibrium velocity, so that $v_1 = 0$, $v_{2n-1} = v_{\max} = 2V_e(\rho)$, and the grid is symmetric with respect to its central point $v_n = V_e(\rho)$. Since $V_e(\rho) \rightarrow 0$ for $\rho \rightarrow \rho_{\max}$, we note that $v_i(\rho) \rightarrow 0$ each $i = 1, \dots, 2n-1$ as the density locally approaches its maximum admissible value. The authors recommend for $V_e(\rho)$ the use of the Bonzani–Mussone's velocity diagram (10). Alternatively, one can use the classical diagram (9) of the LWR model.

The mathematical structure of the discrete kinetic equations to generate particular models relies on the localized Boltzmann-like collisional framework:

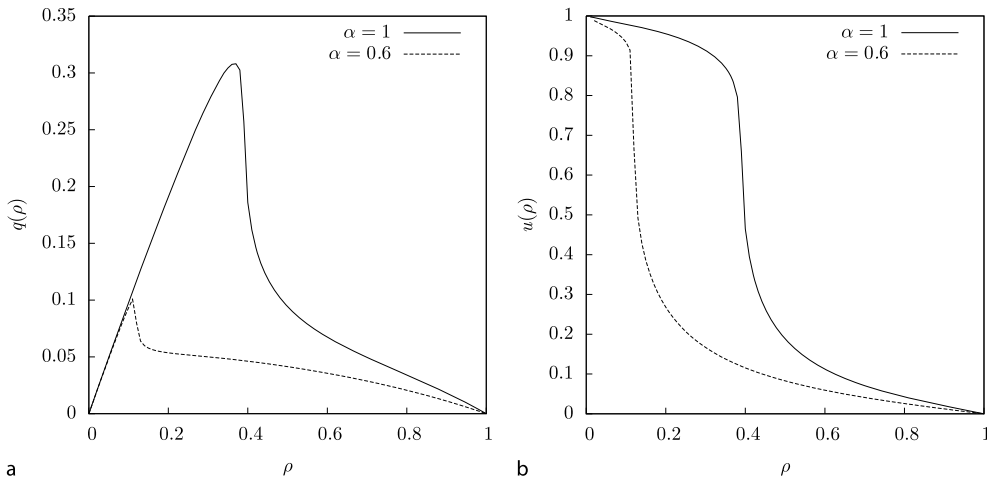
$$\frac{\partial f_i}{\partial t} + \frac{\partial}{\partial x}(v_i(\rho)f_i) = G_i[\mathbf{f}, \mathbf{f}] - f_i L_i[\mathbf{f}], \quad i = 1, \dots, 2n-1$$

for gain and loss operators given respectively by

$$G_i[\mathbf{f}, \mathbf{f}] = \sum_{h,k=1}^{2n-1} \gamma |v_h - v_k| A_{hk}^i f_h f_k,$$

$$L_i[\mathbf{f}] = \sum_{k=1}^{2n-1} \gamma |v_i - v_k| f_k,$$

where $\gamma > 0$ is a constant.



Vehicular Traffic: A Review of Continuum Mathematical Models, Figure 3

Fundamental diagram (a) and velocity diagram (b) computed as stationary dimensionless solutions to Delitala–Tosin's model Eqs. (42)–(44) for two different values of the parameter α of the table of games, corresponding to mediocre ($\alpha = 0.6$) and good ($\alpha = 1$) road conditions

The table of games A_{hk}^i is assumed to be constant in time and space, and is constructed so as to allow interactions only among vehicles belonging to sufficiently close velocity classes ($|h - k| \leq 1$ in [26]). After an interaction, the candidate vehicle can only fall in a velocity class adjacent to its current one, thus the sole potentially non-zero coefficients A_{hk}^i are those for which $i = h - 1$, $i = h$, and $i = h + 1$. In addition, slow and fast cars, which are distinguished by comparing their velocity class to the central class v_n , are supposed to interact only with faster and slower cars, respectively, with a possible tendency to accelerate in the former case and to decelerate in the latter case. If $\epsilon_a, \epsilon_d \in [0, 1]$ denote constant acceleration and deceleration probabilities, the table of games proposed by Coscia and coworkers reads as follows:

(i) for $h < n$

$$A_{h,h+1}^h = 1 - \epsilon_a, \quad A_{h,h+1}^{h+1} = \epsilon_a, \quad A_{hk}^i = 0 \quad \text{otherwise};$$

(ii) for $h > n$

$$A_{h,h-1}^{h-1} = \epsilon_d, \quad A_{h,h-1}^h = 1 - \epsilon_d, \quad A_{hk}^i = 0 \quad \text{otherwise}.$$

A further particularization of these expressions is obtained by setting $\epsilon_a = \epsilon, \epsilon_d = \nu\epsilon$ for $0 \leq \nu \leq 1$, in order to identify a basic reaction probability $\epsilon \in [0, 1]$ and a measure ν of the relative strength of ϵ_a and ϵ_d .

Road Networks

A *road network* is a finite set of $N \in \mathbb{N}$ interconnected roads, which communicate with each other through exchanges of vehicle fluxes at junctions. Therefore, a network can be modeled as an oriented graph in which roads are assimilated to the arcs and junctions to the vertices. Each arcs is represented by an interval $I_i = [a_i, b_i] \subset \mathbb{R}$, $i = 1, \dots, N$, $a_i < b_i$ with possibly either $a_i = -\infty$ or $b_i = +\infty$, whereas each vertex J is univocally identified by the sets of its incoming and outgoing arcs as $J = ((i_1, \dots, i_n), (j_1, \dots, j_m))$, where the first n -uple and the second m -uple contain the indexes of the incoming and the outgoing arcs, respectively ($m, n \leq N$). Hence, the complete model is given by a couple $(\mathcal{I}, \mathcal{J})$, where $\mathcal{I} = \{I_i\}_{i=1}^N$ is the collection of arcs and \mathcal{J} the collection of vertices.

The evolution of traffic on road networks is usually described at a macroscopic level via car densities and other conserved quantities, see Chitour and Piccoli [21], Colclite et al. [22], Garavello and Piccoli [34,35], Herty et al. [43,44], Holden and Risebro [45], Lebacque and Khoshfaryan [53]. Similar ideas were also used for telecommunication networks, see D'Apice et al. [31], gas pipelines networks, see Banda et al. [5], Colombo and Garavello [25],

and supply chains, see Armbruster et al. [2], D'Apice and Manzo [29], Göttlich et al. [37]. In all these cases one is faced with a system of conservation laws:

$$\frac{\partial \mathbf{u}_i}{\partial t} + \frac{\partial}{\partial x} f(\mathbf{u}_i) = 0, \quad i = 1, \dots, N, \quad (45)$$

where $\mathbf{u}_i = \mathbf{u}_i(t, x) : \mathbb{R}_+ \times I_i \rightarrow \mathbb{R}^d$ is the vector of the conserved quantities on the i th arc of the graph and $f : \mathbb{R}^d \rightarrow \mathbb{R}^d$ is the flux function.

In the case of vehicular traffic, Eq. (45) may represent one of the first or second order models (if $d = 1, 2$, respectively) reviewed in Sect. “Macroscopic Modeling”. For instance, choosing the Lighthill–Whitham–Richards model one can identify \mathbf{u}_i with the density of cars $\rho_i = \rho_i(t, x) : \mathbb{R}_+ \times I_i \rightarrow \mathbb{R}$ along the i th road, so that on each arc of the graph the following scalar conservation law is set:

$$\frac{\partial \rho_i}{\partial t} + \frac{\partial}{\partial x} f(\rho_i) = 0, \quad i = 1, \dots, N, \quad (46)$$

where the flux $f : \mathbb{R} \rightarrow \mathbb{R}$ is given by Eq. (8). Conversely, the Aw–Rascle model yields the 2×2 system

$$\frac{\partial}{\partial t} \begin{pmatrix} \rho_i \\ q_i \end{pmatrix} + \frac{\partial}{\partial x} \begin{pmatrix} q_i - \rho_i p(\rho_i) \\ \frac{q_i^2}{\rho_i} - q_i p(\rho_i) \end{pmatrix} = 0, \quad i = 1, \dots, N, \quad (47)$$

where now $\mathbf{u}_i = (\rho_i, q_i)$ with $q_i = \rho_i w_i$ the i th generalized flux (cf. Eq. (19)).

To complete the model, system (45) has to be supplemented by the dynamics at the junctions of the network. A natural assumption is the conservation of the quantities \mathbf{u}_i , $i = 1, \dots, N$ at vertices, which is for instance obtained by requiring that \mathbf{u}_i be a solution at each given vertex: This means that it satisfies Eq. (45), possibly in weak form, for test functions defined on the whole graph and smooth through that vertex. However, in some cases the conservation is not strictly necessary from the modeling point of view. This may either be a modeling choice, like in Garavello and Piccoli [35], or due to some absorption at vertices, e. g. for the presence of queues (Göttlich et al. [37]).

The conservation of the quantities \mathbf{u}_i at vertices is in general not sufficient to describe univocally the dynamics on the network. This was first shown by Holden and Risebro [45], who introduced an additional maximization of some functional at vertices to get uniqueness of the solution to the problem. Then various other choices were proposed, along with techniques to solve Cauchy problems on complete networks. Usually one assigns some traffic distribution rules from incoming to outgoing arcs, joined to

traffic flux (or possibly other functionals) maximization. In some cases, extra rules must be used: For instance, for a junction of a road network with two incoming and one outgoing roads, one needs to describe the right of way of the two incoming roads.

Definition of Solution and Dynamics at Vertices.

Riemann Solvers

In this subsection we briefly report about mathematical details needed to state the concept of solution for a system of conservation laws on a network, including the proper formal definition of the dynamics at the junctions.

We will assume in the sequel that the network load be described on each arc I_i by a vector-valued variable $\mathbf{u}_i = \mathbf{u}_i(t, x) : \mathbb{R}_+ \times I_i \rightarrow \mathbb{R}^d$ satisfying the conservation law (45) for a given flux $f : \mathbb{R}^d \rightarrow \mathbb{R}^d$. The function \mathbf{u}_i is required to be a weak entropic solution to Eq. (45) on $I_i = [a_i, b_i]$, thus for every smooth positive test function $\varphi = \varphi(t, x) : \mathbb{R}_+ \times I_i \rightarrow \mathbb{R}_+$ compactly supported in $(0, +\infty) \times (a_i, b_i)$ the following relation must hold:

$$\int_0^{+\infty} \int_{a_i}^{b_i} \left(\mathbf{u}_i \frac{\partial \varphi}{\partial t} + f(\mathbf{u}_i) \frac{\partial \varphi}{\partial x} \right) dx dt = 0$$

with, in addition, entropy conditions fulfilled, see Bressan [18], Dafermos [27], Serre [63,64]. It is well known that for every initial datum with bounded total variation (possibly sufficiently small, especially in the case of systems of conservation laws) Eq. (45) on \mathbb{R} admits a unique entropic weak solution depending continuously on the initial datum in L^1_{loc} . Moreover, if the initial datum is taken in $L^1 \cap L^\infty$ then Lipschitz continuous dependence of the mapping $t \mapsto \mathbf{u}_i(t, \cdot)$ in L^1 is achieved.

To define solutions at vertices, fix a vertex J with n incoming arcs, say I_1, \dots, I_n , and m outgoing arcs, say I_{n+1}, \dots, I_{n+m} . A weak solution at J is a collection of functions $\mathbf{u}_l : \mathbb{R}_+ \times I_l \rightarrow \mathbb{R}^d$, $l = 1, \dots, n+m$, such that

$$\sum_{l=1}^{n+m} \left[\int_0^{+\infty} \int_{a_l}^{b_l} \left(\mathbf{u}_l \frac{\partial \varphi_l}{\partial t} + f(\mathbf{u}_l) \frac{\partial \varphi_l}{\partial x} \right) dx dt \right] = 0 \quad (48)$$

for every smooth test function $\varphi_l : \mathbb{R}_+ \times I_l \rightarrow \mathbb{R}$ compactly supported either in $(0, +\infty) \times (a_l, b_l]$ if $l = 1, \dots, n$ (incoming arcs) or in $(0, +\infty) \times [a_l, b_l)$ if $l = n+1, \dots, n+m$ (outgoing arcs). Test functions are also required to stick smoothly across the vertex, i. e.,

$$\varphi_i(\cdot, b_i) = \varphi_j(\cdot, a_j), \quad \frac{\partial \varphi_i}{\partial x}(\cdot, b_i) = \frac{\partial \varphi_j}{\partial x}(\cdot, a_j)$$

for all $i = 1, \dots, n$ and all $j = n+1, \dots, n+m$. As a consequence, the solution satisfies the Rankine–Hugoniot condition at the vertex J , namely

$$\sum_{i=1}^n f(\mathbf{u}_i(t, b_i^-)) = \sum_{j=n+1}^{n+m} f(\mathbf{u}_j(t, a_j^+))$$

for almost every $t > 0$. This Kirchhoff-like condition also guarantees the conservation of the solution at vertices.

For a system of conservation laws on the real line, a *Riemann problem* consists in a Cauchy problem for an initial datum of Heaviside type, that is a piecewise constant function with only one discontinuity. Then one looks for self-similar solutions constituted by simple waves, which are the building blocks to deal with more general Cauchy problems via wave-front tracking algorithms (see Bressan [18], Garavello and Piccoli [34]). These solutions are formed by (a combination of) continuous waves, called *rarefactions*, and traveling discontinuities, called *shocks*, whose speeds are related to the eigenvalues of the Jacobian matrix of the flux f (namely, to the derivative of f in the scalar case, see Bressan [18]). A mapping yielding the solution to a Riemann problem as a function of the initial datum is said to be a *Riemann solver*.

Analogously, a Riemann problem for a vertex in a network is the Cauchy problem corresponding to an initial datum which is constant on each arc entering or issuing from that vertex. Correspondingly, the following definition of Riemann solver at a vertex is given:

Definition 1 For an initial datum $\underline{u}^0 = (\mathbf{u}_1^0, \dots, \mathbf{u}_{n+m}^0) \in \mathbb{R}^{d \times (n+m)}$ prescribed at a vertex J , a *Riemann solver* at J is a mapping $RS : \mathbb{R}^{d \times (n+m)} \rightarrow \mathbb{R}^{d \times (n+m)}$ that associates to \underline{u}^0 a vector $\hat{\underline{u}} = (\hat{\mathbf{u}}_1, \dots, \hat{\mathbf{u}}_{n+m}) \in \mathbb{R}^{d \times (n+m)}$ such that:

- On every incoming arc I_i , $i = 1, \dots, n$, the solution is given by the waves produced by the Riemann problem $(\mathbf{u}_i^0, \hat{\mathbf{u}}_i)$;
- On every outgoing arc I_j , $j = n+1, \dots, n+m$, the solution is given by the waves produced by the Riemann problem $(\hat{\mathbf{u}}_j, \mathbf{u}_j^0)$.

Any Riemann solver at J must fulfil the following consistency condition:

$$RS(RS(\underline{u}^0)) = RS(\underline{u}^0).$$

Additional hypotheses are usually stated for a Riemann solver at a vertex, namely:

- (H1) The waves generated from the vertex must have negative speeds on the incoming arcs and positive speeds on the outgoing ones.

- (H2) The solution to a Riemann problem at a vertex must satisfy Eq. (48).
 (H3) The mapping $\mathbf{u}_l^0 \mapsto f(\hat{\mathbf{u}}_l)$ has to be continuous each $l = 1, \dots, n + m$.

Hypothesis (H1) is a consistency condition on the description of the dynamics at the vertex. In fact, if (H1) does not hold then some waves generated by the Riemann solver may disappear through the vertex. Condition (H2) is necessary to have a weak solution at the vertex. However, in some cases (H2) may be violated if only some components of the solution are conserved across the junctions, see for instance Garavello and Piccoli [35]. Finally, (H3) is a regularity condition needed to have a well-posed theory. We simply remark here that continuity of the mapping $\underline{u}^0 \mapsto \hat{u}$ might not hold in case (H1) holds true.

An important consequence of hypothesis (H1) is that some restrictions on the admissible values of the solutions of the problem, and of the corresponding fluxes, arise. For instance, consider a single conservation law for a bounded quantity u , say $u \in [0, u_{\max}]$ for a certain fixed threshold $u_{\max} > 0$, and assume the following:

- (F) The flux $f : [0, u_{\max}] \rightarrow \mathbb{R}$ is strictly concave, with in addition $f(0) = f(u_{\max}) = 0$. Thus f has a unique maximum point $\sigma \in (0, u_{\max})$.

If $\tau : [0, u_{\max}] \rightarrow [0, u_{\max}]$ is defined to be the mapping such that $f(\tau(\varrho)) = f(\varrho)$ for all $\varrho \in [0, u_{\max}]$, with however $\tau(\varrho) \neq \varrho$ for all $\varrho \in [0, u_{\max}] \setminus \{\sigma\}$, then the following results are obtained:

Proposition 2 Consider a single conservation law for a bounded variable $u \in [0, u_{\max}]$ between an incoming arc I_i and an outgoing arc I_j at a vertex J , and assume that the flux function satisfies assumption (F) above. Let $RS : \mathbb{R}^2 \rightarrow \mathbb{R}^2$ be a Riemann solver for the vertex J , where the initial datum $\underline{u}^0 = (u_i^0, u_j^0)$ is prescribed, and set $\hat{\underline{u}} := RS(\underline{u}^0) = (\hat{u}_i, \hat{u}_j)$. Then

$$\begin{aligned} \hat{u}_i &\in \begin{cases} \{u_i^0\} \cup (\tau(u_i^0), u_{\max}] & \text{if } 0 \leq u_i^0 \leq \sigma \\ [\sigma, u_{\max}] & \text{if } \sigma \leq u_i^0 \leq u_{\max}, \end{cases} \\ \hat{u}_j &\in \begin{cases} [0, \sigma] & \text{if } 0 \leq u_j^0 \leq \sigma \\ \{u_j^0\} \cup (0, \tau(u_j^0)) & \text{if } \sigma \leq u_j^0 \leq u_{\max}. \end{cases} \end{aligned}$$

Proposition 3 Consider a single conservation law like in the previous Proposition 2 and assume again the hypothesis (F) on the flux f . For an initial datum $\underline{u}^0 = (u_i^0, u_j^0)$, a Riemann solver at a vertex J complying with the hypothesis (H1) above is univocally defined by prescribing the values $f(\hat{\underline{u}})$ of the flux. Moreover, there exist maximal possible

fluxes in the incoming and outgoing arcs I_i, I_j given respectively by

$$\begin{aligned} f_i^{\max}(\underline{u}^0) &:= \begin{cases} f(u_i^0) & \text{if } 0 \leq u_i^0 \leq \sigma \\ f(\sigma) & \text{if } \sigma \leq u_i^0 \leq u_{\max}, \end{cases} \\ f_j^{\max}(\underline{u}^0) &:= \begin{cases} f(\sigma) & \text{if } 0 \leq u_j^0 \leq \sigma \\ f(u_j^0) & \text{if } \sigma \leq u_j^0 \leq u_{\max}. \end{cases} \end{aligned}$$

After assigning a Riemann solver RS at a vertex J , the admissible solutions \mathbf{u}_l across J are defined as those functions of bounded total variation:

$$TV(\mathbf{u}_l(t, \cdot); I_l) < +\infty, \quad l = 1, \dots, n + m$$

for almost every time t of existence, with the further property:

$$RS(\underline{u}_J(t)) = \underline{u}_J(t)$$

where $\underline{u}_J(t) := (\mathbf{u}_1(t, b_1^-), \dots, \mathbf{u}_n(t, b_n^-), \mathbf{u}_{n+1}(t, a_{n+1}^+), \dots, \mathbf{u}_{n+m}(t, a_{n+m}^+)) \in \mathbb{R}^{d \times (n+m)}$.

Finally, for an arc $I_i = [a_i, b_i]$ such that either $a_i > -\infty$ and I_i is not an outgoing arc of any vertex of the graph or $b_i < +\infty$ and I_i is not an incoming arc of any vertex of the graph, a boundary condition $\boldsymbol{\psi}_i = \boldsymbol{\psi}_i(t) : \mathbb{R}_+ \rightarrow \mathbb{R}^d$ on the unknown \mathbf{u}_i is prescribed. In particular, the latter is required to satisfy

$$\mathbf{u}_i(t, a_i) = \boldsymbol{\psi}_i(t) \quad \text{or} \quad \mathbf{u}_i(t, b_i) = \boldsymbol{\psi}_i(t), \quad \forall t > 0$$

in the sense specified by Bardos et al. [6].

Constructing Solutions on a Network

To solve the Cauchy problem on a network for a prescribed initial datum $\underline{u}^0 = (\mathbf{u}_1^0, \dots, \mathbf{u}_N^0)$, where each $\mathbf{u}_i^0 = \mathbf{u}_i^0(x) : I_i \rightarrow \mathbb{R}^d$ is a measurable function, and possibly a set of suitable boundary conditions amounts to finding N vector-valued functions $\mathbf{u}_i = \mathbf{u}_i(t, x) : \mathbb{R}_+ \times I_i \rightarrow \mathbb{R}^d$ such that:

- The mapping $t \mapsto \|\mathbf{u}_i(t, \cdot)\|_{L_{\text{loc}}^1}$ is continuous each $i = 1, \dots, N$;
- Each \mathbf{u}_i is a weak entropic solution to Eq. (45) on the corresponding arc I_i ;
- At each vertex of the graph the proper collection of incoming and outgoing \mathbf{u}_i defines an admissible solution in the sense discussed in the previous section;
- $\mathbf{u}_i(0, x) = \mathbf{u}_i^0(x)$ for almost every $x \in I_i$.

There is a general strategy to prove existence of admissible solutions on a network, which basically relies on the following steps:

1. Construct approximate solutions via wave-front tracking algorithms, using suitable Riemann solvers at vertices to deal with the interactions among different arcs;
2. Estimate the total variation of the flux at vertices, then on the whole network;
3. Use appropriate compactness properties to pass to the limit and recover the solution to the problem.

The wave-front tracking algorithm invoked by step 1 can be roughly described as follows. First one approximates the initial datum \mathbf{u}_i^0 by a piecewise constant function, then uses classical self-similar solutions to Riemann problems on arcs combined with solutions generated by Riemann solvers at vertices. Rarefaction waves are split in *rarefaction shocks fans*, i. e., collections of small non-entropic shocks. When waves interact, either along arcs or at junctions, new Riemann problems are generated to be sequentially solved. In order to successfully perform this construction, one needs to estimate the number of waves and of interactions, which is achieved via suitable functionals (see Garavello and Piccoli [34,35] for details).

Estimation of the total variation of the flux on the network (step 2) can be reduced to the case of a single junction, thanks to the following result:

Theorem 4 *Let $K \subset \mathbb{R}^{d \times N}$ be a fixed compact set and assume $\underline{u} = (\mathbf{u}_1, \dots, \mathbf{u}_N) \in K$. For each vertex J of the network, consider the new network which has J as unique junction, whose incoming and outgoing arcs are prolonged to infinity. If for this network there exists a constant $C > 0$ such that for every initial datum $\underline{u}^0 = (\mathbf{u}_1^0, \dots, \mathbf{u}_N^0)$ with bounded total variation it results*

$$TV[f(\underline{u}(t))] \leq C \cdot TV[f(\underline{u}^0)],$$

then the same estimate holds for the flux on the entire network with a possibly time-dependent constant $C_t > 0$.

Finally, passing to the limit to obtain the true entropic solution to the original problem as required by step 3 is usually the most delicate task. Indeed, even if some compactness of the sequence $\{f(\underline{u}_v)\}_{v \in \mathbb{N}}$ holds (where $\{\underline{u}_v\}_{v \in \mathbb{N}}$ is the sequence generated by the wave-front tracking algorithm), still u_v may fail to converge. This issue was solved for the scalar case $u_i \in \mathbb{R}$ with concave flux f by proving that the number of waves crossing the maximum of the flux can be controlled. To be precise, assume that condition (F) holds true on the function $f : [0, u_{\max}] \rightarrow \mathbb{R}$, then define

Definition 5 A wave (u_i^-, u_i^+) in the i th arc I_i is said to be a *big shock* if $u_i^- < u_i^+$ and

$$\operatorname{sgn}(u_i^- - \sigma) \cdot \operatorname{sgn}(u_i^+ - \sigma) < 0.$$

Definition 6 Fix a vertex J . An incoming arc I_i is said to have a *good datum* at J at time $t > 0$ if

$$u_i(t, b_i^-) \in [\sigma, u_{\max}]$$

and a *bad datum* otherwise. Conversely, an outgoing arc I_j is said to have a good datum at J at time $t > 0$ if

$$u_j(t, a_j^+) \in [0, \sigma]$$

and a bad datum otherwise.

Then one can prove (see Garavello and Piccoli [34]):

Lemma 7 *If an arc I_i of a vertex J has a good datum, then the datum remains good after all interactions with waves coming in J from other arcs. Furthermore, no big shocks are produced. Conversely, if I_i has a bad datum then after any interaction with waves coming in J from other arcs either the datum of I_i remains unchanged or a big shock is produced with a resulting good new datum.*

Once the number of big shocks is bounded via Lemma 7, one can invert the flux $u \mapsto f(u)$, which allows one to pass to the limit also in the sequence $\{\underline{u}_v\}_{v \in \mathbb{N}}$. The interested reader is referred to the book by Garavello and Piccoli [34] for further details also on this part of the theory.

Riemann Solvers at Vertexes

In this section we focus specifically on vehicular traffic networks, and describe several Riemann solvers at vertices recently proposed in the literature for the Lighthill–Whitham–Richards model (46). In particular, we consider on each arc I_i the density of cars as a bounded variable $\rho_i \in [0, \rho_{\max}^i]$, where ρ_{\max}^i stands for the capacity of the i th road, and we look for Riemann solvers at vertices complying with the hypothesis (H1). Notice that if the flux f is given on each arc by the parabolic profile (8) (with ρ_{\max} replaced by ρ_{\max}^i) then condition (F) is straightforwardly satisfied with $\sigma = \rho_{\max}^i/2$.

According to Proposition 3, a Riemann solver at a vertex J is defined by simply determining the proper values of the flux f . In the papers by Coclite et al. [22] and by D’Apice et al. [31] two different Riemann solvers at vertices, hereafter denoted by R1 and R2, are considered, based on the following algorithms:

- Solver R1:
 - (a) The traffic from incoming roads is distributed on outgoing roads according to fixed rates;
 - (b) Under rule (a), the flow of cars through the junction is maximized.

- Solver R2:

The flow of cars through the junction is maximized over both incoming and outgoing roads.

Concerning the solver R1, for a certain junction J let I_1, \dots, I_n be the n incoming roads and, analogously, I_{n+1}, \dots, I_{n+m} the m outgoing ones. Rule (a) corresponds to defining a stochastic matrix

$$A = (\alpha_{ji})_{\substack{i=1,\dots,n \\ j=n+1,\dots,n+m}} \quad (49)$$

whose entries α_{ji} represent the rate of traffic coming from I_i and directed to I_j . For this, the coefficients α_{ji} are required to satisfy

$$0 < \alpha_{ji} < 1, \quad \sum_{j=n+1}^{n+m} \alpha_{ji} = 1.$$

Notice that the second condition entails in particular that no cars are lost at the junction, indeed if

$$\rho_j = \sum_{i=1}^n \alpha_{ji} \rho_i$$

is the total density of cars flowing through the j th outgoing road after passing the junction then it results

$$\sum_{j=n+1}^{n+m} \rho_j = \sum_{i=1}^n \rho_i.$$

Furthermore, it can be shown that rule (a) implies the fulfillment of hypothesis (H2) by the Riemann solver R1.

In view of Proposition 3, the incoming and outgoing fluxes at J must take values in the sets

$$\begin{aligned} \Omega_{\text{in}} &= \bigotimes_{i=1}^n [0, f_i^{\max}] \subset \mathbb{R}^n, \\ \Omega_{\text{out}} &= \bigotimes_{j=n+1}^{n+m} [0, f_j^{\max}] \subset \mathbb{R}^m. \end{aligned} \quad (50)$$

Moreover, owing to rule (a) the incoming fluxes must specifically belong to the region

$$\tilde{\Omega}_{\text{in}} = \{\gamma \in \Omega_{\text{in}} : A\gamma \in \Omega_{\text{out}}\},$$

A being the matrix defined in Eq. (49), which is a convex subset of Ω_{in} determined by linear constraints. By consequence, rule (b) is equivalent to perform a maximization over the incoming fluxes only, the outgoing ones being univocally recoverable using rule (a). Finally, rules (a) and

(b) give rise to a linear programming problem at vertex J , whose solution always exists and is in addition unique provided the gradient of the cost function (here, the vector with all unit components) is not orthogonal to the linear constraints describing the set $\tilde{\Omega}_{\text{in}}$.

The orthogonality condition cannot hold if $n > m$. To be specific, we consider in the sequel the simple case study $(n, m) = (2, 1)$ corresponding to a junction with two incoming roads I_1, I_2 and one outgoing road I_3 . If not all traffic coming from I_1 and I_2 can flow to I_3 , then one should assign an additional yielding or priority rule:

(c) There exists a priority vector $p \in \mathbb{R}^n$ such that the vector of incoming fluxes must be parallel to p .

In the case under consideration, the matrix A reduces to the vector $(1, 1)$, which gives only the trivial information that all vehicles flow toward the road I_3 . Rule (b) amounts instead to determining the through flux as

$$\Gamma = \min\{f_1^{\max} + f_2^{\max}, f_3^{\max}\}.$$

If $\Gamma = f_1^{\max} + f_2^{\max}$ then one simply takes the maximal flux over both incoming arcs. Conversely, if the opposite happens, consider the set of all possible incoming fluxes (γ_1, γ_2) , which must belong to the region $\Omega_{\text{in}} = [0, f_1^{\max}] \times [0, f_2^{\max}]$, and define the following lines:

$$r_p = \{tp : t \in \mathbb{R}\}, \quad r_\Gamma = \{(\gamma_1, \gamma_2) : \gamma_1 + \gamma_2 = \Gamma\},$$

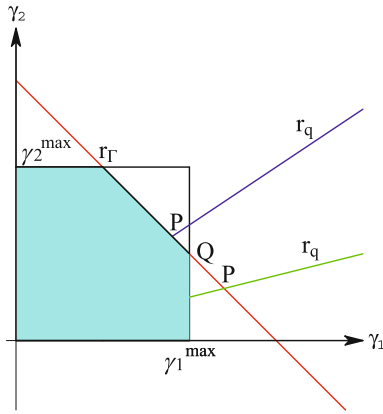
where p is the vector invoked by rule (c). These lines intersect at a point P . As shown by Fig. 4, two situations may arise, namely either P belongs to Ω_{in} or P lies outside Ω_{in} . In the first case the incoming fluxes are individuated by P , whereas in the second case they are determined by the projection Q of P onto the convex set $\Omega_{\text{in}} \cap r_\Gamma$.

The reasoning can be repeated also in the case of n incoming arcs. In \mathbb{R}^n , the general definition of the set Ω_{in} given by Eq. (50) applies; furthermore, the line r_p is defined as above (for $p \in \mathbb{R}^n$), while r_Γ is replaced by the hyperplane

$$H_\Gamma = \left\{ (\gamma_1, \dots, \gamma_n) : \sum_{i=1}^n \gamma_i = \Gamma \right\}.$$

The point $P = r_p \cap H_\Gamma$ exists and is unique. If $P \in \Omega_{\text{in}}$ then it is used again to determine the incoming fluxes, otherwise one chooses its projection Q over $\Omega_{\text{in}} \cap H_\Gamma$. Notice that the point Q is unique since $\Omega_{\text{in}} \cap H_\Gamma$ is a closed convex subset of H_Γ .

It is to check that the hypothesis (H3) is verified for this Riemann solver.



Vehicular Traffic: A Review of Continuum Mathematical Models, Figure 4

The two cases $P \in \Omega_{in}$ and $P \notin \Omega_{in}$

Concerning the solver (R2), one defines the maximal incoming and outgoing fluxes using again Proposition 3:

$$\Gamma_{in} = \sum_{i=1}^n f_i^{\max}, \quad \Gamma_{out} = \sum_{j=n+1}^{n+m} f_j^{\max},$$

so that the through flux is simply determined by

$$\Gamma = \min\{\Gamma_{in}, \Gamma_{out}\}.$$

Then one uses rule (c) over both incoming and outgoing arcs to find the values of the flux over the arcs. Once again hypothesis (H1) is assumed, thus densities are uniquely determined. Property (H2) holds by definition, and (H3) is easily proved. Different Riemann solvers at vertices, along with related qualitative analyzes, are studied by D'Apice and Piccoli [30].

Future Directions

Various research perspectives may be envisaged in the field of vehicular traffic, aimed on the one hand at an improvement of the mathematical framework, in order to include in the theory further specific features of this non-standard system, and on the other hand at a coupling with other topics intimately correlated to traffic, so as to enlarge the scenario of applications to real world problems. Without claiming to be thorough, we simply outline here some possible basic ideas that require to be appropriately developed.

In both macroscopic and kinetic models presented in this review vehicles are described at an essentially mechanical level. Indeed, the macroscopic approach relies on the analogy with fluid particles, hence on principles proper of continuum mechanics, whereas the kinetic approach ac-

counts for a microscopic state of the cars fully characterized by mechanical variables only, such as position and velocity. However, it can be argued that cars are actually not completely mechanical subjects, for the presence of the drivers is likely to affect their behavior in a strongly unconventional way. The concept of fictitious density proposed by De Angelis (see Subsect. “[Fictitious Density Model](#)” and [32]) is an attempt to introduce this aspect of the problem in the macroscopic equations of traffic, but in a sense it is too deterministic to catch the real essence of the human behavior, which is instead quite unpredictable. On the other hand, at the kinetic level of representation no model has been so far introduced in the literature taking the action of the driver explicitly into account. Promising ideas toward this issue are expressed in the recent book by Bellomo [7] dealing with generalized kinetic methods for systems of *active particles*, namely particles whose microscopic state includes, besides the standard mechanical variables, also an additional internal variable named *activity*. In the case of vehicular traffic, the latter may represent the driving ability, or alternatively the personality, of the drivers, and can be conceived so as to affect the velocity transition probabilities in an essentially stochastic way.

Further research perspectives concern, primarily at a macroscopic level of description, the development of new hydrodynamic models and algorithms for real-time reconstruction of traffic flows in a road network by few experimental information. Using few data, as well as few model parameters, is indeed necessary for compatibility reasons with actual traffic measurements, which are usually pointwise scattered on the network. In addition, the development of fluid dynamic and gas dynamic models to simulate the emission and propagation of pollutants produced by cars in an urban context might provide powerful technological tools to rationalize the design and use of public and private transportation resources, and to reduce unpleasant effects of urban traffic on the environment.

Bibliography

1. Arlotti L, Bellomo N, De Angelis E (2002) Generalized kinetic (Boltzmann) models: mathematical structures and applications. *Math Models Methods Appl Sci* 12(4):567–591
2. Armbruster D, Degond P, Ringhofer C (2006) A model for the dynamics of large queuing networks and supply chains. *SIAM J Appl Math (electronic)* 66(3):896–920
3. Aw A, Rascle M (2000) Resurrection of “second order” models of traffic flow. *SIAM J Appl Math* 60(3):916–938
4. Aw A, Klar A, Materne T, Rascle M (2002) Derivation of continuum traffic flow models from microscopic follow-the-leader models. *SIAM J Appl Math (electronic)* 63(1):259–278
5. Banda MK, Herty M, Klar A (2006) Gas flow in pipeline networks. *Netw Heterog Media (electronic)* 1(1):41–56

6. Bardos C, le Roux AY, Nédélec JC (1979) First order quasilinear equations with boundary conditions. *Comm Partial Differential Equations* 4(9):1017–1034
7. Bellomo N (2007) Modelling complex living systems. A kinetic theory and stochastic game approach. *Modeling and Simulation in Science, Engineering and Technology*. Birkhäuser, Boston
8. Bellomo N, Coscia V (2005) First order models and closure of the mass conservation equation in the mathematical theory of vehicular traffic flow. *C R Mec* 333:843–851
9. Bellomo N, Lachowicz M, Polewczak J, Toscani G (1991) Mathematical topics in nonlinear kinetic theory II. The Enskog equation. *Series on Advances in Mathematics for Applied Sciences*, vol 1. World Scientific Publishing, Teaneck
10. Bellomo N, Delitala M, Coscia V (2002) On the mathematical theory of vehicular traffic flow I. Fluid dynamic and kinetic modelling. *Math Models Methods Appl Sci* 12(12):1801–1843
11. Ben-Naim E, Krapivsky PL (1998) Steady-state properties of traffic flows. *J Phys A* 31(40):8073–8080
12. Ben-Naim E, Krapivsky PL (2003) Kinetic theory of traffic flows. *Traffic Granul Flow* 1:155
13. Berthelin F, Degond P, Delitala M, Rascle M (2008) A model for the formation and evolution of traffic jams. *Arch Ration Mech Anal* 187(2):185–220
14. Bertotti ML, Delitala M (2004) From discrete kinetic and stochastic game theory to modelling complex systems in applied sciences. *Math Models Methods Appl Sci* 14(7):1061–1084
15. Bonzani I (2000) Hydrodynamic models of traffic flow: drivers' behaviour and nonlinear diffusion. *Math Comput Modelling* 31(6–7):1–8
16. Bonzani I, Mussone L (2002) Stochastic modelling of traffic flow. *Math Comput Model* 36(1–2):109–119
17. Bonzani I, Mussone L (2003) From experiments to hydrodynamic traffic flow models I. Modelling and parameter identification. *Math Comput Model* 37(12–13):1435–1442
18. Bressan A (2000) Hyperbolic systems of conservation laws. The one-dimensional Cauchy problem. In: *Oxford Lecture Series in Mathematics and its Applications*, vol 20. Oxford University Press, Oxford
19. Cercignani C, Lampis M (1988) On the kinetic theory of a dense gas of rough spheres. *J Stat Phys* 53(3–4):655–672
20. Chakroborty P, Agrawal S, Vasishta K (2004) Microscopic modeling of driver behavior in uninterrupted traffic flow. *J Transp Eng* 130(4):438–451
21. Chitour Y, Piccoli B (2005) Traffic circles and timing of traffic lights for cars flow. *Discret Contin Dyn Syst Ser B* 5(3):599–630
22. Coclite GM, Garavello M, Piccoli B (2005) Traffic flow on a road network. *SIAM J Math Anal* (electronic) 36(6):1862–1886
23. Colombo RM (2002) A 2×2 hyperbolic traffic flow model, traffic flow – modelling and simulation. *Math Comput Model* 35(5–6):683–688
24. Colombo RM (2002) Hyperbolic phase transitions in traffic flow. *SIAM J Appl Math* 63(2):708–721
25. Colombo RM, Garavello M (2006) A well posed Riemann problem for the p -system at a junction. *Netw Heterog Media* (electronic) 1(3):495–511
26. Coscia V, Delitala M, Frasca P (2007) On the mathematical theory of vehicular traffic flow, II. Discrete velocity kinetic models. *Int J Non-Linear Mech* 42(3):411–421
27. Dafermos CM (2005) Hyperbolic conservation laws in continuum physics. *Grundlehren der mathematischen Wissenschaften* [Fundamental Principles of Mathematical Sciences], vol 325, 2nd edn. Springer, Berlin
28. Daganzo CF (1995) Requiem for second-order fluid approximation of traffic flow. *Transp Res* 29B(4):277–286
29. D'Apice C, Manzo R (2006) A fluid dynamic model for supply chains. *Netw Heterog Media* (electronic) 1(3):379–398
30. D'Apice C, Piccoli B (2008) Vertex flow models for network traffic. *Math Models Methods Appl Sci* (submitted)
31. D'Apice C, Manzo R, Piccoli B (2006) Packet flow on telecommunication networks. *SIAM J Math Anal* (electronic) 38(3):717–740
32. De Angelis E (1999) Nonlinear hydrodynamic models of traffic flow modelling and mathematical problems. *Math Comput Model* 29(7):83–95
33. Delitala M, Tosin A (2007) Mathematical modeling of vehicular traffic: a discrete kinetic theory approach. *Math Models Methods Appl Sci* 17(6):901–932
34. Garavello M, Piccoli B (2006) Traffic flow on networks. In: *AIMS Series on Applied Mathematics*, vol 1. American Institute of Mathematical Sciences (AIMS), Springfield
35. Garavello M, Piccoli B (2006) Traffic flow on a road network using the Aw–Rascle model. *Comm Partial Differ Equ* 31(1–3):243–275
36. Gazis DC, Herman R, Rothery RW (1961) Nonlinear follow-the-leader models of traffic flow. *Oper Res* 9:545–567
37. Göttlich S, Herty M, Klar A (2006) Modelling and optimization of supply chains on complex networks. *Commun Math Sci* 4(2):315–330
38. Greenberg JM (2001/02) Extensions and amplifications of a traffic model of Aw and Rascle. *SIAM J Appl Math* (electronic) 62(3):729–745
39. Günther M, Klar A, Materne T, Wegener R (2002) An explicitly solvable kinetic model for vehicular traffic and associated macroscopic equations. *Math Comput Model* 35(5–6):591–606
40. Günther M, Klar A, Materne T, Wegener R (2003) Multivalued fundamental diagrams and stop and go waves for continuum traffic flow equations. *SIAM J Appl Math* 64(2):468–483
41. Helbing D (1998) From microscopic to macroscopic traffic models. In: *A perspective look at nonlinear media*. *Lecture Notes in Phys*, vol 503. Springer, Berlin, pp 122–139
42. Helbing D (2001) Traffic and related self-driven many-particle systems. *Rev Mod Phys* 73(4):1067–1141, doi:10.1103/RevModPhys.73.1067
43. Herty M, Kirchner C, Moutari S (2006) Multi-class traffic models on road networks. *Commun Math Sci* 4(3):591–608
44. Herty M, Moutari S, Rascle M (2006) Optimization criteria for modelling intersections of vehicular traffic flow. *Netw Heterog Media* (electronic) 1(2):275–294
45. Holden H, Risebro NH (1995) A mathematical model of traffic flow on a network of unidirectional roads. *SIAM J Math Anal* 26(4):999–1017
46. Hoogendoorn SP, Bovy PHL (2001) State-of-the-art of vehicular traffic flow modelling. *J Syst Cont Eng* 215(4):283–303
47. Kerner BS (2000) Phase transitions in traffic flow. In: Helbing D, Hermann H, Schreckenberg M, Wolf DE (eds) *Traffic and Granular Flow '99*. Springer, New York, pp 253–283
48. Kerner BS (2004) The physics of traffic. Springer, Berlin
49. Kerner BS, Klenov SL (2002) A microscopic model for phase transitions in traffic flow. *J Phys A* 35(3):L31–L43
50. Klar A, Wegener R (1997) Enskog-like kinetic models for vehicular traffic. *J Stat Phys* 87(1–2):91–114

51. Klar A, Wegener R (2000) Kinetic derivation of macroscopic anticipation models for vehicular traffic. *SIAM J Appl Math* 60(5):1749–1766
52. Klar A, Wegener R (2004) Traffic flow: models and numerics. In: *Modeling and computational methods for kinetic equations. Model Simul Sci Eng Technol*. Birkhäuser, Boston, pp 219–258
53. Lebacque JP, Khoshyaran MM (1999) Modelling vehicular traffic flow on networks using macroscopic models. In: *Finite volumes for complex applications II*. Hermes Sci Publ, Paris, pp 551–558
54. Leutzbach W (1988) *Introduction to the Theory of Traffic Flow*. Springer, New York
55. Lighthill MJ, Whitham GB (1955) On kinematic waves, II. A theory of traffic flow on long crowded roads. *Proc Roy Soc Lond Ser A* 229:317–345
56. Nagel K, Wagner P, Woesler R (2003) Still flowing: approaches to traffic flow and traffic jam modeling. *Oper Res* 51(5): 681–710
57. Paveri Fontana SL (1975) On Boltzmann-like treatments for traffic flow. *Transp Res* 9:225–235
58. Payne HJ (1971) Models of freeway traffic and control. *Math Models Publ Syst Simul Council Proc* 28:51–61
59. Prigogine I (1961) A Boltzmann-like approach to the statistical theory of traffic flow. In: *Theory of traffic flow*. Elsevier, Amsterdam, pp 158–164
60. Prigogine I, Herman R (1971) *Kinetic theory of vehicular traffic*. American Elsevier Publishing, New York
61. Rascle M (2002) An improved macroscopic model of traffic flow: Derivation and links with the Lighthill–Whitham model. *Math Comput Model, Traffic Flow Model Simul* 35(5–6): 581–590
62. Richards PI (1956) Shock waves on the highway. *Oper Res* 4: 42–51
63. Serre D (1996) Hyperbolicité, entropies, ondes de choc. [Hyperbolicity, entropies, shock waves.] In: *Systèmes de lois de conservation, I. Fondations*. [Foundations.] Diderot Editeur, Paris
64. Serre D (1996) Structures géométriques, oscillation et problèmes mixtes. [Geometric structures, oscillation and mixed problems.] In: *Systèmes de lois de conservation, II. Fondations*. [Foundations.] Diderot Editeur, Paris
65. Tosin A (2008) Discrete kinetic and stochastic game theory for vehicular traffic: Modeling and mathematical problems. Ph D thesis, Department of Mathematics, Politecnico di Torino
66. Treiber M, Helbing D (2003) Memory effects in microscopic traffic models and wide scattering in flow-density data. *Phys Rev E* 68(4):046–119, doi:10.1103/PhysRevE.68.046119
67. Treiber M, Hennecke A, Helbing D (2000) Congested traffic states in empirical observations and microscopic simulations. *Phys Rev E* 62(2):1805–1824, doi:10.1103/PhysRevE.62.1805
68. Treiber M, Kesting A, Helbing D (2006) Delays, inaccuracies and anticipation in microscopic traffic models. *Physica A* 360(1): 71–88
69. Villani C (2002) A review of mathematical topics in collisional kinetic theory. In: *Handbook of mathematical fluid dynamics*, vol I. North-Holland, Amsterdam, pp 71–305
70. Wegener R, Klar A (1996) A kinetic model for vehicular traffic derived from a stochastic microscopic model. *Transp Theory Stat Phys* 25(7):785–798
71. Whitham GB (1974) *Linear and nonlinear waves*. Wiley-Interscience, New York

Viral Protein Nano-Actuators, Computational Studies of Bio-nanomachines

ATUL DUBEY, M. SILVINA TOMASSONE

Department of Chemical and Biochemical Engineering,
Rutgers, The State University of New Jersey,
Piscataway, USA

Article Outline

[Glossary](#)

[Definition of the Subject](#)

[Introduction](#)

[The VPL Nanoactuator](#)

[Methods](#)

[Simulation Results and Discussion](#)

[Conclusions](#)

[Future Directions](#)

[Acknowledgments](#)

[Bibliography](#)

Glossary

Nanodevice A Device with size dimensions of the order of the nanometer (10^{-9} m)

Actuator A device used to generate motion by converting some form of energy (such as chemical or light energy) into mechanical energy.

ATP Adenosine Triphosphate molecule used by living organisms to store and transport energy.

End-effector The last link in a robotic assembly that performs the desired tasks by the robot by interacting with or acting upon the elements outside the robot.

Retrovirus A type of virus that has a protein envelope around it, stores its genetic information in an RNA molecule instead of double stranded DNA and transcribes its genome into DNA which integrates into the chromosome of the infected cell thereby replicating the virus when the cell replicates.

Glycoprotein A protein molecule which has a carbohydrate attached to it.

Membrane fusion A process when viral and host cellular membranes fuse together during infection.

Hemagglutinin A type of protein on the surface of the influenza virus.

Fusogenic The unit that facilitates or takes part in membrane fusion.

Disulfide bond A sulfur–sulfur atomic bond which typically joins two biological segments such as protein chains.

Proteolytic cleavage A process of breaking the peptide bond between amino acids in a protein chain.

Endosome Intracellular vesicle formed by the outer cell membrane used to transport material inside the animal cell.

Endocytosis The process of encapsulation of an external element by the cell membrane and subsequent formation of an endosome for transport within the cell.

Nucleocapsid The genome of a virus enclosed in a protein coat.

α -Helix A secondary structure of protein molecules characterized by a helical shape and a specific pitch and stabilized by hydrogen bonds along the length of the helix.

β -Sheet A secondary structure of protein molecules where two or more chains are interconnected by hydrogen bonds forming a sheet-like structure.

Titin A big filamentous protein used by muscles.

Holonomic constraint A constraint that puts a restriction on the motion of a system by the use of integrable system of differential equations.

Chymotrypsin An enzyme in the pancreas which is involved in the catalysis of hydrolysis of proteins in the small intestine.

PDB The protein data bank which contains structural and other information about a large number of protein molecules. <http://www.rcsb.org/pdb/home/home.do>

Implicit solvation A technique used in molecular simulation which allows for a potential function to be used in place of explicit solvent molecules surrounding the molecule of interest.

Protonation The process of accepting a positively charged hydrogen ion or a proton by an amino acid.

Helicity The measure of the helical content of a given peptide molecule.

Denaturation Process of loss of secondary structure of a peptide molecule, which can happen for example due to heating beyond a certain level.

Definition of the Subject

In this paper, we describe computational aspects of an initiative to create a nanodevice for chemo-mechanical energy conversion based on a biological system. We provide insights into the available methods and their applications to gain knowledge about whether a given molecule is suitable to function as a nanoactuator. The field of bio-nanotechnology is new and it is developing fast. Noticeably, its roots go back decades of studies in the fields of biophysics, biochemistry and engineering. These disciplines can now come together to create useful and controllable devices at

the nano-scale thereby adding another dimension to human scientific capabilities. Their applications in the fields of medicine, space exploration and colonization, and military are very promising.

Introduction

There is a persistent need of miniaturization of machines and energy conversion devices for various engineering applications. A great part of modern research is shifting from macro to nano-scale as consumer and scientific devices become smaller, faster and more energy efficient. In the field of robotics, there is a need to develop nano-scale actuators, joints, motors and other machine components. Since these nanodevices can be either single-molecule or macromolecular devices, the laws governing their behavior are different from the ones that govern macro-scale machines. Hence in order to study and develop them it is crucial to fully understand the material properties and the work environment and be able to create appropriate models that account for them.

Miniature molecular machines have been operating for centuries in living organisms. Nature has created and optimized these complex machines to carry out specific tasks, such as moving cellular cargo, and oxidizing high-energy molecules etc. With modern microscopic abilities, finer structural and functional details of these molecules are being discovered. Mechanical motions, structural features, operating principles, limitations, and design features of many natural molecular machines are being investigated. It is possible to use these machines or their individual parts under artificial stimuli in order to perform tasks not necessarily assigned to them by nature. Attempts at creating artificial molecular machines are also being made. Some of the principles and applications of molecular machines have been reviewed [4,5,7,26,32,38,47].

Molecular machines can be broadly classified into protein-based, DNA-based or chemical machines. From each of the three classes, completely different types of machines are obtained. Each of these machines has a different operating environment, force and displacement capabilities, and fuel requirements. Hence all of them figure in a molecular part-list and can be utilized when requirements are specific to them. For example protein-based ATP motors require protons or high energy molecules, whereas DNA-based machines require DNA strands as fuel. Both these machines can be used to produce rotary motion, although in different environmental conditions.

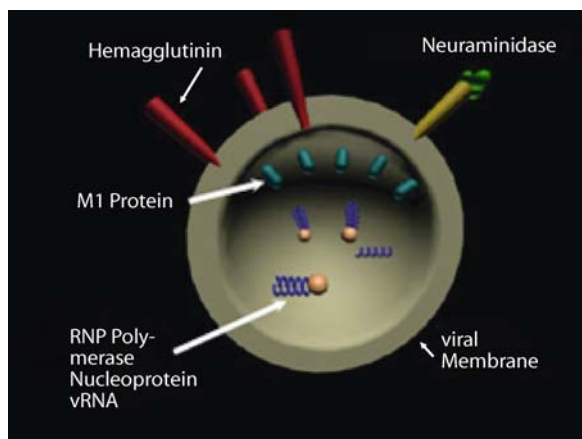
Molecular devices for use in robotics have not yet been thoroughly investigated. There is a need to find nanoscale equivalents of robot parts such as actuators, links, end-eff-

factors, sensors etc. This study aims to develop one such protein based linear actuator, called the Viral Protein Linear (VPL) actuator. The inspiration for this type of actuator comes from nature – from the infection mechanism of some viruses. There is a particular segment of the surface protein of retroviruses such as influenza virus that undergoes a conformational change which can be used as a linear actuator producing about 10 nm of linear motion. In this work, we characterize the VPL protein actuator by computationally studying its behavior and predicting its performance.

The VPL Nanoactuator

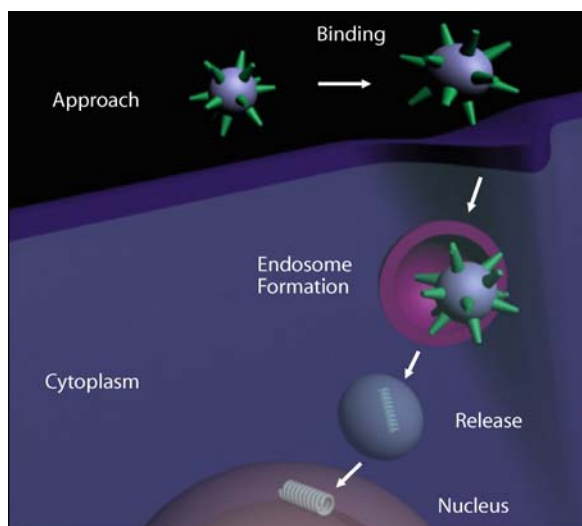
The role of envelope glycoproteins (surface proteins) of various retroviruses in the process of membrane fusion has been investigated and understood over the years. Such viruses infect their target cells by the process of membrane fusion. Membrane fusion is necessary for a large number of diverse processes in biology such as protein trafficking, protein secretion, fertilization, viral invasion and neuro-transmission. The mechanism is best understood among enveloped viruses such as the influenza virus [31,35,43,44]. Specialized viral proteins are required to promote membrane fusion – a process which is otherwise very slow. In many cases, these membrane-fusion proteins also serve as agents that promote the binding of the virus onto the cell surface receptors. In the influenza virus, a protein segment called Hemagglutinin (HA) mediates both the binding of the virus to the cell surface and the subsequent fusion of viral and cellular membranes. The receptor binding subunit of HA is termed HA1, while the fusogenic subunit is denoted as HA2. Figure 1 shows a schematic of the influenza virus.

HA1/HA2 complex consists of the disulfide bonded HA1 and HA2 peptides. Each HA monomer is synthesized as a fusion-incompetent precursor polypeptide known as HA0 which undergoes proteolytic cleavage to give rise to the two chains [25,34]. The two subunits have different functions. For example, in the case of the Human Immunodeficiency Virus (HIV), HIV 1, the precursor glycoprotein is gp160, which is proteolytically cleaved into gp120 and gp41 subunits. The gp120 is the surface subunit and the gp41 is the transmembrane (TM) subunit. The surface subunit serves to recognize the cell to be infected when it comes in the vicinity of the virus with the help of receptors located on the cell surface. The gp41 mediates membrane fusion between the viral and cellular membranes. It has been found that gp41, and corresponding TM subunits in other retroviruses acquire an alpha-helical conformation when the virus is in its active or fusogenic state. The



Viral Protein Nano-Actuators, Computational Studies of Bio-nanomachines, Figure 1

A schematic of the influenza virus. Hemagglutinin (HA) polypeptides lie on the surface of the virus while viral RNA resides inside. HA has subunits that attach to cells and then facilitate membrane fusion in order to infect the cell

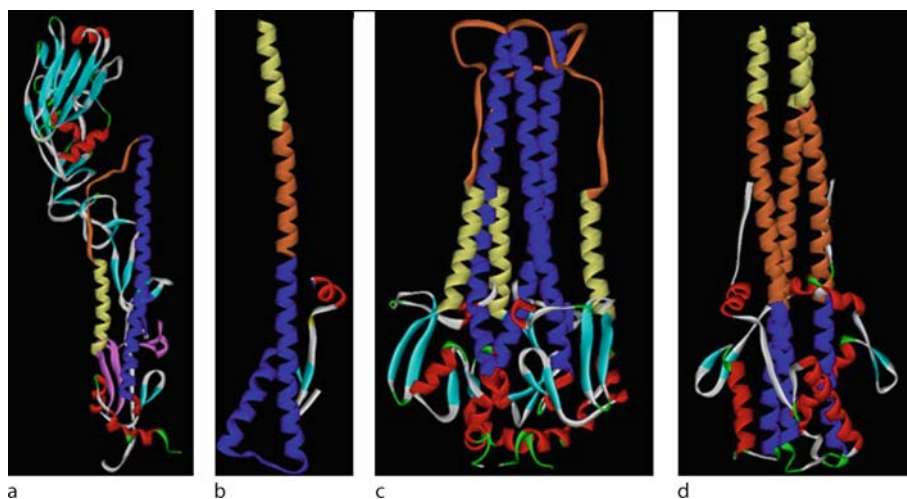


Viral Protein Nano-Actuators, Computational Studies of Bio-nanomachines, Figure 2

Various stages in influenza virus infection. The virus is endocytosed by the cell and an endosome is formed, wherein a conformational change of interest occurs

structure is like a hairpin composed of three coils, having one C terminal (carboxy- end) and the other N terminal (amino-end). The carboxy regions pack in an anti-parallel manner around the three hydrophobic amino ends as shown in Fig. 3.

The native HA1/HA2 complex in the viral envelope is fusion-inactive. The cell-surface receptor needed for the



Viral Protein Nano-Actuators, Computational Studies of Bio-nanomachines, Figure 3

a Hairpin like structure of central HA2 native state monomer. The monomer consists of two segments A and B. At the N-terminal is the fusion peptide contained in segment A (residues 1–25, shown in pink) followed by short anti-parallel β -sheet (residues 26–37, shown in cyan). The outer arm of the hairpin is a small α -helix (residues 38–53, shown yellow) which is connected to a long α -helix (residues 82–125, shown blue) by a loop region (residues 54–81, shown in orange); **b** HA2 chains A and B in fusogenic states. The loop region (orange) converts into a relatively more rigid α -helix and forms a continuation of the long α -helix (blue). The short α -helix is thus translated upwards along with the fusion peptide (not shown). **c** The native state HA2 trimer. The remaining structure other than the helices (bottom) is the fusion peptide from the N-terminal and the other smaller secondary structures following the long helices. **d** Fusogenic state of the HA2 trimer. The helical hairpins open up to form an extended three stranded coiled coil structure with the previously loop regions now helical. Such coiled coil motif is found in many other proteins such as the leucine zipper domain of some transcription factors. The α -helices are wrapped around each other with a left handed superhelical twist

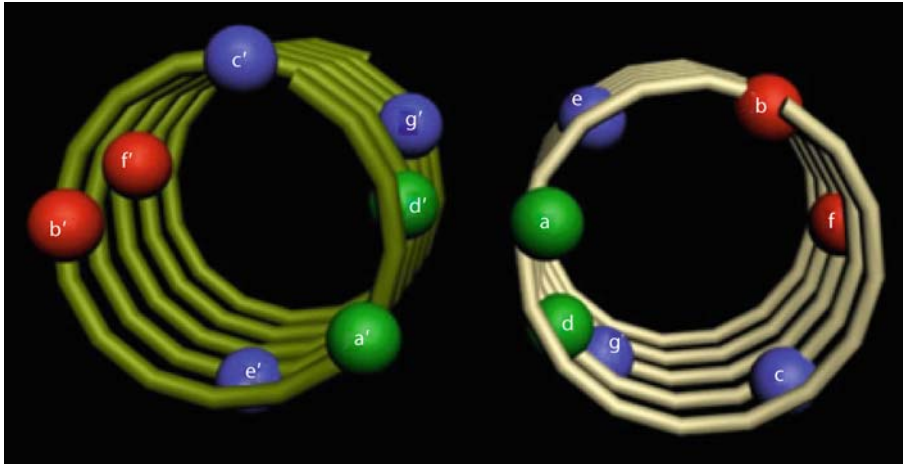
virus to bind onto the cell is known as sialic acid. HA1 binds to this receptor and hence serves the purpose of bringing the virus and cell together. Upon binding with sialic acid, the virus is endocytosed by the cell (Fig. 2). HA remains dormant until the endosome begins to mature, and the pH in the HA surroundings drops to a value of about 5.

At this pH, there is a conformational change in HA2 domain of HA that induces the viral membrane to fuse with the cellular, endosomal membrane, thereby permitting the nucleocapsid of the virus to be deposited into the cytoplasm of the cell. Hence it can be inferred that the acidic pH acts as the physiological trigger for the HA conformational change. Since the low pH also activates membrane fusion, the low pH conformation of HA is also known as fusogenic conformation.

The crystal structures of HA in both the native and the fusogenic conformations are known [8,40,41,45]. As stated above, the HA1 only serves the purpose of cellular recognition and binding to the cell surface receptor and is not of much interest as a nanoactuator. The HA2 subunit, however, is then responsible for the membrane fusion activity. In the native state, the central region of HA2 folds as a helical hairpin-like monomeric structure (Fig. 3a). Two

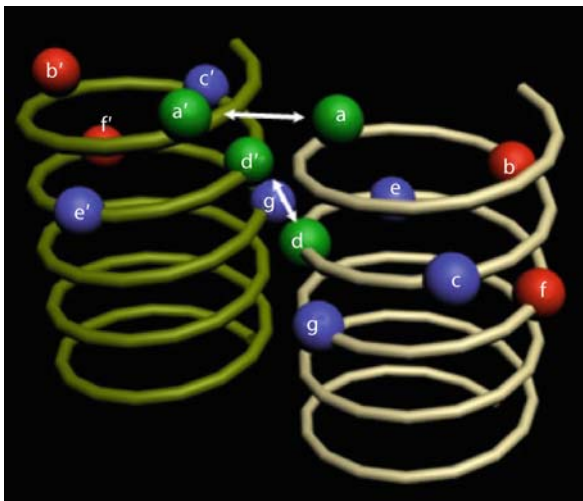
more such subunits (consisting of two segments each) are present to form a trimer together. The long α -helices from each subunit in the native state form a well known structure called the three stranded coiled coil system. Coiled coils can be visualized as an intertwined rope of three interacting helices. As is visible in Fig. 3c and 3d, in addition to the helical domains, there are other regions – small helices, β -sheets, turns and random loop regions. The blue regions in the native stage in Fig. 3c are triple stranded coiled coils wound against each other. They are connected to smaller helices (yellow) in the HA2 domain by loop regions shown in orange. The smaller helices connect to the fusion peptide (residue numbers 1–25). After attachment and pH drop, the orange loop regions convert into extended coiled coils effectively extending the blue coils and moving the fusion peptide by about 10 nm [11].

Coiled coil motifs contain hydrophobic and hydrophilic amino acids in a repeating heptad pattern (positions *a* through *g*) as shown in Figs. 4 and 5. Looking down the axis of the helix, hydrophobic residues tend to occur at the positions *a* and *d* of the heptad repeat and these residues form the interface between the helices. It is believed that HA folds into its thermodynamically most stable state at neutral pH, known as its native state. But



Viral Protein Nano-Actuators, Computational Studies of Bio-nanomachines, Figure 4

Two helices of a coiled coil system. The seven positions (a–e) denote locations of hydrophobic/hydrophilic residues. Hydrophobic residues (green balls) tend to occur on the inside positions a and d whereas the hydrophilic residues (red balls) reside in other positions



Viral Protein Nano-Actuators, Computational Studies of Bio-nanomachines, Figure 5

Packing of two helices of a coiled coil system. The hydrophobic residues in positions a – a' and d – d' of each chain interact with each other to stabilize the coiled coil system

at reduced pH, the fusogenic state becomes thermodynamically more feasible and hence the protein changes conformation in order to achieve it [10]. Another model that is widely accepted suggests that the native state is a metastable state that can be disturbed by any agent, not only pH. It has been observed that heat can also produce this conformational change at neutral pH and so does a denaturant such as urea [10].

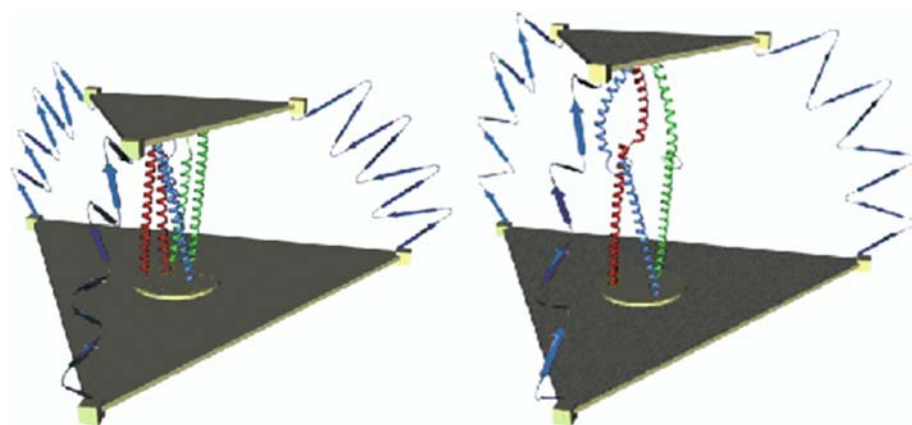
In addition to Influenza, the following other viruses show similar infection mechanism and can be candidates for a VPL-like nanoactuator:

- (i) The Human Immunodeficiency Virus type 1 (HIV 1) peptide gp41 [12]
- (ii) The Human Respiratory Syncytial Virus (HRSV) protein subunit F1 [33]
- (iii) The Simian Immunodeficiency Virus (SIV) protein gp41 [9]
- (iv) The Human T cell Leukemia virus type 1, protein gp21 [23]
- (v) The Simian Parainfluenza Virus peptide unit SV5 [3]
- (vi) Ebola virus protein gp2 [42]

Each one of these peptides can result in a different actuator that can have different properties such as weight, volume, range of motion, force and speed capabilities. However, their principle of actuation is the same. Studies have shown [13,39,43] that the common characteristic in these viruses is the structure of a portion of the envelope glycoprotein and the mode of infection.

Projected Robotic Applications of VPL Nanoactuators

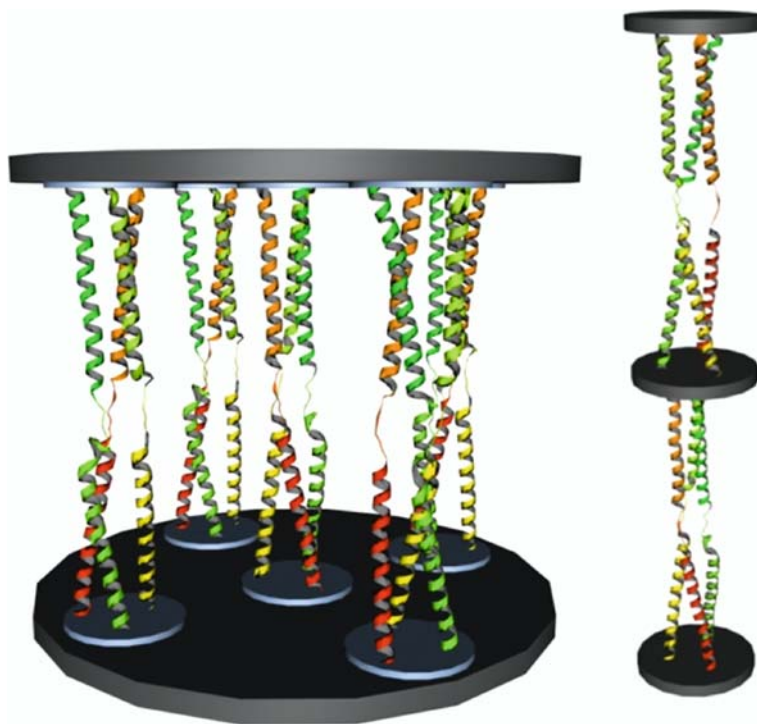
Figure 6 shows a schematic of the VPL motor supporting a moving platform. The motor is shown in its initial, “contracted” phase in the first image that corresponds to the virus’ native state and at its extended, fusogenic state in the second image of the figure. The total outward protrusion is measured to be 10 nanometers. The estimated time for filling up of the hydrophobic membrane defect by lipids



Viral Protein Nano-Actuators, Computational Studies of Bio-nanomachines, Figure 6
A single degree of freedom VPL actuated parallel platform VPL actuator

is 2–4 ns, which gives an idea that the peptide unfolding process takes about the same time. To augment the force capabilities of the VPL motors, several VPL actuating elements could be attached in parallel as it is shown in Fig. 7. Such parallel attachment of multiple VPL motors could result extremely powerful, micro, meso or even macro actuators that will be able to apply ultra large forces while their dimensions are extremely small.

In a similar way, to increase the displacement capability of the VPL motors, several VPL elements could be connected in series (see Fig. 7). For attaching the titin fibers to the platforms DNA joints could be manufactured. By biochemical matching, the platforms could be designed to have proteins that bind to DNA on their corners. DNA strands could then bind onto the corners from one end and to the fibers on the other end to create a flexible joint.



Viral Protein Nano-Actuators, Computational Studies of Bio-nanomachines, Figure 7
Several VPL motors placed in parallel and series

The titin fibers will have to be functionalized in such a way that their ends bind to the DNA as well.

Methods

Targeted Molecular Dynamics (TMD) is a technique used to simulate conformational pathways between two known states by resorting to Newtonian molecular dynamics calculations with a physical potential and a holonomic constraint [29,30]. It provides an approximate modeling of processes that would otherwise span long time-scales (up to milliseconds) in realistic time scales for simulations. Protein folding is a microsecond scale phenomenon [46] and cannot be captured by unbiased MD simulations in realistic time frames. TMD is an example of a biasing technique that drives the trajectory from one known state to another. A number of such techniques have been investigated, for example, internal coordinate constraints [36], minimum biasing methods [20], biased molecular dynamics [27], essential dynamics sampling [14], steered molecular dynamics [22], modified targeted molecular dynamics [2], accelerated molecular dynamics [19] and more recently, the restricted perturbation targeted molecular dynamics (RP-TMD) [37] method.

TMD applies a holonomic constraint that reduces the root mean square deviation (RMSD) of the protein from a predefined target structure by a preset value at each dynamics step [29]. It has been shown that TMD can produce results equivalent to those from traditional MD simulations techniques in a much shorter time by using and lower temperatures. Ferrara et al. [17] have shown using the example of *chymotrypsin inhibitor 2* that the energies of conformation sampled using TMD are in agreement with those obtained from higher temperature unrestrained MD simulations and also with simulations performed using different force fields.

Because the distance to be traveled by the N-terminal of the VPL peptide is relatively very large, unbiased MD techniques cannot be applied to simulate the entire conformational change. High resolution crystal structures of initial and final states of VPL peptides are available from PDB. The closed state was termed as the initial state *I* and the open state as the final state *F*. TMD applies the holonomic constraint to reduce the root mean square deviation (RMSD) from *I* to *F* by a finite value at each MD step. The 3N position coordinates corresponding to N atoms in the molecule can be defined as:

$$\mathbf{X} = (X_1, X_2, \dots, X_{3N})^T, \quad (1)$$

where 3N are the Cartesian coordinates of the position vectors $\mathbf{r}_1, \mathbf{r}_2, \dots, \mathbf{r}_N$ of each individual atom.

The position of an individual atom is time dependent, and is described at time *t* as $X_i(t)$. Let X_{Fi} be the final (target) position of an atom *i*. The holonomic constraint is of the form:

$$\Phi[\underline{X}(t)] = \sum [\underline{X}_i(t) - \underline{X}_{Fi}]^2 - \underline{\rho}^2(t) = 0. \quad (2)$$

The underlined terms indicate that they have been scaled by a factor of $\sqrt{m_i/\langle m \rangle}$ where m_i is the mass of atom *i* and $\langle m \rangle$ is the average atomic mass. This mass scaling helps avoid the net translation of the system as a whole [30]. The holonomic constraint in Eq. (2) gives rise to a constraint force of the form:

$$F_i^c = \lambda \nabla_i \Phi = \frac{2\lambda m_i}{\langle m \rangle} (X_i - X_{Fi}), \quad (3)$$

where λ is a Lagrange multiplier. It is determined by the following method. The Leap-frog [1] propagator is a common method used to update variables along a trajectory of positions. According to this algorithm, the position of an atom *i* at time *t* is given by:

$$\begin{aligned} X_i(t) &= \left[X_i(t - \Delta t) + v_i \left(t - \frac{3}{2} \Delta t \right) \Delta t \right. \\ &\quad \left. + \frac{F_i(t - \Delta t)}{m_i} (\Delta t)^2 \right] + \frac{F_i^c(t - \Delta t)}{m_i} (\Delta t)^2 \quad (4) \\ &= x_i(t) + p_i(t) \end{aligned}$$

In the above equation, Δt is the time increment, F_i is the force on atom *i* due to unbiased Newtonian molecular dynamics, and v_i is the velocity of the atom. The variable $x_i(t)$ is the position of the atom in the absence of the constraint and $p_i(t)$ is the perturbation due to the holonomic constraint [37]. Noting that:

$$p_i(t) = \frac{F_i^c(t - \Delta t)}{m_i} (\Delta t)^2$$

from Eq. (4), and

$$F_i^c(t - \Delta t) = \frac{2\lambda m_i}{\langle m \rangle} \{X_i(t - \Delta t) - X_{Fi}\}$$

from Eq. (3), and defining

$$\gamma = \frac{2(\Delta t)^2 \lambda}{\langle m \rangle}$$

we get:

$$p_i(t) = \gamma [X_i(t - \Delta t) - X_{Fi}]. \quad (5)$$

Hence the perturbation on each atom is now simply the product of a Δt dependent scaling factor γ and the difference in position between the current and previous time

step. In order to obtain γ (and hence λ), substitute Eq. (4) into the original constraint Eq. (2) to get:

$$\Phi[\underline{X}(t)] = \sum [\underline{X}_i(t) - \underline{X}_{Fi}]^2 - \underline{\rho}^2(t) = 0.$$

Which can be written as:

$$\sum \left[\left\{ \underline{x}_i(t) + \underline{p}_i(t) \right\} - \underline{X}_{Fi} \right]^2 - \underline{\rho}^2(t) = 0,$$

and further simplified as:

$$\begin{aligned} & \sum \left[\left\{ \underline{x}_i(t) + \underline{p}_i(t) \right\}^2 \right. \\ & \quad - 2 \left\{ \underline{x}_i(t) + \underline{p}_i(t) \right\} \underline{X}_{Fi} - \underline{X}_{Fi}^2 \left. \right] \\ & \quad - \underline{\rho}^2(t) = 0 \\ & \sum \left[\left\{ \underline{x}_i^2(t) + \underline{p}_i^2(t) + 2\underline{x}_i(t)\underline{p}_i(t) \right\} \right. \\ & \quad - 2\underline{x}_i(t)\underline{X}_{Fi} - 2\underline{p}_i(t)\underline{X}_{Fi} - \underline{X}_{Fi}^2 \left. \right] \\ & \quad - \underline{\rho}^2(t) = 0 \\ & \sum \left[\left\{ \underline{p}_i^2(t) + 2\underline{x}_i(t)\underline{p}_i(t) - 2\underline{p}_i(t)\underline{X}_{Fi} \right\} \right. \\ & \quad + \underline{x}_i^2(t) - 2\underline{x}_i(t)\underline{X}_{Fi} + \underline{X}_{Fi}^2 \left. \right] \\ & \quad - \underline{\rho}^2(t) = 0 \\ & \sum \left[\underline{p}_i^2(t) + 2\underline{p}_i(t)\{\underline{x}_i(t) - \underline{X}_{Fi}\} \right] \\ & \quad + \sum [\underline{x}_i(t) - \underline{X}_{Fi}]^2 - \underline{\rho}^2(t) = 0. \end{aligned} \quad (6)$$

Using Eq. (5) into (6) yields:

$$\begin{aligned} & \sum [\gamma^2 \{\underline{X}_i(t - \Delta t) - \underline{X}_{Fi}\}^2 + 2\gamma \{\underline{X}_i(t - \Delta t) - \underline{X}_{Fi}\} \\ & \quad \cdot \{\underline{x}_i(t) - \underline{X}_{Fi}\}] + \sum [\underline{x}_i(t) - \underline{X}_{Fi}]^2 - \underline{\rho}^2(t) = 0, \end{aligned}$$

which can be rearranged as –

$$\begin{aligned} & \gamma^2 \sum [\{\underline{X}_i(t - \Delta t) - \underline{X}_{Fi}\}^2] \\ & + \gamma \sum 2[\{\underline{X}_i(t - \Delta t) - \underline{X}_{Fi}\}\{\underline{x}_i(t) - \underline{X}_{Fi}\}] \\ & + \sum [\underline{x}_i(t) - \underline{X}_{Fi}]^2 - \underline{\rho}^2(t) = 0. \end{aligned} \quad (7)$$

Defining,

$$\begin{aligned} a &= \sum [\{\underline{X}_i(t - \Delta t) - \underline{X}_{Fi}\}^2], \\ b &= 2 \sum [\{\underline{X}_i(t - \Delta t) - \underline{X}_{Fi}\}\{\underline{x}_i(t) - \underline{X}_{Fi}\}]. \end{aligned}$$

And noting that:

$$\Phi[\underline{x}(t)] = \sum [\underline{x}_i(t) - \underline{X}_{Fi}]^2 - \underline{\rho}^2(t).$$

Equation (7) can be simply written as –

$$a\gamma^2 + b\gamma + \Phi[\underline{x}(t)] = 0. \quad (8)$$

The Eq. (8) yields two roots for γ . In order to minimize the total perturbation $\sum |p_i|$ (from Eq. (5)), the root with lower absolute value is chosen.

The RMSD is decreased by a predetermined (and user defined) value at each time step by a value of $\Delta\rho$ as:

$$\rho(t) = \rho(t - \Delta t) - \Delta\rho. \quad (9)$$

The TMD algorithm steps are:

- (i) Set $\rho = \rho_0 = |\mathbf{x}_I - \mathbf{x}_F|$ where I is the initial and F is the final conformation.
- (ii) Numerically solve the equations of motion with the additional constraint force F^c .
- (iii) After each time step Δt , diminish ρ as in Eq. (9).

At the end of the simulation, the final distance ρ_f is reached. In this way, a monotonous reduction of ρ forces the system to find a pathway from \mathbf{x}_I to a final configuration \mathbf{x}_F .

Simulation Results and Discussion

Molecular Dynamics Simulations were performed on VPL peptides in order to study the performance of the nanoactuator. Specifically, a fragment from the VPL segment, the loop36 was chosen for these studies due to its established role in the conformational change [11]. The large conformational change was simulated using the Targeted Molecular Dynamics (TMD) technique. The TMD analyzes were performed using implicit solvent conditions. In order to simulate the effect of environmental pH change on the VPL motor protein, acidic amino acids were protonated. In the TMD simulations the protein was allowed to undergo a transition from one known state to another. This is a useful approach to ensure the feasibility of the conformational change and to get an idea of the magnitude of the energy change involved. The VPL nanoactuator works in a solution where there are protons bombarding the protein due to a reduction in the solution pH. This allows acidic amino acids in the protein to accept the protons on their negatively charged sites, and hence get protonated. Protonation changes the energy balance of the solvent-protein system and can create conditions that promote a conformational change. Low pH simulations on the small fragment loop36 were performed to study the effect on the protein conformation and the way it interacts energetically with its surroundings.

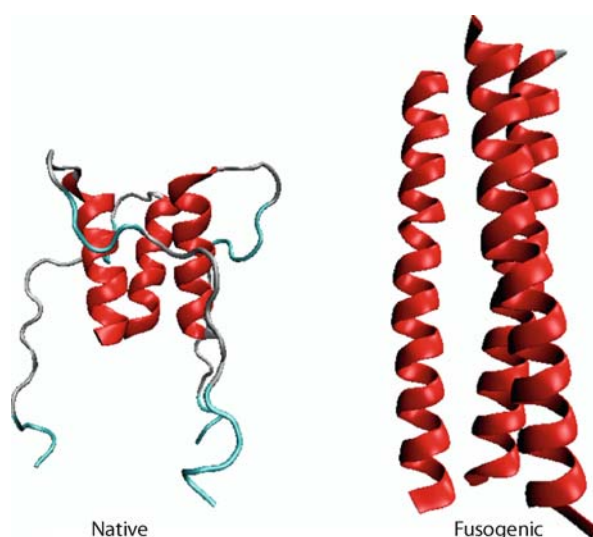
In addition to the TMD analyzes, classical molecular dynamics approaches were performed to quantify some

other aspects such as helicity and free energy of the peptides. In order to be able to perform classical unbiased MD simulations in a realistic time scale, it is important to energize the system by using high temperatures. The open and closed structures were taken from the protein data bank (PDB) with the open state as the target state and the closed state as the starting point [16]. The simulations were performed using an implicit solvation model known as Effective Energy Function for proteins EEF1 [24].

Structural Details of Loop36

Loop36 is a 36 residue long peptide of the VPL protein that forms a hinge region of the viral protein joining the two α -helical regions of each monomer [8,11]. An initial state as obtained from PDB [6] file 1HGF at pH of about 7.0, loop36 consists of a 15 residue long α -helical part with the remaining fragment in a random and flabby form (Fig. 8). It is located in the segment B of the Influenza Hemagglutinin protein sequence from residues 54 to 89. It has been recognized as being critical for a pH dependent conformational change [10,11]. The loop36 wild type (naturally occurring) sequence is as follows:

ARG VAL ILE GLU LYS THR ASN GLU LYS PHE
HIS GLN ILE GLU LYS GLU PHE SER GLU VAL GLU
GLY ARG ILE GLN ASP LEU GLU LYS TYR VAL GLU
ASP THR LYS ILE



Viral Protein Nano-Actuators, Computational Studies of Bio-nanomachines, Figure 8

The peptide loop36 in the initial and final states of the conformational change. Coiled coils are shown in red and the random loop regions in white and cyan. The random loop regions rise and convert into α -helical coiled coils upon activation

The initial and final states of loop36 as obtained by the crystal structures 1HGF (pH \sim 7.0) and 1HTM (pH \sim 5.0) from PDB are shown in Fig. 8.

In order to simulate low pH, the biochemical response of certain amino acids to the acidic conditions was considered. Some amino acids are acidic in nature, some basic and some neutral; and they get protonated at different pH values. Out of the 20 constituent types of amino acids, Glutamic Acid (GLU), Aspartic Acid (ASP), and Histidine (HIS) are in their unprotonated states at neutral pH (7.0). There is only one histidine residue in loop36, whereas there are eight glutamic acid residues and two aspartic acid residues which make a large part of loop36. Hence, overall, there were eleven residues out of the 36 that were protonated.

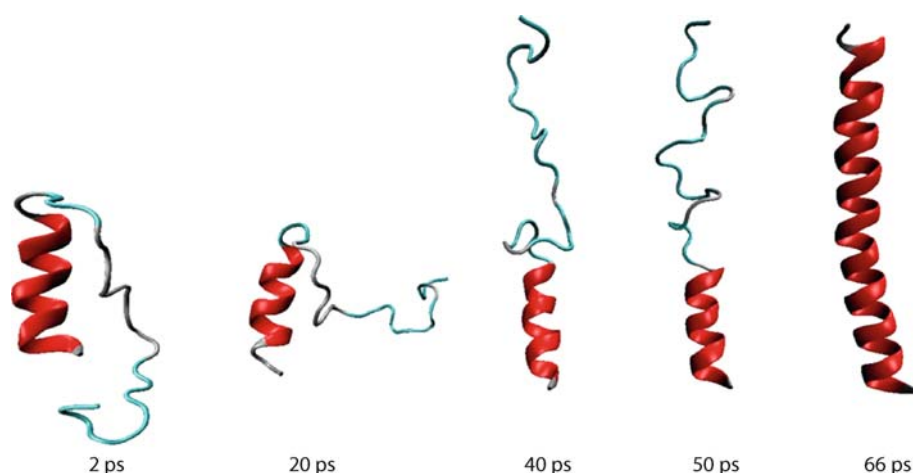
Figure 9 shows the Visual Molecular Dynamics (VMD) [21] rendered transition of a loop36 monomer from initial (closed) state to an open (fusogenic) state. The entire transition is achieved in 66 picoseconds when using TMD, while it is not achievable in 30 nanoseconds using traditional MD techniques. As seen in the figure, after 20 ps the loop regions of the peptide are halfway open and after 50 ps they are completely opened but have not attained an α -helical conformation.

The deviation of the final state from the initial state of the monomer in Fig. 9 can be seen in the root mean square deviation (RMSD) from the open state. Results are depicted in Fig. 10 and values of RMSD indicate that the open and close conformation differ by approximately 19 Å. The rate of opening of the monomer can be estimated by the slope of this curve which in this case is 0.2 Å/ps. It must be kept in mind that to have an estimation of the real rate of opening, this value should be rescaled to account for the increase in speed of the process given by TMD.

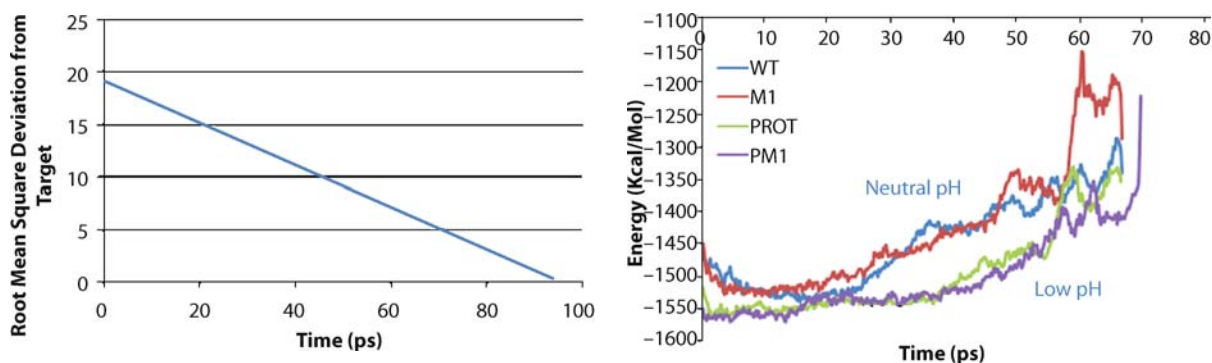
Mutational Analysis

Mutations in a protein can be made by replacing one or more constituent amino acids with different amino acids. The structure and properties of a protein change when they undergo a mutation. It is therefore possible to design a protein according to specific requirements; for example, if a high hydrophobicity is desired, hydrophobic amino acids should replace some of the residues.

The loop36 peptide contains one Glycine residue which is known as a helix-breaker amino acid because its side chain is simply one hydrogen atom. In experimental studies, it is observed that replacing this residue by an Alanine results in better α -helix formation [11]. In line with the experiments, in our simulations the Glycine is replaced



Viral Protein Nano-Actuators, Computational Studies of Bio-nanomachines, Figure 9
Transition of a loop36 monomer from native to fusogenic state during a TMD simulation



Viral Protein Nano-Actuators, Computational Studies of Bio-nanomachines, Figure 10

In the beginning the RMSD from the final state has a maximum value of about 19 Å and it decreases linearly with time as the open state is achieved due to the holonomic constraint applied by TMD

with the Alanine. The glycine (GLY) residue is the 22nd residue in loop36, and a mutated version of the loop36 with GLY replaced by alanine (ALA) is called mutation M1. The unmutated version of the peptide is simply called the wild type (WT). GLY contains no side chain and it has no atom attached to the α -carbon (CA). On the other hand, ALA contains a simple side chain (CH₃) attached to its CA atom.

The four different cases compared in this study are as follows:

- (i) the wild type (no mutation or protonation) guided to an open state
- (ii) one mutation M1
- (iii) protonation of amino acids (with no mutations), and

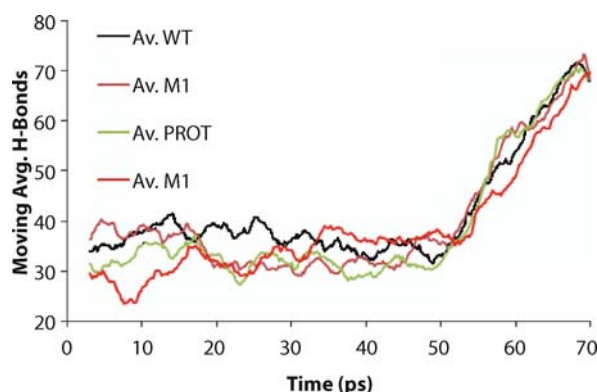
Viral Protein Nano-Actuators, Computational Studies of Bio-nanomachines, Figure 11

Comparison of potential energy paths of four types of loop36 monomers. (i) wild type WT (the protein in this state does not have any mutation or protonation), (ii) mutated type M1 (in this state, GLY (glycine) is replaced by ALA (alanine)), (iii) protonated type PROT (GLU (glutamic acid)) is replaced by protonated GLU, ASP (aspartic acid) by protonated ASP, HIS (histidine) replaced by doubly protonated histidine and (iv) protonated and mutated type PM1 (in this state, the protein has both protonation and mutation). The low pH structures follow lower energy pathways than the neutral pH structures although all structures eventually achieve similar endstate energy values

- (iv) mutation and protonation (PM1). Conformational energies of these simulations are compared in Fig. 11.

H-Bond Analysis

The intra-helical H-bonds stabilize α -helical structures. The hydrogen bonds for the loop36 conformational transition (Fig. 12) were found to be oscillatory in nature and hence a moving average with a period of 15 time units was



Viral Protein Nano-Actuators, Computational Studies of Bio-nanomachines, Figure 12

The number of H-bonds in each of the monomer WT, M1, PROT and PM1 modified structures varies as the open state is achieved. A moving average of 15 points (3 ps) is shown in each curve. The H-bonds oscillate around a constant value up to about 50 ps in each of the cases. A steep rise in the number is observed beyond this point. This region corresponds to the helix formation which results in intra-helical H-bond formation

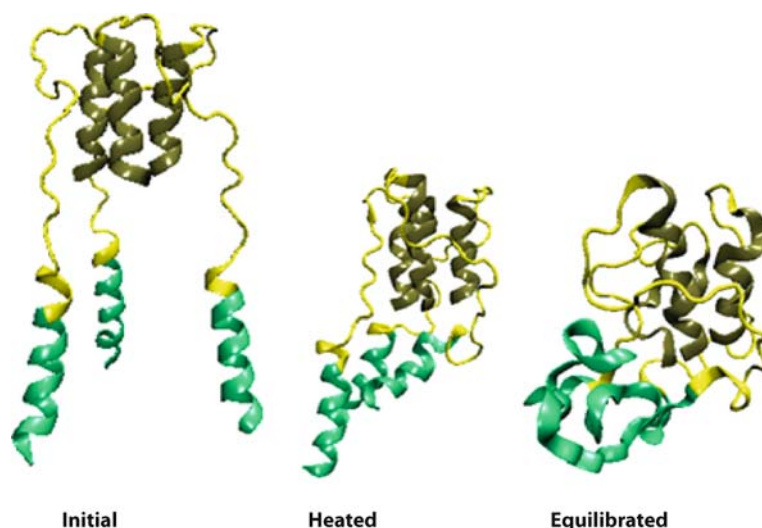
chosen. Each observation was made every 0.2 ps hence 15 points correspond to 3 ps time interval. In the initial stages of the simulation (time < 50 ps) the partial helix of loop36 is the only region with a significant number of H-bonds. The random loop region is converted into α -helix beyond 50 ps and hence a steep increase in the numbers is observed. The variation in the open state contacts, namely

the H-bonds quantitatively describe the achievement of the open state.

Classical Molecular Dynamics Studies

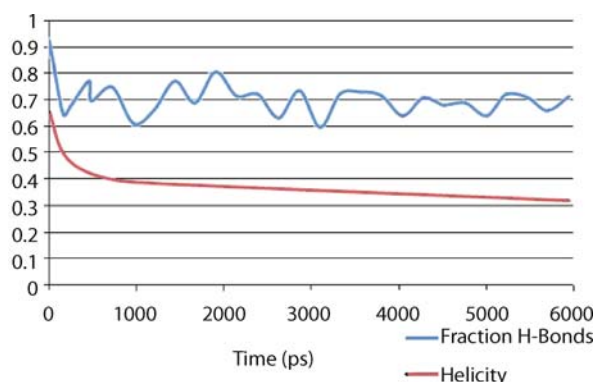
Even though classical methods cannot capture a large conformational change such as that exhibited in the VPL nanoactuator they provide insight into important structural details and properties. Typically higher temperatures are used to accelerate structural events in macromolecule simulations. When the protein is exposed to high temperatures, not only can it fold/unfold but it may also become denatured. Heating a protein corresponds to increasing the kinetic energy of its atoms, and this, in turn causes the molecules to vibrate more, possibly disrupting many of the hydrogen bonds and non-polar interactions and hence the secondary structure of the protein. The classical simulations on VPL protein were performed to understand the behavior of the VPL trimer at elevated temperatures. Knowledge of this will also help to ascertain whether there is a range of temperatures in which changes of structure such as folding or α -helix formation were initiated, before the protein denatures [15]. Figure 13 shows temperature effects on the VPL trimer loop50, which is an extended loop36 trimer. In contrast to the TMD simulations in which the open state was achievable in about 60 ps, the classical simulations need an approximate time of the order of few microseconds to achieve the same results [18].

It has been shown experimentally [28] that viral membrane fusion in the hemagglutinin of influenza virus oc-



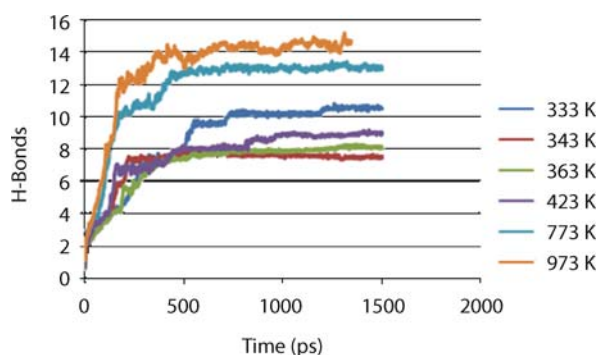
Viral Protein Nano-Actuators, Computational Studies of Bio-nanomachines, Figure 13

Effect of temperature on VPL peptide. The heated state corresponds to 500 °C temperature achieved in 150 ps and the equilibrated state corresponds to a constant temperature equilibration for up to 6 ns. The peptide gets denatured at this point



Viral Protein Nano-Actuators, Computational Studies of Bio-nanomachines, Figure 14

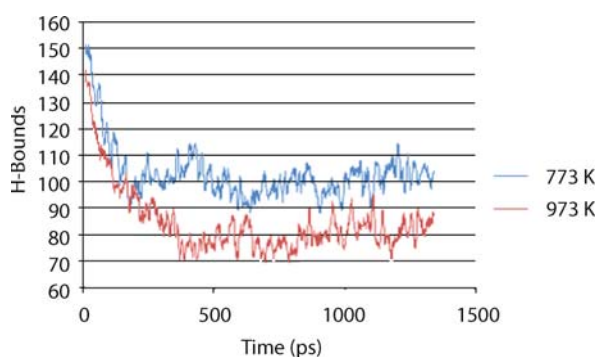
Helicity and fraction of open state contacts for a 6 ns classical high temperature molecular dynamics simulation



Viral Protein Nano-Actuators, Computational Studies of Bio-nanomachines, Figure 15

RMSD of the loop50 trimer from its initial state for each of the simulations ranging from 333 K to 973 K. Higher temperatures take the peptide further away from the initial state which indicates a larger conformational change. However, there is significant denaturation of the peptide at 773 K and 973 K

occurs at 335 K. The loop50 trimer was subjected to a range of simulated temperatures ranging from 333 K to 973 K with an attempt to capture the conformational changes required for fusion and hence the performance of the VPL nanoactuator. The RMSD from the initial equilibrated state at various temperatures is shown in Fig. 15. The expected trend would be that increasing temperature increases the RMSD from the initial state as it allows the peptide to jump energy barriers and denatures it. This was observed in simulations at 773 K and 973 K. However, the 333 K simulation indicates that the peptide has a larger difference with the initial state (larger RMSD values) in the same time frame than those at 343 K, 363 K and 423 K. This result is in agreement with the experimental observation and suggests that larger conformational changes may



Viral Protein Nano-Actuators, Computational Studies of Bio-nanomachines, Figure 16

H-bonding data for the conformational changes achieved at 773 K and 973 K. The higher temperature results in loss of H-bonds

take place in the temperature range of 333–343 K [11]. The extremely high temperatures 773 K and 973 K result in denaturation of the peptides as seen by the H-bond data in Fig. 16.

Conclusions

The recent explosion in nanotechnology has given place to the creation of biomolecular machines and motors such as viral protein linear actuators (VPL). The idea of the VPL motors, whose constituent proteins belong to a family of retroviruses such as HIV and influenza virus, originates from the mechanism they utilize to infect a cell. When these types of viruses are endocytosed by the cell, they experience a drop in pH and change their structure from a coil strand to an alpha helix conformation. In order to exploit the functional mechanism of viral proteins, it is important to characterize and understand the sensing capabilities of the peptides under different conditions of the environment. In this study, some aspects of the response of the VPL motor to different stimuli, using molecular dynamics have been illustrated. For the study of nanoactuators, in particular, molecular simulations provide a very valuable tool, especially since sometimes; experiments at the nanoscale may not be simple to perform. Alteration to the protein sequence (mutations) is a good example of a process in which computational studies are much easier to perform than experimental ones due to the complexities involved. One of the challenges is to learn how to control structural mechanisms, behavior and properties of the basic nanocomponents involved in molecular motors. In this study we learn about changes in the structure experienced by the viral protein actuator monomer as it interacts with other monomers in con-

ditions of trimerization, mutation of its sequence, and changes in temperature.

The VPL undergoes a remarkably large conformational change upon a drop in pH. In order to simulate the motion of the protein, targeted and traditional MD techniques are employed. Structural changes induced by pH variations are studied by protonating a number of amino acids in the peptide sequence. The TMD results showed a clear preference to conformational transition paths at low pH values. Our findings confirm that the protein forms a helical coil at acidic pH values but it shows a coiled structure at neutral pH. More studies are needed to establish conclusive results on the effect of pH and mutations.

The experimental observation that influenza hemagglutinin peptides showed a conformational change with a significant formation of alpha helix occurs in the wild type (unmutated) at 65°C at neutral pH [10]. In our simulations of a reduced loop50 trimer, this conformational change was not captured within 6 ns. Given the remarkably short time frames of our simulations and the size of the peptides, we are unable to observe regeneration of alpha helix. Even more, in order to be able to observe visible conformational changes, we had to work at very high temperatures. Even at that value of the temperature we do not see complete denaturation, again due to the short time frames under study. In an experimental situation the protein denatures at a much lower value of the temperature (at approximately 71°C). At these relatively low temperatures, a much longer time scale (micro- or even millisecond is required to fully capture alpha helix regeneration.

It is important to mention that high temperature approaches remain a valuable tool for conformational exploration; one must understand, however, that torsional transition kinetics are not correct at higher temperatures. Furthermore, rescaling to lower temperatures yields only approximate results. In spite of this, our goal is to present a methodology for studying large conformational changes in nanoscale molecular systems using both targeted and traditional molecular dynamics techniques that can ultimately be extended to much longer time frames using parallel computing.

We are at the dawn of a new era in the development of molecular machinery, and we are just starting to elucidate some of the challenges that these nanoactuators represent. Future studies will involve investigating interfacing with other molecular components such as carbon nanotubes, biological membranes, inorganic substrates, ions etc. As mentioned earlier, the end-effector of VPL can be designed according to the requirement. Moreover, the composition of the peptide can be varied according to the environ-

ment, as long as the rules of having hydrophobic and polar residues to ensure stability of the coiled-coil system are adhered to. The length of the VPL peptides, the role of the solvent (and solvent composition), binding energies to various target objects, are other variables that need to be investigated in order to assess conditions for optimum performance, (i. e. for example maximum force and stability, a given velocity etc.)

The VPL peptides are known to work better with specific mutations [11]. This opens up doors for further mutational analysis of the peptide, again directed towards achieving optimal performance parameters. The goal will be to determine the optimal sequence of the VPL peptide that results in the most stable, quickest, powerful and robust nanoactuator.

Future Directions

The future of this study involves the use of larger peptides, employment of better computational algorithms and interfacing of the VPL nanoactuator to other nanodevices to produce complex nanosystems. This work has shown great potential for further research. Better algorithms need to be developed for the study of the forces exerted by the nanoactuator. These studies have concentrated on developing a suitable approach to characterize and study conformational changes of loop36 and loop50. Preliminary studies have shown that longer peptides, such as loop114 (an extended version of loop50) are promising nanoactuator candidates as they provide a larger displacement (~ 9 nm) and they have a larger helical structure. The added secondary structure may provide more stability and larger forces to the actuator.

Mutations M1 to M7 were applied to loop36. Future studies will involve mutations to loop50 and larger peptides, which provide more mutation points and can significantly alter the performance of the actuator. The VPL nanoactuator can also be interfaced with other protein/lipid based molecular platform/devices such as lipid bilayer membranes. A possible scenario is to attach a cysteine tag to the end of VPL peptide and a lipid bilayer via a disulfide bond. TMD and Steered Molecular Dynamics (SMD) [22] can be used to study the performance of the nanoactuator while bound to a platform.

The TMD algorithm that was used to simulate conformational changes by applying a bias in the force field in this study has recently been succeeded by an updated restricted perturbation TMD (RP-TMD) [37] algorithm. The RP-TMD method depends not only on reduction of RMSD at each time step, but also on the minimal energy path. The two-way check yields lower energy pathways

for the trajectories. The TMD algorithm has a few disadvantages:

- (i) Transition is based solely on RMSD, which is a geometric parameter. No attempt is made to ensure that the conformational transition follows the minimum possible energy pathway.
- (ii) Due to the above, large energy barriers are crossed which may not be realistic.
- (iii) Some trajectories obtained are not reversible.

In the RP-TMD method, the above deficiencies are considerably reduced.

Acknowledgments

The authors gratefully acknowledge support of the National Science Foundation (Grant NSF NIRT #0303950).

Bibliography

1. Allen M, Tildesley D (1987) *Computer Simulation of Liquids*. Oxford University Press, New York
2. Apostolakis J, Ferrara P, Caflisch A (1999) Calculation of conformational transitions and barriers in solvated systems: application to the alanine dipeptide in water. *J Chem Phys* 110(4):2099–2108
3. Baker KA et al (1999) Structural basis for paramyxovirus-mediated membrane fusion. *Mol Cell* 3(3):309–19
4. Balzani VV et al (2000) Artificial Molecular Machines. *Angew Chem Int Edn Engl* 39(19):3348–3391
5. Berg HC (2003) The Rotary Motor of Bacterial Flagella. *Annu Rev Biochem* 72:19–54
6. Berman HM et al (2000) The Protein Data Bank. *Nucl Acids Res* 28(1):235–42
7. Boyer PD (1998) Energy, life, and ATP. *Biosci Rep* 18(3):97–117
8. Bullough PA et al (1994) Structure of influenza haemagglutinin at the pH of membrane fusion. *Nature* 371(6492):37–43
9. Caffrey M et al (1998) Three-dimensional solution structure of the 44 kDa ectodomain of SIV gp41. *EMBO J* 17(16):4572–84
10. Carr CM, Chaudhry C, Kim PS (1997) Influenza hemagglutinin is spring-loaded by a metastable native conformation. *Proc Natl Acad Sci USA* 94(26):14306–13
11. Carr CM, Kim PS (1993) A spring-loaded mechanism for the conformational change of influenza hemagglutinin. *Cell* 73(4):823–32
12. Chan DC et al (1997) Core structure of gp41 from the HIV envelope glycoprotein. *Cell* 89(2):263–73
13. Colman PM, Lawrence MC (2003) The structural biology of type I viral membrane fusion. *Nat Rev Mol Cell Biol* 4(4):309–19
14. Daidone I et al (2003) Molecular Dynamics Simulation of Protein Folding by Essential Dynamics Sampling: Folding Landscape of Horse Heart Cytochrome c. *Biophys J* 85(5):2865–2871
15. Dubey A, Mavroidis C, Tomassone MS (2006) Molecular Dynamic Studies of Viral-Protein Based Nano-Actuators. *J Comput Theor Nanosci* 3:885
16. Dubey A, Sharma G, Mavroidis C, Tomassone MS, Nikitczuk K, Yarmush ML (2004) Computational Studies of Viral Protein Nano-Actuator. *J Comput Theor Nanosci* 1(1):1–11
17. Ferrara P, Apostolakis J, Caflisch A (2000) Targeted Molecular Dynamics Simulations of Protein Folding. *J Phys Chem B* 104:4511–4518
18. Ferrara P, Apostolakis J, Caflisch A (2000) Thermodynamics and Kinetics of Folding of Two Model Peptides Investigated by Molecular Dynamics Simulations. *J Phys Chem B* 104(20):5000–5010
19. Hamelberg D, Mongan J, McCammon JA (2004) Accelerated molecular dynamics: a promising and efficient simulation method for biomolecules. *J Chem Phys* 120(24):11919–29
20. Harvey SC, Gabb HA (1993) Conformational transitions using molecular dynamics with minimum biasing. *Biopolymers* 33(8):1167–72
21. Humphrey W, Dalke A, Schulten K (1996) VMD: visual molecular dynamics. *J Mol Graph* 14(1):27–8, 33–8
22. Isralewitz B, Gao M, Schulten K (2001) Steered molecular dynamics and mechanical functions of proteins. *Curr Opin Struct Biol* 11(2):224–230
23. Kobe B et al (1999) Crystal structure of human T cell leukemia virus type 1 gp21 ectodomain crystallized as a maltose-binding protein chimera reveals structural evolution of retroviral transmembrane proteins. *Proc Natl Acad Sci USA* 96(8):4319–24
24. Lazaridis T, Karplus M (1999) Effective energy function for proteins in solution. *Proteins* 35(2):133–52
25. Lazarowitz SG, Compans RW, Choppin PW (1971) Influenza virus structural and nonstructural proteins in infected cells and their plasma membranes. *Virology* 46(3):830–43
26. Oster G, Wang H (2003) Rotary protein motors. *Trends Cell Biol* 13(3):114–21
27. Paci E, Karplus M (1999) Forced unfolding of fibronectin type 3 modules: an analysis by biased molecular dynamics simulations. *J Mol Biol* 288(3):441–59
28. Ruigrok RW et al (1986) Conformational changes in the hemagglutinin of influenza virus which accompany heat-induced fusion of virus with liposomes. *Virology* 155(2):484–97
29. Schlitter J (1994) Targeted Molecular Dynamics: A New Approach for Searching Pathways of Conformational Transitions. *J Mol Graph* 12:84–89
30. Schlitter JEM, Krüger P, Jacoby E, Wollmer A (1993) Targeted molecular dynamics simulation of conformational change: application to the T \leftrightarrow R transition in insulin. *Mol Simul* 10(2–6):291–308
31. Schoch C, Blumenthal R, Clague MJ (1992) A long-lived state for influenza virus-erythrocyte complexes committed to fusion at neutral pH. *FEBS Lett* 311(3):221–5
32. Seeman NC (2003) DNA in a material world. *Nature* 421(6921):427–31
33. Singh M, Berger B, Kim PS (1999) LearnCoil-VMF: computational evidence for coiled-coil-like motifs in many viral membrane-fusion proteins. *J Mol Biol* 290(5):1031–41
34. Skehel JJ, Waterfield MD (1975) Studies on the primary structure of the influenza virus hemagglutinin. *Proc Natl Acad Sci USA* 72(1):93–7
35. Skehel JJ, Wiley DC (2000) Receptor binding and membrane fusion in virus entry: the influenza hemagglutinin. *Annu Rev Biochem* 69:531–69
36. Tobias DJ, Brooks CL III (1988) Molecular dynamics with internal coordinate constraints. *J Chem Phys* 89:5115–5127
37. van der Vaart A, Karplus M (2005) Simulation of conformational

transitions by the restricted perturbation-targeted molecular dynamics method. *J Chem Phys* 122:114903

38. Vale RD, Milligan RA (2000) The way things move: looking under the hood of molecular motor proteins. *Science* 288(5463):88–95
39. Walker JE (1998) ATP Synthesis by Rotary Catalysis (Nobel Lecture). *Angew Chem Int Edn* 37:2308–2319
40. Weis WI et al (1988) Structure of the influenza virus haemagglutinin complexed with its receptor, sialic acid. *Nature* 333(6172):426–31
41. Weis WI et al (1990) Refinement of the influenza virus hemagglutinin by simulated annealing. *J Mol Biol* 212(4):737–61
42. Weissenhorn W et al (1998) The central structural feature of the membrane fusion protein subunit from the Ebola virus glycoprotein is a long triple-stranded coiled coil. *Proc Natl Acad Sci USA* 95(11):6032–6
43. Weissenhorn W et al (1999) Structural basis for membrane fusion by enveloped viruses. *Mol Membr Biol* 16(1):3–9
44. Wiley DC, Skehel JJ (1987) The structure and function of the hemagglutinin membrane glycoprotein of influenza virus. *Annu Rev Biochem* 56:365–94
45. Wilson IA, Skehel JJ, Wiley DC (1981) Structure of the haemagglutinin membrane glycoprotein of influenza virus at 3 Å resolution. *Nature* 289(5796):366–73
46. Yang W et al (2003) The missing link between thermodynamics and structure in F1-ATPase. *Proc Natl Acad Sci USA* 100(3):874–9
47. Yurke B, Turberfield AJ, Mills AP, Simmel FC, Neumann JL (2000) A DNA-Fuelled Molecular Machine Made of DNA. *Nature* 415:62–65

Volcanic Eruptions: Cyclicity During Lava Dome Growth

OLEG MELNIK^{1,2}, R. STEPHEN J. SPARKS²,
ANTONIO COSTA^{2,3}, ALEXEI A. BARMIN¹

¹ Institute of Mechanics, Moscow State University,
Moscow, Russia

² Earth Science Department, University of Bristol,
Bristol, UK

³ Istituto Nazionale di Geofisica e Vulcanologia,
Naples, Italy

Article Outline

[Glossary](#)

[Definition of the Subject](#)

[Introduction](#)

[Dynamics of Magma Ascent During Extrusive Eruptions](#)

[Short-Term Cycles](#)

[Long-Term Cycles](#)

[Future Directions](#)

[Acknowledgments](#)

[Bibliography](#)

Glossary

Andesite Magma or volcanic rock is characterized by intermediate SiO₂ concentration. Andesite magmas have rheological properties that are intermediate between basalt and rhyolite magmas. Silica content in andesites ranges from approximately 52 to 66 weight percent. Common minerals in andesite include plagioclase, amphibole and pyroxene. Andesite is typically erupted at temperatures between 800 to 1000°C. Andesite is particularly common in subduction zones, where tectonic plates converge and water is introduced into the mantle.

Basalt Magma or volcanic rock contains not more than about 52% SiO₂ by weight. Basaltic magmas have a low viscosity. Volcanic gases can escape easily without generating high eruption columns. Basalt is typically erupted at temperatures between 1100 to 1250°C. Basalt flows cover about 70% of the Earth's surface and huge areas of the terrestrial planets and so are the most important of all crustal igneous rocks.

Bingham liquid is a fluid that does not flow in response to an applied stress until a critical yield stress is reached. Above the critical yield stress, strain rate is proportional to the applied stress, as in a Newtonian fluid.

Bubbly flow A multi-phase flow regime, in which the gas phase appears as bubbles suspended in a continuous liquid phase.

Conduit A channel, through which magma flows towards the Earth's surface. Volcanic conduits can commonly be approximately cylindrical and typically a few 10's meters across or bounded by near parallel sides in a magma-filled fracture. Conduits can be vertical or inclined.

Crystallization Conversion, partial or total, of a silicate melt into crystals during solidification of magma.

Degassing n. (degas v.) The process by which volatiles that are dissolved in silicate melts come out of solution in the form of bubbles. Open- and closed-system degassing can be distinguished. In the former, volatiles can be lost or gained by the system. In the latter, the total amount of volatiles in the bubbles and in solution in the magma is conserved.

Differentiation The process of changing the chemical composition of magma by processes of crystallization accompanied by separation melts from crystals.

Dome A steep-sided, commonly bulbous extrusion of lava or shallow intrusion (cryptodome). Domes are commonly, but not exclusively, composed of SiO₂-rich magmas. In dome-forming eruptions the erupted

magma is so viscous, or the discharge rate so slow, that lava accumulates very close to the vent region, rather than flowing away. Pyroclastic flows can be generated by collapse of lava domes. Recent eruptions producing lava domes include the 1995–2006 eruption of the Soufrière Hills volcano, Montserrat, and the 2004–2006 eruption of Mount St. Helens, USA.

Dyke A sheet-like igneous intrusion, commonly vertical or near vertical, that cuts across pre-existing, older, geological structures. During magmatism, dykes transport magma toward the surface or laterally in fracture-like conduits. In the geologic record, dykes are preserved as sheet-like bodies of igneous rocks.

Explosive eruption A volcanic eruption in which gas expansion tears the magma into numerous fragments with a wide range of sizes. The mixture of gas and entrained fragments flows upward and outward from volcanic vents at high speed into the atmosphere. Depending on the volume of erupted material, eruption intensity and sustainability, explosive eruptions are classified as Strombolian, Vulcanian, sub-Plinian, Plinian or Mega-Plinian; this order is approximately in the order of increasing intensity. Strombolian and Vulcanian eruptions involve very short-lived explosions.

Extrusive flow or eruption A non-explosive (non-pyroclastic) magma flow from a volcanic conduit during a lava dome-building eruption or lava flow.

Mafic Magma, lava, or tephra with silica concentrations of approximately $\text{SiO}_2 < 55\%$.

Magma Molten rock that consists of up three components: liquid silicate melt, suspended crystalline solids, and gas bubbles. It is the raw material of all volcanic processes. Silicate magmas are the most common magma type and consist of long, polymeric chains and rings of Si–O tetrahedra, between which are located cations (e.g. Ca^{2+} , Mg^{2+} , Fe^{2+} , and Na^+). Anions (e.g. OH^- , F^- , Cl^- , and S^-) can substitute for the oxygen in the silicate framework. The greater the silica (SiO_2) content of the magma, the more chains and rings of silicate tetrahedra there are to impede each other and hence the viscosity of the magma increases. The pressure regime and composition of the magma control the minerals that nucleate and crystallize from a magma when it cools or degasses.

Magma chamber A subsurface volume within which magma accumulates, differentiates and crystallizes. Igneous intrusions can constrain the form and size of some magma chambers, but in general the shape and volume of magma chambers beneath active volcanoes are poorly known. Magma reservoir is an equivalent term.

Melt Liquid part of magma. Melts (usually silicate) contain variable amounts of dissolved volatiles. The primary volatiles are usually water and carbon dioxide.

Newtonian liquid A liquid for which the strain rate is proportional to the applied stress. The proportionality coefficient is called the viscosity.

Microlite Crystal with dimensions less than 100 μm . Usually microlites crystallize at shallow levels of magmatic system.

Phenocryst Crystal with dimensions larger than 100 μm . Usually phenocrysts grow in magmatic reservoirs prior to an eruption and or are entrained by magma in the chamber.

Pyroclastic flow or surge A gas-particle flow of pyroclasts suspended in a mixture of hot air, magmatic gas, and fine ash. The flow originates by the gravitational collapse of a dense, turbulent explosive eruption column at the source vent, or by dome collapse, and moves down-slope as a coherent flow. Pyroclastic flows and surges are distinguished by particle concentration in the flow, surges being more dilute. Variations in particle concentration result in differences in the deposits left by flows and surges.

Silicic Magma, lava, or tephra with silica concentrations of approximately $\text{SiO}_2 > 55\%$. The magmas are commonly rich in Al, Na- and K- bearing minerals. Silicic magmas are typically very viscous and can have high volatile contents. Rhyolite is an example of a silicic magma.

Volatile A component in a magmatic melt which can be partitioned in the gas phase in significant amounts during some stage of magma history. The most common volatile in magmas is water vapor H_2O , but there are commonly also significant quantities of CO_2 , SO_2 and halogens.

Definition of the Subject

We consider the process of slow extrusion of very viscous magma that forms lava domes. Dome-building eruptions are commonly associated with hazardous phenomena, including pyroclastic flows generated by dome collapses, explosive eruptions and volcanic blasts. These eruptions commonly display fairly regular alternations between periods of high and low or no activity with time scales from hours to years. Usually hazardous phenomena are associated with periods of high magma discharge rate, thus, understanding the causes of pulsatory activity during extrusive eruptions is an important step towards forecasting volcanic behavior, especially the transition to explosive activity when magma discharge rate increases by a few orders

of magnitude. In recent years the risks have increased because the population density in the vicinity of many active volcanoes has increased.

Introduction

Many volcanic eruptions involve the formation of lava domes, which are extrusions of very viscous, degassed magmas. The magma is so viscous that it accumulates close to the vent. Extrusion of lava domes is a slow and long-lived process, and can continue for many years or even decades [71,83,85]. Typical horizontal dimensions of lava domes are several hundred meters, heights are of an order of tens to several hundred meters, and volumes several million to hundreds of million cubic meters. Typical magma discharge rates (measured as the increase of dome volume with time in dense rock equivalent (DRE)) can reach up to 20–40 m³/s, but are usually below 10 m³/s [83].

Dome-building eruptions are commonly associated with hazardous phenomena, including pyroclastic flows and tsunamis generated by dome collapses, explosive eruptions and volcanic blasts. Dome-building eruptions can also contribute to edifice instability and sector collapse, as occurred on Montserrat on 26 December 1997 [87]. Lava dome activity can sometimes precede or follow major explosive eruptions; the eruption of Pinatubo, Philippines (1991) is an example of the former [37], and the eruption of Mount St. Helens, USA (1980–1986) is an example of the latter [89].

Several lava dome eruptions have been documented in detail and show quite complex behaviors. Substantial fluctuations in magma discharge rate have been documented. In some cases these fluctuations can be quite regular (nearly periodic), as in the extrusion of lava in 1980–1982 on Mount St. Helens [89] and in the 1922–2002 activity of the Santiaguito lava dome, Guatemala [35]. In these cases, periods of high magma discharge rate alternate with longer periods of low magma discharge rate or no extrusion. In some volcanoes, such as Shiveluch, Kamchatka, the intervals of no extrusion are so long compared with the periods of dome growth that the episodes of dome growth have been described as separate eruptions of the volcano rather than episodes of the same eruption. Other dome-building activity can be nearly continuous and relatively steady, as observed at Mount St. Helens in 1983 [89] and at the Soufrière Hills Volcano, Montserrat between November 1999 and July 2003. In yet other cases the behavior can be more complex with quite sudden changes in magma discharge rate, which cannot be related to any well-defined regularity or pattern (e. g. Lascar volcano, Chile, [57]).

Pauses during lava dome-building eruptions are quite common. For example, at Mount St. Helens there were 9 pulses of dome growth with a period of ~74 days, a duration of 1–7 days and no growth in between [89]. The Soufrière Hills Volcano Montserrat experienced a long (20 months) pause in extrusion after the first episode of growth [72]. On Shiveluch volcano in Kamchatka episodes of dome growth occurred in 1980, 1993 and 2000, following a major explosion in 1964 [28]. Each episode of dome growth began with magma discharge rate increasing over the first few weeks to a peak of 8–15 m³/s, with a gradual decline in magma discharge rate over the following year. In between the episodes very minimal activity was recorded.

Fluctuations in magma discharge rate have been documented on a variety of time-scales from both qualitative and quantitative observations. Several lava dome eruptions are characterized by extrusion of multiple lobes and flow units [68,94]. In the case of the Soufrière Hills Volcano, extrusion of shear lobes can be related to spurts in discharge rate and is associated with other geophysical changes, such as onset of seismic swarms and marked changes in temporal patterns of ground tilt [90,91,94]. These spurts in discharge rate have been fairly regular for substantial periods, occurring every 6 to 7 weeks over a 7 month period in 1997 [21,87,91]. These spurts are commonly associated with large dome collapses and pyroclastic flows and, in some cases, with the onset of periods of repetitive Vulcanian explosions [14,26]. Consequently the recognition of this pattern has become significant for forecasting activity for hazard assessment purposes. In the Soufrière Hills Volcano and Mount Pinatubo much shorter fluctuations in magma discharge rate have been recognized from cyclic variations in seismicity, ground tilt, gas fluxes and rock-fall activity [23,91,93]. This cyclic activity has typical periods in the range of 4 to 36 hours. Cyclic activity has been attributed to cycles of gas pressurization and depressurization with surges in dome growth related to degassing, rheological stiffening and stick-slip behavior [23,49,61,91,98].

Dome eruptions can show transitions to explosive activity, which sometimes can be linked to spurts in magma discharge rate. For example, in 1980, periodic episodes of lava dome extrusion on Mount St. Helens were initiated by explosive eruptions, which partly destroyed the dome that had been extruded in each previous extrusion episode [89]. At Unzen Volcano, Japan a single Vulcanian explosive eruption occurred in June 1991 when the magma discharge rate was at its highest [68]. At the Soufrière Hills Volcano, repetitive series of Vulcanian explosions have occurred following large dome collapses in

periods when magma discharge rates were the highest of the eruption [26,88]. In the case of Lascar Volcano, Chile, an intense Plinian explosive eruption occurred on 18 and 19 April, 1993, after nine years of dome extrusion and occasional short-lived Vulcanian explosions [57].

Lava dome eruptions require magma with special physical properties. In order to produce a lava dome rather than a lava flow, the viscosity of the magma must be extremely high so that the lava cannot flow easily from the vent. High viscosity is a consequence of factors such as relatively low temperature (typically 750–900°C), melt compositions rich in network-forming components (principally Si and Al) efficient gas loss during magma decompression, and crystallization as a response to cooling and degassing. Viscosities of silica-rich magmas, such as rhyolites and some andesites, are increased by several orders of magnitude by the loss of dissolved water during decompression. Many, but not all, domes also have high crystal content (up to 60 to 95 vol%), with crystallization being triggered mostly by degassing [10,86]. In order to avoid fragmentation that leads to an explosive eruption, magma must have lost gas during ascent. Consider, for example, a magma at 150 MPa containing 5wt% of dissolved water decompressed to atmospheric pressure. Without gas loss the volume fraction of bubbles, will be more than 99%. Typical dome rock contains less than 20 vol% of bubbles, although there is evidence that magma at depth can be more bubble-rich (e.g., [13,74]). On the other hand, very commonly there is no change in temperature or bulk magma composition in the products of explosive and extrusive eruptions for a particular volcano. This suggests that the properties of magma that are conducive to the formation of lava domes are controlled by physico-chemical transformations that occurred during magma ascent to the surface.

Two other important factors that influence whether lava domes or flows form are topography and discharge rate. The same magma can form a dome if the discharge rate is low, and a lava flow if the rate is high [29,92]. The discharge rate is controlled by overall conduit resistance that is a function of viscosity, conduit size and shape, and driving pressure (the difference between chamber pressure and atmospheric pressure). Additionally the same magma can form a dome on low slopes, such as a flat crater (e.g. the mafic andesite dome of the Soufrière Volcano, St. Vincent; [40]) and a lava flow on steep slopes.

Prior to an eruption, magma is usually stored in a shallow crustal reservoir called a magma chamber. For several volcanoes magma chambers can be detected and characterized by earthquake locations, seismic tomography, petrology or interpretation of ground deformation

data [55]. Typical depths of magma chambers range from a few kilometers to tens of kilometers. Volumes range from less than one to several thousand km³ [55], but are usually less than a hundred km³. Magma chambers are connected to the surface by magma pathways called conduits. There is evidence that the conduits that feed lava dome eruptions can be both dykes or cylindrical. Dykes of a few meters width are commonly observed in the interior of eroded andesite volcanoes. Dyke feeders to lava domes have been intersected by drilling at Inyo crater, California, USA [56] and at Mount Unzen [67]. Geophysical studies point to dyke feeders; for example fault-plane solutions of shallow volcano-tectonic earthquakes indicate pressure fluctuations in dykes [75,76]. Deformation data at Unzen, combined with structural analysis, indicate that the 1991–1995 dome was fed by a dyke [68]. Dykes are also the only viable mechanism of developing a pathway through brittle crust from a deep magma chamber to the surface in the initial stages of an eruption [50,77].

Cylindrical conduits commonly develop during lava dome eruptions. The early stages of lava dome eruptions frequently involve phreatic and phreatomagmatic explosions that create near surface craters and cylindrical conduits [12,73,87,89,96,99]. These explosions are usually attributed to interaction of magma rising along a dyke with ground water. Cylindrical conduits formed by explosions are confined to relatively shallow parts of the crust, probably of order hundreds of meters depth and < 1 km, as indicated by mineralogical studies [73]. Examples of such initial conduit forming activity include Mount Usu (Japan) Mt. St. Helens, and Soufrière Hills Volcano [12,87,99]. Many lava dome eruptions are also characterized by Vulcanian, sub-Plinian and even Plinian explosive eruptions. Examples include Mount Unzen, Mount St. Helens, Santiaguito and Soufrière Hills Volcano [68,87,89,96]. Here the fragmentation front may reach to depths of several kilometers [54] with the possibility of cylindrical conduit development due to severe underpressurization and mechanical disruption of conduit wallrocks. Subsequently domes can be preferentially fed along the cylindrical conduits created by earlier explosive activity. On the Soufrière Hills Volcano, early dome growth was characterized by extrusion of spines with nearly cylindrical shape [87].

Observations of magma discharge rate variations on a variety of time-scales highlight the need to understand the underlying dynamic controls. Research has increasingly focused on modeling studies of conduit flow dynamics during lava-dome eruptions. We will restrict our discussions here to mechanisms that lead to cyclic and quasi-periodic fluctuations in magma discharge rate on various timescales, mainly focusing on long-term cycles. Issues

concerning the transition between explosive and extrusive activity are discussed in detail in [45,80,81,97] and in the special volume of *Journal of Volcanology and Geothermal Research* dedicated to modeling of explosive eruptions [79]. Several papers consider the processes that occur at the surface and relate dome morphology and dimensions with controlling parameters.

Combined theoretical, experimental and geological studies identify four main types of dome: spiny, lobate, platy, and axisymmetric [5,29,30]. These types of dome reflect different regimes which are controlled by discharge rates, cooling rates and yield strength, and the viscosity of the dome-forming material. In recent years mathematical modeling has been used to semi-quantitatively describe spreading of lava domes, including models based on the thin layer approximation [1,2] and fully 2D simulations of lava dome growth which account for visco-elastic and -plastic rheologies [32,33].

Dynamics of Magma Ascent During Extrusive Eruptions

In order to understand the causes of cyclic behavior during extrusive eruptions, first we need to consider the underlying dynamics of volcanic systems, and discuss physical and chemical transitions during magma ascent.

The physical framework for the model of a volcanic system is shown in Fig. 1. Magma is stored in a chamber at depth L , with a chamber pressure P_{ch} that is higher than hydrostatic pressure of magma column and drives magma ascent. Magma contains silicate melt, crystals and dissolved and possibly exsolved volatiles. During ascent of the magma up the conduit the pressure decreases and volatiles exsolve forming bubbles. As the bubble concentration becomes substantial, bubble coalescence take place and permeability develops [27,45], allowing gas to escape from ascending magma, both in vertical (through the magma) and horizontal (to conduit wallrocks) directions. If magma ascends slowly, gas escape results in a significant reduction of the volume fraction of bubbles; such a process is termed open system degassing. In comparison closed system degassing is characterized by a negligible gas escape. Reduction in bubble content, combined with relatively low gas pressures and efficient decoupling of the gas and melt phases, prevents magma fragmentation and, thus, development of explosive eruption [59,60,82].

Due to typical low ascent velocities (from millimeters to a few centimeters per second) magma ascent times to the Earth's surface from the magma chamber range from a several hours to many weeks. These ascent times are often comparable with the times that are re-

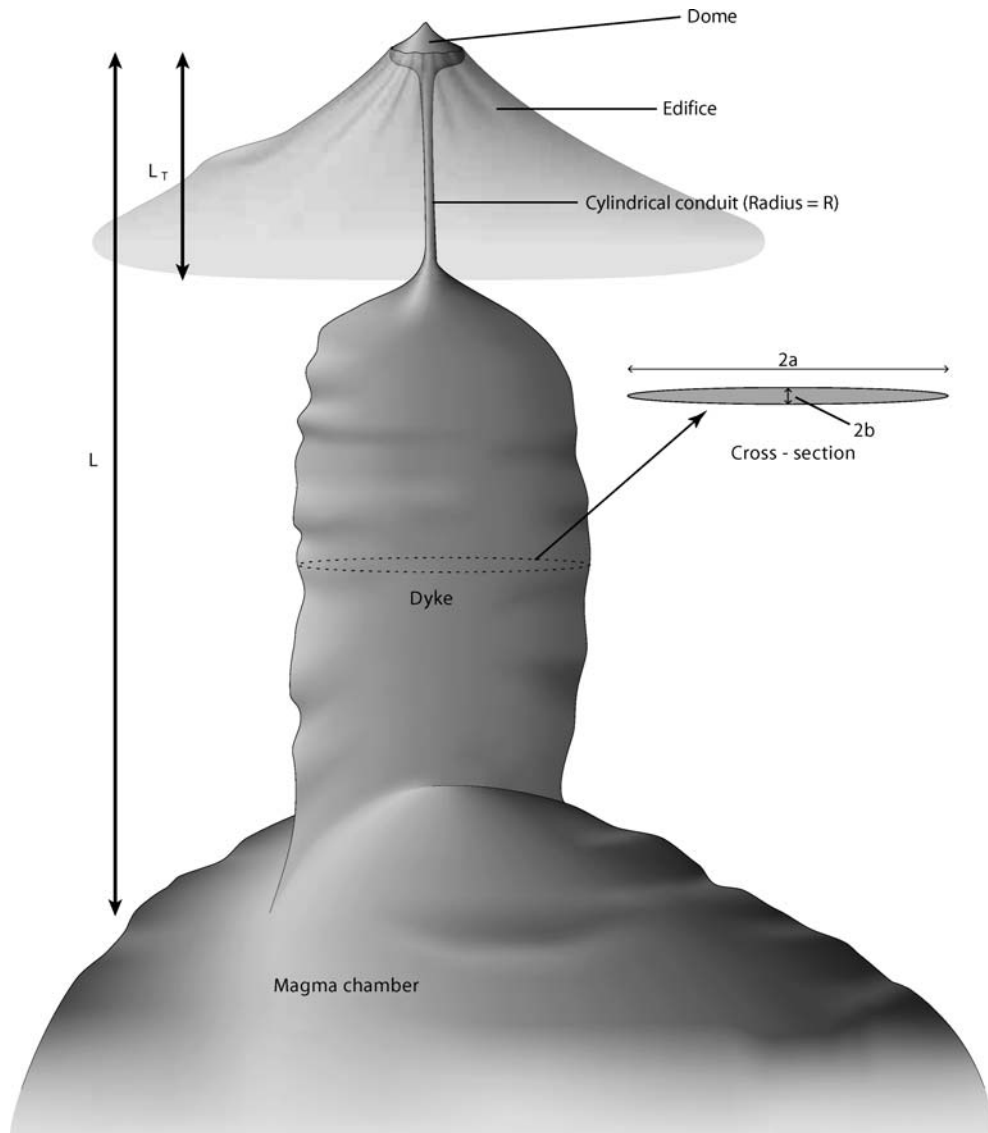
quired for crystals to grow significantly and for heat exchange between magma and wallrocks. The main driving force for crystallization is related to exsolution of volatiles from the magma, leading to increase in the liquidus temperature T_L , and development of magma undercooling $\Delta T = T_L - T$ [10]. Crystallization leads to release of latent heat, and magma temperature can increase with respect to the initial temperature [6]. As a consequence of increasing crystal content, magma viscosity increases by several orders of magnitude [16,20,21] and magma becomes a non-Newtonian fluid [78]. As will be shown later, crystallization induced by degassing can become a key process in causing variable flow rates.

Due to the long duration of extrusive eruptions, the magma chamber can be replenished with significant amounts of magma from underlying sources [41,65]. Replenishment can lead to pressure build-up in the magma chamber, volatile and heat exchange between host and new magmas. The composition of the magma can also change over time, due to differentiation, crustal rock assimilation, or magma mixing. Thus, any model that explains magma ascent dynamics needs to deal with many complexities. Of course there is no single model that can take into account all physical processes in a volcanic system. Additional complications arise from the fact that the physical properties of magma at high crystal contents, such as rheology or crystal growth kinetics and geometry of volcanic systems, are typically poorly constrained. Several issues regarding the dynamics of multiphase systems have not been resolved theoretically, especially for cases where the volume fractions of components of the multiphase system are comparable.

Below we will present a review of existing models that treat cyclic behavior during extrusive eruptions on different timescales.

Short-Term Cycles

Cyclic patterns of seismicity, ground deformation and volcanic activity (Fig. 2 from [23]) have been documented at Mount Pinatubo, Philippines, in 1991 [37] and Soufrière Hills volcano, Montserrat, British West Indies, in 1996–1997 [90,91]. At Soufrière Hills, periodicity in seismicity and tilt ranged from ~ 4 to 30 h, and the oscillations in both records continued for weeks. Cyclic behavior was first observed in the seismicity (RSAM) records beginning in July 1996, when the record of dome growth constrained the average supply rate to between 2 and 3 m³/s [88]. The oscillations in the RSAM records initially had low amplitudes, and no tilt-measurement station was close enough to the vent to detect any pressure oscillations in the con-



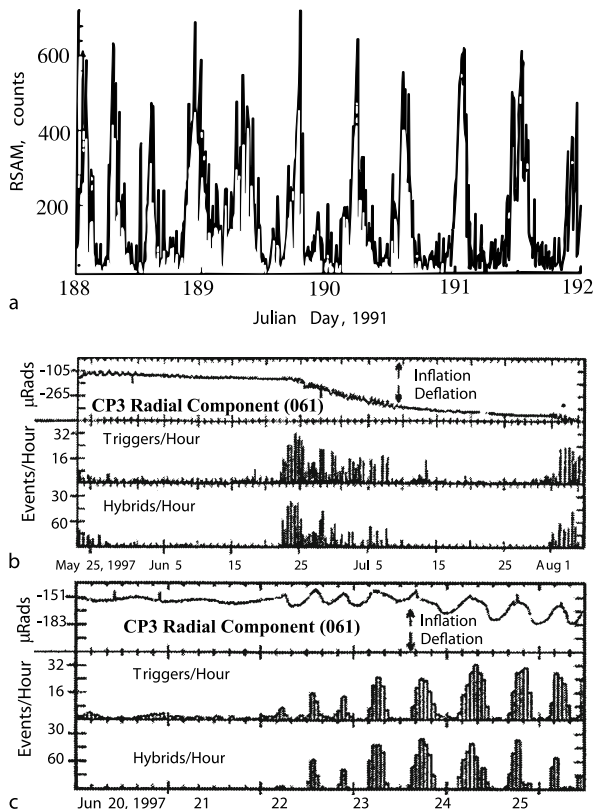
Volcanic Eruptions: Cyclicity During Lava Dome Growth, Figure 1

Schematic view of the volcanic system. In the upper part the conduit is cylindrical with a radius R . A transition from the cylinder to a dyke occurs at depth L_T . The length scale for the transition from cylinder to dyke is w_T . The dyke has an elliptical cross-section with semi-axis lengths a_0 and b_0 . The chamber is located a depth L . In the text we used also the following auxiliary variables: $D = 2R$ for conduit diameter, $L_d = L - L_T$ for the dyke vertical length, $W_d = 2a_0$ for the dyke width, and $H_d = 2b_0$ for the dyke thickness. After [20]

duit. By August 1996, RSAM records showed strong oscillatory seismicity at dome-growth rates between 3 and 4 m³/s. Tilt data, taken close enough to the vent (i.e., Chances Peak [90]) to be sensitive to conduit pressure oscillations, are only available for February 1997 and May–August 1997. In the latter period dome growth rate increase from ~5 m³/s in May to between 6 and 10 m³/s in August. Both near-vent tilt and RSAM displayed oscillatory behavior during this period and were strongly corre-

lated in time. Similar RSAM oscillations having periods of 7 to 10 h were observed at Mount Pinatubo following the climactic eruption in 1991 [37]. At both volcanoes, oscillation periods were observed that do not fit any multiple of Earth or ocean tides.

The cyclic activity at both Pinatubo and Soufrière Hills Volcano are strongly correlated with eruptive behavior and other geophysical phenomena. In the Pinatubo case and on Soufrière Hills Volcano in August, September and



Volcanic Eruptions: Cyclicity During Lava Dome Growth, Figure 2
 Examples of cyclic behavior in a lava dome eruption. RSAM records from Mt. Pinatubo, Philippines following its climatic eruption in June 1991 (a, after [23]). Radial tilt, triggered earthquakes, and hybrid earthquakes for 17 May to 6 August 1997, at Soufrière Hills Volcano (b, after [21,90]). Parts of three 5–7 week cycles are shown, with each cycle showing high amplitude tilt and seismicity pulsations with short time scale that last for several weeks after the start of the cycle. The onset of a cycle is rapid, as detailed in c for the cycle initiating on 22 June 1997

October 1997, the cycles were linked to short-lived volcanic explosions. In the case of the Soufrière Hills Volcano, explosions in August 1997 occurred at the peak in the tilt. The peak in tilt also marked the onset of episodes of increased rock falls [7,8] and [91] is attributed to increased magma discharge rates. SO_2 flux data show that the cycles are linked to surges in gas release, which reach a peak about an hour after the tilt peak [93]. Green et al. [31] have shown that several families of near identical long period earthquakes occur during the tilt cycle, starting at the inflexion point on the up-cycle and finishing before the inflexion point on the down-cycle.

Several models [23,49,70,98,98] have been proposed to explain the observed cyclicity. In these models [23,98] the conduit is divided into two parts. Magma is assumed to be

forced into the lower part of volcanic conduit at a constant rate. In Denlinger and Hoblitt [23] magma in the lower part of the conduit is assumed to be compressible. In Wylie et al. [98] the magma is incompressible but the cylindrical conduit is allowed to expand elastically. In both models the lower part of the conduit, therefore, acts like a capacitor that allows magma to be stored temporally in order to release it during the intense phase of the eruption. In the upper part of the conduit friction is dependent on magma discharge rate, with a decrease in friction resulting in an increase in discharge rate, over a certain range of discharge rates. In Denlinger and Hoblitt [23], when magma discharge rate reaches a critical value, magma detaches from the conduit walls and a stick-slip transition occurs. Rapid motion of magma leads to depressurization of the conduit and a consequent decrease in discharge rate, until at another critical value the magma again sticks to the walls. Pressure starts to increase again due to influx of new magma into the conduit. On a pressure-discharge diagram the path of eruption is represented by a hysteresis loop. In Wylie et al. [98] the friction is controlled by volatile-dependent viscosity. Volatile exsolution delay is controlled by diffusion. When magma ascends rapidly, volatiles have no time to exsolve and viscosity remains low. Depressurization of the upper part of the conduit leads to a decrease in magma discharge rate and an increase in viscosity due to more intense volatile exsolution.

In Neuberg et al. [70] a steady 2D conduit flow model was developed. The full set of Navier–Stokes equations for a compressible fluid with variable viscosity was solved by means of a finite element code. Below some critical depth the flow was considered to be viscous and Newtonian, with a no-slip boundary condition at the wall. Above this depth a plug develops, with a wall boundary condition of frictional slip. The slip criterion was based on the assumption that the shear stress inside the magma overcomes some critical value. Simulations reveal that slip occurs in the shallow part of the conduit, in good agreement with locations of long-period volcanic earthquakes for the Soufrière Hills Volcano, [31]. However, some parameters used in the simulations (low crystallinity, less than 30% and high discharge rate, more than $100 \text{ m}^3/\text{s}$) are inconsistent with observations.

Lensky et al. [49] developed the stick-slip model by incorporating degassing from supersaturated magma together with a sticking plug. Gas diffuses into the magma, which cannot expand due to the presence of a sticking plug, resulting in a build up of pressure. Eventually the pressure exceeds the strength of the plug, which fails in stick-slip motion and the pressure is relieved. The magma sticks again when the pressure falls below the dynamic

friction value. In this model the time scale of the cycles is controlled by gas diffusion. The influence of permeable gas loss, crystallization and elastic expansion of the conduit on the period of pulsations was studied.

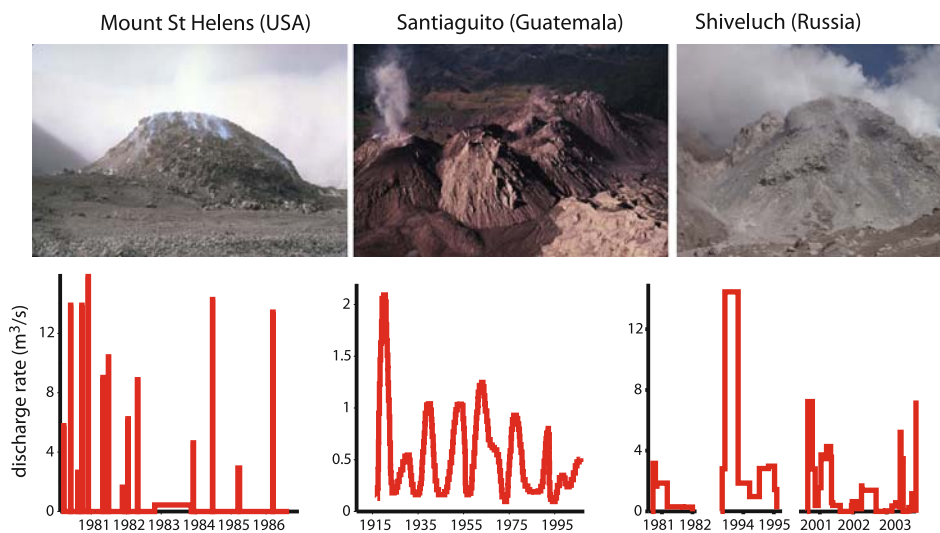
A shorter timescale of order of minutes was investigated in Iverson et al. [43] in relation to repetitive seismic events during the 2004–2006 eruption of Mount St. Helens. The flow dynamics is controlled by the presence of a solid plug that is pushed by a Newtonian liquid, with the possibility of a stick-slip transition. Inertia of the plug becomes important on such short timescales.

Models to explain the occurrence of Vulcanian explosions have also been developed by Connor et al. [15], Jaquet et al. [44] and Clarke et al. [13]. A statistical model of repose periods between explosions by Connor et al. [15] shows that data fit a log-logistic distribution, consistent with the interaction of two competing processes that decrease and increase gas pressure respectively. Jaquet et al. [44] show the explosion repose period data have a memory. The petrological observations of Clarke et al. [13] on clasts from Vulcanian explosions associated with short-term cycles support a model where pressure builds up beneath a plug by gas diffusion, but is opposed by gas leakage through a permeable magma foam. Although these models include some of the key processes and have promising explanatory power, they do not consider the development of the magma plug explicitly. This process is considered in [24], where a model of magma ascent with gas escape is proposed.

Long-Term Cycles

Figure 3 shows views of three lava domes (Mount St. Helens, USA, Santiaguito, Guatemala and Shiveluch, Russia). Measurements of magma discharge rate variations with time are presented below [25,35,89]. Behavior at the first two volcanoes is rather regular, whereas at Shiveluch, long repose periods are followed by an initial rapid increase in eruptive activity with subsequent decrease and complete stop of the eruption. Growth of the lava dome at Unzen volcano, Japan, 1991–1995 was similar to Shiveluch [25,68].

There are three types of conceptual models that attempt to explain long term variation in magma discharge rate. Maeda [53], after [42], considers a simple system that contains a spherical magma chamber located in elastic rocks with a cylindrical conduit located in visco-elastic rocks. Magma viscosity is assumed to be constant. The magma chamber is replenished with a time dependent influx rate. The model reproduces discharge rate variation at Unzen volcano by assuming a bell-shaped form of influx rate dependence on time. There are two controversial assumptions in the model. First, the assumption that the conduit wallrocks are visco-elastic, while the magma chamber wallrocks are purely elastic cannot be justified because near the chamber rock temperature is the highest and it is more reasonable to expect viscous properties for chamber wallrocks rather than for the conduit. The equation that links conduit diameter with



Volcanic Eruptions: Cyclicity During Lava Dome Growth, Figure 3

Observed discharge rate versus time for (a) Mount St. Helens dome growth and (b) Santiaguito volcano and Shiveluch (c). Photos: Mount St. Helens by Lyn Topinka (1985), Santiaguito by Gregg Bluth (2002), Shiveluch by Pavel Plechov (2001)

magmatic overpressure assumes viscous rock properties up to infinity. If the chamber is located in visco-elastic rocks, oscillations in discharge rate are not possible. Second, in order to obtain reasonable timescales, the rock viscosity must be rather small, of order of 10^{13} Pa s, which is only slightly higher than the typical viscosities of the magma.

Another set of models attribute cyclic behavior to heat exchange between ascending magma and wallrocks, which accounts for temperature dependent viscosity [17,95]. The idea of both models is that magma cools down as it ascends, and heat flux is proportional to the difference between the average temperature of the magma and the temperature of the wallrocks. If magma ascends quickly than heat loss is small in comparison with heat advection. Magma viscosity remains low as a consequence and allows high magma discharge rates. In contrast, when magma ascends slowly it can cool substantially and viscosity increases significantly. Both models suggest that, for a fixed chamber pressure, there can be up to three steady state solutions with markedly different discharge rates. Transition between these steady-state solutions leads to cyclic variations in discharge rate. Whitehead and Helfrich [95] demonstrated the existence of cyclic regimes in experiments using corn syrup. In application to magma ascent in a volcanic conduit, these models have strong limitations, because a constant wall-rock temperature is assumed. However, as an eruption progresses the wallrocks heat up and heat flux decreases, a condition that makes periodic behavior impossible for long-lived eruptions. For such a long-lived eruption like Santiaguito (started in 1922) wallrocks are expected to be nearly equilibrated in temperature with the magma, and heat losses from magma became small. It is possible that this decrease in heat flux contributes to a slow progressive increase in temperature that is observed on timescales longer than the period of pulsations. For example, magma at Santiaguito becomes progressively less viscous, resulting in a transition from mainly lava dome to lava flow activity.

Models, developed by authors of this manuscript, consider that degassing-induced crystallization is a major controlling process for the long-term cyclicity during lava dome building eruptions. There is increasing evidence that there is a good correlation between magma discharge rate and crystallinity of the magma [10,68]. An increase in crystal content leads to an increase in magma viscosity [16,20,21] and, thus, influences magma ascent dynamics. First, we consider a simplified model of magma ascent in a volcanic conduit that accounts for crystallization and rheological stiffening.

A Simplified Model

In Barmin et al. [3] the following simplifying assumptions have been made in order to develop a semi-analytical approach to magma ascent dynamics.

1. Magma is incompressible. The density change due to bubble formation and melt crystallization is neglected.
2. Magma is a viscous Newtonian fluid. Viscosity is a step function of crystal content. When the concentration of crystals β reaches a critical value β_* the viscosity of magma increases from value μ_1 to a higher value μ_2 . Later on we will consider magma rheology in more detail (see Sect. “Rheology of Crystal-Bearing Magma and Conduit Resistance”), but a sharp increase in viscosity over a narrow range of crystal content has been confirmed experimentally (e.g., [9,48]).
3. Crystal growth rate is constant and no nucleation occurs in the conduit. The model neglects the fact that magma is a complicated multi-component system and its crystallization is controlled by the degree of undercooling (defined as the difference between actual temperature of the magma and its liquidus temperature). Later in the paper a more elaborate model for magma crystallization will be considered.
4. The conduit is a vertical cylindrical pipe. Elastic deformation of the wallrocks is not included in the model. This assumption is valid for a cylindrical shape of the conduit at typical magmatic overpressures, but is violated when the conduit has a fracture shape. Real geometries of volcanic conduits and their inclination can vary significantly with depth.
5. The magma chamber is located in elastic rocks and is fed from below, with a constant influx rate. For some volcanoes, like Santiaguito or Mount St. Helens, average magma discharge rate remained approximately constant during several periods of pulsation. Thus the assumption of constant influx rate is valid. For volcanoes like Mount Unzen or Shiveluch, there is an evidence of pulse-like magma recharge [25,53].

With above simplification the system of equations for unsteady 1D flow is as follows:

$$\frac{\partial}{\partial t} \rho + \frac{\partial}{\partial x} \rho u = 0; \quad \frac{\partial}{\partial t} n + \frac{\partial}{\partial x} n u = 0 \quad (1a)$$

$$\frac{\partial p}{\partial x} = -\rho g - \frac{32\mu u}{\delta^2}; \quad \mu = \begin{cases} \mu_1, & \beta < \beta_* \\ \mu_2, & \beta \geq \beta_* \end{cases} \quad (1b)$$

$$\frac{\partial}{\partial t} \beta + u \frac{\partial \beta}{\partial x} = 4\pi n r^2 \chi = (36\pi n)^{\frac{1}{3}} \beta^{\frac{2}{3}} \chi \quad (1c)$$

Here ρ is the density of magma, u is the vertical cross-section averaged ascent velocity, n is the number density of

crystals per unit volume, p is the pressure, g is the acceleration due to gravity, δ is the conduit diameter, β is the volume concentration of crystals, β_* is a critical concentration of crystals above which the viscosity changes from μ_1 to μ_2 , r is the crystal radii, χ is the linear crystal growth rate, and x is the vertical coordinate. The first two Eqs. (1a) represent the conservation of mass and the number density of crystals, the second (1b) is the momentum equation with negligible inertia, and the third (1c) is the crystal growth equations with $\chi = \text{constant}$. We assume the following boundary conditions for the system (1):

$$\begin{aligned} x = 0 : \frac{dp_{\text{ch}}}{dt} &= \frac{\gamma}{V_{\text{ch}}} (Q_{\text{in}} - Q_{\text{out}}); \beta = \beta_{\text{ch}}; n = n_{\text{ch}} \\ x = l : p &= 0 \end{aligned}$$

Here γ is the rigidity of the wall-rock of the magma chamber, V_{ch} is the chamber volume, β_{ch} and n_{ch} are the crystal concentration and number density of crystals per unit volume in the chamber, p_{ch} is the pressure in the chamber, l is the conduit length, Q_{in} is the flux into the chamber and $Q_{\text{out}} = \pi \delta^2 u / 4$ is the flux out of the chamber into the conduit. Both β_{ch} and n_{ch} are assumed constant. We neglect the influence of variations of the height of the lava dome on the pressure at the top of the conduit and assume that the pressure there is constant. As the magma is assumed to be incompressible, the pressure at the top of the conduit can be set to zero because the atmospheric pressure is much smaller than magma chamber pressure.

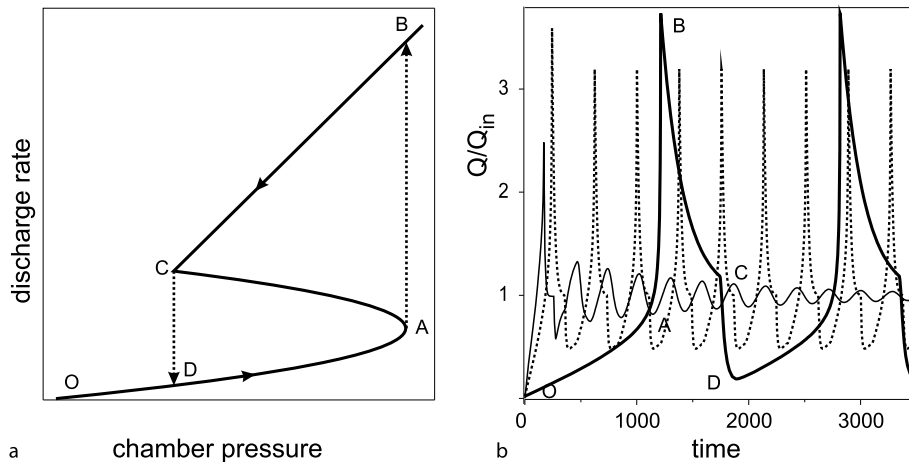
From the mass conservation equation for the case of constant magma density, $u = u(t)$ and $n = n_{\text{ch}}$ everywhere. Equations (1) can be integrated and transformed

from partial differential equations to a set of ordinary differential equations with state-dependent delay representing a “memory” effect on crystal concentration (see [3] for details).

Results and Applications

The general steady-state solution for magma ascent velocity variations with chamber pressure is shown in Fig. 4a. Solutions at high magma ascent velocities, when the critical concentration of crystals is not reached inside the conduit, result in a straight line (CB), which is the same as for the classical Poiseuille solution for a fluid with constant viscosity. At low ascent velocities there is a quadratic relationship (OAC) between chamber pressure and ascent velocity (see [3] for derivation of the equation). A key feature of the steady-state solution is that, for a fixed chamber pressure, it is possible to have three different magma ascent velocities. We note that for $\mu_2/\mu_1 = 1$ only the branch CB exists and for $1 < \mu_2/\mu_1 \leq 2$ there is a smooth transition between the lower branch (ODA) and the upper branch (CB) and multiple steady-state regimes do not exist.

We first consider the case where chamber pressure changes quasi-statically and the value of Q_{in} is between Q_A and Q_C . Starting at point O the chamber pressure increases, because the influx into the chamber is higher than the outflux. At point A, a further increase in pressure is not possible along the same branch of the steady-state solution and the system must change to point B, where the outflux of magma is larger than the influx. The chamber pressure and ascent velocity decrease along BC until the point C is



Volcanic Eruptions: Cyclicity During Lava Dome Growth, Figure 4

The general steady-state solution and possible quasi-static evolution of an eruption. After [3]. Different curves correspond to different values of dimensionless parameter $\kappa = (\pi \delta^2 \gamma) / (4 V_{\text{ch}} \rho g)$ (0.12 – thin line, 0.05 – dotted line, and 0.005 – bold line)

reached and the system must change to point D. The cycle DABC then repeats itself. Provided the chamber continues to be supplied at the same constant rate repetition of this cycle results in periodic behavior. The transitions AB and CD in a cycle must involve unsteady flow.

Oscillations in magma discharge rate involve large variations in magma crystal content. This relation is observed on many volcanoes. For example, pumice and samples of the Soufrière Hills dome that were erupted during periods of high discharge [88] have high glass contents (25 to 35%) and few microlites [65], whereas samples derived from parts of the dome that were extruded more slowly (days to weeks typically) have much lower glass contents (5 to 15%) and high contents of groundmass microlites. These and other observations [34,68] suggest that micro-lite crystallization can take place on similar time scales to the ascent time of the magma.

Of more general interest is to consider unsteady flow behaviour. We assume that the initial distribution of parameters in the conduit corresponds to the steady-state solution of system (1) with the initial magma discharge rate, Q_0 , being in the lowest regime. The behaviour of an eruption with time depends strongly on the value of Q_{in} . If Q_{in} corresponds to the upper or the lower branch of the steady state solution the eruption stabilizes with time with $Q = Q_{in}$ and $dp_{ch}/dt = 0$. However, if Q_{in} corresponds to the intermediate branch of the steady-state solution, with Q_{in} between Q_A and Q_C , periodic behaviour is possible. Figure 4b shows three eruption scenarios for different values of the magma chamber volume V_{ch} . When V_{ch} is small the eruption stabilizes with time. In contrast, undamped periodic oscillations occur for values of V_{ch} larger than some critical value. For very large magma chamber volumes the transient solution almost exactly follows the steady-state solution, with unsteady transitions between the regimes. The time that the system spends in unsteady transitions in this case is much shorter than the period of pulsations. The maximum discharge rate during the cycle is close to Q_B , the minimum is close to Q_D and the average is equal to Q_{in} . The period of pulsations increases as the volume of magma chamber increases.

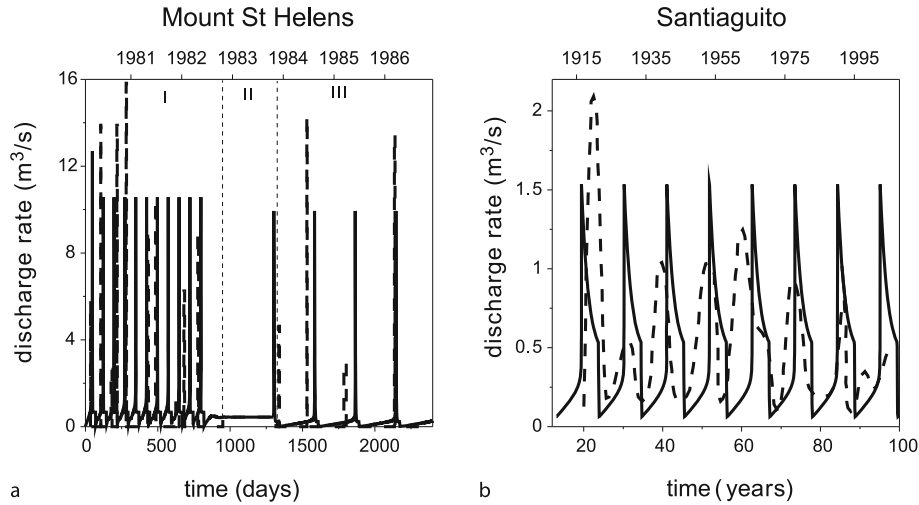
Now we apply the model to two well-documented eruptions: the growth of lava domes on Mount St. Helens (1980–1986) and on Santiaguito (1922–present). Our objective here is to establish that the model can reproduce the periodic behaviors observed at these two volcanoes. Estimates can be obtained for most of the system parameters. However, magma chamber size is not well-constrained and so the model can be used to make qualitative inferences on relative chamber size. Given the uncertainties in the parameter values and the simplifications in the

model development, the approach can be characterized as mimicry. Adjustments in some parameters were made to achieve best fits with observations, but the particular best-fits are not unique.

For Mount St. Helens our model is based on data presented by [89]. Three periods of activity can be distinguished during the period of dome growth. The first period consists of 9 pulses of activity with average peak magma discharge rates $\sim 15 \text{ m}^3/\text{s}$ during 1981–1982. Each pulse lasted from 2 to 7 days (with a mean value of 4 days) with the average period between the pulses being 74 days and the average discharge rate during the period being $Q_1 \sim 0.67 \text{ m}^3/\text{s}$. The second period is represented by continuous dome growth and lasted more than a year (368 days) with a mean magma discharge rate of $Q_2 \sim 0.48 \text{ m}^3/\text{s}$. During the last period there were 5 episodes of dome growth with peak magma discharge rates up to $\sim 15 \text{ m}^3/\text{s}$, an average period of pulsation of ~ 230 days and a mean discharge rate of $Q_3 \sim 0.23 \text{ m}^3/\text{s}$. We assume that the intensity of influx into the magma chamber, Q_{in} , is equal to the average magma discharge rate over the corresponding periods. There might have been a progressive decrease in the intensity of influx during the eruption, but, due to limitations of the model, we assume that Q_{in} changes as a step function between the periods.

The best-fit model for the eruption is presented in Fig. 5a, with the parameters used for the simulation summarized in Table 2 in [3]. During the first period of the eruption $Q_{in} = Q_1$. This corresponds to the intermediate branch of the steady-state solution and cyclic behaviour occurs. In the second period $Q_{in} = Q_2$ the system moves to the lower regime and the eruption stabilizes with time. For the third period of the eruption the parameters of the system have been changed, so that $Q_{in} = Q_3 < Q_2$, corresponding to the intermediate regime once again and periodic behaviour occurs. This condition can be satisfied by a decrease in the diameter of the conduit, or a decrease in crystal growth rate, or the number density of crystals. All these mechanisms are possible: decrease in the diameter could be a consequence of magma crystallization on the conduit walls, while a decrease in either crystal growth rate or number density of crystals could be reflect observed changes in magma composition [89]. The influence of conduit diameter is the strongest because ascent velocity, for the same discharge rate, depends on the square of the diameter. The required change in diameter is from 18 to 12 m, but this change can be smaller if we assume a simultaneous decrease in crystal growth rate.

Since 1922, lava extrusion at Santiaguito has been cyclic [35]. Each cycle begins with a 3–6 year long high ($0.5\text{--}2.1 \text{ m}^3/\text{s}$) magma discharge rate phase, followed by



Volcanic Eruptions: Cyclicity During Lava Dome Growth, Figure 5

Discharge rate versus time for **a** Mount St. Helens dome growth and **b** Santiaguito volcano. Dotted lines represent the observed values of discharge rates and the solid lines are the best fit simulations. After [3]

a longer (3–11 years) low ($\sim 0.2 \text{ m}^3/\text{s}$) discharge rate phase. The time-averaged magma discharge rate was almost constant at $\sim 0.44 \text{ m}^3/\text{s}$ between 1922 and 2000. The first peak in discharge rate had a value $> 2 \text{ m}^3/\text{s}$, whereas the second peak had a much smaller value. The value for the second peak is underestimated as it is calculated based on the dome volume only, but does not include the volume of dome collapse pyroclastic flows. Later peaks show an increase in magma discharge rate until 1960 (Fig. 5b, dashed line). Post-1960, the duration of the low discharge rate phase increased, the peak discharge and the time-averaged discharge rates for each cycle decreased, and the difference between discharge rates during the high and low discharge rate phases of each cycle decreased. Our best-fit model is shown in Fig. 5b and the parameters estimates are listed in Table 2 in [3]. The model reproduces the main features of the eruption, including the period of pulsations, the ratio between low and high magma discharge rates, and the range of observed discharge rates. We cannot, however, reproduce the decrease in the amplitude of pulsations within the framework of the model using fixed parameter values.

The theory provides a potential method to estimate magma chamber volumes. For Mount St. Helens our estimate of the chamber size ($\sim 0.6 \text{ km}^3$) is comparable with the total erupted volume in the entire 1980–1986 eruption and is consistent with the fact that geophysical imaging did not identify a large magma body. Santiaguito volcano erupted more than 10 km^3 in the 1902 explosive eruption [96] and more than 1 km^3 of lava domes since 1922. The best-fit model estimate of a large (64 km^3) chamber is

consistent with much larger eruption volumes, long periods, and longevity of the eruption in comparison to Mount St. Helens. One limitation of the model is that the supply of deep magma from depth to the chamber is assumed to be constant.

Model Development

In this section we further develop models to examine new effects and relax some of the simplifications of earlier models. We investigate a number of effects that were not fully explained or considered in previous studies [3,61,62]. The new model incorporates a more advanced treatment of crystallization kinetics based on the theoretical concepts developed in [38,46], and is calibrated by experimental studies in andesitic systems [22,34]. In particular, we distinguish growth of phenocrysts formed in the magma chamber from crystallization of microlites during magma ascent. Previous models have assumed that magma is always Newtonian, so we study models of conduit flow assuming non-Newtonian rheology, with rheological properties being related to crystal content. Latent heat is released during the crystallization of ascending magma due to degassing and we show that this can have an important influence on the dynamics. Elastic deformation of conduit walls leads to coupling between magma ascent and volcano deformations.

System of Equations We model magma ascent in a dyke-shaped conduit with elliptical cross-section using

a set of 1D transient equations written for horizontally averaged variables [20,21]:

$$\frac{1}{S} \frac{\partial}{\partial t}(S\rho_m) + \frac{1}{S} \frac{\partial}{\partial x}(S\rho_m V) = -G_{mc} - G_{ph} \quad (2)$$

$$\frac{1}{S} \frac{\partial}{\partial t}(S\rho_{mc}) + \frac{1}{S} \frac{\partial}{\partial x}(S\rho_{mc} V) = G_{mc} \quad (3a)$$

$$\frac{1}{S} \frac{\partial}{\partial t}(S\rho_{ph}) + \frac{1}{S} \frac{\partial}{\partial x}(S\rho_{ph} V) = G_{ph} \quad (3b)$$

$$\frac{1}{S} \frac{\partial}{\partial t}(S\rho_d) + \frac{1}{S} \frac{\partial}{\partial x}(S\rho_d V) = -J \quad (4a)$$

$$\frac{1}{S} \frac{\partial}{\partial t}(S\rho_g) + \frac{1}{S} \frac{\partial}{\partial x}(S\rho_g V_g) = J \quad (4b)$$

Here t denotes time, x the vertical coordinate, $\rho_m, \rho_{ph}, \rho_{mc}, \rho_d$ and ρ_g are the densities of melt, phenocrysts, microlites, dissolved gas and exsolved gas respectively, and V and V_g are the velocities of magma and gas, respectively. G_{ph}, G_{mc} represent the mass transfer rate due to crystallization of phenocrysts and microlites, respectively, and J the mass transfer rate due to gas exsolution, S is the cross-section area of the conduit. Equation (2) represents the mass conservation for the melt phase, Eqs. (3a) and (3b) are the conservation equations for microlites and phenocrysts respectively, Eqs. (4a) and (4b) represent the conservation of the dissolved gas and of the exsolved gas respectively.

$$\frac{\partial p}{\partial x} = -\rho g - F_c \quad (5)$$

$$V_g - V = -\frac{k}{\mu_g} \frac{\partial p}{\partial x} \quad (6)$$

Here p is the pressure, ρ the bulk density of magma, g the acceleration due to gravity, μ is the magma viscosity, k is the magma permeability and μ_g is the gas viscosity. Eq. (5) represents the equation of momentum for the mixture as a whole, in which the pressure drops due to gravity and conduit resistance are calculated for laminar flow in an elliptic pipe. Equation (6) is the Darcy law for the exsolved gas flux through the magma.

$$\begin{aligned} \frac{1}{S} \frac{\partial}{\partial t}(S\rho C_m T) + \frac{1}{S} \frac{\partial}{\partial x}(S\rho C_m V T) \\ = L_*(G_{mc} + G_{ph}) - C_m T J - Q_{cl} + Q_{vh} \end{aligned} \quad (7)$$

Here C_m is the bulk specific heat of magma, T is the bulk flow-averaged temperature, L_* is latent heat of crystallization, Q_{cl} denotes the total heat loss by conduction to the conduit walls, and Q_{vh} denotes the total heat generation due to viscous dissipation. Here we consider the case of the latent heat release only. This assumption is valid when

both $Q_{cl} \approx 0$ and $Q_{vh} \approx 0$ or when $Q_{cl} + Q_{vh} \approx 0$. The study of the effects of both heat loss and viscous heating, which are intrinsically two-dimensional [18,19], and their parametrization is the subject of ongoing research.

$$\rho_m = \rho_m^0(1-\alpha)(1-\beta)(1-c); \quad \rho_c = \rho_c^0(1-\alpha)\beta \quad (8a)$$

$$\rho_d = \rho_m^0(1-\alpha)(1-\beta)c; \quad \rho_g = \rho_g^0\alpha \quad (8b)$$

$$\rho = \rho_m + \rho_c + \rho_d + \rho_g \quad (8c)$$

$$\alpha = \frac{4}{3}\pi r_b^3 n; \quad \frac{\partial}{\partial t}(Sn) + \frac{\partial}{\partial x}(SnV) = 0; \quad p = \rho_g^0 RT \quad (9)$$

Here α is the volume concentration of bubble, β is the volume concentration of crystals in the condensed phase (melt plus crystals), and c is mass concentration of dissolved gas (equal to volume concentration as we assume that the density of dissolved volatiles is the same as the density of the melt), ρ_m^0 denotes the mean density of the pure melt phase, ρ_c^0 is density of the pure crystal phase (with $\rho_c = \rho_{ph} + \rho_{mc}$, $\beta = \beta_{ph} + \beta_{mc}$), r_b is the bubble radius, and n the number density of bubble per unit volume. Concerning the parametrization of mass transfer rate functions, we use:

$$J = 4\pi r_b n D \rho_m^0 (c - C_f \sqrt{p}) \quad (10)$$

$$\begin{aligned} G_{mc} = 4\pi \rho_c^0 (1-\beta)(1-\alpha) \\ \times U(t) \int_0^t I(\omega) \left(\int_\omega^t U(\eta) d\eta \right)^2 d\omega \end{aligned} \quad (11a)$$

$$G_{ph} = 3\gamma_s \left(\frac{4\pi N_{ph} \beta_{ph}^2}{3} \right)^{\frac{1}{3}} \rho_c^0 (1-\beta)(1-\alpha) U(t) \quad (11b)$$

Here J is parametrized using the analytical solution described in [69], U is the linear crystal growth rate (m s^{-1}), I is the nucleation rate ($\text{m}^{-3}\text{s}^{-1}$), which defines the number of newly nucleated crystal per cubic meter, and γ_s is a shape factor of the order of unity, D and C_f are the diffusion and the solubility coefficients, respectively. Concerning the mass transfer due to crystallization G_{mc} , we adapt a model similar to that described in [38]. Assuming spherical crystals, the Avrami–Johnson–Mehl–Kolmogorov equation in the form adopted by [46], for the crystal volume increase rate, is:

$$\frac{d\beta}{dt} = 4\pi Y_t U(t) \int_0^t I(\omega) \left(\int_\omega^t U(\eta) d\eta \right)^2 d\omega$$

where $Y_t = (1-\beta)(1-\alpha)$ is the volume fraction of melt remaining uncrystallized at the time t . Therefore, we have $G_{mc} = \rho_{mc} d\beta/dt$. For the phenocryst growth rate $G_{ph}()$

we assume that it is proportional to the phenocryst volume increase rate $d\beta_{\text{ph}}/dt = 4\pi R_{\text{ph}}^2 N_{\text{ph}} U(t)$ times the crystal density ρ_c^0 times the volume fraction of melt remaining uncrystallized at the time t . A detailed description of the parametrization used for the different terms is reported in [63].

For parametrizations of magma permeability k and magma viscosity μ we use:

$$k = k(\alpha) = k_0 \alpha^j \quad (12)$$

$$\mu = \mu_m(c, T) \theta(\beta) \eta(\alpha, Ca) \quad (13)$$

where k is assumed to depend only on bubble volume fraction α . Magma viscosity μ depends on water content, temperature, crystal content, bubble fraction and capillary number as described in detail in the next section.

Regarding equations for semi-axes, a and b , we assume that the elliptical shape is maintained and that pressure change gradually in respect with vertical coordinate and time so that the plain strain analytical solution for an ellipse subjected to a constant internal overpressure [64,66], remains valid:

$$a = a_0 + \frac{\Delta P}{2G} [-(1-2\nu)a_0 + 2(1-\nu)b_0] \quad (14a)$$

$$b = b_0 + \frac{\Delta P}{2G} [2(1-\nu)a_0 - (1-2\nu)b_0] \quad (14b)$$

where ΔP is the overpressure, i. e. the difference between conduit pressure and far field pressure (here assumed to be lithostatic for a sake of simplicity), a_0 and b_0 are the initial values of the semi-axes, ν is the host rock Poisson ratio, and G is the host rock rigidity.

Equations (2)–(14) are solved between the top of the magma chamber and the bottom of the lava dome that provides some constant load by using the numerical method described in [63]. The effects of dome height and morphology changes are not considered in this paper. We consider three different kinds of boundary conditions at the inlet of the dyke: constant pressure, constant influx rate and the presence of a magma chamber located in elastic rocks. The case of constant pressure is applicable when a dyke starts from either a large magma chamber or unspecified source, so that pressure variations in the source region remain small. An estimate of the volume of magma stored in the source region that allows pressure to be approximated as constant depends on wall-rock elasticity, magma compressibility (volatile content), and the total volume of the erupted material. If the magma flow at depth is controlled by regional tectonics, the case of constant influx rate into the dyke may be applicable if total variations

in supply rate are relatively small on the timescale of the eruption.

For the case where magma is stored in a shallow magma chamber prior to eruption, and significant chamber replenishment occurs, the flow inside the conduit must be coupled with the model for the magma chamber. In this case, as explained in detail in [63], we assume that the relationship between the pressure at the top of the magma chamber p_{ch} and the intensity of influx Q_{in} and outflux Q_{out} of magma to and from the chamber is given by:

$$\frac{dp_{\text{ch}}}{dt} = \frac{4G \langle K \rangle}{\langle \rho \rangle V_{\text{ch}} (3 \langle K \rangle + 4G)} (Q_{\text{in}} - Q_{\text{out}}) \quad (15)$$

where V_{ch} is the magma chamber volume, $\langle \rho \rangle$ and $\langle K \rangle$ are the average magma density and magma bulk modulus, respectively, and G is the rigidity of rocks surrounding the chamber.

Cases of constant influx and of constant source pressure are the limit cases of Eq. (15) in the case of infinitely small and infinitely large magma chamber volume. We assume that the volume concentration of bubbles and phenocrysts are determined by equilibrium conditions and that the temperature of the magma is constant. The effect of temperature change on eruption dynamics, due to interaction between silicic and basaltic magma, was studied in [63].

We use a steady-state distribution of parameters along the conduit as an initial condition for the transient simulation. The values are calculated for a low magma discharge rate, but the particular value of this parameter is not important because the system deviates from initial conditions to a cyclic or stabilized state, which does not depend on the initial conditions.

Rheology of Crystal-Bearing Magma and Conduit Resistance

Magma viscosity is modeled as a product of melt viscosity $\mu_m(c, T)$, the relative viscosity due to crystal content $\theta(\beta) = \Theta(\beta) \varphi(\beta)$, and the relative viscosity due to the presence of bubbles $\eta(\alpha, Ca)$. The viscosity of the pure melt $\mu_m(c, T)$ is calculated according to [36]. Viscosity increase due to the presence of the crystals is described through the function $\Theta(\beta)$ [16,20,21]. As crystallization proceeds, the remaining melt becomes enriched in silica and melt viscosity increases. The parametrization of this effect is described by the function $\varphi(\beta)$ in [21,25]. Effects of the solid fraction are parametrized as described in [21].

Effects due to the presence of bubbles are accounted for by adopting a generalization of [51] for an elliptical conduit [20,21].

In the case of Newtonian magma rheology, the friction force in an elliptical conduit can be obtained from

a classical Poiseuille solution for low Reynolds number flow $F_c = 4\mu(a^2 + b^2)/(a^2b^2)V$ [47]. High crystal or bubble content magmas may show non-Newtonian rheology. One possible non-Newtonian rheology is that of a Bingham material characterized by a yield strength τ_b [4]. The stress-strain relation for this material is given by:

$$\begin{aligned}\tau_{ij} &= \left(\mu + \frac{\tau_b}{\gamma_b}\right) \gamma_{ij} \Leftrightarrow \tau > \tau_b \\ \gamma_{ij} &= 0 \Leftrightarrow \tau \leq \tau_b\end{aligned}\quad (16)$$

Here τ_{ij} and γ_{ij} are the stress and strain rate tensors, τ and γ_b are second invariants of corresponding tensors. According to this rheological law, the material behaves linearly when the applied stress is higher than a yield strength. No motion occurs if the stress is lower than a yield strength. In the case of a cylindrical conduit the average velocity can be calculated in terms of the stress on the conduit wall τ_w [52]:

$$V = \frac{1}{12} \frac{r}{\tau_w^3 \mu} (\tau_b^4 + 3\tau_w^4 - 4\tau_b \tau_w^3) \quad (17)$$

Here r is the conduit radii. This form of equation gives an implicit relation between ascent velocity and pressure drop, and is not convenient to use. By introducing dimensionless variables $\Pi = \mu V / \tau_b r$ and $\Omega = \tau_w / \tau_b \geq 1$ relation (17) can be transformed into:

$$\Omega^4 - \frac{1}{6} (8 + 3\Pi) \Omega^3 + \frac{1}{3} = 0 \quad (18)$$

Following [63] a semi-analytical solution can be used for (18) and the conduit friction force can be expressed finally as:

$$F_c = \frac{2\tau_w}{r} = \frac{2\tau_b \Omega (\Pi)}{r}.$$

We note that a finite pressure gradient is necessary to initiate the flow in the case of Bingham liquid, in contrast to a Newtonian liquid.

Results and Applications

Influence of non-Newtonian Properties on Eruption Behaviour Now we compare the dynamics of magma extrusion in the cases of Newtonian and Bingham rheology. We will assume that yield strength is reached when the concentration of crystals reaches a critical value:

$$\tau = \begin{cases} \tau_b & \text{for } \beta > \beta_{cr} \\ 0 & \text{for } \beta \leq \beta_{cr} \end{cases} \quad (19)$$

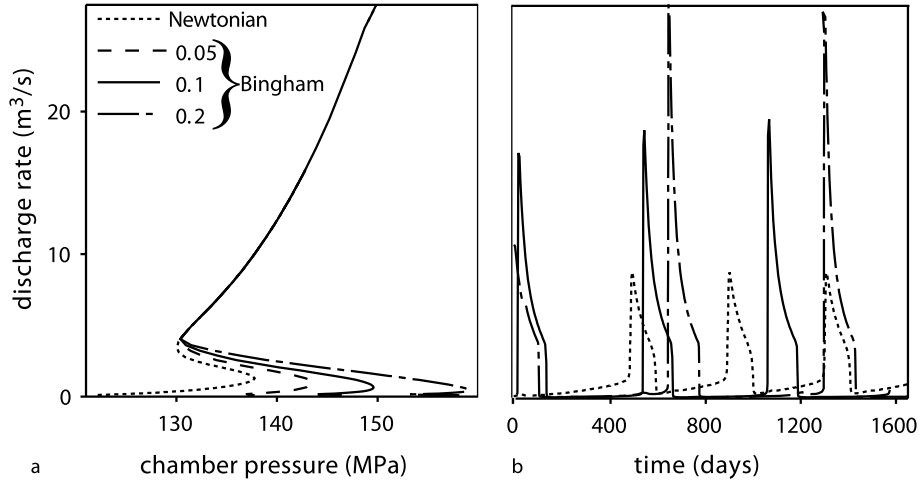
Figure 6a shows a set of steady-state solutions for different values of τ_b . Values of τ_b and β_{cr} depend on crystal shape, crystal size distribution, magma temperature and

other properties, but here are assumed to be constant. To illustrate the influence of Bingham rheology, the value of $\beta_{cr} = 0.65$ was chosen so that, for discharge rate larger than $\sim 5 \text{ m}^3/\text{s}$, the magma has Newtonian rheology (see Fig. 6a). A more detailed study would require measurements of the rheological properties of magma for a wide range of crystal content and crystal size distributions. As the value of τ_b the chamber pressure that is necessary to start the eruption increases.

Figure 6b shows the influence of these two rheological models on the dynamics of magma extrusion. In the case of Bingham rheology, magma discharge rate between the two pulses is zero until a critical chamber overpressure is reached. Then the magma discharge rate increases rapidly with decrease in crystal content, leading to a significant reduction of both magma viscosity and the length of the part of the conduit that is occupied by the Bingham liquid where $\beta_c > \beta_{cr}$. There is a transition in the system to the uppermost flow regime and the pressure then decreases quickly. Because the pressure at the onset of the pulse was significantly larger than in the case of a Newtonian liquid, the resulting discharge rate in the case of Bingham rheology is also significantly higher.

Modeling of Conduit Flow during Dome Extrusion on Shiveluch Volcano The maximum intensity of extrusion was reached at an early stage in all three eruptions (Fig. 3). We therefore suggest that dome extrusion was initiated by high overpressure in the magma chamber with respect to the lithostatic pressure. Depressurization of the magma chamber occurred as a result of extrusion. Without magma chamber replenishment, depressurization results in a decrease in magma discharge rate. In open system chambers replenishment of the chamber during eruption can lead to pulsatory behaviour [3]. The following account is derived from [25]. For the 1980–1981 eruption the monotonic decrease in discharge rate indicates that there was little or no replenishment of the magma chamber. During the 1993–1995 and 2001–2004 episodes, however, the magma discharge rate fluctuated markedly, suggesting that replenishment was occurring. The influx of new magma causes an increase in magma chamber pressure, and a subsequent increase in magma discharge rate. During the 2001–2004 eruption there were at least three peaks in discharge rate. Replenishment of the magma chamber with new hot magma can explain the transition from lava dome extrusion to viscous lava flow that occurred on Shiveluch after 10 May 2004, and which continues at the time of writing (2007).

We simulated dome growth during the 2001–2002, because this dataset is the most complete and is supported



Volcanic Eruptions: Cyclicity During Lava Dome Growth, Figure 6

a Steady-state solutions and dependence of discharge rate on time for Newtonian and Bingham rheology of the magma. Yield strength is a parameter marked on the curves (values in MPa). For Bingham rheology discharge rate remains zero between the pulses of activity. Bingham rheology results in much higher chamber pressures prior to the onset of activity and, therefore, much higher discharge rates in comparison with Newtonian rheology. **b** Comparison of the period of pulsation in discharge rate for Newtonian and Bingham rheologies. After [63]

by petrological investigations [39]. We assume the shape of the influx curve:

$$Q_{\text{in}} = \begin{cases} 0, & t < t_s \\ Q_0, & t_s \leq t \leq t_f \\ 0, & t > t_f \end{cases} \quad (20)$$

Influx occurs with constant intensity Q_0 between times t_s and t_f . We have examined many combinations of values of these parameters within the constraints provided by observations. The best simulation results use the following values of parameters: $Q_0 = 3.8 \text{ m}^3/\text{s}$, $t_s = 77$ and $t_f = 240$ days. A more continuous influx, dependent on time, is plausible, but there is no geophysical evidence that allows us to constrain the intensity of the influx, because ground deformation data are absent for Shiveluch volcano. The output of the model gives a magma chamber volume of 12 km^3 , assuming a spherical chamber. Figure 7a shows the time-dependence of magma discharge rate, and Fig. 7b shows the increase in the volume of erupted material with time after 6th June 2001. The timing of magma influx is in good agreement with the residence time of basaltic magma in the system, as calculated from the olivine reaction rims. For further details see [25].

5 to 7 Weeks Cycles on the Soufriere Hills Volcano: Evidence for a Dyke? An approximately 5 to 7 week cyclic pattern of activity was recognized at the Soufrière Hills Volcano (SHV) [87,91] between April 1997 and March 1998 from

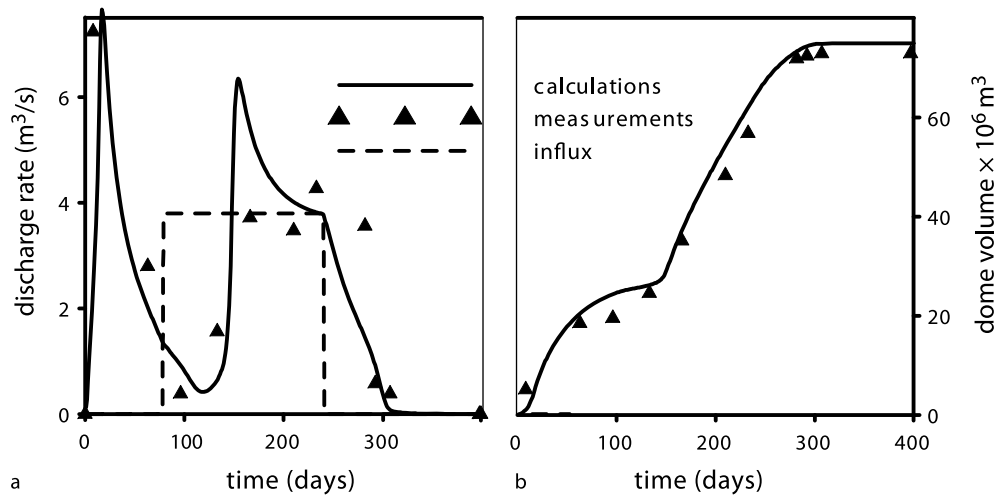
peaks in the intensity of eruptive activity and geophysical data, including tilt and seismicity (Fig. 2).

In models discussed above, the time-scale of pulsations depends principally on the volume of the magma chamber, magma rheology and the cross-sectional area of the conduit. These models might provide an explanation for the 2–3 year cycles of dome extrusion observed at SHV, where deformation data indicate that the magma chamber regulates the cycles. However, the models cannot simultaneously explain the 5–7 week cycles. Thus another mechanism is needed.

The evidence for a dyke feeder at SHV includes GPS data [58], distribution of active vents, and seismic data [76]. We have assumed that, at depth, the conduit has an elliptical shape that transforms to a cylinder at shallow level. In order to get a smooth transition from the dyke at depth to a cylindrical conduit (see Fig. 1) the value of a_0 in Eqs. (14) is parametrized as:

$$a_0(x) = A_1 \arctan\left(\frac{x - L_T}{w_T}\right) + A_2 \quad (21)$$

Here L_T and w_T are the position and the vertical extent of the transition zone between the ellipse and the cylinder and constants A_1 and A_2 are calculated to satisfy conditions $a_0(L) = R$ and $a_0(0) = a_0$, where R is the radius of the cylindrical part of the conduit and a_0 is the length of semi-major axis at the inlet of the dyke. The value of b_0 is calculated in order to conserve the cross-section area of



Volcanic Eruptions: Cyclicity During Lava Dome Growth, Figure 7

a Comparison of calculated and measured discharge rates (**a**) and volumes of the dome (**b**) for the episode of the dome growth in 2001–2002. Influx into the magma chamber is shown by a dashed line in **a**. Time in days begins on 6th June, 2001. After [25]

the unpressurized dyke, although it can also be specified independently.

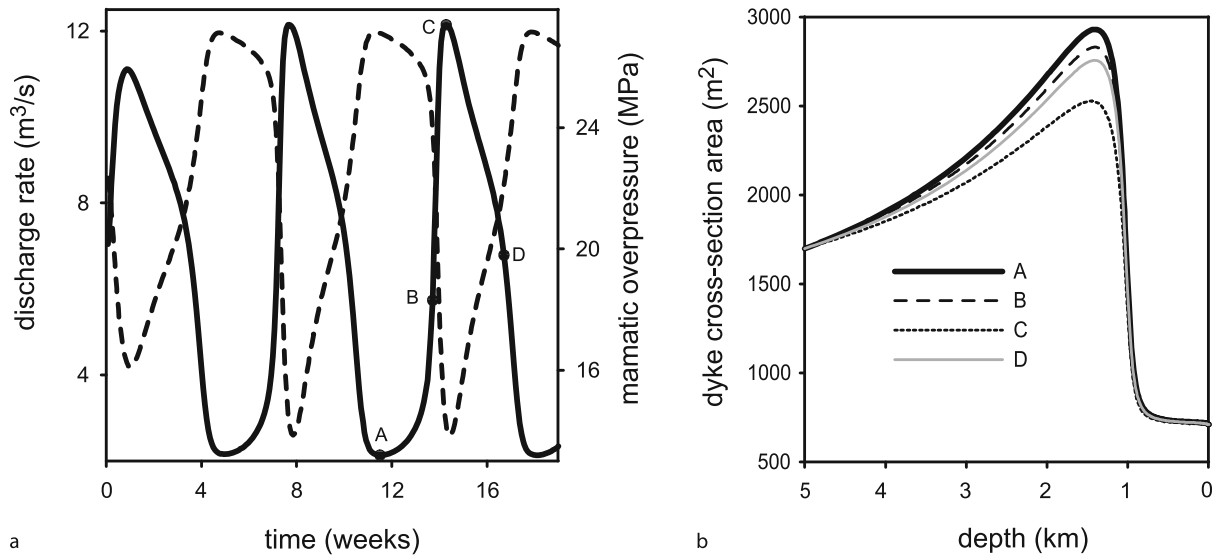
In order to de-couple the influence of the dyke geometry from the oscillations caused by magma chamber pressure variations, we have assumed a fixed chamber pressure as a boundary condition for the entrance to the conduit. This assumption is valid because the timescale of chamber pressure variations are much longer than the period of the cycle (2–3 years in comparison with 5–7 weeks).

Results presented in Figure 8 show that, even with a fixed chamber pressure, there are magma discharge rate oscillations. At the beginning of a cycle the magma discharge rate is at a minimum, while the overpressure (here presented for 1 km depth by a dashed line) and dyke width are at a maximum. At point A in Fig. 8a the crystal content and viscosity have reached their maximum values. Beyond this threshold condition, an increase in magma discharge rate results in decreasing pressure and dyke width. However, crystal content and viscosity also decrease and this effect decreases friction, resulting in flow rate increase and pressure decrease. At C the system reaches minimum viscosity and crystal content, which cannot decline further. Thereafter the magma discharge rate decreases, while the pressure and dyke width increase. The dyke acts like a capacitor, storing volume during this part of the cycle.

The period of oscillation depends on several parameters such as influx rate and dyke aspect ratio a/R . Typically the period decreases with increasing aspect ratio. The range of calculated periods varies between 38 and 51 days for semi major-axis lengths, a , from 175 to 250 m and semi minor-axes, b , from 2 to 4 m. These results match observed

cyclicity at SHV. The start of a cycle is quite sharp (Fig. 2), with the onset of shallow hybrid-type (impulsive, low-frequency coda) earthquakes. The change to shorter period and higher amplitude tilt pulsations indicate a marked increase in average magma discharge rate [91,98]. The model cycles also have rapid onsets. The high-amplitude tilt pulsations lasted for several weeks [91], consistent with the duration of higher magma discharge rates early in each 5–7 week cycle. Tilt data (Fig. 2) are consistent with the model in that the episode of high magma discharge is associated with a marked deflation that lasts several weeks (see dashed curve at Fig. 8, representing magmatic overpressure at 1 km depth). The magma pressure builds up in the swelling dyke and then reaches a threshold, whereupon a surge of partly crystallized magma occurs, accompanied by elevated seismicity.

The models presented above have certain general features that are necessary to show cyclic behaviour. First of all, the resistance of the conduit must depend on magma discharge rate in a way that resistance decreases when discharge rate increases in some range of discharge rate. This dependence is reproduced by a sigmoidal curve. Resistance is a product of viscosity and velocity, and is linearly proportional to discharge rate. This means that magma viscosity must decrease as discharge rate strongly increases. There may be many reasons for this behaviour, including crystallization, temperature variation or gas diffusion. The second condition is that there must be some capacitor in the system that can store magma in a period of low discharge rate and release it in a period of high discharge rate. The role of this capacitor can be played



Volcanic Eruptions: Cyclicity During Lava Dome Growth, Figure 8

a Dependence of magma discharge rate (solid line) and magmatic overpressure at depth of 1 km (dashed line) on time, for $a = 240$ m and $b = 2.25$ m at the inlet of the dyke. The period of cycle is 46 days, average discharge rate is $6.2 \text{ m}^3/\text{s}$, with peak rate about $12 \text{ m}^3/\text{s}$. **b** Profiles of cross-section areas of the conduit during one cycle. Curve A corresponds to the beginning of the cycle, B – to a point on the curve of ascending discharge rate, C – to maximum discharge, and D to the middle of descending discharge curve. At the beginning of the cycle, due to large viscosity of magma (at low discharge rate crystal content is high) large magmatic overpressure develops, reaching a maximum near the transition between the dyke and cylindrical conduit; the dyke inflates providing temporary magma storage. Minimum dyke volume corresponds to maximum discharge rate (curve C). After [21]

by a magma chamber or dyke-shaped conduit located in elastic rocks, or by compressibility of the magma itself. The volumes of these capacitors are different and thus will cause pulsations with different periods. Currently there is no single model that can account for pulsations with multiple timescales.

Future Directions

Our models indicate that magmatic systems in lava dome eruptions can be very sensitive to small changes in parameters. This sensitivity is most marked when the system is close to the cusps of steady-state solutions. If magma discharge rate becomes so high that gas cannot escape efficiently during magma ascent, then conditions for magma fragmentation and explosive eruption can arise. Empirical evidence suggests that conditions for explosive eruption arise when magma discharge rates reach approximately $10 \text{ m}^3/\text{s}$ or more in dome eruptions [45,83]. Calculations show the possibility of such high discharge rates for the system parameters typical of lava dome-building eruptions.

We have illustrated model sensitivity of results by varying only one parameter at a time on plots of chamber pressure and discharge rate. However, magmatic sys-

tems have many controlling parameters that may vary simultaneously. Furthermore, some controlling parameters are likely to be interdependent (such as temperature, volatile content and phenocryst content, for example) and others may be independent (such as magma temperature and conduit dimensions). An eruption can be expected to move through n -parameter space, making simulation and its parameter depiction difficult. Our results are simplified, so system sensitivity and behaviour in the real world may be yet more complex. A volcanic system may be quite predictable when it is within a stable regime, but may become inherently unpredictable [84,85] when variations in the parameters move the system towards transition points and flow regime boundaries.

As in all complex systems there are many controlling parameters. Our models capture some of the key dynamics, but are still simplified in many respects, so do not fully capture the real variations. Our models do not, for example, consider variations in dome height, gas escape to surrounding rocks, strain-rate dependent rheological effects or time dependent changes in conduit diameter. The model for porosity is based on interpretation of measurements of porosity of erupted magma. The role of post-eruptive alterations of pore structure, for example, formation of cooling cracks, cannot be easily estimated. The

model of bubble coalescence and permeability formation is important for understanding gas escape mechanisms and will provide constraints on transitions between extrusive and explosive activity. Because the model remains 1D, lateral distribution of parameters cannot be studied. These includes: lateral pressure gradients, magma crystallization on the conduit walls, wallrocks melting or erosion, formation of shear zones and shear heating, heat flux to surrounding rocks. The models also make the simplifying assumption that influx into the chamber from a deep source is a constant, or given as a function of time. The dynamics of the magma chamber itself are oversimplified in all existing conduit flow models. Changes in magma properties in magma chamber can affect the long-term evolution of eruptions. We have considered water as the only volatile and the addition of other gas species (e.g. CO₂ and SO₂) would add further variability.

There are large uncertainties in some parameters, which are likely to be very strong controls, such as the rheological properties of high crystalline magmas and crystal growth kinetic parameters, notably at low pressures (< 30 MPa) where experiments are very difficult to do (e.g. [22]). More experiments are necessary to understand the rheology of multiphase systems containing melt, crystals and bubbles. The effects of crystal shape, crystal size distribution and strain rate remain largely unclear. Some parameters, such as conduit geometry variation with depth, are highly uncertain. With so many parameters, good fits can be achieved by selecting plausible values for real systems. Barmin et al. [3], for example, were able to reproduce the patterns of discharge rate at Mount St. Helens and Santiaguito quite accurately. However, such models are not unique, partly because the actual values of some parameters may be quite different to the assumed values and partly because of the model simplifications.

Results obtained from waveform inversions of very-long-period seismic data over the past few years point to the predominance of a crack-like geometry for volcanic conduits [11], and it is becoming increasingly evident that the details of this geometry, such as conduit inclination, a sudden change in conduit direction, a conduit bifurcation, or a sudden increase in cross section, are all critically important in controlling magma flow dynamics. Future modeling attempts will need to be closely tied to information on conduit geometry derived from seismology to provide a more realistic view of volcanic processes.

The full simulation of any particular volcanic eruption in such a non-linear and sensitive system may appear a hopeless task. However, some reduction in uncertainties will certainly help to make the models more realistic. Further experimental studies of crystallization kinetics and

the rheological properties of magma at high crystallinities are among the most obvious topics for future research. Advances in understanding the controls on magma input into an open-system chamber would be beneficial, since the delicate balance between input and output is a prime control on periodic behaviour.

Further model development includes 2D effects, elastic deformation effects in dyke-fed domes and coupling between magma chamber and conduit flow dynamics. Even with such improvements, large parameter uncertainties and modeling difficulties will remain. In such circumstances the logical approach is to start quantifying the uncertainties and sampling from them to produce probabilistic outputs based on ensemble models where numerical models of the kind discussed here can be run many times. A future challenge for numerical models will also be to produce simulated outputs which compare in detail with observations, in particular time series of magma discharge rates.

Acknowledgments

This work was supported by NERC research grant reference NE/C509958/1. OM and AB acknowledge Russian Foundation for Basic Research (08-01-00016) and President of Russian Federation program (NCH-4710.2006.1). RSJS acknowledges a Royal Society Wolfson Merit Award. The Royal Society exchange grants and NERC grants had supported the Bristol/Moscow work over the last 10 years.

Bibliography

Primary Literature

1. Balmforth NJ, Burbidge AS, Craster RV (2001) Shallow Lava Theory. In: Balmforth NJ, Provenzale A (eds) *Geomorphological Fluid Mechanics*. Lecture Notes in Physics, vol 582. Springer, Berlin, pp 164–187
2. Balmforth NJ, Burbidge AS, Craster RV, Rust AC, Sassi R (2006) Viscoplastic flow over an inclined surface. *J Non-Newtonian Fluid Mech* 139:103–127
3. Barmin A, Melnik O, Sparks RSJ (2002) Periodic behaviour in lava dome eruptions. *Earth Planet Sc Lett* 199:173–184
4. Bingham EC (1922) *Fluidity and Plasticity*. McGraw-Hill, New York, p 215
5. Blake S (1990) Viscoplastic models of lava domes. In: Fink JH (ed) *Lava flows and domes*, Vol 2. In: Fink JH (ed) *Lava flows and domes; emplacement mechanisms and hazard implications*. Springer, Berlin, pp 88–126
6. Blundy JD, Cashman KV, Humphreys MCS (2006) Magma heating by decompression-driven crystallisation beneath andesite volcanoes. *Nature* 443:76–80. doi:10.1038/nature05100
7. Calder ES, Lockett R, Sparks RSJ, Voight B (2002) Mechanisms of lava dome instability and generation of rockfalls and pyroclastic flows at Soufrière Hills Volcano, Montserrat. In: Druitt TH, Kokelaar BP (eds) *The Eruption of Soufrière Hills Volcano*,

- Montserrat, from 1995 to 1999, Geological Society, London, Memoirs No 21, pp 173–190
8. Calder ES, Cortés JA, Palma JL, Luckett R (2005) Probabilistic analysis of rockfall frequencies during an andesite lava dome eruption: The Soufrière Hills Volcano, Montserrat. *Geophys Res Lett* 32:L16309. doi:10.1029/2005GL023594
 9. Caricchi L, Burlini L, Ulmer P, Gerya T, Vassalli M, Papale P (2007) Non-Newtonian rheology of crystal-bearing magmas and implications for magma ascent dynamics. *Earth Planet Sci Lett* 10.1016/j.epsl.2007.09.032
 10. Cashman KV, Blundy JD (2000) Degassing and crystallization of ascending andesite and dacite. In: Francis P, Neuberg J, Sparks RSJ (eds) Causes and consequences of eruptions of andesite volcanoes. *Phil Trans Royal Soc London A*, pp 1487–1513
 11. Chouet B, Dawson P, Arciniega-Ceballos A (2005) Source mechanism of Vulcanian degassing at Popocatepetl Volcano, Mexico, determined from waveform inversions of very long period signals. *J Geophys Res* 110:B07301. doi:10.1029/2004JB003524
 12. Christiansen RL, Peterson DW (1981) Chronology of the 1980 Eruptive Activity. In: Lipman PW, Mullineaux DR (eds) The 1980 Eruptions of Mount St. Helens. Washington, US Geological Survey Professional Paper 1250, p 844
 13. Clarke AB, Stephens S, Teasdale R, Sparks RSJ, Diller K (2007) Petrological constraints on the decompression history of magma prior to Vulcanian explosions at the Soufrière Hills volcano, Montserrat. *J Volcanol Geotherm Res* 161:261–274. doi:10.1016/j.jvolgeores.2006.11.007
 14. Cole P, Calder ES, Sparks RSJ, Clarke AB, Druitt TH, Young SR, Herd R, Harford CL, Norton GE (2002) Deposits from dome-collapse and fountain-collapse pyroclastic flows at Soufrière Hills Volcano, Montserrat. In: Druitt TH, Kokelaar BP (eds) The eruption of the Soufrière Hills Volcano, Montserrat from 1995 to 1999. Geological Society, London, Memoir No 21, pp 231–262
 15. Connor CB, Sparks RSJ, Mason RM, Bonadonna C, Young SR (2003) Exploring links between physical and probabilistic models of volcanic eruptions: the Soufrière Hills Volcano, Montserrat. *Geophys Res Lett* 30. doi:10.1029/2003GL017384
 16. Costa A (2005) Viscosity of high crystal content melts: dependence on solid fraction. *Geophys Res Lett* 32:L22308. doi:10.1029/2005GL024300
 17. Costa A, Macedonio G (2002) Nonlinear phenomena in fluids with temperature-dependent viscosity: an hysteresis model for magma flow in conduits. *Geophys Res Lett* 29(10). doi:10.1029/2001GL014493
 18. Costa A, Macedonio G (2003) Viscous heating in fluids with temperature-dependent viscosity: implications for magma flows. *Nonlinear Proc Geophys* 10:545–555
 19. Costa A, Macedonio G (2005) Viscous heating in fluids with temperature-dependent viscosity: triggering of secondary flows. *J Fluid Mech* 540:21–38
 20. Costa A, Melnik O, Sparks RSJ (2007) Controls of conduit geometry and wallrock elasticity on lava dome eruptions. *Earth Planet Sci Lett* 260:137–151. doi:10.1016/j.epsl.2007.05.024
 21. Costa A, Melnik O, Sparks RSJ, Voight B (2007) The control of magma flow in dykes on cyclic lava dome extrusion. *Geophys Res Lett* 34:L02303. doi:10.1029/2006GL027466
 22. Couch S, Sparks RSJ, Carroll MR (2001) Mineral disequilibrium in lavas explained by convective self-mixing in open magma chambers. *Nature* 411:1037–1039
 23. Denlinger RP, Hoblitt RP (1999) Cyclic eruptive behaviour of silicic volcanoes. *Geology* 27(5):459–462
 24. Diller K, Clarke AB, Voight B, Neri A (2006) Mechanisms of conduit plug formation: Implications for vulcanian explosions. *Geophys Res Lett* 33:L20302. doi:10.1029/2006GL027391
 25. Dirksen O, Humphreys MCS, Pletchov P, Melnik O, Demyanchuk Y, Sparks RSJ, Mahony S (2006) The 2001–2004 dome-forming eruption of Shiveluch Volcano, Kamchatka: Observation, petrological investigation and numerical modelling. *J Volcanol Geotherm Res* 155:201–226. doi:10.1016/j.jvolgeores.2006.03.029
 26. Druitt TH, Young S, Baptie B, Calder E, Clarke AB, Cole P, Harford C, Herd R, Luckett R, Ryan G, Sparks RSJ, Voight B (2002) Episodes of cyclic Vulcanian explosive activity with fountain collapse at Soufrière Hills volcano, Montserrat. In: Druitt TH, Kokelaar BP (eds) The eruption of the Soufrière Hills Volcano, Montserrat from 1995 to 1999. Geological Society, London, Memoir No 21, pp 231–262
 27. Eichelberger JC, Carrigan CR, Westrich HR, Price RH (1986) Non-explosive silicic volcanism. *Nature* 323:598–602
 28. Fedotov SA, Dvigalo VN, Zharinov NA, Ivanov VV, Seliverstov NI, Khubunaya SA, Demyanchuk YV, Markov LG, Osipenko LG, Smelov NP (2001) The eruption of Shiveluch volcano on May–July 2001. *Volcanol Seis* 6:3–15
 29. Fink JH, Griffiths RW (1990) Radial spreading of viscous gravity currents with solidifying crust. *J Fluid Mech* 221:485–509
 30. Fink JH, Griffiths RW (1998) Morphology, eruption rates, and rheology of lava domes: Insights from laboratory models. *J Geophys Res* 103:527–545
 31. Green, DN, Neuberg J (2006) Waveform classification of volcanic low-frequency earthquake swarms and its implication at Soufrière Hills Volcano, Montserrat. *J Volcanol Geotherm Res* 153:51–63. doi:10.1016/j.jvolgeores.2005.08.003
 32. Hale AJ, Bourgoignie L, Mühlhaus HB (2007) Using the level set method to model endogenous lava dome growth. *J Geophys Res* 112:B03213. doi:10.1029/2006JB004445
 33. Hale AJ, Wadge G (2003) Numerical modeling of the growth dynamics of a simple silicic lava dome. *Geophys Res Lett* 30(19). doi:10.1029/2003GL018182
 34. Hammer JE, Rutherford MJ (2002) An experimental study of the kinetics of decompression-induced crystallization in silicic melt. *J Geophys Res* 107:(B1). doi:10.1029/2001JB000281
 35. Harris AL, Rose WI, Flynn LP (2002) Temporal trends in Lava Dome extrusion at Santiaguito 1922–2000. *Bull Volcanol* 65:77–89
 36. Hess KU, Dingwell DB (1996) Viscosities of hydrous leucogranite melts: A non-Arrhenian model. *Am Mineral* 81:1297–1300
 37. Hoblitt RP, Wolfe EW, Scott WE, Couchman MR, Pallister JS, Javier D (1996) The preclimatic eruptions of Mount Pinatubo, June 1991. In: Newhall CG, Punongbayan RS (eds) Fire and Mud: Eruptions and Lahars of Mount Pinatubo, Philippines. Philippine Institute of Volcanology and Seismology, Quezon City, and University of Washington Press, Seattle, pp 457–511
 38. Hort M (1998) Abrupt change in magma liquidus temperature because of volatile loss or magma mixing: effects of Nucleation, crystal growth and thermal history of the magma. *J Petrol* 39:1063–1076
 39. Humphreys M, Blundy JD, Sparks RSJ (2006) Magma Evolution and Open-system processes at Shiveluch Volcano: insights from phenocryst zoning. *J Petrol* 47(12) 2303–2334. doi:10.1093/petrology/eg1045

40. Huppert HE, Shepherd JB, Sigurdsson H, Sparks RSJ (1982) On lava dome growth, with application to the 1979 lava extrusion of the Soufriere, St Vincent. *J Volcanol Geotherm Res* 14: 199–222
41. Huppert HE, Woods AW (2002) The role of volatiles in magma chamber dynamics. *Nature* 420:493–495
42. Ida Y (1996) Cyclic fluid effusion accompanied by pressure change: Implication for volcanic eruptions and tremor. *Geophys Res Lett* 23:1457–1460
43. Iverson RM et al (2006) Dynamics of seismogenic volcanic extrusion at Mount St. Helens in 2004–05. *Nature* 444:439–443
44. Jaquet O, Sparks RSJ, Carniel R (2006) Magma Memory recorded by statistics of volcanic explosions at the Soufriere Hills Volcano, Montserrat. In: Mader HM, Coles SG, Connor CB, Connor LJ (eds) *Statistics in Volcanology*. Geological Society, London, Special Publication of IAVCEI, vol 1. pp 175–184
45. Jaupart C, Allegre CJ (1991) Gas content, eruption rate and instabilities of eruption regime in silicic volcanoes. *Earth Planet Sci Lett* 102:413–429
46. Kirkpatrick R (1976) Towards a Kinetic Model for the Crystallization of Magma Bodies. *J Geophys Res* 81:2565–2571
47. Landau L, Lifshitz E (1987) *Fluid Mechanics*, 2nd edn. Butterworth–Heinemann, Oxford
48. Lejeune A, Richet P (1995) Rheology of crystal-bearing silicate melts: An experimental study at high viscosity. *J Geophys Res* 100:4215–4229
49. Lensky NG, Sparks RSJ, Navon O, Lyakhovsky V (2007) Cyclic activity at Soufriere Hills volcano, Montserrat: degassing-induced pressurization and stick-slip extrusion. In: Lane SJ, Gilbert JS (eds) *Fluid motions in volcanic conduits: a source of seismic and acoustic signals*. Geological Society, London, Special Publications, vol 307, pp 169–188. doi:10.1144/SP307.100305-8719/08/\$15.00 The Geological Society of London 2008
50. Lister JR, Kerr RC (1991) Fluid mechanical models of crack propagation and their application to magma transport in dykes. *J Geophys Res* 96:10049–10077
51. Llewellyn EW, Manga M (2005) Bubble suspension rheology and implications for conduit flow. *J Geotherm Res* 143: 205–217
52. Loitsyansky LG (1978) *Fluid and gas mechanics*. Nauka, Moscow, pp 847 (in Russian)
53. Maeda I (2000) Nonlinear visco-elastic volcanic model and its application to the recent eruption of Mt. Unzen. *J Volcanol Geotherm Res* 95:35–47
54. Mason RM, Starostin AB, Melnik O, Sparks RSJ (2006) From Vulcanian explosions to sustained explosive eruptions: The role of diffusive mass transfer in conduit flow dynamics. *J Volcanol Geotherm Res* 153:148–165. doi:10.1016/j.jvolgeores.2005.08.011
55. Marsh BD (2000) Reservoirs of Magma and Magma chambers. In: Sigurdsson H (ed) *Encyclopedia of volcanoes*. Academic Press, New York, pp 191–206
56. Mastin GL, Pollard DD (1988) Surface Deformation and Shallow Dike Intrusion Processes at Inyo Craters, Long Valley, California. *J Geophys Res* 93(B11):13221–13235
57. Matthews SJ, Gardeweg MC, Sparks RSJ (1997) The 1984 to 1996 cyclic activity of Lascar Volcano, northern Chile: Cycles of dome growth, dome subsidence, degassing and explosive eruptions. *Bull Volcanol* 59:72–82
58. Mattioli G, Dixon TH, Farina F, Howell ES, Jansma PE, Smith AL (1998) GPS measurement of surface deformation around Soufriere Hills volcano, Montserrat from October 1995 to July 1996. *Geophys Res Lett* 25(18):3417–3420
59. Melnik O (2000) Dynamics of two-phase conduit flow of high-viscosity gas-saturated magma: large variations of sustained explosive eruption intensity. *Bull Volcanol* 62:153–170
60. Melnik O, Barmin A, Sparks RSJ (2005) Dynamics of magma flow inside volcanic conduits with bubble overpressure buildup and gas loss through permeable magma. *J Volcanol Geotherm Res* 143:53–68
61. Melnik O, Sparks RSJ (1999) Non-linear dynamics of lava dome extrusion. *Nature* 402:37–41
62. Melnik O, Sparks RSJ (2002) Dynamics of magma ascent and lava extrusion at Soufriere Hills Volcano, Montserrat. In: Druitt TH, Kokelaar BP (eds) *The eruption of the Soufriere Hills Volcano, Montserrat from 1995 to 1999*. Geological Society, London, Memoir No 21, pp 223–240
63. Melnik O, Sparks RSJ (2005) Controls on conduit magma flow dynamics during lava dome building eruptions. *J Geophys Res* 110(B02209). doi:10.1029/2004JB003183
64. Mériaux C, Jaupart C (1995) Simple fluid dynamic models of volcanic rift zones. *Earth Planet Sci Lett* 136:223–240
65. Murphy MD, Sparks SJ, Barclay J, Carroll MR, Brewer TS (2000) Remobilization origin for andesite magma by intrusion of mafic magma at the Soufriere Hills Volcano. In: Montserrat WI (ed) *A trigger for renewed eruption*. *J Petrol* 41:21–42
66. Muskhelishvili N (1963) *Some Basic Problems in the Mathematical Theory of Elasticity*. Noordhoff, Leiden, The Netherlands
67. Nakada S, Eichelberger JC (2004) Looking into a volcano: drilling Unzen. *Geotimes* 49:14–17
68. Nakada S, Shimizu H, Ohta K (1999) Overview of the 1990–1995 eruption at Unzen Volcano. *J Volcanol Geoth Res* 89:1–22
69. Navon O, Lyakhovsky V (1998) Vesiculation processes in silicic magmas. In: Gilbert J, Sparks RSJ (eds) *The Physics of explosive volcanic eruption*. Geological Society London, Special Publication, vol 145. pp 27–50
70. Neuberg JW, Tuffen H, Collier L, Green D, Powell T, Dingwell D (2006) The trigger mechanism of low-frequency earthquakes on Montserrat. *J Volcanol Geotherm Res* 153:37–50
71. Newhall CG, Melson WG (1983) Explosive activity associated with the growth of volcanic domes. *J Volcanol Geoth Res* 17:111–131
72. Norton GE, Watts RB, Voight B, Mattioli GS, Herd RA, Young SR, Devine JD, Aspinall WP, Bonadonna C, Baptie BJ, Edmonds M, Harford CL, Jolly AD, Loughlin SC, Luckett R, Sparks RSJ (2002) Pyroclastic flow and explosive activity of the lava dome of Soufriere Hills volcano, Montserrat, during a period of no magma extrusion (March 1998 to November 1999). In: Druitt TH, Kokelaar BP (eds) *The eruption of the Soufriere Hills Volcano, Montserrat from 1995 to 1999*. Geological Society, London, Memoir No 21, pp 467–482
73. Ohba T, Kitade Y (2005) Subvolcanic hydrothermal systems: Implications from hydrothermal minerals in hydrovolcanic ash. *J Volcanol Geotherm Res* 145:249–262
74. Robertson R, Cole P, Sparks RSJ, Harford C, Lejeune AM, McGuire WJ, Miller AD, Murphy MD, Norton G, Stevens NF, Young SR (1998) The explosive eruption of Soufriere Hills Volcano, Montserrat 17 September, 1996. *Geophys Res Lett* 25:3429–3432
75. Roman DC (2005) Numerical models of volcanotectonic earthquake triggering on non-ideally oriented faults. *Geophys Res Lett* 32, doi:10.1029/2004GL021549

76. Roman DC, Neuberg J, Luckett RR (2006) Assessing the likelihood of volcanic eruption through analysis of volcanotectonic earthquake fault-plane solutions. *Earth Planet Sci Lett* 248:244–252
77. Rubin AM (1995) Propagation of magma-filled cracks. *Annu Rev Planet Sci* 23:287–336
78. Saar MO, Manga M, Katharine VC, Fremouw S (2001) Numerical models of the onset of yield strength in crystal–melt suspensions. *Earth Planet Sci Lett* 187:367–379
79. Sahagian D (2005) Volcanic eruption mechanisms: Insights from intercomparison of models of conduit processes. *J Volcanol Geotherm Res* 143(1–3): 1–15
80. Slezin YB (1984) Dispersion regime dynamics in volcanic eruptions, 2. Flow rate instability conditions and nature of catastrophic explosive eruptions. *Vulkanol Seism* 1:23–35
81. Slezin YB (2003) The mechanism of volcanic eruptions (a steady state approach). *J Volcanol Geotherm Res* 122:7–50
82. Sparks RSJ (1978) The dynamics of bubble formation and growth in magmas – a review and analysis. *J Volcanol Geotherm Res* 3:1–37
83. Sparks RSJ (1997) Causes and consequences of pressurization in lava dome eruptions. *Earth Planet Sci Lett* 150:177–189
84. Sparks RSJ (2003) Forecasting Volcanic Eruptions. *Earth and Planetary Science Letters Frontiers in Earth Science Series* 210:1–15
85. Sparks RSJ, Aspinall WP (2004) Volcanic Activity: Frontiers and Challenges. In: Forecasting, Prediction, and Risk Assessment. AGU Geophysical Monograph “State of the Planet” 150, IUGG Monograph 19, pp 359–374
86. Sparks RSJ, Murphy MD, Lejeune AM, Watts RB, Barclay J, Young SR (2000) Control on the emplacement of the andesite lava dome of the Soufrière Hills Volcano by degassing-induced crystallization. *Terra Nova* 12:14–20
87. Sparks RSJ, Young SR (2002) The eruption of Soufrière Hills volcano, Montserrat (1995–1999): overview of scientific results. In: Druitt TH, Kokelaar BP (eds) *The eruption of the Soufrière Hills Volcano, Montserrat from 1995 to 1999*. Geological Society, London, Memoir No 21, pp 45–69
88. Sparks RSJ, Young SR, Barclay J, Calder ES, Cole PD, Darroux B, Davies MA, Druitt TH, Harford CL, Herd R, James M, Lejeune AM, Loughlin S, Norton G, Skeritt G, Stevens NF, Toothill J, Wadge G, Watts R (1998) Magma production and growth of the lava dome of the Soufrière Hills Volcano, Montserrat, West Indies: November 1995 to December 1997. *Geophys Res Lett* 25:3421–3424
89. Swanson DA, Holcomb RT (1990) Regularities in growth of the Mount St. Helens dacite dome 1980–1986. In: Fink JH (ed) *Lava flows and domes; emplacement mechanisms and hazard implications*. Springer, Berlin, pp 3–24
90. Voight B, Hoblitt RP, Clarke AB, Lockhart AB, Miller AD, Lynch L, McMahon J (1998) Remarkable cyclic ground deformation monitored in real-time on Montserrat, and its use in eruption forecasting. *Geophys Res Lett* 25:3405–3408
91. Voight B, Sparks RSJ, Miller AD, Stewart RC, Hoblitt RP, Clarke A, Ewart J, Aspinall W, Baptie B, Druitt TH, Herd R, Jackson P, Lockhart AB, Loughlin SC, Lynch L, McMahon J, Norton GE, Robertson R, Watson IM, Young SR (1999) Magma flow instability and cyclic activity at Soufrière Hills Volcano, Montserrat. *Science* 283:1138–1142
92. Walker GPL (1973) Lengths of lava flows. *Philos Trans Royal Soc A* 274:107–118
93. Watson IM et al (2000) The relationship between degassing and ground deformation at Soufrière Hills Volcano, Montserrat. *J Volcanol Geotherm Res* 98(1–4):117–126
94. Watts RB, Sparks RSJ, Herd RA, Young SR (2002) Growth patterns and emplacement of the andesitic lava dome at Soufrière Hills Volcano, Montserrat. In: Druitt TH, Kokelaar BP (eds) *The eruption of the Soufrière Hills Volcano, Montserrat from 1995 to 1999*. Geological Society, London, Memoir No 21, pp 115–152
95. Whitehead JA, Helfrich KR (1991) Instability of flow with temperature-dependent viscosity: a model of magma dynamics. *J Geophys Res* 96:4145–4155
96. Williams SN, Self S (1983) The October 1902 Plinian eruption of Santa Maria volcano, Guatemala. *J Volcanol Geotherm Res* 16:33–56
97. Woods AW, Koyaguchi T (1994) Transitions between explosive and effusive eruption of silicic magmas. *Nature* 370:641–645
98. Wylie JJ, Voight B, Whitehead JA (1999) Instability of magma flow from volatile-dependent viscosity. *Science* 285: 1883–1885
99. Yokoyama I, Yamashita H, Watanabe H, Okada H (1981) Geophysical characteristics of dacite volcanism – 1977–1978 eruption of Usu volcano. *J Volcanol Geotherm Res* 9:335–358

Books and Reviews

- Dobran F (2001) *Volcanic Processes: Mechanisms In Material Transport*. Kluwer, New York, pp 620
- Gilbert JS, Sparks RSJ (eds) (1998) *The Physics of Explosive Volcanism*. Special Publication of the Geological Society of London, vol 145, pp 186
- Gonnermann H, Manga M (2007) The fluid mechanics inside a volcano. *Ann Rev Fluid Mech* 39:321–356
- Lander HM, Coles SG, Connor CB, Connor LJ (2006) *Statistics in Volcanology*. IAVCEI Publications, Geological Society Publishing House, p 296

Volcanic Eruptions, Explosive: Experimental Insights

STEPHEN J. LANE, MICHAEL R. JAMES
Lancaster Environment Centre, Lancaster University,
Lancaster, UK

Article Outline

[Glossary](#)
[Definition of the Subject](#)
[Introduction](#)
[Volcanic Materials](#)
[Volcanic Processes](#)
[Analogue Approach](#)
[Future Directions](#)
[Acknowledgments](#)
[Bibliography](#)

Glossary

Conduit Subterranean pathways to the surface created and sustained by the flow of volcanic materials are known as volcanic conduits. In the laboratory, tubes are used as scale equivalents. The two terminologies ('conduits' and 'tubes') should be kept distinct to avoid inadvertent acceptance that a laboratory experiment is a direct replica of a volcanic process.

Magma When rock melts underground it becomes magma. When magma flows on the surface it is known as lava and when it is projected into the atmosphere it forms pyroclasts. Most magma is silicate-based and comprises a three-phase mixture of solid (crystals, called microlites when small), liquid (melt) and gas (bubbles or vesicles).

Rheology When a force is applied to matter it deforms. The rheology of a material describes the relationship between applied force and the material response. Volcanic materials have a wide range of rheological behaviors dependent on the proportions of gas, liquid and solid, temperature, chemical composition, deformation history and rate of deformation.

Scaling Explosive volcanic eruptions involve temperatures of order 1000°C, pressures of many MPa and physical sizes from μm to km. Laboratory study of these processes generally involves observation and measurement of processes operating at lower temperature or pressure, or at smaller physical size. Scaling is the means of making laboratory-scale analogues representative of volcano-scale natural processes.

Volatiles Explosive volcanic eruptions are driven by the exsolution of a dissolved gas phase as magma pressure falls. These gaseous species, dominated by water vapor on Earth, are known as volatiles.

Definition of the Subject

The magnitude of volcanic eruptions may be classified using the Volcanic Explosivity Index (VEI) [95,99]. The lowest VEI index of zero covers non-explosive activity (such as the production of lava flows) and is generally associated with low magma effusion rates or low viscosity magmas, for example, carbonate-based carbonatites [127]. For silicate-based magmas, which are generally more viscous than carbonatites, the boundary between effusive and explosive volcanism is commonly marked by Hawaiian fire-fountaining activity [96]. Magmas with a high silica content, or a lower temperature (and thus higher viscosity), can erupt either explosively or non-explosively as lava flows or dome-building eruptions [128]. Some eruptions switch between effusive and explosive behavior dependent

on prevailing physicochemical conditions (e. g., [54,62]), with magmas tending to become more explosive at higher effusion rates. High VEI eruptions are, therefore, associated with high flow rates, large erupted volumes and substantial eruption plumes.

Such explosive activity comprises a wide range of phenomena, which result from complex non-linear interactions and feedback mechanisms. Processes that initiate in the subsurface plumbing or conduit system determine the nature of following events and control eruption styles. On emerging from the vent, volcanic material enters the atmosphere and the ensuing interactions are key in determining the consequent transport of volcanic debris that defines the impact on the environment and on human lives and infrastructure. On Earth, our capability to mitigate such volcanic hazard relies in large part on forecasting explosive events, a process which requires a high degree of understanding about the physicochemical factors operating during explosive volcanism.

In common with many science disciplines, the approaches taken to gain an understanding of explosive volcanism have relied on a combination of field observations, theoretical models and laboratory models of materials and mechanisms. Field observations form the 'ground truth' for numerical and experimental modeling (and provide vital historical data), but are often very difficult to unambiguously interpret due to their scarcity in both space and time. Numerical modeling complements field observations by providing much greater information density and, hence, the potential to examine processes in great detail. However, the accuracy of the results depends on correctly including all relevant materials properties and system processes in the model and the results can be difficult to verify against often-unobservable field phenomena. Laboratory investigation of the properties of volcanic materials, their modes of interaction and the behaviors of analogous systems provides the third complementary approach; this is the area we focus on here.

Introduction

In the context of explosive volcanic activity, laboratory experiments cover a wide range of research, the most fundamental of which is to gain an understanding of the properties of the volcanic material involved. Without this to underpin further work, neither accurate computer nor laboratory simulations could be carried out. The materials properties that are relevant to explosive volcanism include the solubility in silicate melts of volatiles (most commonly water and carbon dioxide), melt viscosity as a function of chemical composition, magma rheology as a function of

the size, shape and proportion of crystals and bubbles, gas permeability of magma, magma deformation mode (e. g. brittle or ductile) as a function of strain-rate, and volatile diffusivity. Experimental determination of these parameters and their interdependencies results in empirically formulated relationships that can be used in numerical models and compared with the properties of analogue fluids. We first review aspects of the volcanic materials literature in Sect. “[Volcanic Materials](#)”, with the aim of illustrating the nature of molten rock, the complexity of which underpins most explosive volcanic processes.

Experimental modeling of these processes can then build on the materials understanding. Such experiments involve investigation of the behavior of natural volcanic products at laboratory time and length scales, including the response of magma samples to rapid changes in pressure and temperature, the fall behavior of silicate particles in the atmosphere, and the generation and separation of electrostatic charge during explosive eruptions. Here, we encounter the concept of scaling [[11,20](#)], which links the applicability of experimental results using small samples of natural materials to natural scales that are often several orders of magnitude larger. For experiments that replace natural volcanic products with analogue materials (for example, in order to relax the experimental pressure and temperature requirements), scaling arguments are crucial. A scaling approach permits adjustment of experimental durations and sizes, whilst maintaining similarity with much larger and longer events. Consequently, analogue experimentation has allowed investigation of explosive phenomena in the broader context of fluid-dynamic behavior, and is a powerful means of giving ‘insight’ into volcanic processes.

Burgisser et al. [[20](#)] review and discuss scaling criteria for experiments and natural phenomena involving dilute multiphase mixtures in magmatic systems, and conclude “... that, despite numerous experimental studies on processes relevant to magmatic systems, some and perhaps most geologically important parameter ranges still need to be addressed at the laboratory scale”. This emphasizes that small-scale experiments aiming to mimic larger-scale natural processes need to be considered in two contexts. Firstly, laboratory experiments yield valid results in their own right and provide a means of validating numerical models. Secondly, laboratory experiments are not facsimiles of the natural process, but can give perception into how aspects of natural systems behave provided those aspects are scaled; a process normally considered at design stage. Consequently, comparing experimental results with the natural process must always be undertaken with due caution. The analogue experiment litera-

ture is reviewed in Sects. “[Volcanic Processes](#)” and “[Analogue Approach](#)”.

In Sect. “[Definition of the Subject](#)”, the combined tactics of field observation, numerical model and experimental model was discussed. In practice, complete overlap of these techniques can be difficult to achieve because the parameters measurable in the field are often incompatible with experimentally accessible variables, which in turn may not coincide with the output from numerical models. Explosive volcanism is also a difficult phenomenon to observe in action, and there are three reasons for this. Firstly, explosions do not happen very often, and the larger the explosion the more infrequent it is, with, for example, repeat timescales of order 10^3 years for VEI 6 events like the Krakatau, 1883 eruption. This makes detailed syn-event measurements of large explosive episodes infrequent on the timescale of contemporary volcanology. Secondly, high VEI events tend to destroy near-field observation equipment, making measurements very difficult to obtain even when an event does occur. Thirdly, processes that comprise an explosive event can be difficult to access directly; perhaps a prime example of this is how to obtain data about the nature of flow in the volcanic conduit system during explosive activity. Direct measurements are not possible and our main source of information is the deformation of the conduit wall created by unsteadiness in the flow, which in turn is calculated from the interpretation of ground motion signals detected by seismometers (e. g., [[31](#)]).

These considerations mean that there are many field observations, numerical and experimental models that await comparison with their companion approaches, however, the detailed study of volcanoes with low VEIs is one area where combined tactics are possible. As an example, in Sect. “[Analogue Approach](#)” we review the contribution that experimental modeling has made to the understanding of fluid flow in the conduit feeding VEI 1–2 explosions at Stromboli Volcano, Italy. Here it has been possible to measure signals from many thousand events, over the period of a few years (e. g., [[7](#)]), with a network of seismometers and other instruments, as well as detailed sampling of eruption products (e. g., [[72](#)]). Such field data are key to testing both numerical and experimental models of explosive volcanic activity wherever it occurs.

Volcanic Materials

Magma Rheology

Rheology describes the way in which materials deform and flow under the influence of an applied stress. Explosive eruptions only occur because considerable stress is applied

to magma. The rheology of natural silicate materials was being measured before World War II (e. g., [14]), with empirical models (derived from experimental data) becoming established in the 1960s and 1970s (e. g., [18,92,107] and references therein).

When stress is applied to a solid it deforms or strains elastically, the strain being the macroscopic result of atoms in the solid moving closer together or further apart. These two parameters are related by a constant called a modulus, for example, in solids under tension $\sigma = E\gamma$, where σ is tensile stress, γ is tensile strain and E is Young's modulus. Similar relationships exist for deformation under shear or by pressure change. These moduli are likely to be a constant for a range of values of applied stress, but could become dependent on strain, or indeed strain rate.

When stress (σ) is applied to a fluid (the collective term for gas and liquid), viscosity (η) is the parameter that relates the rate of flow (strain rate, $d\gamma/dt$) to the stress that is being applied to it, giving the relationship $\sigma = \eta d\gamma/dt$. The flow of a fluid is the macroscopic result of fluid molecules moving past each other; therefore, changes that influence molecular motion also affect viscosity. The viscosity can be independent of the rate of flow, a case known as Newtonian behavior, and is best exhibited by gases and liquids of low molecular weight. Fluids whose viscosity is a function of strain-rate are described as non-Newtonian, and many foodstuffs, for instance, exhibit this behavior (e. g. tomato ketchup). Viscosity is also a function of temperature, generally decreasing as temperature increases and molecules move further apart (thermal expansion). An everyday example would be Golden or Maple syrup that becomes easier to pour on heating. The concept of viscosity fails when molecular interactions are rare, for example in gases at low pressure.

Newtonian Viscosity Natural silicates in the liquid state have been assumed to be Newtonian in behavior and demonstrate a strong viscosity dependence on temperature. The relationship was initially represented by an Arrhenius-type equation, such as $\eta = A \exp[E/RT]$, where the constants A and E are dependent on the chemical composition of the silicate melt (e. g., Murase and McBirney [92]), R is the gas constant and T the absolute temperature. With considerable further laboratory effort in measuring the viscosities of a wide compositional range of natural silicate liquids, it became clear that viscosity was not strictly an Arrhenian function of temperature. Hess and Dingwell [49] developed an empirical model to describe laboratory values of viscosity for leucogranitic melts as a function of temperature and water content. The compilation of data used by Hess and Dingwell [49] is shown

in Fig. 1, and the empirical equation generated to fit the data is:

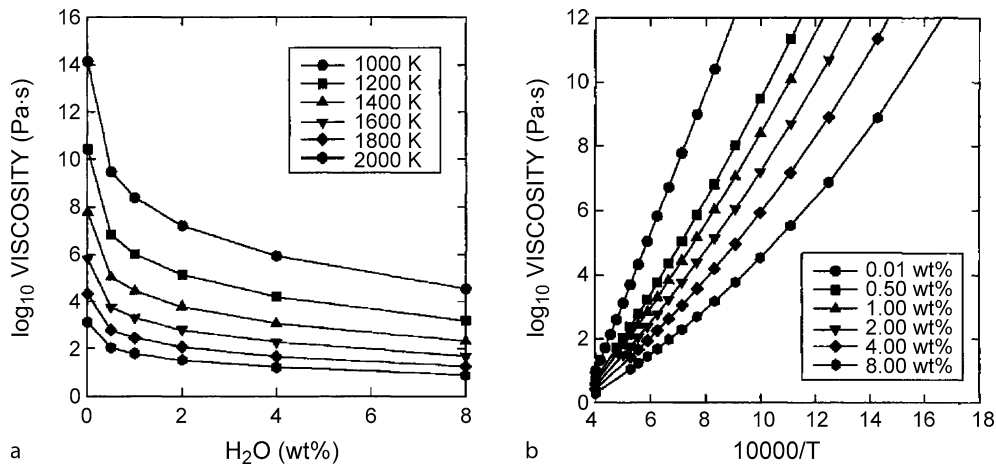
$$\log \eta = \frac{[-3.545 + 0.833 \ln(w)] + [9601 - 2368 \ln(w)]}{\{T - [195.7 + 32.25 \ln(w)]\}},$$

where w is the water % w/w. The constants in this equation will be different for silicate melts of different composition; see Zhang et al. [133] for an updated and modified version of this model. Water is important here because it is a ubiquitous component of explosive volcanism on Earth. The concentration of water has a large and non-linear impact on viscosity (Fig. 1a) because it acts as a network modifier by breaking Si-Si bonds in a silicate melt, thus decreasing the average molecular weight.

The use of laboratory measurement to provide quantitative understanding of the dependence of viscosity on temperature, water content and other parameters has provided a key component in the numerical modeling of the explosive flow behavior of natural silicates, as well as pointing the way to identifying fluids for analogue experiments.

Non-Newtonian Viscosity There is laboratory evidence that the viscosity of liquid magmas is not a constant as once assumed, but may be subtly non-Newtonian [110]. The contents of a volcanic conduit are rarely 100% liquid, with crystals present in many silicate melts below 1250°C, considerably higher than most eruption temperatures. The effect of crystallization is to significantly change the relationship between viscosity and temperature [91], especially as crystal content is both temperature and time dependent. The presence of bubbles is also ubiquitous in explosive volcanic materials, and these too alter magma behavior in response to an applied stress. The presence of both yields a rheologically complex 3-phase material.

Combined laboratory and field-measurement of the viscosity of lavas from Mount Etna [98] showed that above 1120°C Newtonian behavior was exhibited. Eruption temperatures ranged from 1084–1125°C; therefore, for much of this range the magma behaved in a non-Newtonian fashion as a consequence of the interaction between crystals suspended within the liquid silicate melt. The Etnean basalt was found to be thixotropic, meaning that the viscosity decreased the longer it was deformed, perhaps indicating that crystals were becoming aligned and could consequently move past each other more readily. The basalt also showed pseudoplastic or shear-thinning behavior, meaning that viscosity decreased as the rate of flow increased, perhaps again, because of the dynamics of crystal alignment. Finally, the basalt showed a small but measurable yield stress of < 78 Pa, below which it behaved more



Volcanic Eruptions, Explosive: Experimental Insights, Figure 1

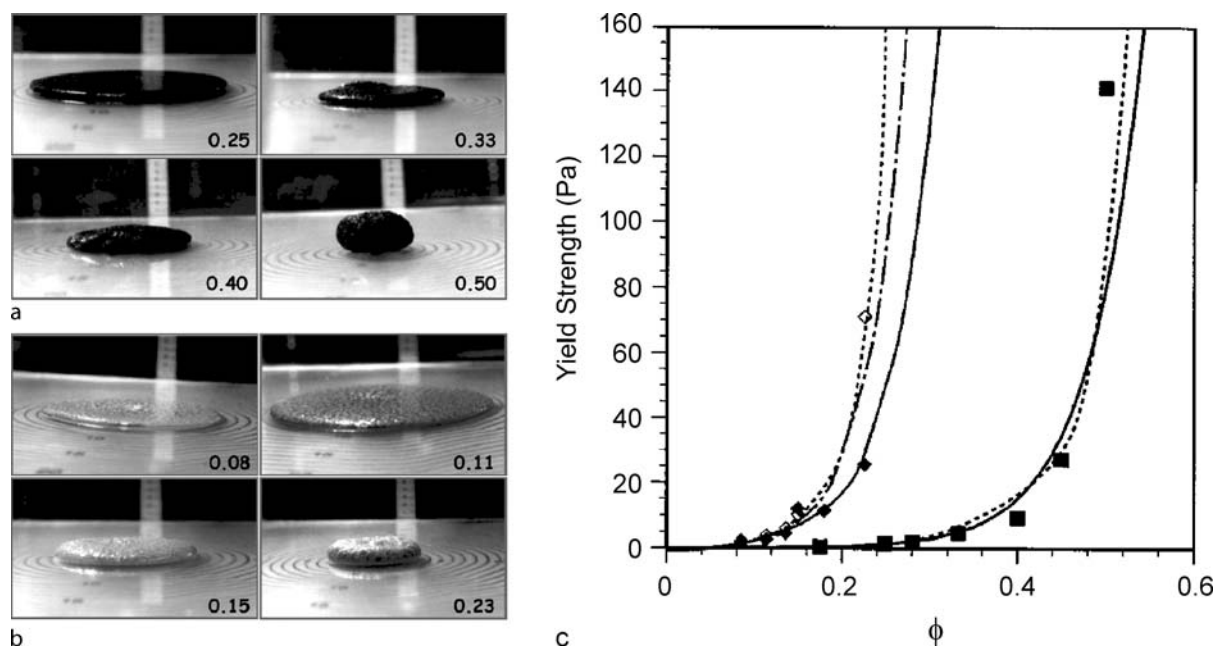
Model curves, based on experimental measurement, of the dependence of viscosity of metaluminous leucogranitic melts on dissolved water content (a) and temperature (b) from a compilation of data (Hess and Dingwell [49]). Note the logarithmic viscosity scale and non-linear nature of the relationships. Explosive volcanic activity often results in water loss from the melt, and cooling results from expansion and interaction with the atmosphere; melt viscosity increases result. The role this plays on the dynamics of expanding vesiculated flows may be studied by analogue experimental means. Figure reproduced with kind permission of the Mineralogical Society of America

like a solid material. The yield stress is likely to be a consequence of crystals weakly binding together into a mesh-like structure. The small nature of the yield stress means that the viscosity of these magmas could be described by a power law equation (i.e., the yield stress was ignored) where $\sigma = \eta (dy/dt)^n$. Above 1120°C, $n = 1$ and Newtonian behavior was observed, but as temperature falls to 1084°C, n decreases to 0.46, meaning that viscosity decreases as strain rate increases. Pinkerton and Norton [98] also noticed that physical motion of the silicate melt could induce crystallization as seen by Kouchi et al. [68]. Similar behavior has been found more recently for laboratory measurements of basalts from Japan [55].

Hoover et al. [51] showed that crystals induce yield strength in magmas at volume fractions as low as 0.2, although this is strongly dependent on crystal shape. These experiments were carried out on natural basaltic samples, as well as using an analogous system of neutrally buoyant particles in corn syrup (Fig. 2). Natural samples do, by definition, provide data directly applicable to the natural system, but analogue experiments are complementary because particles have controlled size, shape and concentration. These experiments provide a good example of the kind of complex interplay of time-dependent processes that can occur in magmatic systems that tend only to be quantified by detailed experimentation.

At eruption temperatures, the non-Newtonian behavior of magmas is due in large part to the presence of crystal

networks; however, during flow, bubbles must also move past each other and contribute to fluid rheology. Explosive eruptions only occur because bubbles form and expand; therefore, understanding bubble behavior is central to understanding explosive processes. When both bubble size and the fluid flow rate are small, then the surface tension between the silicate liquid and the water vapor in the bubble resists viscous forces and is able to minimize the bubble surface area maintaining spherical bubbles; the bubbles act as if they are solid spheres suspended in the silicate melt. However, if bubbles and flow rate are larger, then surface tension is no longer able to maintain a spherical shape against the viscous drag, and bubbles elongate in the flow field. Under conditions of steady flow, when bubble shape is stable with time, these two behaviors may be distinguished by the capillary number, $Ca = \lambda \gamma'$ where $\lambda = a\eta/\sigma$, a being bubble diameter, η viscosity, γ' strain rate and σ surface tension (e.g., Llewellyn and Manga [74]). When Ca is significantly less than unity, surface tension forces dominate and bubbles remain near spherical. However, when Ca is significantly greater than unity surface tension is overcome by the combination of liquid shear and viscosity, forcing bubbles to elongate. Ca provides an example of a parameter that may be used to scale between volcanic behavior and a laboratory experiment. If bubbles preserved in pumice from an eruption were highly elongated, then any experiment simulating this process would need to also produce highly elongated



Volcanic Eruptions, Explosive: Experimental Insights, Figure 2

Magma has complex rheology partly because of its crystal content. Hoover et al. [51] found that basalt with crystals showed solid-like behavior at low stress. Analogue experiments using near-spherical poppy seeds (a) and highly irregular shavings of kaolin/wax (b) in corn syrup demonstrate the role of particle concentration and shape in giving yield strength to solid-liquid mixtures, the number in each panel being the volume fraction of particles. Yield strength increased rapidly (c) for volume fractions of round poppy seed (filled squares) above about 0.4, allowing extruded material to retain considerable vertical topography (a). The same effect occurs at volume fractions around 0.2 for irregular particles (b) because they interact more strongly with each other than spherical particles. Crystals in magma not only act as nucleation sites for bubbles, but also have a very strong rheological influence in their own right. Reprinted with kind permission from Elsevier

bubbles and not spherical bubbles. The shape-change undergone by bubbles provides an added complexity over the effects of crystals, whose shapes are generally constant.

Bagdassarov and Dingwell [8,9] experimentally measured the rheological behavior of vesicular rhyolite, using oscillatory rheometry, with a liquid viscosity between 10^9 and 10^{12} Pa s and gas bubble volume fractions in the region between zero and 0.3. Under these conditions, where $Ca \gg 1$, it was shown that vesicular rhyolite decreased in viscosity with increasing gas volume fraction. Such rheological experiments on hot, high-viscosity natural silicate melts are difficult, and the scaling of the small-strain results to larger scales is not straightforward. Using an oscillating viscometer, Llewellyn et al. [75] measured the viscosity of bubbly Golden Syrup, a fluid analogous to molten silicate with water vapor bubbles, but with liquid viscosity between 10^1 and 10^2 Pa s. The analogous fluid has the advantage of being liquid at room temperature, thereby placing much less stringent demands on any measurement apparatus. Llewellyn et al. [75] showed the effect of increas-

ing gas volume fraction from zero to 0.5 with small deformations ($Ca \ll 1$) caused viscosity to change by over an order of magnitude. They also discriminated between steady flow (bubbles not changing shape) and unsteady flow (bubbles in the process of changing shape) by proposing the dynamic capillary number $Cd = \lambda \gamma'' / \gamma'$, where λ represents the timescale over which a deformed bubble can relax. Under steady flow conditions bubbles tended to increase viscosity, but under conditions of rapidly changing strain rate increasing gas volume fraction reduced viscosity; a result consistent with the oscillatory rheometry results of Bagdassarov and Dingwell [9]. This experimental result largely unified the seemingly contradictory literature that preceded it, and the consequences of these two regimes of behavior are discussed lucidly by Llewellyn and Manga [74], where the influence of bubbles is shown to change some model outcomes by factors of two or more. This is an excellent example of the role that analogue experimental measurement can play in helping to understand complex and inaccessible natural phenomena.

Viscosity or Modulus? The concept of a relaxation time was encountered above in relation to how long a deformed (non-spherical) bubble takes to approach the relaxed spherical shape. This same approach can also be applied at the molecular level as liquids flow. During viscous flow, molecules move past each other, and this requires them to be able to reorient or deform. If the timescale of molecular deformation is much shorter than the timescale required by the strain rate during flow, then liquid or viscous behavior ensues. However, if the strain rate is such that molecules cannot reorient or deform, then the material behaves, at least in part, like an elastic solid, with strain being accommodated by bond stretching, or fracture, if yield stress is exceeded.

Materials that demonstrate aspects of liquid and solid behavior are known as viscoelastic. Viscoelasticity was first investigated in the nineteenth century using materials like rubber and glass. Viscoelastic behavior in volcanic materials begins with the onset of non-Newtonian liquid behavior at deformation timescales about 100 times longer than the relaxation time of silicate molecules in the melt [39]. The onset of non-Newtonian behavior suggests that there is a range of relaxation timescales for different molecules, and this may be a consequence of silicate melts having a range of molecular weights rather than a single value.

The *timescale* of molecular relaxation is given by the Maxwell relation, *viscosity/modulus*, i. e., the relative weighting of liquid to solid response when stress is applied. In volcanic materials the modulus is effectively constant as temperature and composition change, but viscosity changes by a factor of about 10^9 or more. At low magma viscosities, the relaxation timescale is short and viscous liquid behavior occurs at volcanically plausible strain rates. However, magmas of high viscosity have long relaxation timescales. Here, the onset of non-Newtonian behavior, and ultimately the glass transition to brittle solid behavior, occurs at much lower strain rates. Dingwell [38] discusses the relevance of this to explosive volcanic eruptions, and proposes the onset of brittle failure in high-viscosity magma under significant strain rates as a criterion for magma fragmentation. Zhang [130] showed that magma fragmentation also depends on the number density and size of bubbles within the melt.

Volatile Solubility

Volatiles are defined as those compounds that are dissolved within the matrix of a silicate melt at high pressures, but become supersaturated and, consequently, then exsolve in the supercritical or gaseous state as pressure drops towards atmospheric. On Earth, H_2O is the most com-

mon magmatic volatile, with CO_2 , SO_2 , HCl , and the halogens also present. For water, exsolution occurs into the supercritical state, or gas phase at depths less than about 1 km; therefore, understanding the physicochemical behavior of these compounds at volcanic temperatures and pressures is a key component in the modeling of explosive volcanic eruptions. Water itself has been the subject of extensive laboratory and numerical experiments (with Kalinichev [65] providing a review) because of its anthropogenic usefulness as well as geological importance. The densities of volatile species are less than that of the silicate melt, for instance at the depths of exsolution the density of water is about $200\text{--}400\text{ kg m}^{-3}$, a factor of ~ 10 less than magma. The bulk modulus of water (order 10^7 Pa) is much less than that of silicate melt (about 10^{10} Pa, Alidibirov et al. [5]). Consequently, as pressure falls, any exsolved volatile phase expands by about three orders of magnitude more than that of the surrounding silicate melt; this is the fundamental driving mechanism of explosive volcanism.

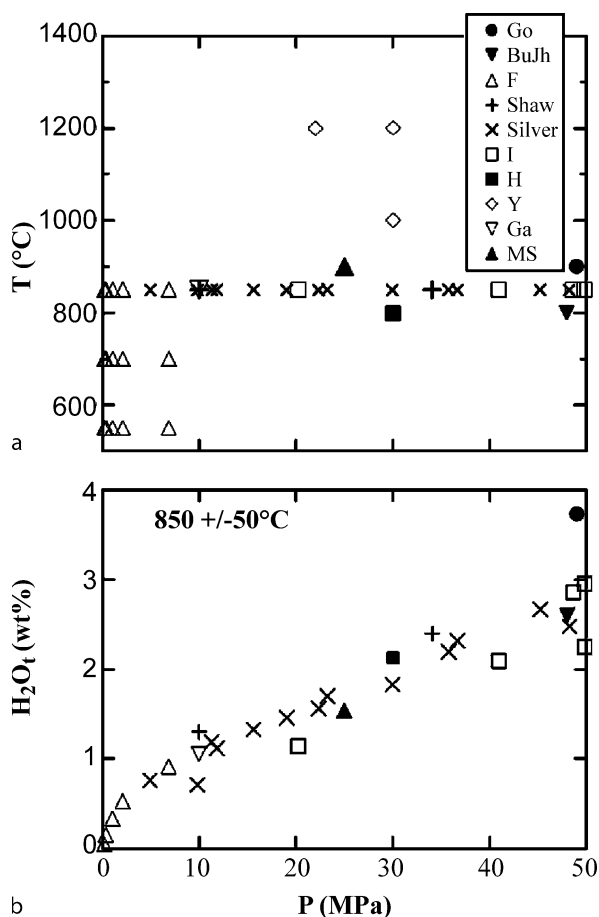
The solubility of volatiles in silicate melts has, and continues to be, the subject of extensive experimentation. Carroll and Holloway [28] review volatiles in magmas, and Liu et al. [73] provide a well-referenced introduction to water and carbon dioxide in rhyolite, and give new experimental data and empirical relationships so important to numerical models of explosive volcanic activity. Empirical H_2O and CO_2 solubility in rhyolitic melt ($700\text{--}1200^\circ\text{C}$ and $0\text{--}500\text{ MPa}$) are expressed by Liu et al. [73] as

$$H_2O_t = \frac{(354.94P_w^{0.5} + 9.623P_w - 1.5223P_w^{1.5})}{T} + 0.0012439P_w^{1.5} + P_{CO_2}(-1.084 \times 10^{-4}P_w^{0.5} - 1.362 \times 10^{-5}P_w),$$

$$CO_2 = \frac{P_{CO_2}(5668 - 55.99P_w)}{T} + P_{CO_2}(0.4133P_w^{0.5} + 2.041 \times 10^{-3}P_w^{1.5}),$$

where H_2O_t is the total dissolved H_2O % w/w, CO_2 content is in mass-ppm, T is absolute temperature and P the partial pressure of water or carbon dioxide.

Figure 3 shows how the solubility of H_2O in rhyolite varies with pressure from a range of experimental work. Experiments focused on explosive volcanism have concentrated on the solubility of water at a temperature of 850°C , because this is a common eruption temperature for rhyolitic melts. Although water solubility increases as pressure increases, this relationship is not linear, especially at lower pressures, and the nature of the non-linearity is dependent on magma composition (see [86] for review). The root of the complexity of water solubility is that water



Volcanic Eruptions, Explosive: Experimental Insights, Figure 3

a shows pressures and temperatures of experiments carried out on rhyolite melts to investigate water solubility as a function of pressure, see Liu et al. [73] for sources. The bulk of the experiments are carried out at 850°C because this is a common temperature for rhyolitic eruptions. b The solubility of water decreases with pressure, becoming increasingly non-linear below 10 MPa (shallower than about 50 m depth for lithostatic pressure). The transition, and consequent expansion, of water going from the dissolved to the vapor (or supercritical) states as pressure decreases is the driving mechanism of explosive volcanic eruptions. Reprinted with kind permission from Elsevier

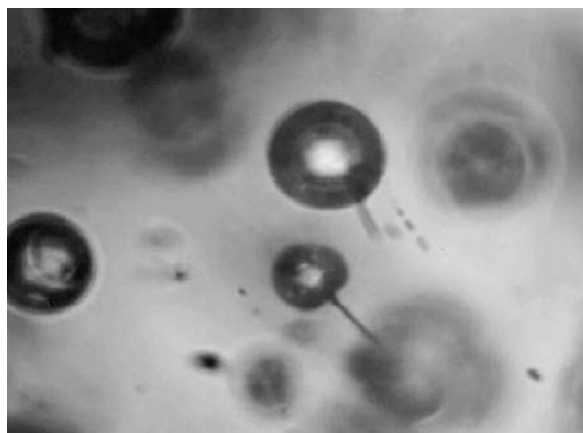
chemically reacts with the silica glass matrix as a network modifier. This reduction in the average molecular weight is responsible for decreasing the viscosity (Fig. 1), as well as having a range of complex geochemical effects (see [12] for popular review).

Nucleation and Diffusion

Decreasing the pressure applied to a volatile-saturated magma causes supersaturation of the volatile species. For

explosive volcanism to occur, the volatile must make the transition from the dissolved state to a lower-density (and therefore higher volume) exsolved state, i.e., the process of bubble nucleation. Determining the degree of volatile supersaturation required for nucleation to take place has been the subject of significant laboratory effort. Magmas are complex chemical compounds that are rarely free of interfaces. Hurwitz and Navon [52] found experimentally that heterogeneous bubble nucleation dominated, with only small supersaturations of water vapor (< 1 MPa, or ~ 50 m head of magma) being required to nucleate bubbles at the surfaces of Fe-Ti oxide microlites. Other crystal-melt interfaces required supersaturations > 10 MPa for nucleation of water bubbles. Even at supersaturations of > 130 MPa, nucleation was heterogeneous even in apparently crystal-free melts.

More recently, Gardner [43] found experimentally that certain crystal interfaces or features acted as nucleation sites, in particular blocky shaped magnetite or the ends of needle-shaped hematite (Fig. 4). Gardner's [43] study, and others cited therein, indicate that bubble nucleation is a complex function of the composition and temperature of the melt, the composition and morphology of crystals, and the degree of supersaturation prevailing. Accurate modeling of bubble nucleation requires detailed knowledge of the melt as it becomes supersaturated. Nucleation could occur at low supersaturations, with conditions never far from equilibrium. Conversely, in the absence of suitable



Volcanic Eruptions, Explosive: Experimental Insights, Figure 4

As pressure decreases, the melt becomes supersaturated in water. During the decompression of small samples of hydrated rhyolite, bubbles of water vapor nucleated then grew at the ends of needle-shaped hematite crystals, but not along their lengths (scale bar = 20 μm, Gardner [43]). Such 'imperfections' allow heterogeneous bubble nucleation and prevent large supersaturations developing. Reprinted with kind permission from Elsevier

nucleation sites, volatile supersaturations of the order of 100 MPa could develop as pressure in the melt decreases, and when nucleation does occur, rapid bubble growth can be expected.

Once bubbles of volatile have nucleated, growth is promoted by diffusion of volatiles from the supersaturated melt, and by expansion during pressure decrease. Any decrease in pressure also acts to increase volatile supersaturation (Fig. 3), encouraging either new bubble nucleation or, if bubbles are nearby, the diffusion of volatile into existing bubbles [17]. The diffusivity of volatiles is, therefore, a key parameter in determining the nature of the degassing process and has been reviewed by Watson [124]. Volatile diffusion into a bubble from the local melt surrounding it implies that the bubble will be surrounded by a shell of melt with relatively low volatile content and, thus, with elevated viscosity (Fig. 1a). This viscous melt shell may play an important role in the dynamics of bubble expansion during eruption, further adding to the importance of understanding diffusivity. Zhang and Behrens [131] experimentally investigated the diffusivity of water in rhyolitic melts, which, in combination with previous studies, covers the parameter range 400–1200°C, 0.1–810 MPa, and 0.1–7.7% w/w total H₂O content. The resulting empirical relationship between diffusivity of molecular water (D) and pressure (P), temperature (T) and water concentration (X) is given by

$$D_{\text{H}_2\text{O}_m} = \exp \left[\left(14.08 - \frac{13128}{T} - \frac{2.796P}{T} \right) + \left(-27.21 + \frac{36892}{T} + \frac{57.23P}{T} \right) X \right].$$

Such experimental determination of water diffusivity then forms key aspects of models of the behavior of silicate melts that undergo decompression, for instance, in how rapidly bubble pressure recovers after a perturbation [32], or in the nature of the resulting explosive activity [84].

Permeability

Erupting magma usually includes gas bubbles, which can approach and interact with each other due to differences in their rise velocities within the melt and due to expansion. If the residence timescale of magma in the plumbing system is long compared to the time required for bubbles to move through it, then the bubbles can be considered to be separating from the melt. This is often the situation in low VEI eruption styles such as Strombolian activity. Here, gas bubbles can ascend through the low viscosity magma relatively rapidly and are able to collide and concentrate,

possibly forming bubble rafts or foam layers. Bubble coalescence may then create fewer, but larger bubbles with significantly increased ascent velocity that, on reaching the surface, result in Strombolian activity.

Conversely, if magma residence timescale is short in comparison to bubble rise velocity, then bubble interactions cannot take place so readily. Under these conditions, the rapid depressurization and expansion of the trapped gas bubbles often results in high VEI events, but not universally. The ability of some such magmas to erupt relatively passively indicates that, as they ascend, they are able to lose gas by some other mechanism. One way for this to happen is for the vesiculated magma to become increasingly able to accommodate gas flow and separation as the volume fraction of bubbles (porosity) increases, allowing gas to move from bubble to bubble to the surface or into the surrounding rock. Such gas escape can be quantified using permeability, which is proportional to the effective pore diameter. Establishing how bubbly magmas become permeable, and the nature of that permeability is, therefore, of key importance to understanding eruption mechanisms.

The permeability of eruption products has only been measured experimentally in recent decades, and by few workers (e. g., [42,67,87,104]). Eichelberger et al. [42] determined the room-temperature gas permeability of rhyolite with between 37% v/v and 74% v/v porosity. Over this range, permeability increased by over nearly four orders of magnitude from 10^{-16} to 10^{-12} m², precipitating the hypothesis that high permeability can suppress explosive behavior in silicic volcanism, provided gas can escape. Klug and Cashman [67] made laboratory measurements on 73 pumice samples with porosities ranging from 30% v/v to 92% v/v. Permeability ranged from 10^{-14} to 10^{-12} m², with the relationship that $k \propto \phi^{3.5}$, where k is permeability and ϕ is porosity. Permeabilities at high porosity values agree between these two investigations, but disagreement at low porosities suggests greater complexity. Saar and Manga [104] demonstrated that there is not a straightforward relationship between permeability and the volume fraction of bubbles. Samples of basaltic scoria, which expand isotropically then cool rapidly, and therefore contain near-spherical bubbles, are well behaved in their permeability-porosity relationship and may be modeled by established percolation theory. However, many multiphase volcanic products do not have spherical bubbles because anisotropic flow causes high values of the capillary number. The elongate nature of the resulting bubbles causes high permeabilities at low porosities [104]. However, the permeability, like the porosity, is no longer isotropic, and gas escapes in directions determined by the local direction

of flow as well as the prevailing pressure gradient. Laboratory measurements of volcanic products have been used to scale and validate theoretical models of magma permeability as a function of porosity. These models have, amongst others, been based on analogy with networks of resistors in electric circuits [16], and combination of classical approaches with fractal pore-space geometry [35]. Such models can then be incorporated into numerical simulations of flow in volcanic conduits that test the importance of permeability on explosive-effusive transitions.

Consequences

The consequences of the materials properties of magmas responsible for explosive volcanic flows might now be explored. At pressures higher than the total volatile vapor-pressure, magma remains bubble-free. When pressure is reduced sufficiently below that of the volatile vapor pressure, then bubbles of volatile nucleate in the magma. These bubbles grow, and as bubble density is less than that of the magma, the bulk magma density decreases. This may act to increase magma ascent rate, creating a mechanism of positive feedback. Simultaneously, the reducing volatile content of the magma rapidly increases the liquid viscosity, reducing the strain rate required for viscoelastic and brittle behavior. This process occurs at the length-scale of diffusion into bubbles as well as within the liquid as a whole and, depending on the timescales, crystal growth may also be changing, or indeed driving, the rheological evolution of the system.

These non-linear interactions underpin the complexity of understanding how magma flows, and illustrate the subsurface control on the nature of eruptions. In order to investigate how the properties of volcanic materials interact during the eruption process, experiments of a different nature are required.

Volcanic Processes

Experiments investigating materials properties are mainly designed to measure parameters under static or steady conditions. However, explosive eruptions are not static and only pseudo-steady at best; therefore, different experiments are needed to explore bulk flow behaviors. Experiments investigating the explosive response of volcanic materials to possible eruption triggers are best conducted using natural silicates that have been well characterized by previous study. These experiments can be designed to minimize the inherent complexity of the overall process by concentrating on specific aspects. Models verified by experiments then contribute to larger models of the whole process.

Explosive Processes

Magma is a hydrated silicate liquid (normally also containing some solid crystals) that, during the explosive eruption process, is converted into silicate fragments ranging in size from 10^1 to 10^{-6} m. The mechanism responsible is fragmentation and understanding fragmentation processes is a major goal of physical volcanology.

Explosive volcanic activity predominantly requires the formation and growth of gas bubbles within magma. Exsolution processes are initiated at pressures generally > 10 MPa, and may extend to pressures of several hundred MPa for water. Such pressures result from overburdens of several kilometers and flow experiments carried out at volcanic temperature and pressure (1100–1500K, up to at least 100 MPa) place severe constraints on containment vessels, measurement transducers and the volume of experimental samples. Another explosive mechanism occurs when volatile species mingle with hot magma at lower pressures resulting in hydrovolcanic activity. This is driven by expansion as liquid turns to gas on heating.

Direct observation of explosive processes is unlikely, but experiments mimicking volcanic conditions give valuable insight. Experimental exploration of explosive processes using natural samples requires that appropriate proportions of gas, liquid and solid are present together with suitable pressures and temperatures.

Hydrovolcanism Experiments investigating the response of hot natural silicate melts to explosive ‘molten fuel-coolant interactions’ (MFCIs) with liquid water have been carried out by Wohletz [126] and Zimanowski et al. [134]. MFCIs are not confined to geological processes and are a dangerous industrial hazard, for example, on 4 November 1975, at the Queen Victoria Blast Furnace, Appleby-Frodingham Steelworks, Scunthorpe, UK, up to 90 tons of molten metal were thrown over a wide area after an MFCI explosion involving about 2 tons of water and 180 tons of molten metal. Berthoud [13] reviews MFCIs from the perspective of the nuclear power and other industries, but the physics described also applies to hydrovolcanism.

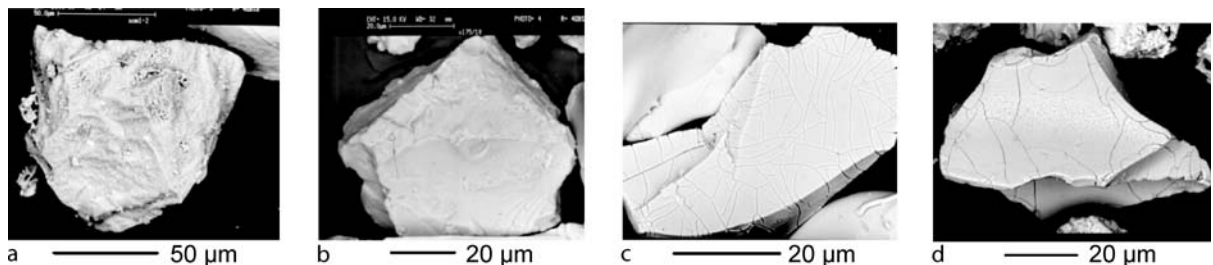
Volcano-specific research into MFCIs has studied the size and morphology of silicate particles from volcanic eruptions and compared them to those generated experimentally by MFCI processes (Wohletz [126]). The ratio of water to magma was found to be a key parameter in determining the nature of the particles resulting from the explosive process, with particle size reducing as explosivity increases. Such experiments provide insight into hydrovolcanic eruptions where magma may interact explosively

with surface water (Surtseyan eruptions) or ground water (phreatomagmatic eruptions). Two processes dominantly produce the explosivity: (1) the rapid ‘flashing’ of liquid water to vapor; and (2) rapid cooling of the silicate melt causing thermal shock. Zimanowski et al. [135] studied how explosive fragmentation of a remelted volcanic rock could be interpreted from the size and shape of expelled silicate fragments. Two methods of fragmentation were used: (1) injection of air at 5 or 10 MPa into the base of the crucible containing the melt (at 1653 K); and (2) initiation of a MFCI using liquid water and a triggering perturbation. With an air injection at 5 MPa pressure, fine particles were uncommon and the particles generally rounded; however, the particle size distribution suggested that two unspecified fragmentation processes had operated. Three unspecified fragmentation modes were implied for the 10 MPa air injections, with finer, but still rounded, particles produced. Interaction with water (MFCI) also had three fragmentation mechanisms, but produced the finest particles, many of which were blocky. The MFCI experiments resulted in a much more complex fragmentation process than the air injection experiments (Zimanowski et al. [135]), with a key difference being the rapid cooling of the silicate melt by interaction with water. The combination of rapid cooling and high strain rates generated by large pressures is considered to cause brittle failure of the melt and generate the fine, blocky fragments during the MFCI experiment.

Although not hydrovolcanism, the air-injection method of Zimanowski et al. [135] has been used by Taddeucci et al. [117] to experimentally investigate the role of crystal volume fraction during the explosive fragmentation of magma. This is of interest because ascending

magmas are thought to have both axial and radial heterogeneity in their crystal contents, both before and during explosive activity. Preliminary results showed a strong correlation between the fragment morphology and the crystal content in both experimental and natural samples, with increasing crystallinity promoting brittle fracture. This suggests a number of interpretations: (1) a higher viscosity liquid phase naturally exists in more crystalline samples; and/or (2) strain-rates in the smaller liquid volume of high crystallinity samples are higher, i.e., there is less liquid to accommodate a similar motion; and/or (3) the macroscopic rheological behavior of the two-phase mixture promotes brittle processes [51].

Comparisons between experimental and natural particles generated by MFCI experiments [22] show that quite subtle surface features can be used to distinguish between events involving either partial or complete water vaporization (Fig. 5). Where vaporization is complete, both experimental and natural particles are blocky and equant in shape, and a brittle fragmentation process is implied from observations of stepped surfaces on the particles, created by mechanical etching. Particles resulting from incomplete vaporization of water show similar features, except that their surfaces host a network of cracks that are considered to be the result of rapid surface cooling (thermal shock), created by interaction with excess liquid water. Büttner et al. [22] comment on the experimental relevance of their research; “In general, the artificial pyroclasts produced in the experiments cover all grain sizes and shape properties of the natural ones, thus illustrating the quality of the experimental scaling in terms of geometry and energy release.” Such phenomenological similarities are a powerful indicator that experimental processes are



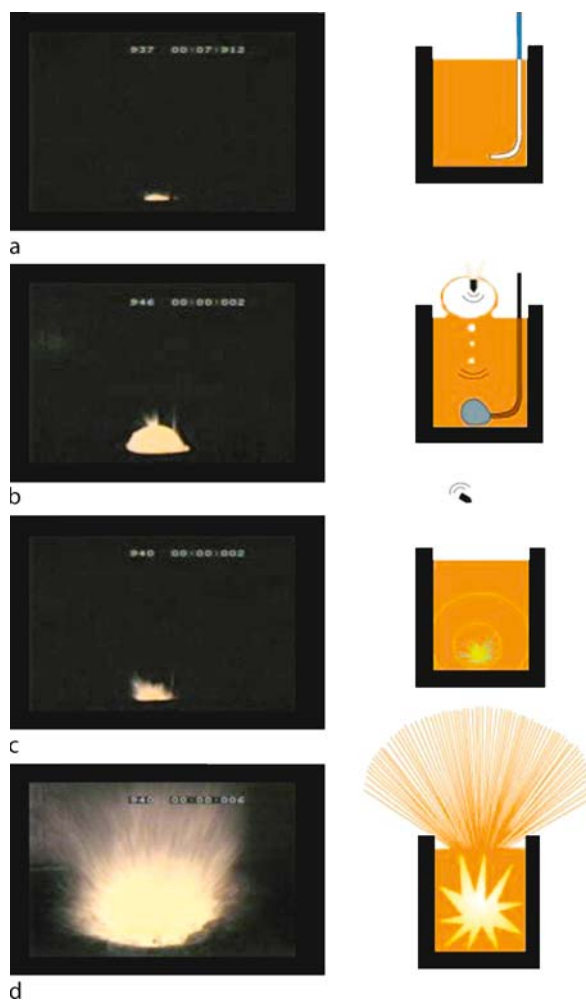
Volcanic Eruptions, Explosive: Experimental Insights, Figure 5

Magma and water may interact explosively during phreatomagmatic eruptions. Molten fuel-coolant interactions (MFCI) or magma-water interactions (MWI) can be carried out experimentally (Fig. 6). **a** shows a fragment generated by experimental MWI (Büttner et al. [22]) where all water was vaporized. **b** shows a fragment from a natural phreatomagmatic eruption that has not interacted with excess water. **c** shows an experimental fragment that ‘erupted’ through excess water, and **d** the product of phreatomagmatic activity thought to have interacted with excess water. The phenomenological similarities between **a** and **b**, and **c** and **d** provide powerful evidence that experiments are mimicking the processes that occurred during natural phreatomagmatic eruptions. Reprinted by kind permission from Macmillan Publishers Ltd: Nature (Büttner et al. [22]), copyright (1999)

mimicking the intended natural processes, and this is additional evidence of similarity. However, the experiments did not mimic all the post-explosion fragmentation processes that lead to the final natural product, demonstrating that care must be taken in comparing the outcomes of controlled experiments with the final product of the volcanic process.

Grunewald et al. [48] introduced a chemical aspect to MFCI experiments by using near-saturated NaCl solution as well as pure water, with the intention that the addition of other species would add complexity. Experimental methods were similar to that of Zimanowski et al. [135] (Fig. 6), with the triggering of a rapid thermal interaction by the injection of hot molten silicate with cool liquid brine. It was found that NaOH and HCl were formed during the heating of the NaCl solution, and that explosion energies were lower than with pure water. The lower explosion energies resulted in more rounded and larger silicate fragments as found by Zimanowski et al. [135]. The reason for the reduced physical energy of fragmentation was attributed to energy coupling into the endothermic chemical process that produced NaOH and HCl, but the heating of brine may well also have introduced a liquid NaCl phase (1074 K–1738 K) that altered the physical MFCI process. These experiments raise the interesting prospect of being able to use the chemistry of volcanic gases and particle surfaces to make inferences about physical processes occurring during hydrovolcanism.

A different experimental approach to studying magma-water interactions (MWI) was used by Trigila et al. [121] in which experiments could be carried out at pressures up to 200 MPa, and temperatures up to 1473 K. In contrast to the method of Zimanowski et al. [135], where water is injected into hot (1650 K), liquid-dominated silicate melt at 0.1 MPa, Trigila et al. [121] ‘infused’ water into permeable sintered samples of solid-dominated basalt at lower temperature (1100 K), but high pressure (8 MPa). The samples were manufactured by grinding basalt to grain sizes of < 10 µm (powder) or about 0.7 mm (granular). These were heated to experimental temperatures and allowed to sinter for 30 minutes to form a permeable cylinder (about 2 cm in diameter and 6 cm in length) into which water was introduced. Only the more permeable granulated samples underwent spontaneous explosive behavior on mixing with water, generating particles similar in size to the original grains. These exploratory experiments indicate the importance of permeability to MFCI processes where groundwater could interact with hot, porous country rock as well as magma. We have already explored the importance of permeability in allowing exsolving volatiles to escape and reduce explosivity; under



Volcanic Eruptions, Explosive: Experimental Insights, Figure 6

Schematic diagrams and frames from high-speed video illustrate one experimental method of simulating explosive phreatomagmatic eruptions (Grunewald et al. [48]). **a** Pre-experiment conditions with water injection tube in crucible of hot (1300°C) basalt melt. **b** 15 ml of water is injected, with the air expelled from the tube forming a bubble. The bubble was impacted by an air gun pellet to trigger **(c)** the explosive mixing of water and melt. **d** rapid transition of water from liquid to vapor results in pressure rise. The melt is fragmented by the subsequent rapid expansion. Reprinted with kind permission from Elsevier

different circumstances we now we see that permeability can also increase explosivity.

Exsolution The nature of geological materials at pressures and temperatures existing within the crust and mantle has been the subject of considerable research by petrologists. Experimental petrology generally studies samples of material in small (millimeter-scale) capsules that are

sealed, then pressurized up to tens of GPa and heated up to 2000 K; easily covering volcanically relevant conditions. Adaptation of this experimental technology to volcanic processes by Hurwitz and Navon [52] was used to study the response of hydrated rhyolite to decompressions up to 135 MPa (equivalent to about 5 km silicate overburden) at eruption temperatures (780°C to 850°C). Extended flow processes cannot be simulated with such small samples at these experimentally challenging conditions, but the pseudo-static response of hydrated silicate melt to pressure decreases of varying rate and magnitude provides important dynamic information about the processes of volatile exsolution (bubble nucleation and growth) and diffusion, as well as crystal growth. Hurwitz and Navon [52] revealed that nucleation of water bubbles (as a supercritical fluid or gas) in natural magmas is likely to be dominated by various heterogeneous processes operating over a range of supersaturations.

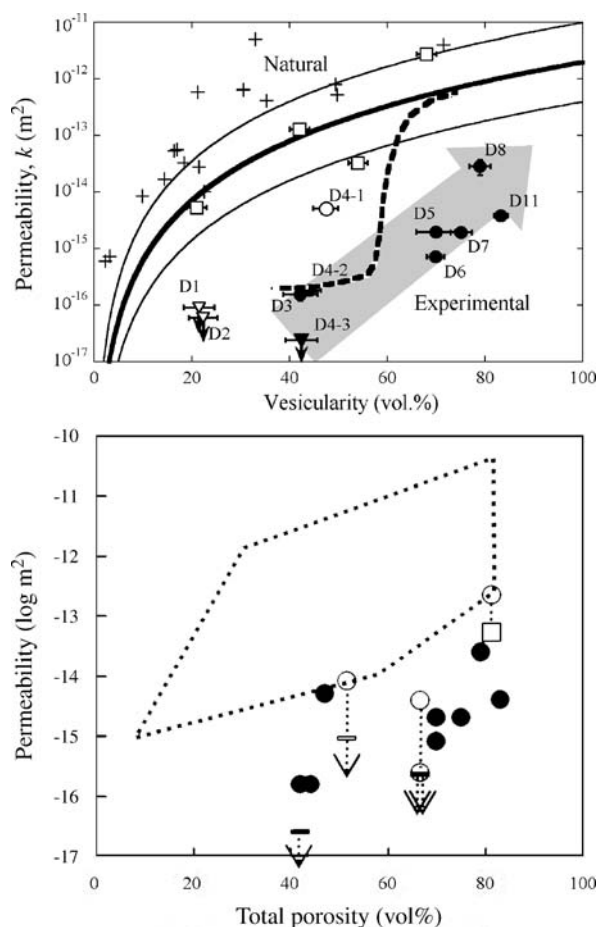
Lyakhovsky et al. [76] carried out further analysis of the experimental results of Hurwitz and Navon [52] to reveal the controls on bubble growth following nucleation. Numerical modeling of the experimental data showed that diffusion of water from the melt into the bubbles controlled bubble growth at modest supersaturations in hydrated melts (3–6% w/w water, viscosity 10^4 – 10^6 Pa s). The viscosity of the melt played a controlling role only when bubble surface area was small in the initial stages (< 1 s) of growth. At high supersaturations, the rapidly increasing area of bubble wall physically moves larger volumes of melt closer to the bubble and volatile advection is a significant contributor to bubble growth under certain conditions. As bubbles grow, the water content of the melt declines and the melt viscosity rapidly increases (Fig. 1a). Bubble growth then again becomes influenced by viscosity. These experimental results indicated that at water concentrations $> 3\%$ w/w in rhyolite, equilibrium degassing was a good approximation. However, as water content declines then equilibrium is not maintained and melt some distance away from a bubble wall, and therefore out of range of significant diffusion, becomes supersaturated in water. Lyakhovsky et al. [76] postulated that these supersaturated melt pockets then encourage additional episodes of bubble nucleation; a process supported by Blower et al. [17] using analogue experimentation and computer modeling. Constrained rapid-decompression experiments provided key insights into the role of continuous nucleation in near-equilibrium degassing of high-viscosity, low-diffusivity melts, with supersaturation limited to that required by heterogeneous nucleation sites.

The role of high viscosities (10^7 – 10^9 Pa s) on bubble nucleation was studied by Gardner [43], using meth-

ods similar to those of Hurwitz and Navon [52]. Heterogeneous and continuous nucleation of water bubbles in a rhyolite with less than 1% v/v microlites of Fe–Ti oxides and plagioclase were again exhibited (Fig. 4). Increasing viscosity and decreasing supersaturation were found to increase bubble nucleation times from a few seconds to greater than 100 s. The controlling parameter for nucleation rate was found not to be temperature, diffusivity or viscosity, but the surface tensions of interfaces between melt, crystal and bubble.

All these experiments were fully sealed, with no opportunity for the exolving volatile phase to escape. This condition was relaxed by Burgisser and Gardner [19] who decompressed 3 mm diameter, 7 mm long cylinders of rhyolite hydrated within gold capsules at 150 MPa and 825°C, with some capsules modified to incorporate a sink for escaping water (pseudo-open conditions). Three bubble growth regimes were identified that depended on balances between diffusivity and viscosity in relation to the rate of sample decompression. The open system experiments showed that, given sufficient time (about 180 s here) water bubbles begin to coalesce once bubble volume fraction exceeds about 43%; note that the permeability of natural samples tends to decline rapidly below about 40% porosity. This is important because bubble coalescence promotes an increase in permeability as preferential degassing pathways form in the melt. The limited volume of the sample, and its confining capsule, prevents the establishment of the range of flow behaviors that exist in volcanic conduits during explosive eruptions. However, the experiments of Burgisser and Gardner [19] provide useful insight into the role of flow on bubble coalescence for this very reason; features seen in the experimental samples are likely to have been difficult to distinguish in any experiments aimed at flow behavior. This demonstrates the usefulness of experiments for investigating spatially and temporally small (but tractable) aspects of a complex bigger picture. The results of such experiments can be used to verify models of the partial-process, with the facility to eventually combine these into a description of the full process.

The link between porosity and permeability was further explored by Takeuchi et al. [119] who isothermally decompressed 5 mm diameter, 15 mm long samples of Usu dacite in gold tubes from 150 MPa at 900°C, to pressures ranging from 50–10 MPa. Samples were then measured for permeability along the tube axis and, with their bubble fraction ranging from 22 to 83% v/v, covered the porosity range over which permeability has been measured in natural samples. However, the experimental samples showed significantly lower permeabilities than natural samples, except for the low porosity data of Eichelberger et al. [42],



and for experiments where bubbles were elongated along the permeability measurement direction (Fig. 7). This suggests that flow processes act to increase permeability by 1–2 orders of magnitude, and that most of the natural samples measured have undergone significant flow; or as Takeuchi et al. [119] state “The quenched experimental products can be considered as snapshots in vesiculating magma during decompression without deformation of vesicular structure in the late stages of eruption”. Describing experiments as snapshots of a larger, more-complex process is an apt analogy. More recently, Takeuchi et al. [118] have revisited their experimental samples and, after removing the gold tubes, found that the sample permeabilities were further reduced (Fig. 7), especially at low vesicularity. The original measurements had included some gas leakage between the silicate sample and the gold tube and, when operating at the limits of permeability detection, the leakage added a significant systematic error to the measurements. The new results further emphasize the importance of the flow history of vesicular materials in the

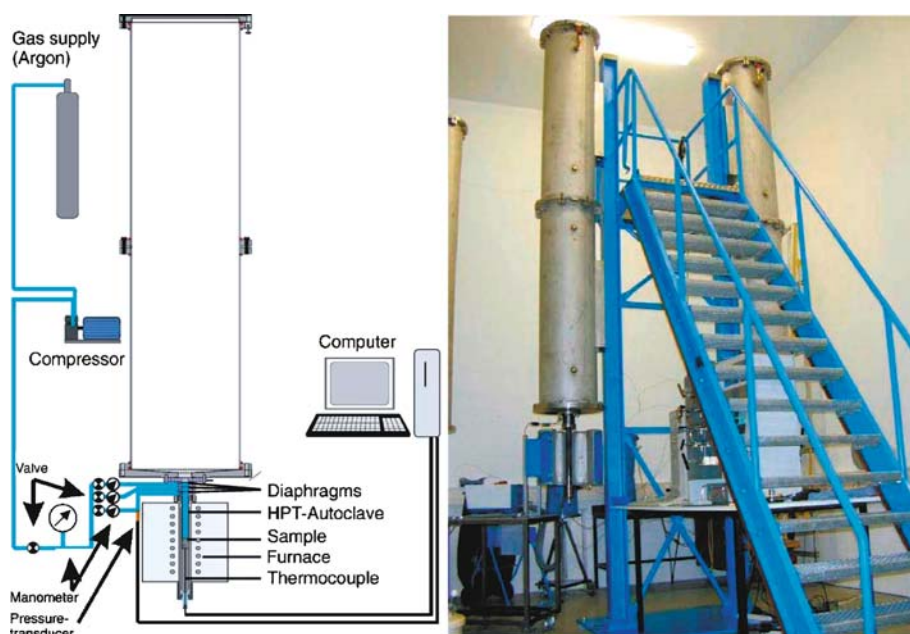
◀ Volcanic Eruptions, Explosive: Experimental Insights, Figure 7

As bubble volume fraction (vesicularity) increases, more bubbles coalesce to allow easy gas exchange between them. The result of this is increasing sample permeability with increasing vesicularity. Permeability allows gas to escape from the magma and reduces explosive potential, making permeability an important parameter in understanding the transition from effusive to explosive volcanism. Experiments carried out by Takeuchi et al. [119] (circles and squares with error bars, the solid and open symbols indicate isotropic and deformed vesicular textures of the products, respectively) are compared with measurement of natural samples in the top panel (dashed curve indicates the relationship of Eichelberger et al. [42], the bold solid curve with two fine satellite lines indicates the relationship of Klug and Cashman [67] with the upper and lower limit of the scattered data, the crosses and squares represent permeabilities of Melnik and Sparks [87], and Takeuchi et al. [119] respectively). Permeabilities have been corrected at a later date because of measurement artefact (bottom panel, Takeuchi et al. [118]). The trend of increasing permeability with vesicularity is demonstrated, but experiments generally show lower permeability than natural samples. One explanation for this could be that most of the natural samples have been subject to significant flow, whereas the experimental samples were generally not (open symbols show some evidence of flow). The role that flow plays in the development of permeability remains unclear. Reprinted with kind permission of AGU

development of permeability, and illustrate the complexity of interactions in the magmatic degassing process that determine the eruptive behavior.

Decompression-Driven Flows At Mt. St. Helens in 1980, a landslide acted to reduce the pressure applied to a body of vesiculated magma. Because the vesicles contained gas, the reduced pressure drove extensive magma expansion. This created the explosive lateral blast that preceded sustained explosive activity on May 18th 1980. Similar behavior may also be exhibited when portions of lava domes collapse. The response of vesiculated magma samples to relatively rapid decompression (10^{-3} – 10^1 GPa s^{-1} (Alidibirov and Dingwell [3])) forms a major area of experimental volcanology.

Laboratory apparatus known as a ‘fragmentation bomb’ (Fig. 8) was conceived by Alidibirov and Dingwell [1,2] and has been developed by others since. This shock-tube apparatus rapidly decompresses experimental samples at 850°C from up to 35 MPa to 0.1 MPa (Spieler et al. [112]). The samples, cylinders of approximate dimensions of 2 cm diameter by 20 cm length, are natural volcanic rocks heated to the required temperature in an atmosphere of Ar within a pressure vessel. On reaching the temperature of interest, the sample is further pressurized with Argon until a system of calibrated rupture discs fail.



Volcanic Eruptions, Explosive: Experimental Insights, Figure 8

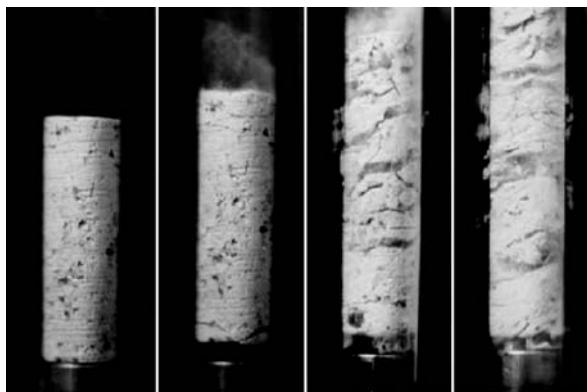
Schematic diagram and photograph of 'fragmentation bomb' shock-tube apparatus (Kueppers et al. [69]). Natural samples are pressurized up to 50 MPa with gas and heated up to 850°C in the autoclave. Samples can be used at room temperature with a transparent experimental section for high-speed imaging (Spieler et al. [111] (Fig. 9); Taddeucci et al. [116] (Fig. 22)). The diaphragms are ruptured to decompress the sample to atmosphere (0.1 MPa) and the resulting flow is collected in the large tank. Pressures, images and fragment morphology then provide information on flow dynamics. Reprinted with kind permission from Elsevier

On failure, the sample rapidly decompresses ($1\text{--}100\text{ GPa s}^{-1}$) and any explosive products freely expand into the collecting tank for further analysis. The use of Ar for these experiments removes any additional complexities that may arise from the nucleation, diffusion and growth of water bubbles allowing the detailed study of the mechanical response of vesiculated silicates to a rapid pressure drop.

Alidibirov and Dingwell [3] provide a review of the findings of experiments to that date. Samples of Mt. St. Helens Dacite from the May 18th 1980 eruption were decompressed by up to 18.5 MPa at temperatures up to 950°C. Observation of the resulting fragments showed angular material characteristic of brittle failure of the samples. Calculations of the strain rates imposed on the samples indicated that, even at the highest temperatures used, the dacite would behave as a brittle solid. Alidibirov and Dingwell [3] analyze three mechanisms that could explain explosive fragmentation of the sample. The dacite samples had interconnected pores and were, therefore, permeable. Rapid removal of the Ar gas above the sample creates a pressure gradient within the sample. If permeability is very high then the Ar gas can readily escape and pressure gradients will be relatively low. At the other extreme, if bubbles are not interconnected then pressure gra-

dients within the sample will be maximized (note, the experimental samples must have some permeability in order to pressurize them with Ar, but this does not need to be the case volcanically). In reality, the samples have a degree of permeability that allows pressure gradients to develop within the dacite. The pressure gradient was found to be at its highest at the fragmentation front, where the yield strength of the sample was exceeded. The fragmentation front was found to intrude the sample at tens of m s^{-1} , much slower than the sound speed and known as the fragmentation wave. In this instance, fragmentation can be described as a pressure-gradient driven change in flow regime from permeable filtration flow where only the gas moves, to two-phase flow where gas and solid are both in motion.

Martel et al. [82] synthesised 2 cm long by 2 cm diameter samples of hydrated haplogranitic glass with water contents ranging from 1.4 to 5.7% w/w. Water bubbles were nucleated and grown within the samples under a range of temperatures and pressures within the fragmentation bomb apparatus (Fig. 8) on timescales of about 1 hour, giving vesicularities ranging from zero to 0.91 v/v. Samples that developed large bubbles and high vesicularities underwent significant expansion and tended to develop



Volcanic Eruptions, Explosive: Experimental Insights, Figure 9

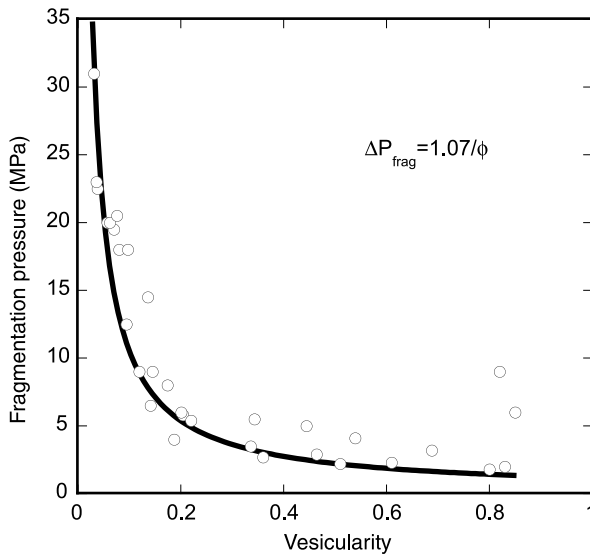
The rapid decompression of a sample of Santorini pumice, at room temperature, by at least 9 MPa (3 times higher than at 850°C) in the ‘fragmentation bomb’ (Fig. 8) results in spalling fragmentation (Spieler et al. [111]). The *first frame* shows the 50-mm length by 20-mm diameter sample just prior to decompression. 0.25 ms after diaphragm rupture (*second frame*) the ejection of fine dust from the sample surface indicates that pressure is falling in the *upper reaches* of the sample and gas is starting to escape from the pores. The combined elastic response of the sample and apparatus has detached the sample from the holder, fracturing the sample base. 0.5 ms after decompression (*third frame*), spalling fragmentation propagates through the sample perpendicular to the axis of decompression. Fragmentation results from the build up of a pressure gradient within gas in the upper sample sufficient to exceed the tensile strength of the bubbly solid. After 0.75 ms (*fourth frame*) primary fragmentation is complete and fragments are ejected into the large tank (Fig. 8). The timescale of this transient flow is of order 1 ms, but such visualizations give great insight into possible volcanological fragmentation mechanisms. Reproduced with kind permission from Springer Science and Business Media

elongated, or tube, bubbles during this process. Subsequent rapid depressurizations of between 5 and 18 MPa resulted in explosive fragmentation of the pre-foamed samples purely from expansion of the gas phase within the bubbles; timescales were too short for any significant further diffusion and exsolution of water from the glass. The resulting fragments were collected and analyzed for size, shape and vesicularity. The primary fragmentation process was found to be a sequential brittle spalling of the upper sample surface exposed to the decompression and was imaged by Spieler et al. [111] using Santorini pumice at room temperature in a transparent pressure vessel (reproduced here in Fig. 9). Low vesicularities and small decompressions were found to yield larger fragments than high vesicularities and large decompressions, a result consistent with the amount of energy released during the decompression process. The fragment size distributions may be dominated by the primary fragmentation mechanism

(surface spalling), but impacts between fragments, and with the apparatus wall, may increase the proportion of the smallest fragments at the expense of the largest, especially with large decompressions (giving high fragment velocities). Interestingly, the presence of tube bubbles acted to decrease fragment size, demonstrating again that flow history is important in determining the products of explosive events.

In a refinement of these experiments, Martel et al. [83] investigated the effect of adding relatively inert alumina particles to the hydrated haplogranitic samples as an analogue to crystals in a silicate melt. Solid particles influenced the final particle size distribution because they tended to remain intact during the experimental fragmentation process. An increasing proportion of alumina particles acted to increase the fragment size for a given decompression, suggesting that energy release was reducing. This would be consistent with the reduced proportion of gas phase that results from an increasing proportion of solids. This effect may also account for the observed increase in the decompression needed to fragment samples as the proportion of crystals increased, with the limit that a zero-vesicularity sample (100% crystals) would not fragment under decompression. Interestingly, tube bubbles were not formed in these experiments due to enhanced heterogeneous bubble nucleation acting to reduce bubble diameter.

Spieler et al. [112] carried out a systematic investigation of the rapid pressure drop required to cause the brittle spalling fragmentation of natural samples with a wide range of chemistry, porosity, permeability and crystallinity. The major control on fragmentation threshold pressure (ΔP_{frag}) was found to be the sample porosity (ϕ). Figure 10 shows the relationship to be approximated by $\Delta P_{\text{frag}} = 1/\phi$, with pressure given in MPa. Such a relationship makes qualitative sense because, as vesicularity tends to zero, ΔP_{frag} will tend to a large value because of little or no gas phase to drive the fragmentation. At large vesicularities, there will be little melt to resist the expansion of the volatile and fragmentation will take place with small decompressions. Figure 10 suggests that the rapid removal of order 100 m of overburden from a vesiculated magma with $\phi > 0.2$ will result in explosive fragmentation caused by pressure-retention in the pores. Such an event could happen by slope failure, for example, at Mt. St. Helens in 1980, or by a dome collapse. At lower vesicularities, the rapid removal of an overburden thickness of order 1000 m is required to initiate explosive fragmentation. However, although smaller overburden removals may not result in immediate spalling fragmentation, slower diffusively driven bubble growth will act to expand the magma and could thus trigger more sustained explosive activity.



Volcanic Eruptions, Explosive: Experimental Insights, Figure 10 Samples of natural volcanic material with a range of vesicularities were heated to 850°C and decompressed in the ‘fragmentation bomb’ (Fig. 8) by Spieler et al. [112]. The pressure drop required to cause explosive brittle fragmentation was inversely related to the sample vesicularity, with the constant of proportionality (here, about 1.07 MPa) being the tensile strength of the solid phase. Intriguingly, this suggests that heterogeneity in vesicularity will result in selective fragmentation of more vesicular regions of magma, particularly at vesicularities below 0.3. Data replotted from Spieler et al. [112]

Another mechanism of increasing pore pressure in magma is by crystallization of the silicate melt (e.g., Sparks [108]). This occurs because water is not incorporated into the structure of growing crystals and concentrates in the declining proportion of melt. Taddeucci et al. [115] used the ‘fragmentation bomb’ to ascertain the fragmentation threshold of crystal-rich magma from the 2001 basalt erupted at Mt. Etna, as a function of porosity. This was combined with models of pressures generated by crystal growth, and calculations of conduit pressures required to eject magma blocks observed during the explosions. This approach supported an explosion model sourced in the heterogeneous fragmentation of crystallizing magma plugs. The particularly interesting aspect of this model is the introduction of porosity heterogeneity within the magma. Figure 10 demonstrates that as porosity increases, the pressure change required for fragmentation decreases. Therefore, the competence of a body of magma will depend on its weakest link, namely any regions of high porosity. Once these begin to fragment, then the less vesicular regions will be removed as large blocks.

Although volcanically accurate materials were used in fragmentation bomb experiments, the effects of reductions in length and timescale by three orders of magnitude remain unknown. Nevertheless, these important experiments give specific insight into key mechanisms that could operate during the rapid decompression (or internal pressurization) of a vesiculated body of magma, and general insight into the behavior of volcanic materials undergoing explosive eruption.

Explosion Products

Explosive expansion of magma, driven by the low bulk modulus of gas-phase volatile species, generates a range of consequent phenomena. The primary magma fragmentation (one mechanism is illustrated in Fig. 6, and another in Fig. 9) involves a large increase in surface area within the volcanic system. The mechanism of this increase is the breaking of molecular bonds.

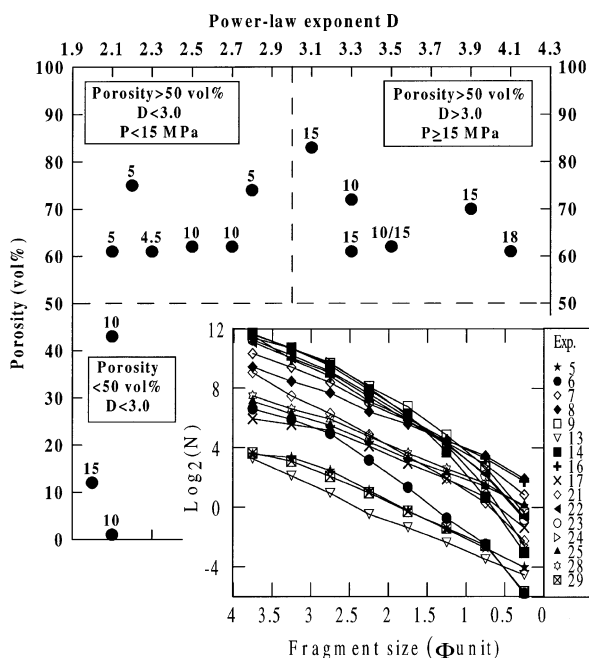
On exiting the volcanic vent, hot silicate fragments and volatile gas (mainly water vapor on Earth) interact with any atmosphere and cool. In the absence of a significant atmosphere, for example on Io, the volcanic ejecta expands, then the silicate fragments follow ballistic trajectories once they have decoupled from any volcanic gases and cool by radiation. Interaction between silicate fragments is now unlikely and their trajectories end when they impact Io’s surface; some may escape Io altogether. On Earth, the presence of an appreciable atmosphere results in different behavior. Explosion products emerge from the vent and interact with the atmosphere. If the silicate fragments are large and the explosive power low then fragment trajectories tend towards ballistic control. Conversely, if eruption power is high and fragments small, then atmospheric interaction may dominate. The mixing of air with hot eruption material and its consequent expansion may result in a thermally buoyant plume that ascends many kilometers into the atmosphere and may circumnavigate the globe by long-range atmospheric transport. If insufficient atmospheric air is entrained in order to develop and maintain buoyancy then some ejecta may fall back to ground to form a pyroclastic flow. On a smaller scale, the presence of electrostatic fields and liquid phases encourages sub-millimeter silicate fragments to aggregate. Many experimental studies have been carried out on the processes that follow explosive volcanic events and we review a selection here.

Fragment Size Distributions The fragment size distribution resulting from explosive volcanic eruption has been found to follow a power law distribution, $N = \lambda r^{-D}$, where N is the number of fragments greater or equal in

size to r , and λ is a constant of proportionality. For a single or primary fragmentation event the exponent (D) is predicted to be less than 3.0. Experiments carried out by Kaminski and Jaupart [66] impacted a sample of Minoan pumice with a solid piston to give an exponent of 2.7. James et al. [57] impacted two pumices together and found an exponent of 3.5. Pyroclastic flow or fall deposits from explosive volcanic eruptions exhibit an exponent range between 2.9 and 3.9.

Martel et al. [82] rapidly decompressed hot vesiculated rhyolite in a 'fragmentation bomb'. Decompressions of less than 15 MPa produced exponents of less than 3.0 for the resulting fragment size distribution, regardless of initial sample vesicularity. However, decompressions of > 15 MPa, for samples of vesicularity > 0.5 , resulted in exponents > 3.0 and ranging up to 4.1 (Fig. 11). These results suggest that secondary fragmentation mechanisms, such as those induced by fragment-wall and fragment-fragment collision, could be occurring within the apparatus after the primary spalling-fragmentation event (Fig. 9). Alternatively, as high exponents were observed at high vesicularities, the highly heterogeneous nature of a foamed silicate could invalidate the assumptions made in suggesting 3.0 as the exponent boundary for primary fragmentation, at least for fragment size ranges smaller than the order of bubble size. Interpretation of fragment size distributions between experimental and natural systems in terms of fragmentation processes is further complicated by difficulties in obtaining complete natural samples from explosive events. For example, winnowing in the atmosphere separates fragments as a function of fall velocity, which is a function of size and shape; therefore, the products of any individual fragmentation process are subsequently separated.

Fall Velocity of Silicate Fragments Understanding the behavior of silicate fragments in the atmosphere requires knowledge of the fall velocities of real volcanic pyroclasts, which rarely conform to an idealized spherical shape. Walker et al. [123] dropped samples of pumice from heights up to 30 m and found that terminal fall velocities were best approximated by the fall equation for cylindrical bodies. Wilson and Huang [125] carried out extensive experiments on silicate crystals and glass fragments in the size range 30 to 500 μm . A fragment shape factor ($F = (b + c)/2a$) was defined in terms of the longest (a), intermediate (b) and shortest (c) principal axes of the fragment, allowing definition of the empirical formula $Cd = (24/\text{Re})F^{-0.828} + 2(1.07 - F)^{0.5}$, where the fragment drag coefficient is given by Cd , as a function of Reynolds number, Re , and the shape factor. Suzuki [114]



Volcanic Eruptions, Explosive: Experimental Insights, Figure 11

Hot samples of bubbly rhyolite glass with a range of vesicularities were decompressed through various pressures in the 'fragmentation bomb' (Fig. 8), and the fragment size distribution (FSD) measured (Martel et al. [82]). The FSD was compared with a power-law distribution given by $N = \lambda r^{-D}$, where N is the number of fragments with radii larger than r . The power-law exponent, D , was found to increase with the magnitude of decompression (numbers next to data points in MPa), as well as with higher vesicularity. Compare this to an exponent of 3.5 for colliding pumices in Fig. 12. Theoretically, $D > 3$ suggests more than one fragmentation process, but these are complex, heterogeneous, multiphase materials and established fragmentation theory based on dense homogeneous materials may not give the full picture. Reprinted with kind permission from Elsevier

revisited the experimental data and proposed a modified equation, $Cd = (24/\text{Re})F^{-0.32} + 2(1.07 - F)^{0.5}$. This empirical, experimentally informed approach allowed calculation of the fall velocity of a fragment in the atmosphere and provided input into numerical models of the dispersal of products from explosive volcanism. Further information can be found in [101,109,120].

Fragment Electrification James et al. [56] investigated possible mechanisms by which silicate fragments could become electrically charged during explosive activity. Two natural pumices were collided together resulting in the generation of particles generally smaller than 70 μm in diameter as the silicate foam fragmented in brittle fashion. Fracto-emission generated ions and charged silicate frag-

ments. Ions were found to have one net charge and silicate fragments the opposite net charge. Experiments carried out at atmospheric pressure produced charge densities similar to those found on ash particles resulting from explosive terrestrial volcanism, whilst those carried out at 0.1 Pa sustained at least an order of magnitude more charge. The absolute amount of charge was dependent on the impact energy, (a result comparable to [23] findings of increasing electric field with greater fragmentation energy), with the net charge representing a slight imbalance between positively and negatively charged fragments. The mechanism of producing charged silicate fragments from pumice-pumice collision adequately accounts for the fragment charges and electric fields measured in proximity to explosive volcanic eruptions. This suggests that pumice-pumice collision, i. e., secondary fragmentation, could be a major source mechanism for sub-100 μm silicate fragments.

Experimental hydrovolcanic explosions were found to produce an electrically charged fragment and ion cloud [24]. Interestingly, fragmentation using high-pressure Argon gas produced electrical effects of smaller magnitude than magma-water interaction, even though expansion rates of the ejecta from the experimental crucible were similar. This suggests that the cooling effect of water does produce much more brittle failure resulting in enhanced fracto-emission [37,40], consistent with the production of smaller blocky fragments from MFCI experiments [135]. It is also possible that polar water molecules dissociated into reactive ions during the MFCI process, a mechanism not so accessible to Argon atoms. Büttner et al. [24] found striking similarities between experimental electric fields and those generated during explosive events at Stromboli volcano.

Silicate Fragments and Their Aggregation Accretionary lapilli are widespread in the deposits from explosive volcanic eruptions, and anomalous variation in the deposit thickness and grain size distribution as a function of distance from the explosive vent is commonly observed. Both of these processes are explainable if silicate fragments smaller than about 100 μm clump together, or aggregate, to form a larger entity which has different aerodynamic properties than its constituent particles. Sparks et al. (see Chapter 16 in [109]) provides a review of particle aggregation in volcanic plumes prior to 1997.

Accretionary lapilli are obvious in the geologic record as millimeter to centimeter sized spheroidal aggregates (density range 1200 to 1600 kg m^{-3}) of silicate fragments and secondary minerals such as gypsum, and they formed the early focus of study into aggregation in volcanic

plumes. Two complementary experimental studies provided insight into the formation mechanisms of accretionary lapilli. Gilbert and Lane [45] focused on formation in atmospheric plumes. A wind tunnel was used to demonstrate experimentally that particles of volcanic ash collide and adhere to the surfaces of objects falling through the atmosphere that are covered with a thin layer of liquid. The liquid layer was found to act as a control on the sizes of silicate fragments that adhere, with high sticking efficiencies at 10 μm diameter, reducing by two orders of magnitude for fragments 100 μm in diameter. A key experimental finding was the importance of hygroscopic chemical species in maintaining thin liquid films. Experimentally this was achieved using NaCl; volcanically, sulphuric acid is the most likely hygroscopic compound that could maintain liquid films at low relative humidity and down to temperatures of -70°C . These experiments strongly suggest that accretionary lapilli are diagnostic of a three-phase environment within the volcanic plume in which they formed, supporting earlier hypotheses (e. g., [88]).

Schumacher and Schmincke [105] focused on accretionary lapilli formation in pyroclastic flow processes. Experiments were carried out providing insight into interpreting the structure of accretionary lapilli in terms of their formation mechanisms. Accretionary lapilli were synthesized by a method similar to the industrial production of fertilizer pellets, with mixtures of volcanic ash and variable proportions of water being rotated in a steel pan. The resulting spheroidal agglomerates varied with the proportion of water present, formation being optimal at between 15 and 25% w/w water, and grain size sorting was found to occur at low water mass fractions. The mechanism of formation, namely capillary binding, is identical to that of Gilbert and Lane [45], but under conditions of much higher fragment number-concentration.

The occurrence of secondary thickness maxima and bimodality of grain size distribution, exemplified by Carey and Sigurdsson [27], implies the mechanism of silicate fragments being transported within aggregates. These aggregates could be accretionary lapilli, but these are often absent from the deposits suggesting that the aggregates are fragile and lose their identities once incorporated into a volcanic deposit. Fragile aggregates have been observed falling from volcanic plumes and one explanation for their formation is the presence of electrostatic charge. During fragmentation, silicate particles become electrostatically charged (see Sect. “Fragment Electrification”), and whilst in the atmosphere these charges have no path to escape to earth unless electric fields exceed the level required for electrostatic discharge in air. This leads to long-lived attractive electrostatic forces between silicate

fragments [81], and consequently the formation of aggregates. Once on the ground an electrically conductive path to earth can be established, especially in the presence of moisture, and the aggregates disintegrate.

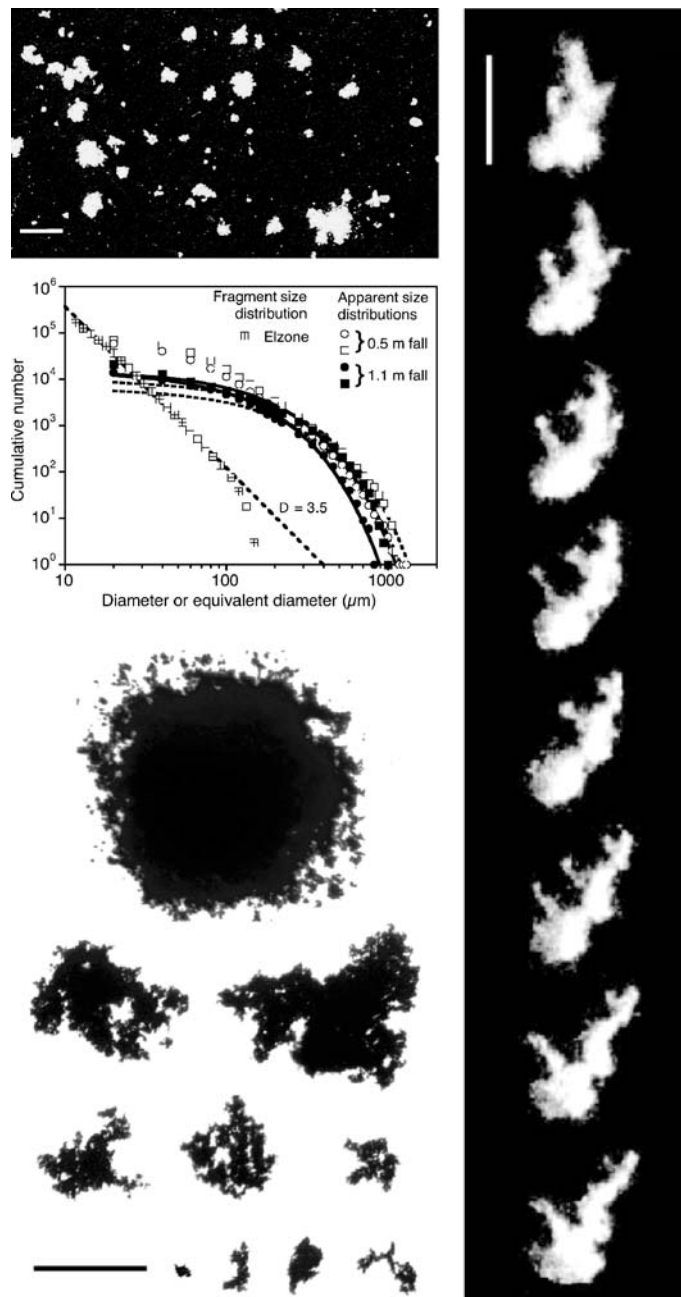
Schumacher and Schmincke [105] carried out experiments using natural volcanic ash and a stream of ions from an electrostatic paint gun. Silicate fragments smaller than about 180 μm diameter were found to rapidly aggregate into loose fragile clusters demonstrating the viability of the electrostatic aggregation process for fine volcanic particles.

James et al. [57] studied the generation of aggregates resulting from the interaction of ions and charged silicate fragments using the fragment generation and charging mechanism of James et al. [56] with pumice from the May 1980, Mount St. Helens fall deposit. Silicate fragments were allowed to fall and interact over a distance of 0.5 to 1.1 m onto a variety of analysis platforms. Fallout was collected and analyzed for fragment size (Fig. 12) using an agitated dispersion of the particles in a conducting electrolyte to maintain disaggregation. The particle size distribution showed power law behavior with exponent 3.5 (Fig. 12), somewhat above the theoretical maximum of 3.0 for a primary fragmentation event. These experiments indicated that the aggregation process happens shortly after the fragmentation event has generated charged silicate fragments and ions (Fig. 12). The aggregation process significantly changes the size distribution relevant to aerodynamic behavior (Fig. 12) from the single-fragment form $N = \lambda r^{-3.5}$ to aggregate form $N = 15\,089 \exp[-0.011d']$, where d' is the aggregate diameter. Experimental measurement of aggregate fall velocities enabled estimation of aggregate densities between 80 and 200 kg m^{-3} , at least an order of magnitude less than both the fragments that comprise aggregates and accretionary lapilli. The main consequence of electrostatic aggregation for sub-100 μm silicate fragments is to reduce atmospheric residence time because aggregation acts to increase fall velocity above the single fragment value. The size distribution of individual fragments within an aggregate was experimentally examined by James et al. [58], who found empirically that for aggregate diameters less than 140 μm , $n = 0.000272d_a^3 [\exp(-0.22d_p) + 0.008 \exp y(-0.083d_p)]$, where n is the number of fragments larger than diameter d_p within an aggregate of diameter d_a . As electrostatic aggregates exceed about 140 μm in diameter the size distribution of their constituent fragments was found to change. This was attributed to the aggregate growth mechanism becoming dominated by aggregate-aggregate interaction rather than aggregate-fragment interaction (Fig. 12), and stabilization of the size distribution of material being incorporated into the aggregate. Electrostatic aggregates can

be represented as spheres of density about 200 kg m^{-3} and an experimentally determined empirical relationship between drag coefficient (C_d) and Reynolds number (Re) for aggregate diameter range 50 to 500 μm is $C_{d\text{agg}} = 23Re^{-0.637}$ (James et al. [58]). Such experimental data can then be used within numerical models of the transport of sub-100 μm volcanic ejecta in the atmosphere, although at the time of writing this has yet to be undertaken.

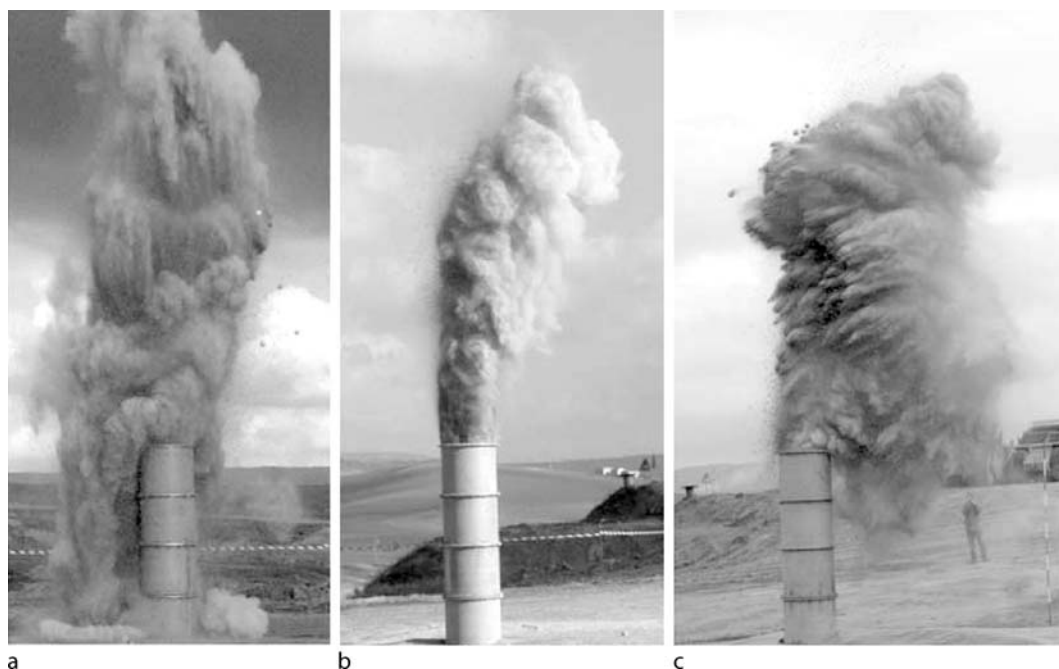
Pyroclastic Flows Pyroclastic flows comprise a hot mixture of silicate particles and gas formed by the collapse of negatively buoyant regions of a volcanic plume or avalanching of material from a growing lava dome. By nature, pyroclastic flows are destructive to infrastructure and almost invariably fatal to plants and animals. Insight into the behavior of pyroclastic flows may be gained by studying their deposits. However, it is difficult to definitively identify fluid dynamic processes operating during a pyroclastic flow from the complex structures within deposits that are revealed once motion has ceased. Here, experiments can help in isolating flow processes and their subsequent effect on deposits. However, scaling between experiment and natural process requires care to ensure behavioral similarity as particles of a range of sizes interact with the gas phase to different degrees.

Dellino et al. [36] designed experiments to investigate the mechanics of pyroclastic flows on a scale comparable to the natural process. In order to approach this, the physical scale of the experiments was such that they required an outdoor laboratory. The experimental material was sourced from a natural pyroclastic flow deposit in order to mimic the interaction between fragments and gas as closely as possible. Varying masses of this material were packed into an experimental tube 60 cm in diameter and 2.2 m high. 14 liters of gas at pressures over 10^7 Pa was rapidly injected into the base of the tube to eject the experimental material, with experiments triggered and logged under computer control. The experiments were carried out at ambient temperature and were, therefore, not scaled for any thermal effects; this has the benefit of reducing both equipment and process complexity. Ejected material could be sampled for analysis and compared to natural pyroclastic deposits. Preliminary experiments showed two main types of behavior as the specific mechanical energy (SME, given by *gas pressure* \times *gas volume* \div *mass of pyroclastic material*) of the system was changed (Fig. 13). At high SME values a dilute particle plume develops with the particles settling out individually. At low SME values the ejected material forms a collapsing column that generates a particle flow similar to a pyroclastic flow. Intermediate



Volcanic Eruptions, Explosive: Experimental Insights, Figure 12

Fragmentation during explosive eruptions produces electrically charged fragments and ions by fracto-emission processes (James et al. [57,58]). Electrostatic forces are significant in comparison to gravity for fragments less than about 100 μm in size, resulting in fragment aggregation. Aggregates have different aerodynamic properties than their constituent fragments, thus altering the fallout behavior of sub-100 μm volcanic ash and consequently its atmospheric transport. The top image shows experimental aggregates collected on a plate (scale 1 mm), with the graph showing the size distribution of the aggregates (*curved lines*), as well as that of the constituent fragments (*straight line*). The bottom panel (scale 0.5 mm) shows that experimental aggregates of different sizes have different morphologies, and the right-hand panel (scale 0.5 mm) shows strobe images of a falling and rotating experimental aggregate. Reprinted with kind permission of AGU



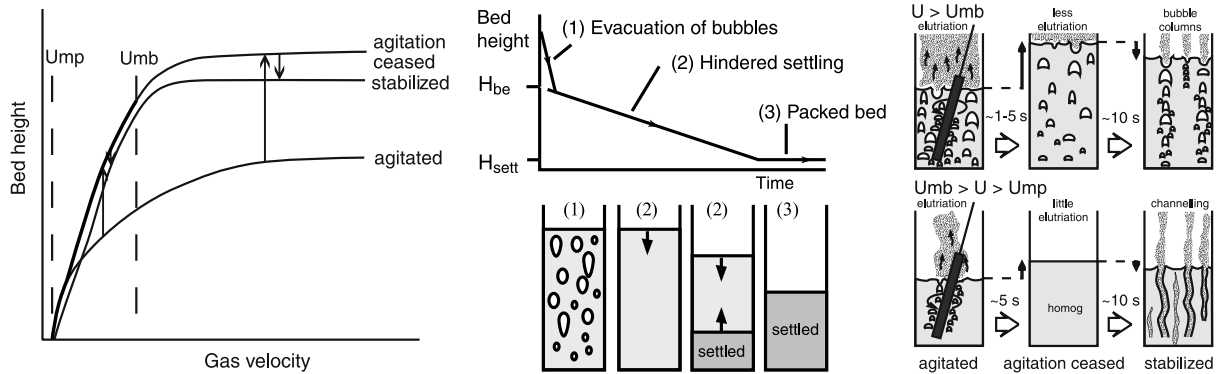
Volcanic Eruptions, Explosive: Experimental Insights, Figure 13

Ejection of natural pyroclastic material by a burst of gas can be used to study both volcanic plumes and pyroclastic flows (Dellino et al. [36]), this also looks enormous fun! a shows an experiment with low specific mechanical energy (SME) generating a collapsing column and (pyro)clastic flow. c shows a high SME experiment generates a plume that, whilst not buoyant, disperses on the prevailing wind, and b shows the transitional case. Such large-scale investigation helps to overcome some of the scaling difficulties imposed by smaller-scale laboratory experiments. Reprinted with kind permission of AGU

SME values give transitional behavior with aspects of both end-members. These experimental observations have considerable phenomenological similarity to natural explosive eruptions where particle-dilute regions ascend in the atmosphere and more particle-concentrated regions fall under gravity to give pyroclastic flows. Such similarity gives added confidence that mechanisms operating in the natural process also operate in the simulation.

Experiments producing a collapsing-column deposited material at the point of impact of the column with the ground. The resulting deposit was found to be structureless, just as many natural proximal pyroclastic deposits, because grain-sorting processes did not operate in this concentrated particle flow. Other similarities included the formation of a concentrated undercurrent, bed load at the base of the turbulent flow, and continuous atmospheric suspension of small silicate particles; this is very interesting in the absence of thermal processes. These preliminary experiments demonstrate great potential for linking processes in scaled experimental flows with the resulting experimental deposits and, therefore, providing a powerful interpretation tool for natural pyroclastic flows.

Experiments carried out at smaller scale, but which included heating of the volcanic ash [41], have also investigated gas retention in pyroclastic flows. A bed of pyroclastic flow material with a wide fragment size range was fluidized by the drag force of rising hot gas. Both the bed expansion and collapse (degassing) after the gas supply was cut were studied. During expansion, smaller fragment size, lower density and higher temperature all promoted more uniform and easier expansion of the fluidizing bed. Figure 14 illustrates the nature of flow patterns that develop. Collapse experiments were imaged using X-rays and carried out between 20°C and 550°C giving temperatures comparable to those in natural flows. The generic collapse process is illustrated in Fig. 14. Experiments and numerical models identified that an aerated bed loses its gas by permeable flow on a diffusive timescale. A fluidized and uniformly expanded bed was controlled by timescales of hindered settling and diffusive degassing of the resulting sediment layer. The relative magnitudes of these timescales depended on the thickness of the degassing bed, with settling dominating in thin beds and diffusion in thick ones. These experiments indicate that hot pyroclas-



Volcanic Eruptions, Explosive: Experimental Insights, Figure 14

The inflation and deflation of a bed of natural pyroclastic material using hot gas shows a range of flow structures (Druitt et al. [41]). During inflation, the bed can be homogeneous or develop gas bubbles or channels, and fine particles can be removed by elutriation. When fluidizing gas velocity exceeds U_{mp} (left panel), the bed inflates and particles start to segregate on the basis of size and density. Bubbling occurs when gas velocity exceeds U_{mb} (upper right panel), and the bed expands only weakly with increasing gas velocity (left panel). Agitation of the flow acts to reduce the gas volume fraction. Once the gas supply is closed off then bubble collapse results in rapid deflation ((1) in middle panel). An extended period of hindered settling then generates a layer of settled material at the base of the bed ((2–3) in middle panel). These experiments were used to investigate the gas retention properties of pyroclastic materials as a function of fragment size and temperature. Gas retention was favored by finer fragment sizes, with high temperature having a secondary retention effect. Hot, fine-grained pyroclastic flows are, therefore, predicted to flow further. Reproduced with kind permission from Springer Science and Business Media

tic flows with small fragment sizes retain gas longer than cool, large fragment flows, with temperature having a secondary effect. The gas retention translates into the distance a flow can travel and these experimental results are consistent with observations of natural pyroclastic flows.

Analogue Approach

Experiments with volcanic materials can suffer constraints placed by the high temperatures and pressures at which the processes of interest occur. If similar processes can be studied under more amenable environments, then the practical limitations are relaxed and, generally, fluid volumes can be increased and a greater range of transducers are available for measurement. This can be achieved by substituting natural fluids with analogues that can be studied at near room temperatures and pressures. However, one difficulty with this approach is in ensuring the relevance of analogue results to volcanic systems and, perversely, natural volcanic materials are now often characterized more fully than many of the analogue fluids used.

Explosive Processes

Direct observation of the motion of magma within volcanic conduits would reveal the how and why of volcanic explosive activity. However, direct observation is considered near-impossible and indirect observation open to interpretation. Experiments with natural materials provide

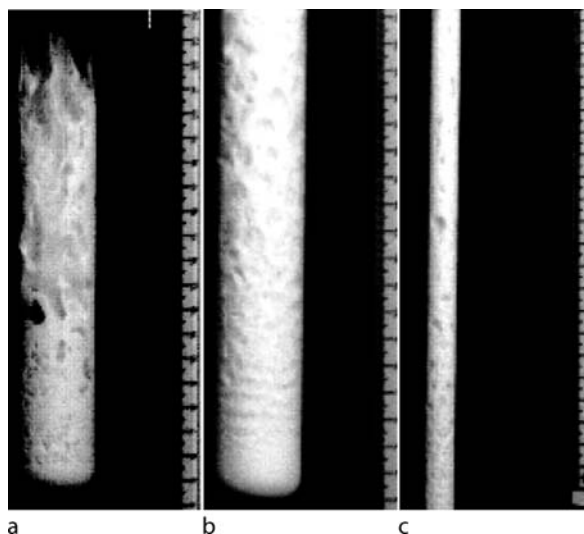
constraints on physico-chemical processes within conduits, but extending the experimental parameter space by using analogue materials provides greater insight and enables testing of numerical models.

High VEI Events Volcanic eruptions of high VEI involve the transition of a low-velocity, high-density, high-viscosity bubbly magma, for which the liquid phase is considered continuous, to a high-velocity, low-density, low-viscosity ‘dusty gas’ where the gas phase is considered continuous. This fragmentation process represents the point at which the liquid and gas phases start to separate. Studies designed to investigate this process in general, but with volcanic application in mind, form a major part of experimental research using the analogue approach.

As pressure declines, the exsolution and expansion of volatile (specifically water) from magma provides the driving mechanism for most explosive events. In order to study similar behavior in analogue systems the shock tube has been almost universally adopted, as it has for the investigation of fragmentation in natural materials (e.g., [1,2]). Such experiments became of great importance around WW2 when understanding of shock waves and flame fronts from explosions, and supersonic flight, became of interest to the fluid dynamic community; volcanological application of shock tubes emerged from this background. Mader [77] provides a review of early shock tube experimentation relating to flow within volcanic con-

duits, we briefly summarize these here, but focus on more recent work.

Post-Fragmentation Flows The decompression of beds of small, incompressible particles with compressible, gas-filled pore space can give insight into the development of two-phase flows within and above the conduit subsequent to primary fragmentation [6]. The resulting rapidly expanding, but transient flows show development of significant heterogeneity, which declines as expansion reduces particle concentration. The development of heterogeneity within expanding particle-laden gas suggests mechanisms for the formation of pyroclastic flows from high-density sections of eruption columns, whilst lower-density sections become buoyant and form an eruption plume. Using smaller particles, Cagnoli et al. [25] carried out similar experiments to explore the dynamics of short-lived Vulcanian explosions. In similarity (we think, but see Fig. 9) with post-fragmentation volcanic flows, the experimental tube was much larger than the particle size. As in Anilkumar et al. [6], these transient flows demonstrated heterogeneous distribution of particles as the mixture expanded and the gas separated from the particles (Fig. 15). These features include sub-horizontal gas-rich regions that invite comparison with those found by Spieler et al. [111] in decompressed pumice samples; the implication being that the primary fragmentation process may be incidental to the nature of the evolving flow. Heterogeneities also comprise gas-rich bubbles, sometimes approaching tube diameter in size, and more elongated towards the flow front. Streamers of particles also emerge from the flow front indicating inhomogeneity in the distribution of gas escaping the particle flow (Fig. 15). As the flow ages and velocities increase, turbulence acts to smear out heterogeneities. The source of the heterogeneities in such transient flows is unclear. They may represent the expansion of gas rich regions in the original packed bed, suggesting that the transient flow reflects heterogeneity in the source material. Variability in permeability, and the dynamics of initial particle acceleration may also act to amplify heterogeneity as the flow expands. These experiments demonstrate the complex nature of even ‘simple’ two-phase flows that are undergoing rapid changes in variables such as pressure and velocity. The volcanic implication is that flow within a volcanic conduit can be highly heterogeneous and that modeling such flows as having smoothly changing density, as a function of time or space, will be far from representing the real richness of the flow physics. Such modeling may give accurate prediction of time-averaged parameters, but will not reflect variability. However, it could be the variability that ultimately results in hazards like pyroclastic flows.



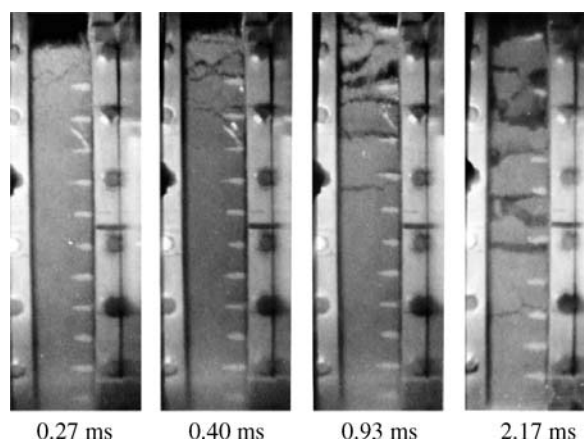
Volcanic Eruptions, Explosive: Experimental Insights, Figure 15 Rapid 20 to 90 kPa decompression of beds of sub-100 μm glass beads generates a particle flow as the gas phase expands in response to the pressure drop (Cagnoli et al. [25]). a shows the decompression of 100 g of beads (with average diameter of 38 μm through 51 kPa) after 28 ms. Note the wispy flow front, indicating escape of gas, and the development of large gas bubbles within the flow (scale shows 1 cm and 0.5 cm gradations). b (150 g of 95 μm beads, 69 kPa decompression, after 23 ms) shows the development of sub-horizontal particle-poor regions, giving some phenomenological similarity to spalling fragmentation (Fig. 9). c shows flow in a narrower tube (100 g of 38 μm beads, 68 kPa decompression, after 20 ms) where large particle-poor regions develop at the flow margin. Reprinted with kind permission from Elsevier

Chojnicki et al. [29] demonstrated that models of explosive volcanic flows based on pseudogas approximations underestimated the initial shock wave strength and velocity. Pseudogas models, and others based on steady-state experiments, then overestimated the subsequent particle bed expansion rate when applied to laboratory scale experiments. Such discrepancies suggest that one or both of the approaches, numerical and experimental, requires modification to reconcile the differences in order to understand the natural phenomena. In this case, Chojnicki et al. [29] identify processes not accounted for in the numerical approach, but which became apparent from experimental observation. Existing theory was then empirically modified to fit the unsteady experimental flow. Volcanically, these experiments suggest that the pressures present in conduits prior to Vulcanian explosive events were underestimated by a factor of approximately five when calculated using established pseudogas and inviscid shock theories. The pressures calculated from equations based

on volcanically relevant experiments are consistent with the overpressures associated with Vulcanian explosions, as well as the rupture strength of volcanic rock. This demonstrates the importance of experimental design to progressing understanding of complex volcanic phenomena, and using the results of these experiments to test, modify and develop the numerical approach.

Decompression-Driven Flows The rapid decompression of natural vesicular solids causes fragmentation if the pressure drop is large enough for pressure gradients within the sample to exceed the tensile strength (Fig. 9). Such transient experiments have also been carried out on analogue solids in order to further characterize the behavior of this system of flows. Decompression of synthetic organic resin, with about 90% porosity and significant permeability (Alidibirov and Panov [4]), resulted in fragmentation phenomenologically similar to that of natural samples (Figs. 9, 16) undergoing brittle failure. A fragmentation front or wave was observed to propagate through the sample creating spalling-type fragmentation. Fragment size was observed to decrease, and exit velocity increase as the magnitude of decompression increases from 0.1 to 0.8 MPa. The propagation velocity of the observed fragmentation wave was less than sound speed in either the solid resin or the gas in the pores. Combining this observation with the dependence of fragment size on pressure drop suggests that fragmentation occurs as gas escapes from the decompressed foam surface, creating a pressure gradient within the foam. When this pressure gradient is sufficiently steep, the foam fails revealing the next gas-escape surface. The expanding gas then accelerates the foam fragments. This implies that fragment size will also depend on sample permeability; an impermeable sample fragmenting on a scale comparable with bubble size and at small decompressions, whilst a permeable sample requires large decompressions and fragments on a scale much larger than bubble size. Very permeable materials will not fragment because the gas can escape without applying sufficient tensile force to the foam. Variability in permeability and porosity may well be reflected in fragment size for any decompression event.

Ichihara et al. [53] depressurized a vesiculated silicone compound and studied the expansion of vesicular materials across the viscoelastic transition by varying the decompression rate (Fig. 17). Fragmentation occurred at decompression rates $> 2.7 \text{ MPa s}^{-1}$, with only sample expansion occurring at $< 2.7 \text{ MPa s}^{-1}$. At high decompression rates, fragmentation occurred before expansion of the fragments. These experiments showed that both the fragmentation threshold and the nature of the fragmentation

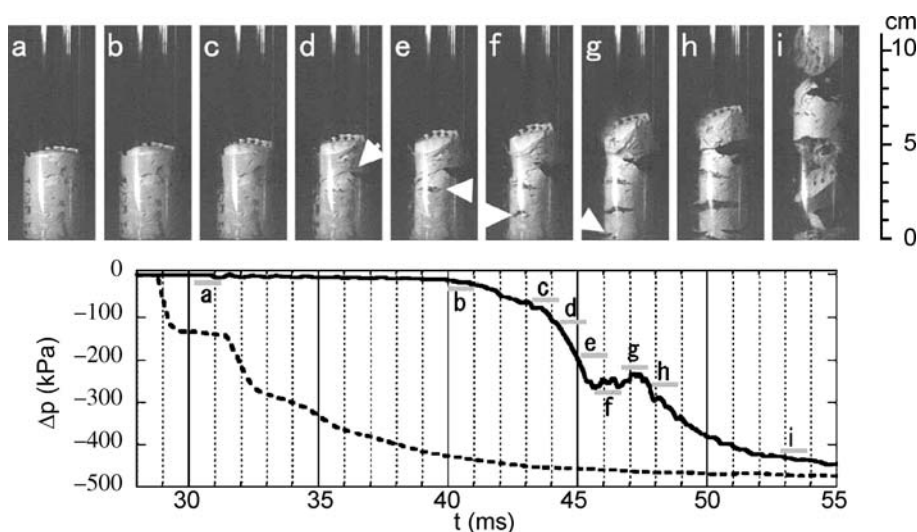


Volcanic Eruptions, Explosive: Experimental Insights, Figure 16

An 0.8-MPa rapid decompression of vesiculated solid foam (Plas-tiprin) shows very similar spalling fragmentation behavior to natural vesiculated magma (compare with Fig. 9). This demonstrates the usefulness of analogue experimentation in identifying the universality (or not) of flow behaviors (Alidibirov and Panov [4]). Reproduced with kind permission from Springer Science and Business Media

process depend not on the magnitude of decompression (above a minimum), but on the rate of pressure change. Furthermore, the rate of decompression needed to exceed the critical value for more than about 0.1 s [53], indicating that a pressure change approaching 300 kPa represents the minimum pressure drop for fragmentation and also relates to the tensile strength of the experimental material. This fragmentation timescale was similar to the structural relaxation time for the glass transition (about 0.3 s), suggesting that crossing the relaxation timescale results in brittle failure of the sample. Coincidentally, the timescale for viscous control of bubble growth in the experimental material is also in the region of 0.1 s, suggesting that bubble expansion may determine the fragmentation timescale. This coincidence occurs because the rigidity of the silicone fluid is within an order of magnitude of the experimental pressure; in magmas the difference is in the region of three orders of magnitude. The nature of the fracture surfaces (Fig. 17, compare with Figs. 9 and 16), and the observation of minimal expansion before fragmentation suggests, however, that fragmentation occurred because instantaneous strain rate exceeded that required for brittle failure.

Using viscoelastic and shear-thinning solutions of 0.1%, 0.3% and 0.5% w/w polysaccharide (xanthan gum) in water, transient flow experiments exploring a wider parameter range, including variable porosity, were undertaken by Namiki and Manga [93]. Air bubbles were introduced using a hand-mixer, giving gas volume fractions



Volcanic Eruptions, Explosive: Experimental Insights, Figure 17

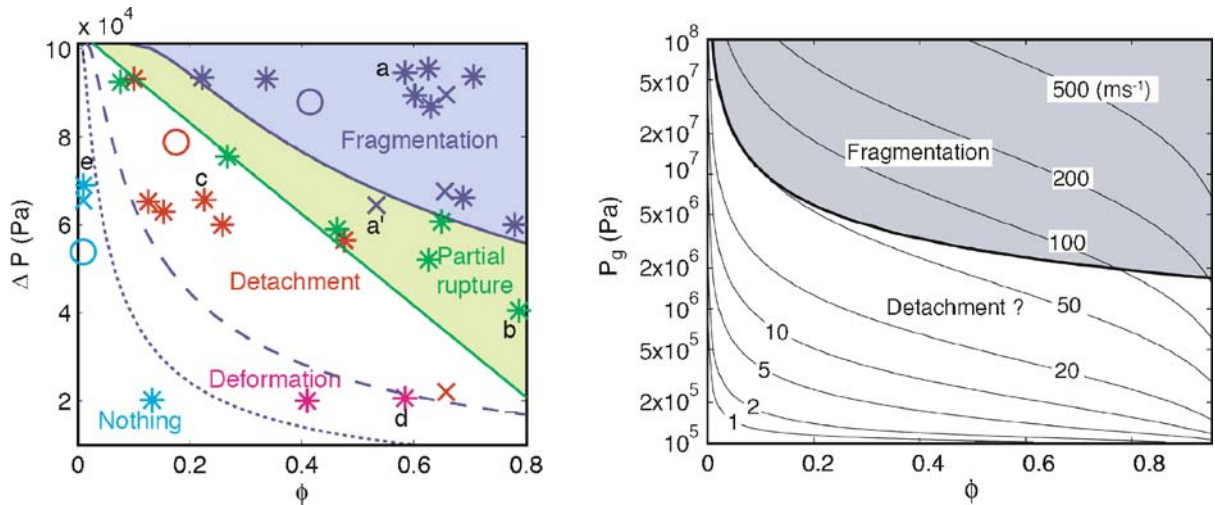
Rapid (50 MPa s^{-1}) 0.5-MPa decompression of a vesiculated dilatant (*shear-thickening*) silicone compound that acts as a brittle solid at high strain rates ($> 3 \text{ s}^{-1}$), but a viscous liquid at low strain rates. Pressure above the sample is given by the *dashed line*, whilst that below by the *solid line*. The surface of the sample is decompressing in (a), but pressure beneath the sample remains steady until (b), decreasing more rapidly from (c). Brittle failure of the sample occurs over a $< 10 \text{ ms}$ time span (d–g) in a spalling-fragmentation manner (Ichihara et al. [53]), about 40 ms after initial decompression. Fractures appear to initiate at the tube wall and then open to expand the flow (h, i). There is little or no expansion of the vesiculated sample or fragments. Reprinted with kind permission of AGU

up to 0.79. Samples were rapidly decompressed from atmospheric pressure to pressures ranging from 0.8 to 0.06 of an atmosphere; pressures much lower than this would encounter the saturated vapor pressure of water, causing the flows to be influenced by the production of water vapor. The shock tube was 0.05 m diameter by 0.25 m length, with fluid added to a depth of about 0.05 m. A range of flow patterns was observed (Fig. 18) as system parameters were varied. These include: fragmentation, partial rupture, detachment, deformation, and nothing; only ‘fragmentation’ results in ejection of fluid from the shock tube. Large decompression of highly vesicular samples leads to fragmenting flows (Fig. 18), which initially expand rapidly, then fragment layer by layer (Fig. 19) showing some similarity to spalling fragmentation (Figs. 9, 16, 17). In ‘partial rupture’, large-scale net-like structures develop that allow gas to escape from the fluid, but the liquid phase does not fragment *en masse*. At lower flow energies, the liquid phase detaches and contracts from the tube wall to yield an inverse annular, or ‘detached’ flow. Transient experiments allow the measurement of flow-front position, thus enabling estimation of strain rates within the flow. In these experiments the flow expansion was found to be independent of viscosity, which ranged from about 30 Pa s to 0.01 Pa s and was strain-rate dependent. For all experiments, it was found that shear rates were sufficient for elas-

tic behavior, consistent with the independence from viscosity.

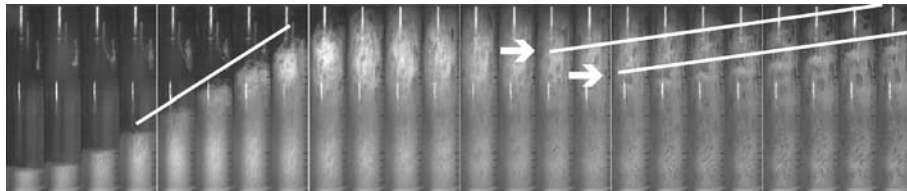
The changes in flow pattern are attributable to the behavior of the bubble walls. Detachment of the fluid from the tube walls can be explained by the Poisson’s ratio of the axially expanding foam, and represents the development of radial heterogeneity within an axial flow. However, if bubble walls rupture, elastic energy is released resulting in radial expansion and, thus, suppression of detachment. This suggests that fragmentation cannot take place from the detached flow pattern. Failure of bubble walls also increases permeability and allows gas to escape. Failure of the thin film, or plateau, between two bubbles, but not of the thicker plateau borders between three or more bubbles, is considered to result in the partial-rupture flow pattern. The plateau borders form the net-like structure. Wholesale failure of plateau and plateau borders results in fragmentation. Application of experimental processes to volcanic scales (Fig. 18) by utilizing results from studies of transient flows of natural materials, gives indication of the decompressions needed to fragment vesicular magma for a range of vesicularities, but defining other flow patterns at volcanic scale requires further research.

Using a similar technique to Ichihara et al. [53], Namiki and Manga [94] investigated the role of transient decompression rate on aqueous xanthan gum so-



Volcanic Eruptions, Explosive: Experimental Insights, Figure 18

Aqueous xanthan gum solutions are shear thinning and develop brittle solid behavior at strain rates above about 0.1 to 1 s^{-1} , depending on concentration. The *left panel* shows that rapid decompressions ($< 0.1 \text{ MPa}$) of pre-vesiculated xanthan gum solution results in a range of flow patterns (Namiki and Manga [93]). Combining data established from the decompression of natural samples with the analogue xanthan gum experiments allows the calculated fragmentation field for explosive volcanic eruptions (*right panel*) in terms of gas pressure and vesicularity. It was not possible to define the parameter space for other experimental flow patterns applied to magmatic systems. Reprinted with kind permission from Elsevier



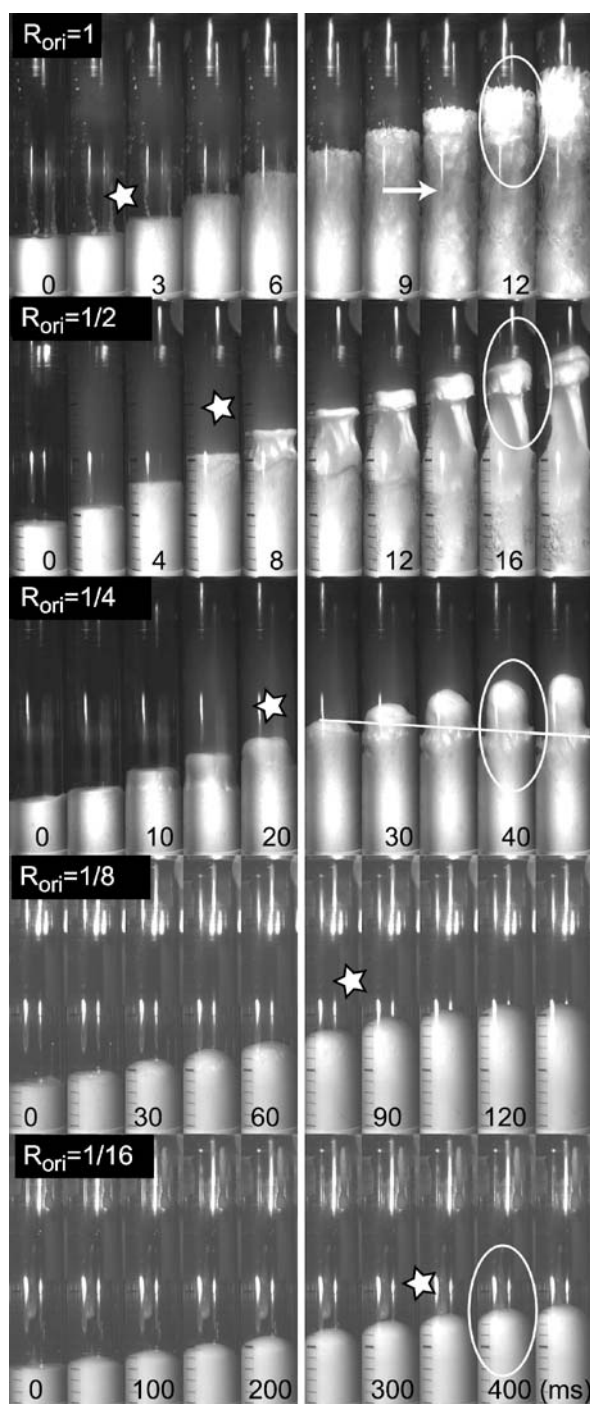
Volcanic Eruptions, Explosive: Experimental Insights, Figure 19

Fragmentation of vesiculated xanthan gum solutions occurs if decompression and vesicularity are high enough (Fig. 18). The *first frame (zero time)* shows the sample of vesiculated solution. On decompression, bubbles expand to give an approximately constant-velocity flow front (Namiki and Manga [93]), shown by the *line in frames 4–8* (3 ms between frames). During expansion, bubbles coalesce through film breakage to increase significantly in size, especially in the *upper parts* of the flow. The foam then fragments layer by layer, as shown by the *two lines* following liquid-poor regions. Most of the xanthan gum is ejected from the shock tube during the experiment. Reprinted with kind permission from Elsevier

lution. The variables here also included porosity (0.19–0.82 v/v) and absolute decompression (0.41–0.94 atmosphere). High decompression rates result in a variety of flow patterns, including fragmentation, depending on porosity and absolute decompression. At low decompression rates only sample deformation or expansion takes place (Fig. 20). Rough upper surfaces develop on flows during high decompression rates, indicating that bubble walls are rupturing; conversely, lower rates of decompression leave flows with smooth upper surfaces. These experiments suggest that decompression rate is an important parameter in determining eruption behavior, in particular the transition between effusive and explosive eruption in

low-viscosity vesiculated magmas subjected to decompression. Explosive response (fragmentation) to decompression results from disequilibrium expansion, where pressure in the bubbles is significantly higher than in the surrounding fluid and bubble expansion is limited by the enthalpy change resulting from the decompression. Bubbles cannot physically expand fast enough to maintain the same pressure as the surrounding fluid. Effusive response results from bubble pressure being close to fluid pressure.

Models of equilibrium and disequilibrium expansion were tested against experimental results. At high decompressions, equilibrium expansion would be faster than dis-



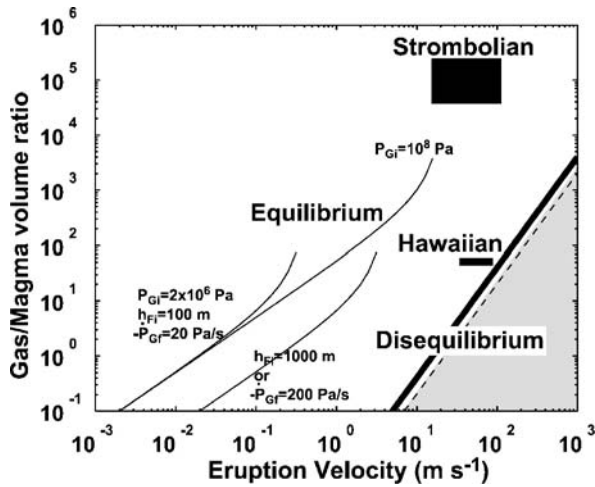
equilibrium expansion; experiments follow the slower disequilibrium expansion model. At lower decompressions the disequilibrium model predicts more rapid expansion than the equilibrium model; experiments again follow the slower expansion, this time in equilibrium. Namiki and

◀ Volcanic Eruptions, Explosive: Experimental Insights, Figure 20

Images of a 60-kPa decomposition of xanthan gum solution of initial vesicularity about 0.6 (Namiki and Manga [94]). In order to study the effect of decompression rate, the top of the shock tube has been choked with an orifice whose radius is a fraction of the tube diameter (R_{ori}). Experiments with rapid decompressions have short durations (time in ms on individual frames), and slow decompressions significantly longer durations, with the star indicating the time decompression ended. For $R_{ori} = 1$, the flow develops a rough surface suggesting rupturing of bubble walls (ellipse), and the arrow indicates the onset of fragmentation. When $R_{ori} = 1/2$, the flow top starts to separate (ellipse), but surfaces are smooth indicating that bubble walls are staying intact. Fragmentation does not occur when $R_{ori} = 1/4$, but the flow detaches from the tube wall as it expands. Smaller orifices result in flow expansion that retains wall contact. Different values of vesicularity and absolute decompression yield different patterns of behavior. Reprinted with kind permission of AGU

Manga [94] gave the critical decompression rate for inviscid explosive behavior as $-P'_{Ot} > (2\gamma/\rho_L\phi_i P_{Gi}(1-\phi_i)(\gamma-1))^{0.5}(P_{Ot}^2/h_{Fi})$, where P_{Ot} is pressure outside bubble during decompression, γ is isentropic exponent, ρ_L is liquid density, ϕ_i is initial gas volume fraction, P_{Gi} is internal bubble pressure and h_{Fi} the initial height of the bubbly fluid column. This experimentally based threshold decompression rate is consistent with the estimated decompression rate for the explosive/effusive transition in natural basaltic eruptions (Fig. 21), with Hawaiian eruptions suggested as mainly driven by the sufficiently rapid decompression of bubbly magma.

Degassing-Driven Flows The decompression and expansion of materials with pre-existing vesicularity provides valuable insight into volcanic behavior. However, magmas also degas on decompression, potentially adding to the explosivity of eruptions. In contrast to experiments with natural materials, where high temperatures and pressures make spatially and temporally extensive flows difficult to achieve, analogue experiments offer the possibility of studying the evolution of flow processes from single phase liquid to multi-phase fragmented flow using high-speed imaging and other data collection. Decompression of an unvesiculated hydrated magma results in, amongst other effects, the nucleation and growth of bubbles of gas phase or supercritical water, complex changes in the rheology of the liquid phase, increasing permeability and decreasing diffusivity. Incorporating all these interdependent variables into an experimental system adds complexity and makes understanding the first order effects more difficult, even if scaling between experiment and volcano is possible. Designing experiments to investigate the domi-



Volcanic Eruptions, Explosive: Experimental Insights, Figure 21

Application of experiments from Fig. 20 to the volcanic case give an estimate of the magma velocity required to cause sufficient decompression rate to initiate explosive eruption (gray region) as a function of magma vesicularity (Namiki and Manga [94]), where P_{Gi} is initial bubble gas pressure, h_{Fi} initial height of bubble column and $-P'_{Gf}$ the bubble decompression rate. Eruptions that result from the rapid expansion of bubbly magma are likely to plot on the thick line separating equilibrium and disequilibrium fields. Hawaiian eruptions approach the transition and, on this basis, result from the rapid expansion of vesiculated basalt magma. Strombolian eruptions, however, are indicated to result from another mechanism. Reprinted with kind permission of AGU

nant physics using a canonical approach reduces complexity and eases scaling requirements. The first order physical process occurring during these flows is the phase change of one system component from liquid (or more strictly, dissolved) to gas, with the associated reduction in bulk modulus and response to pressure change. Therefore, the aim of analogue experiments here is primarily to study the effect of degassing on flow.

The decompression of a liquid below its saturated vapor pressure results in boiling of that liquid as it becomes superheated. Experiments carried out by Hill and Sturtevant [50] used a shock tube to rapidly decompress a refrigerant. The refrigerant was Newtonian in rheology and of low viscosity, which, whilst dissimilar to the physical properties of magma, reduces the experiments to the first order process. Boiling produced a flow of vapor with entrained liquid drops. The superheating of the experimental liquid can be likened to the supersaturation of water in magma, and the liquid boiling to the exsolution of water from magma. The emerging gas phase expands, entrains liquid droplets and rapidly accelerates the flow. These ex-

periments showed the development of a sharply defined plane at which explosive boiling occurred.

The addition of inert particles to a volatile liquid [113] reduces the proportion of volatile phase and maintains particles in the post-fragmentation flow. Decompression, combined with the imposition of a steep pressure gradient within a centrifuge, results in a well-defined fragmentation front when decompressions are large. However, the mass of inert material acts to reduce post-fragmentation acceleration thus maintaining pressure and suppressing heterogeneous bubble growth below the fragmentation front. Small decompressions result in bubble nucleation on the inert particles throughout the mixture, illustrating that system behavior depends on the rates at which processes respond to imposed changes. Although these experiments probably represent end-member behavior, they provided a tantalizing glimpse of possible explosive fragmentation mechanisms that may operate in volcanic conduits given suitable conditions.

Volcanically, only a few weight percent of the magma degasses to drive the flow, whilst boiling experiments represent an extreme expression of degassing flows where all the liquid can change phase to gas. Experiments that retain low liquid viscosity and Newtonian rheology, but degas only a fraction of their mass, extend our knowledge of degassing flows and are likely to behave in a different, possibly more volcanic fashion. Mader et al. [78,79] rapidly generated bubbles of CO_2 in water, and throughout the fluid rather than just at the top interface. In volcanic systems, if bubbles nucleate and grow on timescales over which they can rise and escape then significant fluid expansion does not occur. However, if the CO_2 can be experimentally generated with sufficient supersaturation to drive bubble growth on timescales much shorter than those needed for bubble rise, then the two-phase mixture rapidly expands and fragments in a ductile fashion, producing liquid and foam drops suspended in gas, as the gas volume fraction increases. Two methods were used to achieve CO_2 supersaturation up to 455 times ambient. Water was saturated in CO_2 and decompressed in a shock tube developing high supersaturations. An alternative approach used rapid chemical reaction between K_2CO_3 and HCl to generate a supersaturated CO_2 solution. An intriguing positive feedback mechanism was observed whereby agitation of the liquid by the growing gas bubbles enhanced the release of gas thus increasing the violence of the flow. It was found that considerable expansion and acceleration took place before the major change in flow pattern induced by fragmentation. This contrasts with brittle systems that tend to fragment then expand [53]. Accelerations approached 180 g and were proportional to volatile

supersaturation; velocities peaked at 15 m s^{-1} , and strain rates were in the region of 30 s^{-1} . These are considered to be in the same range to those experienced volcanically and indicate a degree of similarity between laboratory and natural systems, with strain rates suggesting that high-viscosity magmas will be fragmenting in brittle fashion.

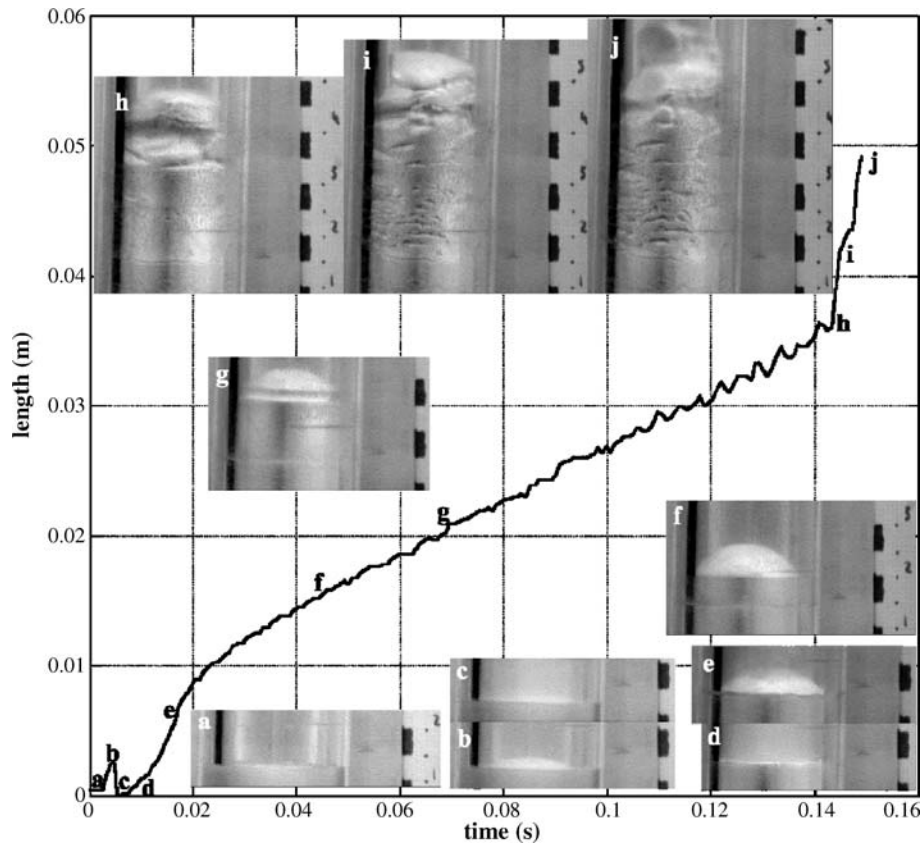
Injection apparatus in the chemical mixing experiments introduces discontinuities in the tube geometry and this appears to play a role in the behavior of the flow. Mader et al. [80] carried out relatively sustained explosive experiments, lasting about 1.5 s, where a considerable volume of carbonated water was decompressed. The vessel used was a round-bottomed flask. The discharge rate of water was found to fluctuate because of flow instabilities at the base of the flask neck, probably accompanied by pressure fluctuations. The flask neck was also found to pin the point of fragmentation as the flow evolved, with similar results being found by Zhang [129]. These experiments demonstrated the importance of sustained flows in allowing quasi-steady behavior to emerge, as well as demonstrating that conduit geometry influences flow patterns.

Although water- CO_2 experiments illuminate the behavior of explosively degassing systems, water is many orders of magnitude less viscous than magma. Zhang et al. [132] investigated the role of viscosity by adding polymers to the water, increasing liquid viscosity by between 1 and 3 orders of magnitude. Degassing styles ranged between passive degassing with little or no expansion for low supersaturation decompressions, through to rapidly expanding and fragmenting flows when pressure reduces by a factor of 50 or more on decompression. Bubbles were found to appear uniformly throughout the liquid on decompression, and were considered to be the result of heterogeneous bubble nucleation on minute particles in the liquid. This differs from boiling liquid flows and is more consistent with heterogeneous bubble nucleation on crystals in magmas. Initial acceleration of the liquid was found to be constant if ambient pressure was constant, with bubbles growing as $\text{time}^{2/3}$. Viscosity was found to be less important than the dissolved gas content in determining explosive capability, indicating that the low solubility of CO_2 in magmas made explosive eruptions driven solely by CO_2 unlikely. Experimental bubble growth was found to match well with models formulated for bubbles in magma, adding to confidence that the experimental system was, at least in part, similar to the natural phenomena.

Taddeucci et al. [116] increased complexity by carrying out degassing experiments with a viscoelastic analogue material, i.e., one that can change from viscous liquid to brittle solid behavior as strain rate increases. The silicate analogue was polydimethyl siloxane, with various addi-

tives, sold commercially as 'Silly Putty'. Silly Putty is a dilatant material with yield strength, and is viscoelastic [26]. The volatile analogue was the inert gas Argon, which had minimal effect on the rheology of the Silly Putty. Pressures up to 10 MPa were also found to have minor effect on rheology. The apparatus used was similar to the 'Fragmentation Bomb' (Fig. 8) used for decompression of non-degassing samples; however, because the Silly Putty experiments were carried out at room temperature, a visibly transparent shock tube could be used to facilitate high-speed imaging. Samples were loaded into the base of the shock tube, then exposed to Ar gas at pressures varying between 4 and 13 MPa, for times between 5 and 340 hours, then rapidly decompressed to 0.1 MPa.

Figure 22 shows the flow response on a depressurization of 11 MPa after 5.7 hours of exposure to Ar gas. On decompression, a small upward bulging of the sample surface was followed by detachment of the upper part of the sample from the tube walls. This is indicated by the change in wall refraction between Figs. 22c and 22d as the Silly Putty 'unsticks' from 'wetting' the tube wall and allows a thin film of gas to change the refractive index structure of the interface. The detachment possibly represents a solid-like radial contraction to axial extension (Poisson's ratio) caused by elastic expansion of the bubble-free sample on decompression. Alternatively, the momentary appearance of doming of the sample surface suggests a significant degree of friction with the tube wall and the generation of high strain rate; the Silly Putty wetting of the tube wall breaks down, but wall friction remains significant. Bubbles nucleate and start to expand. The sample surface domes up, suggesting that despite detachment, wall friction is still appreciable (compare with Fig. 20). The sample then expands and develops fractures at the tube wall. Sharp fractures near the flow head were defined as 'rim fractures', with other more numerous and widespread fractures called 'pervasive fractures'. These fractures represent a solid-like response to the high strain rate imposed at the flow margin and give experimental support for a theoretical process proposed by Gonnermann and Manga [47] who postulated that fragmentation was occurring due to viscous shear along flow edges. The fracturing process may also create seismic signals [122] and act as a trigger for seismically detectable resonant phenomena. The fractures only propagate as far as strain rates maintain brittle behavior, which acts to confine fractures within the outer section of the flow. Fragmentation will occur if the strain rate is sufficient for brittle behavior to persist right to the center of the flow. The fractures were also observed to close and heal because, once formed, lower strain rates caused reversion to viscous behavior. The development of such frac-



Volcanic Eruptions, Explosive: Experimental Insights, Figure 22

An 11-MPa rapid decompression of viscoelastic 'Silly Putty', saturated with Ar gas (Taddeucci et al. [116]), resulted in an expanding degassing flow. The domed flow top indicates the presence of significant wall friction, despite optical indication that the "Silly Putty" did not wet the tube wall during expansion (compare images c and d). Constant velocity expansion then occurred (e to h) with a circumferential fracture forming near the flow front at g. Flow front oscillation is apparent between g and h, but no concurrent pressure data are reported. From h, the flow front velocity increases dramatically as pervasive brittle fractures appear in the flow margin (i and j) where strain rates are highest. Fragmentation did not occur because the fractures did not propagate through the flow center where strain rates were low and viscous behavior persisted. The fractures could then close and heal due to viscous flow once strain rate declined. These experiments give valuable insight into the process of margin fracture, which could provide an efficient means for gas escape, thus suppressing explosive behavior. They also demonstrate a mechanism of generating fluctuations in magma effusion rate. At volcanic scale, margin fracture may be expected to generate a seismic response, and field evidence of such processes exists (Tuffen and Dingwell [122]). Reprinted with kind permission from Elsevier

ture networks has significant implication for mechanisms of magma degassing. The continual formation and healing of margin fractures gives rapid access to the conduit margin for gas deeper in the flow. This has consequences for transitions between effusive and explosive behavior.

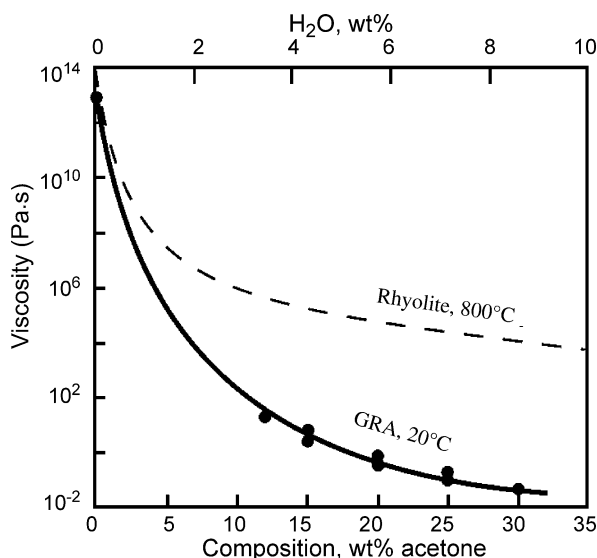
Only a few Silly Putty experiments underwent explosive fragmentation. All these were triggered at a sudden tube widening, emphasizing the importance of conduit geometry on flow behavior in volcanic systems. In comparison, similar decompressions of pre-vesiculated samples [53] resulted in much more extensive fragmentation. This demonstrates that, although there may be more gas

dissolved in an unvesiculated sample than contained in the pores of another non-degassing sample, the pre-vesiculated material is more explosive. The process of bubble nucleation and diffusive growth provides a regulating mechanism on the effective maximum rate of decompression and reduces initial explosive activity. However, the continued supply of volatile into bubbles means that degassing flows are likely to expand more given sufficient time, but in the absence of geometric structures, will they fragment in a brittle solid manner?

The viscosity of the liquid phase in magma increases by several orders of magnitude (Fig. 1) as water degasses,

also decreasing the strain-rates over which viscous flow turns to brittle solid behavior. Water and melt interact to change the lengths of silicate molecules and ‘lubricate’ differential molecular motion, hence changing viscosity. As an analogue material, gum rosin derives from removing volatile compounds from tree sap, leaving 3-ring aromatic hydrocarbons typified by abietic acid ($C_{19}H_{29}COOH$). It is a glassy organic solid at room temperature, but melts in the region of $80^{\circ}C$, and becomes increasingly less viscous as temperature rises. Warm gum rosin behaves in a viscoelastic fashion (Bagdassarov and Pinkerton [10]), being brittle when deformed rapidly but viscous under more gentle treatment. Such behavior is phenomenologically similar to a silicate melt. Phillips et al. [97] found that certain oxygen-bearing organic solvents, such as acetone, dissolved in gum rosin to yield a liquid at room temperature. At concentrations below about 20% w/w solvent these appear to be true solutions [71], with a partial pressure of acetone below that of the pure liquid suggesting some chemical interaction; another phenomenological similarity to hydrated magma. The viscosity of this liquid was found to be a non-linear function of the acetone content of the solution, again similar to a hydrated silicate melt (Fig. 23). Decompression of gum rosin-acetone solution below the saturated vapor pressure of acetone (about 20 kPa at room temperature) was found to result in volatile degassing and consequent increase in liquid viscosity. Slow decompression resulted in the establishment of a degassing interface that consumed the liquid solution. No measures were taken to remove nucleation sites from the liquid, suggesting that nucleation was sensitive to pressure and was confined to a surface layer in the liquid. This is similar behavior to boiling experiments [50,113], where the reaction force from expansion of degassing volatile and accompanying liquid was considered to elevate pressure in the underlying liquid and suppress bubble nucleation and growth, therefore acting to confine rapid degassing to a thin interface. This process may not be as prevalent in H_2O - CO_2 and Silly Putty systems because absolute pressures were larger, in relation to hydrostatic, than in gum rosin-acetone or boiling refrigerant experiments.

Rapid decompressions of gum rosin-acetone resulted in expanding foam growing from the liquid surface [97]. Flow-front acceleration was generally constant, except for large supersaturations with high acetone content where accelerations increased with time. These were reinterpreted by Mourtada-Bonnefoi and Mader [89] in the light of additional experiments that found bubble growth prior to fragmentation is diffusion-driven, but limited by the high-viscosity skins that develop around growing bubbles because of the reducing volatile concentration. This infers



Volcanic Eruptions, Explosive: Experimental Insights, Figure 23

The viscosity of hydrated silicate melts changes non-linearly with water content (Fig. 1). One experimental system uses gum rosin as an analogy for silicate melt, and organic solvents such as acetone and diethyl ether instead of water. The degassing of gum rosin acetone (GRA) results in increasing liquid viscosity (lower scale), in similarity with the degassing of hydrated magma (upper scale) (Mourtada-Bonnefoi and Mader [90]). The volatile content between natural and analogue systems can be compared by quantifying in terms of moles of volatile per unit volume of liquid; 4% water w/w in magma equates to about 20% w/w acetone in gum rosin. The scales here are not matched on this basis. Reprinted with kind permission from Elsevier

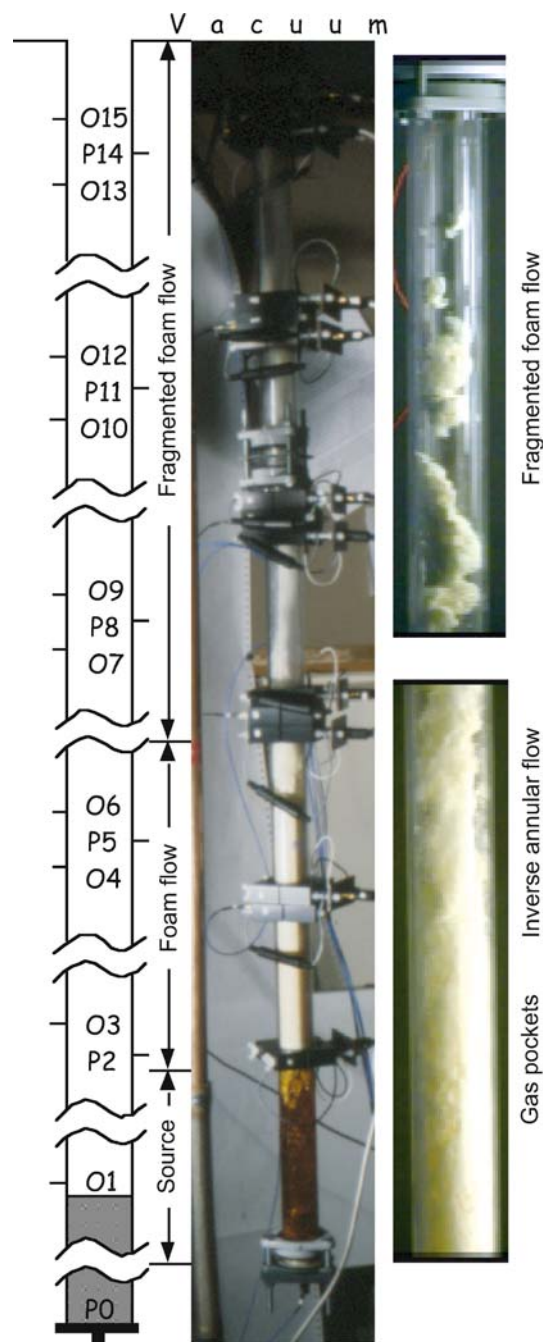
that diffusion-limited degassing is unlikely before fragmentation removes viscous control as a physical mechanism. Accelerations and velocities using gum rosin-acetone were an order of magnitude less than those produced by CO_2 - H_2O experiments, but this is consistent with the order of magnitude lower driving pressures. Experiments carried out with high supersaturations allowed extensive acetone degassing to take place. This resulted in the production of solid gum rosin foam with elongated bubbles, phenomenologically similar to woody or tube pumice.

The experiments of Phillips et al. [97] were carried out using small volumes of solution in un-instrumented and relatively short tubes that did not allow sufficient time or length for flow patterns to develop and stabilize. Lane et al. [70] carried out similar experiments using longer tubes, larger volumes of gum rosin-acetone and gum rosin-diethyl ether solutions, and high-speed pressure measurement. Instantaneous decompression from 10^5 to 10^2 Pa resulted in rapid degassing from the liquid surface. Flow became pseudo-steady after about 0.2 s, with foam expanding from the liquid interface, and continued

explosive behavior for about 1.5 s. Pockets of gas developed at the tube wall, eventually merging to allow the expanding foam to detach from the wall. Removal of wall drag allowed the foam core to accelerate as an inverse annular, or detached flow, and break up into foam fragments that were ejected from the top of the shock tube (Fig. 24). The fragmentation of the foam core was precluded during expansion of a non-degassing system [93], suggesting that degassing systems have different flow patterns to those driven by gas expansion alone. The reason for this difference may lie with the smaller overpressure in bubbles of pseudo-steady degassing systems compared with those in transient expanding flows. The lower bubble pressures prevent bubble wall breakage and stabilize detached flow until fragmentation commences [93]. This suggests that flow behavior preceding fragmentation may differ between explosive volcanism triggered by rapid decompression of vesiculated magma, for example the May 18, 1980 Mt. St. Helens lateral blast triggered by a landslide, and sustained explosive volcanism such as the Plinian eruption which followed the blast. The fragmentation mechanism may also be different, with brittle spalling fragmentation before expansion (Figs. 9, 16 and 17) suggested for the lateral blast and fluid expansion before ‘plastic’ fragmentation (Figs. 19, 20 and 24) for the Plinian eruption.

The size of fragments of gum rosin foam was initially significantly smaller than tube diameter, but increased to near tube diameter and elongated with time, suggesting a declining flow energy. Interestingly, some of the flow features found by Cagnoli et al. [25] in expanding particle beds appear similar to those in expanding gum rosin foams, with bubbles appearing at the margins of both flows and being stretched out (Fig. 15). The sequence of flow pattern changes in the gum rosin flows was found to result in the generation of characteristic pressure fluctuations. Pressure fluctuations may be inherent in the unsteady nature of flows undergoing changes in behavior and such phenomena could be detectable by seismic means during volcanic flow.

Magma can fragment in the presence of pre-existing bubbles alone without any degassing (e. g., Fig. 9), and the presence of crystals increases the number density of nucleation sites (e. g., Fig. 4), and hence the surface area over which degassing can occur. Magmas are decompressed with crystals and bubbles often present, an aspect investigated analogously by Mourtada-Bonnefoi and Mader [90] using gum rosin-acetone mixtures and a variety of particles and existing bubbles. It was found that fragmentation occurred at lower volatile contents and lower decompressions in the presence of particles and bubbles. It was also found that flow behavior depends on the distribu-



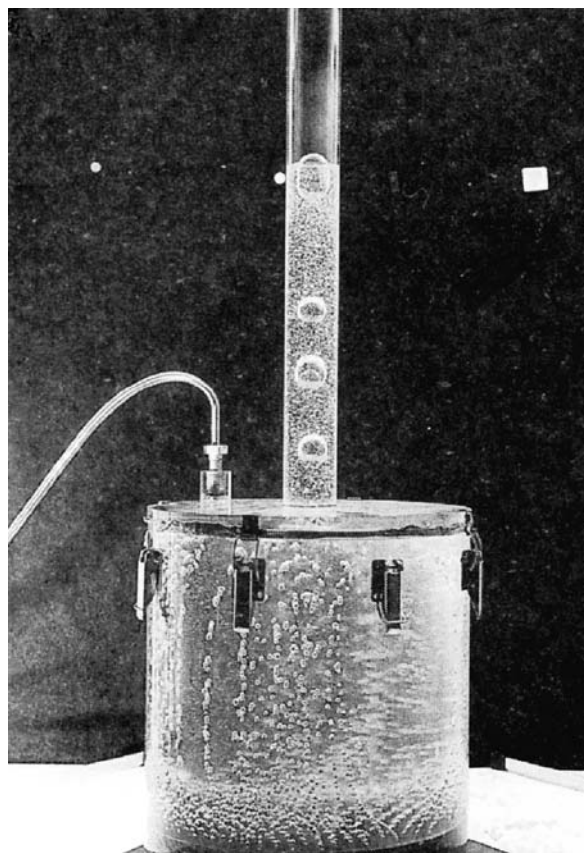
Volcanic Eruptions, Explosive: Experimental Insights, Figure 24

An 0.1-MPa rapid decompression of a solution of gum rosin 19% w/w diethyl ether generates a degassing flow (Lane et al. [70]). Bubble growth occurs predominantly at the upper liquid surface. The expanding flow develops gas pockets at the wall, which merge and allow a central foam core to detach from the tube wall giving inverse annular flow. The detached foam core is no longer constrained by wall drag and expands until it breaks up to give a fragmented flow. The fragments of gum rosin foam are ejected from the shock tube. Reprinted with kind permission of AGU

tion of particles in the liquid, with more rapid degassing where particle concentrations were high. This suggests that heterogeneity in the distribution of crystals and pre-existing bubbles will develop into sizable features within a degassing flow, at least before fragmentation. This raises the possibility that flow heterogeneity over a range of size scales may then play a role in the fragmentation process.

Low VEI Events High VEI events do not occur very frequently compared to anthropogenic timescales, and do not lend themselves readily to detailed field investigation of subterranean flow processes. Conversely, low VEI events, typified by Strombolian activity, occur on anthropogenically short timescales and form relatively safe natural laboratories to study magma flow in the volcanic conduit. Low VEI eruptions commonly occur at volcanoes where magma viscosity is low and degassing water is able to separate relatively easily from the magma; indeed, this separation is required to produce low VEI events. Analogue experiments of separating flows may, therefore, be compared with relatively well-studied natural processes in ways that high-VEI events cannot. Experimental conditions are also simplified in relation to those applied to high-VEI processes, with the assumptions that liquid rheology and temperature remain constant being easier to justify. Low-VEI processes may also be studied without shock tube or high-pressure apparatus, making observation and measurement more straightforward.

Strombolian eruptions are characterized by short-lived explosive events that erupt significantly higher water to silicate mass ratio than that of the bulk magma [15,30]. These events are separated by longer periods of relative quiescence, suggesting the presence of a gas separation process that produces gas-rich regions that rise up the conduit between intervals of relatively gas-depleted magma. In two-phase flow terminology, one such regime is that of slug flow, where large ascending gas slugs can form from the coalescence of many much smaller bubbles. However, evidence from extensive research on water-gas systems indicates that for such a flow pattern to be stable in the conduit the overall gas volume fraction would probably need to exceed about 0.25 [34], and the time intervals between explosions would be similar to, or less than explosion duration. It is also very questionable that slug flow would form from numerous small bubbles in a relatively high viscosity liquid like basalt magma. This suggests that other mechanisms operate to promote formation of gas slugs. Jaupart and Vergnolle [63,64] were among the first to recognize that volcanic conduits are not straight vertical tubes, but exhibit significant geometrical heterogeneity that may play a major role in eruptive behavior. Experiments were car-



Volcanic Eruptions, Explosive: Experimental Insights, Figure 25 Numerous small nitrogen bubbles rising in a silicone oil of viscosity 1 Pa s (Jaupart and Vergnolle [63]) encounter a structural discontinuity in the form of the horizontal roof of the experimental tank. Bubbles trapped under the roof collide and coalesce to emerge up the narrow exit pipe as much larger bubbles. Such a mechanism can be envisaged for the production of large bubbles some 1–3 km beneath the vent at Stromboli volcano (Burton et al. [21]); however, the experimental geometry canonically demonstrates the process rather than simulating conduit structure. Large bubbles emerging from the trap then expand and become overpressured on approach to the surface (James et al. [61]). Reproduced with kind permission of Cambridge University Press

ried out to examine the effect of a flat roof in trapping the numerous small bubbles rising through the magma (Fig. 25). Small air bubbles were injected at variable rate into the base of a tank containing liquids of various viscosities. The bubbles rose to the roof of the tank, which had a vertical small diameter outlet tube. Three modes of system behavior were observed. At lower liquid viscosity, a raft of bubbles formed at the roof. At some critical thickness the bubble raft collapsed on the scale of the tank roof and flowed up the outlet tube as a large gas bubble. This be-

havior was considered analogous to Hawaiian eruptions. At higher liquid viscosities, the bubble raft collapsed on a scale smaller than the tank roof and a series of bubbles that are much larger than those injected, but smaller than the low viscosity case, emerge up the outlet pipe. This gives insight into Strombolian eruptive activity. The final mode of behavior was the development of a relatively stable bubble raft and the escape of small bubbles up the outlet pipe to give bubbly flow at the surface.

The ascent of large gas bubbles, or slugs, up a tube can be controlled by surface tension, liquid viscosity or liquid inertia. In basaltic systems surface tension has negligible control, and inertia dominates with some component of viscous influence [106]. Conveniently, this allows the use of water and air at laboratory scale to give inertia-controlled slug flow. Seyfried and Freundt [106] carried out experiments applying the flow patterns that develop with increasing air flux through a column of water to basaltic volcanism. Single gas slug ascent was found to only occur through sudden incidents of limited volume gas release, with one mechanism being that of foam collapse from a trap [63,64]. It was observed that slug burst in the tube was a gentle process, but that if the liquid level was in the reservoir atop the tube (akin to a lava lake) then burst was more vigorous and could be likened to Strombolian activity; another example of the impact of conduit geometry on flow. Experiments with gas traps in the water column found that the coalescence of trapped gas pockets resulted in significant pressure oscillations that were a potential source mechanism for volcanic tremor; linking volcano-seismic signals to fluid flow could be a powerful method of experimental scaling inaccessible in high VEI events.

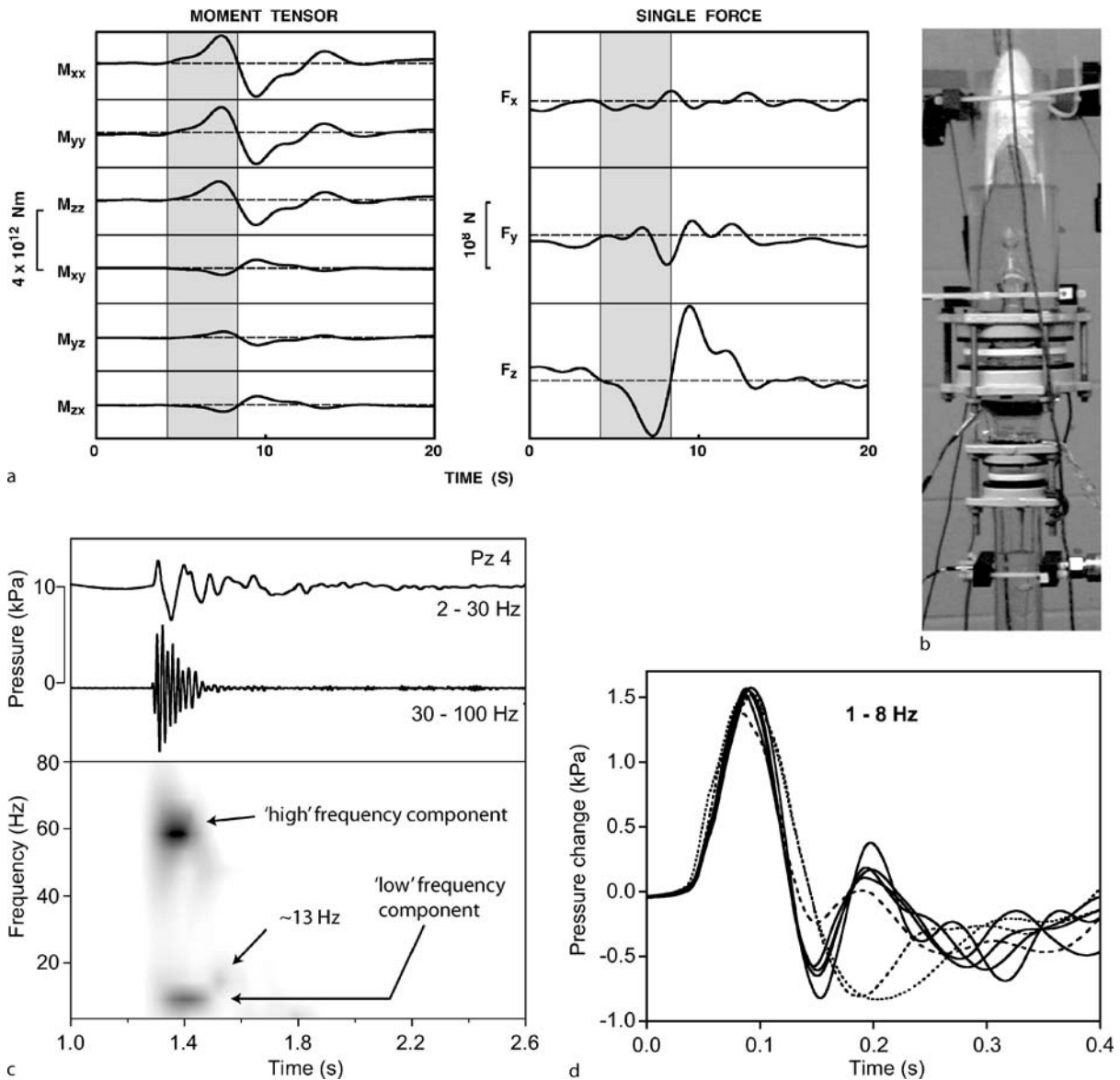
Seismic signals may result from the collapse of a foam layer trapped at a roof. Measurements made within apparatus similar to that of Jaupart and Vergnolle [63,64] reveal pressure fluctuations both within the fluid and in the air above the fluid surface in the outlet tube [102]. These could be linked to seismic and acoustic signals measured at Stromboli volcano and give insight into the role of fluid-flow on the generation of seismo-acoustic waves during explosive volcanism. During the build up of the foam layer, no pressure changes were detected. Collapse of the foam layer and motion of the gas slug up the outlet pipe produced pressure changes in the liquid tank of a few-hundred Pa, and of a few-tenths Pa in the air above the liquid level. Collapse of the foam layer generates upward gas flow in the outlet pipe thereby producing downward motion of the dense liquid phase in the outlet pipe, reducing pressure. Oscillation of liquid on the gas spring of the slug produces pressure oscillations within and above

the liquid. Slug burst results in a sudden increase in oscillation frequency above the liquid, and a small pressure pulse in the liquid due to decay of liquid flow around the slug nose [59]. Ripepe et al. [102] postulate that seismic signals measured at Stromboli are generated during rapid gas expansion during foam collapse, and estimated that the slug be about 4.5 m long and induce a pressure drop of 0.1 MPa in the magma.

Inversion of highly repeatable seismic waveforms measured at Stromboli Volcano, Italy [31,33] has enabled imaging of the conduit as well as revealing the forces and pressures being created by magma flow during Strombolian eruptions. In summary, Stromboli's plumbing system appears to comprise a dyke dipping about 72° that runs from the vent system to an intersection with a dyke dipping about 45° and 900 m below the vent system. Stable and repeatable seismic sources are inferred at a depth of about 220 m below the vent system, and have the characteristics of a dyke segment intersecting the main conduit. Another, weaker, seismic source is located at the intersection of the two main dykes about 900 m below the vents. The dominant seismic source at 220 m below vent generates a downward vertical force of about 10^8 N followed by an upward force of similar magnitude (Fig. 26a). The source volume increases during the downward force and decreases with the upward force. These measurements provided a means of testing laboratory models of Strombolian eruptions.

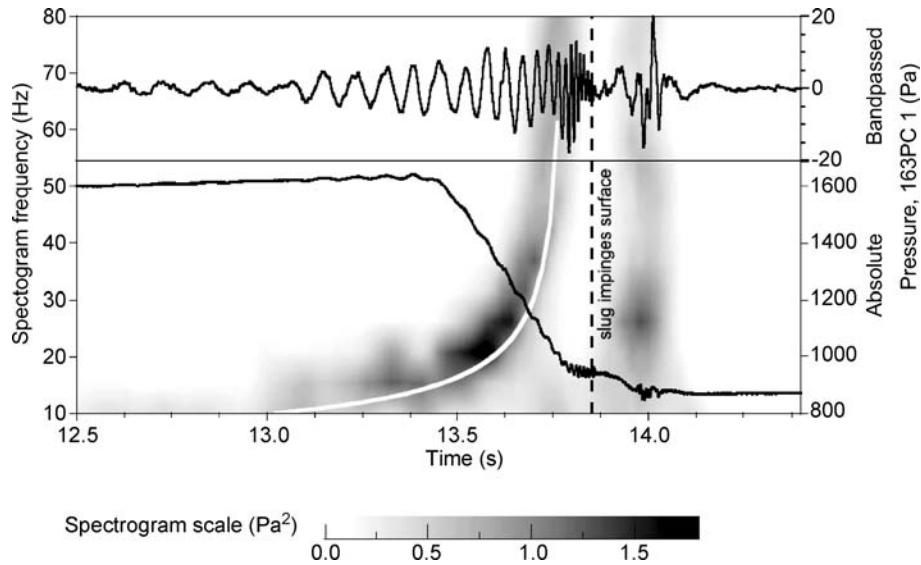
James et al. [59] studied pressure oscillations resulting from the ascent of single gas slugs in a vertical tube. The oscillations observed at the top of the liquid column (Fig. 27) showed an increasing amplitude and decreasing period as the slug ascended, with oscillations ceasing as the slug reached the surface. Burst of the meniscus produced further pressure fluctuation. Modeling of the oscillations revealed the source mechanism as bouncing of the liquid mass above the slug on the spring of gas within the slug. The observed pressure oscillations were not similar to the change in volume of the VLP seismic source at Stromboli (Fig. 26a), nor were oscillation amplitudes sufficient to account for forces of 10^8 N at volcanic scale. Bubble bursting was also quiescent rather than explosive.

Such experiments on Strombolian processes were not scaled for expansion of the gas slug as it rises, and gas chemistry suggests that slug source depths could be in the range 900–2700 m (Burton et al. [21]). A slug ascending from 1000 m in magma will expand about 200 times to reach atmospheric pressure, but in the experiments expansions were in the region of 1.2. In order to investigate more appropriate values, James et al. [61] used low vapor-pressure vacuum pump oil as an analogue liquid and varied



Volcanic Eruptions, Explosive: Experimental Insights, Figure 26

The geometry of experimental tubes has been observed to change flow behavior in a number of instances. James et al. [60] investigated the dynamics of a gas slug ascending through a tube widening. Inversion of seismic data measured at Stromboli volcano (a, Chouet et al. [31]) indicated an initial downward force of about 10^8 N, accompanied by pressure increase expanding the conduit. This was followed by upward force and conduit contraction with a period of about 10 s. The experimental ascent of a gas slug through a tube widening (b) caused breakup of the slug and production of a transient gas jet. Spectral analysis of pressure (c) showed three resonant components. The low frequency component (d, about 6 Hz) showed one to two cycles of pressure increase followed by decrease, qualitatively consistent with pressure change in the conduit at Stromboli during explosive eruption. Measurement of apparatus displacement indicated a peak downward force of 30 N, which when naively scaled by 100^3 for physical dimension and 2.5 for density difference gives a force of 7.5×10^7 N, encouragingly close to that estimated from seismic inversion. Reprinted with kind permission of AGU



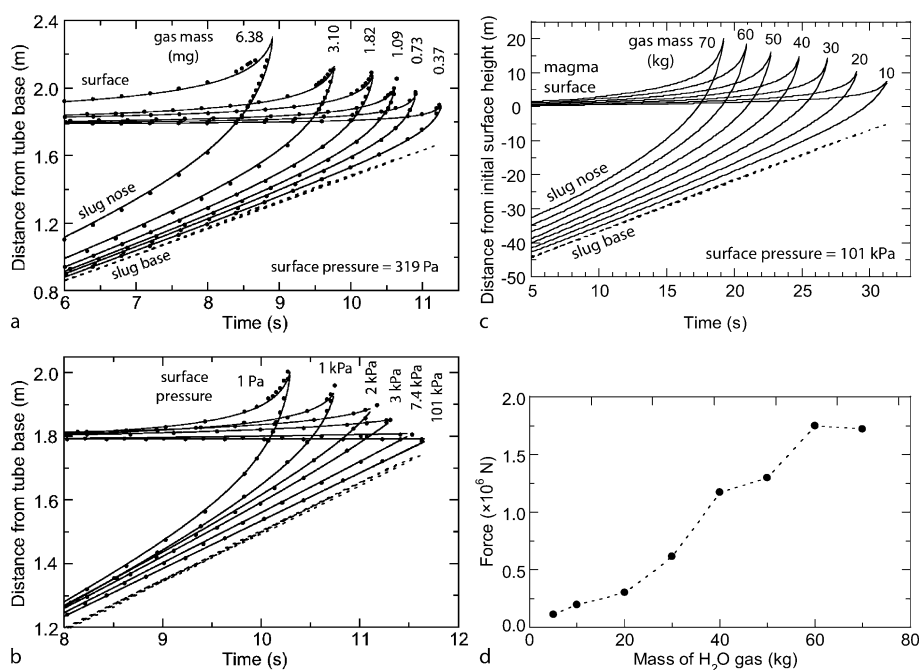
Volcanic Eruptions, Explosive: Experimental Insights, Figure 27

Strombolian eruptions are short-lived, periodic and have high volatile content. For these reasons they are associated with the formation, ascent and bursting of large bubbles of water vapor (often known as slugs), rather than the expansion of a vesicular magma (Fig. 21). The ascent of air slugs in water during small-scale experiments caused pressure oscillations (James et al. [59]). A spectrogram (gray shading) of band-passed (upper trace) pressure data (lower trace) was found to match well with calculations of the oscillation frequency (white trace) of the water above the gas slug bouncing resonantly on the gas slug. This oscillatory mechanism could not be used to account for the seismic signals used to image the conduit at Stromboli (Chouet et al. [31]). Reprinted with kind permission from Elsevier

the ambient pressure above the liquid surface between 10^5 and 10 Pa. The reduction in ambient pressure provided a proxy for slug ascent from depth and allowed potential gas expansions of factors up to 10^4 . The positions of the slug base, slug nose and liquid surface for ascending slugs of various gas masses and ambient pressures are shown in Fig. 28. Regardless of ambient pressure and slug mass, the ascent velocity of the slug base remained essentially constant. However, the slug nose accelerated rapidly on approach to the surface when ambient pressure was low, and burst with a pressure higher than ambient. Gas slugs that underwent little expansion burst at near ambient pressure. Scaling to the volcanic case was undertaken using experimentally verified CFD modeling. This showed that slug burst pressure is a function of conduit radius and slug mass, with large slugs in narrow conduits producing gas overpressures in the region of 1 MPa at burst. This overpressure will fragment the upward-moving (tens of m s^{-1}) meniscus of liquid existing just prior to burst. The effect of such decompression on the vesiculated basalt magma flowing down the conduit walls and slug base could be explosive fragmentation (Namiki and Manga [94]). This would eject pyroclasts, adding greatly to the pyroclast volume from the meniscus and explaining how explosive slug

burst results in the ejection of significant masses of pyroclasts. There is also the possibility that the gas slug is not a single bubble, but more accurately described as a foam raft, although such a structure may not survive the degrees of expansion undergone in ascent from 1000 m depth with its bubble walls intact. The rapid 1 MPa decompression of a foam raft would also produce pyroclasts as the foam fragments.

Rapid slug expansion, which generates the explosivity of Strombolian eruptions, is a process operating within the top few tens of meters of the magma column (Fig. 28c). This, and the fact that the forces generated are of order 10^6 N upward, means that slug expansion is not the fluid dynamic source process responsible for the VLP seismic signals inverted by Chouet et al. [31]. Slug expansion probably plays little role in this particular seismic signal because the magma head is probably too large for the slug to be expanding at any appreciable rate. The stable position of the seismic source suggests geometric control of a flow process, a phenomena we have seen a number of times before. James et al. [60] measured pressure and force as a gas slug ascended from a narrow tube through a flare into a wider tube. The gas slug segmented on passing through the flare and liquid flow during this process generated



Volcanic Eruptions, Explosive: Experimental Insights, Figure 28

Experiments on slug flow are numerous in the engineering literature, but volcanic flows operate under conditions not investigated for anthropogenic purposes. One of these conditions is the large pressure change a gas bubble will experience in rising from some depth. James et al. [61] investigated the dynamics of rapid gas slug expansion as a result of this decompression using an air bubble and vacuum pump oil as analogue fluids. Using surface pressures below atmospheric allows the air bubble to undergo considerable decompression under laboratory conditions. The degree of slug expansion, and hence explosivity on burst, was found to depend on (a) the mass of gas in the slug as well as (b) the applied surface pressure. Computational fluid dynamic modeling was used to apply the experimental findings at volcanic scale (c). The process of slug expansion generated significant pressure change and vertical force (d), but the amplitudes are two orders of magnitude less than those calculated at Stromboli (Chouet et al. [31,33]). Reproduced with kind permission of the Geological Society of London

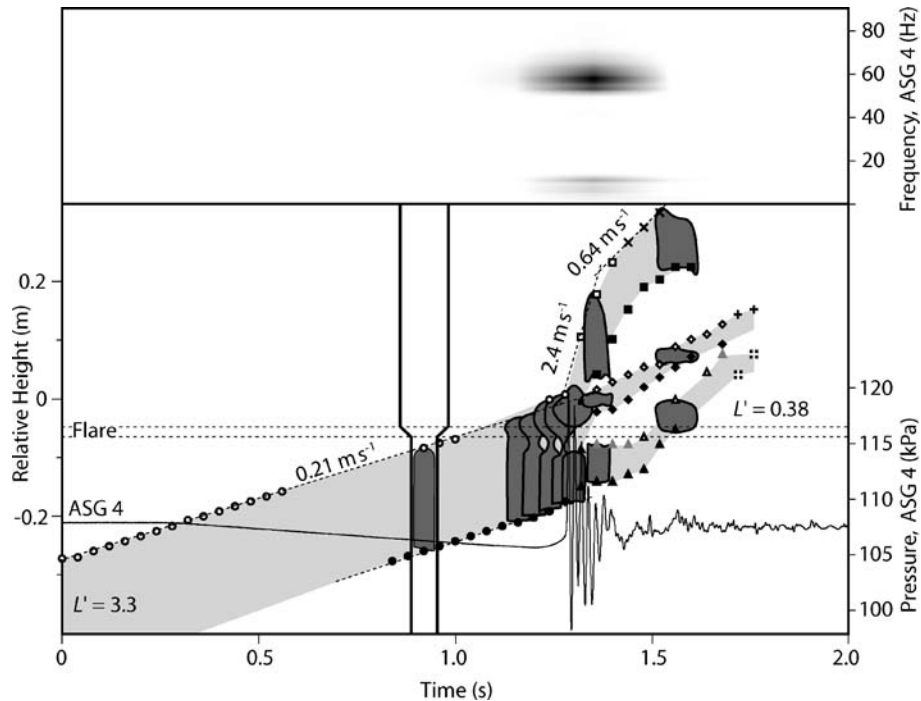
pressure oscillations (Fig. 29). Analysis of these oscillations (Fig. 26) revealed three components centered on 60, 13 and 6 Hz, with the low frequency component showing increasing pressure followed by a decrease, resembling the expansion-contraction waveform from inversion of VLP seismic data (Fig. 26a [31]). The vertical force generated during the experimental pressure increase was 30 N downward. Applying a simplistic scaling based on density and volume differences between laboratory and volcano gives a force in the region of 10^8 N, of similar magnitude to that emerging from inversion of VLP seismic data. It was, therefore, suggested that the source mechanism for VLP seismic signals measured at Stromboli by Chouet et al. [31] was the ascent of slugs sourced at depth [21] through a geometric widening of the feeder dyke inclined at 72° . The upward widening disrupts the downward flow of liquid around the ascending slug, allowing significant thickening of the falling film. As this thickening falls through the downward narrowing, it pinches closed and segments the

slug. The resulting liquid piston continues to descend because of its inertia, and increases pressure below it. The piston then oscillates for a cycle or two before being disrupted by the buoyancy of the gas beneath. Experimental insight suggests that the source mechanism for the VLP seismic signal is the deceleration of the liquid piston.

Explosion Consequences

Various consequences of explosive degassing of magma have been studied by analogue means, and many of these are reviewed in Sparks et al. [109]. Here, we review a sample of more recent literature.

Cinder Cones Explosive volcanic eruptions produce pyroclastic constructs, the most common form being known as cinder or scoria cones. The basis for understanding cinder cone growth was given by McGetchin et al. [85]. These structures, which are piles of generally uncon-



Volcanic Eruptions, Explosive: Experimental Insights, Figure 29

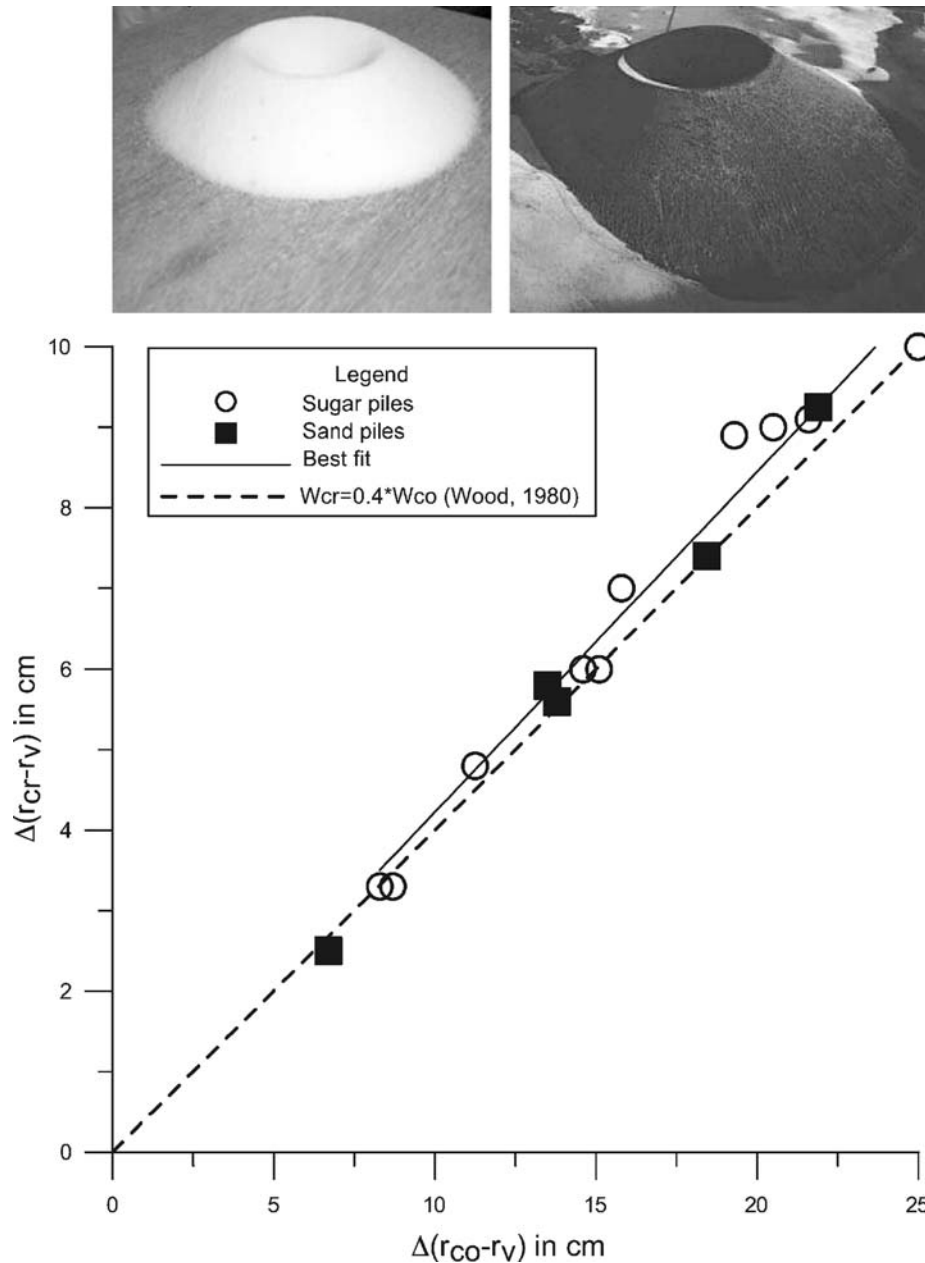
The source mechanism suggested by laboratory experiment (Fig. 26) for seismic signals measured by Chouet et al. [31] at Stromboli Volcano, Italy is the creation and rapid deceleration of a downward-moving liquid piston, formed as a gas slug breaks up in a conduit widening (James et al. [60]). The liquid piston ‘bounces’ on the lower portion of the slug for a cycle or two before being consumed by the ascending remains of the original slug. The cartoon superimposed on the pressure trace correlates the position of gas bubbles with pressure measurement and spectral analysis of pressure fluctuations. The dramatic velocity increase of the slug nose does not appear to play an obvious role as a source mechanism and may be associated with the highly unstable bubble in the tube widening. Reprinted with kind permission of AGU

solidated magma fragments, are prone to gravitational collapse and rapid erosion. To test the hypothesis that cinder cone geometry is controlled by the behavior of unconsolidated fragments, Riedel et al. [100] carried out small-scale analogue experiments using grains of sugar and sand. These were built into cones, drained in the center to represent the crater. These grain piles showed similar geometry to natural cinder cones (Fig. 30). Quantification of the geometry showed that analogue and natural cones were identical in shape to within 5%. This demonstrates that the angles of repose exert fundamental control on cinder cone geometry, with surface grain flow maintaining angle of repose during cone growth. The angle of repose nature of cinder cones emphasizes their vulnerability to erosion and collapse.

Pyroclastic Flows Pyroclastic flows ‘hug’ the ground because their density is greater than that of the atmosphere. Gravity then drives the pyroclastic material in a lateral fashion; hence pyroclastic flows are part of the family

of gravity currents, and the sub-family of particle-driven flows that includes turbidity currents. The flow behavior of pyroclastic flows, which result from explosive volcanism or dome collapse, has been investigated at laboratory scales using analogue materials for a number of years [109]. Gladstone et al. [46] experimentally examined the dynamics of gravity currents that were initially stratified in density using a 3 m long flume. A range of brine solutions of different density were layered into a lock at one end of the flume and released into tap water. The solutions were used singly, in two or three layers to investigate how stratification can develop or be homogenized in pyroclastic flows and turbidity currents. Flows were visualized by coloring the solutions allowing detection of mixing and stratification.

Flow behavior was found to depend on two dimensionless parameters. Firstly, the relative values of buoyancy between brine solutions, B^* , where most salt is in the lower layer for $0 < B^* < 0.5$, and in the upper layer for $0.5 < B^* < 1$. Secondly, the density ratio of the solutions,

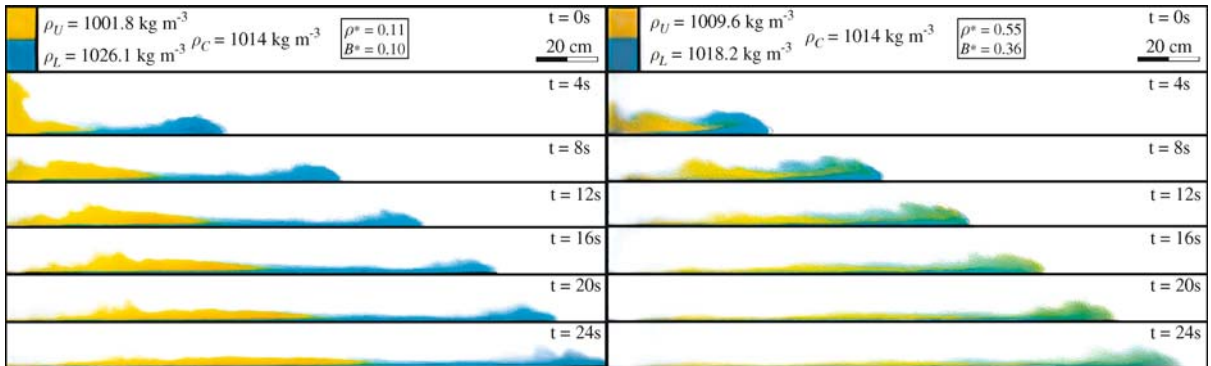


Volcanic Eruptions, Explosive: Experimental Insights, Figure 30

Cinder cones are the proximal expression of fallout from explosive volcanic eruptions. Riedel et al. [100] found that small piles of sugar (left image) or sand look similar in shape to much large piles of cinder (right image). Comparison of characteristic dimensions of laboratory cones (r_{cr} is distance from central hole to crater rim, r_{co} is distance from central hole to pile extremity and r_v is vent radius) with established measurements of natural cinder cones confirms the similarity. These experiments showed that cinder cones grow by the surface transport of grains under gravity to leave the slopes at angle of repose. Reprinted with kind permission from Elsevier

ρ^* , which is small for strong stratification, approaches 1 for weak stratification and equals 1 for unstratified conditions. When the lower layer has a greater proportion of the driving buoyancy ($B^* < 0.5$), it can run ahead lead-

ing to flow stratification (ρ^* approaches 0, Fig. 31), or the layers can mix to produce a homogeneous current (ρ^* approaches 1, Fig. 31). If the upper layer is more buoyant ($B^* > 0.5$), it travels to the nose of the current by mix-



Volcanic Eruptions, Explosive: Experimental Insights, Figure 31

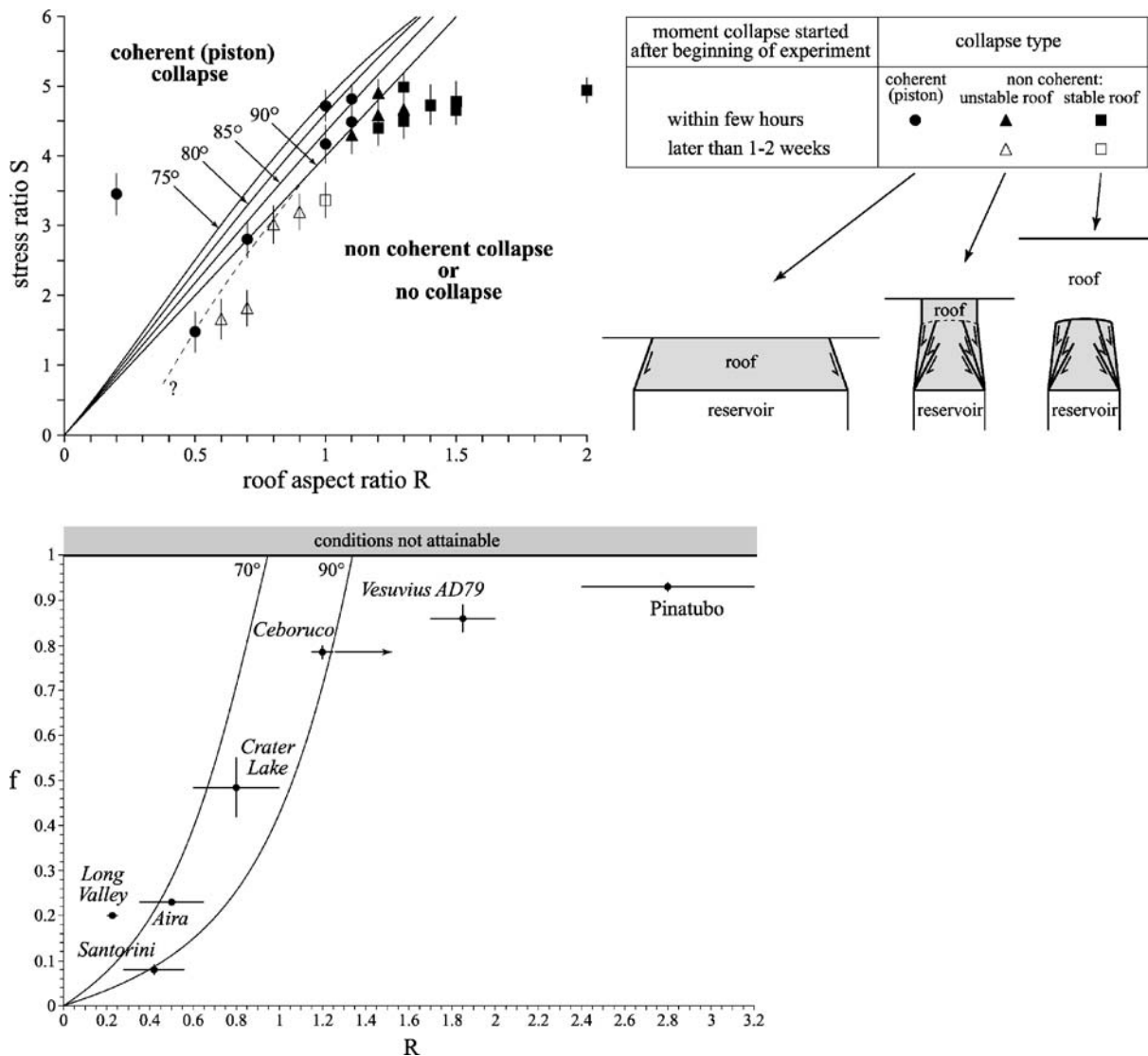
The first order behavior of gravity currents, which include pyroclastic flows, can be studied by analogue experiment using dyed brine solutions of different density propagating in a water-filled flume tank (Gladstone et al. [46]). Density stratification in the flow source material may be preserved under certain conditions of buoyancy and density (*left panel*). Pyroclastic deposits from such flows are likely to show vertical and horizontal stratification. Under other buoyancy and density conditions (*right panel*) the initial stratification is removed by turbulent mixing and resultant pyroclastic flow deposits are expected to be unstratified. Experiments that reduce complexity, as here by not including suspended particles, often give greater insight into primary controlling parameters. Complexity can then be added to understand the smaller scale processes that lead to diagnostic features identifiable in volcanic deposits. Reprinted with kind permission from Blackwell Publishing Ltd

ing to produce a homogeneous flow (ρ^* approaches 1) or overtaking, leading to flow stratification (ρ^* approaches 0). This suggests that buoyancy-contrast controls separation, whilst density-contrast controls mixing. These observations give insights into the origin of stratification and grain size contrast in pyroclastic flow deposits and allow constraint of flow conditions from field observation.

Caldera Collapse The highest VEI eruptions result from the ejection of large volumes of magma. As magma emerges, country rocks overlying the magma storage area subside, resulting in the formation of a caldera. The caldera roof may fail in a number of modes. Roche and Druitt [103] carried out a force balance calculation for a caldera roof to fail as a coherent single piston, predicting that $\Delta P/\tau_c \geq 4R$, where ΔP is the pressure below lithostatic at which failure occurs, τ_c is the rupture shear stress and R is the ratio of roof thickness to diameter. Experiments were carried out using sand or a slightly cohesive sand-flour mixture as an analogue to country rock, and a draining reservoir of silicone fluid to simulate removal of magma. Comparison of experiment and theory (Fig. 32) shows that coherent roof collapse did occur in line with theoretical prediction. The experiments also showed two other more complex modes of collapse that occur at roof aspect ratios larger than the coherent collapse field, and that these collapse mechanisms may take considerable time to complete. Comparison of the experimental data with known parameters for seven calderas suggested

that four had collapsed as coherent pistons, with the other collapses being non-coherent.

Experiments have helped to constrain possible volumes of caldera forming eruptions from pre-caldera conditions [44], showing a potentially powerful route of predicting the time and size of caldera-forming eruptions. Experiments were carried out using a bed of quartz sand as a rock analogue and a deflating water-filled latex balloon to represent the magma body. Extensive arguments are presented to justify application of the experimental results at volcanic scales. Coherent piston collapse was observed at low roof aspect ratios (roof thickness/diameter), becoming more non-coherent as aspect ratio increased. These experiments showed different fault structures and demonstrated the complex 3D nature of the faults that result from caldera collapse (Fig. 33). Fault development was monitored as the balloon was drained to establish the sequence of events prior to, and during, caldera collapse. The relationship between the proportion of water drained from the balloon to make collapse inevitable (f_{crit}) and the aspect ratio of the roof (r) is empirically given as $f_{crit} = 22.4 \ln(r) + 43.5$ (Fig. 33). Data from caldera-forming eruptions were compared to the experimental trend and found to be in reasonable agreement. This suggests that the small-scale experiments mimic the first-order behavior of much larger-scale caldera collapse, but that there are issues of field measurement and second order process that require further investigation. Nevertheless, this work demonstrates the potential of be-



Volcanic Eruptions, Explosive: Experimental Insights, Figure 32

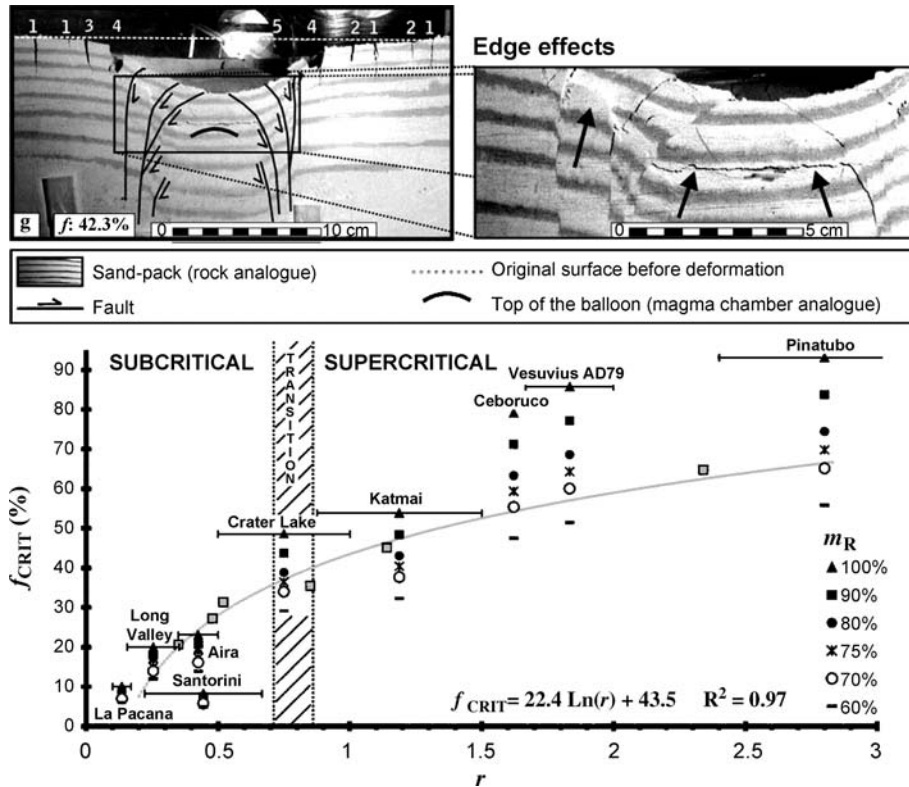
Large VEI eruptions may develop into caldera collapse as the country rock overlying the magma body subsides with pressure drop in the magma. Roche and Druitt [103] experimentally verified a model of coherent, piston-like formation of a caldera (upper left panel). Different modes of collapse were also found experimentally, some of which required significant time to elapse (upper right panel). This suggests that the roof of a deep, narrow magma body may not collapse simultaneously with eruption, but some time afterwards. Comparison of experimentally verified theory and estimates for proportion of magma erupted (f) and roof aspect ratio (R) in natural caldera collapses (bottom panel) indicate that coherent collapse does occur. Reprinted with kind permission from Elsevier

ing able to predict the onset and volume of caldera collapse from combining field observation and laboratory experiment.

Future Directions

Experiments investigating processes that could occur both during, and as a consequence of, explosive volcanic eruptions

are many and varied. All the experiments provide insight into volcanic processes because they are all analogous in certain aspects, whether in size in the case of experiments with natural materials, or with analogue materials as well. Curiosity into the fluid dynamics of degassing and expanding multi-phase flows with non-Newtonian and viscoelastic materials will continue to expand knowledge over a wide parameter range of which volcanic processes



Volcanic Eruptions, Explosive: Experimental Insights, Figure 33

Geyer et al. [44] experimentally ascertained (top panel) the critical proportion of a magma chamber that must be erupted for caldera collapse to occur (f_{CRIT}). This was related to the aspect ratio of the roof (r) by an empirical equation. Experimental data (gray squares) were compared with values estimated for caldera-forming eruptions (bottom panel) for both subcritical (coherent or piston) collapse and supercritical (non-coherent) collapse. The estimated f_{CRIT} values are a function of the percentage of magma actually removable (m_R). This work raises the possibility of being able to forecast the timing and volume of caldera collapse on the basis of previous eruption history and estimates of chamber depth and volume. Reprinted with kind permission from Elsevier

form a small but motivating part. Experiments will form a key part of such research and will continue to inspire numerical models that can provide a data density unavailable experimentally. One future direction could be the development of experiments that use much greater volumes of fluid and run for longer time periods. This would be especially attractive using natural materials, but the apparatus and instrumentation challenge is considerable.

The richness of phenomena that emerge from this complex system suggests that volcanoes are individuals in their eruptive behavior, an observation common to field measurement of volcanoes. Eruption models will increasingly be tested by their ability to account for observed eruption phenomena, and linking of detailed field measurement, volcano-specific experimentation and a unified modeling approach is one of the major current drivers of experimental volcanism. Highly instrumented volcanoes

where measurement, in time and space, of such parameters as wide-spectrum ground and atmosphere motion, thermal outputs, chemistry and physics of magma components, electrical effects, flow rates and flow features are required to drive the understanding and forecasting of volcanic events; a task that, in general, becomes more challenging as VEI increases.

The role of experimental models is in providing a real system that can be repeated and measured in some detail. Computer modeling, verified by many experiments, may then be applied at volcanic scale. Quantitative comparison to field observation then tests the model system. Such combined tactics are likely to play a major role in the advancement of volcanology, and it is possible to envisage near real-time interpretation of field measurement in terms of fluid-dynamic, elasto-dynamic, atmospheric and chemical models built on the results of field, numerical

and experimental volcanism. Such an autonomous system would be a major tool in quantifying fluid behavior in volcanic conduits and provide rapid assessment of changes taking place.

Acknowledgments

We thank Bernard Chouet for a highly constructive review of this chapter, William H. K. Lee for editing this section and the staff at Springer including Julia Koerting and Kerstin Kindler.

Bibliography

Primary Literature

- Alidibirov M, Dingwell DB (1996) Magma fragmentation by rapid decompression. *Nature* 380:146–149
- Alidibirov M, Dingwell DB (1996) An experimental facility for the investigation of magma fragmentation by rapid decompression. *Bull Volcanol* 58:411–416
- Alidibirov M, Dingwell DB (2000) Three fragmentation mechanisms for highly viscous magma under rapid decompression. *J Volcanol Geotherm Res* 100:413–421
- Alidibirov M, Panov V (1998) Magma fragmentation dynamics: experiments with analogue porous low-strength material. *Bull Volcanol* 59(7):481–489
- Alidibirov M, Dingwell DB, Stevenson RJ, Hess K-U, Webb SL, Zinke J (1997) Physical properties of the 1980 Mount St. Helens cryptodome magma. *Bull Volcanol* 59:103–111
- Anilkumar AV, Sparks RSJ, Sturtevant B (1993) Geological implications and applications of high-velocity two-phase flow experiments. *J Volcanol Geotherm Res* 56(1–2):145–160
- Auger E, D'Auria L, Martini M, Chouet B, Dawson P (2006) Real-time monitoring and massive inversion of source parameters of very long period seismic signals: an application to Stromboli Volcano, Italy. *Geophys Res Lett* 33(4):L04301
- Bagdassarov NS, Dingwell DB (1992) A rheological investigation of vesicular rhyolite. *J Volcanol Geophys Res* 50:307–322
- Bagdassarov NS, Dingwell DB (1993) Frequency dependent rheology of vesicular rhyolite. *J Geophys Res* 98:6477–6487
- Bagdassarov N, Pinkerton H (2004) Transient phenomena in vesicular lava flows based on laboratory experiments with analogue materials. *J Volcanol Geotherm Res* 132:115–136
- Barenblatt GI (2003) *Scaling*. Cambridge University Press, Cambridge. ISBN 0-521-53394-5
- Behrens H, Gaillard F (2006) Geochemical aspects of melts: volatiles and redox behavior. *Elements* 2(5):275–280. ISSN 1811-5209
- Berthoud G (2000) Vapor explosions. *Ann Rev Fluid Mech* 32:573–611
- Birch F, Dane EB (1942) Viscosity. In: Birch F, Schairer JF, Spicer HC (eds) *Handbook of physical constants*, vol 97. Geological Society of America Special Paper, vol 36, pp 97–173
- Blackburn EA, Wilson L, Sparks RSJ (1976) Mechanisms and dynamics of Strombolian activity. *J Geol Soc Lond* 132:429–440
- Blower JD (2001) Factors controlling permeability-porosity relationships in magma. *Bull Volcanol* 63:497–504
- Blower JD, Keating JP, Mader HM, Phillips JC (2001) Inferring volcanic degassing processes from vesicle size distributions. *Geophys Res Lett* 28(2):347–350
- Bottinga Y, Weill DF (1972) The viscosity of magmatic silicate liquids: a model for calculation. *Am J Sci* 272:438–475
- Burgisser A, Gardner JE (2005) Experimental constraints on degassing and permeability in volcanic conduit flow. *Bull Volcanol* 67:42–56
- Burgisser A, Bergantz GW, Breidenthal RE (2005) Addressing complexity in laboratory experiments: the scaling of dilute multiphase flows in magmatic systems. *J Volcanol Geotherm Res* 141:245–265
- Burton M, Allard P, Muré F, La Spina A (2007) Magmatic gas composition reveals the source depth of slug-driven Strombolian explosive activity. *Science* 317:227–230
- Büttner R, Dellino P, Zimanowski B (1999) Identifying magma-water interaction from the surface features of ash particles. *Nature* 401(6754):688–690
- Büttner R, Roder H, Zimanowski B (1997) Electrical effects generated by experimental volcanic explosions. *Appl Phys Lett* 70(14):1903–1905
- Büttner R, Zimanowski B, Roder H (2000) Short-time electrical effects during volcanic eruption: Experiments and field measurements. *J Geophys Res* 105(B2):2819–2827
- Cagnoli B, Barmin A, Melnik O, Sparks RSJ (2002) Depressurization of fine powders in a shock tube and dynamics of fragmented magma in volcanic conduits. *Earth Planet Sci Lett* 204(1–2):101–113
- Cambridge Polymer Group (2002) The Cambridge Polymer Group Silly Putty™ “Egg”. <http://www.campoly.com/documents/appnotes/sillyputty.pdf>, accessed 10/10/08
- Carey SN, Sigurdsson H (1982) Influence of particle aggregation on deposition of distal tephra from the May 18, 1980, eruption of Mount St-Helens volcano. *J Geophys Res* 87(NB8):7061–7072
- Carroll MR, Holloway JR (eds) (1994) *Volatiles in magmas*. Rev Miner 30:517. ISBN 0-939950-36-7
- Chojnicki K, Clarke AB, Phillips JC (2006) A shock-tube investigation of the dynamics of gas-particle mixtures: Implications for explosive volcanic eruptions. *Geophys Res Lett* 33:L15309. doi:10.1029/2006GL026414
- Chouet BA, Hamisevicz B, McGetchin TR (1974) Photoballistics of volcanic jet activity at Stromboli, Italy. *J Geophys Res* 79:4961–4976
- Chouet B, Dawson P, Ohminato T, Martini M, Saccorotti G, Giudicepietro F, De Luca G, Milana G, Scarpa R (2003) Source mechanisms of explosions at Stromboli Volcano, Italy, determined from moment-tensor inversions of very-long-period data. *J Geophys Res* 108(B1):2019. doi:10.1029/2002JB001919
- Chouet B, Dawson P, Nakano M (2006) Dynamics of diffusive bubble growth and pressure recovery in a bubbly rhyolitic melt embedded in an elastic solid. *J Geophys Res* 111: B07310
- Chouet B, Dawson P, Martini M (2008) Shallow-conduit dynamics at Stromboli Volcano, Italy, imaged from waveform inversions. In: Lane SJ, Gilbert JS (eds) *Fluid motion in volcanic conduits: a source of seismic and acoustic signals*. Geological

- Society, London. Special Publication 307:57–84, doi:10.1144/SP307.5
34. Clift R, Grace JR, Weber ME (1978) Bubbles, drops and particles. Academic Press, London, p 380. ISBN 012176950X
 35. Costa A (2006) Permeability-porosity relationship: a reexamination of the Kozeny–Carman equation based on a fractal pore-space geometry assumption. *Geophys Res Lett* 33:L02318
 36. Dellino P, Zimanowski B, Büttner R, La Volpe L, Mele D, Sulpizio R (2007) Large-scale experiments on the mechanics of pyroclastic flows: design, engineering, and first results. *J Geophys Res* 112:B04202
 37. Dickinson JT, Langford SC, Jensen LC, McVay GL, Kelso JF, Pantano CG (1988) Fractoemission from fused-silica and sodium-silicate glasses. *J Vac Sci Technol A* 6(3): 1084–1089
 38. Dingwell DB (1996) Volcanic dilemma: flow or blow? *Science* 273(5278):1054–1055
 39. Dingwell DB, Webb SL (1989) Structural relaxation in silicate melts and non-Newtonian melt rheology in geologic processes. *Phys Chem Miner* 16:508–516
 40. Donaldson EE, Dickinson JT, Bhattacharya SK (1988) Production and properties of ejecta released by fracture of materials. *J Adhes* 25(4):281–302
 41. Druitt TH, Avaré G, Bruni G, Lettieri P, Maez F (2007) Gas retention in fine-grained pyroclastic flow materials at high temperatures. *Bull Volcanol* 69(8):881–901
 42. Eichelberger JC, Carrigan CR, Westrich HR, Price RH (1986) Non-explosive silicic volcanism. *Nature* 323:598–602
 43. Gardner JE (2007) Heterogeneous bubble nucleation in highly viscous silicate melts during instantaneous decompression from high pressure. *Chem Geol* 236:1–12
 44. Geyer A, Folch A, Marti J (2006) Relationship between caldera collapse and magma chamber withdrawal: an experimental approach. *J Volcanol Geotherm Res* 157(4):375–386
 45. Gilbert JS, Lane SJ (1994) The origin of accretionary lapilli. *Bull Volcanol* 56(5):398–411
 46. Gladstone C, Ritchie LJ, Sparks RSJ, Woods AW (2004) An experimental investigation of density-stratified inertial gravity currents. *Sedimentology* 51(4):767–789
 47. Gonnermann HM, Manga M (2003) Explosive volcanism may not be the inevitable consequence of magma fragmentation. *Nature* 424:432–435
 48. Grunewald U, Zimanowski B, Büttner R, Phillips LF, Heide K, Büchel G (2007) MFCL experiments on the influence of NaCl-saturated water on phreatomagmatic explosions. *J Volcanol Geotherm Res* 159:126–137
 49. Hess K-U, Dingwell DB (1996) Viscosities of hydrous leucogranitic melts: a non-Arrhenian model. *Am Miner* 81:1297–1300
 50. Hill LG, Sturtevant B (1990) An experimental study of evaporation waves in a superheated liquid. In: Meier GEA, Thompson PA (eds) *Adiabatic waves in liquid-vapor systems*. IUTAM Symposium Göttingen, Germany. Springer, Berlin, pp 25–37. ISBN 3-540-50203-3
 51. Hoover SR, Cashman KV, Manga M (2001) The yield strength of subliquidus basalts – experimental results. *J Volcanol Geotherm Res* 107(1–3):1–18
 52. Hurwitz S, Navon O (1994) Bubble nucleation in rhyolitic melts: experiments at high pressure, temperature, and water content. *Earth Planet Sci Lett* 122(3–4):267–280
 53. Ichihara M, Rittel D, Sturtevant B (2002) Fragmentation of a porous viscoelastic material: implications to magma fragmentation. *J Geophys Res* 107(B10):2229. doi:10.1029/2001JB000591
 54. Ida Y (2007) Driving force of lateral permeable gas flow in magma and the criterion of explosive and effusive eruptions. *J Volcanol Geotherm Res* 162(3–4):172–184
 55. Ishibashi H, Sato H (2007) Viscosity measurements of subliquidus magmas: alkali olivine basalt from the Higashi-Matsuura district, Southwest Japan. *J Volcanol Geotherm Res* 160(3–4):223–238
 56. James MR, Lane SJ, Gilbert JS (2000) Volcanic plume electrification: experimental investigation of a fracture-charging mechanism. *J Geophys Res* 105(B7):16641–16649
 57. James MR, Gilbert JS, Lane SJ (2002) Experimental investigation of volcanic particle aggregation in the absence of a liquid phase. *J Geophys Res* 107(B9):2191
 58. James MR, Lane SJ, Gilbert JS (2003) Density, construction, and drag coefficient of electrostatic volcanic ash aggregates. *J Geophys Res* 108(B9):2435
 59. James MR, Lane SJ, Chouet B, Gilbert JS (2004) Pressure changes associated with the ascent and bursting of gas slugs in liquid-filled vertical and inclined conduits. *J Volcanol Geotherm Res* 129(1–3):61–82
 60. James MR, Lane SJ, Chouet BA (2006) Gas slug ascent through changes in conduit diameter: laboratory insights into a volcano-seismic source process in low-viscosity magmas. *J Geophys Res* 111:B05201. doi:10.1029/2005JB003718
 61. James MR, Lane SJ, Corder SB (2008) Modelling the rapid near-surface expansion of gas slugs in low-viscosity magmas. In: Lane SJ, Gilbert JS (eds) *Fluid motion in volcanic conduits: a source of seismic and acoustic signals*. Geological Society, London. Special Publication 307:147–167, doi:10.1144/SP307.9
 62. Jaupart C, Allegre CJ (1991) Gas content, eruption rate and instabilities of eruption regime in silicic volcanoes. *Earth Planet Sci Lett* 102:413–429
 63. Jaupart C, Vergnolle S (1988) Laboratory models of Hawaiian and Strombolian eruptions. *Nature* 331(6151):58–60
 64. Jaupart C, Vergnolle S (1989) The generation and collapse of a foam layer at the roof of a basaltic magma chamber. *J Fluid Mech* 203:347–380
 65. Kalinichev AG (2001) Molecular simulations of liquid and supercritical water: thermodynamics, structure, and hydrogen bonding. *Rev Miner Geochem* 42:83–129
 66. Kaminski E, Jaupart C (1998) The size distribution of pyroclasts and the fragmentation sequence in explosive volcanic eruptions. *J Geophys Res* 103(B12):29759–29779
 67. Klug C, Cashman KV (1996) Permeability development in vesiculating magmas: implications for fragmentation. *Bull Volcanol* 58:87–100
 68. Kouchi A, Tsuchiyama A, Sunagawa I (1986) Effect of stirring on crystallisation kinetics of basalt: texture and element partitioning. *Contrib Miner Petrol* 93:429–438
 69. Kueppers U, Perugini D, Dingwell DB (2006) “Explosive energy” during volcanic eruptions from fractal analysis of pyroclasts. *Earth Planet Sci Lett* 248(3–4):800–807
 70. Lane SJ, Chouet BA, Phillips JC, Dawson P, Ryan GA, Hurst E (2001) Experimental observations of pressure oscillations and flow regimes in an analogue volcanic system. *J Geophys Res* 106(B4):6461–6476

71. Lane SJ, Phillips JC, Ryan GA (2008) Dome-building eruptions: insights from analogue experiments. In: Lane SJ, Gilbert JS (eds) *Fluid motion in volcanic conduits: a source of seismic and acoustic signals*. Geological Society, London
72. Lautze NC, Houghton BF (2007) Linking variable explosion style and magma textures during 2002 at Stromboli volcano, Italy. *Bull Volcanol* 69(4):445–460
73. Liu Y, Zhang Y, Behrens H (2005) Solubility of H₂O in rhyolitic melts at low pressures and a new empirical model for mixed H₂O–CO₂ solubility in rhyolitic melts. *J Volcanol Geotherm Res* 143:219–235
74. Llewellyn EW, Manga M (2005) Bubble suspension rheology and implications for conduit flow. *J Volcanol Geotherm Res* 143:205–217
75. Llewellyn EW, Mader HM, Wilson SDR (2002) The rheology of a bubbly liquid. *Proc R Soc Lond A* 458:987–1016
76. Lyakhovsky V, Hurwitz S, Navon O (1996) Bubble growth in rhyolitic melts: experimental and numerical investigation. *Bull Volcanol* 58:19–32
77. Mader HM (1998) Conduit flow and fragmentation. *Geol Soc London* 145:51–71
78. Mader HM, Zhang Y, Phillips JC, Sparks RSJ, Sturtevant B, Stolper E (1994) Experimental simulations of explosive degassing of magma. *Nature* 372(6501):85–88
79. Mader HM, Phillips JC, Sparks RSJ, Sturtevant B (1996) Dynamics of explosive degassing of magma: Observations of fragmenting two-phase flows. *J Geophys Res Solid Earth* 101(B3):5547–5560
80. Mader HM, Brodsky EE, Howard D, Sturtevant B (1997) Laboratory simulations of sustained volcanic eruptions. *Nature* 388(6641):462–464
81. Marshall JR, Sauke TB, Cuzzi JN (2005) Microgravity studies of aggregation in particulate clouds. *Geophys Res Lett* 32(11):L11202
82. Martel C, Dingwell DB, Spieler O, Pichavant M, Wilke M (2000) Fragmentation of foamed silicic melts: an experimental study. *Earth Planet Sci Lett* 178:47–58
83. Martel C, Dingwell DB, Spieler O, Pichavant M, Wilke M (2001) Experimental fragmentation of crystal- and vesicle-bearing silicic melts. *Bull Volcanol* 63:398–405
84. Mason RM, Starostin AB, Melnik OE, Sparks RSJ (2006) From Vulcanian explosions to sustained explosive eruptions: the role of diffusive mass transfer in conduit flow dynamics. *J Volcanol Geotherm Res* 153(1–2):148–165
85. McGetchin TR, Settle M, Chouet B (1974) Cinder cone growth modeled after Northeast Crater, Mount Etna, Sicily. *J Geophys Res* 79:3257–3272
86. McMillan PF (1994) Water solubility and speciation models. In: Carroll MR, Holloway JR (eds) *Volatiles in magmas*.
87. Melnik O, Sparks RSJ (2002) Dynamics of magma ascent and lava extrusion at Soufrière Hills Volcano, Montserrat. In: Druitt T, Kokelaar P (eds) *The eruption of Soufrière Hills Volcano, Montserrat, from 1995 to 1999*. Geological Society, London, pp 153–171
88. Moore JG, Peck DL (1962) Accretionary lapilli in volcanic rocks of the western continental United-States. *J Geol* 70(2): 182–193
89. Mourtada-Bonnefoi CC, Mader HM (2001) On the development of highly-viscous skins of liquid around bubbles during magmatic degassing. *Geophys Res Lett* 28(8):1647–1650
90. Mourtada-Bonnefoi CC, Mader HM (2004) Experimental observations of the effects of crystals and pre-existing bubbles on the dynamics and fragmentation of vesiculating flows. *J Volcanol Geotherm Res* 129:83–97. doi:10.1016/S0377-0273(03)00233-6
91. Murase T (1962) Viscosity and related properties of volcanic rocks at 800° to 1400°C. *Hokkaido Univ Fac Sci Jour Ser VII* 1:487–584
92. Murase T, McBirney AR (1973) Properties of some common igneous rocks and their melts at high-temperatures. *Geol Soc Am Bull* 84(11):3563–3592
93. Namiki A, Manga M (2005) Response of a bubble bearing viscoelastic fluid to rapid decompression: implications for explosive volcanic eruptions. *Earth Planet Sci Lett* 236:269–284
94. Namiki A, Manga M (2006) Influence of decompression rate on the expansion velocity and expansion style of bubbly fluids. *J Geophys Res* 111:B11208
95. Newhall CG, Self S (1982) The explosivity index (VEI) – an estimate of explosive magnitude for historical volcanism. *J Geophys Res* 87(NC2):1231–1238
96. Parfitt EA (2004) A discussion of the mechanisms of explosive basaltic eruptions. *J Volcanol Geotherm Res* 134:77–107
97. Phillips JC, Lane SJ, Lejeune A-M, Hilton M (1995) Gum rosin – acetone system as an analogue to the degassing behaviour of hydrated magmas. *Bull Volcanol* 57:263–268
98. Pinkerton H, Norton G (1995) Rheological properties of basaltic lavas at sub-liquidus temperatures – laboratory and field-measurements on lavas from Mount Etna. *J Volcanol Geotherm Res* 68(4):307–323
99. Pyle DM (2000) Sizes of volcanic eruptions. In: Sigurdsson H, Houghton B, McNutt SR, Rymer H, Stix J (eds) *Encyclopaedia of volcanoes*. Academic Press, pp 263–269. ISBN 0-12-643140-X
100. Riedel C, Ernst GGJ, Riley M (2003) Controls on the growth and geometry of pyroclastic constructs. *J Volcanol Geotherm Res* 127(1–2):121–152
101. Riley CM, Rose WI, Bluth GJS (2003) Quantitative shape measurements of distal volcanic ash. *J Geophys Res Solid Earth* 108(B10):2504
102. Ripepe M, Ciliberto S, Della Schiava M (2001) Time constraints for modeling source dynamics of volcanic explosions at Stromboli. *J Geophys Res Solid Earth* 106(B5):8713–8727
103. Roche O, Druitt TH (2001) Onset of caldera collapse during ignimbrite eruptions. *Earth Planet Sci Lett* 191(3–4):191–202
104. Saar MO, Manga M (1999) Permeability-porosity relationship in vesicular basalts. *Geophys Res Lett* 26:111–114
105. Schumacher R, Schmincke HU (1995) Models for the origin of accretionary lapilli. *Bull Volcanol* 56(8):626–639
106. Seyfried R, Freundt A (2000) Experiments on conduit flow and eruption behavior of basaltic volcanic eruptions. *J Geophys Res Solid Earth* 105:23727–23740
107. Shaw HR (1972) Viscosities of magmatic silicate liquids: an empirical method of prediction. *Am Jour Sci* 272:870–893
108. Sparks RSJ (1997) Causes and consequences of pressurisation in lava dome eruptions. *Earth Planet Sci Lett* 150:177–189
109. Sparks RSJ, Bursik MI, Carey SN, Gilbert JS, Glaze LS, Sigurdsson H, Woods AW (1997) *Volcanic plumes*. Wiley, Chichester. ISBN 0-471-93901-3
110. Spera FJ, Borgia A, Strimple J, Feigenson M (1988) Rheology of melts and magmatic suspensions I. Design and calibration of a concentric cylinder viscometer with application to rhyolitic magma. *J Geophys Res* 93:10273–10294

111. Spieler O, Alidibirov M, Dingwell DB (2003) Grain-size characteristics of experimental pyroclasts of 1980 Mount St. Helens cryptodome dacite: effects of pressure drop and temperature. *Bull Volcanol* 65:90–104
112. Spieler O, Kennedy B, Kueppers U, Dingwell DB, Scheu B, Taddeucci J (2004) The fragmentation threshold of pyroclastic rocks. *Earth Planet Sci Lett* 226:139–148
113. Sugioka I, Bursik M (1995) Explosive fragmentation of erupting magma. *Nature* 373(6516):689–692
114. Suzuki T (1983) A theoretical model for dispersion of tephra. In: Shimozuru D, Yokoyama I (eds) *Arc volcanism, physics and tectonics*. Terra Scientific publishing company Terrapub, Tokyo, pp 95–113
115. Taddeucci J, Spieler O, Kennedy B, Pompilio M, Dingwell DB, Scarlato P (2004) Experimental and analytical modeling of basaltic ash explosions at Mount Etna, Italy, 2001. *J Geophys Res* 109:B08203. doi:10.1029/2003JB002952
116. Taddeucci J, Spieler O, Ichihara M, Dingwell DB, Scarlato P (2006) Flow and fracturing of viscoelastic media under diffusion-driven bubble growth: an analogue experiment for eruptive volcanic conduits. *Earth Planet Sci Lett* 243:771–785
117. Taddeucci J, Scarlato P, Andronico D, Cristaldi A, Büttner R, Zimanowski B, Küppers U (2007) Advances in the study of volcanic ash. *Eos Trans AGU* 88(24):253
118. Takeuchi S, Nakashima S, Tomiya A (2008) Permeability measurements of natural and experimental volcanic materials with a simple permeameter: Toward an understanding of magmatic degassing process. *J Volcanol Geotherm Res* doi:10.1016/j.jvolgeores.2008.05.010
119. Takeuchi S, Nakashima S, Tomiya A, Shinohara H (2005) Experimental constraints on the low gas permeability of vesicular magma during decompression. *Geophys Res Lett* 32: L10312
120. Textor C, Graf HF, Longo A, Neri A, Ongaro TE, Papale P, Timmerck C, Ernst GG (2005) Numerical simulation of explosive volcanic eruptions from the conduit flow to global atmospheric scales. *Ann Geophys* 48(4–5):817–842
121. Trigila R, Battaglia M, Manga M (2007) An experimental facility for investigating hydromagmatic eruptions at high-pressure and high-temperature with application to the importance of magma porosity for magma-water interaction. *Bull Volcano* 69:365–372
122. Tuffen H, Dingwell D (2005) Fault textures in volcanic conduits: evidence for seismic trigger mechanisms during silicic eruptions. *Bull Volcanol* 67:370–387
123. Walker GPL, Wilson L, Howell ELG (1971) Explosive volcanic eruptions. 1. Rate of fall of pyroclasts. *Geophys J Royal Astron Soc* 22(4):377–383
124. Watson EB (1994) Diffusion in volatile-bearing magmas. In: Carroll MR, Holloway JR (eds) *Volatiles in magmas*.
125. Wilson L, Huang TC (1979) Influence of shape on the atmospheric settling velocity of volcanic ash particles. *Earth Planet Sci Lett* 44(2):311–324
126. Wohletz KH (1983) Mechanisms of hydrovolcanic pyroclast formation: grain-size, scanning electron microscopy, and experimental studies. *J Volcanol Geotherm Res* 17(1–4): 31–63
127. Woolley AR, Church AA (2005) Extrusive carbonatites: a brief review. *Lithos* 85(1–4):1–14
128. Yokoyama I (2005) Growth rates of lava domes with respect to viscosity of magmas. *Ann Geophys* 48(6):957–971
129. Zhang YX (1998) Experimental simulations of gas-driven eruptions: kinetics of bubble growth and effect of geometry. *Bull Volcanol* 59(4):281–290
130. Zhang Y (1999) A criterion for the fragmentation of bubbly magma based on brittle failure theory. *Nature* 402:648–650
131. Zhang Y, Behrens H (2000) H₂O diffusion in rhyolitic melts and glasses. *Chem Geol* 169:243–26
132. Zhang YX, Sturtevant B, Stolper EM (1997) Dynamics of gas-driven eruptions: experimental simulations using CO₂-H₂O-polymer system. *J Geophys Res Solid Earth* 102(B2): 3077–3096
133. Zhang Y, Xu Z, Liu Y (2003) Viscosity of hydrous rhyolitic melts inferred from kinetic experiments: a new viscosity model. *Am Miner* 88:1741–1752
134. Zimanowski B, Lorenz V, Frohlich G (1986) Experiments on phreatomagmatic explosions with silicate and carbonatitic melts. *J Volcanol Geotherm Res* 30(1–2):149–153
135. Zimanowski B, Büttner R, Lorenz V, Häfele H-G (1997) Fragmentation of basaltic melt in the course of explosive volcanism. *J Geophys Res* 102(B1):803–814

Books and Reviews

- Barnes HA (1997) Thixotropy – a review. *J Non-Newtonian Fluid Mech* 70:1–33
- Barnes HA (1999) The yield strength – a review or ‘πανταρει’ everything flows? *J Non-Newtonian Fluid Mech* 81:133–178
- Chhabra RP (2006) Bubbles, drops, and particles in non-Newtonian fluids. CRC Press, London, p 771. ISBN 0824723295
- Chouet B (2003) Volcano seismology. *Pure and Applied Geophysics* 160:739–788
- De Kee D, Chhabra RP (2002) Transport processes in bubbles, drops, and particles. Taylor and Francis, p 352. ISBN 1560329068
- Fan L-S, Zhu C (1998) Principles of gas-solid flows. Cambridge University Press, Cambridge, p 575. ISBN 0521581486
- Gilbert JS, Sparks RSJ (1998) The physics of explosive volcanic eruptions. The Geological Society, London. ISBN 1-86239-020-7
- Gonnermann HM, Manga M (2007) The fluid mechanics inside a volcano. *Ann Rev Fluid Mech* 39:321–356
- Henderson G, Calas G, Stebbins J (eds) (2006) Glasses and melts: linking geochemistry and materials science. *Elements* 2(5):257–320. ISSN 1811–5209
- Kaminski E, Tait S, Carazzo G (2005) Turbulent entrainment in jets with arbitrary buoyancy. *J Fluid Mech* 526:361–376
- Mather TA, Harrison RG (2006) Electrification of volcanic plumes surveys. *Geophysics* 77(4):387–432
- Moretti R, Richet P, Stebbins JF (2006) Physics, chemistry and rheology of silicate melts and glasses. *Chem Geol* 229(1–3): 1–226
- Parfitt L, Wilson L (2008) Fundamentals of physical volcanology. Blackwell, p 256. ISBN 0632054433
- Sigurdsson H, Houghton B, McNutt SR, Rymer H, Stix J (eds) (2000) *Encyclopaedia of volcanoes*. Academic Press. ISBN 0-12-643140-X
- Tong L-S, Tang YS (1997) Boiling heat transfer and two-phase flow. Taylor and Francis, p 542. ISBN 1560324856
- Webb S (1997) Silicate melts: relaxation, rheology, and the glass transition. *Rev Geophys* 35(2):191–218
- Wood CA (1980) Morphometric evolution of cinder cones. *J Volcanol Geotherm Res* 7:387–413

Volcanic Eruptions: Stochastic Models of Occurrence Patterns

MARK S. BEBBINGTON

Massey University, Palmerston North, New Zealand

Article Outline

Glossary
 Definition of the Subject
 Introduction
 Data
 Temporal Models
 Volcanic Regimes
 Spatial Aspects
 Yucca Mountain
 Interactions with Earthquakes
 Future Directions
 Bibliography

Glossary

Onset The beginning of an eruption. The term **event** will be used interchangeably.

Repose Periods during which an eruption is not in progress.

Onset time Time at which an eruption begins. The i th onset time will be denoted t_i , for $i = 1, \dots, n$.

Inter-onset time Time between successive onsets, denoted by $r_i = t_{i+1} - t_i$, for $i = 1, \dots, n - 1$. In many papers this is termed the **repose time**, which we shall use interchangeably, although the latter is strictly the time between the *end* of one eruption and the *start* of the next.

Polygenetic vent Site of multiple events, in contrast to **monogenetic vents**, at which only one eruption occurs. The latter occur predominately in **volcanic fields**.

Absolute time is denoted by t or s , with the latter usually being the time of the last known event. The **elapsed time** since the last known event is denoted by u , or, equivalently, $t - s$.

A parameter estimate of the parameter λ , say, is denoted by $\hat{\lambda}$.

Definition of the Subject

Depending on the definition, there are approximately 1300 Holocene (last 10,000 years) active volcanoes [83], some 55–70 of which are typically active in any given year. Being tectonic phenomena, they are spatially over-represented along littorals and in island arcs where populations congregate, and millions of lives are potentially at risk. Hence

the quantitative forecasting of hazard has long been a key aim of volcanology. This requires models to quantify the likelihood of future outcomes, which may involve the size, location and/or style of eruption, in addition to temporal occurrence. While a wide range of complex deterministic models exist to model various volcanic processes, these provide little in the way of information about future activity. Being the (partially) observed realization of a complex system, volcanological data are inherently stochastic in nature, and need to be modeled using statistical models. To paraphrase Decker [25] concerning potentially active volcanoes, geologists can find out what did happen, geophysicists can determine what is happening, but to find out what might happen requires statistics. Reminding ourselves that “all models are wrong, but some models are useful”, the most useful models for volcanic eruptions are ones that provide new insight into the physical processes, and can in turn be informed by our present understanding of those physical processes.

Introduction

The hazard is a product of many elements, including the likelihood of an eruption, the distribution of the eruption size, and the style of the eruption. Depending on the nature of the volcanic products, climatological or geographical factors may also play a part.

The style of an eruption strongly determines the relative risks to life and property. Effusive eruptions of molten lava pose little threat to life with, for example, only one life being lost due to a volcanic eruption on Hawaii in the 20th century. However, in the same time period 5% of the island has been covered by new lava flows [25]. Explosive eruptions, in particular pyroclastic flows, travel at high speeds and can cause extensive fatalities such as the 29,000 killed in the Mont Pelee (West Indies) eruption of 1902. Lahars, or mudflows, such as those that killed 25,000 people in the Nevado del Ruiz (Columbia) eruption of 1985, are also a major danger.

Forecasting volcanic eruptions is easier than forecasting earthquakes on several grounds. First, at least in the case of polygenetic volcanoes, there need be no spatial element involved. Second, it is possible using geological techniques to look backward (often a long way, depending on geography and finances) to see what happened in the past. Thirdly, and of most importance for short-term warning, magma intrusions can be detected by seismic networks, although not all seismic signals indicate magma of course, and other monitoring techniques [25].

In this article we will limit our consideration to models of eruption occurrence, omitting techniques for fore-

casting the nature and effect of the eruption. As the track record of a potentially active volcano provides the best method of assessing its future volcanic hazards on a long-term basis [21,25], we will first briefly review the provenance and characteristics of the data available. Various taxonomies for stochastic models are possible. As the majority of models applied to volcanoes are purely temporal, and this also includes the simplest models, we will look at these first. Such models can be further broken down into (nonhomogeneous) Poisson processes, which consider absolute time relative to some fixed origin, and renewal processes, which consider only the time since the previous event. Markov processes, where the state of the process moves between various eruptive and repose states, and models based on eruptive volume, are the simplest ways of incorporating some element of eruption size into the model. Fractals have been used as a descriptive technique for volcanoes, and are reviewed next. The above models, with the exception of the nonhomogeneous Poisson process, all assume that the volcano is in steady state, i. e., that the activity pattern does not change over time. For volcanoes with lengthy records, this appears to be an untenable assumption over longer time scales [99]. This raises the issues of, first, how to detect a departure from stationary stochastic behavior, or change in volcanic regime and, secondly, how to model it, which are discussed in Sect. “[Volcanic Regimes](#)”, illustrated with results from Mount Etna. While purely temporal models are suitable for polygenetic volcanoes, monogenetic volcanic fields require a spatial element, to model the location, as well as the time, of future events. This is usually estimated using kernel smoothing, but in cases where the location can be treated as a discrete variable, such as summit versus flank eruptions, Markov chain techniques can be used. These are reviewed, along with methods for detecting clustering and linear alignments, in Sect. “[Spatial Aspects](#)”. A very high profile, particularly in the USA, exercise in volcanic hazard estimation concerns the risk to a proposed high-level radioactive waste repository planned for Yucca Mountain. The history of published hazard estimates is used in Sect. “[Yucca Mountain](#)” to illustrate the application of both temporal and spatio-temporal models. The final substantive section looks at methods for detecting links between volcanic eruptions and large earthquakes. Determining whether correlation in the occurrence patterns exists is a necessary precursor to formulating models to take advantage of any potential new information from the additional process.

The focus of this article is squarely on the techniques. Hence the applications jump around a bit, as they are those presented in the original paper(s) dealing with the tech-

nique. The examples of Mount Etna and Yucca Mountain were selected for more detailed examination partly on the basis that many, somewhat contradictory, results exist. Different models make different assumptions, and vary in how much information they can extract from data. In addition, the data used often varies from study to study, and the sensitivity of models to data is important, but too often ignored. Subjective judgments on the merits of various techniques is minimized, except for comments on details necessary to their application.

Data

Information about past eruptions forms the basis of any stochastic model for future behavior. Using such data poses a number of challenges because of its inhomogeneity, particularly in the longer records. This inhomogeneity is due to incomplete observation, which becomes more incomplete the further back one goes, and by variations in dating and measurement precision, again becoming less precise the further into the past one looks. We will now outline the nature and limitations of the available information.

There are several functional distinctions in the types of data used in volcanic hazard models. The most fundamental is at the question of scale. Certain volcanoes, notably Stromboli (which lends its name to the behavior) and Soufriere Hills, erupt in distinct events separated by minutes or hours. Hence a catalog of hundreds of events may only cover a few days of activity. More commonly, eruptions are events with durations ranging from days to years. Eruptions are usually modeled simply as a point process of onsets, but a few studies consider duration, volume, or spatial extent.

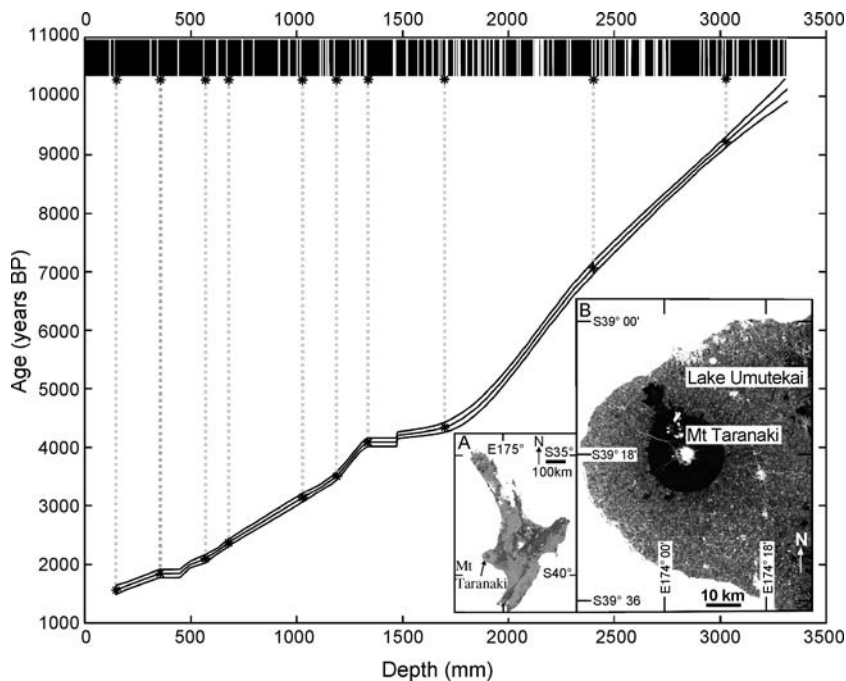
A global catalog of Holocene volcanism is maintained by Seibert and Simkin [82]. This gives onset dates, of various precision, and Volcanic Explosivity Index (VEI) for all known eruptions. The VEI, as a logarithmic measuring scale of eruption size analogous to the magnitude of an earthquake, was proposed by Newhall and Self [68]. It is assigned to historical eruptions on the basis of (in decreasing order of reliability): explosion size; volume of ejecta; column height, classification (‘Hawaiian’, ‘Strombolian’, ‘Vulcanian’, ‘(Ultra-)Plinian’); duration; most explosive activity type; tropospheric and stratospheric injection. Many historical (i. e., observed and recorded at the time) observations also have a duration, and some an estimate of eruptive volume. Estimates of volume, where they exist, typically contain uncertainties of 10–50% [101] or more [54] and, provided the eruption styles are similar, the duration of an eruption can be used as a proxy [3,67].

The frequency of observed volcanic eruptions has increased over the last few hundred years, although this is largely an artifact of the global population increase [84], which indicates that many of the historical records are incomplete. A number of published catalogs for individual volcanoes are of greater detail, and probably more complete. Some of the better known are Etna [65,67,74] and Vesuvius [11,77] (Italy), Ruapehu (New Zealand) [5], Colima (Mexico) [27,63] and Kilauea/Mauna Loa (Hawaii) [46].

While it is reasonably easy, although sometimes controversial, to define events in an historical catalog, it is not so easy in pre-historical cases. Ideally events correspond to eruptions, but subsequent geologic processes can obscure, or even obliterate, the evidence of previous eruptions. The identification of events is dependent on looking in the right place. Pre-historical eruptions can be identified from a combination of stratigraphy (which provides an ordering for the eruptions) and dating techniques. Radiocarbon dating is feasible for material within the last 50,000 years, and provides an estimated age and (Gaussian) error given in C^{14} years. See [28] for an example of such a catalog. Because of the variable rate of C^{14} deposition, this has to be converted to calendar years [8], in

the process losing the Gaussian distribution (and possibly even becoming disjoint). One way [94] of dealing with the resulting untidiness is to treat the data in Monte Carlo fashion, repeatedly drawing random realizations of the eruption sequence from the distributions (ensuring that the stratigraphic ordering is not violated), and fitting the model to each realization to provide a population of hazard models. Beyond 50,000 years, dating is via a number of other techniques, such as K-Ar radiometric age determinations which, with resolutions of the order of 10^6 – 10^7 years, are much less precise. Conway et al. [20] take the approach of simulating event dates from a uniform distribution, bounded by the $\pm 2\sigma$ error limits on the dates, in order to determine the uncertainty in the estimated recurrence rate.

Because of the expense, and due to the difficulty of finding suitable material in the sample to date, it is common to date only a portion of the samples. Geomorphology is then used to interpolate or bound the unknown dates. For example, in a single core, a spline can be fitted to the depth and known dates, representing the sediment deposition rate, and the unknown dates calculated from their depths [94], as shown in Fig. 1. This gets much more complicated when there is a spatial element involved [14].



Volcanic Eruptions: Stochastic Models of Occurrence Patterns, Figure 1

Radiocarbon age versus depth model (mm) for tephra layers in the sediment core from Lake Umutekai (*inset A*: North Island of New Zealand and *inset B*: Taranaki – the lake is directly above the “k-” in “Lake”). The core stratigraphy is displayed at the top of the plot with white representing tephra deposits. Radiocarbon dated layers are indicated by dotted lines

While deposition cores can provide a complete (above a certain minimum size), and ordered tephra record for a given site, the record extracted from another site may only partially overlap. Various criteria of tephra composition and geochemistry can be used to identify common events. Composite records from many sources will almost certainly be incomplete due to missing events, and may well unknowingly contain duplicates of other events.

Temporal Models

Models for the occurrence of volcanic eruptions are based on the idea that the past behavior of a volcano is the best predictor of its future activity. This was dramatically illustrated by Crandell et al. [21] in their somewhat non-quantitative forecast of an eruption of Mount St Helens:

“The repetitive nature of the eruptive activity at Mount St. Helens during the last 4000 years, with dormant intervals typically of a few centuries or less, suggests that the current quiet period will not last a thousand years. Instead, an eruption is likely within the next hundred years, possibly before the end of this century.”

Published in 1975, as a warning that dormant intervals can be a recurring element in the life of a volcano, this forecast shadowed the 1980 eruption and subsequent activity.

Let the number of events in a time interval (s, t) be denoted $N(s, t)$, where we use the shorthand $N(t)$ if $s = 0$.

The *intensity* of a process is

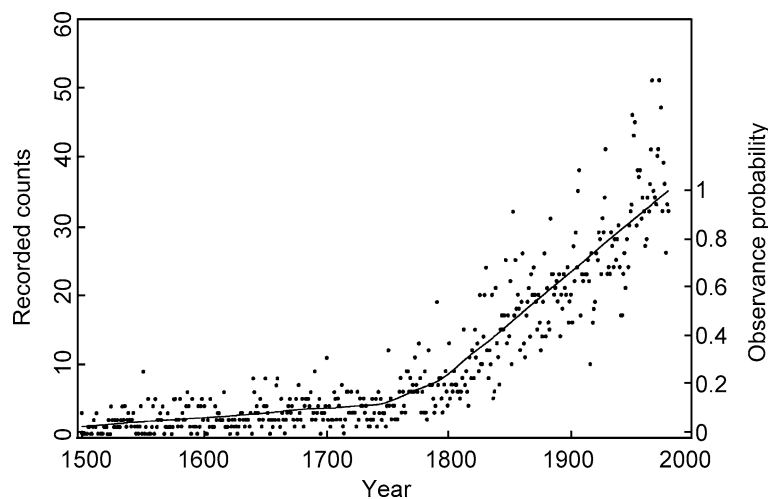
$$\lambda(t) = \lim_{\Delta t \downarrow 0} \frac{\Pr(N(t, t + \Delta t) = 1)}{\Delta t}, \quad (1)$$

i. e., in the short period of time $(t, t + \Delta t)$, the probability of an event is approximately $\lambda(t)\Delta t$.

Guttorp and Thompson [35] provided a non-parametric method of estimating the intensity, based on the observed onset counts Y_k in intervals of length Δ , indexed by $k = 1, \dots, K$. They first estimate the reporting probability $p(t)$ by smoothing the observed onset counts (see [86] for an alternative approach assuming a non-decreasing reporting probability), and calculate $Z_k = Y_k / \int_{(k-1)\Delta}^{k\Delta} p(t)dt$. This is a reconstruction of the underlying process obtained by re-inflating the observed counts by the corresponding observance probability. Assuming that the intensity is locally fairly smooth, an estimate, based on the hanning operation from time-series analysis, is

$$\hat{\lambda}(j\Delta) = \frac{\sum_{i=1}^{K-j-1} Z_i Z_{i+j-1} + 2 \sum_{i=1}^{K-j} Z_i Z_{i+j} + \sum_{i=1}^{K-j+1} Z_i Z_{i+j-1}}{4\Delta(K-j) \sum_{k=1}^K Z_k / K}. \quad (2)$$

Application to the global catalog, assuming a constant rate of underlying events, produced the estimated observance probability in Fig. 2 that increases slowly from 1500 until the second half of the 18th century, and then more sharply at a constant rate to an assumed probability $p(1980) = 1$.



Volcanic Eruptions: Stochastic Models of Occurrence Patterns, Figure 2

Recorded counts (left-hand scale) and estimated observance probability (right-hand scale) for yearly eruption starts in the Simkin catalog from A.D. 1500 on. Reprinted with permission from the *Journal of the American Statistical Association*. Copyright 1991 by the American Statistical Association

The resulting estimated intensity for global eruption starts did not differ from a Poisson (constant intensity) process. However, in order to see if more structure could be observed in a series of eruptions from a restricted area with homogeneous tectonic structure, the methodology was applied to a catalog of Icelandic eruptions. As expected, the estimated observance probability for the last 200 years was approximately constant, which resulted in a periodicity of about 40 years in the estimated intensity, as shown in Fig. 3.

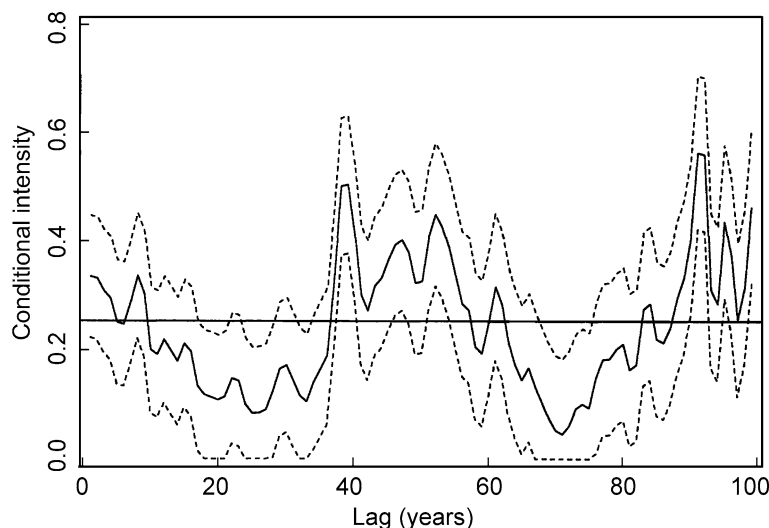
There have been a few other attempts to discern periodic fluctuations in volcanic activity. Mauk and Johnston [62] examined the correlation of the onset dates of 680 eruptions 1900–1971 with the fortnightly solid earth tide. There was a statistically significant tendency for both andesitic and basaltic eruptions to occur at the maxima of the earth tide. In addition, basaltic eruptions had a significant peak at the minima of the earth tide. A more detailed examination of 18 Japanese volcanoes indicated that this may be related to Bouguer anomalies. Similarly, Martin and Rose [54], in Fig. 4, found that eruption onsets of Fuego Volcano, Guatemala were correlated with the fortnightly lunar tidal maxima, with 23 out of 48 eruptions occurring within ± 2 days of the peak gravity acceleration. Casetti et al. [12] binned eruptions at Mt Etna and examined the resulting statistics, in particular the month of an eruption. Eruptions were shown to be significantly more likely during March–April and November, when

there is an increase in the earth-velocity rate. Although Stothers [89] repeated this analysis for a global catalog of eruptions with $\text{VEI} \geq 3$, 1500–1980, and detected no significant monthly or seasonal variation, Mason et al. [61] found that seasonal fluctuations account for 18% of the historical average monthly eruption rate. The idea of a deterministic cycle is incorporated in a renewal model by Jupp et al. [45], but the result was not fitted to data.

Poisson Processes

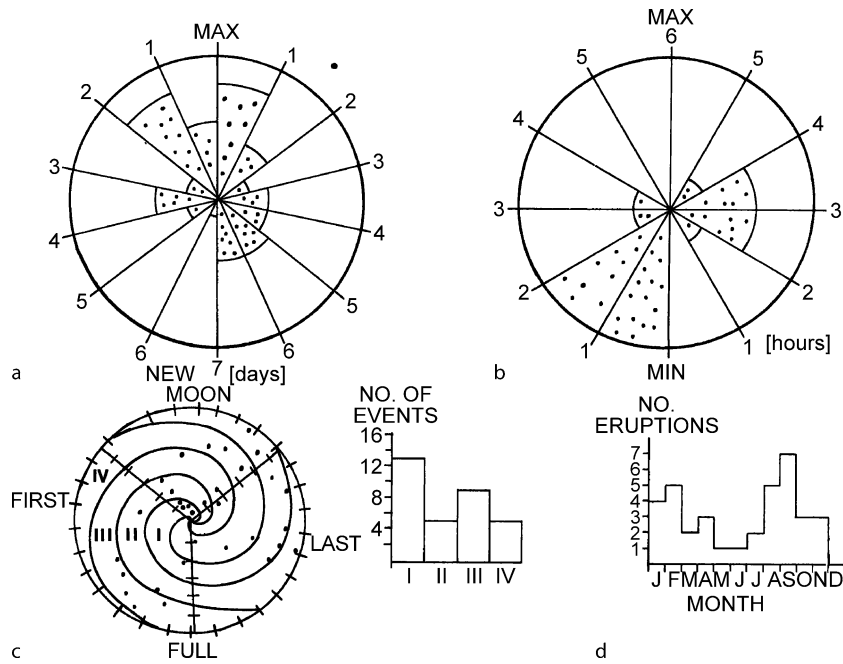
The simplest model is a *simple (homogeneous) Poisson process*, which is characterized by $\lambda(t) = \lambda_0$, a constant independent of t . In this case $N(t)$ has a Poisson distribution with mean $\mu = \lambda_0 t$, and the inter-event times have an exponential distribution with mean $1/\lambda_0$. This is sometimes referred to as *Poissonian behavior*. The parameter is estimated as $\hat{\lambda}_0 = N(T)/T$, for an observed history spanning the time interval $(0, T)$.

In order to weaken the requirement that the mean and variance of $N(t)$ be equal, Ho [36] suggested a Bayesian approach, in which the parameter λ_0 has a gamma prior distribution. This leads to $N(t)$ having a negative binomial distribution. Solow [87] augmented this to an empirical Bayes formulation by suggesting that an informative prior could be constructed from the eruption records of a group of similar volcanoes. Bebbington and Lai [6] introduced a generalized negative binomial distribution incorporating



Volcanic Eruptions: Stochastic Models of Occurrence Patterns, Figure 3

Estimated conditional intensity function for Icelandic eruption starts using data from the last 200 years. The dashed lines are approximate 95% pointwise confidence bands under the assumption of a homogeneous Poisson process. Reprinted with permission from the *Journal of the American Statistical Association*. Copyright 1991 by the American Statistical Association



Volcanic Eruptions: Stochastic Models of Occurrence Patterns, Figure 4

a Lambert equal area polar histogram showing the percentage of eruptions of Fuego since 1800 in relationship to the fortnightly tidal maximum of the vertical gravity acceleration. **b** Lambert equal-area polar histogram showing the percentage of all the known times of the beginning of eruptions since 1957 compared to the 12.4-hour (semi-diurnal) minimum of the vertical gravity acceleration. **c** A spiral diagram indicating the position of an eruption in relation to the synodic month (days plotted around the circumference) and the reduced anomalistic age (days plotted as the radius, with perigee at the center), in which it occurred. There are 27.5 days in the anomalistic cycle, and 29.6 days in the synodic cycle. Right of the spiral diagram, is a histogram of the four spirals of the above diagram, which are drawn around ± 3.5 days of the maxima and minima of the 2 cycles. **d** Monthly histogram of Fuego's eruptions which have occurred since 1800. Reprinted from [54] © 1981 Elsevier B.V., with permission from Elsevier

serial dependence and applied it to eruptions from Mount Sangay (Ecuador).

The Poisson process is stationary in time, in that the distribution of the number of events in an interval depends only on the length of the interval, not its location. In other words, events occur at the same average rate at all times, i.e., there is no trend in the occurrence rate with time. Marzocchi [55] analyzed possible trends by calculating the (biased) autocorrelation function

$$a(s) = \frac{\sum_{i=1}^{n-1-|s|} (r_i - \bar{r})(r_{i+|s|} - \bar{r})}{\sum_{i=1}^{n-1} (r_i - \bar{r})^2}, \quad (3)$$

for $s = 0, \pm 1, \dots, \pm m$, where $r_i, i = 1, \dots, n-1$ is the time between the i th and $(i+1)$ th onsets, $\bar{r} = (1/(n-1)) \sum_{i=1}^{n-1} r_i$ and $m < n-1$. Under the null hypothesis that the process is purely random, the distribution of $a(s)$ is asymptotically normal with mean zero and variance $1/(n-1)$ for $s \neq 0$.

More generally, a process can be a *nonhomogeneous Poisson process*, where $N(t)$ has a Poisson distribution

with mean $\mu(t) = \int_0^t \lambda(s) ds$. Ho [37] used an example of a nonhomogeneous Poisson process known as the *Weibull Process* [2], with

$$\lambda(t) = \frac{\beta}{\theta} \left(\frac{t}{\theta} \right)^{\beta-1}, \quad (4)$$

where t is absolute time with respect to some fixed origin, not the elapsed time since the previous eruption. This includes the homogeneous Poisson process as a special ($\beta = 1$) case, while if $\beta \neq 1$ the process is non-stationary. The intensity (4) is monotonic, and hence can model either an increase or decrease in volcanic activity, but not both. Note that the parameter estimates,

$$\hat{\beta} = N(T) / \sum_{i=1}^{N(T)} \ln(T/t_i) \quad \text{and} \quad \hat{\theta} = T/N(T)^{1/\hat{\beta}}, \quad (5)$$

for the intensity (4) are sensitive to the position of the time origin [4]. Furthermore, estimates of $\hat{\beta} > 2$, which are quite feasible, indicate a constantly accelerating, or

convex, intensity. Neither of these properties is particularly desirable from a physical viewpoint, and hence the Weibull process is not suitable to model entire volcanic histories. Salvi et al. [73] used a statistical technique to identify that the most recent part of the Mount Etna sequence was non-stationary, and fitted the Weibull process to it. The Weibull process can be tested for goodness of fit to a series of data [4] either via a standard χ^2 test, or by using the fact that x_1, \dots, x_{n-1} , where $x_i = \ln(t_n/t_{n-i})$, should be a random sample from an exponential distribution of unknown mean.

Jaquet et al. [44] proposed a temporal occurrence model using the Cox process. This is a doubly stochastic process with

$$\Pr(N(s, s+t) = k) = \mathbb{E} \left(\frac{Z(s, s+t)^k}{k!} e^{-Z(s, s+t)} \right), \quad (6)$$

where

$$Z(s, s+t) = \int_s^{s+t} \omega(t) dt, \quad (7)$$

and $\omega(t)$ is the conditional random frequency of events. The process of determining $\omega(t)$ is not spelt out in detail, involving geostatistical methods, simulation, variograms and a conditioning technique. The advantage of (6) over the Poisson process is that it introduces the possibility of correlation in time.

Renewal Processes

The homogeneous Poisson process without trend is a special case of a *renewal process*. In a renewal process, the intervals between events are independent and identically distributed, and so

$$\lambda(t) = \frac{f(t-s; \theta)}{1 - F(t-s; \theta)}, \quad t > s, \quad (8)$$

where the most recent event occurred at time $s < t$, and $f = F'$ is a density with parameter vector θ . This was first suggested for eruption onsets by Wickman [103], who coined the term *age-specific eruption rate* for (8). The character of the renewal process is that only the elapsed time since the last eruption controls the time to the next eruption. Previous eruptions exert an influence only through their contribution to the parameter estimates $\hat{\theta}$. A number of tests to check whether a series of eruptions is consistent with a renewal process can be found in the paper by Reymont [72]: One first checks for the existence of a trend using the standard normal statistic

$$U = \frac{\sum_{i=1}^n t_i/n - T/2}{T\sqrt{n/12}}, \quad (9)$$

where onsets are observed at times $0 < t_1 < \dots < t_n < T$. If no trend is observed, one can then examine the serial correlation coefficients

$$\rho_j = \frac{\text{Cov}(\mathbf{r}, \mathbf{r}^{(j)})}{\text{Var}(\mathbf{r})}, \quad (10)$$

where $\mathbf{r} = (r_1 \dots r_{n-1-j})$, $\mathbf{r}^{(j)} = (r_{1+j} \dots r_{n-1})$, and r_i is the time between the i th and $(i+1)$ th onsets. For a renewal process, there should be no correlation, and $\text{Var}(\rho_j) \sim 1/(n-j)$. Hence a test of $\rho_j = 0$, $j = 1, 2, \dots$ can be performed using the standard normal statistic $\rho_j \sqrt{(n-j)}$. One can also examine the periodogram [72]. The special case of a Poisson process can be tested in many ways, the easiest of which is to test the inter-onset intervals for exponentiality using, for example, the Kolmogorov–Smirnov statistic of the maximum distance between the empirical and hypothesized distribution functions. Other tests are mentioned in [4,5].

Given a density $f(u; \theta)$ and observed inter-onset times r_i , $i = 1, \dots, n-1$, the parameters θ can be estimated by maximum likelihood. That is, the values are chosen, either algebraically or numerically, to maximize the likelihood

$$L(r_1, \dots, r_{n-1}, t-s; \theta) = [1 - F(t-s; \theta)] \prod_{i=1}^{n-1} f(r_i; \theta), \quad (11)$$

where the first term accounts for the current unfinished interval, and is often omitted. Occasionally other methods are used. The method of moments involves setting the parameter values to equalize the observed and theoretical moments. As many moments are used as one has parameters. For example, two parameters can be fitted using the mean and standard deviation. An alternative is based on minimizing the sum of squared differences between an observed curve and that produced by the model. This is usually done using linear regression, but direct numerical optimization is possible.

If f is the exponential density $f(u) = \nu e^{-\nu u}$, then

$$\lambda(t) = \frac{\nu e^{-\nu(t-s)}}{1 - (1 - e^{-\nu(t-s)})} = \nu, \quad (12)$$

and we recover the homogeneous Poisson process. Klein [46] tested the eruptive patterns of Hawaiian volcanoes against a Poisson process (random model) using this formulation, and showed that repose following large eruptions differed significantly from the whole. The Eq. (12) is sometimes referred to as the memoryless property, as it says that the time elapsed since the last eruption provides no information about the time of the next eruption.

Thorlaksson [93] suggested that an over-dispersed (standard deviation σ greater than the mean μ) sequence of inter-onset intervals should be modeled by the Pareto density $f(u) = a(1 + bu)^{-a/b-1}$, $u > 0$, with intensity

$$\lambda(t) = \frac{a}{1 + b(t-s)}, \quad t > s, \quad (13)$$

where $\hat{a} = 2\sigma^2/(\mu^3 + \mu\sigma^2)$ and $\hat{b} = (\sigma^2 - \mu^2)/(\mu^3 + \mu\sigma^2)$ are estimated by the method of moments. This models a decrease in eruption probability with time, and was applied to Colima by Medina Martinez [63]. For under-dispersed inter-onset intervals, Thorlaksson [93] suggested the density

$$f(u) = \begin{cases} (a + bu) \exp(-au - (b/2)u^2) & \sqrt{4/\pi - 1} < \sigma/\mu < 1 \\ b(u - a) \exp(-(b/2)(u - a)^2) & \sigma/\mu < \sqrt{4/\pi - 1} \end{cases}, \quad u > 0, \quad (14)$$

leading to the intensity

$$\lambda(t) = \begin{cases} a + b(t-s) & \sqrt{4/\pi - 1} < \sigma/\mu < 1 \\ b(t-s-a) H(t-s-a) & \sigma/\mu < \sqrt{4/\pi - 1} \end{cases}, \quad t > s, \quad (15)$$

where

$$H(x) = \begin{cases} 1 & x > 0 \\ 0 & x \leq 0 \end{cases} \quad (16)$$

is the Heaviside function. These imply an increase in eruption probability with time, while the case $\sigma/\mu < \sqrt{4/\pi - 1}$ adds a loading time a , and the parameters can be estimated as $\hat{a} = \mu - \sigma/\sqrt{4/\pi - 1}$ and $\hat{b} = (2 - \pi/2)/\sigma^2$. This latter case was applied to the volcanoes Hekla and Katla, which had ratios σ/μ of 0.44 and 0.43 respectively. Of the other 28 volcanoes examined, none had a ratio less than 0.76, and 23 had a ratio of greater than unity.

Settle and McGetchin [78] fitted a Gaussian density to the inter-onset times of eruptions at Stromboli over four days. Note that the formulation (8) is always strictly positive, even for distributions such as the Gaussian whose support includes the negative axis. However, fitting and simulating such processes presents certain practical difficulties.

Bebbington and Lai [4] fitted renewal models to a number of volcanoes, using the Weibull density with scale parameter β and shape parameter α ,

$$f(u) = \alpha\beta(\beta u)^{\alpha-1} \exp(-(\beta u)^\alpha), \quad u > 0. \quad (17)$$

The intensity is then

$$\lambda(t) = \alpha\beta(\beta(t-s))^{\alpha-1}, \quad t > s. \quad (18)$$

We see that while $\alpha = 1$ is the exponential distribution, $\alpha < 1$ corresponds to an ‘over-dispersed’, or clustering, distribution (cf. [34]), and $\alpha > 1$ to a more periodic distribution with a mode at $u = \beta^{-1}(1 - 1/\alpha)^{1/\alpha}$. The density and intensity are shown in Fig. 5.

De la Cruz-Reyna and Carrasco-Nunez [28] suggested using the gamma density, which also allows for clustering and periodicity, but the computational details are more complex. Also, the Weibull is the consequence of a material failure model [98], and in any case, little qualitative difference is usually observed between Weibull and gamma distributions for small samples, such as eruptive records. Note that the intensity (18) is monotonic, and can model either increasing probability of eruption as the repose time increases, such as at Hekla [103], or decreasing probability with increasing repose time, such as at Colima [63]. Bebbington and Lai [4,5] provided a number of tests for assessing the applicability of the Weibull distribution, based on the fact that r_i^β , where $r_i = t_{i+1} - t_i$, should be exponentially distributed.

The lognormal density,

$$f(u) = \frac{1}{u\sigma\sqrt{2\pi}} \exp\left[-\frac{(\ln u - \mu)^2}{2\sigma^2}\right], \quad u > 0, \quad (19)$$

with intensity

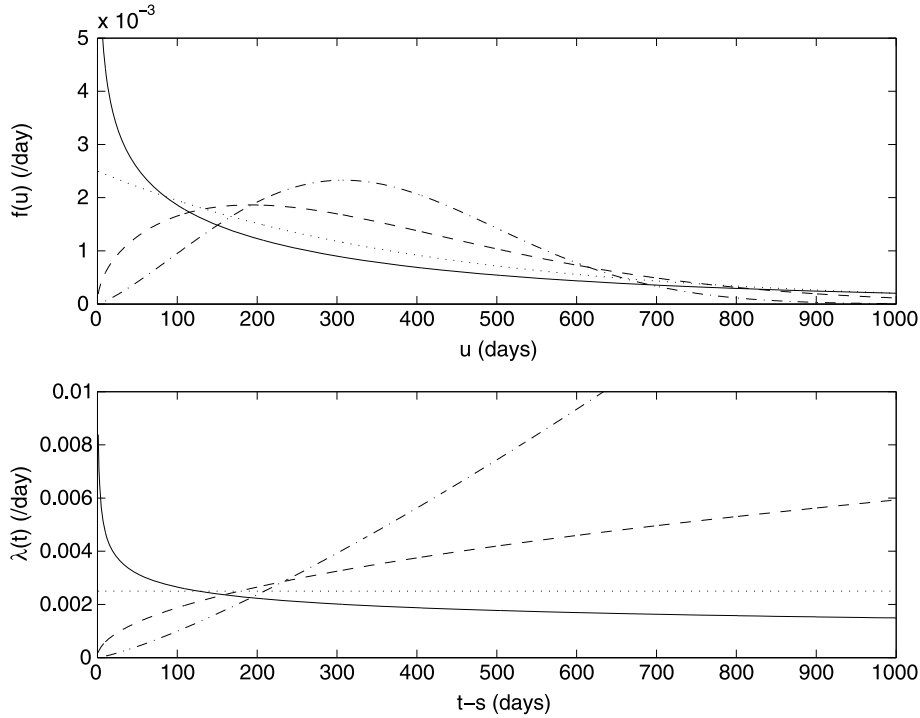
$$\lambda(t) = \frac{\frac{\sqrt{2}}{(t-s)\sigma\sqrt{\pi}} \exp\left[-\frac{(\ln(t-s) - \mu)^2}{2\sigma^2}\right]}{\operatorname{erfc}\left(\frac{\ln(t-s) - \mu}{\sqrt{2}\sigma}\right)}, \quad t > s, \quad (20)$$

was also considered by Bebbington and Lai [4], and used by Marzocchi and Zaccarelli [59] and Eliasson et al. [30]. As the density (19) is unimodal at $u = \exp(\mu - \sigma^2)$, this works better for non-clustering events, such as the very large eruptions considered in [59]. Eliasson et al. [30] noted significant departure from the distribution in one of their models. The density and intensity are shown in Fig. 6. Note that (20) is ‘upside-down bathtub shaped’, i.e., that as t increases it rises to a maximum and then declines.

The log-logistic density,

$$f(u) = \frac{\eta\gamma u^{\gamma-1}}{(1 + \eta u^\gamma)^2}, \quad u > 0, \quad (21)$$

with a mode at $u = \max\{0, (\gamma - 1)/((\gamma + 1)\eta)\}^{1/\gamma}$ was used by Connor et al. [18] to model the intervals between



Volcanic Eruptions: Stochastic Models of Occurrence Patterns, Figure 5

Density f and conditional intensity λ for the Weibull distribution with $\beta = 0.0025$ and $\alpha = 0.75$ (solid line), $\alpha = 1$ (dotted line), $\alpha = 1.5$ (dashed line) and $\alpha = 2.25$ (dot-dash line)

Vulcanian explosions of Soufriere Hills volcano, Montserrat. The density and the intensity

$$\lambda(t) = \frac{\eta\gamma(t-s)^{\gamma-1}}{1 + \eta(t-s)^{\gamma}}, \quad t > s, \quad (22)$$

are shown in Fig. 7. The intensity (22) has a maximum at $t = s + \max\{0, ((\gamma - 1)/\eta)^{1/\gamma}\}$, prior to which it is increasing, subsequently decreasing. Thus we can see that the log-logistic distribution possesses some of the character of the Weibull and of the lognormal distributions.

Pyle [71] used the power-law density

$$f(u | u > c) = \frac{u^{-1-1/b}}{bc^{-1/b}}, \quad u > c > 0 \quad (23)$$

to model the tail of the inter-onset distribution. Note that the density is not defined for $c = 0$. The intensity is

$$\lambda(t) = \frac{1}{b(t-s)}, \quad t > s, \quad (24)$$

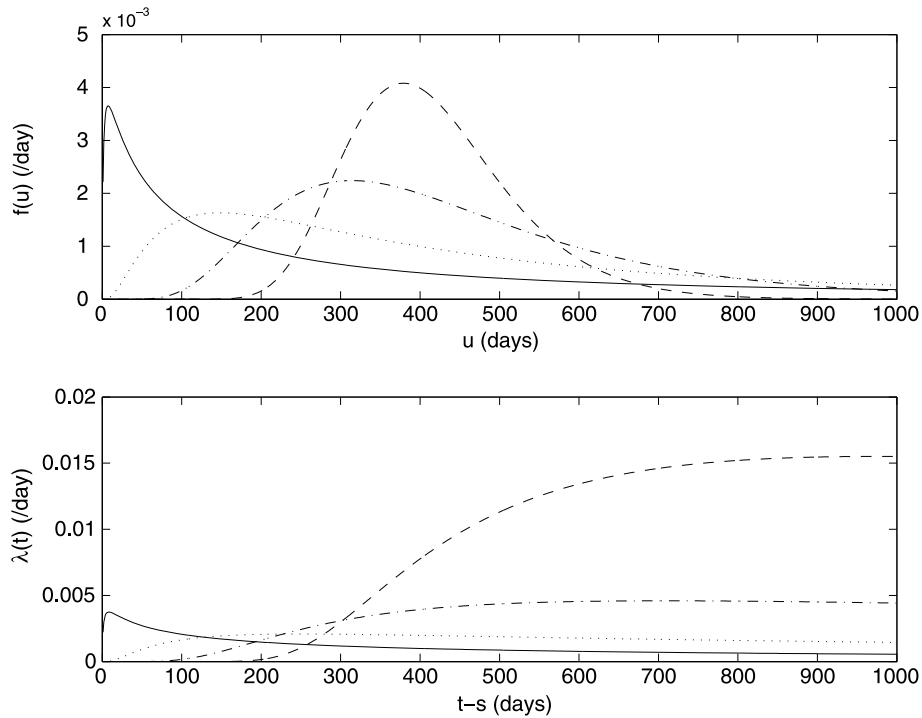
from which we see that the parameter b controls the rate of decay of the intensity, or equivalently, the ‘thickness of the tail’.

Turner et al. [94] fitted a renewal density consisting of a mixture of Weibull densities, as exemplified in Fig. 8, to model a multimodal repose distribution. Cronin et al. [22] proposed a variant on this, where onsets occurred in ‘episodes’, each of variable numbers of eruptions, with different repose distributions corresponding to inter- and intra-episode repose.

The drawback of renewal models is that they commonly fail to explain variations in eruption rate, corresponding to changes in activity level, although Wickman [103] did suggest using a small number of different levels. This idea was taken up in [3], where a renewal process with parameters controlled by a hidden Markov model was fitted to flank eruptions from Mt Etna. Using the Weibull distribution (17) for the inter-onset times, the preferred model had long sequences of approximately Poisson behavior, interspersed with shorter sequences of more frequent and regular eruptions.

Markov Processes

A *Markov process* (continuous time Markov chain) $Z(t), t \geq 0$ has transition intensity matrix $Q = (q_{ij})$,



Volcanic Eruptions: Stochastic Models of Occurrence Patterns, Figure 6

Density f and conditional intensity λ for the lognormal distribution with $\mu = 6$ and $\sigma = 2$ (solid line), $\sigma = 1$ (dotted line), $\sigma = 0.5$ (dashed line) and $\sigma = 0.25$ (dot-dash line)

where

$$q_{ij} = \lim_{t \downarrow 0} \frac{\Pr(Z(s+t) = j \mid Z(s) = i)}{t} \geq 0, \quad (25)$$

for all $i \neq j$, and $-q_i = q_{ii} = -\sum_{j \neq i} q_{ij}$. Thus the sojourn time in state i is exponential with mean $1/q_i$, and when it ends, the process moves to state j with probability $p_{ij} = q_{ij} / \sum_{k \neq i} q_{ik}$.

Wickman [104] proposed the use of Markov processes to model eruption-repose patterns. This entailed defining a number of eruptive and repose states, with prescribed permitted transitions between them. The initial models [104] allowed for one or two magma chambers, with eruptions and ‘solidification’ of the vent occurring in Poisson processes of differing rate. In the two-state case this solidification can only be removed by an eruption from the second, larger and deeper, magma chamber. If the two magma chambers erupt at rates ν and μ ($\nu > \mu$), respectively, and the vent solidifies at rate η , then the eruption rate can be derived as

$$\lambda(t) = \frac{\mu\eta + \nu(\mu + \nu + \eta) \exp[-(\nu + \eta)(t-s)]}{\eta + \nu \exp[-(\eta + \nu)(t-s)]}, \quad t > s, \quad (26)$$

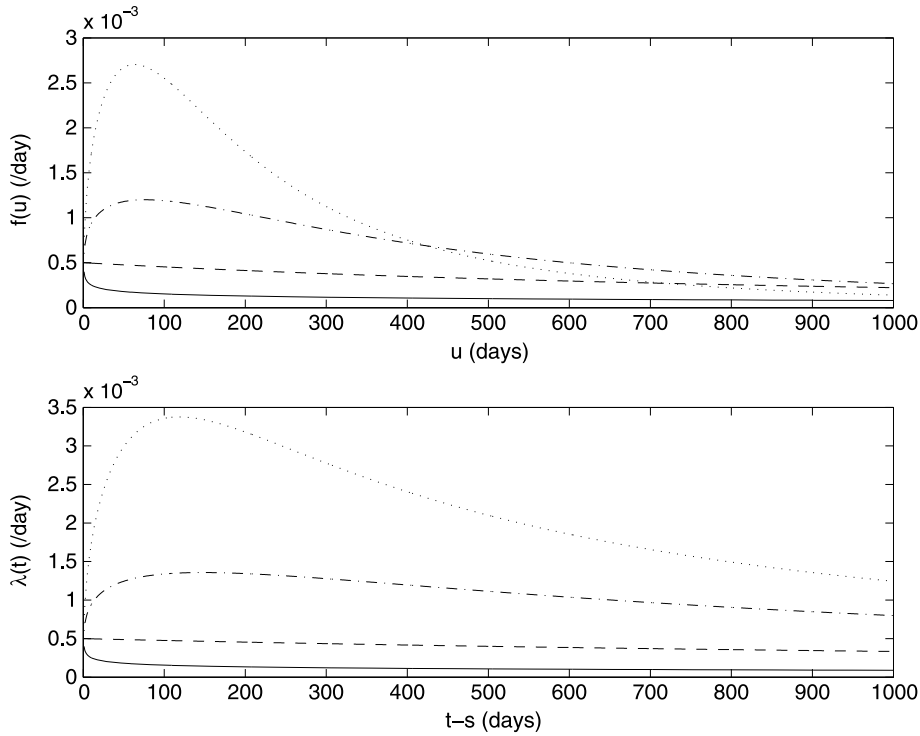
where the previous eruption occurred at time s . The pa-

rameters can be estimated by numerically fitting this equation to the empirical renewal intensity.

Wickman [105] extended this to six possibilities modeled on various well-known volcano types, and simulated them to produce reasonable appearing synthetic data. The process of fitting these models to observed data has required manual identification of the various states in the data [11,54], but the use of hidden Markov model techniques to automate the process has been suggested [3]. In a Markov process, the time between onsets is the passage time through the eruptive and repose states, which will have a compound exponential distribution, i.e., be the sum of a number of exponential random variables of differing means.

Time and Size Predictable Models

Bacon [1] noted that the intervals between rhyolitic and basaltic eruptions in the Coso Range (California) appeared to be proportional to the volume of the preceding eruption. This *time-predictable* behavior (cf. [81]) is most simply explained by assuming that the rate of magma input is constant, and an eruption occurs when a certain magma level is reached. However, Bacon [1] suggested the covariate of accumulated extensional strain as the controlling



Volcanic Eruptions: Stochastic Models of Occurrence Patterns, Figure 7

Density f and conditional intensity λ for the log-logistic distribution with $\eta = 0.0005$ and $\gamma = 0.8$ (solid line), $\gamma = 1$ (dashed line), $\gamma = 1.2$ (dot-dash line) and $\gamma = 1.4$ (dashed line)

variable, and considered eruptions a passive response of the magmatic system to the tectonic stress field.

Similar behavior was observed for Fuego Volcano, Guatemala [54], together with a weaker proportionality between volume and the length of repose before an eruption, although the authors did note that “the volume estimates probably have an error of less than ± 1 order of magnitude”. Martin and Rose [54] also examined a possible link between the length of repose before an eruption and its geochemical composition. Santacroce [75] found a similar phenomenon at the Somma-Vesuvius complex, and suggested that eruptions there occur in cycles, of approximately 3000 years, each initiated by a large-scale Plinian eruption, and terminated by a long repose of several centuries. Klein [46] found evidence of time-predictable behavior at both Kilauea and Mauna Loa (Hawaii).

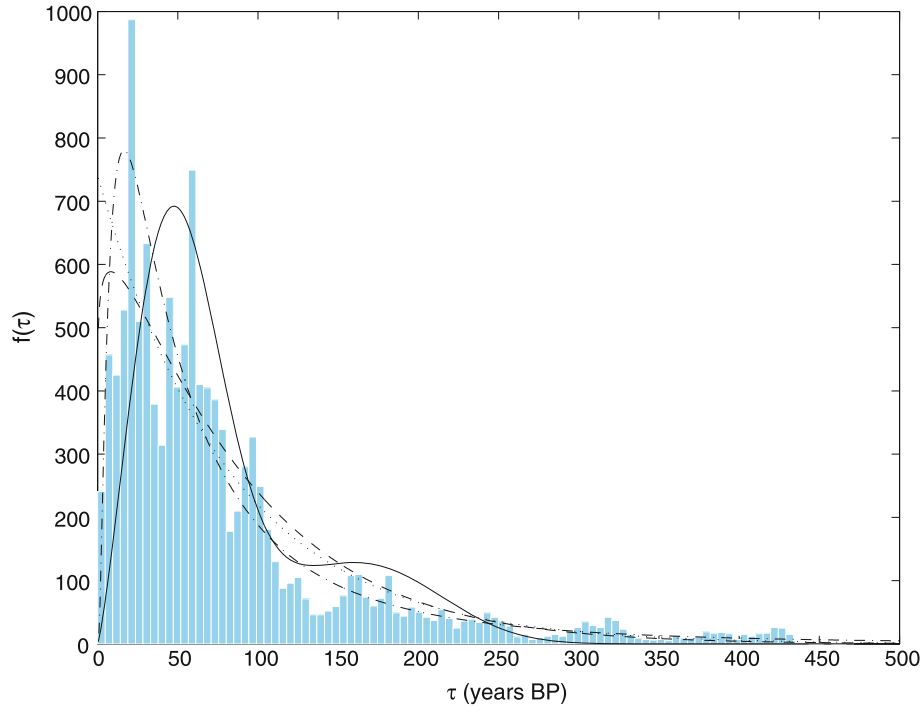
Wadge and Guest [101] suggested that the time-predictable model has a limited predictive ability, based on drawing an empirical envelope on the recent eruptive volume curve. This has a slope determined as the mean eruptive volume rate, and limits defined by the extreme points of the curve in the considered history. This enables a forecast of both the longest the current repose is likely to

last, and the maximum volume of the next eruption, provided that steady-state is maintained. Figure 9 shows an example using flank eruptions from Mt Etna 1970–2006. Wadge [99] estimated, however, that volcanoes may spend only 1/4–1/2 of the time in steady-state, being dormant much of the remainder. Changes in eruptive rate have also been found in a number of historical records [9,26,65].

De la Cruz-Reyna [26] proposed a general *load-and-discharge* model, where the ‘energy’ of the volcano increases at a constant rate σ between eruptions. The i th eruption occurs when this exceeds the threshold H_i , during which the stored energy drops to the threshold L_i , releasing an energy $\xi_i = H_i - L_i$. The interval between eruptions is thus

$$r_i = t_{i+1} - t_i = \frac{H_{i+1} - H_i + \xi_i}{\sigma}. \quad (27)$$

Hence successive repose intervals are not independent, as they include a common threshold term, and should be negatively correlated. In general, the thresholds can be random, but this formulation includes the time-predictable model. In this, the thresholds H_i are constant, and



Volcanic Eruptions: Stochastic Models of Occurrence Patterns, Figure 8

Histogram of 122,000 sampled inter-event times for Mt Taranaki based on 1000 Monte Carlo runs. Curves show the fitted densities for this data set: *Dotted line* = exponential distribution, *dot-dash* = lognormal, *dashed* = Weibull, *solid* = mixture of Weibulls

thus the interval

$$r_i = \xi_i / \sigma \quad (28)$$

is proportional to the energy of the preceding eruption, and successive intervals are independent. Alternatively, if the thresholds L_i are held constant ($= L$, say), $H_i = \xi_i - L$ and from (27)

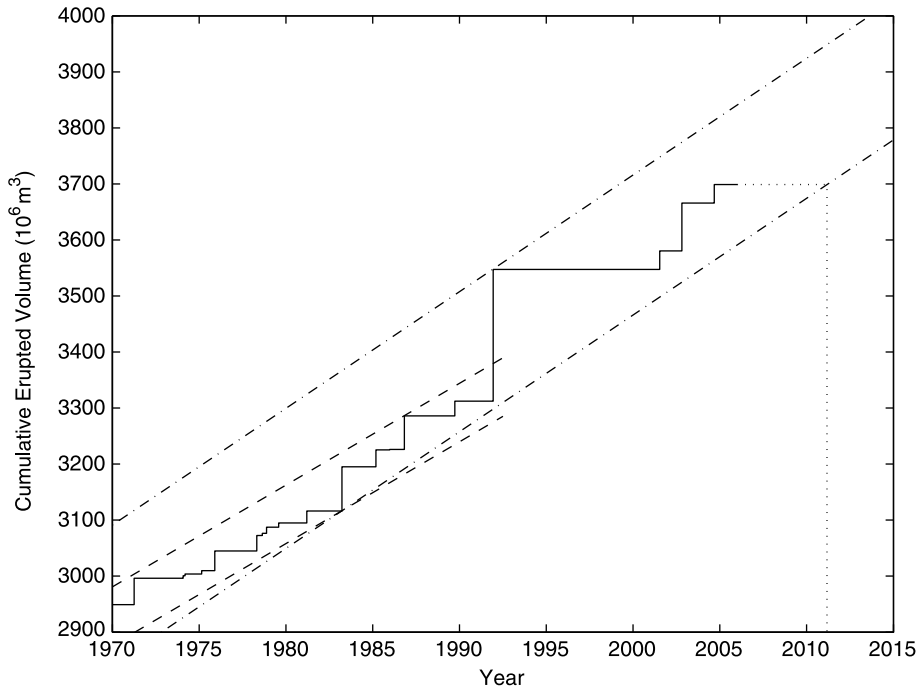
$$r_i = (H_{i+1} - L) / \sigma. \quad (29)$$

Thus successive intervals are again uncorrelated, and the energy drop of the eruption is proportional to the length of the interval preceding it. This is termed the *size-predictable* model.

In a global analysis of eruptions, De la Cruz-Reyna [26] noted the existence of a regression relationship $\log \lambda_0 = 3.494 - 0.789 \text{VEI}$ with correlation -0.999 , where λ_0 is the Poisson intensity for eruptions of a given VEI. This led De la Cruz-Reyna [27] (see also [28]) to model the onsets of different VEI events as independent Poisson processes, in a special case of the size-predictable model. This approach was also used in the quantification of volcanic risk due to Vesuvius by Scandone et al. [76], based on the sequence of equilibrium states (re-

pose, persistent activity, intermediate eruption, final eruption) identified by Carta et al. [11].

Burt et al. [9], in an examination of the basaltic volcano Nyamuragia (Zaire), formulated the ‘pressure-cooker’ and ‘water-butt’ models. The former, where an eruption occurs when the magma volume reaches a threshold determined by the rock strength and reservoir shape, is the time-predictable model, while the latter, where eruptions always drain the magma reservoir to the same level, is the size-predictable model. Burt et al. [9] suggested physical explanations for stochastic perturbations observed in these models, and proposed that a volcano could be tested for time-predictability by performing a regression analysis of $(v_i^{(1)})$ on (r_i) , where $r_i = t_{i+1} - t_i$, and $t_i, v_i^{(1)}$ are the onset time and eruptive volume of the i th eruption. Similarly the size-predictable model entails a regression analysis of $(v_i^{(2)})$ on (r_i) , where $v_i^{(2)} = v_{i+1}^{(1)}$. Sandri et al. [74] generalized the test for time-predictability to a regression analysis of $(\log v_i^{(1)})$ on $(\log r_i)$, so that an estimated slope of b significantly greater than zero implies a time-predictable relation $v_i^{(1)} \propto r_i^b$. Marzocchi and Zaccarelli [59] performed a similar regression analysis of $(\log v_i^{(2)})$ on $(\log r_i)$ for the size predictable model, resulting in a relation $v_i^{(2)} \propto r_i^b$. Be-



Volcanic Eruptions: Stochastic Models of Occurrence Patterns, Figure 9

Volume-time curve for Mt Etna flank eruptions (solid line). Dashed limits based on 1970–1990 data were exceeded, or equivalently the volcano departed from steady-state, by the 1991 eruption. Dot-dash limits based on 1970–2006 data have a steeper slope and wider limits to accommodate the 1991 eruption. The dotted lines show that the method predicts the next eruption to occur by the end of February 2011, and the eruptive volume to be less than $142.1 + 20.8t$ (10^6 m^3), where t is the number of years to the date of the eruption from January 2007

cause both the repose and volume distributions are highly skewed, the logarithmic transformation is advisable to reduce the high leverage of the tail points.

Marzocchi et al. [57] estimated the VEI of the next eruption of Mt Vesuvius by considering a) the global catalog, b) a catalog of ‘analog’ volcanoes, and c) the catalog of Vesuvius itself. In each case, the catalogs are trimmed to those eruptions following a repose interval of at least the presently observed 60 years. The estimated probability of an eruption of $\text{VEI} \geq 5$ ranged from 1% to 20%, and could not be considered negligible. This has implications for the Emergency Plan of Mount Vesuvius, which assumes a maximal $\text{VEI} = 4$.

Marzocchi and Zaccarelli [59] proposed a renewal model based on the time-predictable model. In their *open conduit system* model, the probability density of the time u to the next eruption is conditional on the previous eruptive volume v . Using a log-normal distribution, this is

$$f(u | v) = \frac{1}{u\sigma\sqrt{2\pi}} \exp \left[-\frac{(\log u - (a + bv))^2}{2\sigma^2} \right], \quad (30)$$

where a, b are the intercept and slope regression coefficients from the regression of $(\log v_i^{(1)})$ on $(\log r_i)$.

Chaos and Fractals

A sufficiently complicated deterministic model is indistinguishable by finite observation from a random process. However, it is possible to construct systems with few degrees of freedom, but very complex dynamics, which are known as *chaotic systems*, or *strange attractors*. This possibility can be tested by examining the correlation properties of the observation sequence. The underlying principle of fractals is one of *self-similarity*, i. e., that the statistical properties of the process are invariant at differing time (or space) scales.

Sornette et al. [88] computed the dimension D of the attractor as a function of the dimension d of the embedding phase space. Given onset times t_i , let $X_i^{(k)} = r_{i+k-1}$ for $k = 1, \dots, d-1$, where $r_i = t_{i+1} - t_i$, for $i = 1, \dots, n-1$. Then the correlation function is determined as

$$C_d(w) = \frac{1}{n^2} \# \{i, j: \|\mathbf{X}_i - \mathbf{X}_j\| < w\}, \quad (31)$$

where \mathbf{X}_i is the vector $(X_i^{(1)} \dots X_i^{(d)})$. The correlation dimension is then defined by the power law relation

$$C(w) \sim w^{D(d)}. \quad (32)$$

If this saturates at some value D_{\max} as d increases, this is taken as evidence that the underlying dynamics is deterministic and has dimension of the order of D_{\max} . Applications to the volcanoes Piton de la Fournaise (La Reunion Island) and Mauna Loa/Kilauea (Hawaii) produced estimates of D_{\max} of 1.7 and 4.6, respectively. The latter value was interpreted as evidence of two independent dynamical systems for the two Hawaiian volcanoes, contradicting the conclusion of Klein [46]. Sornette et al. [88] also constructed a series of ‘return maps’ (r_{i+1} as a function of r_i) by truncating the data in various ways.

Dubois and Cheminee [29] used the Cantor dust model for volcanic eruption onsets. In this method, the eruptive record is divided into segments of length T , and the fraction of these intervals containing at least one onset is denoted X . If fractal clustering with fractal dimension D is present, then $X \sim T^{1-D}$. This implies a renewal model with intensity $\lambda(t) = D/(t-s)$, $t > s$, where the last eruption occurred at time s (cf. Eq. (24)). An obvious method for estimating D is a regression analysis of $(\log X_i)$ against $(\log T_i)$ for various interval lengths T_i . Applied to the Piton de la Fournaise (La Reunion Island), two slopes were observed, one with $D \approx 0.5$ for $T < 10$ months, and one with $D \approx 0.7$ for $T > 10$ months. Kilauea had two regimes with $D = 0.58$ for $T < 24$ months and $D = 0.81$ for $T > 24$ months, while Mauna Loa had $D \approx 0.35$ for $T < 6$ years and $D \approx 0.85$ for $T > 6$ years. The two regimes all indicated clustering at short repose lengths, and more regular activity for eruptions separated by longer repose. This was interpreted as evidence of multiple magma chambers, with different sizes and recharge rates, at different depths. Applied to a combined catalog of flank and summit eruptions of Mt Etna 1950–1987, the result was a single regime with $D = 0.88$. This high value of D was interpreted as being characteristic of the regular eruptive activity of the volcano.

Marzocchi [55] calculated the statistic

$$a_{\max} = \max_{1 \leq s \leq 5} a(s), \quad (33)$$

where $a(s)$ is defined in (3), although a process might first be de-trended by subtracting an auto-regressive model. A value $a_{\max} > a_c^*$ indicates a chaotic system, while a value $a_{\max} < a_s^*$ indicates a stochastic system. Intermediate values provide insufficient evidence for either. The critical values a_c^* and a_s^* are determined by simulation. Both Vesuvius and Etna evidenced significantly stochastic behavior.

A multifractal analysis using the Grassberger–Procaccia algorithm was performed by Godano and Ci-

vetta [33]. The correlation interval is calculated as

$$C(t, q) = \frac{1}{n-1} \sum_{i=1}^{n-1} \left[\frac{1}{n-2} \sum_{j \neq i} H(t - |r_i - r_j|) \right]^q, \quad (34)$$

where r_1, \dots, r_{n-1} are the inter-onset times, and $H(\cdot)$ is the Heaviside function. The *generalized dimensions* are then evaluated as

$$D_{q+1} = \phi(q)/q, \quad (35)$$

where $\phi(q)$ is the estimated slope from a regression analysis of $\log C(t, q)$ versus $\log t$. The fractal, information, and correlation dimensions are D_0 , D_1 and D_2 , respectively. More generally, D_{q+1} is constant as q varies for a homogeneous fractal distribution, but varies with q for a multifractal distribution. The latter implies that local clustering properties are different from global clustering properties. Applied to eruptions of Vesuvius, the estimated dimensions were $D_0 = 1.05 \pm 0.07$, $D_2 = 0.75 \pm 0.04 \approx D_\infty = 0.73 \pm 0.02$ and $D_{-\infty} = 1.09 \pm 0.13$. This indicates that at a global scale, the catalog exhibits Poissonian behavior ($D = 1$), and the most intense clustering is not a particularly strong effect. The catalog exhibits only weak multifractal behavior, and this only for $q < 1$. Thus the cyclic behavior outlined by Carta et al. [11] cannot be identified statistically, as the intervals between events in a cycle are not distinguishable from those between cycles.

Nishi et al. [69] examined the long term memory of the time series of 3796 eruptions of Sakurajima 1981–1999 using the Hurst exponent. Let $r_i = t_{i+1} - t_i$, $i = 1, \dots, n-1$, be the inter-onset times, and set

$$X(k, t, m) = \sum_{i=1}^k \left(r_{i+t-1} - \frac{1}{m} \sum_{j=1}^m r_{j+t-1} \right). \quad (36)$$

Then the *self-adjust range* is

$$R(t, m) = \max_{1 \leq k \leq t} X(k, t, m) - \min_{1 \leq k \leq t} X(k, t, m), \quad (37)$$

which is re-scaled by the standard deviation

$$S(t, m) = \sqrt{\frac{1}{t} \sum_{i=1}^t \left(r_{i+m-1} - \frac{1}{m} \sum_{j=1}^m r_{j+t-1} \right)^2}, \quad (38)$$

and averaging over the length of the time series, the *Hurst exponent* H is then defined by

$$\frac{\sum_{m=1}^{n-1} R(t, m)}{\sum_{m=1}^{n-1} S(t, m)} = \left(\frac{t}{2} \right)^H. \quad (39)$$

The value of H can be estimated by a regression analysis of (39), after taking logarithms. The Poisson process produces a value of $H = 0.5$. A value of H greater than this implies persistent behavior, with each value depending on the previous one. Anti-persistence behavior is characterized by $H < 0.5$. The Hurst exponents for Sakurajima were $H = 0.72$ for the whole series, and $H = 0.74$ for a ‘high frequency’ period 1983–1985. A Monte Carlo test consisting of randomly reordering the observed inter-onset times and recalculating H confirms that these values are significantly greater than 0.5. Telesca and Lapenna [92] performed the same analysis for eruptions of $\text{VEI} \geq 0$ of 14 volcanoes worldwide. The requirements were a minimum of 40 events during 1800–2000. Seven of the volcanoes, with Hurst exponents ranging from 0.79 to 1.3, were characterized by persistent behavior, while the remainder, with Hurst exponents ranging from 0.60 to 0.73, were not significantly different from a Poisson process.

Telesca et al. [91] examined 35 sequences of $\text{VEI} \geq 0$ eruptions (minimum 25 eruptions 1800–2000) using the Fano factor method. The Fano factor is defined as the variance of the number of events in a specified interval width Δ divided by the mean,

$$\text{FF}(\Delta) = \frac{(\Delta/T) \sum_{i=1}^{T/\Delta} N_i^2 - \left((\Delta/T) \sum_{i=1}^{T/\Delta} N_i \right)^2}{(\Delta/T) \sum_{i=1}^{T/\Delta} N_i}, \quad (40)$$

where $N_i = N((i-1)\Delta, i\Delta)$. Telesca et al. [91] represented the FF of a fractal point process as a monotonic power law

$$\text{FF}(\Delta) = 1 + \left(\frac{\Delta}{\Delta_0} \right)^\alpha, \quad (41)$$

for $\Delta > \Delta_0$, where Δ_0 is the fractal onset time, marking the lower limit for significant scaling behavior, with negligible clustering below this. Again the fractal exponent α is estimated by a regression analysis of (41), after taking logarithms. For Poisson processes, the FF is approximately one for all interval lengths, and so $\alpha \approx 0$. Of the 35 sequences examined, 30 had fractal exponents ranging from 0.2 to 0.9 (mean of 0.5). The remaining five exhibited no value Δ_0 above which (41) held.

Gusev et al. [34] examined clustering of eruptions on Kamchatka during the last 10,000 years using the Weibull density (17) for the inter-onset times, the correlation dimension (32), and the Hurst exponent (39). No self-similar behavior was found for intervals greater than 800 years, but for shorter delays there was a significant degree of clustering. Gusev et al. [34] also generalized the correla-

tion dimension by replacing (31) by a weighted version, where the contribution of a pair of events is proportional to the product of their eruptive volumes. This identified self-similar behavior over the entire range of inter-onset times (100–10,000 years).

Fractals have basically been used in volcanology as a descriptive technique. They can provide, at the level of a single volcano, some indication of the sort of stochastic model that might fit the observed behavior. Applied to multiple volcanoes, they can provide a similarity index, useful for sorting volcanoes into homogeneous groups.

Volcanic Regimes

Apart from the nonhomogeneous model (4), the parametric models examined above have all been stationary, in the sense that the statistical properties of the intensity function do not vary over time. However, Wadge [99] postulated that, while a volcano could be in steady state on a time scale of years to decades, in the longer term the activity can wax and wane. Thus, particularly for long-term hazard forecasts, it is desirable to formulate methods of detecting (and modeling) such non-stationary activity.

Wickman [103] suggested that the activity of a volcano could change over time, perhaps in discrete steps, which we will term *regimes*. Mulargia et al. [65] addressed the importance of objectively identifying regimes of a volcano, noting however that a) the number of regimes is unknown, b) they may follow different distributions, and c) sample sizes are generally small. Different patterns of eruption and magma output are supposedly features of most volcanoes, and fundamental to the understanding and modeling of eruptions. These regimes may represent changes in the eruption mechanism, the mechanism for transport of magma to the surface, or the eruptive style (see, for example, the interpretation by Wadge et al. [102]). The estimated properties of such regimes can exclude certain models or mechanisms of volcanic eruption [46].

Various methods have been used to identify changes in regime, one based on cumulative eruptive volume [99,102] already having been illustrated in Fig. 9. Another uses a running mean of time between onsets. Suppose that the individual repose are denoted by $r_i = t_{i+1} - t_i$, $i = 1, \dots, n-1$, and that $\sum_{i=1}^{n-1} r_i = T$. If the repose are divided into disjoint groups of m consecutive repose, then $(2(n-1)/T) \sum_{i=(k-1)m+1}^{km} r_i$, for $k = 1, \dots, \lfloor (n-1)/m \rfloor$, where $\lfloor \cdot \rfloor$ is the greatest integer function, are independent and have a chi-square distribution with $2m$ degrees of freedom [46].

Mulargia et al. [65] presented a method based on the theory of change-point problems. Suppose that we have

a time series of data X_1, \dots, X_n , which might be, for example, inter-onset intervals, eruptive volumes, or effusion rates. The algorithm begins by setting a significance level α , and examining the time series to determine the most significant change point. If a change point is found, the time series is divided into two parts at this point, and each examined to determine the most significant change point. The algorithm proceeds recursively until no further significant change points are found. The most significant change point is identified by a search process: For $m = 3, \dots, n - 3$, divide the time series into two segments $X^{(1)} = X_1, \dots, X_m$, and $X^{(2)} = X_{m+1}, \dots, X_n$, and calculate the Kolmogorov–Smirnov (two-tail) statistic as

$$J = \left(\frac{m(n-m)}{n} \right)^{1/2} \max_x |F_1(x; m) - F_2(x; n-m)|, \quad (42)$$

where $F_j(x; k) = \#\{i: X_i^{(j)} \leq x\}/k$ is the empirical distribution function of the first segment, et cetera. For large $m, n - m (> 30)$, the approximate critical value J_α of the statistic can be determined from

$$\Pr(J < J_\alpha) = \sum_{k=-\infty}^{\infty} (-1)^k \exp(-2k^2 J_\alpha^2) = 1 - \alpha. \quad (43)$$

Exact critical values for small $m, n - m$ are also available.

Later approaches used the cumulative count of eruptions in a statistical control chart [39], applied by Burt et al. [9] to Nyamuragia, and rank order statistics for the size of event [71]. Bebbington [3] noted that a hidden Markov model for the activity, with the unobserved state representing the regime, provides for regime identification via the Viterbi algorithm, which finds the most likely path through the hidden states.

Mount Etna

Mount Etna possesses one of the most complete records of volcanism known. A variety of eruption styles have been displayed, but since 1500 the activity has been predominantly effusive eruptions from lateral vents on the volcano's flanks, or from the central craters. The record of summit eruptions is incomplete prior to 1970 [101], but data for flank eruptions is considered complete since 1600 or so [65]. The volumes of all such eruptions have been estimated [74], and these have been shown to be well correlated with the observed duration [67]. As the summit eruptions appear to be of different style [102], and to have different mechanisms to the flank eruptions [66] the longer record of the latter can be analyzed in isolation. In addition,

only flank eruptions pose a major threat to inhabited areas [73].

Using the cumulative erupted volume curve, Wadge and Guest [101] found that the volume output was in steady state 1971–1981. Mulargia et al. [67] found that the events 1600 to 1980 were satisfactorily fit by a stationary Poisson process, but that the distribution of eruptive durations changed at the end of the 17th century, confirming the observation of Wadge et al. [102]. However, Mulargia et al. [65] identified a change point in the inter-onset times at 1865, both parts being consistent with a Poisson process, and, when augmented by volume data, change points at 1670 and 1750. Using the effusion rate (= volume/duration), Mulargia et al. [65] found a change point at 1950 in the 1600–1980 data, with the later sequence being of significantly lower rate. A repeat of the analysis by Gasperini et al. [31] for the data 1978–1987 identified a change point in the inter-onset times at November 1978, although no change point occurred in the volume series. Ho [39] fitted a statistical control chart based on the Weibull process, and found departures from the trend (4) in 1702 and 1759. Marzocchi [55] found some evidence of a trend in inter-onset times in the 1600–1994 data, while Sandri et al. [74] found no change points in the inter-onset times or eruptive volumes in the 1971–2002 data. Salvi et al. [73] determined that the activity 1536–2001 was not Poissonian, and although there was no trend 1536–1980, there was a trend in the data 1536–2001. They therefore concluded that the last 20 years of data is from a nonhomogeneous Poisson process, and fitted a Weibull process model with increasing trend.

The regime change points identified in the Mount Etna flank eruption data are summarized in Table 1. The lack of consistency is due to differences in both models and, via the fitting of them, in the coverage of the data. These models are ‘first order’ in the data being analyzed. Using hidden Markov models, Bebbington [3] was able to examine the ‘second order’ quantity of the correlation between durations and subsequent repose. The conclusion was that changes in volcanic regime may be more frequent and/or fleeting, and thus undetectable by change-point methods, than has been thought. Notably, the identified change points corresponded closely to those identified manually by Behncke and Neri [7], showing that these are statistically identifiable. The complex relation between the duration of an eruption and the subsequent repose appears to be at least partially explained by an open/closed conduit system model with transitions between them. On the other hand, the correlation between repose and subsequent durations may be sensitive to the longer of the two cycles identified by Behncke and Neri [7]. This would indi-

Volcanic Eruptions: Stochastic Models of Occurrence Patterns, Table 1

Regime change points for Etna flank eruptions

Data type	Source	Date Range	Change Points
Onset counts	Mulargia et al. [67]	1600–1980	None
Inter-onset times	Mulargia et al. [65]	1600–1978	1865
	Gasperini et al. [31]	1978–1987	1987
	Ho [39]	1600–1978	1702, 1759
	Marzocchi [55]	1600–1994	(Trend)
	Sandri et al. [74]	1971–2002	None
	Salvi et al. [73]	1536–2001	1980
Volume -repose	Wadge et al. [102]	1535–1974	1610, 1669, 1759/1763
	Wadge and Guest [101]	1971–1981	None
	Mulargia et al. [65]	1600–1978	1670, 1750, 1950
	Gasperini et al. [31]	1978–1987	None
	Sandri et al. [74]	1971–2002	None

cate that flank eruptions are being fed from more than one magma chamber, of widely different sizes and recharge rates.

Spatial Aspects

In the case of polygenetic cones, the major aspect of hazard modeling is temporal. Spatial aspects are limited to the direction of flank eruptions (cf. [73]), and the likely paths of lava flows and lahars. In monogenetic volcanic fields, where cones correspond to single eruptions, there is a true spatio-temporal element to modeling occurrence data.

Spatio-temporal Intensities

The models used to describe spatio-temporal eruption occurrence have been largely nonparametric, or kernel-type. Connor and Hill [17] gave three methods:

1. Spatio-temporal nearest-neighbor estimate: Suppose we have n volcanoes, that the formation of the i th volcano occurred at time t_i , and let u_i be the area of a circle with radius equal to the distance between the point x of interest and the i th volcano. Further, let $j = 1, \dots, m$ index the m th nearest neighbors to the point x using the distance metric $u_i(t - t_i)$. Then the estimated intensity at the point x is

$$\lambda(x, t; m) = \frac{m}{\sum_{j=1}^m u_j(t - t_j)}, \quad (44)$$

where m is the number of nearest neighbors used in the estimation, which was set equal to the number of volcanoes, although a smaller choice is possible. The temporal hazard for an area A can then be obtained by integrating the intensity (44) over the area. Note that in

practice, to avoid singularities, $u_i > c$, a constant, and the intensity is summed over a grid. The choice of c may be an interesting question.

Condit and Connor [14] proposed that the optimal m can be determined by matching the average recurrence rate $\int_{x \in A} \lambda(x, t; m) dx$ to the observed average recurrence rate $\hat{\lambda}(t) = N(t - s, t)/As$, in a window of length s , for the area A . Further, Condit and Connor [14] also suggested that overestimation during rapidly waning stages of activity can be addressed by defining a threshold time beyond which prior eruptions are not included in the calculation.

2. Kernel estimate: If we have n volcanoes, then using the Epanechnikov kernel

$$\kappa_i = \max \left\{ 0, \frac{2}{\pi} \left[1 - \left(\frac{d_i}{h} \right)^2 \right] \right\}, \quad (45)$$

where d_i is the distance from x to the i th volcano, we have the spatial intensity

$$\lambda(x) = \frac{1}{e_h} \sum_{i=1}^n \frac{\kappa_i}{h^2}, \quad (46)$$

where e_h is an edge correction. Conway et al. [20] use the Gaussian kernel instead. The parameter h is a smoothing constant. A small value of h concentrates the probability close to existing volcanoes, while a large value distributes it more uniformly. Estimating the best value of h is a difficult task – see Vere-Jones [96] for an earth sciences based discussion.

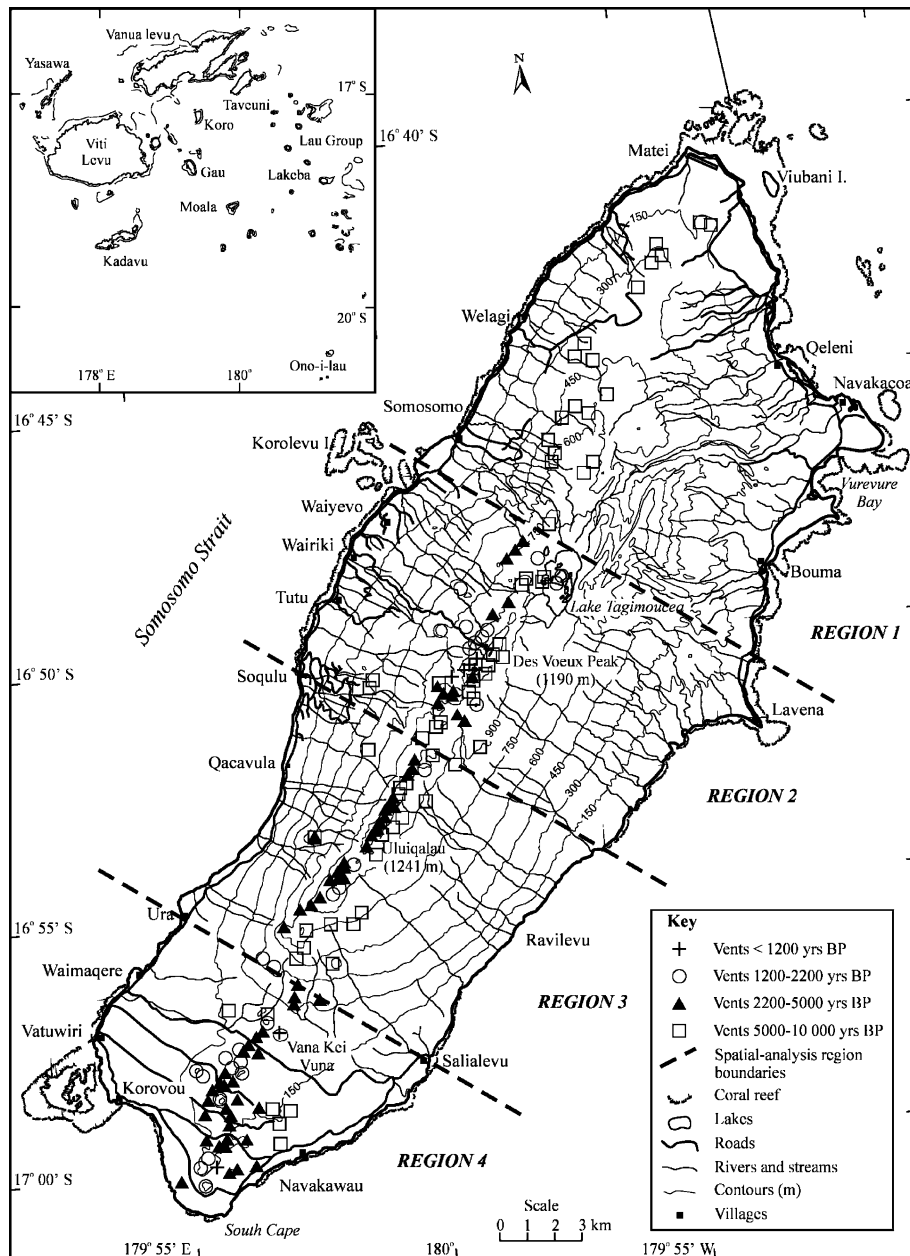
3. Nearest-neighbor kernel estimate: Here we replace the smoothing constant h in the Kernel estimate with $d_{(m)}$, the distance to the m th nearest neighbor using the d_i metric.

The two (spatial) kernel estimates above can then be made into spatio-temporal estimates by multiplying them by a spatially independent temporal rate $\hat{\lambda}_0 = N/T$, resulting in

$$\lambda(x, t) = \lambda(x)\hat{\lambda}_0. \quad (47)$$

Ho and Smith [42] generalized (47) by replacing $\hat{\lambda}_0$ by the Weibull process intensity (4).

Martin et al. [53] extended the spatio-temporal idea with a Bayesian formulation to incorporate information from other geophysical data such as P-wave velocity perturbations or geothermal gradients. The spatio-temporal



Volcanic Eruptions: Stochastic Models of Occurrence Patterns, Figure 10

Location map of Taveuni (inset: Fiji group), with main villages, positions of Holocene mapped vents, and regions used for the spatial analysis. From [22], Figure 1, © Springer-Verlag 2001. With kind permission of Springer Science and Business Media

intensity (46) is used as an a priori intensity $P(x)$, and a likelihood function $L(\theta | x)$ is generated by conditioning the geophysical data θ on the locations of volcanic events. The a posteriori intensity can then be obtained from Bayes' theorem as

$$P(x | \theta) = \frac{P(x)L(\theta | x)}{\int_{y \in A} P(y)L(\theta | y)dy}, \quad (48)$$

where A is the volcanic field.

Markov Chains

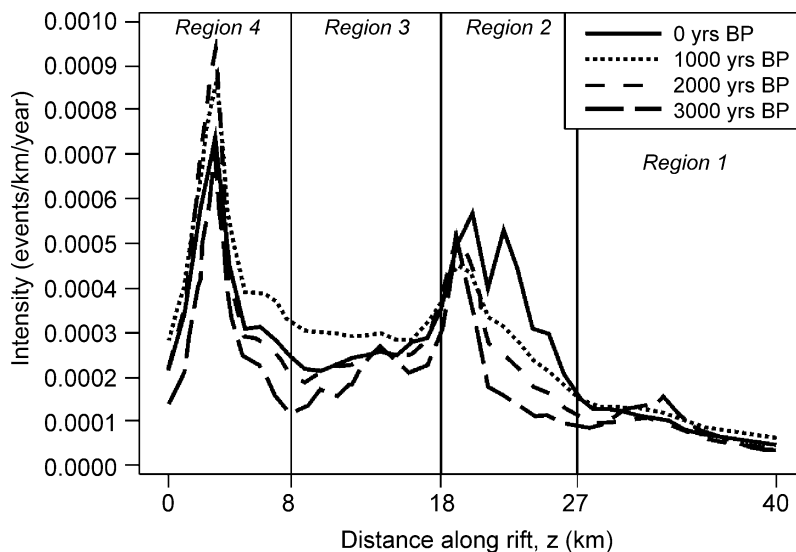
In the case where there is a geologically useful spatial classification, and sufficient data, a simple Markov chain approach can be used. If the i th eruption occurs in spatial region X_i , then the transition matrix is $P = (p_{jk})$, where $p_{jk} = \Pr(X_{i+1} = k | X_i = j)$. The maximum likelihood estimates are $\hat{p}_{jk} = N_{jk} / \sum_l N_{jl}$, where N_{jk} is the number of transitions from j to k observed in the data. The Markov chain can be tested against a null hypothesis of independence using the statistic

$$\chi^2 = 2 \sum_j \sum_k N_{jk} \log \left[\frac{N_{jk} / \sum_l N_{jl}}{\sum_l N_{lk} / \sum_l \sum_m N_{lm}} \right], \quad (49)$$

which asymptotically has a χ^2 distribution with K^2 degrees of freedom, where K is the number of states. Cronin et al. [22] used this approach, made feasible by the essentially linear rift formation shown in Fig. 10, to estimate the hazard at the heavily populated south-west end of Taveuni,

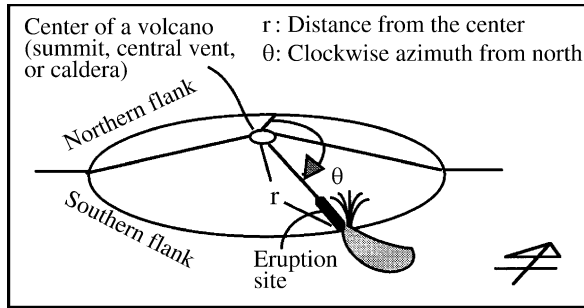
Fiji. This was combined (cf. Eq. (47)) with a hierarchical renewal model for the temporal aspect to provide an alternative to the spatio-temporal hazard estimate from (44) shown in Fig. 11. Eliasson et al. [30] likewise divided the Katla caldera, Iceland, into three sectors to examine the spatial progression of volcanogenic flood events.

In the same vein, a few studies have considered possible correlations between multiple vents on the same volcano. Klein [46] showed using a runs test that eruptions and intrusions at Kilauea tend to cluster in time, and that intrusions occur in place of eruptions during long repose. By dividing Kilauea repose into summit-summit, summit-flank, flank-summit and flank-flank pairs, and finding that their distributions did not differ statistically, Klein [46] showed that the location of the previous event provided no information about the time of the next eruption. At Mauna Loa, however, repose following flank eruptions were significantly longer than those following summit eruptions, consistent with the fact that the former are generally more voluminous than the latter. Examination of the sequences of summit and flank eruptions disclosed that Kilauea summit eruptions tend to occur in runs, due solely to the long summit sequence of 1924–1954, while Mauna Loa displays no tendency for clustering or alternation of summit and flank eruptions. However, Lockwood [49], in an analysis of 170 well-dated prehistoric lava flows from Mauna Loa, identifies cycling between summit overflows and flank eruptions with a periodicity of about 2000 years.



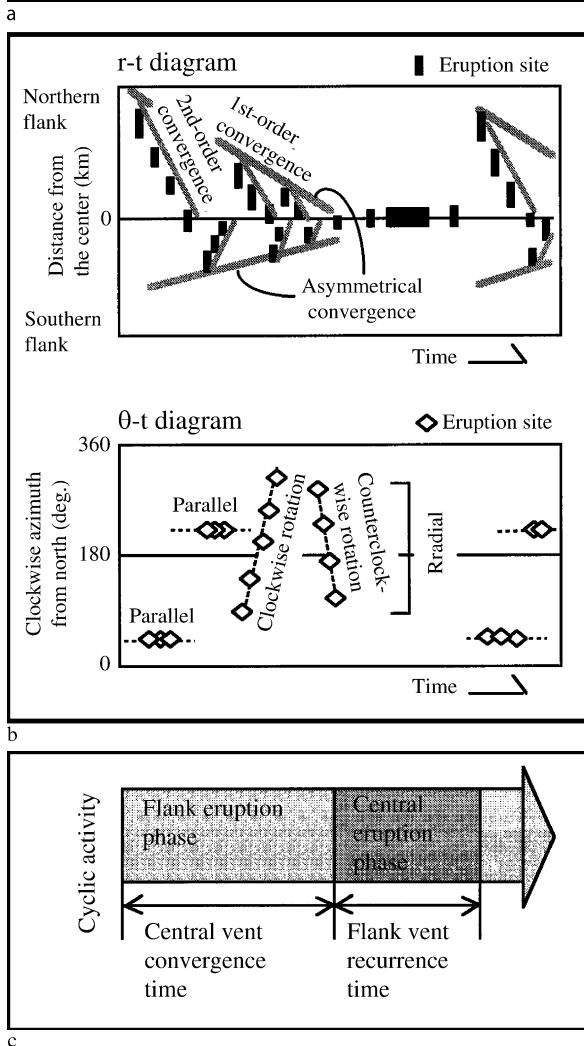
Volcanic Eruptions: Stochastic Models of Occurrence Patterns, Figure 11

Plot of spatio-temporal intensities (events/km year⁻¹) over the length of the Taveuni rift zone and at different times between 3000 B.P. and the present. From [22], Figure 8, © Springer-Verlag 2001. With kind permission of Springer Science and Business Media

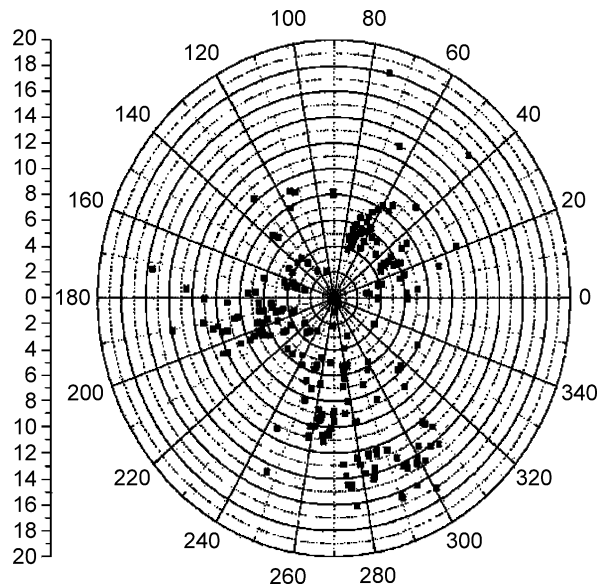


◀ Volcanic Eruptions: Stochastic Models of Occurrence Patterns, Figure 12

a Parameters representing the position of an eruption site. The flank of a volcano is divided into two regions, e.g., the northern flank and the southern one. **b** Two types of time-series diagram for eruption sites, representing the distance of eruption sites from the center (r - t diagram) and the clockwise azimuth from the north (θ - t diagram), respectively. **c** Schematic cyclic activity consisting of flank eruption and central eruption phases From [90], Figure 1, © Springer-Verlag 1997. With kind permission of Springer Science and Business Media



Takada [90] proposed using time-series plots, as shown in Fig. 12, to visually express the temporal relationship between flank and summit eruptions, in particular plots of flank-vent distance and direction from the central vent. Central eruption phases, defined as periods where at least 70% of eruptions are central vent eruptions without accompanying flank eruptions, alternate with flank erup-



Volcanic Eruptions: Stochastic Models of Occurrence Patterns, Figure 13

Azimuthal distribution of cones of lateral eruption on Etna. The center is located on "La Voragine" central crater. The scale on the left is in km from the center. Reprinted from [73], © 2006 Elsevier B.V., with permission from Elsevier

tion phases. Salvi et al. [73] considered the azimuth distribution of flank eruptions from Mount Etna, as in Fig. 13, determining that there is no significant difference in the pre- and post-1536 distributions.

Klein [46] also examined the relation between activity at the nearby volcanoes of Kilauea and Mauna Loa. Separating the record into three parts at the longest repose of each volcano disclosed that the activities were inversely related. The rank correlation of the number of events in five year periods 1915–1980 was -0.646 , significant at a level of 0.01, which indicates that they share the same magma source. Bebbington and Lai [5] repeated this analysis for the New Zealand volcanoes Ruapehu and Ngauruhoe, finding that the combined eruption sequence was indistinguishable from a superposition of indepen-

dent Poisson processes. This independence of the eruption sequences argues for separate magma sources.

Alignments and Clusters

There has also been considerable interest in detecting alignments or clusters of volcanic vents, in the hope that these can be related to geological features.

Lutz [50] proposed the ‘two-point azimuth method’, where the azimuth between every two vents is measured, generating $n(n-1)/2$ measurements for n vents. These are then binned in 10° intervals, although the bin size could vary, and the result tested for departure from randomness. As non-circular fields and/or a non-homogeneous density of points can produce a preferred orientation, a correction must be made in these cases. One way of doing this is to use Monte Carlo simulation of random points to produce a reference distribution from which departures can be detected. Lutz and Gutmann [51] noted that using kernel smoothing methods for the vent location provides an improved distribution from which to perform the Monte Carlo simulation.

Wadge and Cross [100] suggested the use of the Hough transform. In this technique, a point (x, y) is converted into the normal parameterization (ρ, θ) , where $\rho = x \cos \theta + y \sin \theta$. Thus each point generates a curve in the (ρ, θ) plane as θ varies, and multiple (more than two curves) intersections of these define the alignment of co-linear points. In practice the scales for ρ and θ are quantized into discrete bins, which allows for a small degree of departure from strict co-linearity. Significance levels can be obtained via Monte Carlo techniques.

Connor [15] suggested the use of uniform kernel density fusion cluster analysis, using the distance metric

$$d(i, j) = \begin{cases} \frac{1}{2} \left(\frac{1}{m_i(w)} + \frac{1}{m_j(w)} \right), & \|x_i - x_j\| < w \\ \infty, & \text{otherwise,} \end{cases} \quad (50)$$

where $\|\cdot\|$ denotes map distance, and $m_i(w)$ is the number of cones within a circle of radius w centered on the i th vent. Cones are linked into clusters starting with the smallest values of d . Clusters are only combined if the ‘density fusion’ d between the clusters is greater than the maximum d between any two events within either cluster. This makes it possible to recognize overlapping clusters. The search radius w is determined experimentally.

Connor [15] and Connor et al. [16] used the two-point azimuth method, Hough transform and cluster analysis to map clusters of multiple cones with common alignments in the TransMexican volcanic belt and Springerville volcanic field (Arizona).

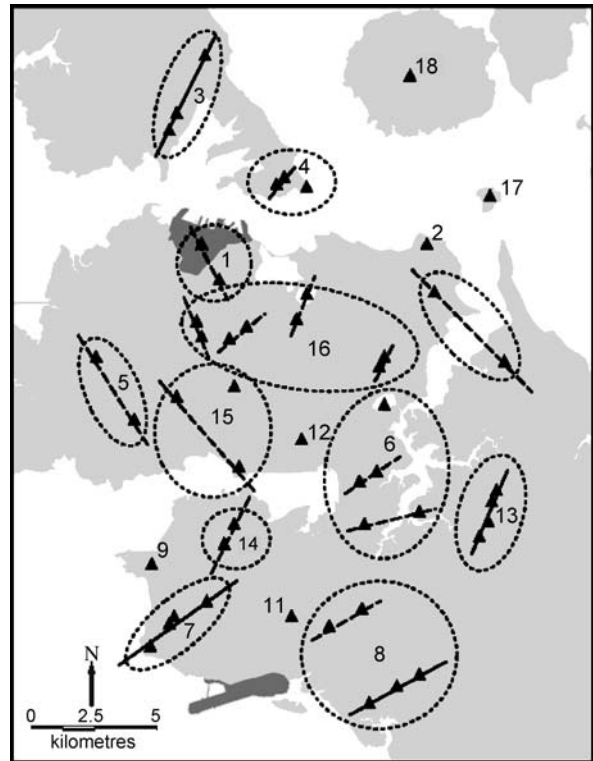
Magill et al. [52] measured vent clustering in the Auckland volcanic field using the statistic

$$L(d) = \sqrt{\frac{K(d)}{\pi}} - d, \quad (51)$$

where

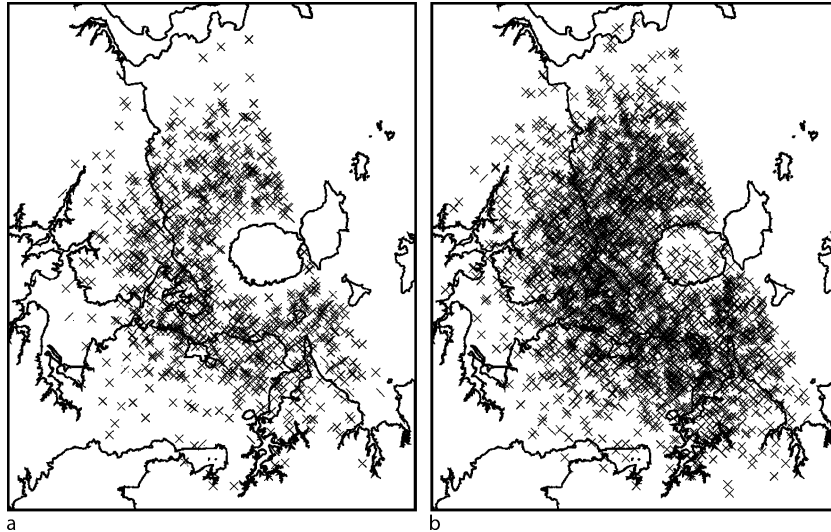
$$K(d) = \frac{A}{n} \sum_{j=1}^n \sum_{i \neq j} \frac{H(d - d_{ij})}{w_{ij}} \quad (52)$$

is Ripley’s K-function, A is the area of the field, d_{ij} is the distance between the i th and j th vents, $H(\cdot)$ is the Heaviside function, and w_{ij} is an edge correction. Peaks of positive $L(d)$ indicate clustering, and troughs of negative values regularity, at that distance. The Auckland field exhibits clustering at between 900 and 1600 m, and spatial regularity at about 4600 m. This clustering was used to collapse



Volcanic Eruptions: Stochastic Models of Occurrence Patterns, Figure 14

Groups and alignments of vents within the Auckland volcanic field, identified by position and age, and their relative order of eruption. Solid lines indicate alignments for which there are three or more vents. Dashed lines are alignments inferred from two vents. From [52], Figure 5, © 2005 International Association for Mathematical Geology. With kind permission of Springer Science and Business Media



Volcanic Eruptions: Stochastic Models of Occurrence Patterns, Figure 15

a event centroid locations, and **b** eruption locations for 1000 simulated events. From [52], Figure 8, © 2005 International Association for Mathematical Geology. With kind permission of Springer Science and Business Media

49 cones into 18 events. Magill et al. [52] then examined the distance separating consecutively erupted vents, and the distance between clustered eruptions, concluding that eruptions do not occur randomly, and occur preferentially closer to the previous eruption. Vent alignments in NE–SW and NW–SE directions were observed within clusters, as shown in Fig. 14. Using these observations, Magill et al. [52] constructed a Monte Carlo simulation model for the location of the next vent. Based on the last vent location (Rangitoto), the distance to the center of the next cluster was simulated from a distribution fitted to the observed distances. The number of vents was described by a negative binomial distribution, and vent locations were then simulated from a fitted distribution for the distance from the center of the cluster, modified by the observed alignment distribution, with the results shown in Fig. 15. Some 57% of the simulated eruption locations occur either on land, or within 1 km of the coast, rising to 69% if one considers the probability of at least one eruption from the next cluster falling within these limits.

Yucca Mountain

After Mount Etna, the next most studied volcano is probably the volcanic field at Yucca Mountain, Nevada (cf. Fig. 16), due to the high-level radioactive waste repository planned there. The available data [13] consists of a large number of basaltic volcanoes, of ages 80,000 years to 10,500,000 years. These of course have large dating er-

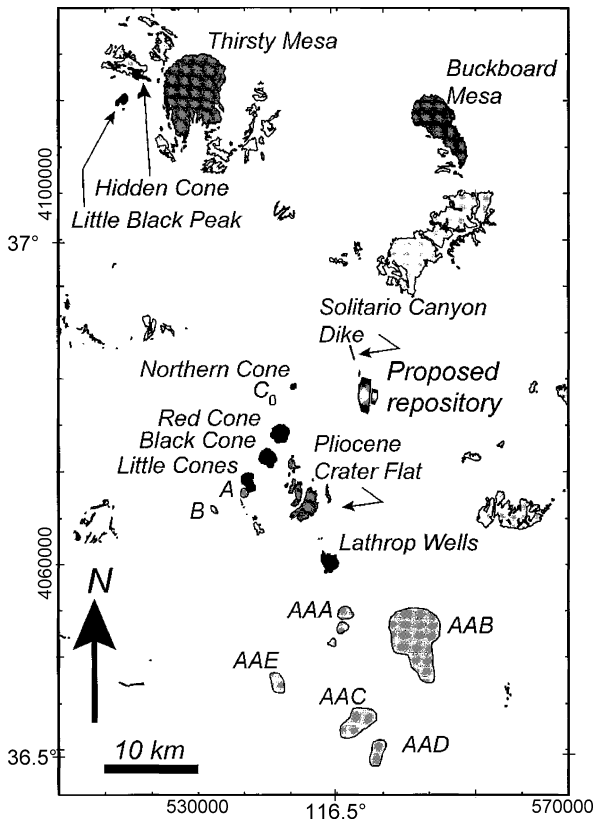
rors associated with them, but most analysis do not seem to have included this. The object is to estimate the probability of disruption of the repository by a volcanic intrusion. This is dependent on the probability of an intrusion, the distribution of the intrusion's dimensions, and on the dimensions of the repository itself.

The first analysis [23] used a Poisson process for the probability of an event, coupled with a Bernoulli probability of an event disrupting the repository:

$$\begin{aligned} \Pr(\text{no disruption before time } t) &= \sum_{n=0}^{\infty} \frac{(\lambda t)^n}{n!} (1-p)^n \\ &= e^{-\lambda t p}. \end{aligned} \quad (53)$$

The probability of an event being disruptive was estimated as $p = a/A$, where a is the area of the repository, and A the area, including the repository, used to define λ . The latter was estimated as N/T , where N is the number of scoria cones, and T the corresponding time period. Ho et al. [43] elaborated on means of estimating λ through event counts, repose intervals and magma volumes, and Ho [38] suggested a Bayesian framework for estimating p .

The next approach [38] attempted to incorporate a trend in the rate of volcanism using the Weibull process (4). As the data consisted of a number of clusters each containing several cones, but only the former had been dated, the event dates input to the Weibull process



Volcanic Eruptions: Stochastic Models of Occurrence Patterns, Figure 16

Distribution of basaltic rocks in the Yucca Mountain Region: *light gray shading*, Miocene; *dark gray shading*, Pliocene; *black shading*, Quaternary. Magnetic anomalies are shown in *light gray shading*, but only AAB is dated (Pliocene). Location is given in latitude/longitude, and in Universal Transverse Mercator (UTM) coordinate pairs (in meters). From [19], Figure 1b, © 2000 by the American Geophysical Union

consisted of multiples of each of a few dates. Depending on the details of the implementation, there was either a strong ($\beta > 2$) increasing trend, or no significant trend at all. Notably, Ho [38] used a homogeneous Poisson process, with rate equal to the fitted Weibull process intensity at the present, for future prediction, although a continuing Weibull process was one possibility considered in the sensitivity analysis [40]. Ho and Smith [41] combined the Weibull process and Bayesian estimation of p in a formulation allowing the incorporation of ‘expert knowledge’.

Sheridan [80] included a spatial element by fitting a bivariate Gaussian distribution with five parameters (the (x, y) coordinates of the center, the length of the major and minor axes, and their orientation) to the volcanic field

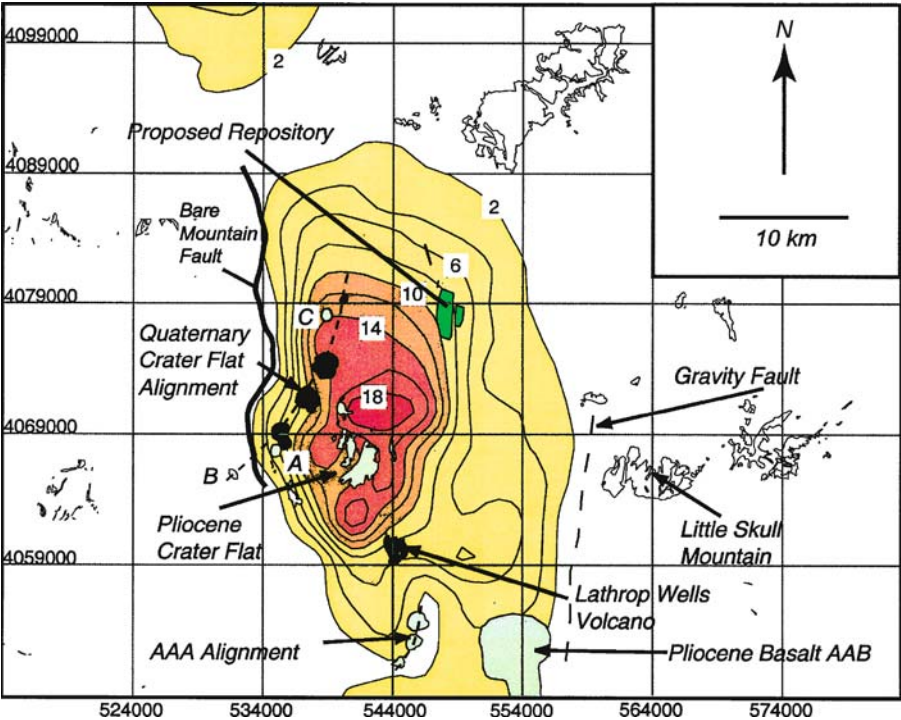
as a whole. Connor and Hill [17] used the spatio-temporal estimate (44), and integrated the resulting intensity over the area of the proposed repository, using a Gamma distribution for the area of a new volcano. The effects on the intensity of future events beyond the vicinity of the repository were ignored. Similar results were obtained using kernel-type estimators. Ho and Smith [42] elaborated on the latter by making the independent temporal component a Weibull process, while Connor et al. [19], while retaining the temporal Poisson process component, imposed a variety of geological constraints from crustal density, vent and fault alignments, and vent positions, on the spatial Gaussian kernel intensity in Fig. 17. A sensitivity analysis restricting the vent locations to various date-subsets was also conducted.

Crowe et al. [24], in their ‘final report’ of hazard studies at Yucca Mountain, summarized previous work, in particular that of Geomatrix Consultants [32]. They also fitted uniform, triangular (two varieties) and normal distributions to event count data, and simulated the results to obtain hazard estimates.

Smith et al. [85] suggested that the volcanism in the Yucca Mountain area could be episodic volcanism, and linked to an area of hot mantle. This would make possible another future peak of volcanism, with consequent underestimation of the recurrence rate. It was suggested that recurrence rates up to four times those previously used might be feasible. On the other hand, Coleman et al. [13] considered the lack of any detected dikes in or above the potential repository block, treating intrusions as an isolated Poisson process with zero observations in 13,000,000 years (although there was one ‘near-miss’). The conclusion was that high probabilities (10^{-6} per year) of disruption are ‘unrealistic’. Table 2 summarizes the published hazard estimates.

Interactions with Earthquakes

A common question is whether an eruption is related to a preceding large regional earthquake (or vice-versa). Stress changes from earthquakes resolved at dike locations tend to be small, in fact smaller than those associated with solid earth tides. The exception are those earthquakes within a few fault-lengths. However, small increments of stress may of course advance the occurrence of an already imminent eruption. On a longer scale, as both eruptions and earthquakes are tectonic in nature, they must be related. Any such correlation may provide additional information about the likelihood of an imminent eruption which may be caused, or at least ‘detected’, by seismic activity. Alternatively, one might be interested in the likeli-



Volcanic Eruptions: Stochastic Models of Occurrence Patterns, Figure 17

The spatial recurrence rate (volcanic events/km²) contoured for the Yucca Mountain Region, based on the distribution of Quaternary volcanism and its relationship to the Bare Mountain Fault. The contour interval is 2×10^{-4} volcanic events/km². Location is given in Universal Transverse Mercator (UTM) coordinate pairs (in meters). From [19], Plate 2, © 2000 by the American Geophysical Union

Volcanic Eruptions: Stochastic Models of Occurrence Patterns, Table 2

Summary of hazard assessment for Yucca Mountain

Source	Estimation Method		Probability of disruption in 10 ⁵ years
	Temporal	Spatial	
Crowe et al. [23]	Poisson process	$p = a/A$	10^{-5} to 10^{-3}
Ho et al. [43]	Poisson process	$\langle p \rangle$	$0.5p$
Sheridan [80]	$\langle \lambda \rangle$	bivariate Gaussian	$6\lambda \times 10^{-3}$ to $1.7\lambda \times 10^{-2}$
Ho [38]	Weibull (past)/ Poisson (future) process	Bayesian	10^{-3} to 7×10^{-3} (10 ⁴ years)
Ho [40]	Weibull process	Bayesian	2×10^{-5} to 7×10^{-3}
Connor and Hill [17]	Spatio-temporal		10^{-4} to 5×10^{-4} (10 ⁴ years)
Connor and Hill [17]	Poisson process	Kernel	10^{-4} to 5×10^{-4} (10 ⁴ years)
Geomatrix [32]	Expert Panel: Various		5×10^{-5} to 5×10^{-3}
Ho and Smith [41]	Weibull process	Bayesian	10^{-3} to 3×10^2
Crowe et al. [24]	Summary: Various		7×10^{-5} to 4×10^{-3}
Ho and Smith [42]	Weibull process	Kernel	10^{-4} to 6×10^{-4}
Connor et al. [19]	Weighted spatio-temporal		10^{-3} to 10^{-2}
Coleman et al. [13]	Poisson process		10^{-3} to 10^{-2}

hood of potentially dangerous earthquakes during a period of volcanic activity.

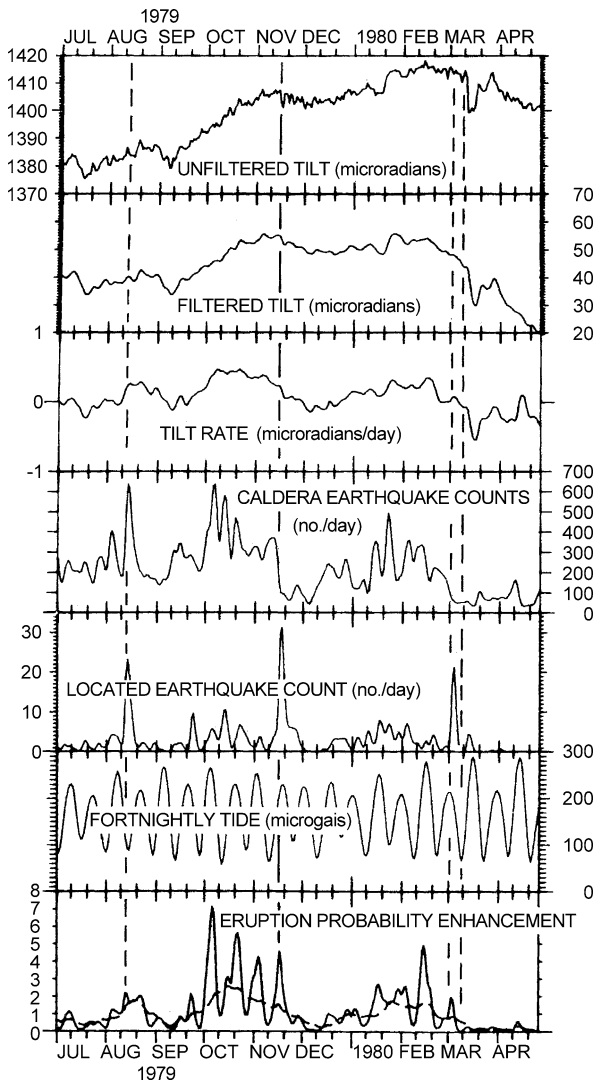
Sharp et al. [79] considered the relationship between eruptions of Mount Etna and earthquakes from various

structural zones of southern Italy. Both the earthquakes and eruption onsets were treated as Poisson processes, an assumption that had to be tested, with intensities λ_a and λ_b , respectively. A variable $\xi(t)$ is formed by summing

the number of A-series events in the intervals $(B_i, B_i + t)$, where (B_i) are the observed times of the B-series events. If the two series are independent, then $\xi(t)$ should have a Poisson distribution with mean $\hat{\lambda} = \hat{\lambda}_a \hat{\lambda}_b T$, where T is the length of the observation period, and $\hat{\lambda}_i = N_i(T)/T$, for $i = a, b$. For example, if B-series events consistently lead A-series events by some interval less than t , ξ will be significantly larger than $\hat{\lambda}$. The significance of an observed $\xi(t)$, or confidence limits, can be obtained from the null distribution, which is Poisson with mean $\hat{\lambda}$. Repeating the procedure for varying t identifies significant correlations. Sharp et al. [79] found that the earthquakes were not Poissonian, but could be represented as a non-stationary Poisson process. A significant relationship was found between local earthquakes and subsequent flank eruptions within a few hundred days. Also, summit eruptions were found to occur before flank eruptions not preceded by earthquakes, but the summit eruptions themselves were not correlated with earthquakes. This suggests two mechanisms for flank eruptions of Etna: Those preceded by summit eruptions may be caused by magma pressure in the reservoir, while those preceded by earthquakes may be due to fracturing of the flank by earthquakes caused by tensile forces associated with the east-west extension of eastern Sicily.

Klein [47] examined various precursors of volcanic eruptions at Kilauea by examining the ratio of these precursors preceding an eruption to their long-term average value. The candidates included summit tilt, daily counts of small caldera earthquakes, repose since the last eruption, earth tides, and rainfall, as shown in Fig. 18. The number of caldera earthquakes was highly significant as a short-term (10 days or less) predictor, but tilt rate was a better predictor beyond 20 days. The fortnightly earth tidal modulation was also significant (cf. [54]), as it appears to trigger a volcano that is nearly ready to erupt anyway. Similarly, Mulargia et al. [66] used a statistical non-parametric pattern-recognition algorithm to examine possible precursors of eruptions at Mount Etna 1974–1990, including the number of earthquakes in five surrounding tectonic regions, and their maximum magnitude. An eighty day interval straddling the eruption onset was considered, and the pattern of 12 factors in each interval noted. The only statistically significant result was that flank eruptions were linked to seismicity with more than six earthquakes in the surrounding regions during the 80 day period. All 11 of the flank eruptions considered satisfied this condition, but only 11 out of 24 (in a total of 62) windows with this level of seismicity corresponded to earthquakes. Summit eruptions possessed no discernable pattern.

Mulargia [64] used the intensity cross product for two series of events at times $0 < s_1 < \dots < s_{M(T)} < T$ and



Volcanic Eruptions: Stochastic Models of Occurrence Patterns, Figure 18

Kilauea volcano: Several parameters and eruption probability enhancement at an expanded time scale. The figure spans 10 months during 1979–1980 and includes the November 16, 1979, eruption (solid vertical line), and intrusions on August 12, 1979, and March 2 and 10, 1980 (dashed vertical lines). Intrusions, like eruptions, are generally accompanied by summit deflation, an earthquake swarm and harmonic tremor, but magma fails to reach the surface. The eruption probability enhancement is plotted as a 1-day outlook (solid line) and 30-day outlook (dashed line). The 1-day probability depends on the fortnightly tide and oscillates with it. The 30-day probability is a function of smoothed tilt and earthquake parameters and does not depend on the tide. Note that eruption probability enhancement was higher than average (greater than 1) for about 2 months prior to the November 1979 eruption and March 1980 intrusions. From [47], Figure 4 © 1984 by the American Geophysical Union

$0 < t_1 < \dots < t_{N(T)} < T$. For a lag u , this is estimated by

$$\hat{p}_{MN}(u) = \frac{n(u, h)}{2hT}, \quad (54)$$

where $n(u, h) = \#\{i: t_j + u - h \leq s_i \leq t_j + u + h, \text{ for some } j\}$ is the number of events from the process M that occur within a window of length $2h$ of the lag of a point in the process N . Under a null hypothesis of two independent Poisson processes, the significance level can be calculated as

$$P = \sum_{k=n(u, h)}^{N(T)} \binom{k}{N(T)} \left(\frac{2hM(T)}{T} \right)^k. \quad (55)$$

This was applied to the flank eruptive activity and local seismicity at Mt Etna 1974–1990. The data consisted of 11 eruptions and 12 seismic sequences [31]. Using a window of length $2h = 10$ days, Mulargia [64] found a highly significant association peak at a lag u between -7 and 3 days. This indicates that local earthquakes and flank eruptions are largely concomitant phenomena.

Marzocchi et al. [58] examined the correlation between eruptions of Vesuvius and earthquakes of $M > 5.4$ in the southern Apennines, Calabrian Arc and Sicily, 1631–1944. The eruptions and earthquakes were binned into intervals of 1, 2, 3 and 4 years, and the Spearman rank correlation

$$\rho_{XY}(k) = \frac{\sum_{i=1}^m R(X_{i+k})R(Y_i) - m(m+1)^2/4}{\left(\sum_{i=1}^m R(X_{i+k})^2 - m(m+1)^2/4\right)^{1/2} \cdot \left(\sum_{i=1}^m R(Y_i)^2 - m(m+1)^2/4\right)^{1/2}} \quad (56)$$

calculated, where X_i, Y_i are the total seismic moment and number of eruptions in the i th time bin, $R(\cdot)$ is the rank, from smallest to largest, of the quantities, and k is the lag. Varying this lag produces the Spearman correlogram. Marzocchi et al. [58] observed changes in eruptive activity following increases in seismicity in the southern Apennines after 6–13 years, and with delays of 27–30 years and 36–39 years for earthquakes in Sicily and the Calabrian arc, respectively. Nostro et al. [70] investigated this coupling (cf. Fig. 19) in terms of the Coulomb stress change on a magma body beneath Vesuvius caused by a slip on Apennine normal faults (promoting eruptions by earthquakes) and on fault planes caused by voiding a buried magma body (promoting earthquakes by eruptions), as shown in Fig. 20. Using these results to select earthquakes and eruptions improved the significance of the Marzocchi et al. [58] analysis.

Cardaci et al. [10] used a cross-correlation technique to investigate the relation between seismic and volcanic data

at Mount Etna 1975–1987. The seismic and eruptive data were averaged over seven day intervals, with the cross-correlation being

$$\rho_{XY}(k) = \frac{\sigma_{XY}(k)}{\sqrt{\sigma_X^2 \sigma_Y^2}} \quad (57)$$

for $k = 0, \pm 1, \dots, \pm K$, where

$$\sigma_{XY}(k) = \begin{cases} (1/n) \sum_{i=1}^{n-k} (X_i - \mu_X)(Y_{i+k} - \mu_Y) & k = 0, 1, \dots, K \\ (1/n) \sum_{i=1-k}^n (X_i - \mu_X)(Y_{i+k} - \mu_Y) & k = -1, \dots, -K \end{cases} \quad (58)$$

is the cross covariance function and μ_X, μ_Y and σ_X^2, σ_Y^2 are the means and variances, respectively, of the two time series X_1, \dots, X_n and Y_1, \dots, Y_n . The significance of the cross-correlation can be assessed from the fact that $\rho_{XY}(k) \sqrt{(m-2)/(1-\rho_{XY}(k))}$, is asymptotically distributed as a t -distribution with $m-2$ degrees of freedom, where m is the number of overlapped positions between the two series. Cardaci et al. [10] arrived at a similar conclusion to Mulargia et al. [66], identifying low frequency events, whose rate of occurrence increases from 17 to 108 days prior to flank eruptions, as the best precursor. Summit events had a less clear relation with volcanic tremor rather than seismic activity.

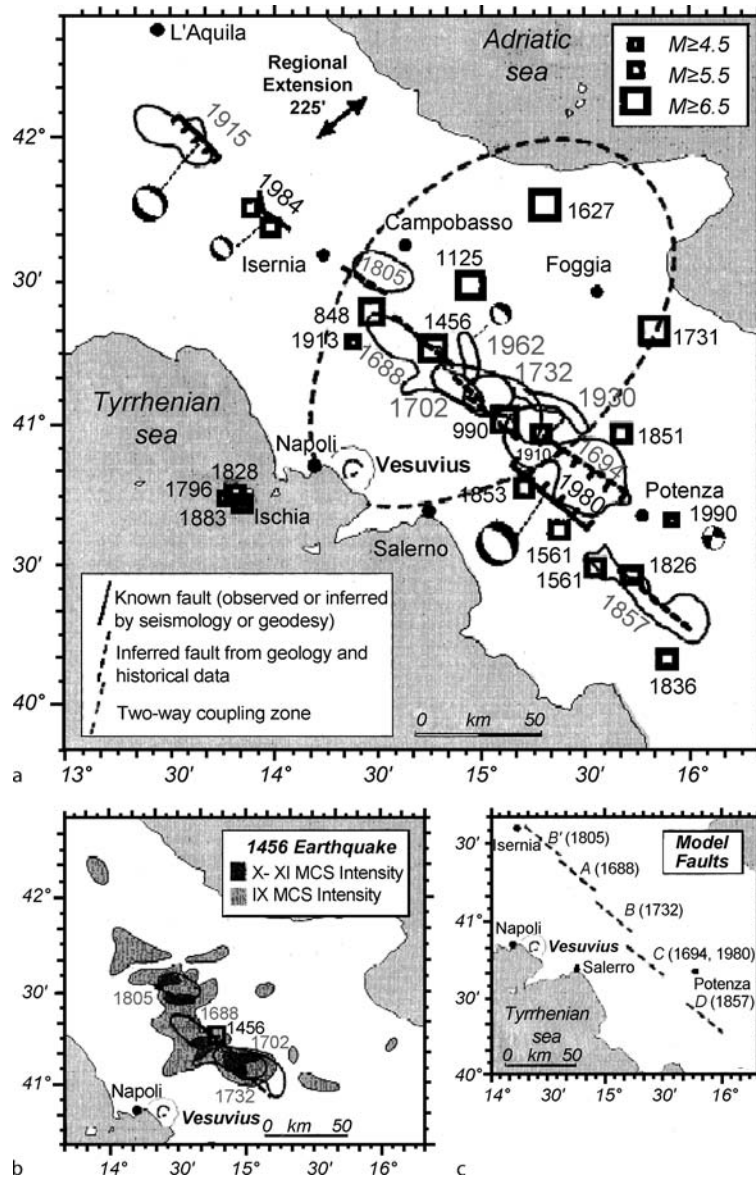
Linde and Sacks [48] examined the historical record of eruptions ($\text{VEI} \geq 2$) and large earthquakes, to see whether there are more of the former within two days of the latter. For earthquakes with ($M \geq 8$), there are a significant excess of eruptions within 750 km of the epicenter, while for earthquakes with $7.0 \leq M \leq 7.9$, the effect is only observed within a radius of 200 km. In all, 20 such earthquake-volcano pairs are observed 1587–1974. In addition, Linde and Sacks [48] hypothesized that eruptions in unison of volcanoes separated by hundreds of kilometers could be due to the second eruption being triggered by earthquakes associated with the first. Marzocchi [56] elaborated on this analysis by defining a perturbation function

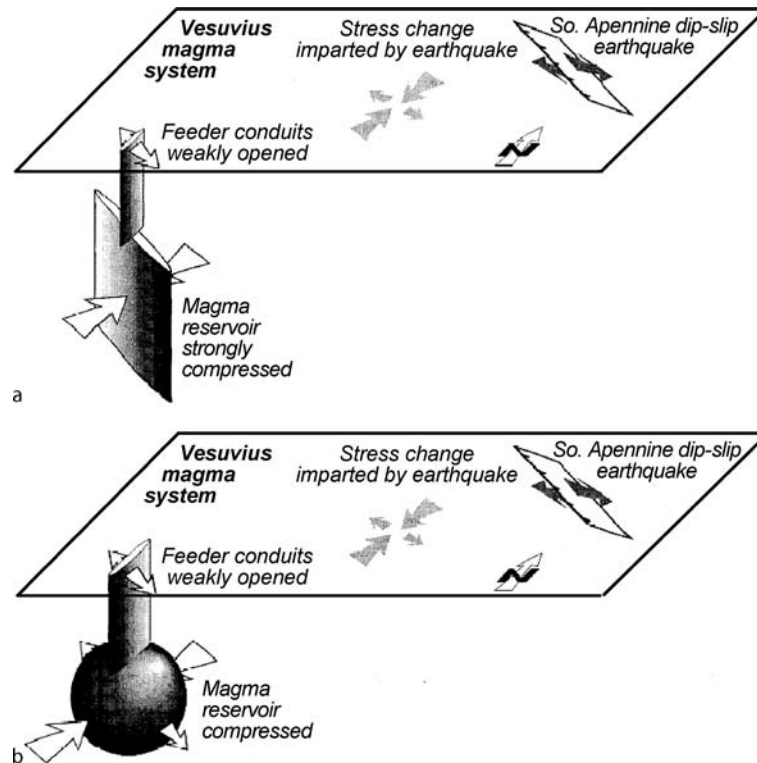
$$\phi_i^{(k)}(\Delta) = \sum_j M_j w(d_{jk}) \mathbf{I}_{((i-1)\Delta, i\Delta)}(t_k - s_j), \quad (59)$$

where

$$\mathbf{I}_A(x) = \begin{cases} 1 & x \in A \\ 0 & x \notin A \end{cases} \quad (60)$$

is the indicator function, s_j and M_j are the time and seismic moment of the j th earthquake, t_k is the onset time of





Volcanic Eruptions: Stochastic Models of Occurrence Patterns, Figure 20

Schematic illustration of the response of a hypothetical Vesuvius magmatic system to a southern Apennine normal-faulting earthquake for (a) a buried dike in which at least one fissure or feeder conduit strikes NE and (b) a buried spherical magma chamber with a NE striking fissure. From [70], Figure 3 © 1998 by the American Geophysical Union

the 62 20th Century eruptions with $VEI \geq 4$, identifying peaks at 0–5 and 20–35 years. The perturbations for $VEI \geq 4$ eruptions were shown to be significantly larger than those for $VEI = 1$ and $VEI = 2$ eruptions. This suggests that the likelihood of large explosive eruptions is affected by post-seismic stress variations induced by large earthquakes up to decades earlier and hundreds of km distant. No spatio-temporal clustering of the earthquakes and eruptions was detected.

Future Directions

There are two places in the above review where the effect of a second process on the likelihood of eruptions has been identified, but an appropriate model incorporating this is lacking. These are deterministic (fortnightly and/or annual) cycles in the intensity, and correlation between eruptions and large earthquakes. A candidate to model the first is a cyclic Poisson process [97], and the second could be examined via a bivariate Point process, or perhaps a non-homogeneous hidden Markov model.

More generally, much of the relevant literature on stochastic processes has not been applied to problems in volcanology. In particular, (marked) point processes, alternating renewal processes, and semi-Markov processes would seem to be natural candidates for modeling volcanic activity. A number of techniques from time series analysis (see [106] for a brief review) may prove useful for the investigation of volcanic data at various time scales.

In the application of stochastic models, and the understanding to be gleaned from them, volcanology lags well behind seismology. This is despite the inherent advantages of a phenomenon in which spatial degrees of freedom can often be ignored. An obvious future direction is the borrowing of more techniques from seismology. Unlike seismology, a certain amount of effort (and money) can often produce additional data through coring and dating. This is a great advantage in statistical terms, especially as the data can be 'targeted' to some degree as required by the model. This additional data makes it possible in volcanology to detect, and forecast, non-stationary behavior, and to relate this to physical changes in the volcano [95].

Although this article has concentrated on models for occurrence patterns, actual volcanic hazard is dependent on the nature and behavior of volcanic products such as lava, ash fall, lahars and pyroclastic flows. Incorporating existing sophisticated numerical models of such behavior with stochastic models of occurrence, location/direction and magnitude will allow more accurate estimation of the hazard to life and property.

Bibliography

Primary Literature

- Bacon CR (1982) Time-predictable bimodal volcanism in the Coso range, California. *Geology* 10:65–69
- Bain LJ (1978) *Statistical Analysis of Reliability and Life Testing Models*. Marcel Dekker, New York
- Bebbington MS (2007) Identifying volcanic regimes using hidden Markov models. *Geophys J Int*, 171:921–942
- Bebbington MS, Lai CD (1996) On nonhomogeneous models for volcanic eruptions. *Math Geol* 28:585–600
- Bebbington MS, Lai CD (1996) Statistical analysis of New Zealand volcanic occurrence data. *J Volcanol Geotherm Res* 74:101–110
- Bebbington MS, Lai CD (1998) A generalised negative binomial and applications. *Commun Statist Theor Methods* 27:2515–2533
- Behncke B, Neri M (2003) Cycles and trends in the recent eruptive behaviour of Mount Etna (Italy). *Canadian J Earth Sci* 40:1405–1411
- Bronk Ramsey C (1995) Radiocarbon calibration and analysis of stratigraphy: The OxCal program. *Radiocarbon* 37:425–430
- Burt ML, Wadge G, Scott WA (1994) Simple stochastic modelling of the eruption history of a basaltic volcano: Nyamuragira, Zaire. *Bull Volcanol* 56:87–97
- Cardaci C, Falsaperla S, Gasperini P, Lombardo G, Marzocchi W, Mulargia F (1993) Cross-correlation analysis of seismic and volcanic data at Mt Etna volcano, Italy. *Bull Volcanol* 55: 596–603
- Carta S, Figari R, Sartoris G, Sassi R, Scandone R (1981) A statistical model for Vesuvius and its volcanological implications. *Bull Volcanol* 44:129–151
- Casetti G, Frazzetta G, Romano R (1981) A statistical analysis in time of the eruptive events on Mount Etna (Italy) from 1323 to 1980. *J Volcanol Geotherm Res* 44:283–294
- Coleman NM, Abramson LR, Marsh BD (2004) Testing claims about volcanic disruption of a potential geologic repository at Yucca Mountain, Nevada. *Geophys Res Lett* 31:L24601
- Condit CD, Connor CB (1996) Recurrence rates of volcanism in basaltic volcanic fields: an example from the Springerville volcanic field, Arizona. *Geol Soc Am Bull* 108:1225–1241
- Connor CB (1990) Cinder cone clustering in the TransMexican volcanic belt: Implications for structural and petrologic models. *J Geophys Res* 95:19395–19405
- Connor CB, Condit CD, Crumpler LS, Aubele JC (1992) Evidence of regional structural controls on vent distribution: Springerville volcanic field, Arizona. *J Geophys Res* 97: 349–359
- Connor CB, Hill BE (1995) Three nonhomogeneous Poisson models for the probability of basaltic volcanism: application to the Yucca Mountain region, Nevada. *J Geophys Res* 100:10107–10125
- Connor CB, Sparks RSJ, Mason RM, Bonadonna C, Young SR (2003) Exploring links between physical and probabilistic models of volcanic eruptions: The Soufriere Hills volcano, Montserrat. *Geophys Res Lett* 30:1701
- Connor CB, Stamatakis JA, Ferrill DA, Hill BE, Ofoegbu GI, Conway FM, Sagar B, Trapp J (2000) Geologic factors controlling patterns of small-volume basaltic volcanism: Application to a volcanic hazards assessment at Yucca Mountain, Nevada. *J Geophys Res* 105:417–432
- Conway FM, Connor CB, Hill BE, Condit CD, Mullaney K, Hall CM (1998) Recurrence rates of basaltic volcanism in SP cluster, San Francisco volcanic field, Arizona. *Geology* 26:655–658
- Crandell DR, Mullineaux DR, Rubin M (1975) Mount St. Helens volcano: Recent and future behaviour. *Science* 187:438–441
- Cronin S, Bebbington M, Lai CD (2001) A probabilistic assessment of eruption recurrence on Taveuni volcano, Fiji. *Bull Volcanol* 63:274–288
- Crowe BM, Johnson ME, Beckman RJ (1982) Calculation of the probability of volcanic disruption of a high-level radioactive waste repository within southern Nevada, USA. *Radioact Waste Manag* 3:167–190
- Crowe BM, Wallmann P, Bowker LM (1998) Probabilistic modeling of volcanism data: Final volcanic hazard studies for the Yucca Mountain site. In: Perry FV et al. (eds) *Volcanism Studies: Final Report for the Yucca Mountain project*. Los Alamos National Laboratory Report LA-13478, Los Alamos National Laboratory, Los Alamos, 415 pp
- Decker RW (1986) Forecasting volcanic eruptions. *Ann Rev Earth Planet Sci* 14:267–291
- De la Cruz-Reyna S (1991) Poisson-distributed patterns of explosive eruptive activity. *Bull Volcanol* 54:57–67
- De la Cruz-Reyna S (1993) Random patterns of occurrence of explosive eruptions at Colima volcano, Mexico. *J Volcanol Geotherm Res* 55:51–68
- De la Cruz-Reyna S, Carrasco-Nunez G (2002) Probabilistic hazard analysis of Citlaltepetl (Pico de Orizaba) volcano, eastern Mexican volcanic belt. *J Volcanol Geotherm Res* 113: 307–318
- Dubois J, Cheminee JL (1991) Fractal analysis of eruptive activity of some basaltic volcanoes. *J Volcanol Geotherm Res* 45:197–208
- Eliasson J, Larsen G, Gudmundsson MT, Sigmundsson F (2006) Probabilistic model for eruptions and associated flood events in the Katla caldera, Iceland. *Comput Geosci* 10: 179–200
- Gasperini P, Gresta S, Mulargia F (1990) Statistical analysis of seismic and eruptive activities at Mt. Etna during 1978–1987. *J Volcanol Geotherm Res* 40:317–325
- Geomatrix Consultants (1996) Probabilistic volcanic hazard analysis for Yucca Mountain, Nevada. Report BA0000000-1717-220-00082. Geomatrix Consultants, San Francisco
- Godano C, Civetta L (1996) Multifractal analysis of Vesuvius volcano eruptions. *Geophys Res Lett* 23:1167–1170
- Gusev AA, Ponomareva VV, Braitseva OA, Melekestsev IV, Sulerzhitsky LD (2003) Great explosive eruptions on Kamchatka during the last 10,000 years: Self-similar irregularity of the output of volcanic products. *J Geophys Res* 108(B2):2126

35. Guttorp P, Thompson ML (1991) Estimating second-order parameters of volcanicity from historical data. *J Amer Statist Assoc* 86:578–583
36. Ho CH (1990) Bayesian analysis of volcanic eruptions. *J Volcanol Geotherm Res* 43:91–98
37. Ho CH (1991) Nonhomogeneous Poisson model for volcanic eruptions. *Math Geol* 23:167–173
38. Ho CH (1992) Risk assessment for the Yucca Mountain high-level nuclear waste repository site: Estimation of volcanic disruption. *Math Geol* 24:347–364
39. Ho CH (1992) Statistical control chart for regime identification in volcanic time-series. *Math Geol* 24:775–787
40. Ho CH (1995) Sensitivity in volcanic hazard assessment for the Yucca Mountain high-level nuclear waste repository site: The model and the data. *Math Geol* 27:239–258
41. Ho CH, Smith EI (1997) Volcanic hazard assessment incorporating expert knowledge: application to the Yucca Mountain region, Nevada, USA. *Math Geol* 29:615–627
42. Ho CH, Smith EI (1998) A spatial-temporal/3-D model for volcanic hazard assessment: application to the Yucca Mountain region, Nevada. *Math Geol* 30:497–510
43. Ho CH, Smith EI, Feuerbach DL, Naumann TR (1991) Eruptive probability calculation for the Yucca Mountain site, USA: Statistical estimation of recurrence rates. *Bull Volcanol* 54:50–56
44. Jaquet O, Low S, Martinelli B, Dietrich V, Gilby D (2000) Estimation of volcanic hazards based on Cox stochastic processes. *Phys Chem Earth (A)* 25:571–579
45. Jupp TE, Pyle DM, Mason BG, Dade WB (2004) A statistical model for the timing of earthquakes and volcanic eruptions influenced by periodic processes. *J Geophys Res* 109:B02206
46. Klein FW (1982) Patterns of historical eruptions at Hawaiian volcanoes. *J Volcanol Geotherm Res* 12:1–35
47. Klein FW (1984) Eruption forecasting at Kilauea Volcano, Hawaii. *J Geophys Res* 89:3059–3073
48. Linde AT, Sacks IS (1998) Triggering of volcanic eruptions. *Nature* 395:888–890
49. Lockwood JP (1995) Mauna Loa eruptive history – the preliminary radiocarbon record, Hawai'i. In: Rhodes JM, Lockwood JP (eds) *Mauna Loa Revealed: Structure, Composition, History, and Hazards*. American Geophysical Union Monograph, vol 92. American Geophysical Union, Washington DC, pp 81–94
50. Lutz TM (1986) An analysis of the orientation of large-scale crustal structures: A statistical approach based on areal distributions of pointlike features. *J Geophys Res* 91:421–434
51. Lutz TM, Gutmann JT (1995) An improved method for determining and characterizing alignments of pointlike features and its implications for the Pinacate volcanic field, Sonora, Mexico. *J Geophys Res* 100:17659–17670
52. Magill CR, McAneney KJ, Smith IEM (2005) Probabilistic assessment of vent locations for the next Auckland volcanic field event. *Math Geol* 37:227–242
53. Martin AJ, Umeda K, Connor CB, Weller JN, Zhao D, Takahashi M (2004) Modeling long-term volcanic hazards through Bayesian inference: An example from the Tohoku volcanic arc, Japan. *J Geophys Res* 109:B10208
54. Martin DP, Rose WI (1981) Behavioral patterns of Fuego volcano, Guatemala. *J Volcanol Geotherm Res* 10:67–81
55. Marzocchi W (1996) Chaos and stochasticity in volcanic eruptions the case of Mount Etna and Vesuvius. *J Volcanol Geotherm Res* 70:205–212
56. Marzocchi W (2002) Remote seismic influence on large explosive eruptions. *J Geophys Res* 107:2018. doi:10.1029/2001JB000307
57. Marzocchi W, Sandri L, Gasparini P, Newhall C, Boschi E (2004) Quantifying probabilities of volcanic events: The example of volcanic hazard at Mount Vesuvius. *J Geophys Res* 109:B11201
58. Marzocchi W, Scandone R, Mulargia F (1993) The tectonic setting of Mount Vesuvius and the correlation between its eruptions and the earthquakes of the southern Apennines. *J Volcanol Geotherm Res* 58:27–41
59. Marzocchi W, Zaccarelli L (2006) A quantitative model for the time-size distribution of eruptions. *J Geophys Res* 111: B04204
60. Marzocchi W, Zaccarelli L, Boschi E (2004) Phenomenological evidence in favor of a remote seismic coupling for large volcanic eruptions. *Geophys Res Lett* 31:L04601
61. Mason BG, Pyle DM, Dade WB, Jupp T (2004) Seasonality of volcanic eruptions. *J Geophys Res* 109:B04206
62. Mauk FJ, Johnston MJS (1973) On the triggering of volcanic eruptions by earth tides. *J Geophys Res* 78:3356–3362
63. Medina Martinez F (1983) Analysis of the eruptive history of the Volcan de Colima, Mexico (1560–1980). *Geof Int* 22: 157–178
64. Mulargia F (1992) Time association between series of geophysical events. *Phys Earth Plan Int* 71:147–153
65. Mulargia F, Gasperini P, Tinti S (1987) Identifying regimes in eruptive activity: An application to Etna volcano. *J Volcanol Geotherm Res* 34:89–106
66. Mulargia F, Marzocchi W, Gasperini P (1992) Statistical identification of physical patterns which accompany eruptive activity on Mount Etna, Sicily. *J Volcanol Geotherm Res* 53: 289–296
67. Mulargia F, Tinti S, Boschi E (1985) A statistical analysis of flank eruptions on Etna volcano. *J Volcanol Geotherm Res* 23: 263–272
68. Newhall CG, Self S (1982) The volcanic explosivity index (VEI): An estimate of explosive magnitude for historical volcanism. *J Geophys Res* 87:1231–1238
69. Nishi Y, Inoue M, Tnaka T, Murai M (2001) Analysis of time sequences of explosive volcanic eruptions of Sakurajima. *J Phys Soc Japan* 70:1422–1428
70. Nostro C, Stein RS, Cocco M, Belardinelli ME, Marzocchi W (1998) Two-way coupling between Vesuvius eruptions and southern Apennine earthquakes, Italy, by elastic stress transfer. *J Geophys Res* 103:24487–24504
71. Pyle DM (1998) Forecasting sizes and repose times of future extreme volcanic events. *Geology* 26:367–370
72. Reymont RA (1969) Statistical analysis of some volcanologic data regarded as series of point events. *Pure Appl Geophys* 74:57–77
73. Salvi F, Scandone R, Palma C (2006) Statistical analysis of the historical activity of Mount Etna, aimed at the evaluation of volcanic hazard. *J Volcanol Geotherm Res* 154:159–168
74. Sandri L, Marzocchi W, Gasperini P (2005) Some insights on the occurrence of recent volcanic eruptions of Mount Etna volcano (Sicily, Italy). *Geophys J Int* 163:1203–1218
75. Santacroce R (1983) A general model for the behaviour of the Somma-Vesuvius volcanic complex. *J Volcanol Geotherm Res* 17:237–248
76. Scandone R, Arganese G, Galdi F (1993) The evaluation of

- volcanic risk in the Vesuvian area. *J Volcanol Geotherm Res* 58:263–271
77. Scandone R, Giacomelli L, Gasparini P (1993) Mount Vesuvius: 2000 years of volcanological observations. *J Volcanol Geotherm Res* 58:5–25
 78. Settle M, McGetchin TR (1980) Statistical analysis of persistent explosive activity at Stromboli, 1971: Implications for eruption prediction. *J Volcanol Geotherm Res* 8:45–58
 79. Sharp ADL, Lombardo G, David PM (1981) Correlation between eruptions of Mount Etna, Sicily, and regional earthquakes as seen in historical records from AD 1582. *Geophys J R astr Soc* 65:507–523
 80. Sheridan MF (1992) A Monte Carlo technique to estimate the probability of volcanic dikes. In: High-Level Radioactive Waste Management: Proceedings of the Third Annual International Conference, Las Vegas, April 12–16, 1992. American Nuclear Society, La Grange Park, pp 2033–2038
 81. Shimazaki K, Nakata T (1980) Time-predictable recurrence model for large earthquakes. *Geophys Res Lett* 7:279–282
 82. Siebert L, Simkin T (2002) Volcanoes of the World: an Illustrated Catalog of Holocene Volcanoes and their Eruptions, Smithsonian Institution, Global Volcanism Program Digital Information Series, GVP-3. <http://www.volcano.si.edu/world/>. Accessed 20 Jun 2008
 83. Simkin T (1993) Terrestrial volcanism in space and time. *Ann Rev Earth Planet Sci* 21:427–452
 84. Simkin T (1994) Distant effects of volcanism – how big and how often? *Science* 264:913–914
 85. Smith EI, Keenan DL, Plank T (2002) Episodic volcanism and hot mantle: Implications for volcanic hazard studies at the proposed nuclear waste repository at Yucca Mountain, Nevada. *GSA Today* April 2002:4–9
 86. Solow AR (1993) Estimating record inclusion probability. *The Amer Statist* 47:206–208
 87. Solow AR (2001) An empirical Bayes analysis of volcanic eruptions. *Math Geol* 33:95–102
 88. Sornette A, Dubois J, Cheminee JL, Sornette D (1991) Are sequences of volcanic eruptions deterministically chaotic? *J Geophys Res* 96:11931–11945
 89. Stothers RB (1989) Seasonal variations of volcanic eruption frequencies. *Geophys Res Lett* 16:453–455
 90. Takada A (1997) Cyclic flank-vent and central-vent eruption patterns. *Bull Volcanol* 58:539–556
 91. Telesca L, Cuomo V, Lapenna V, Macchiato M (2002) Time-clustering analysis of volcanic occurrence sequences. *Phys Earth Planet Int* 131:47–62
 92. Telesca L, Lapenna V (2005) Identifying features in time-occurrence sequences of volcanic eruptions. *Environmetrics* 16:181–190 58
 93. Thorlaksson JE (1967) A probability model of volcanoes and the probability of eruptions of Hekla and Katla. *Bull Volcanol* 31:97–106
 94. Turner M, Cronin S, Bebbington M, Platz T (2008) Developing a probabilistic eruption forecast for dormant volcanoes; a case study from Mt Taranaki, New Zealand. *Bull Volcanol* 70: 507–515
 95. Turner M, Cronin S, Smith I, Bebbington M, Stewart RB (2008) Using titanomagnetite textures to elucidate volcanic eruption histories. *Geology* 36:31–34
 96. Vere-Jones D (1992) Statistical methods for the description and display of earthquake catalogs. In: Walden AT, Guttorp P (eds) *Statistics in the Environmental and Earth Sciences*, Edward Arnold, London, pp 220–246
 97. Vere-Jones D, Ozaki T (1982) Some examples of statistical estimation applied to earthquake data. *Ann Inst Statist Math* 34:189–207
 98. Voight B (1988) A method for prediction of volcanic eruptions. *Nature* 332:125–130
 99. Wadge G (1982) Steady state volcanism: Evidence from eruption histories of polygenetic volcanoes. *J Geophys Res* 87:4035–4049
 100. Wadge G, Cross A (1988) Quantitative methods for detecting aligned points: An application to the volcanic vents of the Michoacan–Guanajuato volcanic field, Mexico. *Geology* 16: 815–818
 101. Wadge G, Guest JE (1981) Steady-state magma discharge at Etna 1971–1981. *Nature* 294:548–550
 102. Wadge G, Walker WPL, Guest JE (1975) The output of Etna volcano. *Nature* 255:385–387
 103. Wickman FE (1966) Repose-period patterns of volcanoes. I. Volcanic eruptions regarded as random phenomena. *Arch Mineral Geol* 4:291–367
 104. Wickman FE (1966) Repose-period patterns of volcanoes. V. General discussion and a tentative stochastic model. *Arch Mineral Geol* 4:351–367
 105. Wickman FE (1976) Markov models of repose-period patterns of volcanoes. In: Merriam DF (ed) *Random Processes in Geology*. Springer, New York, pp 135–161
 106. Young PC (2006) New approaches to volcanic time-series analysis. In: Mader HM, Coles SG, Connor CB, Connor LJ (eds) *Statistics in Volcanology*. Geological Society of London, London, pp 143–160

Books and Reviews

- Guttorp P (1995) *Stochastic Modeling of Scientific Data*, Chapman and Hall, London
- Hill DP, Pollitz FP, Newhall C (2002) Earthquake-volcano interactions. *Phys Today* 55:41–47
- Lindsay JK (2004) *Statistical Analysis of Stochastic Processes in Time*. Cambridge University Press, Cambridge
- Karr AF (1991) *Point Processes and Their Statistical Inference*, 2nd edn. Marcel Dekker, New York
- Mader HM, Coles SG, Connor CB, Connor LJ (eds) (2006) *Statistics in Volcanology*. Geological Society of London, London

Volcanic Hazards and Early Warning

ROBERT I. TILLING
Volcano Hazards Team, US Geological Survey,
Menlo Park, USA

Article Outline

Glossary
Definition of the Subject
Introduction
Scope of Problem:

Challenge for Emergency–Management Authorities
 Variability in Possible Outcomes of Volcano Unrest
 Some Recent Examples of Actual Outcomes
 of Volcano Unrest
 Challenges in Achieving Refined Predictive Capability
 Future Directions
 Acknowledgments
 Bibliography

Glossary

Volcano hazards Potentially damaging volcano-related processes and products that occur during or following eruptions [see [31,37] for overviews]. In quantitative hazards assessments, the probability of a given area being affected by potentially destructive phenomena within a given period of time.

Volcano risk Probability of harmful consequences – individual or societal – or expected losses (deaths, injuries, property, livelihoods, economic activity disrupted or environment damaged) resulting from interactions between volcano hazards, human development, and vulnerable conditions. Though definitions vary in detail, risk is conventionally expressed by the general relation: $risk = hazards \times vulnerability$ [13].

Vulnerability The conditions determined by physical, social, economic, and environmental factors or processes, which increase the susceptibility of a community to the impact of hazards [13].

Volcano status The current activity or mode of behavior of a volcano. Status is commonly described as follows: *active* (having one or more recorded historical eruptions); *dormant* (currently inactive but having potential for renewed eruptive activity); and *extinct* (dormant for long time and not expected to erupt again). These terms, while commonly used in the scientific literature, are imperfect and are undergoing serious reexamination within the global volcanological community.

Factual statement Following the recommended definition of Swanson et al. [35], is the description of the current status and conditions of a volcano but does not anticipate future events.

Forecast As defined by Swanson et al. [35], is a comparatively imprecise statement of the time, place, and nature of expected activity; forecasts of eruptions and earthquakes sometimes are probabilistic (e.g., [43,47]). A forecast usually covers a longer time period than that for a prediction.

Prediction As defined by Swanson et al. [35], is a comparatively precise statement of the time, place, and, ide-

ally, the nature and size of impending activity. Forecasts and predictions can be either *long term* (typically years to decades or longer) or *short term* (typically hours to months).

Volcano unrest Visual and (or) measurable physical and (or) chemical changes, surface or subsurface, in the status of the volcano, relative to its “normal” historical behavior; duration of unrest can vary from hours to decades. The initiation or escalation of volcano unrest, regardless of duration, may or may not culminate in eruption.

Magma intrusion The subsurface movement or injection of *magma* (molten rock containing associated crystals and gases) from one part of a volcanic system into another. Typically, an intrusion involves transport of magma from a central zone of storage (i.e., magma “reservoir”) into peripheral, structurally weaker zones (e.g., faults or rifts). Some intrusions culminate in surface eruptive outbreaks, others do not.

Volcano monitoring The systematic collection, analysis, and interpretation of visual observations and instrumental measurements of changes at volcanoes before, during, and after the onset of volcano unrest and (or) eruptive activity.

“Baseline” monitoring data Volcano-monitoring data acquired for a volcanic system documenting its range of variation during its “normal” behavior prior to volcano unrest and (or) eruptions. The longer the time span covered by “baseline” monitoring, the more diagnostic the dataset for identifying any significant departures from normal behavior in anticipating the possible outcomes of escalating volcano unrest.

Volcanic crisis An unstable situation or time of heightened public concern when the level of volcano unrest exceeds its “baseline” level, thereby increasing the prospects of possible eruption at some future, but indeterminate time. In general, during a crisis, emergency managers face a relatively narrow “decision window” in which to take timely mitigative actions to ensure public safety.

“Decision window” The period of time – typically weeks to months, but can be longer – during a developing volcanic crisis between the onset or escalation of volcano unrest. During this time, emergency managers are under high-stress political and public pressure to make decisions regarding mitigative actions, including possible evacuation of populations at risk.

Warning An official message issued by government authorities, usually given to a specific community or communities when a direct response to a volcanic threat is required. To be useful, warnings must be cred-

ible and effectively communicated – in clear, easily understandable language – with sufficient lead-time, ideally, well before the volcano unrest escalates into a volcanic crisis.

Definition of the Subject

The hazards and risks posed by volcanic eruptions are increasing inexorably with time. This trend is the direct result of continuing exponential growth in global population and progressive encroachment of human settlement and economic development into hazardous volcanic areas. One obvious strategy in reducing volcano risk is the total abandonment of hazardous volcanic regions for human habitation. Clearly, this is utterly unrealistic; many hazardous volcanoes are located in densely populated areas, for most of which land-use patterns have been fixed by history, culture, and tradition for centuries or millennia. Moreover, people also are exposed to potential volcano hazards by simply being passengers aboard commercial airliners flying over volcanic regions and possibly encountering a drifting volcanic ash cloud from a powerful explosive eruption [5]. Thus, the only viable option in reducing volcano risk is the timely issuance of early warning of possible impending eruptions, allowing emergency-management officials to take mitigative actions. It is then imperative for volcanologists to effectively communicate the best-possible hazards information to emergency-management authorities, and to convince them to implement timely mitigative countermeasures, including evacuation, if necessary, of people at risk. However, volcanologists face daunting challenges in providing reliable, precise early warnings that government officials demand and need to make informed decisions to ensure public safety.

Introduction

About 1500 volcanoes have erupted one or more times during the Holocene (i. e., past 10,000 years); since A.D. 1600, volcanic disasters have killed about than 300,000 people and resulted in property damage and economic loss exceeding hundreds of millions of dollars [39,40]. During recent centuries, on average 50 to 70 volcanoes worldwide are in eruption each year – about half representing activity continuing from the previous year and the other half new eruptive outbreaks [32]. Most of these erupting volcanoes are located in developing countries, which often lack sufficient scientific and economic resources to conduct adequate volcano-monitoring studies. Moreover, in any given year, many more volcanoes exhibit observable and (or) measurable anomalous behavior (*volcano unrest*) that does not lead to eruption.

For scientists and emergency-management authorities alike, the critical issues in providing early warning of possible eruption, or of possible escalation of an ongoing but weak eruption, involve basic questions such as (1) will the initiation of unrest at a currently dormant volcano culminate in eruption?; (2) if so, what would be its time of onset, eruptive mode (explosive, non-explosive, etc.) and duration?; (3) at an already restless or weakly erupting volcano, what are the prospects of escalation to major activity?; and (4) what would be the nature and severity of the associated hazards and which sectors of the volcano are the most vulnerable?

Systematic geoscience studies of a volcano's geologic history and past behavior can provide answers to some of the above-listed and related questions relevant to *long-term* forecasts of a volcano's present and possible future activity. In general, the fundamental premise applied in making long-term forecasts is that the volcano's past and present behavior provides the best clues to its future behavior. However, data from volcano monitoring – showing increased activity relative to pre-crisis or “background” levels – constitute the only scientific basis for *short-term* forecasts or predictions of a possible future eruption or a significant change during an ongoing eruption. To respond effectively to a developing volcanic crisis, timely early warnings are absolutely essential, and these warnings must be reliable and precise. Improvement in the reliability and precision of warnings can be achieved only by a greatly improved capability for eruption prediction, which in turn depends on the quantity and quality of volcano-monitoring data and the diagnostic interpretation of such information [36,38,40].

At the outset, it must be emphasized that, in this article, the term *prediction* is used in the strict sense (see Glossary) proposed by Swanson et al. [35]; thus, for a forecast or prediction to be genuine, it must be included in an official warning statement made publicly in advance of the predicted event. While retrospective forecasts and predictions serve valid scientific purposes in testing or verifying theories or models, they are of little or no use to emergency-management authorities. It is beyond the scope of this brief paper to consider in detail volcano-monitoring studies and their applications to eruption prediction. Suffice it to say that instrumental volcano monitoring is a multi-faceted, multidisciplinary endeavor that involves the ground- and (or) satellite-based measurement of seismicity, ground deformation, gas and fluid chemistry, temperature variations, secular changes in micro-gravity and geomagnetism, etc. For more information about volcano-monitoring approaches, techniques, and instrumentation, interested readers are referred to nu-

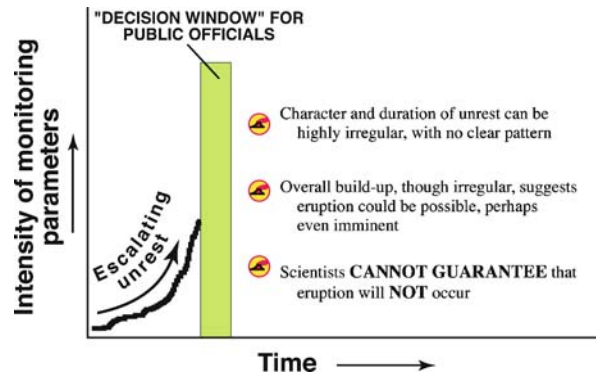
merous recent comprehensive reviews and references cited therein (e. g., [6,10,21,22,23,36] ► [Volcanoes, Non-linear Processes in](#)). Instead, this paper highlights the range in possible outcomes of volcano unrest and reviews some recent examples of the actual outcomes documented for several well-monitored volcanoes. Some implications from the observations discussed in this paper are considered in the final two parts of this article (Sect. “[Challenges in Achieving Refined Predictive Capability](#)” and “[Future Directions](#)”).

Scope of Problem: Challenge for Emergency–Management Authorities

Because earthquake and eruption dynamics intrinsically involve non-linear processes (the focus of this volume), the attainment of a reliable capability to predict eruptions (especially explosive events) still eludes volcanologists. This dilemma persists despite notable advances in volcanology and the availability in recent decades of increasingly sophisticated models, stochastic and deterministic. Such models, which commonly involve pattern-recognition methodologies, are developed from theoretical or statistical analysis of volcano-monitoring data, eruption-occurrence patterns, or other time-space attributes for a volcanic system (e. g., [14,15,18,25,29,33,45,46] ► [Volcanic Eruptions: Stochastic Models of Occurrence Patterns](#)). The non-attainment of predictive capability to date reflects the reality that most volcanic systems are highly complex and that the relevant datasets for the vast majority of volcanoes are too inadequate and (or) incomplete to enable reliable and precise predictions.

Given the fact that the emerging science of eruption prediction is still nascent, scientists and emergency-management officials are at a substantial disadvantage when a long-dormant or weakly active volcano begins to exhibit unrest above its historical (i. e., “normal”) levels. A principal concern is that the heightened unrest, should it persist or escalate, could culminate in renewed or greatly increased, possibly hazardous activity. Because of public-safety and socio-economic issues and consequences, emergency managers in particular must have a definitive answer to the question: What is the most likely outcome of the escalating unrest? The answer(s) to this critical question then shape(s) possible decisions they must make – within a narrow “decision window” (typically weeks to months), generally under confusing, stressful conditions – in managing the growing volcanic crisis.

Figure 1 depicts a common scenario during a volcanic crisis and lists some major factors that complicate the determination of the most likely outcome of the unrest. Un-



Volcanic Hazards and Early Warning, Figure 1

A common scenario confronting emergency-management authorities when unrest initiates or escalates at a volcano, as documented by increasing intensity of monitoring parameters (seismicity, ground deformation, gas emission, thermal, microgravity, etc.) during a volcanic crisis. The “decision window”, though shown schematically, represents a very real and usually short timeframe during which emergency managers must decide and implement – by legal requirement, political and (or) citizen pressure, or moral conscience – strategies and actions to mitigate the potential risk from volcano hazards. (Figures 1 and 2 modified from unpublished conceptual sketches of C. Dan Miller, US Geological Survey)

fortunately, despite advances in volcanology and volcano-monitoring techniques, scientists are unable to give emergency-management authorities the specific information they require. The greatest frustration for the authorities is that scientists cannot guarantee that an eruption will *not* occur. In the section below, I review some common possible outcomes of volcano unrest, and, in Sect. “[Some Recent Examples of Actual Outcomes of Volcano Unrest](#)”, some actual outcomes of recent episodes of volcano unrest.

Variability in Possible Outcomes of Volcano Unrest

Experience worldwide for historical eruptions demonstrates a great range in possible outcomes of volcano unrest. The three types of outcomes discussed below – for which adequate eruptive-history and volcano-monitoring data exist – probably represent the commonest possibilities. Given the non-linear nature of eruptive phenomena, however, other scenarios can be envisaged.

Culmination in Major Eruption or Return to Dormancy Following Short Duration of Unrest

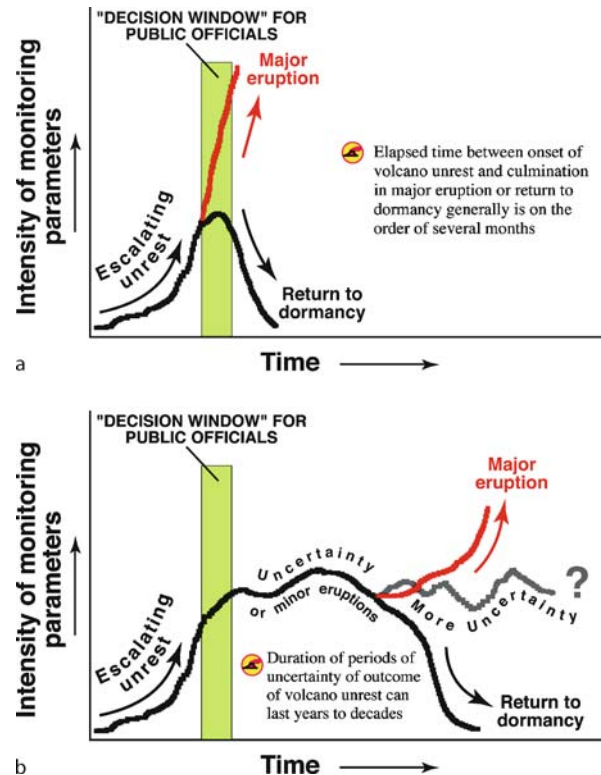
Perhaps the simplest scenario – and certainly the most easily manageable for public officials – is when a volcano reawakens from a long dormancy (i. e., greater than a century) and begins to exhibit significant unrest. Such unrest

then persists at a high level for a relatively short duration (several weeks or months) before culminating in a major eruption (Fig. 2a). With adequate volcano-monitoring studies, preferably in real time or near-real time, conducted during the precursory build-up, scientists may be able to make a short-term forecast or prediction of the impending eruption. The emergency-management authorities then could have the needed guidance during the “decision window” in issuing early warnings and implementing mitigative countermeasures. Alternatively, diagnostic analysis of the volcano-monitoring data, combined with detailed knowledge of eruptive history, could lead the scientists to conclude that an eruption is not likely. In this situation, emergency managers also receive the required scientific input they need to make informed decisions to manage the volcanic crisis, including the declaration of the end of the crisis and the cancellation of any warnings in effect. In either case, scientists need sufficient information to try to determine whether an imminent eruption or a return of the volcano to dormancy is the most likely outcome. However, it must be emphasized that scientists in assessing possible outcomes can reach incorrect conclusions, even using abundant scientific data and constraints from quantitative models.

Culmination in Major Eruption or Return to Dormancy Following a Long Lull in Unrest

A scenario fraught with greater uncertainty is one that, after an initial short period (weeks to months) of sustained and heightened volcano unrest, the volcano neither erupts nor quickly returns to quiescence. Instead, the volcanic system exhibits a decreased level of activity characterized by fluctuating but low-level unrest and (or) weak, non-hazardous eruptions that may persist for years or decades, before possibly exhibiting another episode of heightened unrest. Under such circumstances, scientists and public officials confront anew the crisis conditions and challenges inherent in attempting to anticipate the outcome of the renewed unrest.

This scenario is similar to that previously discussed above (Sect. “[Culmination in Major Eruption or Return to Dormancy Following Short Duration of Unrest](#)”) but differs by the complication posed by another possible outcome in addition to those of an imminent eruption or a return to dormancy: namely, the possibility that the volcano could revert to a mode of continuing uncertainty involving only low-level activity or cessation of unrest for an indeterminate period of time (Fig. 2b). The prolongation of the periods of uncertainty has some unfortunate consequences, including (1) the potential for scien-



Volcanic Hazards and Early Warning, Figure 2

a Two common possible outcomes of volcano unrest that are arguably the most tractable for public officials managing a volcanic crisis (see text). **b** Some other possible outcomes of volcano unrest that pose much greater challenges for scientists and public officials alike during a volcanic crisis (see text)

tists and public officials to lose credibility by incorrectly anticipating the outcomes during the pulses of heightened unrest and by issuing warnings (“false alarms”) of events that fail to materialize (see Sect. “[The Dilemma of “False Alarms”](#)”); and (2) increased difficulty in maintaining public interest in, and awareness of, potential hazards posed by some eventual volcanic crisis that actually culminates in eruption.

Ongoing Unrest over Long Periods with no Clear Indication of Possible Future Activity

Some long-dormant volcanic systems undergo unrest that can persist for many years to decades, fluctuating in intensity but not showing any long-term definitive trend suggestive of possible renewed eruptive activity (Fig. 2b). It is extremely difficult, perhaps impossible, to anticipate possible outcomes of such long-duration, ongoing unrest. The reasons for this problem are simply that the eruptive his-

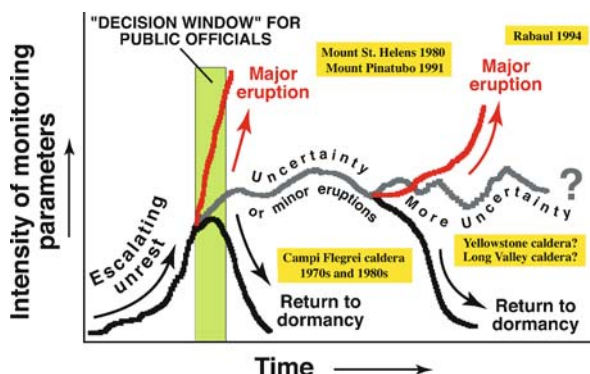
tories and dynamics of long-dormant systems are poorly understood and (or) their eruption frequencies are longer than the time span of the available pre-eruption *baseline* monitoring data. Some examples of such modes of volcano unrest include: Three Sisters volcanic center, Oregon, USA [48]; Long Valley caldera, California, USA [2,12]; Yellowstone caldera, Wyoming–Montana, USA [48]; and Campi Flegrei Caldera, Italy [3,42].

Some Recent Examples of Actual Outcomes of Volcano Unrest

The previous discussion of possible hypothetical outcomes of volcano unrest (Sect. “[Variability in Possible Outcomes of Volcano Unrest](#)”) has its basis in several recent examples of actual volcano unrest, as documented by detailed investigations. These examples are reviewed herein (Fig. 3).

Mount St. Helens (USA) and Mount Pinatubo (Philippines)

In 1975, on the basis of many years of detailed stratigraphic and dating studies, together with an analysis of repose intervals, scientists of the US Geological Survey (USGS) made a long-term forecast of possible renewed eruptive activity at Mount St. Helens Volcano, Washington State, which had been dormant since 1857. This forecast, albeit qualitative, was remarkably prescient, stating: “...an eruption is likely within the next hundred years, possibly before the end of this century” (see p. 441 in [7]).



Volcanic Hazards and Early Warning, Figure 3

Some actual outcomes of recent episodes of volcano unrest at selected volcanoes. Even though these well-studied volcanoes are closely monitored in real time or near-real time by instrumental arrays, it was or is not possible to determine the outcome of the unrest at most of them (see text for discussion)



Volcanic Hazards and Early Warning, Figure 4

19 km-high eruption column of the climactic magmatic eruption of Mount St. Helens Volcano, Washington State, USA, on 18 May 1980. This eruption occurred following about two months of volcano unrest that began after a 123-year quiet period. (Photograph by Austin Post taken about noon on 18 May 1980)

Five years after the forecast, phreatic eruptions began at Mount St. Helens in late March 1980 following a week of precursory seismicity. Sustained seismicity, accompanied by large-scale ground deformation of the volcano’s north flank, ultimately produced a cataclysmic magmatic eruption on 18 May 1980 (Fig. 4). This catastrophic event caused the worst volcanic disaster in the history of the United States (see [16] and chapters therein for detailed summary).

For Mount St. Helens, the volcano unrest, which was well monitored visually and instrumentally, lasted for only about three months before culminating in a major eruption (Fig. 3). Scientists monitoring Mount St. Helens were not able to make a precise prediction of the 18 May events (flank collapse, laterally directed blast, and vertical magmatic eruption). From analysis of the volcano-monitoring data and hazards assessments, however, they were able to give early warning and to convince emergency-management authorities to order evacuation and take other risk-reduction actions well within the “decision window” prior to the paroxysmal eruption.

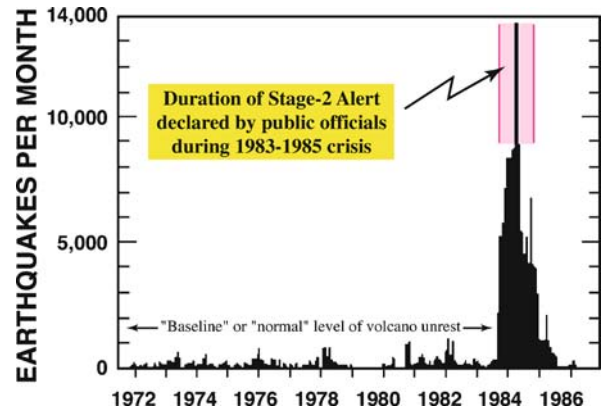
Another illustrative example of a major eruptive activity following a brief duration of volcano unrest was the 1991 eruption of Mount Pinatubo, Luzon, Philippines (see [26], and chapters therein). Prior to 1991, Pinatubo had been quiescent for about 600 years with no recorded

historical eruptions; it had been little studied and was not monitored. In March 1991, Pinatubo began to stir from its long sleep, as indicated by increased fumarolic activity and precursory earthquakes, some large enough to be felt by local inhabitants. Phreatic explosions began in early April, and the first magmatic activity (dome intrusion) was observed on 7 June. On the basis of the analysis and interpretation of data from volcano monitoring (initiated in late April), combined with observation of increased frequency of high (> 15 km) eruption columns, scientists of the Philippine Institute of Volcanology and Seismology (PHIVOLCS) and the USGS Volcano Disaster Assistance Program (VDAP) issued warnings and made a forecast on 12 June that a major eruption was imminent. The PHIVOLCS-USGS scientific team recommended to the Commandant of the US Clark Air Base and the Philippine emergency-management authorities to order major evacuations of the air base and other population centers around the volcano. In all, more than 300,000 people were evacuated from hazardous zones. Three days later on 15 June, Pinatubo's climactic eruption occurred. Even though this eruption was the largest in the world since the 1912 eruption of Novarupta (Alaska, USA), the timely early warnings and evacuations saved many thousands of lives and minimized economic loss.

Rabaul Caldera (Papua New Guinea)

The outcomes for the volcano unrest at Mount St. Helens (1980) and Pinatubo (1991) represent examples of simple (linear?) and relatively short progression (several months) from onset of precursory activity to major eruption. However, most other recent episodes of volcano unrest involve complex or uncertain outcomes; below I discuss one well-documented example of a complex outcome.

Rabaul caldera, Papua New Guinea, after being quiescent for several decades began to exhibit volcano unrest in the mid-1980s, as manifested by dramatically increased seismicity (Fig. 5) and accompanying caldera uplift of more than 1 m [20]. This intense and rapidly escalating unrest prompted the scientists of the Rabaul Volcanological Observatory (RVO) to warn of possible imminent eruption. In response, emergency-management authorities declared in October 1983 a "Stage-2 Alert" (Fig. 5), stating that the volcano could erupt within weeks. Accordingly, the civil authorities implemented a number of mitigative measures – including widening of roads to serve as evacuation routes, preparation of contingency plans, conduct of evacuation drills, etc. – to prepare for the expected soon-approaching eruption. However, soon after the issuance of the alert, the volcano unrest, after peaking



Volcanic Hazards and Early Warning, Figure 5

Occurrences of earthquakes at Rabaul Caldera, Papua New Guinea, during the period 1972–1986 (modified from McKee et al. [20]). The dramatically increased seismicity during 1983–1985, together with significant ground deformation, constituted a serious volcanic crisis and prompted public officials to declare a "Stage-2 Alert" (see text). The time span bracketed by this alert (pink shading) is somewhat comparable to the "decision window" schematically shown in Figs. 1–3. However, the 1983–1985 unrest did not immediately culminate in eruption, which did occur ten years later

in early 1985, began to diminish sharply and returned to normal levels within 6 months (Fig. 5). No eruption occurred, and the "Stage-2 Alert" was lifted in November 1984.

The abrupt cessation of volcano unrest and the non-occurrence of the forecasted eruption were generally viewed as a needless, disruptive "false alarm". As fallout from the unanticipated turn of events, the scientists of the RVO lost credibility with the emergency-response authorities, who in turn lost the confidence of the general population.

Ultimately however, the initially unsatisfactory outcome of the 1983–1985 unrest positively influenced the successful response to a later major eruption. After remaining at the normally low level of activity after for about ten years the mid-1980s crisis, Rabaul erupted suddenly on 19 September 1994 following only 27 hours of precursory seismicity [4]. This major eruption (Fig. 6) devastated nearly all of Rabaul City, but fortunately caused only 5 deaths. The lower-than-expected fatalities can in part be attributable to the fact that people largely "self-evacuated" without waiting for official advisories to do so. They apparently well remembered the lessons (e. g., enhanced awareness of volcano hazards, measures to take in case of eruption, evacuation drills) learned from the volcanic crisis ten years earlier.



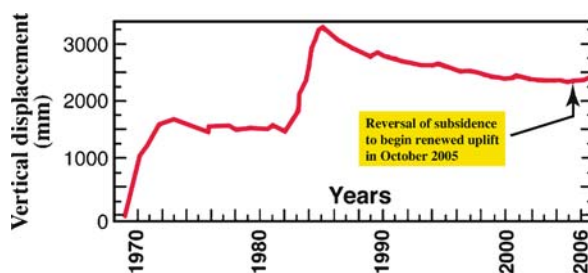
Volcanic Hazards and Early Warning, Figure 6

View from space of the powerful explosive eruption of 19 September 1994 from Rabaul Caldera. (Photograph courtesy of astronauts aboard the NASA Shuttle)

Ongoing Irregular Long-Duration Volcano Unrest but no Clear Indication of Possible Eruption

Recent volcano unrest at several calderas, which are well studied and systematically monitored in real time or near-real time by geophysical and geochemical networks, provide good examples of the difficulty in determining the most likely outcomes of unrest. Because of the abundance of historical observations and volcano-monitoring data, Campi Flegrei Caldera, Italy, located adjacent to Vesuvius Volcano in the Naples metropolitan area, is a particularly instructive example. During the early 1970s and again during 1983–1985, the caldera exhibited pronounced episodes of volcano unrest (Fig. 7) that generated scientific and public concern. Neither of these unrest episodes culminated in eruption, and each was followed by longer intervals of relatively low, fluctuating activity or net subsidence, hinting of an outcome whereby the restless volcano would return to dormancy.

From a recent study by Troise et al. [42], however, the post-1985 subsidence trend reversed in late 2005, and the caldera since has risen by a few centimeters (Fig. 7). Historical records, extending back in time for more than two millennia (see Fig. 1a in [42]), demonstrate a pattern of relatively short-duration uplifts (lasting years to decades) interspersed with long-lived gradual subsidence (lasting centuries). Of these several ups and downs of Campi Flegrei caldera over the past two millennia, only one episode of volcano unrest culminated in eruptive activity – the Monte Nuovo eruption in 1538 [9]. The historical behavior of Campi Flegrei emphasizes the challenging task of attempt-



Volcanic Hazards and Early Warning, Figure 7

Uplift and subsidence at Campi Flegrei Caldera, Italy, during the period 1969–2006 (modified from Fig. 1b in [42]). Vertical displacements measured by precise leveling, together with associated horizontal displacements and increased seismicity, indicate two episodes of caldera uplift, one during 1969–1973 and another during 1982–1985. Neither episode culminated in eruption (see text). Note that the current “baseline” level of activity is higher than that prior to 1982

ing to determine the outcome of volcano unrest with only a few years or decades of volcano-monitoring data.

Similarly, in recent years, ground-based and space-based geodetic data [e.g., Interferometric Synthetic Aperture Radar (InSAR) and GPS], combined with seismic monitoring and other geophysical and geochemical investigations, have documented uplift and (or) subsidence at several other well-monitored long-dormant volcanic systems (e.g., Three Sisters volcanic center, Oregon; Long Valley Caldera, California; and Yellowstone Caldera, Wyoming–Montana). For more information concerning these systems as well as other volcanic systems, the interested reader is referred to the following works: Wicks et al. [48,49]; Battaglia et al. [2]; Hill [12]; and Dzurisin [10 and chapters therein]. It is important to stress that, while the level and intensity at these restless volcanic systems have varied within the periods of systematic instrumental monitoring (only a few decades at most), the available datasets and interpretations are inadequate to determine whether or not the ongoing unrest will culminate in eruption.

Kilauea Volcano, Hawaii (USA)

Brief mention should be made of frequently active volcanic systems – typically basaltic in composition – that are characterized by conspicuous and measurable unrest occurring nearly continuously over long time periods. Perhaps the best-studied volcanic systems exhibiting such behavior are those of Kilauea and Mauna Loa volcanoes on the Island of Hawaii (see [8] and chapters therein). These two volcanoes are among the most active in the world and have been well monitored since the establishment in 1912

of the Hawaiian Volcano Observatory, operated continuously by the USGS since 1948. Abundant “baseline” monitoring data, particularly for Kilauea, demonstrate well-defined patterns and outcomes of unrest (e. g., Fig. 5 in [41]; Fig. 8 in [37]). However, it must be emphasized that the behavior and outcomes of unrest observed for Kilauea – culminating either in subsurface intrusion only or in eruption – occur over much shorter time scales than those for the examples of explosive volcanoes discussed in this paper (e. g., Figs. 2, 3, and 7).

For Kilauea, because of its high eruption frequency and, at times, nearly continuous activity (e. g., [11]), the outcomes of its volcano unrest and the need to issue early warnings are manageable for the civil authorities with little or no anxiety. This fortunate situation reflects a positive circumstance: because of the volcano’s frequent and, at times, continuous eruptive activity, the dissemination of hazards information and early warnings is easily and routinely accomplished among the scientists, emergency-management officials, news media, and the affected public. Moreover, analyses of data for well-monitored, frequently active volcanoes, such as Kilauea, provide many case histories that can serve to test and refine volcano-monitoring techniques as well as eruption-forecasting methodologies. Nonetheless, it should be noted that eruptions at Kilauea and other basaltic volcanoes differ fundamentally from those of more explosive – hence, potentially more dangerous – stratovolcanoes that erupt more viscous materials of intermediate composition (e. g., Mount St. Helens, Mount Pinatubo).

Challenges in Achieving Refined Predictive Capability

The discussion in the preceding sections paints a somewhat discouraging picture: namely, possibly with very rare exceptions (e. g., the Mount St. Helens and Pinatubo case histories), to date scientists still lack a reliable capability for precisely and accurately predicting the outcomes of unrest at explosive volcanoes with low eruption frequency. This unsatisfactory state of affairs does not well serve societal needs to reduce the risks of volcanic hazards and demands improvement. Considered below are some elements that I deem to be essential to achieve refined predictive capability and early warnings of possible eruptive activity.

More Geologic Mapping and Dating Studies of Volcanoes

Of the world’s active and potentially active volcanoes, only a handful (mostly in the developed countries) have been studied sufficiently for the detailed and complete re-

construction of their past behavior, eruption frequencies, and associated hazards. Specifically, geologic mapping (at a scale of 1:25,000 or better) and dating studies of stratigraphically well-controlled eruptive products have been done for only a few volcanoes. Recorded historical eruptions for most volcanoes – especially those in the New World – rarely extend back in time for more than five centuries. Their eruptive histories generally are too short to serve as a comprehensive time-series dataset for quantitative statistical analysis of eruption frequency or repose intervals. Thus, it is essential to expand the time-series dataset by obtaining radiometric ages of prehistoric eruptive products. Moreover, in studies of eruption frequency, no matter how abundant the data used, the calculated frequencies obtained are necessarily *minima*, because the products of small eruptive events are lost to erosion and not preserved in the geologic record.

More Volcano Monitoring at More Volcanoes: Importance of Establishing Long-Term “Baseline” Behavior

As noted by Tilling (see p. 9 in [40]), most volcanologists believe that “... if a volcano is monitored extensively in real- or near-real time by well-deployed instrumental networks, it should be possible to make much better forecasts of the outcomes of volcano unrest.” Unfortunately, many of the world’s active and potentially active volcanoes are poorly monitored, and some are not monitored at all. Thus, to advance our understanding of eruptive dynamics in order to make more precise early warnings, initiating or expanding volcano monitoring at many more volcanoes is imperative. Ideally, volcano monitoring should be conducted in real- or near-real time, and it should involve a combination of monitoring techniques rather than reliance on any single one [36]. Moreover, the longer the time span of volcano monitoring, the more diagnostic is the relevant database needed for detecting and interpreting any significant departure from the overall variation in the long-term “baseline” behavior of the volcano.

The Dilemma of “False Alarms”

With the current state-of-the-art in volcanology and monitoring techniques, it is difficult, and generally impossible, for volcanologists to determine with any certainty: (1) the most likely outcome of onset of unrest at a long-dormant volcano; and (2) the eventual possible occurrence of a major eruption in the course of long-duration, but relatively low-level ongoing unrest. Nonetheless, scientists still have an obligation to emergency managers and the threatened populations to provide the best-possible hazards in-

formation, forecasts or predictions, and warnings within the limitations of available knowledge, technology, and volcano-monitoring techniques. In so doing, the scientists run the unavoidable risk of raising a “false alarm” and the associated criticism and loss of credibility when the forecasted event fails to materialize. On the other hand, emergency-management officials as well as the general public must be prepared to accept the disruptive socio-economic consequences and costs of occasional “false alarms”. The Rabaul case history (previously discussed in Sect. “[Rabaul Caldera \(Papua New Guinea\)](#)”) underscores the sentiment of Banks et al. (see p. 78 in [1]): “... False alarms themselves can provide, through objective assessment of the scientific and public response to a volcanic crisis that ended without eruption, valuable lessons useful ... for the next crisis, which could culminate in an eruption.” Even so, every attempt should be made to minimize “false alarms” to the extent possible, in order to maintain scientific credibility and the confidence of the emergency-management authorities and the populace at risk.

Future Directions

An obvious critical need is the comprehensive geoscience studies of more volcanoes, to reconstruct their prehistoric eruptive histories, thereby extending the time-series database needed for quantitative analysis and interpretation. In addition, volcano monitoring, even if rudimentary – deploying only 1 to 3 seismometers and making simple field observations and measurements [34] – is needed for many more volcanoes, both to establish “baselines” and to provide early warning. Obviously, future research necessarily should also be focused on methodologies to make more robust the acquisition and processing of real- or near-real-time volcano-monitoring data, using or refining *existing* instrumentation and techniques, volcano databases, analytical tools, and empirical and theoretical models. An especially promising avenue of future research would require the wider utilization of broadband instruments in seismic-monitoring networks at active and potentially volcanoes. This would enable systematic and quantitative analysis and interpretation of Long-Period (LP) and Very-Long-Period (VLP) seismicity, which from worldwide experience precedes and accompany nearly all eruptions ► [Volcanoes, Non-linear Processes in](#).

A long-standing and vexing problem for volcanologists is that, at present, no geophysical or geochemical criteria exist to identify the distinguishing characteristics between volcano unrest that merely ends in a subsurface intrusion of magma and unrest that culminates with magma breaking the surface to produce an eruption. From

the vantage point of the emergency-management officials, subsurface intrusion or movement of magma, while of great academic interest to volcanologists in deciphering volcano dynamics, poses no threat to public safety. In contrast, the threat of an imminent eruption requires timely decisions and mitigative actions to ensure public safety. Thus, the future development, if possible, of quantitative criteria to distinguish the precursory pattern of a subsurface intrusion from that for an eruption would mark a quantum leap in the young science of volcanology. In this regard, an improved understanding of magma intrusion vs. eruptive dynamics might provide scientists more powerful tools in choosing between the various paths shown in Fig. 3 as the most likely outcome of volcano unrest.

In attempting to quantify estimates of the probabilities of specified hazardous volcanic events within specified timeframes (i.e., eruption predictions), scientists have made increasing use of “materials-failure” models (e.g., [25,45,46]), “event trees” (e.g., [27]), and more statistically rigorous variants of the “event-tree”, “decision-tree”, “pattern-recognition”, and “occurrence-pattern” approaches (e.g., [17,18,19,24,29] ► [Volcanic Eruptions: Stochastic Models of Occurrence Patterns](#)). Depending on the particular circumstances of the volcano(es) and eruptions under study, these and other statistical tools have their individual strengths and weaknesses. Taken together, however, the utility and potential successful application of such approaches are inherently hampered by the incompleteness and (or) too-short time span of the eruptive-history or volcano-monitoring datasets analyzed. Thus, to become more robust, the probabilistic methodologies must employ larger and more complete datasets. In any case, while useful, the existing techniques or models cannot yield results with the precision and accuracy that emergency-managers demand and need as they confront a “decision window” during a volcanic crisis. Simply stated, even if the calculated results prove to be accurate, their error bars generally exceed the time span bracketed by the “decision window”.

In recent years, the World Organization of Volcano Observatories (WOVO) – a Commission of the International Association of Volcanology and Chemistry of the Earth’s Interior – has launched an ambitious but poorly funded effort, called *WOVOdat*, to construct a global database of empirical data on volcanic unrest. This database is being developed as a user-friendly Internet-based system with query and analysis tools [30]. Even though a basic design and schema now exist for the construction of *WOVOdat* [44], the actual compilation and integration of data are just barely beginning. The *WOVOdat* project recently received major funding from

the Singapore Government and Nanyang Technological University [28]. This favorable development brightens the prospects for it ultimately to become a powerful tool in evaluating patterns and possible outcomes of volcanic unrest. Nonetheless, until *WOVOdat* becomes fully operational, we must continue to rely on the available datasets – however imperfect – and to employ and refine the existing analytical methodologies and statistical models.

Acknowledgments

This article has benefited from constructive reviews and helpful suggestions by L. J. Patrick Muffler and Fred Klein (both of the US Geological Survey, Menlo Park) on an earlier draft. To them, I offer them my sincere thanks. The views expressed in this article have been shaped by my personal involvement in responses to several of the volcanic crises in recent decades, and by enlightening and instructive interactions and discussions with many colleagues in the global volcanological community.

Bibliography

Primary Literature

1. Banks NG, Tilling RI, Harlow DH, Ewert JW (1989) Volcano monitoring and short-term forecasts. In: Tilling RI (ed) *Short Courses in Geology*, vol 1. Volcanic Hazards, American Geophysical Union, Washington, DC, chap 4, pp 51–80
2. Battaglia M, Roberts C, Segall P (2003) The mechanics of unrest at Long Valley caldera, California: 2. Constraining the nature of the source using geodetic and micro-gravity data. *J Volcanol Geotherm Res* 127:219–245
3. Berrino G, Corrado G, Luongo G, Toro B (1984) Ground deformation and gravity changes accompanying the 1982 Pozzuoli uplift. *Bull Volcanol* 47:187–200
4. Blong R, McKee C (1995) The Rabaul eruption 1994: Destruction of a Town. Natural Hazards Research Centre, Macquarie University, Sydney, 52 pp
5. Casadevall TJ (ed) (1994) Volcanic ash and aviation safety: Proceedings of the First International Symposium on Volcanic Ash and Aviation Safety. US Geological Survey Bulletin 2047. Government Printing Office, Washington, 450 pp
6. Chouet B (2004) Volcano seismology. *Pure Appl Geophys* 160:739–788
7. Crandell DR, Mullineaux DR, Rubin M (1975) Mount St. Helens volcano: Recent and future behaviour. *Science* 187:438–441
8. Decker RW, Wright TL, Stauffer PH (eds) (1987) *Volcanism in Hawaii*. US Geological Survey Professional Paper 1350. vol 1 and 2. U.S. Government Printing Office, Washington, 1667 pp
9. De Vito M, Lirer L, Mastrolorenzo G, Rolandi G (1987) The 1538 Monte Nuovo eruption (Campi Flegrei, Italy). *Bull Volcanol* 49:608–615
10. Dzurisin D (ed) (2006) *Volcano deformation: Geodetic Monitoring Techniques*. Springer-Praxis, Berlin, 441 pp
11. Heliker C, Swanson DA, Takahashi TJ (eds) (2003) The Pu'u O'o-Kupaianaha Eruption of Kilauea Volcano, Hawaii: The first 20 years. US Geological Survey Professional Paper 1676. U.S. Geological Survey, Reston, 206 pp
12. Hill DP (2006) Unrest in Long Valley Caldera, California, 1978–2004. *Geol Soc London* 269:1–24
13. ISDR (2004) *Living with Risk: International Strategy for Disaster Reduction (ISDR)*. United Nations, New York and Geneva vol 1, 431 pp and vol 2, 126 pp
14. Klein F (1982) Patterns of historical eruptions at Hawaiian volcanoes. *J Volcanol Geotherm Res* 12:1–35
15. Klein F (1984) Eruption forecasting at Kilauea Volcano, Hawaii. *J Geophys Res* 89(B5):3059–3073
16. Lipman PW, Mullineaux DR (eds) (1981) The 1980 eruptions of Mount St. Helens, Washington. US Geological Survey Professional Paper 1250. U.S. Government Printing Office, Washington, 844 pp
17. Marzocchi W (1996) Chaos and stochasticity in volcanic eruptions the case of Mount Etna and Vesuvius. *J Volcanol Geotherm Res* 70:205–212
18. Marzocchi W, Sandri L, Gasparini P, Newhall C, Boschi E (2004) Quantifying probabilities of volcanic events: The example of volcanic hazards at Mt. Vesuvius. *J Geophys Res* 109:B11201. doi:10.1029/2004JB003155
19. Marzocchi W, Sandri L, Selva J (2008) BET_EF: A probabilistic tool for long- and short-term eruption forecasting. *Bull Volcanol* 70(5):623–632. <http://dx.doi.org/>
20. McKee CO, Johnson RW, Lowenstein PL, Riley SJ, Blong RJ, de St. Ours P, Talai B (1985) Rabaul caldera, Papua New Guinea: Volcanic hazards, surveillance, and eruption contingency planning. *J Volcanol Geotherm Res* 23:195–237
21. McNutt SR (1996) Seismic monitoring and eruption forecasting of volcanoes: A review of the state of the art and case histories. In: Scarpa R, Tilling RI (eds) *Monitoring and Mitigation of Volcano Hazards*. Springer, Heidelberg, pp 99–146
22. McNutt SR (2000) Seismic monitoring. In: Sigurdsson H, Houghton B, McNutt SR, Rymer H, Stix J (eds) *Encyclopedia of Volcanoes*. Academic Press, San Diego, chap 68, pp 1095–1119
23. McNutt SR (2000) Synthesis of volcano monitoring. In: Sigurdsson H, Houghton B, McNutt SR, Rymer H, Stix J (eds) *Encyclopedia of Volcanoes*. Academic Press, San Diego, chap 71, pp 1167–1185
24. Mulargia F, Gasparini P, Marzocchi W (1991) Pattern recognition applied to volcanic activity: Identification of the precursory patterns to Etna recent flank eruptions and periods of rest. *J Volcanol Geotherm Res* 45:187–196
25. Murray JB, Ramirez Ruiz JJ (2002) Long-term predictions of the time of eruptions using remote distance measurement at Volcán de Colima, México. *J Volcanol Geotherm Res* 117(1–2): 79–89
26. Newhall CG, Punongbayan RS (eds) (1996) *Fire and Mud: Eruptions and Lahars of the Mount Pinatubo*, Philippines. Philippine Institute of Volcanology and Seismology, Quezon City, and University of Washington Press, Seattle, 1126 pp
27. Newhall CG, Hoblitt RP (2002) Constructing event trees for volcanic crises. *Bull Volcanol* 64:3–20
28. Newhall CG (2008) written communication, 11 February 2008
29. Sandri L, Marzocchi W, Zaccarelli L (2004) A new perspective in identifying the precursory patterns of eruptions. *Bull Volcanol* 66:263–275
30. Schwandner FM, Newhall CG (2005) *WOVOdat: The World Organization of Volcano Observatories database of volcanic un-*

- rest. European Geosciences Union, Geophysical Research Abstracts, vol 7, abstract # 05-J-09267 (extended abstract), 2 pp
31. Sigurdsson H, Houghton B, McNutt SR, Rymer H, Stix J (eds) (2000) Encyclopedia of Volcanoes (and chapters therein). Academic Press, San Diego, 1417 pp
 32. Simkin T, Siebert L (1994) Volcanoes of the World: A Regional Directory, Gazetteer, and Chronology of Volcanism During the Last 10,000 Years, 2nd edn. Smithsonian Institution, Washington and Geoscience Press, Inc., Tucson, Arizona, 349 pp
 33. Sparks RSJ (2003) Frontiers: Forecasting volcanic eruptions. *Earth Planet Sci Lett* 210(1–2):1–15
 34. Swanson DA (1992) The importance of field observations for monitoring volcanoes, and the approach of “Keeping Monitoring as Simple as Practical”. In: Ewert JW, Swanson DA (eds) *Monitoring volcanoes: Techniques and Strategies used by the staff of the Cascades Volcano Observatory, 1980–90*. US Geological Survey Bulletin, vol 1966. U.S. Government Printing Office, Washington, 219–223
 35. Swanson DA, Casadevall TJ, Dzurisin D, Holcomb RT, Newhall CG, Malone SD, Weaver CS (1985) Forecasts and predictions of eruptive activity at Mount St. Helens, USA: 1975–1984. *J Geodyn* 3:397–423
 36. Tilling RI (1995) The role of monitoring in forecasting volcanic events. In: McGuire WJ, Kilburn CRJ, Murray JB (eds) *Monitoring Active Volcanoes: Strategies, Procedures, and Techniques*. UCL Press, London, pp 369–402
 37. Tilling RI (2002) Volcanic Hazards. In: Meyer RA (ed) *Encyclopedia of Physical Science and Technology*, vol 17, 3rd edn. Academic Press, San Diego, pp 559–577
 38. Tilling RI (2003) Volcano monitoring and eruption warnings. In: Zschau J, Küppers AN (eds) *Early Warning Systems for Natural Disaster Reduction*. Springer, Berlin, chap 5, pp 505–510
 39. Tilling RI (2005) Volcano Hazards. In: Martí J, Ernst G (eds) *Volcanoes and the Environment*. Cambridge University Press, Cambridge, chap 2, pp 56–89
 40. Tilling RI (2008) The critical role of volcano monitoring in risk reduction. *Adv Geosci* 14:3–11
 41. Tilling RI, Dvorak JJ (1993) The anatomy of a basaltic volcano. *Nature* 363:125–133
 42. Troise C, De Natale G, Pingue F, Obrizzo F, De Martino P, Tammaro U, Boschi E (2007) Renewed ground uplift at Campi Flegrei caldera (Italy): New insight on magmatic processes and forecast. *Geophys Res Lett* 34:L03301. doi:10.1029/2006GL28545
 43. Turner MB, Cronin SJ, Bebbington MS, Platz T (2008) Developing probabilistic eruption forecasts for dormant volcanoes: A case study from Mt. Taranaki, New Zealand. *Bull Volcanol* 70:507–515
 44. Venezky DY, Newhall CG (2007) WOVodat design document: The schema, table descriptions, and create table statements for the database of worldwide volcanic unrest (WOVodat version 1.0). US Geological Survey Open-File Report 2007-1117, 184 pp
 45. Voight B (1988) A method for prediction of volcanic eruptions. *Nature* 332:125–130
 46. Voight B, Cornelius RR (1991) Prospects for eruption prediction in near real-time. *Nature* 350:695–698
 47. WG99, Working Group on California Earthquake Probabilities (1999) Earthquake probabilities in the San Francisco Bay region: 2000 to 2030 – A summary of findings. US Geological Survey Open-File Report 99-517, 60 pp
 48. Wicks C, Dzurisin D, Ingebritsen S, Thatcher W, Lu Z, Iverson RM (2002) Magmatic activity beneath the quiescent Three Sisters volcanic center, central Oregon Cascade Range, USA. *Geophys Res Lett* 29(7):26–751,26–754. doi:10.1029/2001GL014205
 49. Wicks C, Thatcher W, Dzurisin D, Svarc J (2006) Uplift, thermal unrest, and magmatic intrusion at Yellowstone Caldera. *Nature* 440:72–75

Books and Reviews

- Chester D (1993) *Volcanoes and Society*. Edward Arnold (a Division of Hodder & Stoughton), London, 351 pp
- Martí J, Ernst G (eds) (2005) *Volcanoes and the Environment*. Cambridge University Press, Cambridge, 471 pp
- Scarpa R, Tilling RI (eds) (1996) *Monitoring and Mitigation of Volcano Hazards*. Springer, Heidelberg, 841 pp

Volcanoes, Non-linear Processes in

BERNARD CHOUET

US Geological Survey, Menlo Park, USA

Article Outline

Glossary

Definition of the Subject

Introduction

Description of Seismic Sources in Volcanoes

Sources of Long-Period Seismicity

Source Processes of Very-Long-Period Signals

Future Directions

Acknowledgment

Bibliography

Glossary

Bubbly liquid Liquid-gas mixture in which the gas phase is distributed as discrete bubbles dispersed in a continuous liquid phase.

Choked flow Flow condition where the transonic flow of a compressible fluid through a constriction becomes choked. As the fluid flows through a narrowing channel, it accelerates at a rate that depends on the ratio of channel inlet pressure to channel outlet pressure. At a critical pressure ratio, which is a function of the fractional change of cross-sectional area, the speed of the fluid accelerating through the nozzle-like constriction reaches a maximum value equal to its sound speed. This flow condition is termed choked flow.

Crack wave A dispersive wave generated by fluid-solid interaction in a fluid-filled crack embedded in an elastic solid. The crack-wave speed is always smaller than the acoustic speed of the fluid.

Diffuse interface Thin mixing layer constituting the interface between two immiscible fluids. Interface dynamics is governed by molecular forces and is described by the mixing energy of the two fluid components.

Gas slug A gas bubble whose diameter is approximately the diameter of the pipe in which the slug is flowing. In a slug ascending a vertical pipe, the nose of the bubble has a characteristic spherical cap and the gas in the rising bubble is separated from the pipe wall by a falling film of liquid.

Long-period (LP) event A seismic event originating under volcanoes with emergent onset of *P* waves, no distinct *S* waves, and a harmonic signature with periods in the range 0.2–2 s as compared to a tectonic earthquake of the same magnitude. LP events are attributed to the involvement of fluid such as magma and/or water in the source process (see also VLP event).

Magma Molten rock containing variable amounts of dissolved gases (principally water vapor, carbon dioxide, and sulfur dioxide), crystals (principally silicates and oxides), and, occasionally, preexisting solid rock fragments.

Moment tensor A symmetric second-order tensor that completely characterizes an internal seismic point source. For an extended source, it represents a point-source approximation and can be quantified from an analysis of seismic waves whose wavelengths are much longer than the source dimensions.

Nonlinear process Process involving physical variables governed by nonlinear equations that reflect the fundamental micro-scale dynamics of the system. Nonlinear phenomena can arise from a number of different sources, including convective acceleration in fluid dynamics, constitutive relations, boundary conditions representing gas-liquid interfaces, nonlinear body forces, and geometric nonlinearities arising from large-scale deformation.

Phase-field method Method treating the interface between two immiscible fluids as a diffuse thin layer; also known as the diffuse interface method. In this approach, the physical and chemical properties of the interfacial layer are defined by a phase-field variable ϕ , whose dynamics are expressed by the Cahn–Hilliard convection-diffusion equation. Use of the phase-field variable avoids the necessity of tracking the interface and yields the correct interfacial tension from the free energy stored in the mixing layer.

Very-long-period (VLP) event A seismic event originating under volcanoes with typical periods in the range 2–100 s. VLP events are attributed to the involvement

of fluid such as magma and/or water in the source process. Together with LP events, VLP events represent a continuum of fluid oscillations, including acoustic and inertial effects resulting from perturbations in the flow of fluid through conduits.

Volatile A chemical compound that is dissolved in magma at high pressure and exsolves from the melt and appears as a low-density gas at low pressure. The most common volatiles in magma are water, carbon dioxide, and sulfur dioxide.

Waveform inversion Given an assumed model of the wave-propagation medium, a procedure for determining the source mechanism and source location of a seismic event based on matching observed waveforms with synthetics calculated with the model.

Definition of the Subject

Magma transport is fundamentally episodic in character as a result of the inherent instability of magmatic systems at all time scales. This episodicity is reflected in seismic activity, which originates in dynamic interactions between gas, liquid and solid along magma transport paths involving complex geometries. The geometrical complexity plays a central role in controlling flow disturbances and also providing specific sites where pressure and momentum changes in the fluid are effectively coupled to the Earth.

Recent technological developments and improvements in the seismological instrumentation of volcanoes now allow the surface effects of subterranean volcanic processes to be imaged in unprecedented detail. Through detailed analyses of the seismic wavefields radiated by volcanic activity, it has become possible for volcano seismologists to make direct measurements of the volcanic conduit response to flow processes, thus opening the way for detailed modeling of such processes.

However, unlike the description of seismic waves, which is based on the linear equations of elastodynamics, the description of the flow processes underlying the observed seismic source mechanisms is governed by the nonlinear equations of fluid dynamics. In the classic Navier–Stokes equations of fluid mechanics, the nonlinearity resides in the convective acceleration terms in the equations of conservation of momentum. In volcanic fluids, further complexity arises from the strong nonlinear dependence of magma rheology on temperature, pressure, and water and crystal content, and nonlinear characteristics of associated processes underlying the physico-chemical evolution of liquid-gas mixtures constituting magma. An example of nonlinearity in two-phase fluid mixtures

are the changing boundary conditions associated with the internal surfaces separating the phases, a situation commonly encountered during the spinodal decomposition of binary fluids [61]. Spinodal decomposition occurs when a mixture of two species *A* and *B* of fluid forming a homogeneous mixture at high temperature undergoes spontaneous demixing following a temperature drop (quench) below some critical temperature. As the temperature drops below the critical temperature, the initially homogeneous mixture becomes locally unstable, and a period of interdiffusion is initiated, which leads to the formation of patches of *A*-rich and *B*-rich fluids separated by sharp interfaces. In the late stages of demixing following a deep quench, the interfacial thickness reaches a molecular scale and the interfacial tension approaches an equilibrium surface tension. As it approaches local equilibrium, the mixture continues to evolve toward a minimization of energy by reducing its interfacial area, and stresses arising from changes in the local interfacial curvature drive fluid motion. A smooth evolution of the interfacial structure ensues, occasionally interrupted by local coalescence, breakup and reconnection, until final equilibrium is reached between the two bulk domains. Similar processes underlie the physics that governs the vesiculation, fragmentation, and collapse of bubble-rich suspensions to form separate melt and vapor in response to decreasing pressure along the ascent path of magma.

All of the above factors contribute to a diversity of oscillatory processes that intensifies as magma rheology becomes more complex; increasingly diverse behavior also characterizes hydrothermal fluids. Heat transfer to the hydrothermal system from magmatic gases streaming through networks of fractures pervading the rock matrix may induce boiling in ground water, resulting in the formation of steam bubbles and attendant bubble oscillations, thereby generating sustained tremor of hydrothermal origin.

Refined understanding of magma and hydrothermal transport dynamics therefore requires multidisciplinary research involving detailed field measurements, laboratory experiments, and numerical modeling. The comprehensive breadth of seismology must be used to understand and interpret the wide variety of seismic signals encountered in various volcanic processes. This effort must then be complemented by laboratory experiments and numerical modeling to better understand the complex flow dynamics at the origin of the source mechanisms imaged from seismic data. Such research is fundamental to monitoring and interpreting the subsurface migration of magma that often leads to eruptions, and thus enhances our ability to forecast hazardous volcanic activity.

Introduction

Degassing is the main driving force behind most volcanic phenomena. The separation of vapor and melt phases leads to the formation of bubbles, the presence of which decreases magma density, enhances magma buoyancy and propels magma ascent [140]. Bubbles in magma also naturally increase magma compressibility, resulting in a low acoustic speed of the bubbly mixture compared to that of the liquid phase [28,36,37,56]. At shallow depths, the high compressibility of the bubbles may further contribute to the generation of pressure oscillations in bubble clouds [28,145]. Bubble coalescence and fragmentation can also contribute to pressure disturbances [85]. In hydrothermal fluids, the collapse of small vapor bubbles can be the source of pressure pulses and sustained tremor [70,72].

Bubble dynamics play a key role in the transport of magmatic and hydrothermal fluids, not only as sources of acoustic energy, but also in providing a sharp contrast in velocity between the fluid and encasing solid, which facilitates the entrapment of acoustic energy at the source. This aspect of the source often manifests itself in the form of long-lasting, long-period harmonic oscillations produced by sustained resonance at the source.

Other types of gaseous fluid mixtures also favor source resonance. For example, gases laden with solid particles, or gases mixed with liquid droplets, may produce velocity contrasts that are similar to, or stronger, than those associated with bubbly liquids. Indeed, dusty gases made of micron-sized particles, or misty gases made of micron-sized droplets, can sustain resonance at the source over durations that far exceed those achieved with bubbly fluids [77].

Large gas slugs bursting at the liquid surface can act as active sources of acoustic and seismic radiation [59,118,136]. Gas slugs traversing discontinuities in conduit geometry can also cause transient liquid motions inducing pressure and momentum changes [60], which radiate elastic waves via their coupling to the conduit walls [32,35,109]. In magmas where a high fluid viscosity impedes flow, the diffusion of volatiles from a super-saturated melt may result in gradual pressurization of the melt and attendant deformation of the encasing rock matrix [33,34,104,124]. The fluid motions resulting from unsteady slug dynamics, large degassing bursts, and diffusion-dominated processes typically produce signals with characteristic periods longer than those commonly associated with acoustic resonance.

Oscillatory processes are thus ubiquitous during magma flow and are a natural expression of the release of

thermo-chemical and gravitational energy from volcanic fluids. The radiated elastic energy reflects both active and passive processes at the source, and features a large variety of signals over a wide range of periods.

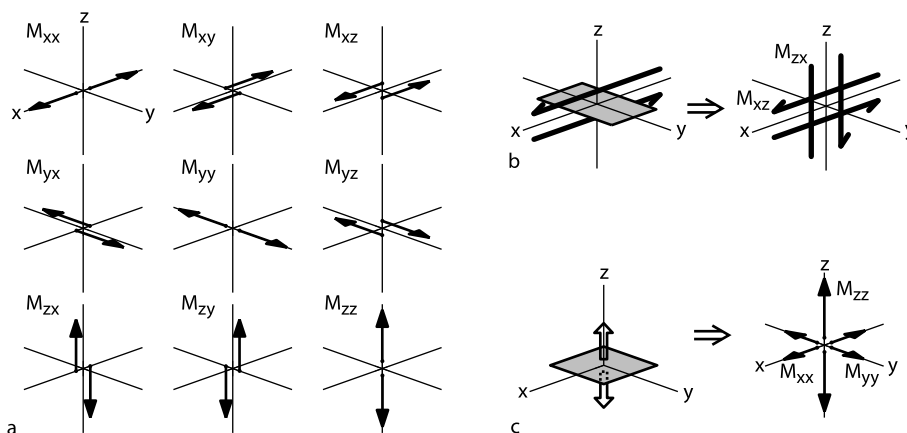
Seismic signals originating in the dynamics of magmatic and hydrothermal fluids typically include Long-Period (LP) events and tremor [27,28]. LP events resemble small tectonic earthquakes in duration but differ in their characteristic frequency range and harmonic signature. Tremor is characterized by a harmonic signal of sustained amplitude lasting from minutes to days, and sometimes for months or even longer. In many instances, LP events and tremor are found to have essentially the same temporal and spectral components, suggesting that a common source process, differing only in duration, underlies these two types of events. Accordingly, LP events and tremor are often grouped under the common appellation LP seismicity. The periods in which LP seismicity is observed typically range from 0.2 to 2 seconds, and the characteristic oscillations of LP signals are commonly viewed as a result of acoustic resonance in a fluid-filled cavity. Slower processes involving inertial forces associated with unsteady mass transport may radiate seismic signals extending to periods much longer than 2 seconds. These types of signals commonly fall under the appellation of Very-Long-Period (VLP) seismicity. Collectively, LP and VLP seismicities provide a comprehensive view of mass transport dynamics under a volcano.

The present chapter offers a brief review of the state of the art in volcano seismology and addresses basic is-

ssues in the quantitative interpretation of processes operative in active volcanic systems. The chapter starts with an introduction of the seismic methodology used to quantify the source of volcano seismicity, with emphasis on sources originating in the dynamics of volcanic fluids. A review of some of the representative source mechanisms of LP and VLP signals and of their implications for volcanic processes follows in Sects. “Sources of Long-Period Seismicity” and “Source Processes of Very-Long-Period Signals”. A final section describes a mesoscale computational approach for simulating two-phase flows of complex magmatic fluids. This method, called the phase-field method, grew out of the original work of [19], and relies on an energy-based variational formalism to treat interfacial dynamics and complex rheology in a unified framework. The phase-field method has been successfully applied to the modeling of complex micro-structured two-phase fluids in the field of engineering materials and appears well adapted to the numerical simulation of nonlinear volcanic processes.

Description of Seismic Sources in Volcanoes

A general kinematic description of seismic sources in volcanoes is commonly based on a moment-tensor and single-force representation of the source [3] (Fig. 1a). The seismic-moment tensor consists of nine force couples, with each corresponding to one set of opposing forces (dipoles or shear couples). This symmetric second-order tensor allows a description of any generally oriented dis-



Volcanoes, Non-linear Processes in, Figure 1

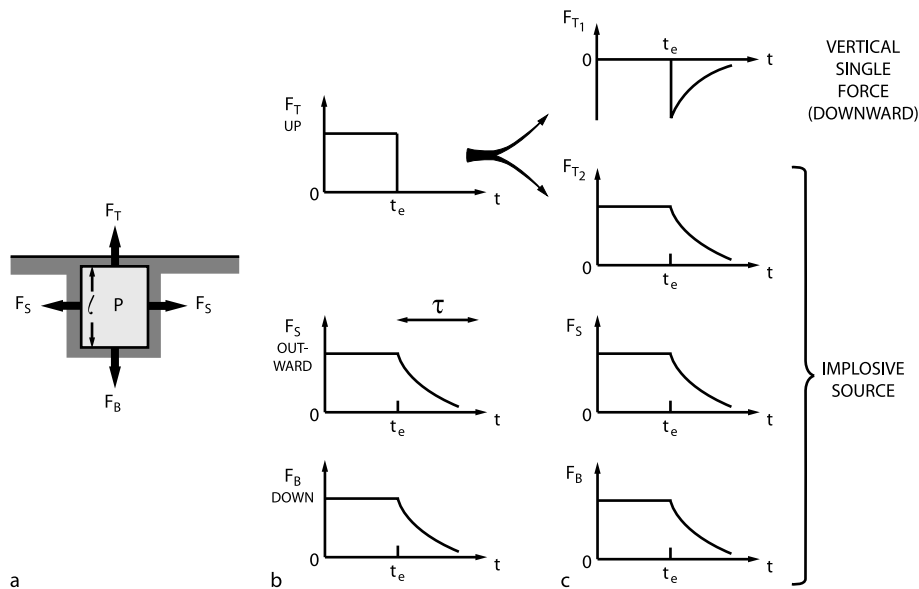
a The nine possible couples corresponding to the moment-tensor components describing the equivalent force system for a seismic source in the Earth. **b** Slip on a fault can be described by a superposition of two force couples, in which each force couple is represented by a pair of forces offset in the direction normal to the force. Sources involving slip on a fault thus have an equivalent force system in the form of a double couple composed of four forces. **c** A tensile crack has a representation in the form of three vector dipoles, in which each dipole consists of a pair of forces offset in the direction of the force

continuity in the Earth in terms of equivalent body forces. For example, slip on a fault can be represented by an equivalent force system involving a superposition of two force couples of equal magnitudes – a double couple (Fig. 1b). Similarly, a tensile crack has an equivalent force system made of three vector dipoles, with dipole magnitudes with ratios $1:1:(\lambda + 2\mu)/\lambda$, in which λ and μ are the Lamé coefficients of the rock matrix [28], and where the dominant dipole is oriented normal to the crack plane (Fig. 1c). Injection of fluid into the crack will cause the crack to expand and act as a seismic source. In general, magma movement between adjacent segments of conduit can be represented through a combination of volumetric sources of this type. Because mass-advection processes can also generate forces on the Earth, a complete description of volcanic sources commonly requires the consideration of single forces in addition to the volumetric source components expressed in the moment tensor. For example, a volcanic eruption can induce a force system that includes a contraction of the conduit/reservoir system in response to the ejection

of fluid, and a reaction force from the eruption jet [64] (Fig. 2). Some volcanic processes can be described by a single-force mechanism only. An example is the single-force mechanism attributed to the massive landslide observed at the start of the 1980 eruption of Mount St. Helens [63,66]. A single-force source model was also proposed by Uhira et al. [134] to explain the mechanism of dome collapses at Unzen Volcano, Japan. In general terms, a single force can be generated by an exchange of linear momentum between the source and the rest of the Earth [129]. Thus, a single force on the Earth may result from an acceleration of the center of mass of the source in the direction opposite to the force, or deceleration of the center of mass of the source in the same direction as the force [129].

Waveform Inversion

Waveform inversions solving for the amplitudes and time histories of the moment-tensor and single-force components of the source have become the primary tool to



Volcanoes, Non-linear Processes in, Figure 2

Force system equivalent to a volcanic eruption (after [64]). **a** Pressurized cavity model for a volcanic eruption. A shallow vertically oriented cylindrical cavity initially sealed at the top by a lid contains a pressurized inviscid fluid which exerts an upward vertical force F_T on the lid, a horizontal outward force F_S on the sidewall, and a vertical downward force F_B on the bottom of the cylinder. **b** Time histories of forces acting on the top, side, and bottom cavity walls of the cavity. The eruption is simulated by the sudden removal of the lid at time $t = t_e$, at which point the force F_T vanishes instantaneously and the fluid pressure in the cylinder starts to decrease with a characteristic time constant τ fixed by the mass flux of the eruption, i.e., $\tau \sim \ell/v$, where ℓ is the length of the cylinder and v is the mean fluid velocity inside the cylinder. Since the forces F_S and F_B are both proportional to pressure, they decrease with the same time constant τ . **c** Decomposition of the force system to a downward single force and implosive source. The force F_T in **b** is decomposed into a vertical downward component F_{T1} and vertical upward component F_{T2} in such a way that F_{T2} has the same time history as F_S and F_B . As a result, the three forces F_{T2} , F_S , and F_B form an implosive source so that the eruption mechanism is represented by the superposition of a downward vertical force (the reaction force of the volcanic jet) with this volumetric implosion

identify and understand the mechanisms of generation of LP and VLP signals recorded by broadband seismometers. When the wavelengths of observed seismic waves are much longer than the spatial extent of the source, the source may be approximated by a point source, and the force system represented by the moment-tensor and single-force components is localized at this point. The waveform inversion procedure requires a calculation of the impulse responses (Green's functions) of the medium to this force system for each receiver component. The displacement field generated by a seismic source is described by the representation theorem which, for a point source, may be written as e. g., Chouet, [28]

$$u_n(t) = F_p(t) * G_{np}(t) + M_{pq}(t) * G_{np,q}(t), \\ p, q = x, y, z, \quad (1)$$

where $u_n(t)$ is the n -component of seismic displacement at a receiver at time t , $F_p(t)$ is the time history of the force applied in the p -direction, $M_{pq}(t)$ is the time history of the pq -component of the moment tensor, and $G_{np}(t)$ is the Green tensor which relates the n -component of displacement at the receiver position with the p -component of impulsive force at the source position. The notation, q indicates spatial differentiation with respect to the q -coordinate and the symbol $*$ denotes convolution. Summation over repeated indices is implied.

A common approach to the quantification of the seismic source mechanism relies on a discretized representation of the volcanic edifice based on a digital elevation model. Using this model, Green's functions are then calculated by the finite difference method [107]. Once the Green's functions are known, the nine independent mechanisms in Eq. (1) are retrieved through least-squares inversion expressing the standard linear problem $\mathbf{d} = \mathbf{Gm}$ in this equation [32].

Sources of Long-Period Seismicity

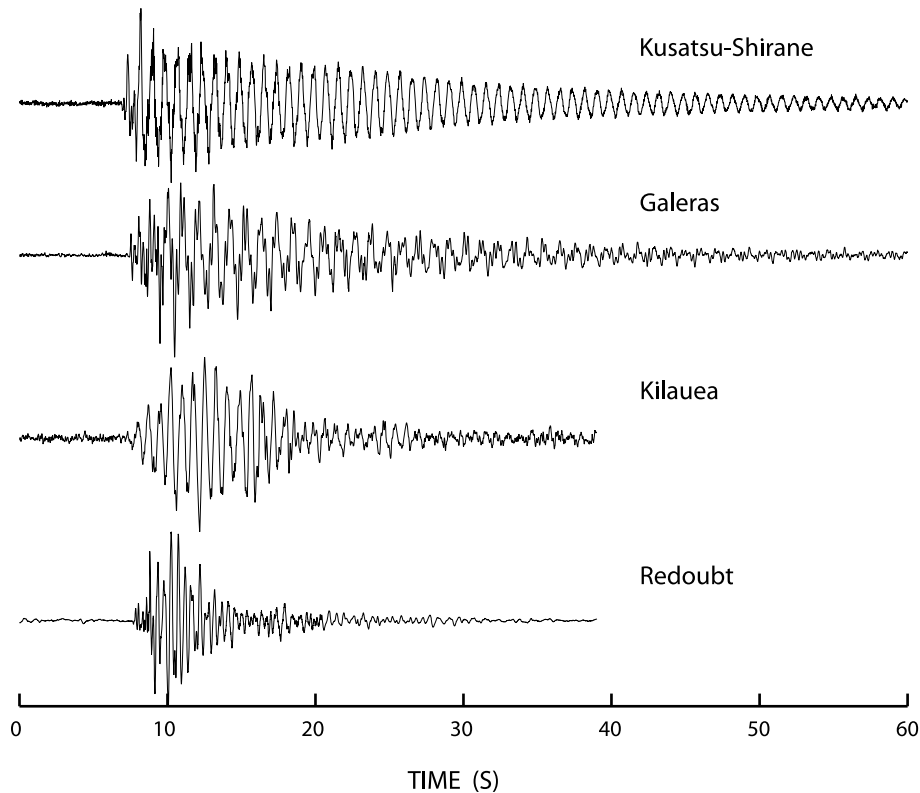
Long-Period (LP) seismicity, including individual LP events and tremor, is commonly observed in relation to magmatic and hydrothermal activities in volcanic areas and is recognized as a precursory phenomenon for eruptive activity (e. g., Chouet, [27]). The waveform of the LP event is characterized by simple decaying harmonic oscillations except for a brief interval at the event onset (Fig. 3). This signature is commonly interpreted as oscillations of a fluid-filled resonator in response to a time-localized excitation. By the same token, tremor may be viewed as oscillations of the same resonator in response to a sustained excitation. LP events are particularly useful in the quantification of magmatic and hydrothermal processes because

the properties of the resonator system at the source of this event can be inferred from the properties of the decaying oscillations in the tail of the seismogram. The damped oscillations in the LP coda are quantified by two parameters, T , and Q , where T is the period of the dominant mode of oscillation, and Q is the quality factor of the oscillatory system representing the combined effects of intrinsic and radiation losses.

Interpretations of the oscillating characteristics of LP sources have mostly relied on a model of fluid-driven crack [23,24,25]. This model, which has the most natural geometry that satisfies mass-transport conditions at depth beneath a volcano, is supported by results from inversions of LP waveforms recorded at several volcanoes [80,82,97,137]. A simplified two-dimensional model of fluid-driven crack was originally proposed by Aki et al. [2]. Although this model considered both the driving excitation and geometry appropriate for transport, the fluid inside the crack was only treated as a passive cushion that did not support the acoustic propagation of the pressure disturbance caused by the motion of the crack wall. An extension of this model including active fluid participation was proposed by Chouet and Julian [22], who considered a simultaneous solution of the elastodynamics and fluid dynamics for a two-dimensional crack. This model was further extended to three dimensions by Chouet [23] and was extensively studied by Chouet [24,25].

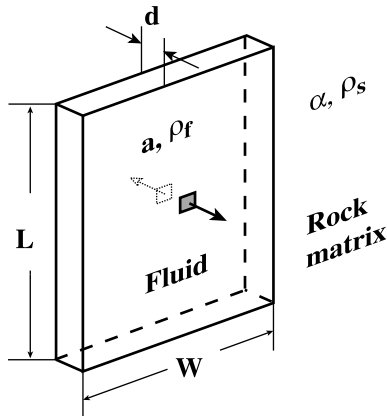
Chouet's three-dimensional model consists of a single isolated rectangular crack embedded in an infinite elastic body and assumes zero mass transfer in and out of the crack (Fig. 4). Crack resonance is excited by a pressure transient applied symmetrically on both walls over a small patch of crack wall. In this model, the crack aperture is assumed to be much smaller than the seismic wavelengths of interest and the motion of the fluid inside the crack is treated as two-dimensional in-plane motion. The fluid dynamics are represented by the conservation of mass and momentum for the two in-plane components of fluid velocity averaged over the crack aperture, and convective terms in the momentum equations are neglected assuming their contributions are negligibly small compared to the time derivatives of pressure and flow velocity. A solution of the coupled equations of fluid dynamics and elastodynamics is then obtained by using a finite-difference approach. As formulated, the model accounts for the radiation loss only; intrinsic losses due to dissipation mechanisms within the fluid are treated separately [77].

Figure 5 shows snapshots of the normal component of particle velocity on the crack wall obtained at four different times following the onset of crack resonance. In this particular example, the crack excitation is triggered by a step



Volcanoes, Non-linear Processes in, Figure 3

Typical signatures of long-period events observed at Kusatsu-Shirane, Galeras, Kilauea, and Redoubt Volcanoes. The signatures are all characterized by a harmonic coda following a signal onset enriched in higher-frequencies

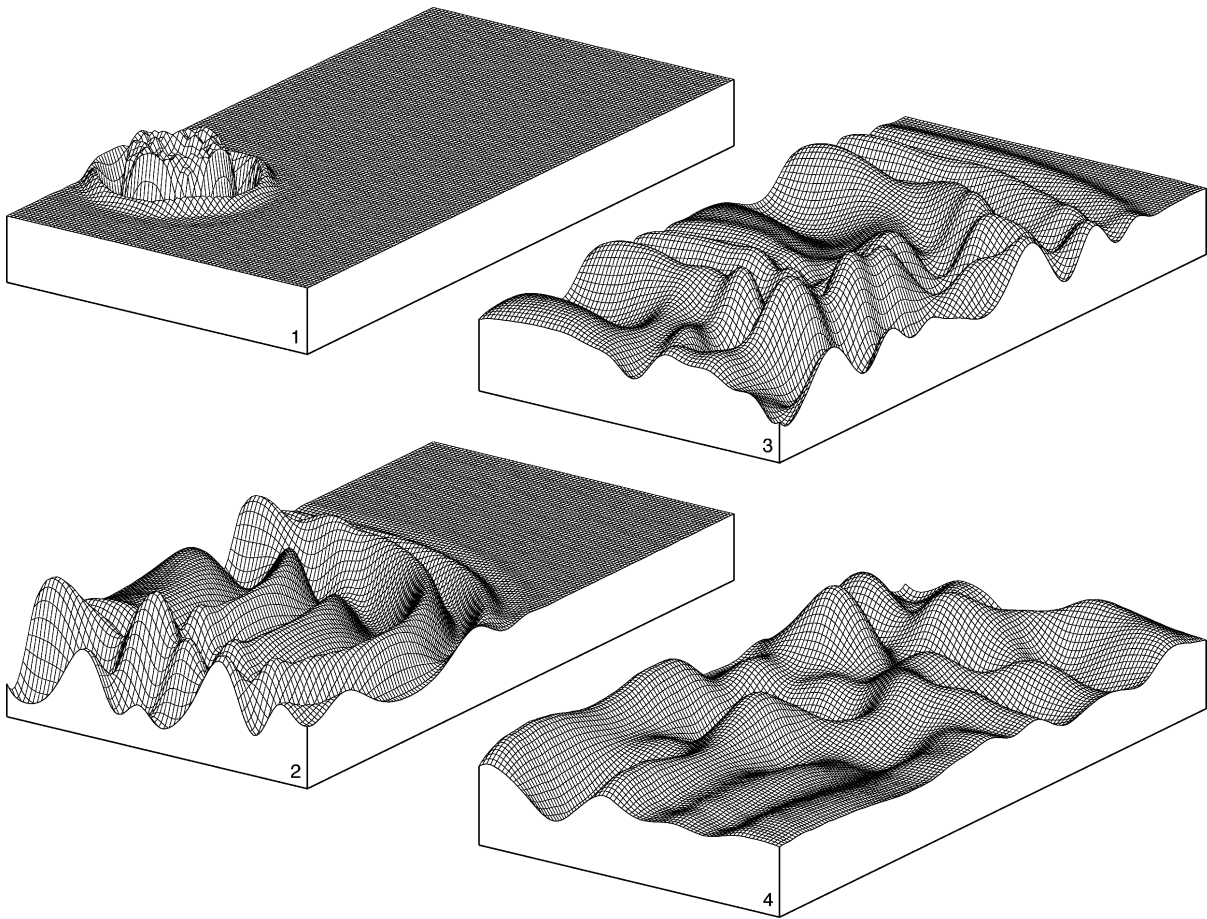


Volcanoes, Non-linear Processes in, Figure 4

Geometry of the fluid-filled crack model of Chouet [23]. The crack has length L , width W , and aperture d , and contains a fluid with sound speed a and density ρ_f . The crack is embedded in an elastic solid with compressional wave velocity α and density ρ_s . Excitation of the crack is provided by a pressure transient applied symmetrically on both walls over the small areas such as that indicated by the gray patch and dotted small square

in pressure applied at a point located a quarter of the crack width from the left edge of the crack and a quarter of the crack length from the front edge of the crack. The first snapshot at the upper left shows the propagation of the elastic disturbance on the crack surface shortly after the onset of the pressure transient. The second snapshot at the lower left shows the motion of the crack wall following the first reflections from the front, left and right edges of the crack. The third snapshot at the upper right represents the wall motion immediately preceding the reflection from the back edge of the crack, and the fourth snapshot at the lower right depicts the shape of the lateral and longitudinal modes of crack resonance, which by then are well established.

The excitation of modes in the crack model depends on the position of the pressure transient, the extent of crack surface affected by the transient, the temporal characteristics of the transient, and crack stiffness $C = (b/\mu)(L/d)$, where b is the bulk modulus of the fluid, μ is the rigidity of the rock, L is the crack length, and d is the crack aperture [2,23]. An example of synthetic seismo-

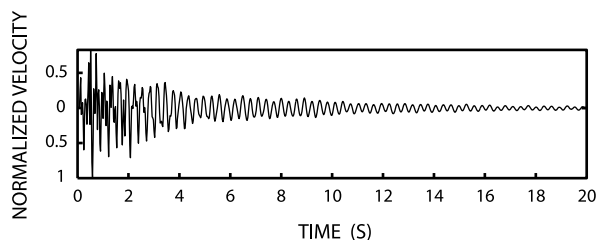


Volcanoes, Non-linear Processes in, Figure 5

Snapshots of the normal component of particle velocity on the surface of a fluid-filled crack excited by a step in pressure applied over a small patch of the crack wall. The snapshots (1–4) show the propagation of the disturbance on the crack wall at four different times in the history of crack oscillation specified by the number of time steps, N , in the finite-difference solution obtained by Chouet [23]. The time step has size $\Delta t = 0.003125L/\alpha$ (see Fig. 4 for explanation of symbols). Depicted are the shape of the wall motion at $N = 72$ (snapshot 1), $N = 312$ (snapshot 2), $N = 560$ (snapshot 3), and $N = 1200$ (snapshot 4). (See text for discussion)

gram representing the vertical ground velocity response in the near field of a fluid-filled crack excited into resonance by a step transient in pressure is shown in Fig. 6. The synthetics display sustained oscillations that bear strong resemblance to observed LP waveforms (compare with Fig. 3), convincingly demonstrating the critical involvement of active fluid participation in the source process of volcanic signals.

Chouet's studies demonstrated the existence of a slow wave propagating along the crack wall, which he named the "crack wave". The asymptotic behavior of this wave was investigated by Ferrazini and Aki [42] in an analytical study of normal modes trapped in a liquid layer sandwiched between two elastic half spaces. The crack wave speed is slower than the sound velocity of the liquid and



Volcanoes, Non-linear Processes in, Figure 6

Synthetic velocity waveform observed at an epicentral distance of 500 m and azimuth of 45° from the crack trace for a vertical crack (vertical extent $L = 150$ m and horizontal extent $W = 75$ m) buried at a depth of 500 m in a homogeneous half space. The aspect ratio is $L/d = 10^4$, and the parameters of the fluid and solid are $a = 300$ m/s, $\rho_f = 2120$ kg/m³, and $\alpha = 4500$ m/s, $\rho_s = 2650$ kg/m³. (Reproduced from [77])

decreases with increasing crack stiffness and increasing wavelength; this result reflects the elasticity of the crack wall, whose effect is to decrease the effective bulk modulus of the fluid. These slow characteristics of the crack wave lead to more realistic estimates of crack dimensions compared to estimates based on the sound speed of a fluid embedded in a resonator with perfectly rigid walls. Source dimensions estimated from LP data based on this model typically range from tens to several hundred meters [79, 82, 120]. Detailed analyses of the dependence of crack resonance on fluid composition carried out by Kumagai and Chouet [77], and systematic investigations of LP signatures based on their results, suggest that dusty gases or bubbly basalt are common fluids in LP events of magmatic origin [27, 45, 76], and that wet gases, steam and bubbly water are typically representative of the source of LP events of hydrothermal origin [79, 120].

The model of Chouet [23] does not address the excitation mechanism of LP events or tremor. Rather, the spatio-temporal properties of the pressure transient triggering the crack resonance are preset as kinematic conditions in the model. The usefulness of this model is thus restricted to a quantification of the crack resonance and properties of the fluids at the source of LP events. For a better perspective of the excitation mechanism of LP seismicity, observations of the source over a wider band of frequencies are necessary, along with an adequate sampling of the evolutionary characteristics of volcanic seismicity. Observations carried out in different volcanic settings point to a wide variety of LP excitation mechanisms originating in magmatic-hydrothermal interactions, as well as magmatic instabilities.

Magmatic-Hydrothermal Interactions

In hydrothermal systems, LP seismicity can be induced by surges in the heat transfer from an underlying magma body. Kusatsu-Shirane Volcano in central Japan provides a prime example of the character of such interactions. Three crater lakes (Yugama, Mizugama, and Karagama) occupy the summit of the volcano along with numerous hot springs, pointing to an active magmatic system and enhanced circulation of hydrothermal fluids. Geochemical studies provide further support for hydrothermal activity resulting from the interaction of hot volcanic gases with groundwater [55, 106]. LP events marked by nearly monochromatic oscillatory signatures have been frequently observed at this volcano (see Fig. 3) [43, 46], and temporal variations in the decay characteristics of these events have also been documented [96]. Kumagai et al. [79] performed a systematic study of the temporal

characteristics of LP events observed at Kusatsu-Shirane over a period from August 1992 through January 1993, and Kumagai et al. [80] carried out waveform inversions of a typical event during this time interval. Results from these studies point to the repeated excitation of a fixed sub-horizontal crack at depths near 200 m under the Yugama crater lake, and consistently explain temporal variations in LP signatures by the dynamic response of this crack to a magmatic heat pulse. In this interpretation, the crack contains an initially wet gas, which became gradually drier with time, suggesting a “drying out” of the hydrothermal system in response to the heat pulse. Further analyses by Nakano et al. [97] based on waveform inversions of the effective excitation functions (the signal components remaining after removal of the resonance characteristics) of individual LP events confirm the crack mechanism imaged by Kumagai et al. [80] and shed further light on the source process. This process involves a collapse and recovery of the sub-horizontal crack accompanied by an upward-directed force, and is consistent with a gradual buildup of pressure in the crack causing repeated discharges of steam from the crack. The vertical force imaged with the volumetric component of the source reflects the release of gravitational energy that occurs as a slug of steam ejected from the crack ascends toward the surface and is replaced by a downward flow of cooler water within a conduit linking the crack to the base of the Yugama crater lake. In this scenario, crack resonance is triggered by the sudden collapse of the crack induced by the venting of steam.

Similar mechanisms of interaction between magmatic and hydrothermal systems have been inferred for Kilauea, Mount St. Helens, and Redoubt Volcanoes. At Kilauea Volcano, Hawaii, Almendros et al. [4] imaged a shallow hydrothermal system from frequency-slowness analyses of LP seismicity recorded on three small-aperture seismic arrays deployed in the summit caldera. Located within the top 500 m below the caldera floor, this reservoir is perched immediately above the shallowest segment of magma conduit identified by [109] from inversions of VLP signals produced during a transient in the magma flow feeding the long-lived and ongoing east rift eruption of this volcano [48]. Episodic deflations of the Kilauea summit during brief pauses in the flow of magma are commonly followed by rapid reinflation of the summit during the resumption of flow, and subsequent slower deflation back to an original state preceding the pause [21]. Larger summit reinflation episodes associated with more energetic surges of magma are accompanied by the emission of VLP signals, production of shallow brittle failure earthquakes, and enhanced LP seismicity in the hydrothermal reservoir [39, 109]. Detailed analyses of seismic array data by

Almendros et al. [5] further document the persistence of low-amplitude tremor generated by shallow hydrothermal activity in response to the flux of heat from the underlying magma conduit. Additional support for this scenario also comes from analyses of the source process of a hydrothermal LP event [82], which point to the resonance of a horizontal crack at depth of ~ 150 m immediately above the conduit imaged by Ohminato et al. [109]. The observed frequencies and attenuation characteristics of crack resonance are consistent with a crack filled with either bubbly water or steam [82].

The inferred scenario of magmatic-hydrothermal interactions at Kilauea, which is in harmony with all of the above observations, involves a chain of causes and effects that starts with a volumetric deformation of the underlying shallow segment of magma conduit induced by the surging magma. This conduit response causes brittle fractures in the surrounding rock matrix, and thus enhances the upward transport of magmatic gases through the fractured medium to shallow depths, where the hot gases heat and activate the hydrothermal system. The boiling of ground-water and attendant production of steam then raise the overall pressure of hydrothermal fluids in fractures permeating the medium, thereby leading to repeated impulsive discharges of fluid and resonant excitation of individual fractures.

The current dome-building eruption of Mount St. Helens Volcano, Washington, is marked by the extrusion of a stiff plug of dacitic magma [40,91] accompanied by shallow, repetitive LP events that have been dubbed “drumbeats” by scientists monitoring Mount St. Helens [94]. VLP signals commonly accompany the LP events, but are generally detected only in the immediate vicinity of the crater. Using high-quality data from a temporary broadband seismic network deployed in 2004–2005, Waite et al. [137] carried out systematic waveform inversions for both LP and VLP signals. Results from these inversions point to the perturbation of a common crack system linking the magma conduit and shallow water-saturated region of the volcano. A scenario consistent with the imaged source mechanisms involves the repeated pressurization of a sub-horizontal crack that lies beneath the growing lava dome in the southern part of the crater. Steam produced by the heating of ground water, as well as steam exsolved from the magma, feed into the crack and pressurize it. Upon reaching a critical pressure threshold, steam is vented out of the crack through fractures leading to the surface. The drop in pressure triggers a partial collapse of the crack, which resonates for 5 to 10s of seconds. The collapse of the crack in turn induces sagging of the overlying dome and triggers a passive response in the magma

conduit that is observed in the VLP band. The observed force and volumetric components of this VLP response are both consistently explained as the result of a perturbation in an otherwise smooth steady flow of magma upward through a dike and into a sill underlying the old dome. In this model, the dike represents the top of the old conduit that fed the 1980–1986 dome-building eruptions, and the sill represents a bypass below the old dome. According to this interpretation, at the start of renewed activity in September 2004, magma moving up the conduit found an easier pathway to the surface by breaking out of the conduit near the surface and pushing sub-horizontally to the south rather than intruding the older dome complex. The imaged sill represents this segment of conduit, and the hydrothermal crack represents an extension of this fracture into the shallow water-soaked region beneath the crater floor. This picture of Mount St. Helens as a steam engine is quite distinct from an earlier model in which the seismic drumbeats were assumed to represent stick-slip motion between the extruding lava and conduit walls (see below). A sustained supply of heat and fluid from the magmatic system is necessary to keep the crack pressurized and keep the drumbeats beating in the model elaborated by Waite et al. [137]. As for Kilauea, a proper interpretation of this activity has important implications for the assessment of the potential for phreatic eruptions at Mount St. Helens.

Another perspective on a different type of instability presumed to be associated with dome growth activity at Mount St. Helens was proposed by Iverson et al. [57]. Their model, originally developed before results from the detailed seismic analyses by Waite et al. [137] became available, hypothesizes that repetitive stick-slip motion along the perimeter of the extruding solid plug may cause observable earthquakes. Although not supported by the character of LP seismicity observed at Mount St. Helens, this model nevertheless offers an intriguing view into a possible oscillatory behavior of plug flow. Oscillations in extrusion velocity originate in the interaction of plug inertia, a variable upward force due to magma pressure, and downward force due to plug mass. Assuming that a steady ascent of compressible magma drives the upward extrusion of a solidified plug exhibiting nonlinear rate-weakening friction along its margins, Iverson et al. [57] infer that stick-slip oscillations might be an inevitable component of such an extrusion process; however, the predicted amplitude of individual slip events, estimated at a few millimeters, suggests this mechanism may be difficult to detect. The seismic source associated with a stick-slip extrusion event may manifest itself as a combination of a near-vertical force (assuming vertical spine growth) representing the

reaction force on the Earth due to the upward acceleration of mass, and double couple resulting from shear near the plug margins where viscosity is very high and magma is in the glass transition. This particular mechanism does not involve LP source resonance and is apparently not part of the dominant expression of seismicity at Mount St. Helens, but could possibly be operating at a level below the threshold of seismic detection. Such mechanism may be observable in dome-building eruptions where the extrusion rate is sufficiently large and unsteady to produce oscillations of this type.

The reawakening of Redoubt Volcano, Alaska on 13 December, 1989, after 23 years of quiescence, was heralded by a rapidly accelerating swarm of repetitive LP events that merged into sustained tremor a few hours before the eruption onset [26,126]. These LP events were interpreted by Chouet et al. [26] as the resonant excitation of a crack linking a shallow, low-pressure hydrothermal system to a deeper supercharged magma-dominated reservoir. The initiation of the swarm was attributed by these authors to the failure of a barrier separating the two reservoirs. The actual mechanism triggering the LP excitation in this model is the unsteady choking of a supersonic flow of magmatic steam driven by the pressure gradient existing between the two reservoirs. Unsteady choking itself is the result of fluctuations in crack outlet pressure associated with the reaction of the hydrothermal system to the injection of mass and heat from below. Similarly, the emergence of sustained tremor late in the swarm is interpreted as a change in choked-flow regime related to a gradual weakening of the pressure gradient driving the flow [92]. Numerical simulations of the transonic flow through a crack featuring a nozzle-like constriction were performed by Morrissey and Chouet [95] using the Navier–Stokes equations representing a mixture of gas and suspended solid particles. In these simulations, shock waves develop immediately downstream from the nozzle-like constriction, and the flow acts as an energy transducer that converts smooth low-amplitude fluctuations of outlet flow pressure into strongly-amplified and repetitive step-like pressure transients applied to the crack wall immediately downstream from the nozzle. The magnitude of the pressure transient at the walls is fixed by the pressure of the supplying reservoir and the geometry of the nozzle aperture, presumably remaining constant as long as these conditions prevail. The temporal pattern of outlet pressure fluctuations controls the areal extent of the crack wall impacted by shock waves and, given a roughly constant shock magnitude, fixes the amplitude of the force applied to the wall by the fluid. This variable force applied at a fixed location along the crack wall is viewed as the force responsible for

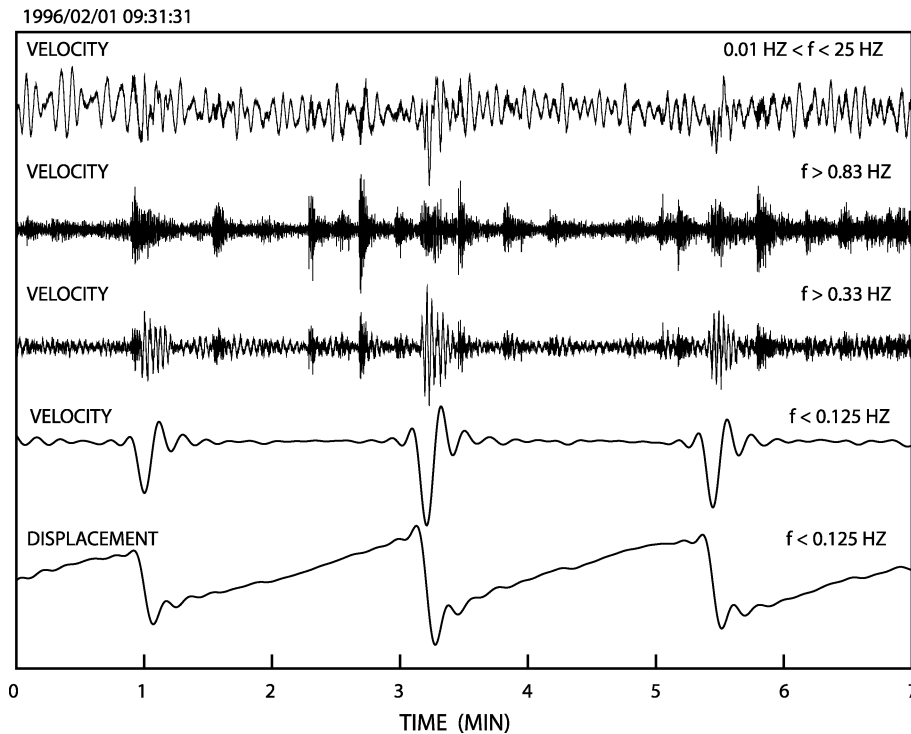
the scaling of amplitudes and the similarity of waveforms observed in the LP swarm at Redoubt [26].

Magmatic LP Events

In low-viscosity basaltic systems, LP seismicity may be part of a broadband source process associated with the unsteady transport of magma and gases through conduits. This is well illustrated in a broadband seismic record obtained at Kilauea (Fig. 7); most interesting is the displacement record shown at bottom of figure. This record, obtained after filtering the raw broadband signal (top trace in Fig. 7) with a 0.125 Hz low-pass filter, features a repetitive sawtooth signal with rise time of 2–3 min and drop time of 5–10 s. The observed repetitiveness of the VLP signal is a clear indication of the repeated action of a non-destructive source. Noteworthy also are the characteristic LP signatures obtained by filtering the broadband signal with a 0.33-Hz high-pass filter (third trace from the top). These LP events display a fixed dominant period of 2.5 s, whose onsets coincide with the start of the dropdown in the VLP sawtooth displacement signals. Such coincidence is strongly suggestive of a causative relationship between the VLP and LP signals.

The data in Fig. 7 are part of a seismic sequence observed during a surge in the magma flow feeding the ongoing east rift eruption of Kilauea, and the source mechanism of the VLP signals obtained by Ohmiato et al. [109] from waveform inversions of these data points to a repeated cycle of deformation of a sub-horizontal crack located roughly 1 km below the floor of the summit caldera. Each sawtooth in the recorded displacement signal represents a slow dilation of the crack, followed by a rapid collapse of the crack. The volume change associated with individual sawtooths ranges from 1000 to 4000 m³ [109].

A conceptual model consistent with the seismic source mechanism imaged by Ohmiato et al. [109] is shown in Fig. 8. This model involves the injection of a large slug of gas into a sub-horizontal crack with a narrow constricted outlet; both liquid magma and gas flow through this outlet constriction. Initially, liquid magma occupies the entire outlet cross section and gas accumulates in the crack, forming a layer of gas on top of the liquid and deforming the crack walls as the back pressure of gas increases in the crack. Eventually, when the back pressure buildup in the crack reaches a critical threshold, the gas slug deforms and rapidly squeezes past the constriction along with the liquid, triggering a rapid deflation (collapse) of the crack in the process. This sequence is then repeated with the next gas slug. In this scenario, the restraining force of the liquid on the gas acts like a self-activated viscosity-controlled



Volcanoes, Non-linear Processes in, Figure 7

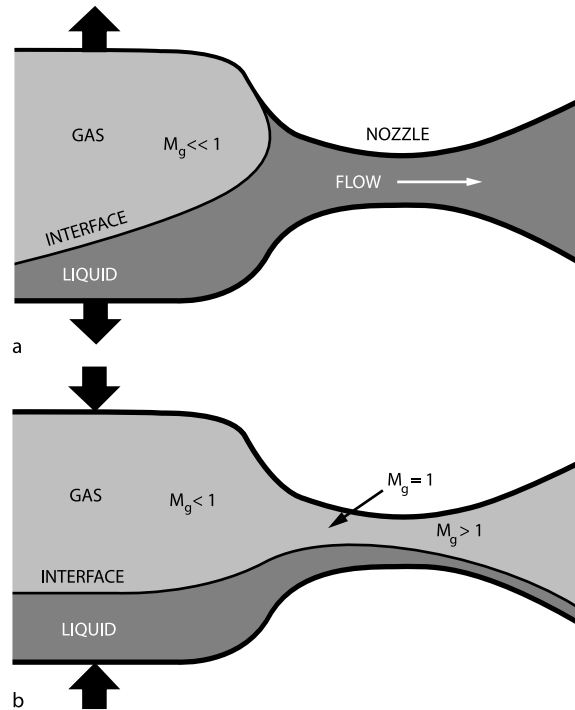
Broadband record and associated filtered signals obtained at Kilauea Volcano during a volcanic event on February 1, 1996. The broadband signal represents ground velocity and is filtered in various frequency bands to produce five records for the same 7-min time interval. The top trace shows the broadband signal ($0.01 < f < 25$ Hz), which is dominated by the oceanic wave-action microseism with dominant periods in the range 3 to 7 s. The second trace shows the signal obtained after application of a high-pass filter ($f > 0.83$ Hz). The result is equivalent to a typical short-period record and shows a series of events superimposed on a background of tremor. The third trace also has a high-pass filter applied but with a lower corner frequency ($f > 0.33$ Hz); LP signals with a dominant period of about 2.5 s are enhanced in this record. The fourth trace shows the signal when a low-pass filter is applied ($f < 0.125$ Hz); a repetitive VLP signal consisting of pulses with period of about 20 s is observed. The fifth trace is the corresponding displacement record obtained with the same low-pass filter ($f < 0.125$ Hz), showing a repetitive sawtooth pattern with rise time of 2–3 min and drop time of 5–10 s. Notice that the onset of the LP signal seen above coincides with the onset of the dropdown in the VLP displacement. (Reproduced from [38])

valve. In the stratified flow through the nozzle, the liquid moves at a steady slow pace on the order of m/s but the gas flow itself is choked in the narrow opening between the liquid/gas interface and the upper wall [138]. The formation of a shock associated with compound choking of the flow is viewed here as a trigger of acoustic oscillations of the liquid/gas mixture, which is at the origin of the LP signature with characteristic period of 2.5 s observed in conjunction with the rapidly downgoing part of the sawtooth displacement signal shown in Fig. 7.

At Stromboli Volcano, Italy, broadband seismic signals including strong VLP and LP components are seen to accompany explosions. Waveform inversions of the VLP signals performed by Chouet et al. [32] show that the processes associated with eruptions involve volumetric changes marking a cycle of pressurization-depressur-

ization-repressurization of the conduit, coupled with a single force component, both of which may be viewed as the result of a piston-like action of the magma associated with the disruption of a gas slug transiting through a sudden enlargement in conduit aperture in the steeply-inclined upper segment of conduit [32,60] (see Sect. “[Slug Distribution at Stromboli](#)” for details). The LP signal in that case is attributed to the oscillatory response of the shallowest segment of the fluid-filled conduit associated with the rapid expansion and ejection of the slug [29].

LP seismicity is also intimately linked with Vulcanian activity. The complex magma rheology, marked by a strong nonlinear dependence of viscosity on water content and temperature [49,147], finite yield strength, strain-rate dependent viscosity, and transition to brittle solid behavior at high strain rates [133] contributes to



Volcanoes, Non-linear Processes in, Figure 8

Conceptual model of separated gas-liquid flow through a converging-diverging nozzle under choked conditions (see pp. 71–74 in [138]). **a** Inflation phase showing gas accumulation upstream of the nozzle, leading to pressure buildup and deformation of the crack. The gas slug is essentially stationary and the Mach number of the gas is $M_g \ll 1$. This stage coincides with the upgoing ramp in the sawtooth displacement signal at the bottom of Fig. 7. **b** Separated gas-liquid flow through the nozzle under compound choked conditions. The gas flow is choked ($M_g = 1$) in the nozzle defined by the gas-liquid interface and upper solid wall, and is supersonic ($M_g > 1$) immediately downstream of the nozzle. There exists a maximum possible gas flow rate that is fixed by the rate of liquid discharge for given upstream conditions and fixed throat geometry. In the limit, liquid fills the duct entirely and there is no gas flow. (Reproduced from [109])

widely varying oscillatory behaviors seen in Vulcanian systems. At Galeras Volcano, Colombia, LP events displaying extended quasi-monochromatic coda were found to be linked to the release of ash-laden gases from a shallow magma body through a preexisting system of cracks bisecting the dome capping the vent [45]. Similar to Galeras, eruptive activity at Popocatepetl Volcano, Mexico, is dominated by emissions of steam, gas and ash, and by repeated formation and destruction of lava domes, all of which generate a wide variety of signals [10,11]. LP events accompanying degassing bursts are commonly associated with VLP signals and display waveform features that remain stationary from event to event. The source of these events coincides with, or is very close to, the source of VLP signals, 1.5 km below the crater floor [11,33]. This LP activity represents an integral part of a degassing process similar to that inferred for Galeras, where the sudden expulsion of a pressurized pocket of gases induces elastic deformation

of the conduit coupled with acoustic resonance of the conduit (see further discussion in Sect. “Coupled Diffusive-Elastic Pressurization at Popocatepetl Volcano”).

LP events at Soufrière Hills, Montserrat, have been linked to the action of a repetitive, non-destructive, stationary source 1.5 km below the crater floor [100]. The temporal relationship between LP events and tilt patterns at Soufrière Hills clearly shows that LP seismicity starts in synchronicity with the passage of tilt through a turning point marked by a maximum in time derivative of the tilt signal. Seismicity subsequently ceases as tilt goes through a second turning point [100]. This correlation between LP events and inflation-deflation cycles is evidence of a strong relationship linking LP seismicity to magma movement and pressure conditions at depth. Based on these observations, [100] proposed a mechanism of LP excitation originating in the brittle failure of a highly viscous magma under high strain rate. In their model, loss of gas and heat

from the magma at the conduit wall leads to the generation of a sharp viscosity gradient at the wall. This in turn leads to a buildup of shear stress near the wall, where the flowing magma undergoing glass transition can fail in a brittle manner. The resulting brecciated zone along the conduit boundary provides a natural pathway for escaping gases. The LP events may then be viewed as an expression of acoustic resonance occurring in well-defined channels in this zone, or possibly as an expression of acoustic energy trapped in an adjacent region of conduit filled with bubbly magma [36,56].

The LP sources described so far all represent shallow sources occurring in the top 2 km below the surface. Although thoroughly documented, such sources do not represent the total expression of LP seismicity. An activity of deep (> 5 km depth) LP events has also been noted in several areas of the world. In particular, episodes of deep (30–60 km) and intermediate-depth (5–15 km) LP seismicity are often observed under Kilauea [74,75]. Analyses of the intermittency of LP activity were carried out by Shaw and Chouet [122] and Shaw and Chouet [123], who viewed such tremor episodes as the relaxation oscillations of a percolation network of coupled magma-filled fractures. In their interpretation, each individual fracture in the network acts as a source of LP events, and sets of fractures give rise to multiple LP events and episodes of tremor. The aggregate nature of fracture propagation and vibration then lead to the existence of universal scaling laws that give rise to the long-recognized frequency invariance of LP events [122,123].

Other episodic bursts have been noted at depths of 10–20 km under Mammoth Mountain, California, where LP and VLP events have been seen to occur synchronously with spasmodic bursts of small brittle failure earthquakes [54]. A process involving the transport of a slug of CO₂-rich hydrous magmatic fluid derived from a plexus of basaltic dikes and sills has been invoked to explain such occurrences [54]. LP events at depths near 30 km under Mount Pinatubo, Philippines, have been attributed to a basaltic intrusion thought to have triggered processes leading to the cataclysmic eruption of June 15 [139]. Small LP events attributed to magmatic activity have also been detected at depths of 25–40 km beneath active volcanoes in northeastern Japan [47], and at depths of 10–45 km below volcanoes of the Aleutian Arc [114]. In all these instances, the occurrence of deep LP events appears to be more directly related to deep magma supply dynamics than near-surface or surface activity. Because of our lack of knowledge concerning the character and dynamics of deep-seated fluid transport under volcanoes, the actual origins of these events remain enigmatic.

Summary of Inferred Excitation Mechanisms for LP Seismicity

Shallow hydrothermal LP events at Kusatsu-Shirane, Kilauea, and Mount St. Helens all share a common excitation mechanism involving the repeated pressurization of a steam-filled fracture, causing the venting of steam, collapse of the fracture and recharge, in response to heat transfer from an underlying magma body. At Mount St. Helens, where the LP source is located very close to the magma conduit, LP activity is also seen to trigger a passive response of the conduit itself. LP seismicity observed at Redoubt represents a more energetic form of magmatic-hydrothermal interaction where an unsteady choked flow of magmatic gases provides a natural source of pressure perturbation at the origin of LP events and tremor. Magmatic LP events produced during bursts of ash-laden gases associated with Vulcanian activity at Galeras and Popocatepetl involve a pumping mechanism in shallow fractures similar to that inferred for hydrothermal LP events at Kusatsu-Shirane, Kilauea, and Mount St. Helens. LP events accompanying endogeneous dome growth at Soufrière Hills appear to be related to a more complex process involving the production of shear fractures in highly viscous magma at the glass transition, injection of dusty gases into these fractures, and resonance of the fracture network and/or possibly resonance of a bubble-rich magma excited by the energy release from the brittle failure. Magmatic LP events in the basaltic systems at Kilauea and Stromboli are the result of pressure disturbances generated during the transit of large slugs of gas through conduit discontinuities.

A nonlinear excitation mechanism of LP seismicity by fluid flow has also been proposed by Julian [62]. Using a simple lumped-parameter model, Julian investigated the elastic coupling of the fluid and solid as a means to produce self-excited oscillations in a viscous incompressible liquid flowing through a channel with compliant walls. In his model, an increase in flow velocity leads to decrease of fluid pressure via the Bernoulli effect. As a result, the channel walls move inward and constrict the flow, causing an increase in fluid pressure and forcing the channel open again. The cyclic repetition of this process is the source of sustained oscillations in Julian's model. Julian demonstrated that with increasing driving pressure the model can exhibit various oscillatory behaviors resembling tremor.

As illustrated in the above examples, magmatic-hydrothermal interactions and magmatic oscillations can take on a variety of forms. Studies of the mechanisms of tremor excitation are still very much in their infancy, owing to the paucity of accurate and detailed seismic ob-

servations essential in documenting and analyzing such processes.

Source Processes of Very-Long-Period Signals

Unlike the LP signals, which are mainly interpreted as manifestations of acoustic resonance, VLP signals are viewed as the results of inertial forces associated with perturbations in the flow of magma and gases through conduits. An increasingly widespread use of broadband seismometers on volcanoes has led to an increasing number of observations, and VLP signals have by now been documented in volcanic areas all over the world, including Sakurajima [67,68], Unzen [134], Aso [65,69,86,143], Satsuma-Iwojima [108,110], Iwate [101], Miyakejima [44,78], Usu [144], Bandai [103], Hachijo [81,83], and Asama [111] in Japan; Stromboli [14,30,32,35,99] in Italy; Merapi [50,51,52] in Indonesia; Kilauea [6,7,38,39,109] in Hawaii; Long Valley [53,54] and Mount St. Helens [137] in the United States; Erebus [13,119] in Antarctica; Popocatepetl [9,10,33] in Mexico; and Cotopaxi and Tungurahua [84] in Ecuador.

The wavelengths of VLP signals are in the range of tens to hundreds of kilometers, which greatly facilitates their analysis. Inversions of VLP waveforms have imaged crack geometries at the source in the forms of dikes or sills [32,81,109,143], as well as more complicated geometrical configurations involving a composite of a dike intersecting a sill [33], or composites of intersecting dikes [7,35], or two chambers connected to each other by a narrow channel [101]. Based on the characteristic period of VLP signals recorded at Hachijo Island, Japan, Kumagai [83] estimated a source with dimensions of a few km. The decaying harmonic oscillations with periods near 10 s and duration up to 300 s of the VLP signals seen at Hachijo are similar to the features of LP events with periods near 1 s (see Fig. 3) and appear consistent with the resonance of a dike containing a bubbly basalt. In that sense, these VLP signals probably represent a unique end member of the family of sources associated with resonant conduit excitation. Interestingly, the dominant periods and associated decay characteristics of the VLP signals at Hachijo were both found to vary with time, and these temporal variations were attributed by Kumagai [83] to a change in source dimensions, assuming fixed acoustic properties of the fluid at the source. A spread of about 4 km was also estimated by Chouet et al. [101] for two chambers at Iwate Volcano. The modeling of VLP waveforms at Stromboli by Nishimura et al. [35] points to two point sources, each involving two intersecting dikes, whose relative positions and orientations represent individual con-

duit segments with dimensions of a few hundred meters. Systematic modeling of sustained VLP tremor accompanying episodes of deflation-inflation-deflation at Kilauea has suggested a complex magma pathway composed of a plexus of intersecting dikes extending over the depth range 0.6–1.6 km below the summit caldera [7]. A crack-like conduit extending over the depth range 0.3–2.5 km has also been inferred under Aso Volcano, Japan [143].

Contrasting the above-discussed findings are results obtained by Ohminato [111] from waveform inversions of VLP signals produced by Vulcanian explosions at Asama Volcano, Japan. At Asama, the contribution from a vertical single force with magnitude $10^{10} - 10^{11}$ N was found to dominate the observed waveforms, and no obvious volumetric component was identified at the source. The depth of the VLP source is ~ 200 m beneath the summit crater, and the source-time history features two downward force components separated by an upward force component. The initial downward component was attributed by Ohminato [111] to the sudden removal of the lid capping the pressurized conduit (this force is analogous to the force F_{T_1} in Fig. 2), and the subsequent upward force was interpreted by these authors as a drag force induced by viscous magma moving up the conduit. Ohminato [111] also attributed the final downward force component to an explosive fragmentation of the magma, whose effect is to effectively cancel viscous drag so that the downward force due to jet recoil again dominates the VLP signal.

Available studies demonstrate that detailed investigations of the VLP oscillation characteristics of the source are critically important to our understanding of volcanic fluid dynamics. Below, I review two in-depth investigations of VLP signals representative of Vulcanian degassing bursts at Popocatepetl and gas-slug transport dynamics at Stromboli.

Coupled Diffusive-Elastic Pressurization at Popocatepetl Volcano

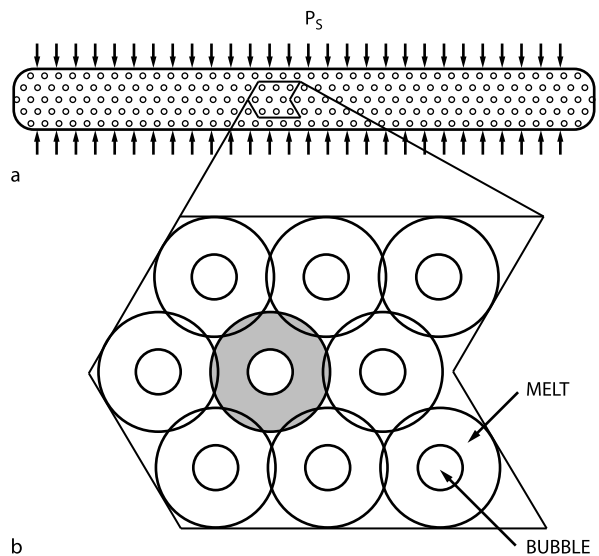
Vulcanian degassing bursts at Popocatepetl Volcano, Mexico, have been observed to be closely linked to the degassing of a sill-shaped volume of magma at a depth of 1.5 km below its summit crater [33]. The variations in volume of this sill were interpreted by Chouet et al. [33] as reflecting cyclic pressure oscillations originating in the magma filling the sill. Based on these observations, these authors proposed a model in which static magma in the sill becomes supersaturated because of groundmass crystallization. In this conceptual view, volatile exsolution and diffusion of gas from the melt into bubbles increase the internal pressure of the bubbles, because bubble expansion

is impeded by the viscous resistance of the surrounding liquid and by the confining effects due to the finite yield strength of the overlying column of magma and surrounding solid rock. Elastic inflation of the sill occurs as a result of bubble pressurization, and this inflation proceeds until the critical yield strength of the magma column is exceeded and magma starts flowing out of the sill. Magma fragmentation induced by viscous shear near the conduit wall then causes coalescence and collapse of bubbles intersected by fractures, allowing gas escape through a transient network of fractures. This, in turn, induces a pressure decrease in the sill, which results in the collapse and welding of the fracture network that shuts down the gas-escape pathway. Repeated cycles of shear-induced fracture and welding of magma provide a ratchet mechanism by which the separated gas phase in the magma can be recharged and evacuated.

The expansion dynamics of bubbles in supersaturated magma have been addressed in many previous studies under conditions of constant melt pressure [87,88,90,115,117,121,125], or constant decompression rate [116,131,132]. A canonical model of bubble growth in magma that includes the effect of finite spacing of bubbles in the melt was first developed by Proussevitch et al. [115]. This model considers a suspension of gas bubbles in an incompressible volatile-bearing liquid. The suspension is modeled as a three-dimensional lattice of closely-packed spherical cells, where each identical elementary cell is composed of a gas bubble surrounded by a shell of liquid. A step drop in pressure in the melt induces volatile exsolution and bubble expansion is driven by the diffusion of gas into the bubble. In this model, only the volatiles contained in the shell of liquid surrounding the bubble contribute to the bubble expansion so that bubble growth is limited by how closely packed the bubbles are in the liquid. Using the model of Proussevitch et al. [115], Chouet et al. [34] and Shimomura et al. [124] obtained a dynamic solution that includes the effect of melt compressibility. In their model, pressure recovery is driven by bubble growth in a supersaturated magma that is stressed by the surrounding crust as the magma volume increases with bubble expansion. Both models consider the pressure recovery following an instantaneous pressure drop in the melt. The magma is embedded in an infinite, homogeneous, elastic solid and consists of a melt containing numerous small spherical gas bubbles of identical size. No new bubbles are created and no bubbles are lost during pressure recovery, and the gas in the bubbles is assumed to be a perfect gas. Gravity and other body forces are not considered.

The conduit geometry considered by Chouet et al. [34] applies specifically to the observation made at Popocate-

petl [33] and consists of a penny-shaped crack containing a melt with an isotropic distribution of bubbles (Fig. 9a). The initial oversaturation of the melt resulting from a pressure drop ΔP_0 is distributed uniformly in the melt, and each bubble grows by diffusion of volatiles from a surrounding shell of melt with finite radius (Fig. 9b). As diffusion is a slow process, with time scale much longer than that of heat transfer into the bubble [56], bubble growth is assumed to be isothermal. The mathematical model describing an elementary cell therefore consists of three equations: (1) a diffusion equation governing the transfer of volatiles in the melt shell; (2) an equation expressing the radial motion of the bubble; and (3) a relation representing the ideal gas approximation. These equations are then subjected to three boundary conditions expressing the phase equilibrium at the bubble wall, mass flux at the bubble wall, and zero mass flux through the outer shell wall. As the bubble grows by mass transfer from the melt, melt is compressed and the surrounding rock ma-



Volcanoes, Non-linear Processes in, Figure 9

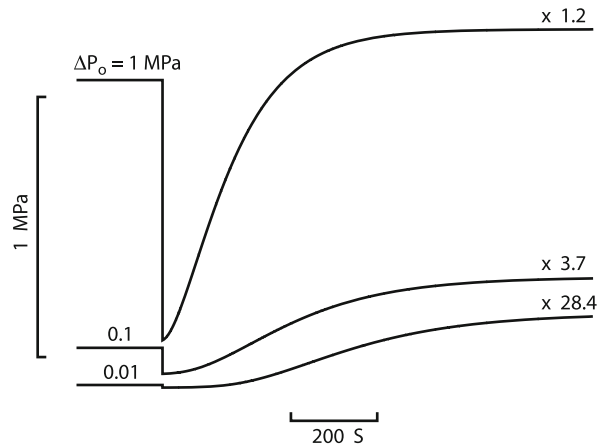
Model used by Chouet et al. [34] to interpret the source mechanism of Vulcanian degassing bursts at Popocatepetl Volcano, Mexico. **a** Schematic illustration (cross section) of penny-shaped crack embedded in an elastic solid. The crack is under confining pressure P_s , and contains a melt with an isotropic distribution of gas bubbles of identical sizes. **b** Detailed view of the distribution of elementary cells composing the bubbly liquid (after [115]). Each cell (as in gray-shaded example) consists of a gas bubble surrounded by a finite volume of melt. The elementary cells are organized in a three-dimensional lattice with slight overlap of the cells, where the volumes of intersecting melt and gaps are equal, so that the gas-volume fraction is $(R/S)^3$, where R is the bubble radius and S is the outer shell radius

trix is deformed as a result. The pressure in the melt is balanced by the stress applied by the surrounding elastic medium, and in both Chouet et al. [34] and Shimomura et al. [124], this is formalized by assuming a quasi-static deformation of the magma conduit. Melt shrinkage from dehydration [105] is assumed to be negligible compared to melt compression due to bubble growth and is not considered.

In their treatment of the initial condition in the bubble, Chouet et al. [34] follow Proussevitch et al. [115] and assume an instantaneous drop in gas pressure inside the bubble. This induces an instantaneous drop in volatile concentration at the bubble wall, thereby producing a step-like gradient of concentration that kick-starts the diffusion process. This condition is different from that assumed by Shimomura et al. [124], who follow the model of Navon and Lyakhovsky [98], in which the bubble initially retains the original gas pressure and immediately expands in response to the difference between internal and external pressures. The relaxation expansion of the bubble then induces a decrease in gas pressure inside the bubble, which leads to the establishment of a gradient in volatile concentration at the bubble wall that starts the diffusion. Although this leads to distinct features in the instantaneous bubble response, this has essentially no effect on the volumetric response of the bubble at longer time scales.

Figure 10 shows the pressure recovery calculated by Chouet et al. [34] for input step drops $\Delta P_0 = 0.01, 0.1$, and 1 MPa applied to a bubbly rhyolitic melt encased in a penny-shaped crack with radius 100 m and thickness 5 m under ambient pressure $P_s = 40$ MPa appropriate for the depth of the source imaged for Popocatepetl Volcano [33]. The bubbles have a fixed initial radius 10^{-6} m, and the bubble number density is 10^{12} m^{-3} . Melt density, viscosity, and diffusivity are 2300 kg m^{-3} , 10^6 Pa s , and $10^{-11} \text{ m}^2 \text{ s}^{-1}$, respectively; surface tension is 0.2 Nm^{-1} , and the bulk modulus of melt and elastic rigidity of the rock are both 10^{10} Pa . The amplitude ratio of pressure recovery to initial pressure drop displays a strong non-linear sensitivity to the magnitude of the input pressure drop, resulting in magnifications ranging from about 1 to nearly 30 over the range of input transients considered (Fig. 10). This overpressurization upon recovery was previously noted in a static solution obtained earlier by Nishimura [104] and becomes largest for tiny bubbles and a stiff elastic medium [34,124]. Figure 10 also indicates that the speed of recovery is a function of the input transient, with the crack response becoming markedly slower for small pressure transients compared to larger ones.

The variation of time and amplitude scales seen in Fig. 10 suggests that a wide range of responses may

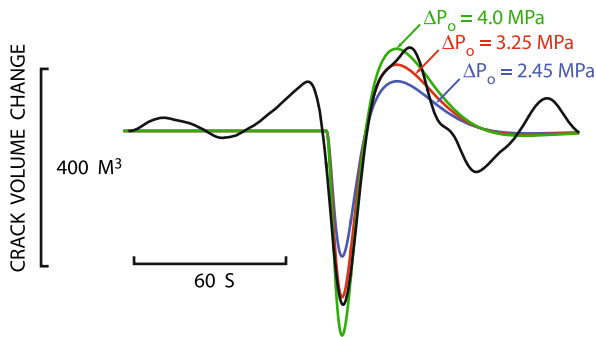


Volcanoes, Non-linear Processes in, Figure 10

Dependence of pressure recovery on the size of the input transient, ΔP_0 , in the model of Chouet et al. [34]. The magnification factor for each response is indicated at the upper right of each pressure trace

be possible for cracks containing melts with a wider population of bubble sizes than the single-size bubble populations considered by Chouet et al. [34]. The net drop in volatile concentration associated with diffusion-driven bubble growth is quite small. Indeed, the results obtained by Chouet et al. [34] point to concentration drops $\sim 0.003 - 0.035 \text{ wt\%}$ for initial bubble radii of $10^{-5} - 10^{-7} \text{ m}$ in penny-shaped cracks with aperture to radius ratios $0.01 - 0.25$. The net concentration drop is small because pressure recovery in the melt acts to raise the saturation level of volatiles in the melt. This has important implications for the overall history of degassing in a Vulcanian system, as it suggests that this process may be repeated many times without significantly depleting the gases in the melt body.

The source process imaged under Popocatepetl involves a sequence of inflation, deflation, and reinflation, reflecting a cycle of pressurization, depressurization, and repressurization within a time interval of 3–5 min [33]. The volumetric component of the source processes in the sill associated with an eruption on 23 May 2000 is shown in Fig. 11. Other eruptions were found to produce similar waveform characteristics, hence the event in Fig. 11 may be viewed as an appropriate representation of overall source dynamics associated with these Vulcanian eruptions. For comparison, Fig. 11 also shows the volume change of a magma-filled sill calculated with the model of Chouet et al. [34]. The sill response has been band-pass filtered in the same band as the observed signal, and is illustrated for three distinct pressure drops. The model pa-



Volcanoes, Non-linear Processes in, Figure 11

Source-time function of volume change obtained by Chouet et al. [33] for a sill under Popocatepetl Volcano during a degassing burst on 23 May 2000 (black line), and corresponding volume changes in a sill filled with a bubbly melt in response to a step drop ΔP_0 in pressure (colored lines). The data from Popocatepetl and solutions from the crack model have both been band-pass filtered in the 15–70 s band

parameters in Fig. 11 are identical to those used in Fig. 10. A realistic fit of the peak-to-trough amplitude of the volume change imaged at Popocatepetl is obtained for an input pressure drop $\Delta P_0 = 3.25$ MPa.

Unfortunately, the longer-period components and other specific features of the sill response in the model are lost in the band-limited version of the signal compatible with observations made at Popocatepetl, so that the responses obtained in this band for different model parameters are all very similar [34]. Although it is not possible to infer specific values of melt viscosity, volatile diffusivity, initial bubble radius, bubble number density, or sill aperture to radius ratio based on available seismic data, these results strongly support the idea that diffusion pumping of bubbles in the magma under Popocatepetl provides a viable mechanism for pressure recovery following a pressure drop induced by a degassing event.

Slug Disruption at Stromboli

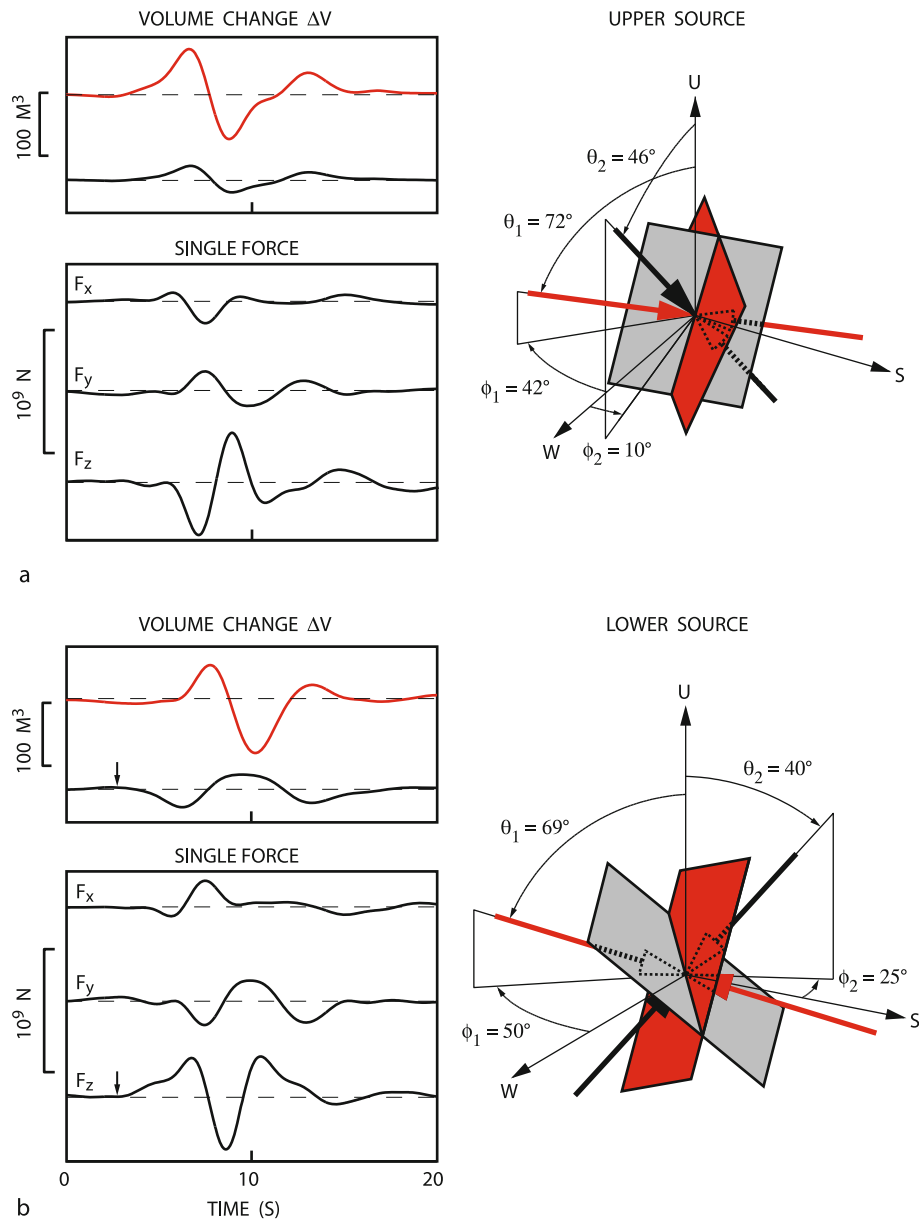
Eruptive behavior at Stromboli is characterized by mild, intermittent explosive activity, during which well-collimated jets of gases laden with molten lava fragments burst in short eruptions typically lasting 5–15 s. Modeling of VLP seismic data recorded during explosive activity in 1997 has imaged two distinct dike structures representative of explosive eruptions from two different vents located near the northern and southern perimeters of the summit crater [32,35].

Figures 12 and 13 show two representations of the conduit geometry underlying the northern vent area. Figure 12 shows the seismic source mechanisms obtained

from inversion of VLP waveforms; the mechanisms include two point sources, each of which marks a flow disruption site along the upper conduit. The upper source (Fig. 12a) is located 300 m below the crater floor and represents a bifurcation in the conduit; this is the main flow disruption site for gas slugs ascending toward the northern vent. The lower source (Fig. 12b), located roughly 500 m below the upper source, involves a sharp corner in the conduit and represents a secondary flow disruption site. Both upper and lower sources feature a dominant crack sustaining the largest volume change (colored red), and a subdominant crack undergoing a smaller volume change (shaded gray). Both cracks in Fig. 12a display a similar sequence of inflation-deflation-inflation. The dominant crack in the lower source displays a volumetric response similar to that seen in the dominant crack at the upper source, but delayed by about 1 s with respect to the upper source. This implies a propagation speed of roughly 500 m/s between the two sources, consistent with the slow speed expected for the crack wave.

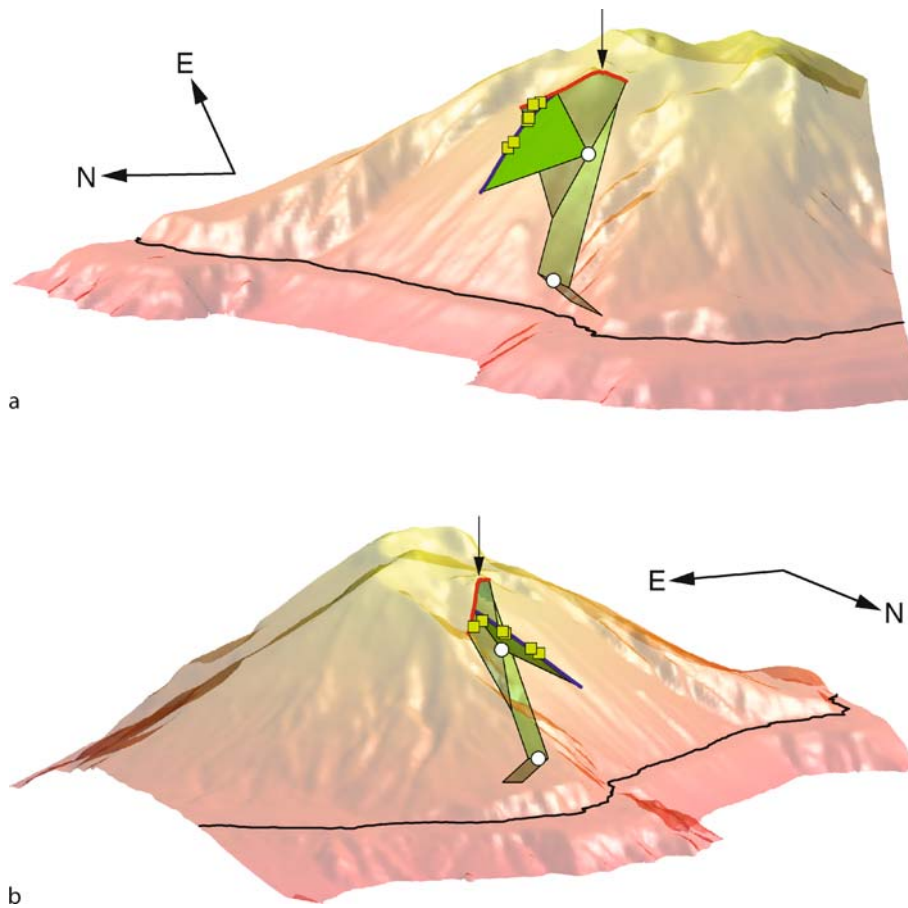
Figure 13 shows a picture of the upper conduit geometry consistent with the seismic source mechanisms imaged in Fig. 12. The closely matching dips of the two dominant cracks in Fig. 12 point to a conduit that extends essentially straight from 80 m below sea level to the crater floor, 760 m above sea level. At a depth of 80 m below sea level the conduit features a sharp corner leading into a dike segment dipping 40° to the southeast. The upper dominant dike segment, and deep segment below the abrupt corner both strike northeast-southwest along a direction parallel to the elongation of the volcanic edifice and a prominent zone of structural weakness, as expressed by lineaments, dikes, and brittle structures. The surface trace of the main dike segment trends through the northern vent area, while that of the upper subsidiary segment extends northwest-southeast in rough alignment with several vents active in the northwest quadrant of Stromboli in 2002–2003 [1]; the subsidiary dike trace intersects the main dike trace ~ 170 m north of the northern vent area.

A striking aspect of the mechanisms imaged for the two sources in Fig. 12 is the presence of dominantly vertical single-force components with common-looking time histories, except for a polarity reversal in one source compared to the other. The upper source (Fig. 12a) displays an initially downward force followed by an upward force, while an upward force followed by a downward force is manifest in the lower source (Fig. 12b). These force components compensate each other so that the total momentum in the overall source volume is conserved. In contrast to the delay of ~ 1 s in the volumetric components noted above, no significant delay is noted in the onsets of the ver-



Volcanoes, Non-linear Processes in, Figure 12

Seismic source mechanisms imaged for the two flow disruption sites in the shallow conduit structure underlying the northern vent area at Stromboli. The two point-source mechanisms were obtained by Chouet et al. [35] from inversions of VLP waveforms recorded during explosions at Stromboli, and are positioned at different depths in the volcanic edifice (see text for details). Each source consists of two intersecting cracks and a single force with components F_x (east), F_y (north), and F_z (up). Volume changes are color-coded with the color of the cracks they represent in each source. Crack orientations are provided by the azimuth ϕ and polar angle θ of the dominant dipole normal to the crack plane, with arrow directions marking crack deflation (see Fig. 1c). The reference coordinates are W (west), S (south), and U (up). **a** Upper source. **b** Lower source. Small arrows in left panels mark the onset of deflation of the lower dike (gray dike in right panel) and synchronous start of the upward force. (Reproduced from [35])



Volcanoes, Non-linear Processes in, Figure 13

Geometry of the upper 1 km of conduit underlying the northern vent area of Stromboli. A semi-transparent view of the northwest quadrant of the volcanic edifice provides the reference for the location and geometry of the conduit, which is derived from the seismic source mechanisms in Fig. 12. Thin black line indicates sea level. The summit of the volcano is 924 m above sea level (no vertical exaggeration). The two flow disruption sites that are sources of VLP elastic radiation are indicated by small circles. The irregular red and blue lines, respectively, represent the surface traces of the dominant and subdominant dike segments constituting the shallowest portions of the conduit system. The eruptive vent is marked by an arrow, and vents temporarily active during the flank eruption in 2002–2003 are marked by green squares. The lateral extents of individual dike segments are unknown and are shown for illustrative purpose only. **a** East-looking view. **b** South-looking view

tical forces at the two sources, suggesting that transmission of the force between the two sources occurs via the faster speed (3.5 km/s [32]) of the compressional wave in the rock matrix.

Laboratory simulations carried out by James et al. [60] provide insights into the origin of the initial pressurization and downward force observed at the upper source in Fig. 12a. These experiments investigate the ascent of a slug of gas in a vertical liquid-filled tube featuring a flare that abruptly doubles the cross sectional area. The tube is instrumented with pressure transducers mounted flush with the inner tube wall, and one accelerometer mounted on the exterior of the tube, and the whole assembly is free

to move in the vertical direction. Detailed measurements of the flow transients obtained by James et al. [60] show that the transit of a gas slug through the tube flare involves complex changes in flow pattern. A characteristic pinching of the slug tail is observed to occur synchronously with strong pressure and acceleration transients at the time the slug clears the flare, a picture consistent with the downward and inward motion of a liquid piston formed by the thickening film of liquid falling past the slug expanding in the wider tube. The sudden deceleration of the liquid annulus as it impinges the narrower inlet to the lower tube segment generates a pressure pulse in the liquid below the flare and also induces a downward force on the apparatus.

These observations are consistent with the pressurization phase and initial downward force imaged for the upper source at Stromboli and a similar funneling mechanism was inferred by Chouet et al. [35] to be operative there. The repeatability of recorded pressure data and dependence of the magnitude of the pressure transient on slug size seen in the experiments of James et al. [60] are also in harmony with the observed spatio-temporal properties of VLP signals at Stromboli [32,35].

At the lower source, the start of the vertical force signal is synchronous with the onset of deflation of the lower dike segment (see arrows in the left panels in Fig. 12b). As the amplitude of the upward force increases, the lower dike segment continuously deflates. During the same interval, the dominant dike (red-colored volumetric trace in Fig. 12b) remains in a slightly deflated state. The lower dike reaches maximum deflation at the time the upper dike segment goes through a transition from weak contraction to expansion, and the upward force reaches its peak amplitude ~ 0.5 s later. This picture is consistent with a compression of the lower dike synchronous with a downward acceleration of the liquid mass, both of which are suggestive of increasing external pressure on the conduit wall resulting from the downward vertical force acting at the upper source. Compression of the lower dike segment proceeds unimpeded until this process is overprinted by the arrival of the much slower volumetric expansion signal from the upper source.

Although not illustrated here, a similar slug disruption mechanism was imaged in the dike system underlying the southern vent [35]. In both conduit systems, the early response of the lower source relative to the volumetric disturbance arriving from the upper source may be interpreted as the passive response of the liquid to the movement of the conduit wall induced by elastic radiation from the force acting at the upper source. The scenario emerging from these dynamics is that of an upper source representing an active fluid phase and passive solid phase, and a lower source representing an active solid phase and passive fluid phase. The overall seismic source process associated with eruptions at Stromboli may then be summarized as follows. A slug of gas formed in the deeper reaches of conduit [18] rises through the lower conduit corner (the lower seismic source). At this point, the slug is most likely a few meters long and traverses this corner aseismically; past this corner, the slug expands on its way to the upper conduit bifurcation (the upper seismic source). The transit time from the lower to the upper seismic source is probably in the range of 5–15 minutes [60], hence related changes in magmatic head are well beyond the capability of broadband seismometers to detect and are not appar-

ent within the VLP band imaged in Fig. 12. As it traverses the upper seismic source, the slug length has expanded to tens of meters and the slug is by then seismically noisy. Gravitational slumping of the liquid occurs as the slug expands through a flare in the conduit at this location. The slumping liquid rapidly decelerates in the narrowing dike neck, increasing the liquid pressure and inducing a volume expansion in the main conduit and its subsidiary branch. The rapid deceleration and associated pressurization of the liquid couples to the conduit wall via the flare shoulders and induces a downward vertical force on the Earth. The volumetric signal propagates along the conduit at the slow speed of the crack wave, while the force signal itself propagates in the solid at the much higher speed of the compressional wave in the rock matrix, arriving at the lower conduit corner well before the crack wave. At this corner, the downward displacement of the rock induced by the force acting at the upper source impinges the bottom dike and squeezes this segment of conduit; this segment essentially acts like a spring that absorbs the downward motion of the rock. This scenario is consistent with both the small volume change of the lower dike segment, as well as its early response. The subsequent conduit response then reflects the combined effects of volumetric and mass oscillations of this liquid/gas/solid system, which are damped and eventually terminated by changing flow conditions.

The analyses carried out by Chouet et al. [35] illuminate the subsurface processes driving eruptions at Stromboli and clearly point to the key role played by the conduit geometry in controlling fluid motion and resultant processes. Each irregularity or discontinuity in the conduit provides a site where pressure and momentum changes resulting from flow processes associated with the transit of a gas slug through the discontinuity are coupled to the Earth, or where the elastic response of the conduit can couple back into pressure and momentum changes in the fluid. The resulting processes are naturally oscillatory and involve diverse dynamics that reflect the complex physico-chemical behavior of the volcanic system from the surface downward.

Future Directions

Seismology alone cannot directly see into the conduit and resolve details of the actual fluid dynamics at the origin of the seismic source mechanisms revealed by analyses of LP or VLP signals. To develop a better understanding of fluid behavior responsible for these signals, laboratory experiments are required to explore the links between known flow processes and the resulting pressure and momentum changes. The pressure and mo-

mentum changes generated under laboratory conditions may then be compared with the pressure and momentum changes estimated from the time-varying moment-tensor and single-force components imaged from seismic data, yielding clues about the physical flow processes linked to the seismic source mechanism. Recent laboratory studies [59,60,85] have elucidated self-excitation mechanisms inherent to the fluid nonlinearity that are providing new insights into the mechanisms imaged from seismic data. In particular, the results obtained by James et al. [60] demonstrate that direct links between the moment-tensor and single-force seismic-source mechanism and fluid-flow processes are possible and could potentially provide a wealth of information not available from seismic data alone. Together with these laboratory advances, numerical studies of multiphase flows are required to shed light on both the micro- and macrophysics of such flows (e.g., Badalassi [15]), along with models exploring the coupled dynamics of fluid and solid [102]. The key to a better understanding of volcanic processes lies in a sustained effort aimed at cross-fertilization between increasingly realistic numerical and experimental models of the fluid dynamics and elastodynamics, spatially and temporally dense field measurements of diverse geophysical signals at all frequencies, and chemical and physical evidence recorded in the eruptive products. In the next section, I present a brief summary of a modeling approach to two-phase fluids that holds great promise for the quantification of volcanic and hydrothermal source processes.

Phase-Field Method

Liquid-gas mixtures are an ubiquitous feature of magmatic and hydrothermal systems. A major challenge in addressing these types of fluids is the description of the moving and deforming interface between the two components of fluid. Traditional fluid dynamics treats these as sharp interfaces on which matching boundary conditions must be imposed, which generally leads to intractable problems. Another difficulty is posed by the complex rheology of each component, whose internal microstructure is coupled with the flow field. The *phase-field method*, also known as the *diffuse-interface model*, circumvents these difficulties by considering the interface between components as a thin diffuse layer within which the two components are mixed and store a mixing energy. This idea follows from the original work of van der Waals [135] and expresses the properties of the interface by molecular forces and a mixing energy. In the limit of an interface width approaching zero, the diffuse-interface model reduces to the classical sharp-interface model and results in the proper

expression for interfacial tension. Lowengrub and Truskinovsky [89] provide a detailed formulation of the conservative dynamics of the diffuse-interface model based on the classical procedure of Lagrangian mechanics. A review of diffuse-interface methods and related applications can also be found in Anderson et al. [8]. Noteworthy are the more recent applications by Kendon et al. [71], Xu et al. [141], Xu et al. [142], and Yue et al. [146]. The following discussion is restricted to a brief description of the basic principles of the method based on the work of Kendon et al. [71], who consider the evolution of a symmetric binary fluid mixture after a deep quench.

Equilibrium State A two-phase mixture is described by two scalar fields n_A and n_B expressing the local molar densities of the fluid components A and B . The corresponding local density, ρ , is given by:

$$\rho = m_A n_A + m_B n_B, \quad (2)$$

where m_A and m_B are the molecular weights of phases A and B , respectively. The local composition of the fluid is quantified by a dimensionless parameter, ϕ ,

$$\phi = \frac{n_A - n_B}{n_A + n_B}, \quad (3)$$

called the order parameter; the values of ϕ span the range $[-1, +1]$ with the value $+1$ denoting the pure phase A and the value -1 denoting the pure phase B .

The chemical equilibrium between the two phases is described through a minimization of the free energy \mathcal{F} , which represents the integral over the body of the local free-energy density (with units of Jm^{-3} or, equivalently, Nm^{-2}), a function of the fluid composition and its gradient [19]:

$$\mathcal{F} = \int \left\{ f_0(\phi, P) + \frac{1}{2} \kappa (\nabla \phi)^2 \right\} \text{d}\mathbf{r}. \quad (4)$$

The term $f_0(\phi, P)$ in the above equation represents the bulk free-energy density, which is assumed to take the form of a double-well with respect to ϕ . The detailed functional form of the double-well potential is not important [17,71,127,128,141,142,146] and may be set as [71,141]:

$$f_0(\phi, P) = \frac{a}{2} \phi^2 + \frac{b}{4} \phi^4 + P \ln \frac{P}{P_0}, \quad (5)$$

where the polynomial terms represent the bulk properties of the fluid. The parameter $a < 0$ and parameter b is always positive [141]. The term in P yields a positive

background pressure and does not affect the phase behavior (see discussion of pressure below). The form of this latter term is selected here for convenience, with P_0 representing an arbitrary reference pressure. As defined above, the function f_0 features two minima for $\phi = \pm\sqrt{-a/b}$ that correspond to the coexisting pure bulk phases. Assuming $b = -a$, one obtains the equilibrium values $\phi = \pm 1$ [141].

The squared gradient term in Eq. (4), with κ a positive constant, represents weakly non-local interactions between the components. The effect of these interactions favors mixing of the components in contrast to the tendency of the bulk free energy f_0 , which is toward total separation of the phases into domains of pure components [146].

According to the model represented by Eq. (5), minimization of the free energy is achieved through the creation of two bulk domains at compositions $\phi = \pm 1$ separated by interfaces across which the composition varies smoothly from one phase to the other. The change in \mathcal{F} induced by a small local change in composition is described by the chemical potential, μ ,

$$\mu = \frac{\delta \mathcal{F}}{\delta \phi}, \quad (6)$$

and equilibrium between the coexisting bulk phases is reached when μ is everywhere zero [19,71]. Using Eqs. (4) and (5), one obtains the following expression for μ :

$$\mu = a\phi + b\phi^3 - \kappa \nabla^2 \phi. \quad (7)$$

The equilibrium interfacial profile is given by $\phi(x) = \tanh(2x/\xi)$, where x is the coordinate normal to the interface [141]. With the choice $b = -a$, this yields an interfacial width, $\xi = 2\sqrt{-2\kappa/a}$, and surface tension, $\sigma = (2/3)\sqrt{-2a\kappa}$ [141]. The interface thickness may then be defined as the width over which 90% of the variation of ϕ occurs; this yields an equilibrium interface thickness of 1.47222ξ .

As interfaces in the fluid can exert non-isotropic forces, pressure is a tensor. The thermodynamic pressure tensor P_{ij}^{th} is obtained from the free energy as [41,71,127]

$$\begin{aligned} P_{ij}^{\text{th}} &= \left(P \frac{\delta \mathcal{F}}{\delta P} + \phi \frac{\delta \mathcal{F}}{\delta \phi} - \left[f_0(\phi, P) + \frac{1}{2} \kappa (\nabla \phi)^2 \right] \right) \delta_{ij} \\ &\quad + \kappa \frac{\partial \phi}{\partial x_i} \frac{\partial \phi}{\partial x_j} \\ &= P + P_{ij}^{\text{chem}}, \end{aligned} \quad (8)$$

where P is the bulk pressure, and P_{ij}^{chem} is the chemical pressure component given by

$$\begin{aligned} P_{ij}^{\text{chem}} &= \left[\frac{1}{2} a \phi^2 + \frac{3}{4} b \phi^4 - \kappa \phi \nabla^2 \phi - \frac{1}{2} \kappa (\nabla \phi)^2 \right] \delta_{ij} \\ &\quad + \kappa \frac{\partial \phi}{\partial x_i} \frac{\partial \phi}{\partial x_j}, \end{aligned} \quad (9)$$

in which δ_{ij} is the Kronecker symbol ($\delta_{ij} = 0$ for $i \neq j$, and $\delta_{ij} = 1$ for $i = j$). Note that the expression between brackets contributes to the isotropic fluid pressure and that only the last term is anisotropic.

Conservation Equations The temporal evolution of the fluid composition ϕ is described by the Cahn–Hilliard diffusion-advection equation [20]

$$\frac{\partial \phi}{\partial t} + \mathbf{v} \cdot \nabla \phi = \nabla \cdot (\gamma \nabla \mu), \quad (10)$$

where γ is the order-parameter mobility and $\mathbf{v}(\mathbf{r})$ is the fluid velocity.

The dynamics of the fluid are described by the Navier–Stokes equations, whose exact forms depend on the system considered. The equations describing a viscous, compressible, isothermal flow are the conservation of mass:

$$\frac{\partial \rho}{\partial t} + \nabla \cdot (\rho \mathbf{v}) = 0, \quad (11)$$

and conservation of momentum:

$$\rho \left[\frac{\partial \mathbf{v}}{\partial t} + (\mathbf{v} \cdot \nabla) \mathbf{v} \right] = -\nabla \cdot \mathbf{P}^{\text{th}} + \nabla \cdot \boldsymbol{\tau} + \rho \mathbf{g}, \quad (12)$$

where \mathbf{g} is the acceleration of gravity vector, \mathbf{P}^{th} is the thermodynamic pressure tensor with components given by Eqs. (8) and (9), and $\boldsymbol{\tau}$ is the viscous stress tensor, which for a newtonian fluid is given by

$$\tau_{ij} = \lambda e_{kk} \delta_{ij} + 2\eta e_{ij}, \quad (13)$$

where η is the coefficient of viscosity (dynamic viscosity) and λ is the second coefficient of viscosity generally defined as $\lambda = -(2/3)\eta$ [130]. Summation over repeated indices is implied. In this equation e_{ij} is the strain rate tensor given by:

$$e_{ij} = \frac{1}{2} \left(\frac{\partial v_i}{\partial x_j} + \frac{\partial v_j}{\partial x_i} \right). \quad (14)$$

The field variables are the order parameter ϕ , the three components of fluid velocity \mathbf{v} , density ρ , and bulk pressure P . Under isothermal conditions P may be specified

through a van der Waals equation of state. The diffusion-advection Eq. (10), continuity Eq. (11), and the three momentum Eqs (12), along with an equation of state for P , therefore provide a complete description of the physico-chemical evolution of the binary fluid mixture. All other quantities can be obtained from the relations (2), (3), (7), (8), (9), (13), and (14). For non-isothermal flow, a complete description is obtained from Eqs. (10–12), along with two additional equations describing the conservation of energy and entropy production [8].

The thermodynamic properties of the two-phase system enter the above equations through the chemical potential $\mu = \delta \mathcal{F} / \delta \phi$, and pressure tensor \mathbf{P}^{th} , which are both obtained from the free energy Eq. (4). As a result, interfaces between the different fluid phases appear naturally within the model and do not need to be put in as boundary conditions. The procedure is quite general and may conceivably be applied to any complex fluid with a properly defined free energy.

The coupled Cahn–Hilliard/Navier–Stokes system of equations representing binary fluid systems is analytically intractable, and efforts have mainly been directed toward the development of robust, stable numerical schemes. The description of the fluid in terms of a smooth variation of the composition $\phi(\mathbf{r})$ provides a coarse-grained representation of the fluid where the smallest length scale is larger than the average distance between molecules. Under dynamical conditions, care must be taken to ensure that this coarse-grained description adequately represents the underlying microscopic physics. For the nominal interfacial thickness representing 90% of the variation of ϕ this typically requires 7–10 grids to resolve [146]. Numerical applications include the Lattice Boltzmann Method (LBM) [16,71,112,113,127,128,141,142], and various finite-difference approaches based on an Implicit-Explicit (IMEX) discretization [12], semi-implicit discretization [15,146], fully implicit discretization [73], or fully explicit central-differenced staggered-grid discretization [58].

An example of application of this method that may provide a useful metaphor for the process of Vulcanian degassing discussed in Sect. “Coupled Diffusive-Elastic Pressurization at Popocatepetl Volcano” is the 3D spinodal decomposition of a density-matched binary fluid mixture in a channel under shear [15]. A remarkable feature of this type of flow is the formation of string-like structures. Similar structures have been observed in immiscible viscoelastic systems subjected to complex flow fields [93], and such process may also play a role in the formation of degassing channels in a rhyolitic bubbly magma driven by slow pressurization in response to crystallization and de-

gassing. A 2D application of the method to the dynamics of a gas slug ascending in a liquid-filled conduit featuring a flare is described in the chapter by *D’Auria and Martini*. The numerical results obtained by these authors reproduce the basic behavior observed in the experimental simulations of James et al. [59] and James et al. [60] and hold great potential as a key link between the seismic source mechanisms imaged at Stromboli (see Sect. “Slug Disruption at Stromboli”) and the underlying volcanic fluid dynamics.

Acknowledgment

I am grateful to Phil Dawson for his assistance in drafting figures. I am indebted to Robert Tilling and David Hill for careful reviews and helpful suggestions.

Bibliography

1. Acocella V, Neri M, Scarlato P (2006) Understanding shallow magma emplacement at volcanoes: Orthogonal feeder dykes during the 2002–2003 Stromboli (Italy) eruption. *Geophys Res Lett* 33:L17310. doi:10.1029/2006GL026862
2. Aki K, Fehler M, Das S (1977) Source mechanism of volcanic tremor: Fluid-driven crack models and their application to the 1963 Kilauea eruption. *J Volcanol Geotherm Res* 2:259–287
3. Aki K, Richards PG (1980) *Quantitative Seismology*. Freeman, New York, p 932
4. Almendros J, Chouet B, Dawson P (2001) Spatial extent of a hydrothermal system at Kilauea Volcano, Hawaii, determined from array analyses of shallow long-period seismicity. *J Geophys Res* 106:13581–13597
5. Almendros J, Chouet B, Dawson P, Huber C (2002) Mapping the sources of the seismic wave field at Kilauea Volcano, Hawaii, using data recorded on multiple seismic antennas. *Bull Seismol Soc Am* 92:2333–2351
6. Almendros J, Chouet B, Dawson P, Bond T (2002) Identifying elements of the plumbing system beneath Kilauea Volcano, Hawaii, from the source locations of very-long-period signals. *Geophys J Int* 148:303–312
7. Almendros J, Chouet B, Dawson P (2008) Shallow magma transport pathway under Kilauea Volcano, Hawaii, imaged from waveform inversions of very-long-period seismic data. 2-Source modeling *J Geophys Res*, submitted
8. Anderson DM, McFadden GB, Wheeler AA (1998) Diffuse-interface methods in fluid mechanics. *Annu Rev Fluid Mech* 30:139–165
9. Arciniega-Ceballos A, Chouet BA, Dawson P (1999) Very-long-period signals associated with Vulcanian explosions at Popocatepetl Volcano, Mexico. *Geophys Res Lett* 26: 3013–3016
10. Arciniega-Ceballos A, Chouet B, Dawson P (2003) Long-period events and tremor at Popocatepetl Volcano (1994–2000) and their broadband characteristics. *Bull Volcanol* 65: 124–135
11. Arciniega-Ceballos A, Chouet B, Dawson P, Asch G (2008) Broadband seismic measurements of degassing activity as-

- sociated with lava effusion at Popocatepetl Volcano, Mexico. *J Volcanol Geotherm Res* 170:12–23
12. Ascher UM, Ruuth SJ, Wetton BTR (1995) Implicit-explicit methods for time-dependent partial differential equations. *SIAM J Numer Anal* 3:797–823
 13. Aster R, Mah S, Kyle P, McIntosh W, Dunbar N, Johnson J, Ruiz M, McNamara S (2003) Very long period oscillations of Mount Erebus Volcano. *J Geophys Res* 108(B11). doi:10.1029/2002JB002101
 14. Auger E, D'Auria L, Martini M, Chouet B, Dawson P (2006) Real-time monitoring and massive inversion of source parameters of very long period seismic signals: An application to Stromboli Volcano, Italy. *Geophys Res Lett* 33:L04301. doi:10.1029/2005GL024703
 15. Badalassi VE, Cenicerio HD, Banerjee S (2003) Computation of multiphase systems with phase field models. *J Comput Phys* 190:371–397
 16. Balazs AC, Verberg R, Pooley CM, Kuksenok O (2005) Modeling the flow of complex fluids through heterogeneous channels. *Soft Matter* 1:44–54
 17. Bray AJ (1994) Theory of phase-ordering kinetics. *Adv Phys* 43:357–459
 18. Burton M, Allard P, Muré F, La Spina A (2007) Magmatic gas composition reveals the source depth of slug-driven Strombolian explosive activity. *Science* 317(5835):227–230
 19. Cahn JW, Hilliard JE (1958) Free energy of a nonuniform system. I. Interfacial free energy. *J Chem Phys* 28:258–267
 20. Cahn JW, Hilliard JE (1959) Free energy of a nonuniform system. III, Nucleation in a two-component incompressible fluid. *J Chem Phys* 31:688–689
 21. Cervelli PF, Miklius A (2003) The shallow magmatic system of Kilauea Volcano. *US Geol Surv Prof Paper* 1676:149–163
 22. Chouet B, Julian BR (1985) Dynamics of an expanding fluid-filled crack. *J Geophys Res* 90:11187–11198
 23. Chouet B (1986) Dynamics of a fluid-driven crack in three dimensions by the finite difference method. *J Geophys Res* 91:13967–13992
 24. Chouet B (1988) Resonance of a fluid-driven crack: Radiation properties and implications for the source of long-period events and harmonic tremor. *J Geophys Res* 93:4375–4400
 25. Chouet B (1992) A seismic source model for the source of long-period events and harmonic tremor. In: Gasparini P, Scarpa R, Aki K (eds) *IAVCEI Proceedings in Volcanology*, vol 3. Springer, New York, pp 133–156
 26. Chouet BA, Page RA, Stephens CD, Lahr JC, Power JA (1994) Precursory swarms of long-period events at Redoubt Volcano (1989–1990), Alaska: Their origin and use as a forecasting tool. *J Volcanol Geotherm Res* 62:95–135
 27. Chouet B (1996) Long-period volcano seismicity: its source and use in eruption forecasting. *Nature* 380:309–316
 28. Chouet B (1996) New methods and future trends in seismological volcano monitoring. In: Scarpa R, Tilling RI (eds) *Monitoring and Mitigation of Volcano Hazards*. Springer, New York, pp 23–97
 29. Chouet B, Saccorotti G, Martini M, Dawson P, De Luca G, Milana G, Scarpa R (1997) Source and path effects in the wave fields of tremor and explosions at Stromboli Volcano, Italy. *J Geophys Res* 102:15129–15150
 30. Chouet B, Saccorotti G, Dawson P, Martini M, Scarpa R, De Luca G, Milana G, Cattaneo M (1999) Broadband measurements of the sources of explosions at Stromboli Volcano, Italy. *Geophys Res Lett* 26:1937–1940
 31. Chouet B (2003) Volcano seismology. *PAGEOPH* 160(3–4): 739–788
 32. Chouet B, Dawson P, Ohminato T, Martini M, Saccorotti G, Giudicepietro F, De Luca G, Milana G, Scarpa R (2003) Source mechanisms of explosions at Stromboli Volcano, Italy, determined from moment-tensor inversions of very-long-period data. *J Geophys Res* 108(B1):2019. doi:10.1029/2002JB001919
 33. Chouet B, Dawson P, Arciniega-Ceballos A (2005) Source mechanism of Vulcanian degassing at Popocatepetl Volcano, Mexico, determined from waveform inversions of very long period signals. *J Geophys Res* 110:B07301. doi:10.1029/2004JB003524
 34. Chouet B, Dawson P, Nakano M (2006) Dynamics of bubble growth and pressure recovery in a bubbly rhyolitic melt embedded in an elastic solid. *J Geophys Res* 111:B07310. doi:10.1029/2005JB004174
 35. Chouet B, Dawson P, Martini M (2008) Shallow-conduit dynamics at Stromboli Volcano, Italy, imaged from waveform inversion. In: Lane SJ, Gilbert JS (eds) *Fluid Motions in Volcanic Conduits A Source of Seismic and Acoustic Signals*. Geol Soc Lond Special Pub 307:57–84
 36. Collier L, Neuberg JW, Lensky N, Lyakhovsky V, Navon O (2006) Attenuation in gas-charged magma. *J Volcanol Geotherm Res* 153:21–36
 37. Commander KW, Prosperetti A (1989) Linear pressure waves in bubbly liquids: Comparison between theory and experiments. *J Acoust Soc Am* 85:732–746
 38. Dawson PB, Dietel C, Chouet BA, Honma K, Ohminato T, Okubo P (1998) A digitally telemetered broadband seismic network at Kilauea Volcano, Hawaii. *US Geol Surv Open-File Rep* 98–108:1–121
 39. Dawson P, Whilldin D, Chouet B (2004) Application of near real-time radial semblance to locate the shallow magmatic conduit at Kilauea Volcano, Hawaii. *Geophys Res Lett* 31:L21606. doi:10.1029/2004GL021163
 40. Dzurisin D, Vallance JW, Gerlach TM, Moran SC, Malone SD (2005) Mount St. Helens reawakens. *Eos Trans AGU* 86:25,29. doi:10.1029/2005EO030001
 41. Evans R (1979) The nature of the liquid-vapour interface and other topics in the statistical mechanics of non-uniform, classical fluids. *Adv Phys* 28:148–200
 42. Ferrazini V, Aki K (1987) Slow waves trapped in a fluid-filled infinite crack: Implications for volcanic tremor. *J Geophys Res* 92:9215–9233
 43. Fujita E, Ida Y, Oikawa J (1995) Eigen oscillation of a fluid sphere and source mechanism of harmonic volcanic tremor. *J Volcanol Geotherm Res* 69:365–378
 44. Fujita E, Ukawa M, Yamamoto E (2004) Subsurface cyclic magma sill expansions in the 2000 Miyakejima Volcano eruption: Possibility of two-phase flow oscillation. *J Geophys Res* 109:B04205. doi:10.1029/2003JB002556
 45. Gil Cruz F, Chouet BA (1997) Long-period events, the most characteristic seismicity accompanying the emplacement and extrusion of a lava dome in Galeras Volcano, Colombia, in 1991. *J Volcanol Geotherm Res* 77:121–158
 46. Hamada N, Jingu H, Ikumoto K (1976) On the volcanic earthquake with slowly decaying coda wave (in Japanese with English abstract). *Bull Volcanol Soc Jpn* 21:167–183
 47. Hasegawa A, Zhao D, Hori S, Yamamoto A, Horiuchi S (1991)

- Deep structure of the northeastern Japan arc and its relationship to seismic and volcanic activity. *Nature* 352:683–689
48. Heliker C, Mattox T (2003) The first two decades of the Pu'u O'o-Kupaianaha eruption: Chronology and selected bibliography. *US Geol Surv Prof Paper* 1676:1–27
 49. Hess K, Dingwell DB (1996) Viscosities of hydrous leucogranitic melts: A non-Arrhenian model. *Am Mineral* 81:1297–1300
 50. Hidayat D, Voight B, Langston C, Ratdomopurbo A, Ebeling C (2000) Broadband seismic experiment at Merapi Volcano, Java, Indonesia: Very-long-period pulses embedded in multi-phase earthquakes. *J Volcanol Geotherm Res* 100:215–231
 51. Hidayat D, Chouet B, Voight B, Dawson P, Ratdomopurbo A (2002) Source mechanism of very-long-period signals accompanying dome growth activity at Merapi Volcano, Indonesia. *Geophys Res Lett* 29(23):2118. doi:10.1029/2002GL015013
 52. Hidayat D, Chouet B, Voight B, Dawson P, Ratdomopurbo A (2003) Correction to Source mechanism of very-long-period signals accompanying dome growth activity at Merapi Volcano, Indonesia. *Geophys Res Lett* 30(10):2118. doi:10.1029/2003GL017211
 53. Hill DP, Dawson P, Johnston MJS, Pitt AM, Biasi G, Smith K (2002) Very-long-period volcanic earthquakes beneath Mammoth Mountain, California. *Geophys Res Lett* 29(10):1370. doi:10.1029/2002GL014833
 54. Hill DP, Prejean S (2005) Magmatic unrest beneath Mammoth Mountain, California. *J Volcanol Geotherm Res* 146:257–283
 55. Hirabayashi J (1999) Formation of volcanic fluid reservoir and volcanic activity. *J Balneol Soc Jpn* 49:99–105
 56. Ichihara M, Kameda M (2004) Propagation of acoustic waves in a visco-elastic two-phase system: Influences of the liquid viscosity and the internal diffusion. *J Volcanol Geotherm Res* 137:73–91
 57. Iverson RM, Dzurisin D, Gardner CA, Gerlach TM, LaHusen RG, Lisowski M, Major JJ, Malone SD, Messerich JA, Moran SC, Pallister JS, Qamar AI, Schilling SP, Vallance JW (2006) Dynamics of seismogenic volcanic extrusion at Mount St. Helens in 2004–05. *Nature* 444:439–443. doi:10.1038/nature05322
 58. Jacqmin D (1999) Calculation of two-phase Navier–Stokes Flows using phase-field modeling. *J Comput Phys* 155:96–127
 59. James MR, Lane SJ, Chouet B, Gilbert JS (2004) Pressure changes associated with the ascent and bursting of gas slugs in liquid-filled vertical and inclined conduits. *J Volcanol Geotherm Res* 129:61–82
 60. James MR, Lane SJ, Chouet BA (2006) Gas slug ascent through changes in conduit diameter: Laboratory insights into a volcano-seismic source process in low-viscosity magmas. *J Geophys Res* 111:B05201. doi:10.1029/2005JB003718
 61. Jones RAL (2002) *Soft Condensed Matter*. Oxford University Press, Oxford, p 195
 62. Julian BR (1994) Volcanic tremor, Nonlinear excitation by fluid flow. *J Geophys Res* 99:11859–11877
 63. Kanamori H, Given JW (1982) Analysis of long-period waves excited by the May 18, 1980, eruption of Mount St. Helens – A terrestrial monopole? *J Geophys Res* 87:5422–5432
 64. Kanamori H, Given JW, Lay T (1984) Analysis of seismic body waves excited by the Mount St. Helens eruption of May 18:1980. *J Geophys Res* 89:1856–1866
 65. Kaneshima S, Kawakatsu H, Matsubayashi H, Sudo Y, Tsutsui T, Ohminato T, Ito H, Uhira K, Yamasato H, Oikawa J, Takeo M, Iidaka T (1996) Mechanism of phreatic eruptions at Aso Volcano inferred from near-field broadband seismic observations. *Science* 273:642–645
 66. Kawakatsu H (1989) Centroid single force inversion of seismic waves generated by landslides. *J Geophys Res* 94:12363–12374
 67. Kawakatsu H, Ohminato T, Ito H, Kuwahara Y (1992) Broadband seismic observation at Sakurajima Volcano, Japan. *Geophys Res Lett* 19:1959–1962
 68. Kawakatsu H, Ohminato T, Ito H (1994) 10-s-period volcanic tremors observed over a wide area in southwestern Japan. *Geophys Res Lett* 21:1963–1966
 69. Kawakatsu H, Kaneshima S, Matsubayashi H, Ohminato T, Sudo Y, Tsutsui T, Uhira K, Yamasato H, Ito H, Legrand D (2000) Aso94: Aso seismic observation with broadband instruments. *J Volcanol Geotherm Res* 101:129–154
 70. Kedar S, Sturtevant B, Kanamori H (1996) The origin of harmonic tremor at Old Faithful Geyser. *Nature* 379:708–711
 71. Kendon VM, Cates ME, Pagonabarraga I, Desplat J-C, Bladon P (2001) Inertial effects in three-dimensional spinodal decomposition of a symmetric binary fluid mixture: A lattice Boltzmann study. *J Fluid Mech* 440:147–203
 72. Kieffer SW (1977) Sound speed in liquid-gas mixtures: Water-air and water-steam. *J Geophys Res* 82:2895–2904
 73. Kim J, Kang K, Lowengrub J (2004) Conservative multigrid methods for Cahn–Hilliard fluids. *J Comput Phys* 193:511–543
 74. Klein FW, Koyanagi RY, Nakata JS, Tanigawa WR (1987) The seismicity of Kilauea's magma system. In: Decker RW, Wright TL, Stauffer RW (eds) *Volcanism in Hawaii*. US Geol. Surv. Prof. Pap., 1350. US government printing office, Washington, pp 1019–1185
 75. Koyanagi RY, Chouet B, Aki K (1987) Origin of volcanic tremor in Hawaii. Part I: Compilation of seismic data from the Hawaiian Volcano Observatory, 1972 to 1985. In: Decker RW, Wright TL, Stauffer RW (eds) *Volcanism in Hawaii*, US Geol. Surv. Prof. Pap., 1350. US government printing office, Washington, pp 1221–1257
 76. Kumagai H, Chouet BA (1999) The complex frequencies of long-period seismic events as probes of fluid composition beneath volcanoes. *Geophys Int* 138:F7–F12
 77. Kumagai H, Chouet BA (2000) Acoustic properties of a crack containing magmatic or hydrothermal fluids. *J Geophys Res* 105:25493–25512
 78. Kumagai H, Ohminato T, Nakano M, Ooi M, Kubo A, Inoue H, Oikawa J (2001) Very-long-period seismic signals and caldera formation at Miyake Island, Japan. *Science* 293:687–690
 79. Kumagai H, Chouet BA, Nakano M (2002) Temporal evolution of a hydrothermal system in Kusatsu-Shirane Volcano, Japan, inferred from the complex frequencies of long-period events. *J Geophys Res* 107(B10):2236. doi:10.1029/2001JB000653
 80. Kumagai H, Chouet BA, Nakano M (2002) Waveform inversion of oscillatory signatures in long-period events beneath volcanoes. *J Geophys Res* 107(B11):2301. doi:10.1029/2001JB001704
 81. Kumagai H, Miyakawa K, Negishi H, Inoue H, Obara K, Suet-sugu D (2003) Magmatic dyke resonances inferred from very-long-period seismic signals. *Science* 299:2058–2061
 82. Kumagai H, Chouet BA, Dawson PB (2005) Source process of a long-period event at Kilauea Volcano, Hawaii. *Geophys J Int* 161:243–254
 83. Kumagai H (2006) Temporal evolution of a magmatic dike

- system inferred from the complex frequencies of very long period seismic signals. *J Geophys Res* 111:B06201. doi:10.1029/2005JB003881
84. Kumagai H, Yepes H, Vaca M, Caceres V, Nagai T, Yokoe K, Imai T, Miyakawa K, Yamashina T, Arrais S, Vasconez F, Pinajota E, Cisneros C, Ramos C, Paredes M, Gomezjurado L, Garcia-Arztizabal A, Molina I, Ramon P, Segovia M, Palacios P, Troncoso L, Alvarado A, Aguilar J, Pozo J, Enriquez W, Mothes P, Hall M, Inoue I, Nakano M, Inoue H (2007) Enhancing volcano-monitoring capabilities in Ecuador. *Eos Trans Am Geophys Union* 88:245–246
 85. Lane SJ, Chouet BA, Phillips JC, Dawson P, Ryan GA, Hurst E (2001) Experimental observations of pressure oscillations and flow regimes in an analogue volcanic system. *J Geophys Res* 106:6461–6476
 86. Legrand D, Kaneshima S, Kawakatsu H (2000) Moment tensor analysis of near-field broadband waveforms observed at Aso Volcano, Japan. *J Volcanol Geotherm Res* 101:155–169
 87. Lensky NG, Lyakhovsky V, Navon O (2002) Expansion dynamics of volatile-saturated liquids and bulk viscosity of bubbly magmas. *J Fluid Mech* 460:39–56
 88. Lensky NG, Navon O, Lyakhovsky V (2004) Bubble growth during decompression of magma: experimental and theoretical investigation. *J Volcanol Geotherm Res* 129:7–22
 89. Lowengrub J, Truskinovsky L (1998) Quasi-incompressible Cahn-Hilliard fluids and topological transitions. *Proc Royal Soc Lond A* 454:2617–2654
 90. Lyakhovsky V, Hurwitz S, Navon O (1996) Bubble growth in rhyolitic melts: experimental and numerical investigation. *Bull Volcanol* 58:19–32
 91. Major JJ, Scott WE, Driedger C, Dzurisin D (2005) Mount St. Helens erupts again – Activity from September 2004 through March 2005. US Geological Survey Fact Sheet FS2005-3036. US government printing office, Washington, p 4
 92. Meier GEA, Grabitz G, Jungowsky WM, Witzczak KJ, Anderson JS (1978) Oscillations of the supersonic flow downstream of an abrupt increase in duct crosssection. *Mitteilungen aus dem Max-Planck Institut für Strömungsforschung und der Aerodynamischen Versuchsanstalt* 65:1–172
 93. Migler KB (2001) String formation in sheared polymer blends: coalescence, breakup, and finite size effects. *Phys Rev Lett* 86(6):1023–1026
 94. Moran SC, Malone SD, Qamar AI, Thelen W, Wright AK, Caplan-Auerbach J (2007) 2004–2005 seismicity associated with the renewed dome-building eruption of Mount St. Helens. In: Sherrod DR, Scott WE, Stauffer PH (eds) *A Volcano rekindled: the first year of renewed eruptions at Mount St. Helens, 2004–2006*. US Geological Survey Prof. Pap. 2007-XXXX
 95. Morrissey MM, Chouet BA (1997) A numerical investigation of choked flow dynamics and its application to the triggering mechanism of long-period events at Redoubt Volcano, Alaska. *J Geophys Res* 102:7965–7983
 96. Nakano M, Kumagai H, Kumazawa M, Yamaoka K, Chouet BA (1998) The excitation and characteristic frequency of the long-period volcanic event: An approach based on an inhomogeneous autoregressive model of a linear dynamic system. *J Geophys Res* 103:10031–10046
 97. Nakano M, Kumagai H, Chouet BA (2003) Source mechanism of long-period events at Kusatsu-Shirane Volcano, Japan, inferred from waveform inversion of the effective excitation functions. *J Volcanol Geotherm Res* 122:149–164
 98. Navon O, Lyakhovsky V (1998) Vesiculation processes in silicic magmas. *Geol Soc Lond Special Pub* 145:27–50
 99. Neuberg J, Luckett R, Ripepe M, Braun T (1994) Highlights from a seismic broadband array on Stromboli Volcano. *Geophys Res Lett* 21:749–752
 100. Neuberg JW, Tuffen H, Collier L, Green D, Powell T, Dingwell D (2006) The trigger mechanism of low-frequency earthquakes on Montserrat. *J Volcanol Geotherm Res* 153:37–50
 101. Nishimura T, Nakamichi H, Tanaka S, Sato M, Kobayashi T, Ueki S, Hamaguchi H, Ohtake M, Sato H (2000) Source process of very long period seismic events associated with the 1998 activity of Iwate Volcano, northeastern Japan. *J Geophys Res* 105:19135–19147
 102. Nishimura T, Chouet B (2003) A numerical simulation of magma motion, crustal deformation, and seismic radiation associated with volcanic eruptions. *Geophys. J Int* 153: 699–718
 103. Nishimura T, Ueki S, Yamawaki T, Tanaka S, Hasino H, Sato M, Nakamichi H, Hamaguchi H (2003) Broadband seismic signals associated with the 2000 volcanic unrest of Mount Bandai, northeastern Japan. *J Volcanol Geotherm Res* 119:51–59
 104. Nishimura T (2004) Pressure recovery in magma due to bubble growth. *Geophys Res Lett* 31:L12613. doi:10.1029/2004GL019810
 105. Ochs FA, Lange RA (1999) The density of hydrous magmatic liquids. *Science* 283:1314–1317
 106. Ohba T, Hirabayashi J, Nogami K (2000) D/H and $^{18}\text{O}/^{16}\text{O}$ ratios of water in the crater lake of Kusatsu-Shirane Volcano, Japan. *J Volcanol Geotherm Res* 97:329–346
 107. Ohminato T, Chouet BA (1997) A free-surface boundary condition for including 3D topography in the finite-difference method. *Bull Seismol Soc Am* 87:494–515
 108. Ohminato T, Ereditato D (1997) Broadband seismic observations at Satsuma-Iwojima Volcano, Japan. *Geophys Res Lett* 24:2845–2848
 109. Ohminato T, Chouet BA, Dawson PB, Kedar S (1998) Waveform inversion of very-long-period impulsive signals associated with magmatic injection beneath Kilauea volcano, Hawaii. *J Geophys Res* 103:23839–23862
 110. Ohminato T (2006) Characteristics and source modeling of broadband seismic signals associated with the hydrothermal system at Satsuma-Iwojima volcano, Japan. *J Volcanol Geotherm Res* 158:467–490
 111. Ohminato T, Takeo M, Kumagai H, Yamashina T, Oikawa J, Koyama E, Tsuji H, Urabe T (2006) Vulcanian eruptions with dominant single force components observed during the Asama 2004 volcanic activity in Japan. *Earth Planets Space* 58:583–593
 112. Orlandini E, Swift MR, Yeomans JM (1995) A Lattice Boltzmann Model of binary fluid mixtures. *Europhys Lett* 32:463
 113. Pooley CM, Kuksenok O, Balasz AC (2005) Convection-driven pattern formation in phase-separating binary fluids. *Phys Rev E* 71:030501(R)
 114. Power JA, Stihler SD, White RA, Moran SC (2004) Observations of deep long-period (DLP) seismic events beneath Aleutian Arc Volcanoes, 1989–2002. *J Volcanol Geotherm Res* 138:243–266
 115. Proussevitch AA, Sahagian DL, Anderson AT (1993) Dynamics of diffusive bubble growth in magmas: Isothermal case. *J Geophys Res* 98:22283–22307
 116. Proussevitch AA, Sahagian DL (1996) Dynamics of coupled

- diffusive and decompressive bubble growth in magmatic systems. *J Geophys Res* 101:17447–17455
117. Proussevitch AA, Sahagian DL (1998) Dynamics and energetics of bubble growth in magmas: Analytical formulation and numerical modeling. *J Geophys Res* 103:18223–18251
 118. Ripepe M, Poggi P, Braun T, Gordeev E (1996) Infrasonic waves and volcanic tremor at Stromboli. *Geophys Res Lett* 23:181–184
 119. Rowe CA, Aster RC, Kyle PR, Schlue JW, Dibble RR (1998) Broadband recording of Strombolian explosions and associated very-long-period seismic signals on Mount Erebus Volcano, Ross Island, Antarctica. *Geophys Res Lett* 25:2297–2300
 120. Saccorotti G, Chouet B, Dawson P (2001) Wavefield properties of a shallow long-period event and tremor at Kilauea Volcano, Hawaii. *J Volcanol Geotherm Res* 109:163–189
 121. Scriven LE (1959) On the dynamics of phase growth. *Chem Eng Sci* 10:1–13
 122. Shaw HR, Chouet B (1989) Singularity spectrum of intermittent seismic tremor at Kilauea Volcano, Hawaii. *Geophys Res Lett* 16:195–198
 123. Shaw HR, Chouet B (1991) Fractal hierarchies of magma transport in Hawaii and critical self-organization of tremor. *J Geophys Res* 96:10191–10207
 124. Shimomura Y, Nishimura T, Sato H (2006) Bubble growth processes in magma surrounded by an elastic medium. *J Volcanol Geotherm Res* 155:307–322
 125. Sparks R (1978) The dynamics of bubble formation and growth in magmas: A review and analysis. *J Volcanol Geotherm Res* 3:1–38
 126. Stephens CD, Chouet BA (2001) Evolution of the December 14, 1989 precursory long-period event swarm at Redoubt Volcano, Alaska. *J Volcanol Geotherm Res* 109:133–148
 127. Swift MR, Osborn WR, Yeomans JM (1995) Lattice Boltzmann simulation of nonideal fluids. *Phys Rev Lett* 75(5):0–833
 128. Swift MR, Orlandini E, Osborn WR, Yeomans JM (1996) Lattice Boltzmann simulations of liquid-gas and binary fluid systems. *Phys Rev E* 54(5):5041–5052
 129. Takei Y, Kumazawa M (1994) Why have the single force and torque been excluded from seismic source models? *Geophys J Int* 118:20–30
 130. Tannehill JC, Anderson DA, Pletcher RH (1997) *Computational Fluid Mechanics and Heat Transfer*, 2nd edn. Taylor and Francis, Philadelphia, p 792
 131. Toramaru A (1989) Vesiculation process and bubble size distributions in ascending magmas with constant velocities. *J Geophys Res* 94:17523–17542
 132. Toramaru A (1995) Numerical study of nucleation and growth of bubbles in viscous magmas. *J Geophys Res* 100:1913–1931
 133. Tuffen H, Dingwell DB, Pinkerton H (2003) Repeated fracture and healing of silicic magma generates flow banding and earthquakes? *Geology* 31:1089–1092
 134. Uhira K, Yamasato H, Takeo M (1994) Source mechanism of seismic waves excited by pyroclastic flows observed at Unzen Volcano, Japan. *J Geophys Res* 99:17757–17773
 135. van der Waals JD (1979) The thermodynamic theory of capillarity under the hypothesis of a continuous variation of density. *Verhandel Konink. Acad. Wet. Amsterdam*, (Sect. 1), 1, pp 1–56. Translation by Rowlingson JS. *J Statist Phys* 20:197–244
 136. Vergnolle S, Brandeis G, Mareschal JC (1996) Strombolian explosions, 2. Eruption dynamics determined from acoustic measurements. *J Geophys Res* 101:20449–20466
 137. Waite GP, Chouet BA, Dawson PB (2008) Eruption dynamics at Mount St. Helens imaged from broadband seismic waveforms: Interaction of the shallow magmatic and hydrothermal systems. *J Geophys Res* 113, B02305. doi:10.1029/2007JB005259
 138. Wallis GB (1969) *One-dimensional Two-phase Flow*. MacGraw-Hill, New York, pp 408
 139. White RA (1996) Precursory deep long-period earthquakes at Mount Pinatubo: Spatio-temporal link to a basalt trigger. In: Newhall CG, Punongbayan RS (eds) *Fire and Mud: Eruptions and Lahars of Mount Pinatubo, Philippines*. University of Washington Press, Seattle, pp 307–326
 140. Wilson L, Head JW (1981) Ascent and eruption of basaltic magma on the earth and moon. *J Geophys Res* 86:2971–3001
 141. Xu A, Gonnella G, Lamura A (2003) Phase-separating binary fluids under oscillatory shear. *Phys Rev E* 67:056105
 142. Xu A, Gonnella G, Lamura A (2004) Phase separation of incompressible binary fluids with lattice Boltzmann methods. *Physica A* 331:10–22
 143. Yamamoto M, Kawakatsu H, Kaneshima S, Mori T, Tsutsui T, Sudo Y, Morita Y (1999) Detection of a crack-like conduit beneath the active crater at Aso Volcano, Japan. *Geophys Res Lett* 26:3677–3680
 144. Yamamoto M, Kawakatsu H, Yomogida K, Koyama J (2002) Long-period (12 sec) volcanic tremor observed at Usu 2000 eruption: seismological detection of a deep magma plumbing system. *Geophys Res Lett* 29(9):1329. doi:10.1029/2001GL013996
 145. Yoon SW, Crum LA, Prosperetti A, Lu NQ (1991) An investigation of the collective oscillations of a bubble cloud. *J Acoust Soc Am* 89:700–706
 146. Yue P, Feng JJ, Liu C, Shen J (2004) A diffuse-interface method for simulating two-phase flows of complex fluids. *J Fluid Mech* 515:293–317
 147. Zhang Y, Xu Z, Liu Y (2003) Viscosity of hydrous rhyolitic melts inferred from kinetic experiments: A new viscosity model. *Am Mineral* 88:1741–1752

Volcano Seismic Signals, Source Quantification of

HIROYUKI KUMAGAI^{1,2}

¹ National Research Institute for Earth Science and Disaster Prevention, Tsukuba, Japan

² IAVCEI/IASPEI Joint Commission on Volcano Seismology, Tsukuba, Japan

Article Outline

Glossary

Definition of the Subject

Introduction

Phenomenological Representation of Seismic Sources

Waveform Inversion

[Spectral Analysis](#)
[Fluid-Solid Interactions](#)
[Future Directions](#)
[Acknowledgment](#)
[Appendix A: Green's Functions](#)
[Appendix B: Moment Tensor for a Spherical Source](#)
[Appendix C: Moment Tensor for a Cylindrical Source](#)
[Bibliography](#)

Glossary

Moment tensor A point seismic source representation defined by the first-order moment of the equivalent body force or the stress glut. Slip on a fault as well as volumetric changes such as an isotropic expansion and tensile crack can be represented by the moment tensor.

Waveform inversion An approach to estimate source mechanisms and locations of seismic events by finding the best fits between observed and synthesized seismograms.

Autoregressive equation A difference form of the equation of motion of a linear dynamic system, which is a basic equation to determine the complex frequencies (frequencies and Q factors) of decaying harmonic oscillations in observed signals.

Crack wave A dispersive wave generated by fluid-solid interactions in a crack. The phase velocity of the crack wave is smaller than the acoustic velocity of the fluid in the crack.

Definition of the Subject

Volcano seismicity produces a wide variety of seismic signals that provide glimpses of the internal dynamics of volcanic systems. Quantitative approaches to analyze and interpret volcano-seismic signals have been developed since the late 1970s. The availability of seismic equipments with wide frequency and dynamic ranges since the early 1990s revealed a further variety of volcano-seismic signals in oscillation periods longer than a few seconds. Quantification of the sources of volcano-seismic signals is crucial to achieving a better understanding of the physical states and dynamics of magmatic and hydrothermal systems.

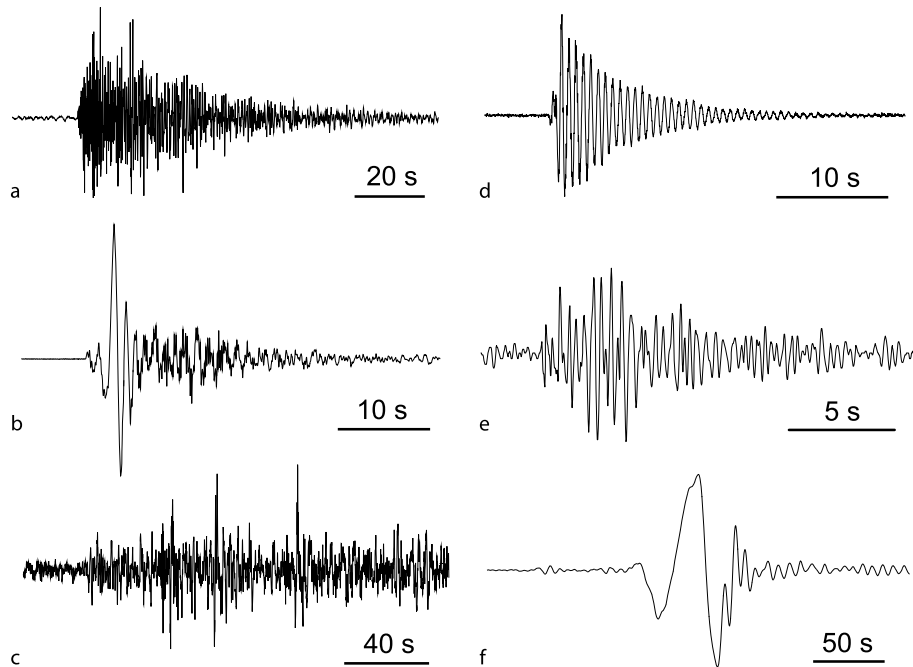
Introduction

Volcanoes occur in tectonically active regions of the earth where magmatic and hydrothermal fluids display complex interactions with volcanic rocks and the atmosphere. Volcano seismicity is the manifestation of such complex interactions occurring inside of volcanic edifices. Volcano seismology aims at achieving a better understanding of the

physical states and dynamics of magmatic and hydrothermal systems beneath active volcanoes through observation, analysis, and interpretation of volcano-seismic signals. It is well known that volcano-seismic signals have a wide variety of signatures (Fig. 1), which have been classified by various schemes e. g., [25,61,80,84]. The volcano-tectonic (VT) earthquake, low-frequency (LF) or long-period (LP) event, tremor, very-long-period (VLP) event, hybrid event, and explosion earthquake have been traditionally used to specify volcano-seismic signals. Here, LF denotes frequencies between 0.5 and 5 Hz [61], and LP and VLP denote periods between 0.2 and 2 s and longer than a few seconds, respectively [25].

In contrast to the various classification schemes, source processes of volcano-seismic signals may be classified into three main families: (i) brittle failure in volcanic rock triggered by fluid movement, (ii) transient pressure disturbance caused by mass transport and/or volumetric change, and (iii) resonance of a fluid-filled resonator excited by a pressure disturbance. These three processes may be linked to the signals as follows: (i) VT earthquake, (ii) VLP event and explosion earthquake, (iii) LF or LP event, tremor, and VLP event, and (i)+(iii) hybrid event. VT earthquakes, sometimes called high-frequency (HF) earthquakes, are indistinguishable from ordinary tectonic earthquakes, but occur in volcanic regions due to process (i). LF or LP events have signals characterized by decaying oscillations, whereas the signature of tremor shows continuous oscillations. These oscillatory signatures can be interpreted as process (iii), in which the excitations are impulsive for LF or LP events and successive for tremor. Most VLP events are characterized by impulsive signatures, which may be generated by process (ii). However, some VLP events show sustained oscillations or decaying harmonic oscillations, which may reflect process (iii). Hybrid events show mixed characters of both VT earthquakes and LP events, suggesting that processes (i) and (iii) both take place at the source. Explosion earthquakes occur in association with eruptions in which process (ii) is dominant.

Recently, there have been remarkable advances in quantitative understanding of the sources of volcano-seismic signals. These advances were made possible by the development of source models and analysis techniques coupled with increased computer capacity and the availability of seismic observation equipment with wide frequency and dynamic ranges. Major studies that have contributed to these advances are summarized as follows: Detailed magma intrusion processes imaged by VT earthquakes e. g., [19,43,46,86,111,112,123]; Quantitative interpretations of oscillations in LP and VLP events and tremor



Volcano Seismic Signals, Source Quantification of, Figure 1

Various volcano-seismic signals: **a** volcano-tectonic earthquake that occurred between Miyakejima and Kozujima, Japan; **b** explosion earthquake observed at Asama volcano, Japan; **c** tremor that occurred beneath Mt. Fuji, Japan; **d** long-period event observed at Kusatsu-Shirane volcano, Japan; **e** long-period event observed at Guagua Pichincha volcano, Ecuador; **f** very-long-period event that occurred beneath Miyakejima, Japan (low-pass filtered at 20 s)

to diagnose the states of fluids at the sources of these signals e. g., [2,7,21,22,23,24,28,29,38,39,40,41,42,44,52,53,65,66,67,70,71,73,77,78,85,87,88,90,91,92,93,94,95,98,134]; Tracking the sources of LP events and tremor e. g., [3,4,5,13,30,45,82,113,114]; Waveform analysis of impulsive and oscillatory signatures in VLP events and explosion earthquakes to investigate source dynamics e. g., [6,8,9,10,11,31,32,33,34,36,47,48,49,51,54,55,56,57,58,59,60,64,69,72,76,97,102,103,105,107,108,110,120,122,126,132,133]. These volcano seismological studies have been reviewed by various authors [25,26,27,61,80,81,96].

The purpose of this article is to provide a systematic presentation of the theoretical basis for quantification of the sources of volcano-seismic signals suitable for readers, including graduate students and young researchers, who are new to the study of volcano seismology. I focus on four subjects: (1) phenomenological representation of seismic sources, (2) waveform inversion to estimate source mechanisms, (3) spectral analysis based on an autoregressive model, and (4) physical properties of fluid-solid coupled waves. Some additional notes are provided in Appendixes. These constitute the basic elements needed to quantify the sources of volcano-seismic signals. Applica-

tions of quantitative approaches are not fully reviewed in this manuscript. Readers are encouraged to consult both the original research papers and the review papers cited above.

Phenomenological Representation of Seismic Sources

We first derive the phenomenological representation of seismic sources using single force and moment tensor. This representation provides the basis to study source processes of volcano seismicity. I follow the approach presented by Backus and Mulcahy [12] (hereafter referred to as BM) and Aki and Richards [1] for the moment tensor representation. The theory elaborated by Takei and Kumazawa [118,119] is used to introduce single force in seismic sources.

Stress Glut

We consider indigenous seismic sources occurring within the closed earth system. This means that external bodies and detached mass are excluded. Let us assume an isotropic medium for the earth, which is represented by

density ρ and Lamé's constants λ and μ . The exact equation of motion of the earth is given by

$$\rho \frac{\partial^2 u_i}{\partial t^2} = \frac{\partial \sigma_{ni}^{\text{true}}}{\partial x_n}, \quad (1)$$

where u_i and $\sigma_{ni}^{\text{true}}$ are the true displacement field and true stress tensor, respectively, actually produced in the earth. These are functions of space $\mathbf{x} = (x_1, x_2, x_3)$ and time t . The summation convention for repeated subscripts is used throughout this paper unless otherwise stated. In BM's theory, the failure of the elastic stress-strain relationship in source processes, such as slip across a plane that can not be described by the linear elastodynamics, is represented by an equivalent body force. We use a model stress $\sigma_{ni}^{\text{model}}$ given by the elastic stress-strain relationship as

$$\sigma_{ni}^{\text{model}} = \lambda \frac{\partial u_k}{\partial x_k} \delta_{ni} + \mu \left(\frac{\partial u_n}{\partial x_i} + \frac{\partial u_i}{\partial x_n} \right), \quad (2)$$

where δ_{ni} is the Kronecker symbol ($\delta_{ni} = 0$ for $n \neq i$ and $\delta_{ni} = 1$ for $n = i$). By replacing the true stress by the model stress, Eq. (1) can be rewritten as follows:

$$\rho \frac{\partial^2 u_i}{\partial t^2} = \frac{\partial \sigma_{ni}^{\text{model}}}{\partial x_n} + f_i^S, \quad (3)$$

where f_i^S is the equivalent body force defined as

$$f_i^S = \frac{\partial}{\partial x_n} (\sigma_{ni}^{\text{true}} - \sigma_{ni}^{\text{model}}). \quad (4)$$

The difference between $\sigma_{ni}^{\text{true}}$ and $\sigma_{ni}^{\text{model}}$ is called the stress glut. The equivalent body force, which is the spatial derivative of the stress glut, describes the source and vanishes outside the source region for motion in a completely elastic medium.

We introduce Green's function $G_{ij}(\mathbf{x}, t; \boldsymbol{\eta}, \tau)$, which is the i th component of displacement at (\mathbf{x}, t) excited by the

unit impulse applied at $\mathbf{x} = \boldsymbol{\eta}$ and $t = \tau$ in the j -direction. $G_{ij}(\mathbf{x}, t; \boldsymbol{\eta}, \tau)$ satisfies the following equation:

$$\rho \frac{\partial^2 G_{ij}}{\partial t^2} = \frac{\partial}{\partial x_n} \left\{ \lambda \frac{\partial G_{kj}}{\partial x_k} \delta_{ni} + \mu \left(\frac{\partial G_{nj}}{\partial x_i} + \frac{\partial G_{ij}}{\partial x_n} \right) \right\} + \delta(\mathbf{x} - \boldsymbol{\eta}) \delta(t - \tau) \delta_{ij}. \quad (5)$$

Note that $G_{ij}(\mathbf{x}, t; \boldsymbol{\eta}, \tau) = G_{ij}(\mathbf{x}, t - \tau; \boldsymbol{\eta}, 0)$. The displacement u_i can then be described by using the equivalent body force and Green's functions as follows ("Appendix A: Green's Functions"):

$$u_i(\mathbf{x}, t) = \int_{-\infty}^{\infty} \iiint_V f_j^S(\boldsymbol{\eta}, \tau) G_{ij}(\mathbf{x}, t - \tau; \boldsymbol{\eta}, 0) dV(\boldsymbol{\eta}) d\tau. \quad (6)$$

BM expanded f_j^S in terms of polynomial moments at a particular point $\boldsymbol{\xi}_0$ as

$$\begin{aligned} f_j^S(\boldsymbol{\eta}, \tau) &= F_j^{S0}(\boldsymbol{\xi}_0, \tau) \delta(\boldsymbol{\eta} - \boldsymbol{\xi}_0) \\ &\quad + F_{jk}^{S1}(\boldsymbol{\xi}_0, \tau) \frac{\partial \delta(\boldsymbol{\eta} - \boldsymbol{\xi}_0)}{\partial \eta_k} + \dots \\ &= f_j^{S0}(\boldsymbol{\eta}, \tau) + f_j^{S1}(\boldsymbol{\eta}, \tau) + \dots \end{aligned} \quad (7)$$

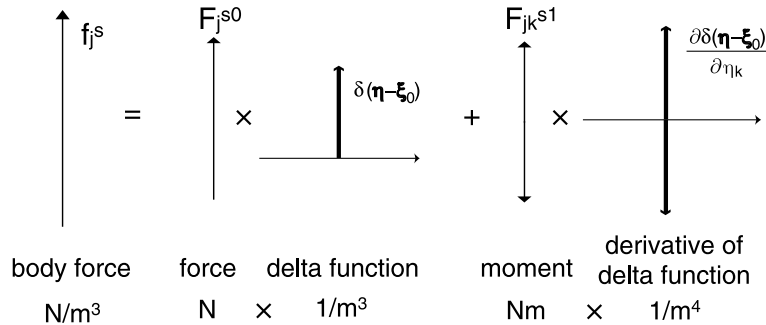
This expansion is schematically shown in Fig. 2, which may help the reader to understand that F_j^{S0} and F_{jk}^{S1} have the dimensions of force and moment, respectively.

Single Force

F_j^{S0} is given as

$$F_j^{S0}(\boldsymbol{\xi}_0, \tau) = \iiint_V f_j^S(\boldsymbol{\eta}, \tau) dV(\boldsymbol{\eta}), \quad (8)$$

which is the total force. This must be zero because of the conservation of linear momentum (no force appears or



Volcano Seismic Signals, Source Quantification of, Figure 2

Schematic diagram of the expansion of the equivalent body force f_j^S in terms of polynomial moments

disappears in the earth). Therefore,

$$\iiint_V f_j^S(\boldsymbol{\eta}, \tau) dV(\boldsymbol{\eta}) = 0. \quad (9)$$

This states that no single force exists in any indigenous seismic sources in the scheme presented by BM. However, we will see later that a single force exists in indigenous sources if the non-linear effect of mass advection is taken into account.

Moment Tensor

We next examine the equivalent body force arising from the first-order moment,

$$f_j^{S1}(\boldsymbol{\eta}, \tau) = F_{jk}^{S1}(\boldsymbol{\xi}_0, \tau) \frac{\partial \delta(\boldsymbol{\eta} - \boldsymbol{\xi}_0)}{\partial \eta_k}. \quad (10)$$

If we consider a displacement discontinuity across a surface Σ , f_j^{S1} may be expressed as [1]

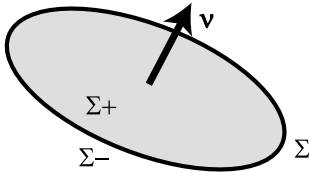
$$f_j^{S1}(\boldsymbol{\eta}, \tau) = - \iint_{\Sigma} m_{jk}(\boldsymbol{\xi}, \tau) \frac{\partial}{\partial \eta_k} \delta(\boldsymbol{\eta} - \boldsymbol{\xi}) d\Sigma(\boldsymbol{\xi}), \quad (11)$$

where m_{jk} is the moment density tensor given as

$$m_{jk} = \lambda v_l [u_l] \delta_{jk} + \mu (v_j [u_k] + v_k [u_j]). \quad (12)$$

Here, $[u]$ is the displacement discontinuity defined by $[u] = u|_{\Sigma+} - u|_{\Sigma-}$ and $\mathbf{v} = (v_1, v_2, v_3)$ is the unit vector normal to Σ , where $u|_{\Sigma+}$ and $u|_{\Sigma-}$ are displacements on the Σ_+ and the Σ_- sides of Σ , respectively (see Fig. 3). An explicit expression of m_{jk} is

$$\mathbf{m} = \begin{pmatrix} \lambda v_k [u_k] + 2\mu v_1 [u_1] & \mu (v_1 [u_2] + v_2 [u_1]) & \mu (v_1 [u_3] + v_3 [u_1]) \\ \mu (v_2 [u_1] + v_1 [u_2]) & \lambda v_k [u_k] + 2\mu v_2 [u_2] & \mu (v_2 [u_3] + v_3 [u_2]) \\ \mu (v_3 [u_1] + v_1 [u_3]) & \mu (v_3 [u_2] + v_2 [u_3]) & \lambda v_k [u_k] + 2\mu v_3 [u_3] \end{pmatrix}. \quad (13)$$



Volcano Seismic Signals, Source Quantification of, Figure 3

An internal surface Σ across which a displacement discontinuity occurs. The displacement discontinuity is denoted by $[u] = u|_{\Sigma+} - u|_{\Sigma-}$, where $u|_{\Sigma+}$ and $u|_{\Sigma-}$ are displacements on the Σ_+ and Σ_- sides of Σ , respectively [1]

Therefore $m_{jk} = m_{kj}$. Using Green's functions, the displacement field due to f_j^{S1} is expressed as

$$\begin{aligned} u_i^{S1}(\mathbf{x}, t) &= \int_{-\infty}^{\infty} \iiint_V f_j^{S1}(\boldsymbol{\eta}, \tau) G_{ij}(\mathbf{x}, t - \tau; \boldsymbol{\eta}, 0) dV(\boldsymbol{\eta}) d\tau \\ &= \int_{-\infty}^{\infty} \iiint_V \left[- \iint_{\Sigma} m_{jk}(\boldsymbol{\xi}, \tau) \frac{\partial}{\partial \eta_k} \delta(\boldsymbol{\eta} - \boldsymbol{\xi}) d\Sigma(\boldsymbol{\xi}) \right] \\ &\quad \cdot G_{ij}(\mathbf{x}, t - \tau; \boldsymbol{\eta}, 0) dV(\boldsymbol{\eta}) d\tau \\ &= \int_{-\infty}^{\infty} \iint_{\Sigma} \left[m_{jk}(\boldsymbol{\xi}, \tau) \iiint_V - \frac{\partial}{\partial \eta_k} \delta(\boldsymbol{\eta} - \boldsymbol{\xi}) G_{ij}(\mathbf{x}, t - \tau; \boldsymbol{\eta}, 0) dV(\boldsymbol{\eta}) \right] d\Sigma(\boldsymbol{\xi}) d\tau \\ &= \int_{-\infty}^{\infty} \iint_{\Sigma} m_{jk}(\boldsymbol{\xi}, \tau) \frac{\partial}{\partial \xi_k} G_{ij}(\mathbf{x}, t - \tau; \boldsymbol{\xi}, 0) d\Sigma(\boldsymbol{\xi}) d\tau, \end{aligned} \quad (14)$$

where I used the following property:

$$\begin{aligned} \iiint_V \frac{\partial}{\partial \eta_k} \delta(\boldsymbol{\eta} - \boldsymbol{\xi}) G_{ij}(\mathbf{x}, t - \tau; \boldsymbol{\eta}, 0) dV(\boldsymbol{\eta}) \\ = - \frac{\partial}{\partial \xi_k} G_{ij}(\mathbf{x}, t - \tau; \boldsymbol{\xi}, 0). \end{aligned} \quad (15)$$

We assume that the source is small compared to the wavelengths of seismic waves and approximate the source as a point at $\boldsymbol{\xi}_0$. Then, Eq. (14) can be written as

$$u_i^{S1}(\mathbf{x}, t) = \int_{-\infty}^{\infty} M_{jk}(\boldsymbol{\xi}_0, \tau) \frac{\partial}{\partial \xi_k} G_{ij}(\mathbf{x}, t - \tau; \boldsymbol{\xi}_0, 0) d\tau, \quad (16)$$

where M_{jk} is the moment tensor defined as

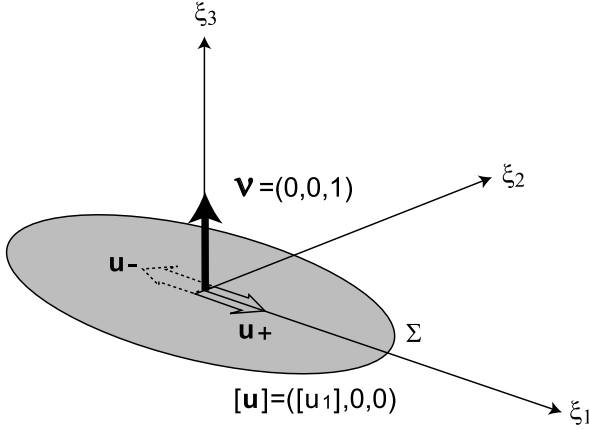
$$M_{jk}(\boldsymbol{\xi}_0, \tau) = \iint_{\Sigma} m_{jk}(\boldsymbol{\xi}, \tau) d\Sigma(\boldsymbol{\xi}). \quad (17)$$

Slip on a Fault We consider slip $[u_1]$ in the plane $\xi_3 = 0$ (see Fig. 4). In this case, $\mathbf{v} = (0, 0, 1)$ and $[u] = ([u_1], 0, 0)$. Substituting \mathbf{v} and $[u]$ into Eq. (13), we obtain the moment density tensor m_{jk} as

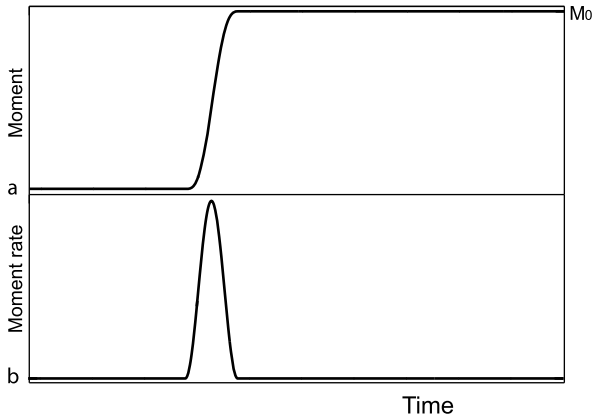
$$\mathbf{m} = \begin{pmatrix} 0 & 0 & \mu [u_1(\boldsymbol{\xi}, \tau)] \\ 0 & 0 & 0 \\ \mu [u_1(\boldsymbol{\xi}, \tau)] & 0 & 0 \end{pmatrix}, \quad (18)$$

and the moment tensor M_{jk} as

$$\mathbf{M} = M(\boldsymbol{\xi}_0, \tau) \begin{pmatrix} 0 & 0 & 1 \\ 0 & 0 & 0 \\ 1 & 0 & 0 \end{pmatrix}, \quad (19)$$



Volcano Seismic Signals, Source Quantification of, Figure 4
Slip $[u_1]$ in the plane $\xi_3 = 0$



Volcano Seismic Signals, Source Quantification of, Figure 5
Moment and moment-rate functions for slip across a plane in the form of a step-like function

where

$$M(\xi_0, \tau) = \mu \iint_{\Sigma} [u_1(\xi, \tau)] d\Sigma(\xi). \quad (20)$$

This is called the moment function or source-time function. The time history of slip across a plane is typically represented by a step-like function, and therefore $M(\xi_0, \tau)$ displays a step-like function (Fig. 5a). We can also define the time derivative of M as

$$\dot{M}(\xi_0, \tau) = \mu \frac{\partial}{\partial \tau} \iint_{\Sigma} [u_1(\xi, \tau)] d\Sigma(\xi). \quad (21)$$

This is called the moment-rate function, which is an impulsive function (Fig. 5b). After slip stops, M has a finite value M_0 (Fig. 5a), which is given as

$$M_0 = \mu A \bar{u}_1. \quad (22)$$

A and \bar{u}_1 are the slip area and average slip, respectively, which are defined as

$$A = \iint_{\Sigma} d\Sigma, \quad (23)$$

$$\bar{u}_1 = \frac{\iint_{\Sigma} [u_1(\xi, \tau = \infty)] d\Sigma}{A}, \quad (24)$$

where $\tau = \infty$ represents time after the termination of slip. M_0 is called the seismic moment. When $\tau = \infty$, M_{jk} becomes

$$\mathbf{M} = M_0 \begin{pmatrix} 0 & 0 & 1 \\ 0 & 0 & 0 \\ 1 & 0 & 0 \end{pmatrix}. \quad (25)$$

This matrix can be diagonalized to

$$\mathbf{M}' = M_0 \begin{pmatrix} 1 & 0 & 0 \\ 0 & 0 & 0 \\ 0 & 0 & -1 \end{pmatrix}, \quad (26)$$

where three eigenvalues (1, 0, and -1) correspond to the T (maximum compression), B (null), and P (minimum compression) axes, respectively. As shown in Fig. 6, this system constitutes a double couple, which is equivalent to fault slip.

Tensile Crack We examine a crack such that slip $[u_3]$ is nonzero in the plane $\xi_3 = 0$ (a horizontal crack; see Fig. 7). In this case, $\mathbf{v} = (0, 0, 1)$ and $[\mathbf{u}] = (0, 0, [u_3])$. Therefore, we find from Eq. (13) that

$$\mathbf{m} = \begin{pmatrix} \lambda[u_3(\xi, \tau)] & 0 & 0 \\ 0 & \lambda[u_3(\xi, \tau)] & 0 \\ 0 & 0 & (\lambda + 2\mu)[u_3(\xi, \tau)] \end{pmatrix}. \quad (27)$$

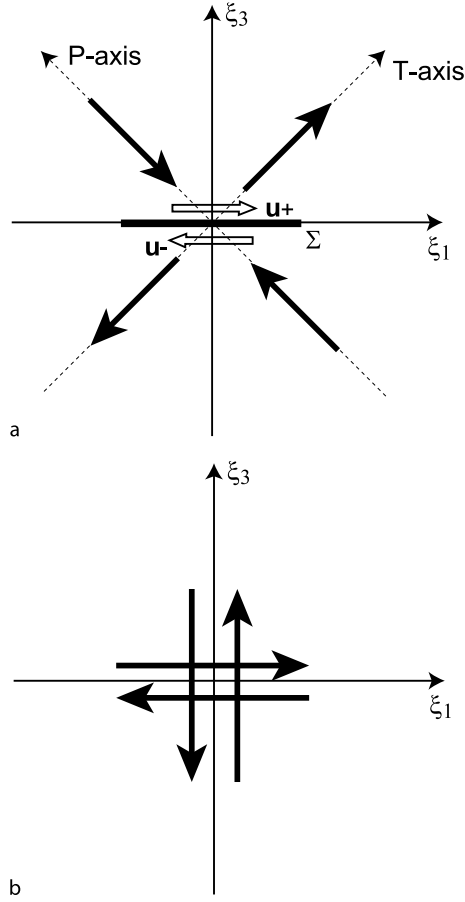
The moment tensor for a horizontal crack is given as

$$\mathbf{M} = M(\xi_0, \tau) \begin{pmatrix} \lambda/\mu & 0 & 0 \\ 0 & \lambda/\mu & 0 \\ 0 & 0 & \lambda/\mu + 2 \end{pmatrix}, \quad (28)$$

and

$$\begin{aligned} M(\xi_0, \tau) &= \mu \iint_{\Sigma} [u_3(\xi, \tau)] d\Sigma(\xi) \\ &= \mu A \bar{u}_3(\tau) \\ &= \mu \Delta V(\tau), \end{aligned} \quad (29)$$

where ΔV represents the incremental volume change of the crack.



Volcano Seismic Signals, Source Quantification of, Figure 6
a Force system for slip $[u_1]$ in the plane $\xi_3 = 0$. **b** A double couple equivalent to the force system in Fig. 6a

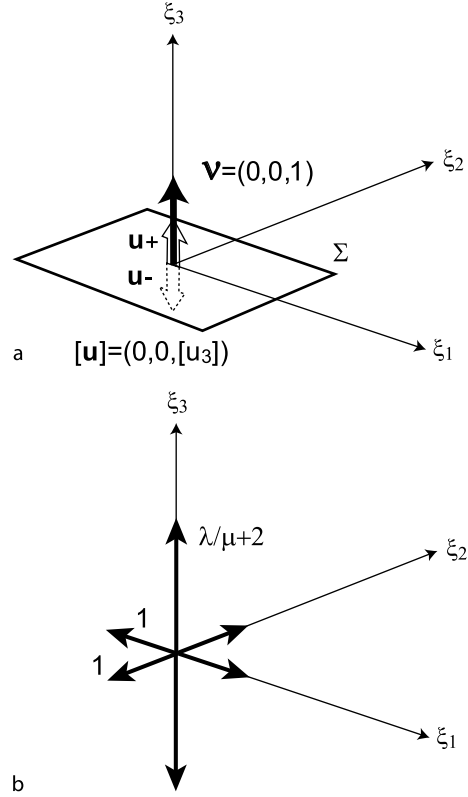
Figure 8a is a tensile crack with normal direction (θ, ϕ) , and we find that $\mathbf{v} = (\sin \theta \cos \phi, \sin \theta \sin \phi, \cos \theta)$ and $[\mathbf{u}] = [u](\sin \theta \cos \phi, \sin \theta \sin \phi, \cos \theta)$. Using Eqs. (13) and (17), we obtain the moment tensor for the crack:

$$\mathbf{M} = \mu \Delta V \begin{pmatrix} \lambda/\mu + 2 \sin^2 \theta \cos^2 \phi & 2 \sin^2 \theta \sin \phi \cos \phi & 2 \sin \theta \cos \theta \cos \phi \\ 2 \sin^2 \theta \sin \phi \cos \phi & \lambda/\mu + 2 \sin^2 \theta \sin^2 \phi & 2 \sin \theta \cos \theta \sin \phi \\ 2 \sin \theta \cos \theta \cos \phi & 2 \sin \theta \cos \theta \sin \phi & \lambda/\mu + 2 \cos^2 \theta \end{pmatrix}, \quad (30)$$

where $\Delta V = \iint_{\Sigma} [u] d\Sigma$.

For a vertical crack ($\theta = \pi/2$),

$$\mathbf{M} = \mu \Delta V \begin{pmatrix} \lambda/\mu + 2 \cos^2 \phi & 2 \sin \phi \cos \phi & 0 \\ 2 \sin \phi \cos \phi & \lambda/\mu + 2 \sin^2 \phi & 0 \\ 0 & 0 & \lambda/\mu \end{pmatrix}. \quad (31)$$



Volcano Seismic Signals, Source Quantification of, Figure 7

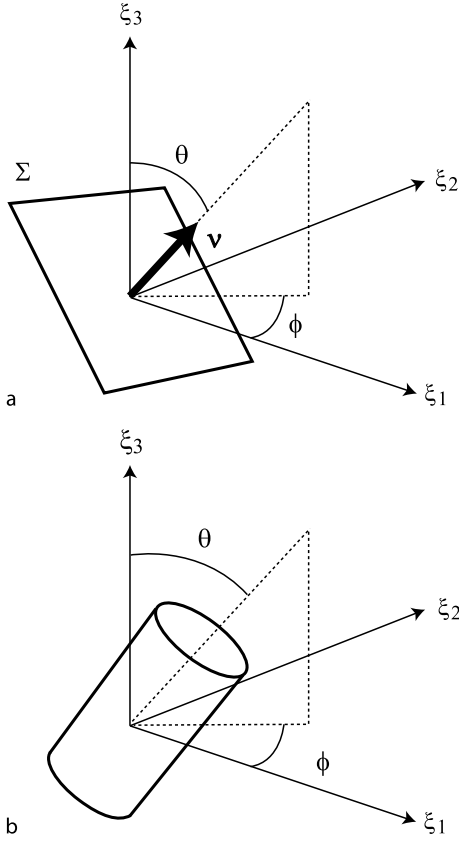
a A tensile horizontal crack in which slip $[u_3]$ is nonzero in the plane ξ_3 . **b** Force system equivalent to a tensile horizontal crack

A tensile crack is equivalent to a superposition of three vector dipoles with amplitude ratios $1:1:(\lambda + 2\mu)/\lambda$ (Fig. 7). If $\lambda = \mu$, the amplitude ratios are represented by 1:1:3. If $\lambda = 2\mu$, which may be appropriate either for volcanic rock near liquidus temperature or for a highly heterogeneous medium, the ratios become 1:1:2.

Spherical Source The moment tensor for a spherical source is given as

$$\mathbf{M} = (\lambda + 2\mu) \Delta V_s \begin{pmatrix} 1 & 0 & 0 \\ 0 & 1 & 0 \\ 0 & 0 & 1 \end{pmatrix}, \quad (32)$$

where $\Delta V_s = 4\pi R^2 \Delta_s$ is the volume change caused by the displacement Δ_s of a spherical surface of radius R [89] (see “Appendix B: Moment Tensor for a Spherical Source”). The moment tensor for a spherical source may be useful to describe the source of explosion earthquakes e. g., [56].



Volcano Seismic Signals, Source Quantification of, Figure 8
Source coordinates and geometries for **a** a crack and **b** a cylinder

Cylindrical Source The moment tensor for a vertical cylinder is

$$\mathbf{M} = \frac{\lambda + 2\mu}{\lambda + \mu} \mu \Delta V_c \begin{pmatrix} \lambda/\mu + 1 & 0 & 0 \\ 0 & \lambda/\mu + 1 & 0 \\ 0 & 0 & \lambda/\mu \end{pmatrix}, \quad (33)$$

where $\Delta V_c = 2\pi RL\Delta_c$ is the volume change caused by the radial displacement Δ_c of the surface of a cylinder of radius R and length L [89,126] (see “Appendix C: Moment Tensor for a Cylindrical Source”).

The moment tensor for a cylinder with axis orientation angles (θ, ϕ) (Fig. 8b) is given as

$$\mathbf{M} = \frac{\lambda + 2\mu}{\lambda + \mu} \mu \Delta V_c \times \begin{pmatrix} \lambda/\mu + (\cos^2 \theta \cos^2 \phi + \sin^2 \phi) & \sin^2 \theta \sin \phi \cos \phi & \sin \theta \cos \theta \cos \phi \\ \sin^2 \theta \sin \phi \cos \phi & \lambda/\mu + (\cos^2 \theta \sin^2 \phi + \cos^2 \phi) & \sin \theta \cos \theta \sin \phi \\ \sin \theta \cos \theta \cos \phi & \sin \theta \cos \theta \sin \phi & \lambda/\mu + \sin^2 \theta \end{pmatrix} \quad (34)$$

(see “Appendix C: Moment Tensor for a Cylindrical Source”). Radial volumetric changes of a pipe may occur in association with mass transport in a cylindrical conduit e.g., [126].

Inertial Glut

In the scheme presented by BM, no single force exists in indigenous seismic sources because of the requirement for conservation of linear momentum. However, Takei and Kumazawa [118] presented a theoretical justification for the existence of a single force in indigenous sources, if the non-linear effect of mass advection is taken into account.

Following the theory of Takei and Kumazawa [118], we consider the exact equation of motion of the earth, given as

$$\rho^{\text{true}} \frac{D^2 u_i}{Dt^2} = \frac{\partial \sigma_{ni}^{\text{true}}}{\partial x_n}, \quad (35)$$

where ρ^{true} is true density as a function of both space and time. $\frac{D}{Dt}$ is the particle derivative:

$$\frac{D}{Dt} = \frac{\partial}{\partial t} + v_k \frac{\partial}{\partial x_k}, \quad (36)$$

where $v_k = \frac{Du_k}{Dt}$ is particle velocity. Using model density ρ^{model} and model stress $\sigma_{ni}^{\text{model}}$ from Eq. (2), Eq. (35) can be rewritten as follows:

$$\rho^{\text{model}} \frac{\partial^2 u_i}{\partial t^2} = \frac{\partial \sigma_{ni}^{\text{model}}}{\partial x_n} + f_i^V. \quad (37)$$

This equation is similar to Eq. (3), but the equivalent body force f_i^V is defined in this case as

$$\begin{aligned} f_i^V &= \left(\frac{\partial \sigma_{ni}^{\text{true}}}{\partial x_n} - \frac{\partial \sigma_{ni}^{\text{model}}}{\partial x_n} \right) \\ &+ \left(\rho^{\text{model}} \frac{\partial^2 u_i}{\partial t^2} - \rho^{\text{true}} \frac{D^2 u_i}{Dt^2} \right) \\ &= f_i^S + f_i^I. \end{aligned} \quad (38)$$

Here, f_i^V is f_i^S , arising from the stress glut, plus f_i^I , representing the difference between the inertia terms, which is called the inertial glut [118].

In the same way as presented by BM, we expand f_i^I in terms of polynomial moments at a particular point ξ_0 as

$$f_i^I(\eta, \tau) = F_i^{I0}(\xi_0, \tau) \delta(\eta - \xi_0) + \text{higher-order terms}, \quad (39)$$

where

$$\begin{aligned} F_i^{I0} &= \iiint_V f_i^I(\eta, \tau) dV(\eta) \\ &= - \iiint_V \left(\rho^{\text{true}} \frac{D^2 u_i}{Dt^2} - \rho^{\text{model}} \frac{\partial^2 u_i}{\partial t^2} \right) dV(\eta). \end{aligned} \quad (40)$$

By using mass conservation

$$\frac{\partial \rho^{\text{true}}}{\partial t} + \frac{\partial}{\partial x_k}(\rho^{\text{true}} v_k) = 0 \quad (41)$$

and Gauss' theorem

$$\iiint_V \frac{\partial v_k}{\partial x_k} dV = \iint_{S_e} v_k v_k dS_e, \quad (42)$$

the first integral of Eq. (40) is expressed as

$$\begin{aligned} \iiint_V \rho^{\text{true}} \frac{D^2 u_i}{Dt^2} dV &= \frac{\partial}{\partial t} \iiint_V \rho^{\text{true}} v_i dV \\ &+ \iint_{S_e} (\rho^{\text{true}} v_i v_k) v_k dS_e, \end{aligned} \quad (43)$$

where S_e is the surface of the earth. The second term in the right-hand side of Eq. (43) vanishes because it is a surface integral of a non-linear term, which is infinitesimal. Therefore, we find that

$$\begin{aligned} \iiint_V \rho^{\text{true}} \frac{D^2 u_i}{Dt^2} dV &= \frac{\partial}{\partial t} \iiint_V \rho^{\text{true}} v_i dV \\ &= \dot{L}_i^t. \end{aligned} \quad (44)$$

Here, \dot{L}_i^t is the time derivative of the total linear momentum, which is zero at any given time because of conservation of linear momentum of the earth. The second integral in Eq. (40) is given as

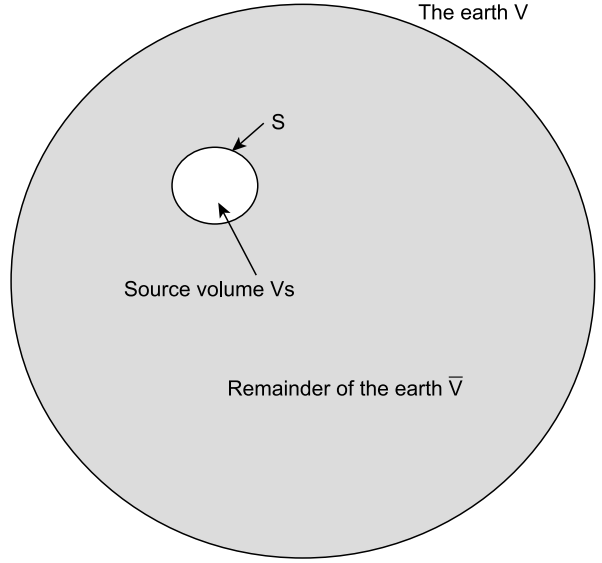
$$\begin{aligned} \iiint_V \rho^{\text{model}} \frac{\partial^2 u_i}{\partial t^2} dV &= \frac{\partial}{\partial t} \iiint_V \rho^{\text{model}} \frac{\partial u_i}{\partial t} dV \\ &= \dot{L}_i^m, \end{aligned} \quad (45)$$

which is the time derivative of linear momentum defined by the model density. Therefore, Eq. (40) is written as

$$\begin{aligned} F_i^{I0} &= -(\dot{L}_i^t - \dot{L}_i^m) \\ &= \dot{L}_i^m, \end{aligned} \quad (46)$$

which shows that force F_i^{I0} exists as an apparent change of the total linear momentum of the earth referred to a biased model density structure.

Takei and Kumazawa [118] stated that F_i^{I0} originates from (a) the difference of density structure of the prescribed model from the actual value in the source region before the event, and from (b) a temporal change of the density structure in the source region caused by finite displacement of mass during the event. The latter is a non-linear effect caused by mass advection, which may occur by fluid flow, especially in volcanic regions.



Volcano Seismic Signals, Source Quantification of, Figure 9

The earth V divided into a source volume V_s enclosed by a surface S and the remainder of the earth \tilde{V}

Single Force Defined by Action and Reaction

We further consider the single force from the viewpoint of the interaction force between the source volume and the rest of the earth. Following Takei and Kumazawa [119], we define the source region V_s enclosed by a surface S and the remaining part of the earth \tilde{V} (Fig. 9). Using Eqs. (38), (9), (44), and (45), we obtain

$$\begin{aligned} \iiint_V f_i^V dV &= \iiint_V (f_i^S + f_i^I) dV \\ &= \iiint_V f_i^I dV \\ &= -\frac{\partial}{\partial t} \iiint_V \left(\rho^{\text{true}} v_i - \rho^{\text{model}} \frac{\partial u_i}{\partial t} \right) dV \\ &= -\frac{\partial}{\partial t} \left[\iiint_{V_s} \left(\rho^{\text{true}} v_i - \rho^{\text{model}} \frac{\partial u_i}{\partial t} \right) dV \right. \\ &\quad \left. - \iiint_{\tilde{V}} \left(\rho^{\text{true}} v_i - \rho^{\text{model}} \frac{\partial u_i}{\partial t} \right) dV \right], \end{aligned} \quad (47)$$

where infinitesimal surface integral terms are omitted. The second integral in the right-hand side of Eq. (47) vanishes because $\rho^{\text{true}} = \rho^{\text{model}}$ and $v_i = \partial u_i / \partial t$ in \tilde{V} . f_i^V exists only in the source region, and thus the volume integral of f_i^V in the left hand side of Eq. (47) can be limited to V_s .

Therefore, Eq. (47) is written as

$$\iiint_{V_s} f_i^V dV = -\frac{\partial}{\partial t} \iiint_{V_s} \left(\rho^{\text{true}} v_i - \rho^{\text{model}} \frac{\partial u_i}{\partial t} \right) dV. \quad (48)$$

This equation is then rewritten as

$$\begin{aligned} \frac{\partial}{\partial t} \iiint_{V_s} \rho^{\text{true}} v_i dV &= \frac{\partial}{\partial t} \iiint_{V_s} \rho^{\text{model}} \frac{\partial u_i}{\partial t} dV \\ &\quad - \iiint_{V_s} f_i^V dV \\ &= \iiint_{V_s} \left(\rho^{\text{model}} \frac{\partial^2 u_i}{\partial t^2} - f_i^V \right) dV. \end{aligned} \quad (49)$$

From Eq. (37), we find that the integrand of the right-hand side of Eq. (49) equals $\partial \sigma_{ni}^{\text{model}} / \partial x_n$. Therefore, we obtain

$$\begin{aligned} \frac{\partial}{\partial t} \iiint_{V_s} \rho^{\text{true}} v_i dV &= \iiint_{V_s} \frac{\partial \sigma_{ni}^{\text{model}}}{\partial x_n} dV \\ &= \iint_S \sigma_{ni}^{\text{model}} v_n dS. \end{aligned} \quad (50)$$

This indicates that a temporal change of linear momentum in the source region is equivalent to the total force exerted on the boundary S . Therefore, $\iint_S \sigma_{ni}^{\text{model}} v_n dS$ can be regarded as the action force originating from non-linear processes in the source volume V_s . In \bar{V} , the reaction force opposite to $\iint_S \sigma_{ni}^{\text{model}} v_n dS$ acts through the boundary S . We define traction P_i on S , which satisfies the following condition:

$$\sigma_{ni}^{\text{model}} v_n = -P_i \quad \text{on } S. \quad (51)$$

Then, we find that

$$\begin{aligned} \iint_S P_i dS &= -\iint_S \sigma_{ni}^{\text{model}} v_n dS \\ &= -\frac{\partial}{\partial t} \iiint_{V_s} \rho^{\text{true}} v_i dV, \end{aligned} \quad (52)$$

which is the reaction force opposite to the action force.

If the source is small compared to the wavelengths of seismic waves, the action force originating in a closed small source volume V_s may not be observable outside the source volume \bar{V} . Instead, the traction P_j exerted on S may be viewed in \bar{V} as a traction discontinuity on S . As shown by Aki and Richards [1], a traction discontinuity is the source of seismic waves represented by an equivalent body

force. We consider seismic waves in \bar{V} , and the equation of motion in \bar{V} may be expressed as

$$\rho^{\text{model}} \frac{\partial^2 u_i}{\partial t^2} = \frac{\partial \sigma_{ni}^{\text{model}}}{\partial x_n} + f_i \quad \text{in } \bar{V}, \quad (53)$$

where f_i is the equivalent body force due to the traction discontinuity on S , given as

$$f_i(\eta, \tau) = \iint_S P_i(\xi, \tau) \delta(\eta - \xi) dS(\xi). \quad (54)$$

Note that

$$\iiint_{\bar{V}} f_i(\eta, \tau) dV(\eta) = \iint_S P_i(\xi, \tau) dS(\xi), \quad (55)$$

which is the total force acting through S in \bar{V} .

We may use Green's functions estimated from the model structure because the effect of the true structure in the source volume is negligible in the point source approximation. Therefore, by using Eq. (54), the displacement field u_i^f due to the single force may be described as

$$\begin{aligned} u_i^f(\mathbf{x}, t) &= \int_{-\infty}^{\infty} \iiint_{\bar{V}} f_j(\eta, \tau) G_{ij}(\mathbf{x}, t - \tau; \eta, 0) dV(\eta) d\tau \\ &= \int_{-\infty}^{\infty} \iiint_{\bar{V}} \left[\iint_S P_j(\xi, \tau) \delta(\eta - \xi) dS(\xi) \right] \\ &\quad \cdot G_{ij}(\mathbf{x}, t - \tau; \eta, 0) dV(\eta) d\tau \\ &= \int_{-\infty}^{\infty} \iint_S P_j(\xi, \tau) G_{ij}(\mathbf{x}, t - \tau; \xi, 0) dS(\xi) d\tau, \end{aligned} \quad (56)$$

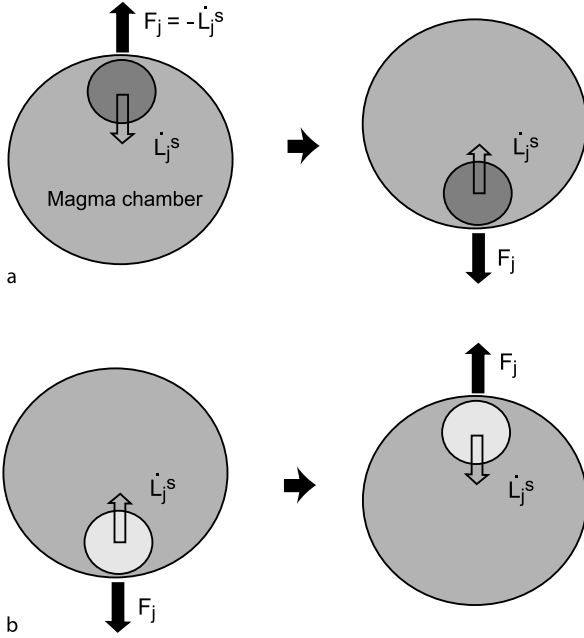
or, equivalently,

$$u_i^f(\mathbf{x}, t) = \int_{-\infty}^{\infty} F_j(\xi_0, \tau) G_{ij}(\mathbf{x}, t - \tau; \xi_0, 0) d\tau, \quad (57)$$

where

$$\begin{aligned} F_j(\xi_0, \tau) &= \iint_S P_j(\xi, \tau) dS(\xi) \\ &= -\frac{\partial}{\partial t} \iiint_{V_s} \rho^{\text{true}} v_j dV \\ &= -\dot{L}_j^s. \end{aligned} \quad (58)$$

Here, L_j^s is the total linear momentum inside the source volume. This single force representation in terms of the traction P_j is consistent with the relationship between the traction modes and equivalent body force given by Takei and Kumazawa [119] in small-source and long-wavelength approximations.



Volcano Seismic Signals, Source Quantification of, Figure 10
Schematic illustration of the reaction force (F_j) opposite to the action force (\dot{L}_j^s) generated by nonlinear processes in a source volume: **a** dense materials falling in a magma chamber and **b** light materials ascending in a magma chamber

F_j is the reaction force opposite to the action force generated by non-linear processes in the source volume. A simple example is dense materials falling in a magma chamber (Fig. 10a). During the acceleration stage of falling dense materials, \dot{L}_j^s is a downward force and we therefore observe an upward single force as the reaction force; during the deceleration stage, we observe a downward single force (Fig. 10a). In the case of lighter materials ascending in a magma chamber, we observe a downward single force during the acceleration stage of ascending lighter materials, and an upward single force is observed during the deceleration stage of ascending lighter materials (Fig. 10b).

Summary

Here, we summarize the phenomenological representation of indigenous seismic sources. For point sources, the displacement field u_i can be expressed by the superposition of the displacement fields excited by single force u_i^f of Eq. (57) and moment tensor u_i^{s1} of Eq. (16):

$$u_i(\mathbf{x}, t) = \int_{-\infty}^{\infty} F_j(\xi_0, \tau) G_{ij}(\mathbf{x}, t - \tau; \xi_0, 0) d\tau + \int_{-\infty}^{\infty} M_{jk}(\xi_0, \tau) \frac{\partial}{\partial \xi_k} G_{ij}(\mathbf{x}, t - \tau; \xi_0, 0) d\tau, \quad (59)$$

where

$$F_j(\xi_0, \tau) = \iint_S P_j(\xi, \tau) dS(\xi) \quad (60)$$

and

$$M_{jk}(\xi_0, \tau) = \iint_{\Sigma} m_{jk}(\xi, \tau) d\Sigma(\xi). \quad (61)$$

Here, P_j is the traction exerted on the boundary S between the source volume and the rest of the earth and m_{jk} is the moment density tensor defined by the displacement discontinuity across the surface Σ . F_j is related to the total linear momentum within the source volume L_j^s as

$$F_j = -\dot{L}_j^s \quad (j = 1, 2, 3). \quad (62)$$

M_{jk} is the moment tensor consisting of six independent components:

$$\mathbf{M} = \begin{pmatrix} M_{11} & M_{12} & M_{13} \\ M_{12} & M_{22} & M_{23} \\ M_{13} & M_{23} & M_{33} \end{pmatrix}. \quad (63)$$

Waveform Inversion

Waveform inversion is a quantitative tool used to estimate the source mechanisms and locations of volcano-seismic signals. The source parameters are determined by finding the best fits between observed and synthetic seismic waveforms. This can be performed by solving an inverse problem by using the concept of linear inverse theory e. g., [83].

We may reasonably assume that the source of a tectonic earthquake is represented by the moment tensor corresponding to a double couple. However, volcano-seismic signals may be generated by complex source processes, requiring a general source representation consisting of single force and moment tensor. Furthermore, while we can assume a step-like function for the source-time function of a tectonic earthquake, we must determine the complex time history at the source of volcano-seismic signals, which involves more unknowns. Waveform inversion of volcano-seismic signals is thus a more complicated task than the inversion of a tectonic earthquake.

We assume a single force and moment tensor at a particular source location, and obtain from Eq. (59) the following relationship:

$$u_i(t) = \int_{-\infty}^{\infty} [F_j(\tau) G_{ij}(t - \tau) + M_{jk}(\tau) G_{ij,k}(t - \tau)] d\tau, \quad (64)$$

where $G_{ij,k} = \partial G_{ij} / \partial \xi_k$. We rewrite Eq. (64) in the following form:

$$u_i(t) = \sum_{j=1}^9 \int_{-\infty}^{\infty} m_j(\tau) \Gamma_{ij}(t - \tau) d\tau, \quad (65)$$

where

$$m_j = [F_1, F_2, F_3, M_{11}, M_{22}, M_{33}, M_{12}, M_{23}, M_{13}] \quad (66)$$

and

$$\Gamma_{ij} = [G_{i1}, G_{i2}, G_{i3}, G_{i1,1}, G_{i2,2}, G_{i3,3}, G_{i1,2}, G_{i2,1}, G_{i2,3} + G_{i3,2}, G_{i1,3} + G_{i3,1}]. \quad (67)$$

We discretize t and τ as $t = k\Delta t$ ($k = 0, \dots, N_t - 1$) and $\tau = l\Delta t$ ($l = 0, \dots, N_t - 1$), respectively, where Δt is the sampling interval. This yields the discrete form of Eq. (65) given as

$$u_i(k\Delta t) = \sum_{j=1}^9 \sum_{l=0}^{N_t-1} m_j(l\Delta t) \Gamma_{ij}(k\Delta t - l\Delta t) \Delta t. \quad (68)$$

If we have N_c traces of u_i , Eq. (68) is written in matrix form

$$\mathbf{u} = \mathbf{\Gamma} \mathbf{m}, \quad (69)$$

where

$$\mathbf{u} = [u_1(0), \dots, u_1((N_t - 1)\Delta t), \dots, u_{N_c}(0), \dots, u_{N_c}((N_t - 1)\Delta t)]^T, \quad (70)$$

$$\mathbf{m} = [m_1(0), \dots, m_1((N_t - 1)\Delta t), \dots, m_9(0), \dots, m_9((N_t - 1)\Delta t)]^T, \quad (71)$$

$$\mathbf{\Gamma} = \begin{bmatrix} \Gamma_{11}(0) & \cdots & \Gamma_{11}((1 - N_t)\Delta t) & \cdots \\ \vdots & \vdots & \vdots & \vdots \\ \Gamma_{11}((N_t - 1)\Delta t) & \cdots & \Gamma_{11}(0) & \cdots \\ \vdots & \vdots & \vdots & \vdots \\ \Gamma_{N_c 1}(0) & \cdots & \Gamma_{N_c 1}((1 - N_t)\Delta t) & \cdots \\ \vdots & \vdots & \vdots & \vdots \\ \Gamma_{N_c 1}((N_t - 1)\Delta t) & \cdots & \Gamma_{N_c 1}(0) & \cdots \\ \cdots & \Gamma_{19}(0) & \cdots & \Gamma_{19}((1 - N_t)\Delta t) \\ \vdots & \vdots & \vdots & \vdots \\ \cdots & \Gamma_{19}((N_t - 1)\Delta t) & \cdots & \Gamma_{19}(0) \\ \vdots & \vdots & \vdots & \vdots \\ \cdots & \Gamma_{N_c 9}(0) & \cdots & \Gamma_{N_c 9}((1 - N_t)\Delta t) \\ \vdots & \vdots & \vdots & \vdots \\ \cdots & \Gamma_{N_c 9}((N_t - 1)\Delta t) & \cdots & \Gamma_{N_c 9}(0) \end{bmatrix} \Delta t. \quad (72)$$

Here T denotes transpose. $\mathbf{\Gamma}$ is called the data kernel, which is an $N \times M$ matrix, and \mathbf{u} and \mathbf{m} are vectors of lengths N and M , respectively, where $N = N_c N_t$ and $M = 9 N_t$.

We denote observed waveforms as \mathbf{u}^{obs} , which satisfy the following equation:

$$\mathbf{u}^{\text{obs}} - \mathbf{\Gamma} \mathbf{m} = \mathbf{e}, \quad (73)$$

where \mathbf{e} is the prediction error or misfit. In the case of $N > M$, we estimate \mathbf{m} by minimizing the residual R , defined as

$$R = \frac{\mathbf{e}^T \mathbf{e}}{\mathbf{u}^{\text{obs}T} \mathbf{u}^{\text{obs}}} = \frac{\sum_{i=1}^N e_i^2}{\sum_{i=1}^N u_i^{\text{obs}}}, \quad (74)$$

where

$$\mathbf{e}^T \mathbf{e} = (\mathbf{u}^{\text{obs}} - \mathbf{\Gamma} \mathbf{m})^T (\mathbf{u}^{\text{obs}} - \mathbf{\Gamma} \mathbf{m}). \quad (75)$$

To minimize R is to find values of \mathbf{m} that satisfy the following equations:

$$\frac{\partial R}{\partial m_q} = 0 \quad (q = 1, \dots, M). \quad (76)$$

This leads to the following relationship (the normal equation)

$$\mathbf{\Gamma}^T \mathbf{\Gamma} \mathbf{m} - \mathbf{\Gamma}^T \mathbf{u}^{\text{obs}} = 0. \quad (77)$$

Therefore, we have the following solution:

$$\mathbf{m}^{\text{est}} = [\mathbf{\Gamma}^T \mathbf{\Gamma}]^{-1} \mathbf{\Gamma}^T \mathbf{u}^{\text{obs}}, \quad (78)$$

which is the least-squares solution. This least-squares approach in the time domain has been used in many volcano seismological studies e. g., [32,33,48,69,71,72,73,92,94,102,105,107,108,120,122].

As can be seen from Eq. (68), u_i is calculated by the convolution of m_j with Γ_{ij} . This means that the displacement $u_i(k\Delta t)$ includes the entire effect of the time history of the single force and moment tensor as well as Green's functions before time $k\Delta t$. This may be easily understood if we consider $u_i((N_t - 1)\Delta t)$ in Eq. (68):

$$\begin{aligned} u_i((N_t - 1)\Delta t) = \Delta t \sum_{j=1}^9 [& m_j(0) \Gamma_{ij}((N_t - 1)\Delta t) \\ & + m_j(\Delta t) \Gamma_{ij}((N_t - 2)\Delta t) + \cdots \\ & + m_j((N_t - 2)\Delta t) \Gamma_{ij}(\Delta t) \\ & + m_j((N_t - 1)\Delta t) \Gamma_{ij}(0)]. \end{aligned} \quad (79)$$

The convolution relationship leads to the large matrix of \mathbf{F} of Eq. (69), which requires long computation time to obtain the least-squares solution. A better alternative is to solve the inverse problem in the frequency domain [11,95,116]. The Fourier transform of Eq. (65) is given by

$$\tilde{u}_i(\omega) = \sum_{j=1}^9 \tilde{m}_j(\omega) \tilde{\Gamma}_{ij}(\omega), \quad (80)$$

where ω is the angular frequency and \tilde{u}_i , \tilde{m}_j , and $\tilde{\Gamma}_{ij}$ are the Fourier transforms of u_i , m_j , and Γ_{ij} . This frequency domain equation is discretized as follows:

$$\tilde{u}_i(k\Delta\omega) = \sum_{j=1}^9 \tilde{m}_j(k\Delta\omega) \tilde{\Gamma}_{ij}(k\Delta\omega), \quad (81)$$

where $\Delta\omega = 2\pi/(N_t\Delta t)$ and $k = 0, \dots, N_t/2$. Note that the Fourier transformed components are complex and we have a set of the equations corresponding to real and imaginary parts; therefore, Eq. (81) consists of N_t equations. We further note that \tilde{u}_i , \tilde{m}_j , and $\tilde{\Gamma}_{ij}$ in Eq. (81) depend only on $k\Delta\omega$. This indicates that individual frequency components of \tilde{u}_i , \tilde{m}_j , and $\tilde{\Gamma}_{ij}$ are independent of each other and Eq. (81) can be solved separately. This is different from the time-domain Eq. (65): u_i is a function of $k\Delta t$, whereas m_j is a function of $l\Delta t$, and Γ_{ij} is a function of $k\Delta t$ and $l\Delta t$, so we cannot separate the time-domain equation in individual values of $k\Delta t$. The use of the frequency-domain equation results in a smaller size of the data kernel, as shown below.

If we have N_c traces of \tilde{u}_i , Eq. (81) is written in matrix form

$$\tilde{\mathbf{u}} = \tilde{\mathbf{F}} \tilde{\mathbf{m}}. \quad (82)$$

Here, $\tilde{\mathbf{u}}$ is a vector consisting of \tilde{u}_i , which is arranged in individual frequency components as follows:

$$\begin{aligned} \tilde{\mathbf{u}} = & [\tilde{u}_1(0), \tilde{u}_2(0), \dots, \tilde{u}_{N_c}(0), \tilde{u}_1(\Delta\omega), \\ & \tilde{u}_2(\Delta\omega), \dots, \tilde{u}_{N_c}(\Delta\omega), \dots, \tilde{u}_1((N_t/2)\Delta\omega), \\ & \tilde{u}_2((N_t/2)\Delta\omega), \dots, \tilde{u}_{N_c}((N_t/2)\Delta\omega)]^T \end{aligned} \quad (83)$$

or, equivalently,

$$\tilde{\mathbf{u}} = [\tilde{\mathbf{u}}(0), \tilde{\mathbf{u}}(\Delta\omega), \dots, \tilde{\mathbf{u}}(k\Delta\omega), \dots, \tilde{\mathbf{u}}(N_t/2\Delta\omega)]^T, \quad (84)$$

where

$$\tilde{\mathbf{u}}(k\Delta\omega) = [\tilde{u}_1(k\Delta\omega), \tilde{u}_2(k\Delta\omega), \dots, \tilde{u}_{N_c}(k\Delta\omega)]^T. \quad (85)$$

Similarly, $\tilde{\mathbf{m}}$ is a vector consisting of \tilde{m}_j , which is arranged in individual frequency components as

$$\begin{aligned} \tilde{\mathbf{m}} = & [\tilde{m}_1(0), \tilde{m}_2(0), \dots, \tilde{m}_9(0), \tilde{m}_1(\Delta\omega), \\ & \tilde{m}_2(\Delta\omega), \dots, \tilde{m}_9(\Delta\omega), \dots, \tilde{m}_1((N_t/2)\Delta\omega), \\ & \tilde{m}_2((N_t/2)\Delta\omega), \dots, \tilde{m}_9((N_t/2)\Delta\omega)]^T \end{aligned} \quad (86)$$

or

$$\tilde{\mathbf{m}} = [\tilde{\mathbf{m}}(0), \tilde{\mathbf{m}}(\Delta\omega), \dots, \tilde{\mathbf{m}}(k\Delta\omega), \dots, \tilde{\mathbf{m}}((N_t/2)\Delta\omega)]^T, \quad (87)$$

where

$$\tilde{\mathbf{m}}(k\Delta\omega) = [\tilde{m}_1(k\Delta\omega), \tilde{m}_2(k\Delta\omega), \dots, \tilde{m}_9(k\Delta\omega)]^T. \quad (88)$$

Accordingly, $\tilde{\mathbf{F}}$ is given as

$$\tilde{\mathbf{F}} = \begin{bmatrix} \tilde{\mathbf{F}}(0) & & & & \\ & \tilde{\mathbf{F}}(\Delta\omega) & & & 0 \\ & & \ddots & & \\ & & & \tilde{\mathbf{F}}(k\Delta\omega) & \\ 0 & & & & \ddots \\ & & & & & \tilde{\mathbf{F}}((N_t/2)\Delta\omega) \end{bmatrix}, \quad (89)$$

where $\tilde{\mathbf{F}}(k\Delta\omega)$ is

$$\tilde{\mathbf{F}}(k\Delta\omega) = \begin{bmatrix} \tilde{\Gamma}_{11}(k\Delta\omega) & \cdots & \tilde{\Gamma}_{19}(k\Delta\omega) \\ \vdots & \vdots & \vdots \\ \tilde{\Gamma}_{N_c1}(k\Delta\omega) & \cdots & \tilde{\Gamma}_{N_c9}(k\Delta\omega) \end{bmatrix}. \quad (90)$$

Since $\tilde{\mathbf{F}}$ is the block diagonal matrix, Eq. (82) can be reduced to

$$\tilde{\mathbf{u}}(k\Delta\omega) = \tilde{\mathbf{F}}(k\Delta\omega) \tilde{\mathbf{m}}(k\Delta\omega) \quad (k = 0, \dots, N_t/2). \quad (91)$$

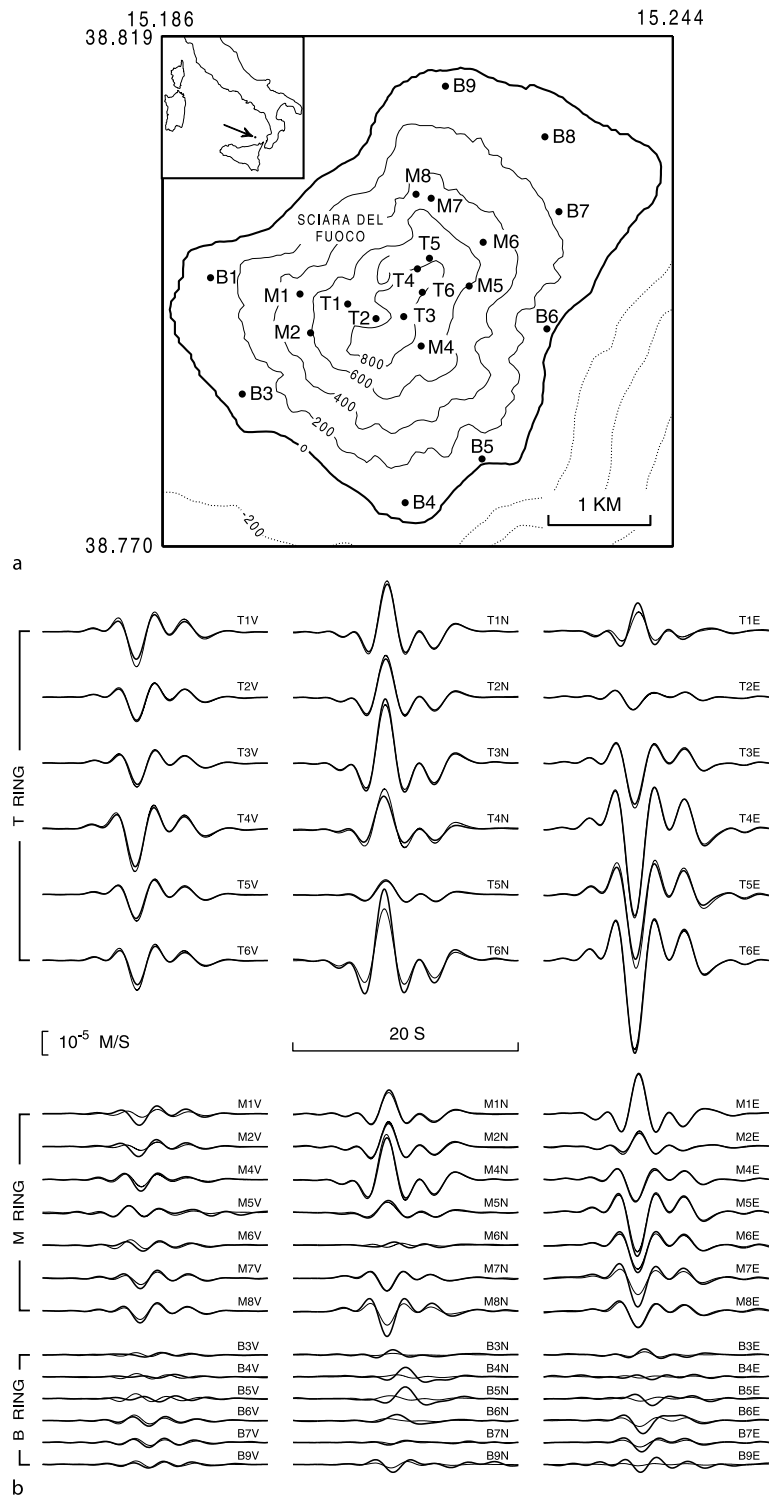
The dimension of matrix $\tilde{\mathbf{F}}(k\Delta\omega)$ is $N_c \times 9$, which is N_t^2 times smaller than that of \mathbf{F} in the time domain (Eq. (72)). This is because convolution in the time domain is equivalent to the multiplication in the frequency domain. The smaller size of $\tilde{\mathbf{F}}(k\Delta\omega)$ contributes to faster computation of the least-squares solution. We denote the $k\Delta\omega$ component of the Fourier transform of observed seismograms as

$$\tilde{\mathbf{u}}^{\text{obs}}(k\Delta\omega) = [\tilde{u}_1^{\text{obs}}(k\Delta\omega), \tilde{u}_2^{\text{obs}}(k\Delta\omega), \dots, \tilde{u}_{N_c}^{\text{obs}}(k\Delta\omega)]^T. \quad (92)$$

The least-squares solution in the frequency domain for the $k\Delta\omega$ component is then given by

$$\begin{aligned} \tilde{\mathbf{m}}^{\text{est}}(k\Delta\omega) = & [\tilde{\mathbf{F}}^H(k\Delta\omega) \tilde{\mathbf{F}}(k\Delta\omega)]^{-1} \\ & \tilde{\mathbf{F}}^H(k\Delta\omega) \tilde{\mathbf{u}}^{\text{obs}}(k\Delta\omega), \end{aligned} \quad (93)$$

where H denotes the adjoint (Hermitian conjugate). We perform the inverse Fourier transform of $\tilde{\mathbf{m}}^{\text{est}}(k\Delta\omega)$ ($k = 0, \dots, N_t/2$) to obtain the solution in the time domain.



Volcano Seismic Signals, Source Quantification of, Figure 11

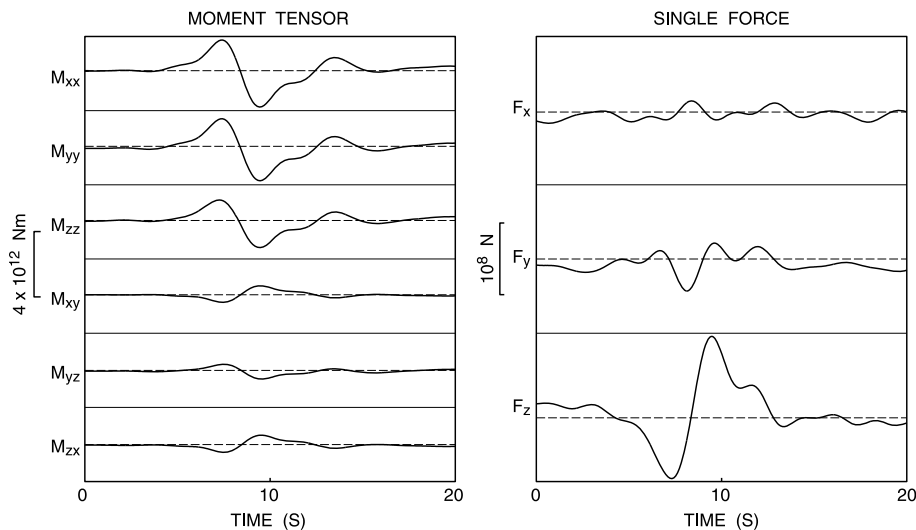
a Locations of broadband seismic stations at Stromboli Volcano, Italy. b Observed VLP velocity waveforms (*thick lines*) bandpassed between 2 and 20 s and the best-fit synthetic seismograms (*thin lines*) obtained from waveform inversion assuming six moment tensor and three single force components for the source mechanism [32]

The use of appropriate Green's functions is critically important to obtain the correct solution \mathbf{m}^{est} in either the time or frequency domains. If the source is located in a medium that can be approximated by a homogeneous or layered structure with a flat surface, Green's functions can be calculated by using propagator matrices e.g., [63] and the discrete wavenumber method e.g., [16,17,20]. However, this situation is not common in volcanic regions, and we need to take into account the steep topographies and heterogeneous structures of volcanoes. The boundary integral equation method e.g., [18] and boundary element method e.g., [62] can be used to quantify the effect of three-dimensional topography in a homogeneous or layered structure. To treat both topography and structural heterogeneity simultaneously, the finite-difference method e.g., [106,109] and the discrete lattice method [104] are suitable. Once Green's functions (and their spatial derivatives) are calculated, we can obtain the least-squares solution \mathbf{m}^{est} through Eq. (78) or (93). This solution is, however, obtained for a particular source point and a grid search in space is required to find the best-fit source location.

An example of waveform inversion is provided in Figs. 11 and 12. The source mechanism of VLP signals observed by a dense broadband seismic network at Stromboli volcano, Italy, was estimated by using the waveform inversion method in the time domain [32]. In the inversion, VLP waveforms from 18 stations (Fig. 11) were used, and six moment tensor and three single force components

for a point source were assumed. Green's functions were calculated by the finite-difference method [106] using the topography of the volcano. The inversion result (Fig. 12) points to volumetric changes accompanying a dominantly vertical single force at the source of the VLP signals. The mechanism is interpreted as the movement of a magma column in response to the piston-like rise of a slug of gas in an inclined crack-like conduit of Stromboli volcano [32].

The waveform inversion approach discussed above might be successful if we have many (more than 10) stations covering the entire edifice of a volcano. However, such dense seismic networks exist at only a limited number of volcanoes. Many volcanoes are monitored by networks of just a few seismic stations. It is also possible that signals would be detected by only a few stations close to the source even in a dense seismic network. Nakano and Kumagai [92] proposed a practical approach for quantifying the source of volcano-seismic signals observed by a small number of seismic stations. In this approach, possible source geometries such as a crack and pipe, are assumed as a priori information in waveform inversion. This assumption reduces the number of free parameters and enables us to estimate the source mechanism and location with waveform data from 2 to 3 three-component seismic stations. Their approach is summarized as follows. The moment tensors for a crack and pipe are given in Eqs. (30) and (34), respectively. If we assume a value for λ/μ , free parameters in the moment tensors are the source-time function, θ , and ϕ . We can determine the source-time



Volcano Seismic Signals, Source Quantification of, Figure 12

Source-time functions of six moment tensor and three single force components estimated by waveform inversion for the VLP signals shown in Fig. 11b [32]

function by the waveform inversion discussed above, in which a grid search with respect to θ and ϕ is conducted to find the best-fit angles at a fixed location. A grid search in space is also conducted to find the combination of the best-fit angles and source location, and their residuals are compared to adopt the best model. The applicability of this simple approach has been demonstrated by synthetic tests and observed seismograms [92].

Spectral Analysis

Volcano-seismic signals often show harmonic oscillatory signatures, which are interpreted as oscillations of fluid-filled resonators at the source of these signals. To determine the frequency characteristics of observed oscillations is essential to quantify the characteristic properties of the resonator systems. The discrete Fourier transform (DFT) has traditionally been used for this purpose. In DFT, the discrete time series $u(k\Delta t)$ ($k = 0, \dots, N_t - 1$) is transformed into the discrete frequency series

$$\bar{u}(l\Delta\omega) = \Delta t \sum_{k=0}^{N_t-1} u(k\Delta t) e^{2\pi i l k / N_t} \quad (l = 0, \dots, N_t - 1), \quad (94)$$

where $\Delta\omega = 2\pi/(N_t\Delta t)$ and $i = \sqrt{-1}$. DFT is the decomposition of time series into a linear combination of the orthogonal basis functions $e^{2\pi i l k / N_t}$ in the frequency domain. Because of the stationary nature of the basis functions, DFT is especially useful to analyze stationary periodic signals. However, volcano-seismic signals often show decaying harmonic oscillations. These may be viewed as the impulsive response of a resonator system, which inherently contains dissipation mechanisms. A decaying harmonic oscillation can be represented by the complex frequency, which cannot be directly estimated by DFT based on the real frequency. The complex frequencies can be determined by solving an inverse problem for parameters in an appropriate model of a given time series. The Sompi method [75] is one such approach that is based on an autoregressive (AR) model of a linear dynamic system. This method has been successfully used to determine the complex frequencies of decaying harmonic oscillations in LP and VLP events. We follow the theory of Sompi presented by Kumazawa et al. [75] and Hori et al. [50].

Let us consider the equation of motion for a linear dynamic system consisting of a block and spring:

$$b \frac{d^2}{dt^2} x(t) + v \frac{d}{dt} x(t) + \kappa x(t) = 0, \quad (95)$$

where b is the mass of a block, κ is the spring constant, and $v(dx(t)/dt)$ represents a dissipation term caused by friction, which is proportional to velocity. We set $x(t) = e^{i\omega t}$ in Eq. (95), which is an eigenfunction of this system. We then obtain

$$b(i\omega)^2 + v(i\omega) + \kappa = 0. \quad (96)$$

This is the characteristic equation of the system. If we consider oscillation solutions ($v^2 - 4b\kappa < 0$), Eq. (96) has two characteristic solutions:

$$i\omega_1 = \frac{-v + i\sqrt{4b\kappa - v^2}}{2b}, \quad i\omega_2 = i\omega_1^*, \quad (97)$$

where $*$ denotes the complex conjugate. If we set $\omega = 2\pi(f - ig)$, we obtain

$$f_1 = -f_2 = \frac{1}{2\pi} \sqrt{\frac{\kappa}{b} - \frac{v^2}{4b^2}}, \quad (98)$$

$$g_1 = g_2 = -\frac{1}{2\pi} \frac{v}{b}. \quad (99)$$

Let us consider the following difference equation:

$$\sum_{j=0}^2 a(j)x((k-j)\Delta t) = 0 \quad (100)$$

or

$$a(0)x(k\Delta t) + a(1)x(k\Delta t - \Delta t) + a(2)x(k\Delta t - 2\Delta t) = 0. \quad (101)$$

If we set $x(k\Delta t) = z^k$, where $z = e^{i\omega\Delta t}$, Eq. (100) is given as

$$a(0)z^k + a(1)z^{k-1} + a(2)z^{k-2} = 0 \quad (102)$$

or, equivalently,

$$a(0)z^2 + a(1)z + a(2) = 0. \quad (103)$$

Equation (103) is the characteristic equation of the difference equation. If we consider oscillation solutions ($a^2(1) - 4a(0)a(2) < 0$), Eq. (103) has the following two characteristic solutions:

$$z_1 = \frac{-a(1) + i\sqrt{4a(0)a(2) - a^2(1)}}{2a(0)}, \quad z_2 = z_1^*. \quad (104)$$

These two solutions constitute complex conjugate pairs. By setting $\omega = 2\pi(f - ig)$, we obtain

$$f_1 = -f_2 = \frac{1}{2\pi\Delta t} \tan^{-1} \left(-\sqrt{\frac{4a(0)a(2)}{a^2(1)} - 1} \right), \quad (105)$$

$$g_1 = g_2 = \frac{1}{2\pi\Delta t} \ln \sqrt{\frac{a(2)}{a(0)}}. \quad (106)$$

These solutions are equivalent to the solutions of the linear dynamic system given in Eqs. (98) and (99). Therefore, Eq. (100) is a difference form of the equation of motion (95).

We further consider a dynamic system consisting of two block-spring subsystems, which are coupled to each other. The equations of motion for this system are written as

$$M_1 \frac{d^2}{dt^2} x_1(t) + L_1 \frac{d}{dt} x_1(t) + K_1 x_1(t) = C(x_2 - x_1), \quad (107)$$

$$M_2 \frac{d^2}{dt^2} x_2(t) + L_2 \frac{d}{dt} x_2(t) + K_2 x_2(t) = C(x_1 - x_2), \quad (108)$$

where M_i , L_i , and K_i are the mass, dissipation coefficient, and spring constant of the i th block and C is the spring constant between the blocks. The set of the equations of motion (107) and (108) can be equivalently given in the following form:

$$\begin{pmatrix} M_1 \frac{d^2}{dt^2} + L_1 \frac{d}{dt} + K_1 + C & -C \\ -C & M_2 \frac{d^2}{dt^2} + L_2 \frac{d}{dt} + K_2 + C \end{pmatrix} \cdot \begin{pmatrix} x_1(t) \\ x_2(t) \end{pmatrix} = 0. \quad (109)$$

These equations have non-trivial solutions of $x_i(t)$ if, and only if,

$$\det \begin{vmatrix} M_1 \frac{d^2}{dt^2} + L_1 \frac{d}{dt} + K_1 + C & -C \\ -C & M_2 \frac{d^2}{dt^2} + L_2 \frac{d}{dt} + K_2 + C \end{vmatrix} = 0. \quad (110)$$

This leads to the following 4th-order differential equation:

$$\left[\left(M_1 \frac{d^2}{dt^2} + L_1 \frac{d}{dt} + K_1 + C \right) \cdot \left(M_2 \frac{d^2}{dt^2} + L_2 \frac{d}{dt} + K_2 + C \right) - C^2 \right] x_i(t) = 0, \quad (111)$$

where $i = 1, 2$. Each 4th-order differential equation has four complex frequencies, of which two are complex conjugates. Therefore, each block has two independent complex frequencies in this dynamic system. Similarly, a dynamic system consisting of m block-spring subsystems,

which are all connected to each other, can be described by the following $2m$ -order differential equation:

$$\sum_{j=0}^{2m} b_j \frac{d^j}{dt^j} x_i(t) = 0 \quad (i = 1, 2, \dots, m), \quad (112)$$

where b_j denotes the coefficients determined by the characteristic properties of the system. Each block has m independent complex frequencies in this case. A difference form of Eq. (112) is

$$\sum_{j=0}^{2m} a(j) x_i(k\Delta t - j\Delta t) = 0, \quad (113)$$

which is a homogeneous $2m$ -order AR equation. Although we have considered block-spring systems as an example, Eq. (112) is a general equation to describe the free oscillations of any linear systems. We use its difference form, Eq. (113), as the basic equation to determine the characteristic complex frequencies of linear systems from time series records.

Hereafter, I set $\Delta t = 1$ to simplify the following notations. We assume that observed discrete time series $u(k)$ consists of signal $x(k)$ and white noise $e(k)$:

$$u(k) = x(k) + e(k) \quad (k = 0, 1, \dots, N_t - 1), \quad (114)$$

and $x(k)$ satisfies the following homogeneous AR equation:

$$\sum_{j=0}^{2m} a(j) x(k - j) = 0. \quad (115)$$

To determine the $2m + 1$ AR coefficients, we minimize the residual R :

$$R = \frac{1}{N_t - 2m} \sum_{k=2m}^{N_t-1} \left[\sum_{j=0}^{2m} a(j) u(k - j) \right]^2. \quad (116)$$

Since Eq. (115) is homogeneous, we cannot determine absolute values of the AR coefficients. To avoid the trivial solution $a(j) = 0$ ($j = 0, 1, \dots, 2m$), we impose the condition

$$\sum_{j=0}^{2m} a^2(j) = 1. \quad (117)$$

To minimize the residual R under the condition of Eq. (117) is a conditional minimization problem. This problem can be solved by minimizing the residual R' :

$$R' = R - \beta \left(\sum_{j=0}^{2m} a^2(j) - 1 \right), \quad (118)$$

where β is a constant. Consequently, we solve the following equation:

$$\frac{\partial}{\partial a(l)} R' = 0 \quad (l = 0, 1, \dots, 2m). \quad (119)$$

This equation leads to an eigenvalue problem

$$\mathbf{P}\mathbf{a} = \beta \mathbf{a}, \quad (120)$$

where $\mathbf{a} = (a(0), a(1), \dots, a(2m))^T$ and \mathbf{P} is a non-Toeplitz matrix given by

$$\mathbf{P} = \frac{1}{N_t - 2m} \begin{bmatrix} \sum_{n=2m}^{N_t-1} u(n)u(n) & \cdots & \sum_{n=2m}^{N_t-1} u(n-2m)u(n) \\ \vdots & \ddots & \vdots \\ \sum_{n=2m}^{N_t-1} u(n)u(n-2m) & \cdots & \sum_{n=2m}^{N_t-1} u(n-2m)u(n-2m) \end{bmatrix}. \quad (121)$$

By solving the eigenvalue problem of Eq. (120) we obtain $2m + 1$ eigenvalues $\beta^{(r)} (r = 1, 2, \dots, 2m + 1)$ and corresponding eigenvectors $\mathbf{a}^{(r)} (r = 1, 2, \dots, 2m + 1)$. Note that the residual R in Eq. (116) is given as

$$R = \mathbf{a}^T \mathbf{P} \mathbf{a} = \mathbf{a}^T \beta \mathbf{a} = \beta. \quad (122)$$

Therefore, each eigenvector gives a local minimum of the residual R . We therefore adopt the eigenvector corresponding to the minimum eigenvalue, which minimizes the residual R . Hereafter, \mathbf{a} denotes the eigenvector corresponding to the minimum eigenvalue.

The next step is to determine the complex frequencies from the eigenvector \mathbf{a} . The characteristic equation of the $2m$ -order homogeneous AR equation is given as

$$\sum_{j=0}^{2m} a(j)z^{-j} = 0. \quad (123)$$

This equation is the $2m$ -degree algebraic equation for z^{-1} , and has $2m$ complex solutions, which can be solved by a numerical procedure. As mentioned before, a complex solution is always accompanied by its complex conjugate, and therefore there are m independent solutions $z_l (l = 1, 2, \dots, m)$ in Eq. (123). These solutions are related to the complex frequencies $(f_l - ig_l)$ as

$$z_l = e^{2\pi i(f_l - ig_l)} \quad (124)$$

or

$$f_l - ig_l = \ln z_l / (2\pi i). \quad (125)$$

The Q factor is defined through the complex frequencies as

$$Q_l = f_l / (-2g_l). \quad (126)$$

The final step is to determine the amplitudes of the solutions z_l . If we set a conjugate pair as $z_l = z_{m+l}^*$, the general solution of Eq. (123) is given as

$$\begin{aligned} x(k) &= \sum_{l=1}^m (\alpha_l z_l^k + \alpha_{m+l} z_{m+l}^k) \\ &= \sum_{l=1}^m (\alpha_l z_l^k + (\alpha_l z_l^k)^*). \end{aligned} \quad (127)$$

Here α_l is the complex amplitude given as

$$\alpha_l = r_l e^{i\phi_l}, \quad (128)$$

where r_l and ϕ_l are the real amplitude and phase, respectively. This is equivalently written as

$$\alpha_l = \alpha_l^r + i\alpha_l^i, \quad (129)$$

where α_l^r and α_l^i are the real and imaginary parts of α_l , respectively. Then, the general solution of Eq. (127) can be rewritten

$$x(k) = \sum_{l=1}^m (2\alpha_l^r C_l(k) - 2\alpha_l^i S_l(k)), \quad (130)$$

where $C_l(k) = e^{2\pi g_l k} \cos(2\pi f_l k)$ and $S_l(k) = e^{2\pi g_l k} \sin(2\pi f_l k)$. The observed time series thus satisfies the following equation

$$\begin{aligned} u(k) - \sum_{l=1}^m (2\alpha_l^r C_l(k) - 2\alpha_l^i S_l(k)) &= e(k) \\ (k &= 0, 1, \dots, N_t - 1) \end{aligned} \quad (131)$$

or, in matrix form

$$\mathbf{u} - \mathbf{A}\boldsymbol{\alpha} = \mathbf{e}, \quad (132)$$

where

$$\mathbf{u} = (u(0), u(1), \dots, u(N_t - 1))^T, \quad (133)$$

$$\boldsymbol{\alpha} = (2\alpha_1^r, \dots, 2\alpha_m^r, 2\alpha_1^i, \dots, 2\alpha_m^i)^T, \quad (134)$$

$$\mathbf{e} = (e(0), e(1), \dots, e(N_t - 1))^T, \quad (135)$$

and

$$A = \begin{bmatrix} C_1(0) & \cdots & C_m(0) \\ \vdots & & \vdots \\ C_1(N_t - 1) & \cdots & C_m(N_t - 1) \\ -S_1(0) & \cdots & -S_m(0) \\ \vdots & & \vdots \\ -S_1(N_t - 1) & \cdots & -S_m(N_t - 1) \end{bmatrix}. \quad (136)$$

We estimate α by minimizing the residual R_a as follows:

$$R_a = (\mathbf{u} - A\alpha)^T(\mathbf{u} - A\alpha). \quad (137)$$

This is an ordinary least-squares problem, and the solution is given as

$$\alpha = [A^T A]^{-1} A^T \mathbf{u}. \quad (138)$$

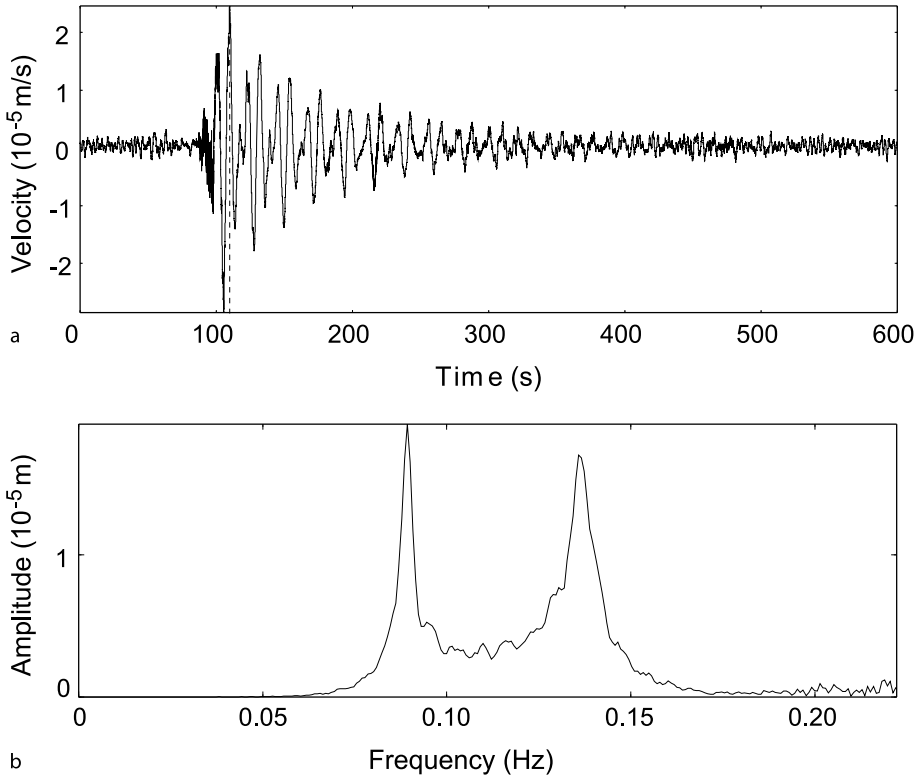
The real amplitudes r_l and phases ϕ_l at $k = 0$ are determined from estimated α as

$$r_l = \sqrt{(\alpha_l^r)^2 + (\alpha_l^i)^2} \quad (l = 1, \dots, m), \quad (139)$$

$$\phi_l = \tan^{-1}(\alpha_l^i / \alpha_l^r) \quad (l = 1, \dots, m). \quad (140)$$

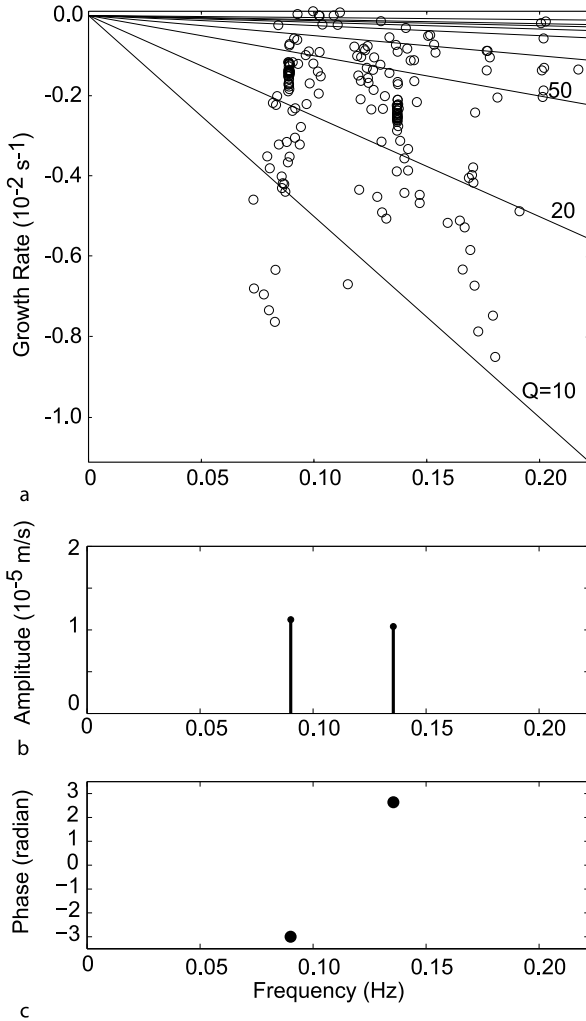
An example of the Sompi analysis of a VLP waveform (Fig. 13a) is shown in Fig. 14. The VLP waveform in Fig. 13a shows decaying harmonic oscillations, which are interpreted as the resonances of a magmatic dike triggered by a time-localized excitation [65,72]. The amplitude spectrum of the VLP waveform based on DFT is shown in Fig. 13b, which indicates two dominant peaks. As such, DFT provides frequency and amplitude information simultaneously. Q values may be determined by the bandwidths of these spectral peaks at halves their peak amplitudes. The estimated Q values, however, can be biased, because the whole waveform including the tail of decaying oscillations as well as the onset of growing oscillations is used in this approach. A box-car window can be applied to extract the decaying oscillations, but this distorts the spectrum and may lead to biased estimations of Q values.

In Sompi, on the other hand, we delete the onset portion of the signal and use the decaying harmonic oscillations only, which satisfy the homogeneous assumption of the AR equation. Since the number of signals (oscilla-



Volcano Seismic Signals, Source Quantification of, Figure 13

a VLP waveform observed at Hachijo Island, Japan, associated with a VT earthquake swarm [65,72]. **b** Amplitude spectrum of the waveform displayed in Fig. 13a



Volcano Seismic Signals, Source Quantification of, Figure 14

An example of the Sompi spectral analysis of the VLP waveform of Fig. 13a, in which Sompi was applied to the waveform after the time of the maximum amplitude indicated by the dashed line in Fig. 13a. **a** A frequency-growth rate diagram for estimated complex frequencies using trial AR orders between 4 and 60. *Solid lines* represent lines along which the Q factor is constant. We can identify two densely populated regions, which represent the signal, while other *scattered points* represent incoherent noise. **b** Amplitudes and **c** phases at the time of the maximum amplitude using the two complex frequencies determined at an AR order of 40

tions) is not known a priori, we use trial AR orders and solve the eigenvalue problems for individual trial AR orders to determine the complex frequencies, which are plotted in a frequency-growth rate (f-g) diagram. Figure 14a is the f-g diagram of the complex frequencies determined from the VLP waveform by using trial AR orders between

4 and 60. Densely populated regions on the f-g diagram represent the signal for which the complex frequencies are stably determined for different AR orders, while scattered points represent incoherent noise. Sompi then determines the complex amplitudes $re^{i\phi}$ by using the estimated complex frequencies. The optimum AR order and the number of signals may be determined by the two-parameter Akaike information criterion (AIC) [79] or the extended information criterion (EIC) [128]. Figure 14b and c plot the amplitudes r and phases ϕ , respectively, at the beginning of the decaying harmonic oscillations and using the two complex frequencies determined at an AR order of 40.

Some remarks on the theory of the Sompi method may be required. Although Hori et al. [50] and Kumazawa et al. [75] stated that Sompi is a new spectral method. This may be incorrect, as suggested by Ulrych and Sacchi [128]. Let us consider again the AR Eq. (115), which is equivalently rewritten as

$$x(k) = \sum_{j=1}^{2m} a'(j)x(k-j), \quad (141)$$

where $a'(j) = -a(j)/a(0)$. From Eq. (114), we have

$$\begin{aligned} u(k) &= x(k) + e(k) \\ &= \sum_{j=1}^{2m} a'(j)x(k-j) + e(k). \end{aligned} \quad (142)$$

Substituting $u(k-j) = x(k-j) + e(k-j)$ into Eq. (142) we obtain

$$u(k) = \sum_{j=1}^{2m} a'(j)u(k-j) + e(k) - \sum_{j=1}^{2m} a'(j)e(k-j). \quad (143)$$

This is the special autoregressive-moving average (ARMA) model discussed by Ulrych and Clayton [127], who showed that the AR coefficients in Eq. (143) can be determined by an eigenvalue problem that is essentially the same as that given in Eq. (120). In this sense, Sompi is not a new method. However, the Sompi theory, which is based not only on mathematics or information theory but also on physical concepts, yielded a systematic approach to estimate the complex frequencies and complex amplitudes, which can be directly related to the characteristic properties of a linear dynamic system and the system excitation. This approach has been favorably used in analysis of LP and VLP events to estimate the complex frequencies and their temporal variations e.g., [38,65,66,70,72,78,85,91,93].

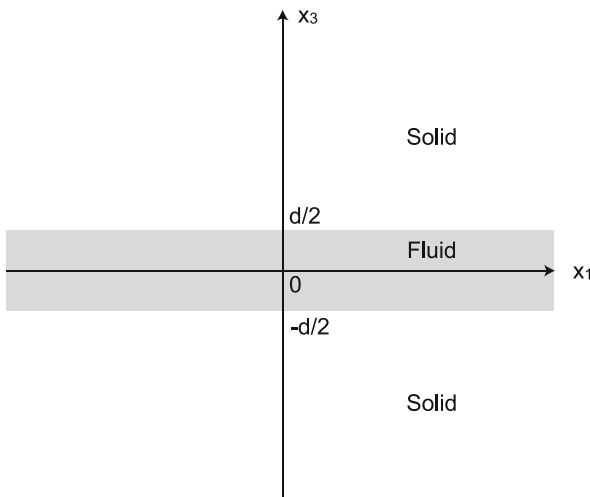
Fluid-Solid Interactions

Understanding the physics of the fluid-solid interactions is crucial to interpreting source mechanisms and spectral characters of volcano-seismic signals. The pioneering study on the fluid-solid interaction was by Biot [14], who studied seismic waves in a fluid-filled borehole and showed the existence of a slow wave propagating along the borehole boundary. This is called the tube wave. Aki et al. [2] first studied a fluid-filled crack, although the motion of the fluid in the crack was not adequately treated in their study. Chouet [22,23,24] fully studied the fluid-filled crack and demonstrated the existence of a slow wave in the fluid-filled crack, which was called the crack wave. We first consider a fluid layer sandwiched between two homogeneous elastic half-spaces following Ferrazzini and Aki [39] to examine the physical properties of the crack wave. Then, we examine the resonance of a crack of finite size containing a fluid by using the approach proposed by Chouet [22]. For simplicity, we assume an inviscid fluid.

Crack Wave

Let us consider a compressible fluid layer of thickness d , which is sandwiched between two elastic half-spaces bounded at $x_3 = -d/2$ and $x_3 = d/2$ (Fig. 15). The equation of motion for the fluid is given by

$$\rho_f \frac{\partial^2 u_1^f}{\partial t^2} = -\frac{\partial p}{\partial x_1}, \quad (144)$$



Volcano Seismic Signals, Source Quantification of, Figure 15
A fluid layer of thickness d sandwiched between two elastic half-spaces bounded at $x_3 = -d/2$ and $x_3 = d/2$

$$\rho_f \frac{\partial^2 u_3^f}{\partial t^2} = -\frac{\partial p}{\partial x_3}. \quad (145)$$

Here, ρ_f is the fluid density, u_1^f and u_3^f are the x_1 and x_3 components of the displacement in the fluid, respectively, and p is the fluid pressure satisfying the following continuity equation:

$$p = -b \left(\frac{\partial u_1^f}{\partial x_1} + \frac{\partial u_3^f}{\partial x_3} \right), \quad (146)$$

where b is the bulk modulus of the fluid. The equation of motion for the solid is

$$\rho_s \frac{\partial^2 u_1}{\partial t^2} = \frac{\partial \sigma_{11}}{\partial x_1} + \frac{\partial \sigma_{13}}{\partial x_3}, \quad (147)$$

$$\rho_s \frac{\partial^2 u_3}{\partial t^2} = \frac{\partial \sigma_{13}}{\partial x_1} + \frac{\partial \sigma_{33}}{\partial x_3}. \quad (148)$$

Here, ρ_s is the solid density, u_1 and u_3 are the x_1 and x_3 components of the displacement in the solid, respectively, and σ_{11} , σ_{33} , and σ_{13} are the components of stress:

$$\sigma_{11} = \lambda \left(\frac{\partial u_1}{\partial x_1} + \frac{\partial u_3}{\partial x_3} \right) + 2\mu \left(\frac{\partial u_1}{\partial x_1} \right), \quad (149)$$

$$\sigma_{33} = \lambda \left(\frac{\partial u_1}{\partial x_1} + \frac{\partial u_3}{\partial x_3} \right) + 2\mu \left(\frac{\partial u_3}{\partial x_3} \right), \quad (150)$$

$$\sigma_{13} = \mu \left(\frac{\partial u_1}{\partial x_3} + \frac{\partial u_3}{\partial x_1} \right). \quad (151)$$

The boundary conditions at the fluid-solid interfaces ($x_3 = \pm d/2$) are

$$u_3 = u_3^f, \quad (152)$$

$$\sigma_{33} = -p, \quad (153)$$

$$\sigma_{13} = 0. \quad (154)$$

The first and second conditions mean that the normal displacement and stress across the interface are both continuous. The third condition states that the shear stress vanishes at the interface.

For waves propagating in the x_1 direction, the displacements in the fluid may be written in the forms

$$u_1^f = r_1(x_3; k, \omega) e^{i(kx_1 - \omega t)}, \quad (155)$$

$$u_3^f = ir_2(x_3; k, \omega) e^{i(kx_1 - \omega t)}, \quad (156)$$

Substituting these equations into Eq. (146) we obtain

$$p = -ir_3 e^{i(kx_1 - \omega t)}, \quad (157)$$

where k and ω are the wavenumber and angular frequency, respectively

$$r_3 = b \left(kr_1 + \frac{dr_2}{dx_3} \right). \quad (158)$$

Substituting Eqs. (155) and (156) into Eqs. (144) and (145), respectively, and using Eq. (158) we have

$$\rho_f \omega^2 r_1 = kr_3, \quad (159)$$

$$-\rho_f \omega^2 r_2 = \frac{dr_3}{dx_3}. \quad (160)$$

Equations (158), (159), and (160) can be arranged in the following matrix form:

$$\begin{bmatrix} \frac{dr_2}{dx_3} \\ \frac{dr_3}{dx_3} \end{bmatrix} = \begin{bmatrix} 0 & \frac{1}{b} - \frac{k^2}{\rho_f \omega^2} \\ -\rho_f \omega^2 & 0 \end{bmatrix} \begin{bmatrix} r_2 \\ r_3 \end{bmatrix}. \quad (161)$$

For the solid, the displacement components of waves propagating in the x_1 direction may be written as

$$u_1 = y_1(x_3; k, \omega) e^{i(kx_1 - \omega t)}, \quad (162)$$

$$u_3 = iy_2(x_3; k, \omega) e^{i(kx_1 - \omega t)}. \quad (163)$$

Substituting these equations into Eqs. (147), (148), (149), (150), and (151) we obtain the relationship:

$$\begin{bmatrix} \frac{dy_1}{dx_3} \\ \frac{dy_2}{dx_3} \\ \frac{dy_3}{dx_3} \\ \frac{dy_4}{dx_3} \end{bmatrix} = \begin{bmatrix} 0 & k & \frac{1}{\mu} & 0 \\ \frac{-k\lambda}{\lambda+2\mu} & 0 & 0 & \frac{1}{\lambda+2\mu} \\ k^2\zeta - \rho_s \omega^2 & 0 & 0 & \frac{k\lambda}{\lambda+2\mu} \\ 0 & -\rho_s \omega^2 - k & 0 & 0 \end{bmatrix} \begin{bmatrix} y_1 \\ y_2 \\ y_3 \\ y_4 \end{bmatrix}, \quad (164)$$

where $\zeta = \frac{4\mu(\lambda+\mu)}{\lambda+2\mu}$ and

$$y_3 = \mu \left(\frac{dy_1}{dx_3} - ky_2 \right), \quad (165)$$

$$y_4 = (\lambda + 2\mu) \frac{dy_2}{dx_3} + k\lambda y_1. \quad (166)$$

The boundary condition Eqs.(152), (153), and (154) can then be written as

$$y_2 = r_2, \quad (167)$$

$$y_4 = r_3, \quad (168)$$

$$y_3 = 0, \quad (169)$$

respectively, at $x_3 = \pm d/2$. The systems of Eqs. (161) and (164) are to be solved under the boundary conditions

of Eqs. (167), (168), and (169), in which we seek solutions satisfying the following two additional conditions

$$r_2(-x_3) = -r_2(x_3) \quad -d/2 \leq x_3 \leq d/2, \quad (170)$$

$$y_1, y_2 \rightarrow 0 \quad x_3 \rightarrow \pm\infty. \quad (171)$$

The first condition means that motion in the fluid layer is symmetric with respect to x_3 . There is the antisymmetric motion in the fluid layer with respect to x_3 . This motion is the same as that observed in a fluid layer overlying a solid half-space, such as ocean, and has been investigated by Biot [15] and Tolstoy [124]. This motion does not produce the slow wave, and I do not discuss it here.

The solution for the systems of Eqs. (161) and (164) under the conditions mentioned above can be determined by the following numerical procedure, which was proposed by Takeuchi and Saito [121]. Since we assume symmetric motion in the fluid layer, it is enough to consider the region $x_3 \geq 0$. We choose $x_3 = h$, where h is appropriately far from the fluid-solid interface to satisfy $y_1 = y_2 = 0$. At $x_3 = h$, we assume two independent initial values $y_1 = y_2 = y_4 = 0, y_3 = 1$ and $y_1 = y_2 = y_3 = 0, y_4 = 1$ and integrate the equation for the solid (164) with values of k and ω by the Runge-Kutta method. Then, we have two independent solutions $y_i^A(x_3; k, \omega)$ and $y_i^B(x_3; k, \omega)$ ($i = 1, 2, 3, 4$). Any solution of Eq. (164) may be expressed as a linear combination of the two solutions:

$$y_i(x_3; k, \omega) = Ay_i^A(x_3; k, \omega) + By_i^B(x_3; k, \omega) \quad (i = 1, 2, 3, 4), \quad (172)$$

where A and B are arbitrary constants of integration for the two solutions. At $x_3 = 0$, we assume initial values $r_2 = 0$ and $r_3 = 1$, and integrate the equation for the fluid (161) with values of k and ω . Then, we have a solution $r_i^C(x_3; k, \omega)$ ($i = 1, 2$), and any solution of Eq. (161) may be given as

$$r_i(x_3; k, \omega) = Cr_i^C(x_3; k, \omega) \quad (i = 2, 3), \quad (173)$$

where C is an arbitrary constant of integration. From the boundary conditions of Eqs. (167), (168), and (169), we have the following relationships at $x_3 = d/2$:

$$\begin{aligned} Ay_2^A(d/2; k, \omega) + By_2^B(d/2; k, \omega) - Cr_2^C(d/2; k, \omega) &= 0, \\ Ay_4^A(d/2; k, \omega) + By_4^B(d/2; k, \omega) - Cr_3^C(d/2; k, \omega) &= 0, \\ Ay_3^A(d/2; k, \omega) + By_3^B(d/2; k, \omega) &= 0. \end{aligned} \quad (174)$$

These equations have a nontrivial solution if, and only if,

$$\det \begin{vmatrix} y_2^A(d/2; k, \omega) & y_2^B(d/2; k, \omega) & -r_2^C(d/2; k, \omega) \\ y_4^A(d/2; k, \omega) & y_4^B(d/2; k, \omega) & -r_3^C(d/2; k, \omega) \\ y_3^A(d/2; k, \omega) & y_3^B(d/2; k, \omega) & 0 \end{vmatrix} = 0. \quad (175)$$

The dispersion relation of the fluid-solid coupled waves can be determined by searching for k and ω that satisfy Eq. (175). From Eq. (174) we have

$$\frac{B}{A} = -\frac{y_3^A(d/2; k, \omega)}{y_3^B(d/2; k, \omega)}, \quad (176)$$

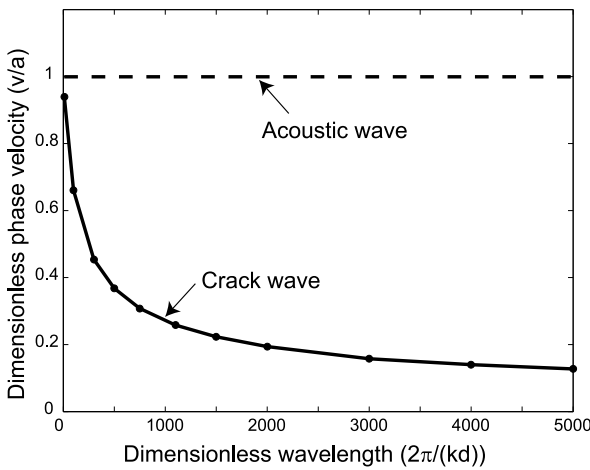
$$\frac{C}{A} = \frac{y_2^A(d/2; k, \omega)}{r_2^C(d/2; k, \omega)} - \frac{y_3^A(d/2; k, \omega)}{y_3^B(d/2; k, \omega)} \frac{y_2^B(d/2; k, \omega)}{r_2^C(d/2; k, \omega)}, \quad (177)$$

and the eigenfunctions are given as

$$y_i(x_3; k, \omega)/A = y_i^A(x_3; k, \omega) + (B/A)y_i^B(x_3; k, \omega) \quad (i = 1, 2, 3, 4), \quad (178)$$

$$r_i(x_3; k, \omega)/A = (C/A)r_i^C(x_3; k, \omega) \quad (i = 2, 3). \quad (179)$$

The dispersion relationship and eigenfunctions of the crack wave calculated by the above procedure are shown in Figs. 16 and 17, respectively. In this example, I used the following parameter values: $\rho_s = 1.10\rho_f$, $b = 0.06\mu$, and $\lambda = 2\mu$, which mimic a dike containing basaltic magma with a gas-volume fraction of 15%. The dispersion rela-



Volcano Seismic Signals, Source Quantification of, Figure 16
The phase velocities of the acoustic wave (dashed line) and crack wave (solid line). These are normalized by the fluid acoustic velocity, and plotted as a function of the wavelength normalized by the thickness of the fluid layer

tionship in Fig. 16 clearly indicates that the phase velocity of the fluid-solid coupled wave depends on the wavelength, in which the velocity decreases as the wavelength increases. This wave is called the crack wave. Figure 17 displays dimensionless normal displacements (y_2 and r_2) and normal stress and pressure (y_4 and r_3) as a function of dimensionless x_3 . Figure 17 indicates that the normal displacement is symmetric with respect to x_3 . This motion causes the deformation of the fluid-solid boundary. The deformation has the effect of lowering the phase velocity, which is examined below.

Fluid-Filled Crack Model

Chouet [22,23,24] studied the motion of a finite crack containing a fluid in an infinite elastic medium. Following Chouet [22], we consider a crack set in the plane $x_3 = 0$, which extends from $-W/2$ to $W/2$ along the x_1 axis and from 0 to L in the x_2 direction (Fig. 18). The thickness of the crack is d , which is much smaller than L . Chouet [22] used the equations of motion for the solid given as

$$\rho_s \frac{\partial v_i}{\partial t} = \frac{\partial \sigma_{ij}}{\partial x_j}, \quad (180)$$

with the stress-strain relationship

$$\frac{\partial \sigma_{ij}}{\partial t} = \lambda \frac{\partial v_k}{\partial x_k} \delta_{ij} + \mu \left(\frac{\partial v_i}{\partial x_j} + \frac{\partial v_j}{\partial x_i} \right), \quad (181)$$

where v_j is particle velocity of the solid and $i = 1, 2, 3$. The equations of motion for the fluid are given as

$$\rho_f \frac{\partial^2 u_i^f}{\partial t^2} = -\frac{\partial p}{\partial x_i}, \quad (182)$$

with the equation of continuity

$$p = -b \frac{\partial u_k^f}{\partial x_k}. \quad (183)$$

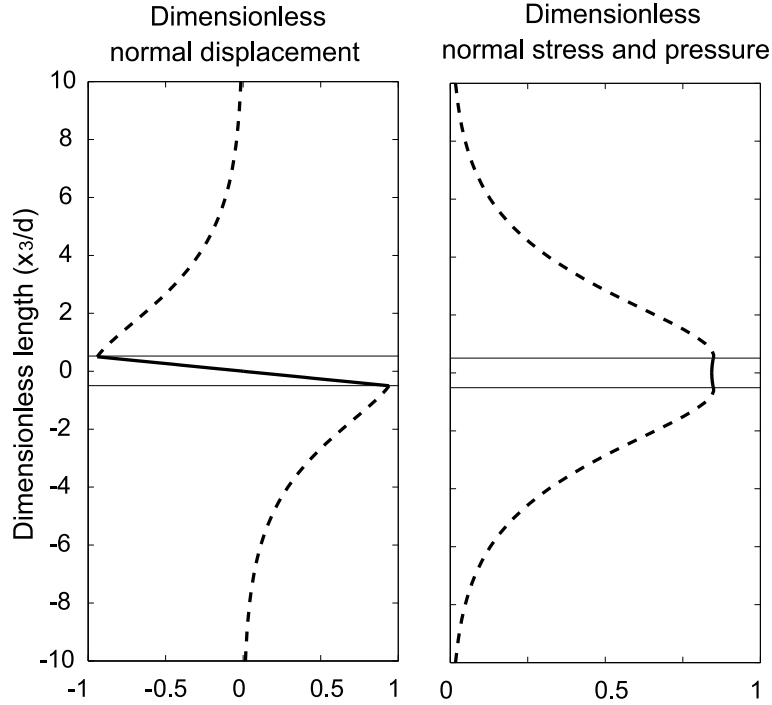
The boundary conditions on the crack surface S_1 are

$$u_3^f = u_3, \quad \sigma_{33} = -p, \quad \sigma_{13} = \sigma_{23} = 0, \quad (184)$$

which are the continuity of normal displacement and stress and the vanishment of shear stress on S_1 . Let us introduce u_d , which represents the normal displacement of the crack wall and is identical to $u_3^f = u_3$ on S_1 .

We integrate Eq. (183) with respect to x_3 within the crack and divide it by d :

$$\begin{aligned} \frac{1}{d} \int_{-d/2}^{d/2} p dx_3 \\ = -b \frac{1}{d} \int_{-d/2}^{d/2} \left[\frac{\partial u_1^f}{\partial x_1} + \frac{\partial u_2^f}{\partial x_2} + \frac{\partial u_3^f}{\partial x_3} \right] dx_3. \end{aligned} \quad (185)$$



Volcano Seismic Signals, Source Quantification of, Figure 17

Dimensionless normal displacements, normal stress, and pressure as a function of x_3 normalized by the thickness of the fluid layer. *Thin solid lines* represent the boundaries between the fluid and solid, and *thick dashed and solid lines* represent the functions in the fluid and solid regions, respectively

If we define

$$P = \frac{1}{d} \int_{-d/2}^{d/2} p dx_3 \quad (186)$$

and

$$U_i^f = \frac{1}{d} \int_{-d/2}^{d/2} u_i^f dx_3 \quad (i = 1, 2), \quad (187)$$

Eq. (185) is written as

$$P = -b \left(\frac{\partial U_1^f}{\partial x_1} + \frac{\partial U_2^f}{\partial x_2} + \frac{1}{d} \int_{-d/2}^{d/2} \frac{\partial u_3^f}{\partial x_3} dx_3 \right). \quad (188)$$

Since u_3^f is symmetric with respect to x_3 ($u_3^f(-x_3) = -u_3^f(x_3)$), we find that

$$\int_{-d/2}^{d/2} \frac{\partial u_3^f}{\partial x_3} dx_3 = \int_{-d/2}^{d/2} du_3^f = [u_3^f]_{-d/2}^{d/2} = 2u_3^f(d/2). \quad (189)$$

Note that $u_3^f(d/2) = u_3(d/2) = u_d$ from the boundary condition of Eq. (184) and, therefore, we have

$$P = -b \left(\frac{\partial U_1^f}{\partial x_1} + \frac{\partial U_2^f}{\partial x_2} + \frac{2}{d} u_d \right). \quad (190)$$

From Eq. (182) we obtain

$$\rho_f \frac{\partial^2 U_1^f}{\partial t^2} = -\frac{\partial P}{\partial x_1}, \quad (191)$$

$$\rho_f \frac{\partial^2 U_2^f}{\partial t^2} = -\frac{\partial P}{\partial x_2}. \quad (192)$$

Using the fluid velocity, Eqs. (191), (192), and (190) can be equivalently written as

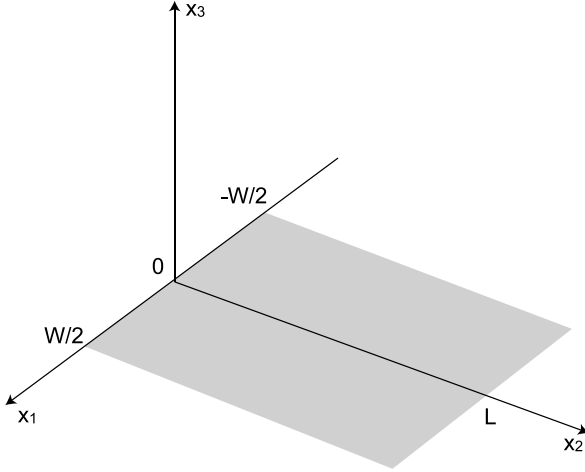
$$\rho_f \frac{\partial V_1^f}{\partial t} = -\frac{\partial P}{\partial x_1}, \quad (193)$$

$$\rho_f \frac{\partial V_2^f}{\partial t} = -\frac{\partial P}{\partial x_2}, \quad (194)$$

$$\frac{\partial P}{\partial t} = -b \left(\frac{\partial V_1^f}{\partial x_1} + \frac{\partial V_2^f}{\partial x_2} + \frac{2}{d} v_d \right), \quad (195)$$

where $V_i^f = \partial U_i^f / \partial t$ ($i = 1, 2$) and v_d is the normal velocity of the crack wall.

Thus, the three-dimensional equations of motion and continuity are reduced to two-dimensional equations with



Volcano Seismic Signals, Source Quantification of, Figure 18
Coordinates and geometry of a crack set in the plane $x_3 = 0$, which extends from $-W/2$ to $+W/2$ on the x_1 axis and from 0 to L on the x_2 axis

respect to V_1^f , V_2^f , P , and v_d . In this problem, the boundary conditions are

$$\sigma_{33} = -p, \quad \sigma_{13} = \sigma_{23} = 0, \quad \text{on } S_1, \quad (196)$$

$$u_3 = 0, \quad \sigma_{13} = \sigma_{23} = 0, \quad \text{on } S_2, \quad (197)$$

where S_1 denotes the crack surface and S_2 denotes the crack plane outside the crack. The latter condition expresses that the displacement in the solid is symmetric with respect to x_3 . In addition to these boundary conditions, Chouet [22] assumed zero mass transfer in and out of the crack, which are as follows:

$$V_1^f = v_1 \quad \text{along } |x_1| = W/2, 0 \leq x_2 \leq L, \quad (198)$$

$$V_2^f = v_2 \quad \text{along } -W/2 \leq x_1 \leq W/2, x_2 = 0 \quad x_2 = L. \quad (199)$$

The equations of motion and stress-strain relationship for the solid in the form of Eqs. (180) and (181) and the equations of motion and continuity for the fluid in the forms of Eqs. (193), (194) and (195) are solved under the boundary conditions of Eqs. (196), (197), (198), and (199). Chouet [22] solved this problem by using a finite-difference method, in which the following scaling was used:

$$\tilde{x}_i = x_i/L, \quad (200)$$

$$\tilde{t} = \alpha t/L, \quad (201)$$

$$\tilde{\sigma}_{ij} = \sigma_{ij}/\sigma_0, \quad (202)$$

$$\tilde{u}_i = u_i\mu/(L\sigma_0), \quad (203)$$

$$\tilde{v}_i = v_i\mu/(\alpha\sigma_0), \quad (204)$$

where nondimensional variables are indicated by a bar, σ_0 is an effective stress, and α is the compressional wave velocity $\alpha = \sqrt{(\lambda + 2\mu)/\rho_s}$. Let us define the first-order difference operators in time and space as:

$$\Delta_t f(l; i, j, k) = f(l + 1; i, j, k) - f(l; i, j, k), \quad (205)$$

$$\Delta_{x1} f(l; i, j, k) = f(l; i + 1, j, k) - f(l; i, j, k), \quad (206)$$

$$\Delta_{x2} f(l; i, j, k) = f(l; i, j + 1, k) - f(l; i, j, k), \quad (207)$$

$$\Delta_{x3} f(l; i, j, k) = f(l; i, j, k + 1) - f(l; i, j, k), \quad (208)$$

where $f(l; i, j, k)$ represents any function at time $l\Delta t$ and position $[i\Delta, j\Delta, k\Delta]$ or $[i\Delta_a, j\Delta_a, k\Delta_a]$. Here, Δt is the time increment and Δ and Δ_a are the grid spacings for the solid and fluid, respectively. A difference form of Eq. (195) is then obtained as

$$\frac{\Delta_t P}{\Delta t} = -b \left(\frac{\Delta_{x1} V_1^f}{\Delta_a} + \frac{\Delta_{x2} V_2^f}{\Delta_a} + \frac{2}{d} v_d \right) \quad (209)$$

or

$$\Delta_t P = -b H_a \left(\Delta_{x1} V_1^f + \Delta_{x2} V_2^f \right) - 2 \frac{b}{d} \Delta t v_d, \quad (210)$$

where $H_a = \Delta t/\Delta_a$. Using the scaling given by Eqs. (200) to (204), Eq. (210) can be further modified to a nondimensional form:

$$\Delta_t \tilde{P} = - \left(\frac{b}{\mu} \right) \alpha H_a \left(\Delta_{x1} \tilde{V}_1^f + \Delta_{x2} \tilde{V}_2^f \right) - 2 C \Delta \tilde{t} \tilde{v}_d, \quad (211)$$

where $C = (b/\mu)(L/d)$ is called the crack stiffness [2]. In a similar manner, we obtain nondimensional difference forms of equations of motion for the fluid (193) and (194) as

$$\Delta_t \tilde{V}_1^f = - \left(\frac{a}{\alpha} \right)^2 \left(\frac{\mu}{b} \right) \alpha H_a \Delta_{x1} \tilde{P}, \quad (212)$$

$$\Delta_t \tilde{V}_2^f = - \left(\frac{a}{\alpha} \right)^2 \left(\frac{\mu}{b} \right) \alpha H_a \Delta_{x2} \tilde{P}, \quad (213)$$

where $a = \sqrt{b/\rho_f}$ is the acoustic velocity of the fluid and the ratios α/a and b/μ are related to ρ_f and ρ_s through the relationship

$$\frac{\rho_f}{\rho_s} = \left(\frac{\mu}{\lambda + 2\mu} \right) \left(\frac{\alpha}{a} \right)^2 \left(\frac{b}{\mu} \right). \quad (214)$$

Nondimensional difference forms of the equations of motion and the stress-strain relationship for the solid

(Eqs. (180) and (181)) are

$$\Delta_t \tilde{v}_i = \frac{1}{2 + (\lambda/\mu)} \alpha H \Delta_{xi} \tilde{\sigma}_{ij}, \quad (215)$$

$$\Delta_t \tilde{\sigma}_{ij} = \alpha H \left[\frac{\lambda}{\mu} \Delta_{xk} \tilde{v}_k \delta_{ij} + (\Delta_{xi} \tilde{v}_j + \Delta_{xj} \tilde{v}_i) \right], \quad (216)$$

where $H = \Delta t / \Delta$. To satisfy the conditions for numerical stability in the solid and fluid, Chouet [22] used the following relationships:

$$H = \frac{\Delta t}{\Delta} = \frac{1}{4\alpha}, \quad (217)$$

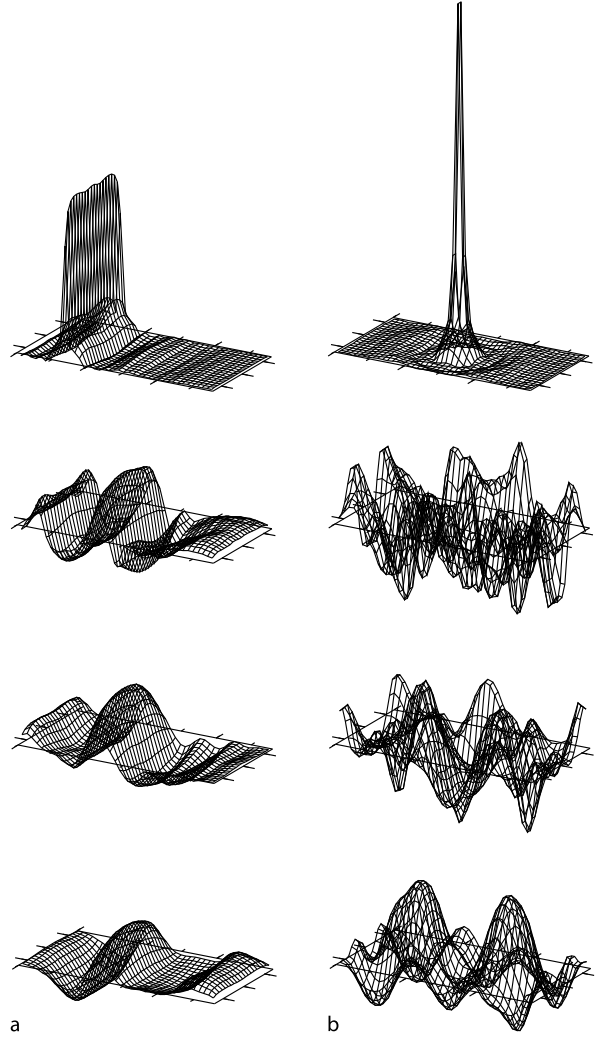
$$H_a = \frac{\Delta t}{\Delta_a} = \frac{1}{2a}. \quad (218)$$

Applying a step increase in the fluid pressure over an area of the crack, the nondimensional difference equations for the solid and fluid are solved by a finite-difference method with a staggered grid scheme [129] to determine the normal velocity of the crack wall v_d . This source space-time function is used to synthesize the ground response to the fluid-filled crack. Note that Chouet [22] added an artificial dissipation term to the equations for particle velocities in the solid (Eq. (215)) and for fluid velocities (Eqs. (212) and (213)) to suppress spurious numerical oscillations associated with discretization in time and space in the finite difference calculations.

Snapshots of the normal velocity of the crack wall v_d for a fluid-filled crack excited by a step increase in the pressure applied over a strip extending over the entire width of the crack are shown in Fig. 19a. The results show that the crack oscillation is dominated by the longitudinal modes with wavelengths L and $2L/5$. Figure 19b shows snapshots of v_d for the crack with the excitation applied over a small area at the center of the crack. The crack oscillation shown in Fig. 19b displays more complex spatial patterns than those of Fig. 19a, in which both the longitudinal and transverse modes with wavelengths $2L/3$ and $2W/3$, respectively, are dominantly excited. Chouet [22] showed that the dimensionless phase velocity v/a of the crack wave sustaining the crack resonance depends on the crack stiffness C . The Q factor of the crack resonance almost monotonically increases with the increasing α/a [67,68].

The slow wave and its dependence on the crack stiffness may be understood by the following simple theoretical consideration. Using Eqs. (190), (191), and (192), we obtain the following relationship:

$$\frac{\partial^2}{\partial t^2} \left(P + \frac{2b}{d} u_d \right) = \left(\frac{b}{\rho_f} \right) \left(\frac{\partial^2 P}{\partial x_1^2} + \frac{\partial^2 P}{\partial x_2^2} \right). \quad (219)$$



Volcano Seismic Signals, Source Quantification of, Figure 19

a Snapshots of the normal velocity of the crack wall v_d for a fluid-filled crack excited by a step increase in the pressure applied over a strip extending over the entire width of the crack. **b** Snapshots of v_d for the crack with the excitation applied over a small area at the center of the crack (modified from Nakano et al. [95])

Note that $a = \sqrt{b/\rho_f}$ is the acoustic velocity of the fluid. Let us consider a simple case for which u_d is proportional to P :

$$u_d = \epsilon P, \quad (220)$$

where ϵ is a proportionality constant. Using the scaling given in Eqs. (202) and (203), the constant ϵ may be written in a nondimensional form as

$$\epsilon = \bar{\epsilon} L / \mu, \quad (221)$$

where $\bar{\epsilon}$ is a nondimensional proportionality constant. Using Eqs. (220) and (221), Eq. (219) can be written as

$$\left(1 + 2\bar{\epsilon} \frac{b}{\mu} \frac{L}{d}\right) \frac{\partial^2 P}{\partial t^2} = \left(\frac{b}{\rho_f}\right) \left(\frac{\partial^2 P}{\partial x_1^2} + \frac{\partial^2 P}{\partial x_2^2}\right) \quad (222)$$

or, equivalently,

$$\frac{\partial^2 P}{\partial t^2} = \left(\frac{b_e}{\rho_f}\right) \left(\frac{\partial^2 P}{\partial x_1^2} + \frac{\partial^2 P}{\partial x_2^2}\right), \quad (223)$$

where b_e is an effective bulk modulus defined as

$$b_e = b/(1 + 2\bar{\epsilon}C). \quad (224)$$

Here, $C = (b/\mu)(L/d)$ is the crack stiffness. Equation (223) is the two-dimensional wave equation with phase velocity $a_e = \sqrt{b_e/\rho_f}$. If no deformation of the crack wall occurs ($\bar{\epsilon} = 0$), the phase velocity a_e is equal to the fluid acoustic velocity a . If the deformation of the crack wall occurs such that the wall moves inward to increase fluid pressure ($\bar{\epsilon} < 0$), a_e becomes smaller than a through a reduction of the effective bulk modulus, which depends on the crack stiffness as given in Eq. (224).

The slow crack wave leads to more realistic estimates of the size and volume of a fluid-filled resonator as compared to a resonator with spherical geometry e. g. [35,40,41,115]. The slow wave has been used to interpret spectral characteristics of LP and VLP events observed at various active volcanoes [29,44,52,65,66,67,70,72,73,85,88,91,98,117,131].

Future Directions

Recent volcano seismological studies have contributed greatly to achieving a better understanding of magmatic and hydrothermal systems. It is clear that the theoretical development of source models and analysis techniques has played an essential role in recent advances. The current studies in volcano seismology may be summarized as follows: (a) physical understanding and modeling of source dynamics of LP and VLP events [34,99,100,125], (b) development of a waveform inversion method of volcano-seismic signals for an extended source to achieve a better understanding of the resonance characteristics and triggering mechanisms [95], (c) extension of the crack model to incorporate more realistic fluid acoustic properties [65,131], and (d) dense broadband seismic observation and the use of waveform inversion techniques to monitor active volcanoes e. g., [11,37,74]. Future studies building on these will contribute further to our ability to quantify the sources of volcano-seismic signals, which will help us in our efforts to

predict eruptive behavior and thus mitigate volcanic hazards through improved seismic monitoring of magmatic and hydrothermal activity.

Acknowledgment

I am deeply grateful to Masaru Nakano for numerous discussions on all the subjects presented in this manuscript. I thank Yasuko Takei for constructive comments on the phenomenological source representation. Comments from Pablo Palacios, Luca D'Auria, Takeshi Nishimura, and an anonymous reviewer helped improve the manuscript. I used the Generic Mapping Tools (GMT) [130] in the preparation of figures.

Appendix A: Green's Functions

Here, I briefly explain the relationship between the displacement and Green's functions. To simplify the explanation, I use two-dimensional equations in an infinite medium. The extension of the equations into three-dimension is straightforward. Green's functions defined by Eq. (5) are explicitly written as

$$\rho \frac{\partial^2 G_{11}}{\partial t^2} = (\lambda + 2\mu) \frac{\partial^2 G_{11}}{\partial x_1^2} + (\lambda + \mu) \frac{\partial^2 G_{21}}{\partial x_2 \partial x_1} + \mu \frac{\partial^2 G_{11}}{\partial x_2^2} + \delta(\mathbf{x} - \boldsymbol{\eta}) \delta(t - \tau), \quad (A1)$$

$$\rho \frac{\partial^2 G_{21}}{\partial t^2} = (\lambda + 2\mu) \frac{\partial^2 G_{21}}{\partial x_2^2} + (\lambda + \mu) \frac{\partial^2 G_{11}}{\partial x_2 \partial x_1} + \mu \frac{\partial^2 G_{21}}{\partial x_1^2}, \quad (A2)$$

$$\rho \frac{\partial^2 G_{12}}{\partial t^2} = (\lambda + 2\mu) \frac{\partial^2 G_{12}}{\partial x_1^2} + (\lambda + \mu) \frac{\partial^2 G_{22}}{\partial x_2 \partial x_1} + \mu \frac{\partial^2 G_{12}}{\partial x_2^2}, \quad (A3)$$

$$\rho \frac{\partial^2 G_{22}}{\partial t^2} = (\lambda + 2\mu) \frac{\partial^2 G_{22}}{\partial x_2^2} + (\lambda + \mu) \frac{\partial^2 G_{12}}{\partial x_2 \partial x_1} + \mu \frac{\partial^2 G_{22}}{\partial x_1^2} + \delta(\mathbf{x} - \boldsymbol{\eta}) \delta(t - \tau). \quad (A4)$$

Note that (G_{11}, G_{21}) represents the x_1 and x_2 components of the wavefield at (\mathbf{x}, t) , which is excited by the impulse in the x_1 direction applied at $\mathbf{x} = \boldsymbol{\eta}$ and $t = \tau$. Similarly, (G_{12}, G_{22}) represents the x_1 and x_2 components of the wavefield excited by the impulse in the x_2 direction at $\mathbf{x} = \boldsymbol{\eta}$ and at $t = \tau$. Therefore, i and j in G_{ij} represent the component and direction of the impulse, respectively. To specify the relationship between the receiver and source, we use the notation $G_{ij}(\mathbf{x}, t; \boldsymbol{\eta}, \tau)$. We

obtain $G_{ij}(\mathbf{x}, t; \boldsymbol{\eta}, \tau) = G_{ij}(\mathbf{x}, t - \tau; \boldsymbol{\eta}, 0)$, since Green's functions are independent of the time of origin.

The displacement $u_i(\mathbf{x}, t)$ satisfies Eq. (3), which is explicitly written as

$$\rho \frac{\partial^2 u_1}{\partial t^2} = (\lambda + 2\mu) \frac{\partial^2 u_1}{\partial x_1^2} + (\lambda + \mu) \frac{\partial^2 u_2}{\partial x_1 \partial x_2} + \mu \frac{\partial^2 u_1}{\partial x_2^2} + f_1^S(\mathbf{x}, t), \quad (\text{A5})$$

$$\rho \frac{\partial^2 u_2}{\partial t^2} = (\lambda + 2\mu) \frac{\partial^2 u_2}{\partial x_2^2} + (\lambda + \mu) \frac{\partial^2 u_1}{\partial x_1 \partial x_2} + \mu \frac{\partial^2 u_2}{\partial x_1^2} + f_2^S(\mathbf{x}, t). \quad (\text{A6})$$

Equation (6) indicates that u_i is described by the following relationships:

$$u_1(\mathbf{x}, t) = \int_{-\infty}^{\infty} \int_{-\infty}^{\infty} [f_1^S(\boldsymbol{\eta}, \tau) G_{11}(\mathbf{x}, t - \tau; \boldsymbol{\eta}, 0) + f_2^S(\boldsymbol{\eta}, \tau) G_{12}(\mathbf{x}, t - \tau; \boldsymbol{\eta}, 0)] d\eta_1 d\eta_2 d\tau, \quad (\text{A7})$$

$$u_2(\mathbf{x}, t) = \int_{-\infty}^{\infty} \int_{-\infty}^{\infty} [f_1^S(\boldsymbol{\eta}, \tau) G_{21}(\mathbf{x}, t - \tau; \boldsymbol{\eta}, 0) + f_2^S(\boldsymbol{\eta}, \tau) G_{22}(\mathbf{x}, t - \tau; \boldsymbol{\eta}, 0)] d\eta_1 d\eta_2 d\tau. \quad (\text{A8})$$

We can verify that the displacement given by Eqs. (A7) and (A8) satisfies Eqs. (A5) and (A6) in the following way. We can rewrite Eqs. (A5) and (A6) as

$$f_1^S(\mathbf{x}, t) = \rho \frac{\partial^2 u_1}{\partial t^2} - (\lambda + 2\mu) \frac{\partial^2 u_1}{\partial x_1^2} - (\lambda + \mu) \frac{\partial^2 u_2}{\partial x_1 \partial x_2} - \mu \frac{\partial^2 u_1}{\partial x_2^2}, \quad (\text{A9})$$

$$f_2^S(\mathbf{x}, t) = \rho \frac{\partial^2 u_2}{\partial t^2} - (\lambda + 2\mu) \frac{\partial^2 u_2}{\partial x_2^2} - (\lambda + \mu) \frac{\partial^2 u_1}{\partial x_1 \partial x_2} - \mu \frac{\partial^2 u_2}{\partial x_1^2}. \quad (\text{A10})$$

We denote the right-hand side of Eq. (A9) as L_1 , which is derived from Eqs. (A7) and (A8) as

$$L_1 = \int_{-\infty}^{\infty} \int_{-\infty}^{\infty} \left[\rho \left(f_1^S \frac{\partial^2 G_{11}}{\partial t^2} + f_2^S \frac{\partial^2 G_{12}}{\partial t^2} \right) - (\lambda + 2\mu) \left(f_1^S \frac{\partial^2 G_{11}}{\partial x_1^2} + f_2^S \frac{\partial^2 G_{12}}{\partial x_1^2} \right) - (\lambda + \mu) \left(f_1^S \frac{\partial^2 G_{21}}{\partial x_1 \partial x_2} + f_2^S \frac{\partial^2 G_{22}}{\partial x_1 \partial x_2} \right) - \mu \left(f_1^S \frac{\partial^2 G_{11}}{\partial x_2^2} + f_2^S \frac{\partial^2 G_{12}}{\partial x_2^2} \right) \right] d\eta_1 d\eta_2 d\tau. \quad (\text{A11})$$

This equation can be modified as follows:

$$L_1 = \int_{-\infty}^{\infty} \int_{-\infty}^{\infty} \left[f_1^S \left\{ \rho \frac{\partial^2 G_{11}}{\partial t^2} - (\lambda + 2\mu) \frac{\partial^2 G_{11}}{\partial x_1^2} - (\lambda + \mu) \frac{\partial^2 G_{21}}{\partial x_1 \partial x_2} - \mu \frac{\partial^2 G_{11}}{\partial x_2^2} \right\} + f_2^S \left\{ \rho \frac{\partial^2 G_{12}}{\partial t^2} - (\lambda + 2\mu) \frac{\partial^2 G_{12}}{\partial x_1^2} - (\lambda + \mu) \frac{\partial^2 G_{22}}{\partial x_1 \partial x_2} - \mu \frac{\partial^2 G_{12}}{\partial x_2^2} \right\} \right] d\eta_1 d\eta_2 d\tau. \quad (\text{A12})$$

From Eq. (A3), we find that the second integral of Eq. (A12) is zero. Therefore, Eq. (A12) from Eq. (A1) becomes

$$L_1 = \int_{-\infty}^{\infty} \int_{-\infty}^{\infty} f_1^S(\boldsymbol{\eta}, \tau) \delta(\mathbf{x} - \boldsymbol{\eta}) \delta(t - \tau) d\eta_1 d\eta_2 d\tau = f_1^S(\mathbf{x}, t). \quad (\text{A13})$$

Similarly, we can show that the right-hand side of Eq. (A10) is equivalent to $f_2^S(\mathbf{x}, t)$, and thus the displacement in the forms of Eqs. (A7) and (A8) satisfies the equation of motion (A5) and (A6).

Appendix B: Moment Tensor for a Spherical Source

Let us consider the moment density tensors for three tensile cracks in the planes $\xi_1 = 0$, $\xi_2 = 0$, and $\xi_3 = 0$. If we sum and average these three tensors and assume that $[u_1] = [u_2] = [u_3] = D_s$, we obtain the following moment density tensor:

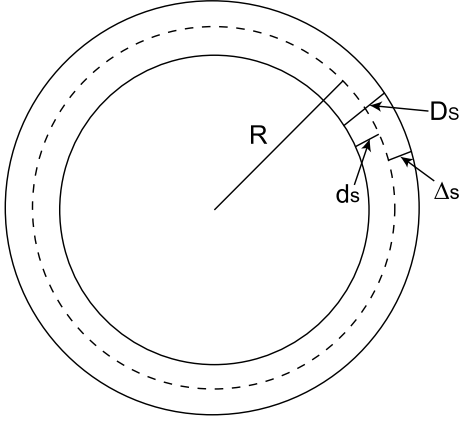
$$\mathbf{m} = D_s \begin{pmatrix} \lambda + 2\mu/3 & 0 & 0 \\ 0 & \lambda + 2\mu/3 & 0 \\ 0 & 0 & \lambda + 2\mu/3 \end{pmatrix}. \quad (\text{B1})$$

This represents the moment density tensor for the isotropic expansion of a cubic element. Following Müller [89], we consider a spherical crack surface of radius R where a constant radial expansion $D_s = (d_s + \Delta_s)$ occurs (Fig. A1). Here, the inner wall of the crack moves inward by d_s and the outer wall moves outward by Δ_s . The moment tensor of the spherical expansion may be obtained by integration of the moment density tensor (B1) over the surface R :

$$\mathbf{M} = \Delta V \begin{pmatrix} \lambda + 2\mu/3 & 0 & 0 \\ 0 & \lambda + 2\mu/3 & 0 \\ 0 & 0 & \lambda + 2\mu/3 \end{pmatrix}, \quad (\text{B2})$$

where ΔV is the volume given as

$$\Delta V = 4\pi R^2 D_s = 4\pi R^2 (d_s + \Delta_s). \quad (\text{B3})$$



Volcano Seismic Signals, Source Quantification of, Figure A1

A spherical crack surface of radius R where a constant radial expansion $D_s = (d_s + \Delta_s)$ occurs. Here, the inner wall of the crack moves inward by d_s and the outer wall moves outward by Δ_s [89]

The volume $4\pi R^2 d_s$ is caused by the inward motion, which compresses the sphere. The volume $\Delta V_s = 4\pi R^2 \Delta_s$, on the other hand, is caused by the outward motion, which excites seismic waves in the region outside the sphere. ΔV_s can be determined by solving an elastostatic boundary-value problem in the following way. We assume an isotropic medium, and denote the regions inside and outside the sphere as regions 1 and 2, respectively. Since the motion is radial only, the equation of motion is given as e. g., [121]

$$\rho \frac{\partial^2 u}{\partial t^2} = \frac{1}{r^2} \frac{\partial}{\partial r} (r^2 \sigma_{rr}) - \frac{1}{r} (\sigma_{\theta\theta} + \sigma_{\phi\phi}) \quad (\text{B4})$$

and

$$\sigma_{rr} = (\lambda + 2\mu) \frac{\partial u}{\partial r} + \lambda \frac{2}{r} u, \quad (\text{B5})$$

$$\sigma_{\theta\theta} = \sigma_{\phi\phi} = \lambda \frac{\partial u}{\partial r} + (\lambda + \mu) \frac{2}{r} u, \quad (\text{B6})$$

where u is the radial displacement and σ_{rr} , $\sigma_{\theta\theta}$, and $\sigma_{\phi\phi}$ are the stress components in the spherical coordinate. Equations (B4) and (B5) apply to both regions 1 and 2. Substituting Eq. (B5) into Eq. (B4) and setting $\rho(\partial^2 u_r / \partial t^2) = 0$, we obtain the following static equilibrium equation:

$$\frac{\partial^2 u}{\partial r^2} + \frac{2}{r} \frac{\partial u}{\partial r} - \frac{2}{r^2} u = 0. \quad (\text{B7})$$

This equation has two solutions: $u = ar$ and $u = b/r^2$, where a and b are constants. The former is the interior solution for region 1 ($r \leq R$), and the latter is the exterior

solution for region 2 ($r \geq R$). I denote the interior and exterior solutions as u_i and u_e , respectively. The constants a and b are determined by the boundary conditions for the radial displacement and the continuity of the radial stress at $r = R$:

$$u_e(R) - u_i(R) = \frac{b}{R^2} - aR = D_s, \quad (\text{B8})$$

$$\sigma_{rr}^i(R) - \sigma_{rr}^e(R) = -\frac{4\mu}{R^3} b - (3\lambda + 2\mu)a = 0, \quad (\text{B9})$$

where σ_{rr}^i and σ_{rr}^e are the radial stresses in regions 1 and 2, respectively. Accordingly, we obtain

$$u_i(r) = -\frac{4\mu D_s}{3(\lambda + 2\mu)} \frac{r}{R} \quad (r \leq R), \quad (\text{B10})$$

$$u_e(r) = \frac{(\lambda + 2\mu/3) D_s}{\lambda + 2\mu} \frac{R^2}{r^2} \quad (r \geq R). \quad (\text{B11})$$

Then, we obtain

$$d_s = -u_i(R) = \frac{4\mu D_s}{3(\lambda + 2\mu)}, \quad (\text{B12})$$

$$\Delta_s = u_e(R) = \frac{(\lambda + 2\mu/3) D_s}{\lambda + 2\mu}. \quad (\text{B13})$$

Equation (B3) can be modified as

$$\Delta V = 4\pi R^2 \Delta_s (D_s / \Delta_s) = \frac{\lambda + 2\mu}{\lambda + 2\mu/3} \Delta V_s. \quad (\text{B14})$$

Finally, we obtain the moment tensor for the spherical expansion as

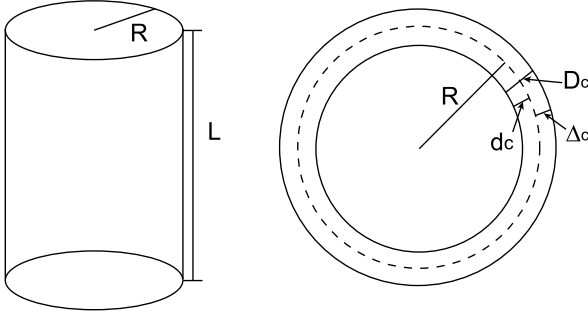
$$\mathbf{M} = (\lambda + 2\mu) \Delta V_s \begin{pmatrix} 1 & 0 & 0 \\ 0 & 1 & 0 \\ 0 & 0 & 1 \end{pmatrix}. \quad (\text{B15})$$

Appendix C: Moment Tensor for a Cylindrical Source

We consider the moment density tensors for two tensile cracks in the planes $\xi_1 = 0$ and $\xi_2 = 0$, where ξ_1 and ξ_2 are two horizontal axes. If we sum and average these two tensors and assume that $[u_1] = [u_2] = D_c$, we obtain

$$\mathbf{m} = D_c \begin{pmatrix} \lambda + \mu & 0 & 0 \\ 0 & \lambda + \mu & 0 \\ 0 & 0 & \lambda \end{pmatrix}. \quad (\text{C1})$$

This represents the moment density tensor for the expansion of a cubic element in the two horizontal directions. Let us consider a vertical cylinder of length L and radius R . The cylinder surface at radius R can be regarded as a cylindrical crack, where the radial expansion $D_c = (d_c + \Delta_c)$



Volcano Seismic Signals, Source Quantification of, Figure A2

A vertical cylinder of length L and radius R . The cylinder surface can be regarded as a cylindrical crack, where the radial expansion $D_c = (d_c + \Delta_c)$ occurs. Here, the inner wall of the crack moves inward by d_c and the outer wall moves outward by Δ_c [89]

occurs (Fig. A2). The moment tensor for the radial expansion of the cylinder may be obtained by integration of the moment density tensor (C1) over the surface R :

$$\mathbf{M} = \Delta V \begin{pmatrix} \lambda + \mu & 0 & 0 \\ 0 & \lambda + \mu & 0 \\ 0 & 0 & \lambda \end{pmatrix}, \quad (\text{C2})$$

where ΔV is the volume given as

$$\Delta V = 2\pi R L D_c = 2\pi R L (d_c + \Delta_c). \quad (\text{C3})$$

We obtain the static equilibrium equation for the radial expansion of the cylinder u as

$$\frac{\partial^2 u}{\partial r^2} + \frac{1}{r} \frac{\partial u}{\partial r} - \frac{1}{r^2} u = 0. \quad (\text{C4})$$

This equation has internal and external solutions, which are given as $u = ar$ and $u = b/r$, respectively. The constants a and b are determined by the boundary conditions

$$u_e(R) - u_i(R) = \frac{b}{R} - aR = D_c, \quad (\text{C5})$$

$$\sigma_{rr}^i(R) - \sigma_{rr}^e(R) = -\frac{2\mu}{R^2} b - 2(\lambda + \mu)a = 0, \quad (\text{C6})$$

where superscripts i and e denote the interior and exterior solutions. We then obtain

$$d_c = -u_i(R) = \frac{\mu D_s}{(\lambda + 2\mu)}, \quad (\text{C7})$$

$$\Delta_c = u_e(R) = \frac{(\lambda + \mu) D_c}{\lambda + 2\mu}, \quad (\text{C8})$$

and

$$\Delta V = \frac{\lambda + 2\mu}{\lambda + \mu} \Delta V_c. \quad (\text{C9})$$

The moment tensor for the vertical cylinder is therefore given as

$$\mathbf{M} = \frac{\lambda + 2\mu}{\lambda + \mu} \Delta V_c \begin{pmatrix} \lambda + \mu & 0 & 0 \\ 0 & \lambda + \mu & 0 \\ 0 & 0 & \lambda \end{pmatrix}. \quad (\text{C10})$$

Let us rotate the vertical cylinder with axis orientation angles ϕ and θ (Fig. 8b). This can be done in the following steps: (1) fix the cylinder and (2) rotate the ξ_1 and ξ_2 axes around the ξ_3 axis through an angle $-\phi$, and (3) further rotate the ξ_1 and ξ_3 axes around the ξ_2 axis through an angle $-\theta$. The rotation matrix \mathbf{R} is given as

$$\mathbf{R} = \begin{pmatrix} \cos \theta & 0 & -\sin \theta \\ 0 & 1 & 0 \\ \sin \theta & 0 & \cos \theta \end{pmatrix} \begin{pmatrix} \cos \phi & -\sin \phi & 0 \\ \sin \phi & \cos \phi & 0 \\ 0 & 0 & 1 \end{pmatrix} \quad (\text{C11})$$

$$= \begin{pmatrix} \cos \theta \cos \phi & -\cos \theta \sin \phi & -\sin \theta \\ \sin \phi & \cos \phi & 0 \\ \sin \theta & -\sin \theta \sin \phi & \cos \theta \end{pmatrix}. \quad (\text{C12})$$

Using the matrix \mathbf{R} , we obtain the moment tensor for a cylinder with the axis orientation angles (ϕ, θ) as

$$\mathbf{M}' = \mathbf{R}^T \mathbf{M} \mathbf{R}, \quad (\text{C13})$$

which leads to Eq. (34).

Bibliography

Primary Literature

1. Aki K, Richards PG (2002) Quantitative seismology, 2nd ed. University Science Books, Sausalito
2. Aki K, Fehler M, Das S (1977) Source mechanism of volcanic tremor: Fluid-driven crack models and their application to the 1963 Kilauea eruption. *J Volcanol Geotherm Res* 2:259–287
3. Almendros J, Chouet BA, Dawson PB (2001) Spatial extent of a hydrothermal system at Kilauea Volcano, Hawaii, determined from array analyses of shallow long-period seismicity 1. Method. *J Geophys Res* 106:13565–13580
4. Almendros J, Chouet BA, Dawson PB (2001) Spatial extent of a hydrothermal system at Kilauea Volcano, Hawaii, determined from array analyses of shallow long-period seismicity 2. Results. *J Geophys Res* 106:13581–13597
5. Almendros J, Chouet BA, Dawson PB, Huber C (2002) Mapping the sources of the seismic wave field at Kilauea Volcano, Hawaii, using data recorded on multiple seismic antennas. *Bull Seism Soc Am* 92:2333–2351
6. Almendros J, Chouet BA, Dawson PB, Bond T (2002) Identifying elements of the plumbing system beneath Kilauea Volcano, Hawaii, from the source locations of very-long-period signals *Geophys J Int* 148:303–312

7. Aoyama H, Takeo M (2001) Wave properties and focal mechanisms of N-type earthquakes at Asama volcano. *J Volcanol Geotherm Res* 105:163–182
8. Arciniega-Ceballos A, Chouet BA, Dawson PB (1999) Very long-period signals associated with vulcanian explosions at Popocatepetl Volcano, Mexico. *Geophys Res Lett* 26: 3013–3016
9. Arciniega-Ceballos A, Chouet BA, Dawson PB (2003) Long-period events and tremor at Popocatepetl volcano (1994–2000) and their broadband characteristics. *Bull Volcanol* 65: 124–135
10. Aster R, Mah S, Kyle P, McIntosh W, Dunbar N, Johnson J, Ruiz M, McNamara S (2003) Very long period oscillations of Mount Erebus Volcano. *J Geophys Res* 108:2522. doi:10.1029/2002JB002101
11. Auger E, D'Auria L, Martini M, Chouet BA, Dawson PB (2006) Real-time monitoring and massive inversion of source parameters of Very-Long-Period (VLP) seismic signals: An application to Stromboli Volcano, Italy. *Geophys Res Lett* 33:L04301. doi:10.1029/2005GL024703
12. Backus G, Mulcahy M (1976) Moment tensors and other phenomenological descriptions of seismic sources—I. Continuous displacements. *Geophys J R Astr Soc* 46:341–361
13. Battaglia J, Aki K (2003) Location of seismic events and eruptive fissures on the Piton de la Fournaise volcano using seismic amplitudes. *J Geophys Res* 108:2364. doi:10.1029/2002JB002193
14. Biot MA (1952) Propagation of elastic waves in a cylindrical bore containing a fluid. *J Appl Phys* 23:997–1005
15. Biot MA (1952) The interaction of Rayleigh and Stoneley waves in the ocean bottom. *Bull Seism Soc Am* 42:82–92
16. Bouchon M (1979) Discrete wave number representation of elastic wave fields in three-space dimensions. *J Geophys Res* 84:3609–3614
17. Bouchon M (1981) A simple method to calculate Green's functions for elastic layered media. *Bull Seism Soc Am* 71:959–971
18. Bouchon M, Schultz CA, Toksöz MN (1996) Effect of 3D topography on seismic motion. *J Geophys Res* 101:5835–5846
19. Brandsdóttir B, Einarsson P (1979) Seismic activity associated with the September 1977 deflation of the Krafla central volcano in northeastern Iceland. *J Volcanol Geotherm Res* 6: 197–212
20. Chouet BA (1982) Free surface displacements in the near field of a tensile crack expanding in three dimensions. *J Geophys Res* 87:3868–3872
21. Chouet BA (1985) Excitation of a buried magmatic pipe: A seismic source model for volcanic tremor. *J Geophys Res* 90:1881–1893
22. Chouet BA (1986) Dynamics of a fluid-driven crack in three dimensions by the finite difference method. *J Geophys Res* 91:13967–13992
23. Chouet BA (1988) Resonance of a fluid-driven crack: Radiation properties and implications for the source of long-period events and harmonic tremor. *J Geophys Res* 93:4375–4400
24. Chouet BA (1992) A seismic model for the source of long-period events and harmonic tremor. In: Gasparini P, Scarpa R, Aki K (eds) *Volcanic Seismology*. Springer, Berlin, pp 133–156
25. Chouet BA (1996) New methods and future trends in seismological volcano monitoring. In: Scarpa R, Tilling RI (eds) *Monitoring and Mitigation of Volcano Hazards*. Springer, New York, pp 23–97
26. Chouet BA (1996) Long-period volcano seismicity: its source and use in eruption forecasting. *Nature* 380:309–316
27. Chouet BA (2003) *Volcano Seismology*. Pure Appl Geophys 160:739–788
28. Chouet BA, Julian B (1985) Dynamics of an expanding fluid-filled crack. *J Geophys Res* 90:11187–11198
29. Chouet BA, Page RA, Stephens CD, Lahr JC, Power JA (1994) Precursory swarms of long-period events at Redoubt Volcano (1989–1990), Alaska: Their origin and use as a forecasting tool. *J Volcanol Geotherm Res* 62:95–135
30. Chouet BA, Saccorotti G, Martini M, Dawson PB, De Luca G, Milana G, Scarpa R (1997) Source and path effects in the wavefields of tremor and explosions at Stromboli volcano, Italy. *J Geophys Res* 102:15129–15150
31. Chouet BA, Saccorotti G, Dawson PB, Martini M, Scarpa R, De Luca G, Milana G, Cattaneo M (1999) Broadband measurements of the sources of explosions at Stromboli Volcano, Italy. *Geophys Res Lett* 26:1937–1940
32. Chouet BA, Dawson PB, Ohminato T, Martini M, Saccorotti G, Guidicepierto F, De Luca G, Milana G, Scarpa R (2003) Source mechanisms of explosions at Stromboli Volcano, Italy, determined from moment-tensor inversions of very-long-period data. *J Geophys Res* 108:2331. doi:10.1029/2003JB002535
33. Chouet BA, Dawson PB, Arciniega-Ceballos A (2005) Source mechanism of Vulcanian degassing at Popocatepetl Volcano, Mexico, determined from waveform inversions of very long period signals. *J Geophys Res* 110:B07301. doi:10.1029/2004JB003524
34. Chouet BA, Dawson PB, Nakano M (2006) Dynamics of diffusive bubble growth and pressure recovery in a bubbly rhyolitic melt embedded in an elastic solid. *J Geophys Res* 111:B07310. doi:10.1029/2005JB004174
35. Crosson RS, Bame DA (1985) A spherical source model for low frequency volcanic earthquakes. *J Geophys Res* 90:10237–10247
36. Dawson PB, Dietel C, Chouet BA, Honma K, Ohminato T, Okubo P (1998) A digitally telemetered broadband seismic network at Kilauea Volcano, Hawaii. *US Geol Surv Open File Report* 98–108:1–121
37. Dawson PB, Whilldin D, Chouet BA (2004) Application of near real-time semblance to locate the shallow magmatic conduit at Kilauea Volcano, Hawaii. *Geophys Res Lett* 31:L21606. doi:10.1029/2004GL021163
38. De Angelis S, McNutt SR (2005) Degassing and hydrothermal activity at Mt. Spurr, Alaska during the summer of 2004 inferred from the complex frequencies of long-period events. *Geophys Res Lett* 32:L12312. doi:10.1029/2005GL022618
39. Ferrazzini V, Aki K (1987) Slow waves trapped in a fluid-filled infinite crack: Implication for volcanic tremor. *J Geophys Res* 92:9215–9223
40. Fujita E, Ida Y (2003) Geometrical effects and low-attenuation resonance of volcanic fluid inclusions for the source mechanism of long-period earthquakes. *J Geophys Res* 108:2118. doi:10.1029/2002JB001806
41. Fujita E, Ida Y, Oikawa J (1995) Eigen oscillation of a fluid sphere and source mechanism of harmonic volcanic tremor. *J Volcanol Geotherm Res* 69:365–378
42. Fujita E, Ukawa M, Yamamoto E (2004) Subsurface cyclic magma sill expansions in the 2000 Miyakejima volcano eruption: Possibility of two-phase flow oscillation. *J Geophys Res* 109:B04205. doi:10.1029/2003JB002556

43. Fukuyama E, Kubo A, Kawai H, Nonomura K (2001) Seismic remote monitoring of stress field. *Earth Planets Space* 53: 1021–1026
44. Gil Cruz F, Chouet BA (1997) Long-period events, the most characteristic seismicity accompanying the emplacement and extrusion of a lava dome in Galeras Volcano, Colombia, in 1991. *J Volcanol Geotherm Res* 77:121–158
45. Goldstein P, Chouet BA Array measurements and modeling of sources of shallow volcanic tremor at Kilauea volcano, Hawaii. *J Geophys Res* 99:2637–2652
46. Hayashi Y, Morita Y (2003) An image of a magma intrusion process inferred from precise hypocenter migrations of the earthquake swarm east of the Izu Peninsula. *Geophys J Int* 153:159–174
47. Hidayat D, Voight B, Langston C, Ratdomopurbo A, Ebeling C (2000) Broadband seismic experiment at Merapi volcano, Java, Indonesia: very-long-period pulses embedded in multiphase earthquakes. *J Volcanol Geotherm Res* 100: 215–231
48. Hidayat D, Chouet BA, Voght B, Dawson P, Ratdomopurbo A (2002) Source mechanism of very-long-period signals accompanying dome growth activity at Merapi volcano, Indonesia. *Geophys Res Lett* 23:2118. doi:10.1029/2002GL015013
49. Hill DP, Dawson PB, Johnston MJS, Pitt AM (2002) Very-long-period volcanic earthquakes beneath Mammoth Mountain, California. *Geophys Res Lett* 29:1370 doi:10.1029/2002GL014833
50. Hori S, Fukao Y, Kumazawa M, Furumoto M, Yamamoto A (1989) A new method of spectral analysis and its application to the earth's free oscillations: the "Sompi" method. *J Geophys Res* 94:7535–7553
51. Iguchi M (1994) A vertical expansion source model for the mechanisms of earthquakes originated in the magma conduit of an andesitic volcano: Sakurajima, Japan. *Bull Volcanol Soc Jpn* 39:49–67
52. Jousset P, Neuberg JW, Sturton S (2003) Modelling the time-dependent frequency content of low-frequency volcanic earthquakes. *J Volcanol Geotherm Res* 128:201–223
53. Julian BR (1994) Volcanic tremor: Nonlinear excitation by fluid flow. *J Geophys Res* 99:11859–11877
54. Julian BR, Miller AD, Foulger GR (1998) Non-double-couple earthquakes 1. Theory. *Rev Geophys* 36:525–549
55. Kanamori H, Given J (1982) Analysis of long-period seismic waves excited by the May 18, 1980, eruption of Mount St. Helens – A terrestrial monopole. *J Geophys Res* 87: 5422–5432
56. Kanamori H, Given J, Lay T (1984) Analysis of seismic body waves excited by the Mount St. Helens eruption of May 18, 1980. *J Geophys Res* 89:1856–1866
57. Kaneshima S et al (1996) Mechanism of phreatic eruptions at Aso volcano inferred from near-field broadband observations. *Science* 273:642–645
58. Kawakatsu H, Ohminato T, Ito H, Kuwahara Y, Kato T, Tsuruga K, Honda S, Yomogida K (1992) Broadband seismic observation at Sakurajima Volcano, Japan. *Geophys Res Lett* 19: 1959–1962
59. Kawakatsu H, Ohminato T, Ito H (1994) 10s-period volcanic tremors observed over a wide area in southwestern Japan. *Geophys Res Lett* 21:1963–1966
60. Kawakatsu H et al (2000) Aso-94: Aso seismic observation with broadband instruments. *J Volcanol Geotherm Res* 101:129–154
61. Kawakatsu H, Yamamoto M (2007) Volcano Seismology. In: Kamanori H (ed) *Treatise on Geophysics. Earthquake Seismology*, vol 4. Elsevier, Amsterdam, pp 389–420
62. Kawase H (1988) Time domain response of a semi-circular canyon for incident SV, P and Rayleigh waves calculated by the discrete wavenumber boundary element method. *Bull Seism Soc Am* 78:1415–1437
63. Kennet LN, Kerry NJ (1979) Seismic waves in a stratified half-space. *Geophys J R Astr Soc* 57:557–583
64. Kobayashi T, Ohminato T, Ida Y (2003) Earthquakes series preceding very long period seismic signals observed during the 2000 Miyakejima volcanic activity. *Geophys Res Lett* 30:1423. doi:10.1029/2002GL016631
65. Kumagai H (2006) Temporal evolution of a magmatic dike system inferred from the complex frequencies of very long period seismic events. *J Geophys Res* 111:B06201. doi:10.1029/2005JB003881
66. Kumagai H, Chouet BA (1999) The complex frequencies of long-period seismic events as probes of fluid composition beneath volcanoes. *Geophys J Int* 138:F7–F12
67. Kumagai H, Chouet BA (2000) Acoustic properties of a crack containing magmatic or hydrothermal fluids. *J Geophys Res* 105:25493–25512
68. Kumagai H, Chouet BA (2001) The dependence of acoustic properties of a crack on the mode and geometry. *Geophys Res Lett* 28:3325–3328
69. Kumagai H, Ohminato T, Nakano M, Ooi M, Kubo A, Inoue H, Oikawa J (2001) Very-long-period seismic signals and caldera formation at Miyake Island, Japan. *Science* 293:687–690
70. Kumagai H, Chouet BA, Nakano M (2002) Temporal evolution of a hydrothermal system in Kusatsu-Shirane Volcano, Japan, inferred from the complex frequencies of long-period events. *J Geophys Res* 107:2236. doi:10.1029/2001JB000653
71. Kumagai H, Chouet BA, Nakano M (2002) Waveform inversion of oscillatory signatures in long-period events beneath volcanoes. *J Geophys Res* 107:2301. doi:10.1029/2001JB001704
72. Kumagai H, Miyakawa K, Negishi H, Inoue H, Obara K, Suet-sugu D (2003) Magmatic dike resonances inferred from very-long-period seismic signals. *Science* 299:2058–2061 (10.1126/science.1081195)
73. Kumagai H, Chouet BA, Dawson PB (2005) Source process of a long-period event at Kilauea Volcano, Hawaii. *Geophys J Int* 161:243–254
74. Kumagai H et al (2007) Enhancing volcano-monitoring capabilities in Ecuador. *Eos trans AGU* 88:245–246
75. Kumazawa M, Imanishi Y, Fukao Y, Furumoto M, Yamamoto A (1990) A theory of spectral analysis based on the characteristic property of a linear dynamic system. *Geophys J Int* 101:613–630
76. Legrand D, Kaneshima S, Kawakatsu H (2000) Moment tensor analysis of near field broadband waveforms observed at Aso volcano, Japan. *J Volcanol Geotherm Res* 101:155–169
77. Lesage P, Glangeaud F, Mars J (2002) Applications of autoregressive models and time-frequency analysis to the study of volcanic tremor and long-period events. *J Volcanol Geotherm Res* 114:391–417
78. Lin CH, Konstantinou KI, Liang WT, Pu HC, Lin YM, You SH, Huang YP (2005) Preliminary analysis of volcanoseismic sig-

- nals recorded at the Tatun Volcano Group, northern Taiwan. *Geophys Res Lett* 32:L10313. doi:10.1029/2005GL022861
79. Matsuura T, Imanishi Y, Imanari M, Kumazawa M (1990) Application of a new method of high-resolution spectral analysis, "Sompil", for free induction decay of nuclear magnetic resonance. *Appl Spectrosc* 44:618–626
 80. McNutt SR (1996) Seismic monitoring and eruption forecasting of volcanoes: A review of the state-of-the art and cased histories. In: Scarpa R, Tilling RI (eds) *Monitoring and Mitigation of Volcano Hazards*. Springer, New York, pp 99–146
 81. McNutt SR (2005) Volcanic Seismology. *Annu Rev Earth Planet Sci* 33:461–491
 82. Métaxian JP, Lesage P, Dorel J (1997) Permanent tremor of Masaya volcano, Nicaragua: wavefield analysis and source location. *J Geophys Res* 102:22529–22545
 83. Menke W (1989) *Geophysical data analysis: Discrete inverse theory*, Revised edition. Academic Press, San Diego
 84. Minakami T (1974) Seismology of volcanoes in Japan. In: Civetta L, Gasparini P, Luongo G, Rapolla A (eds) *Physical Volcanology*. Elsevier, Amsterdam, pp 1–27
 85. Molina I, Kumagai H, Yepes H (2004) Resonances of a volcanic conduit triggered by repetitive injections of an ash-laden gas. *Geophys Res Lett* 31:L03603. doi:10.1029/2003GL018934
 86. Morita Y, Nakao S, Hayashi Y (2006) A quantitative approach to the dike intrusion process inferred from a joint analysis of geodetic and seismological data for the 1998 earthquake swarm off the east coast of Izu Peninsula, central Japan. *J Geophys Res* 111:B06208. doi:10.1029/2005JB003860
 87. Morrissey M, Chouet BA (1997) A numerical investigation of choked flow dynamics and its application to the triggering mechanism of long-period events at Redoubt Volcano, Alaska. *J Geophys Res* 102:7965–7983
 88. Morrissey M, Chouet BA (2001) Trends in long-period seismicity related to magmatic fluid compositions. *J Volcanol Geotherm Res* 108:265–281
 89. Müller G (2001) Volume change of seismic sources from moment tensors. *Bull Seism Soc Am* 91:880–884
 90. Nakamichi H, Hamaguchi H, Tanaka S, Ueki S, Nishimura T, Hasegawa A (2003) Source mechanisms of deep and intermediate-depth low-frequency earthquakes beneath Iwate volcano, northeastern Japan. *Geophys J Int* 154:811–828
 91. Nakano M, Kumagai H (2005) Response of a hydrothermal system to magmatic heat inferred from temporal variations in the complex frequencies of long-period events at Kusatsu-Shirane Volcano, Japan. *J Volcanol Geotherm Res* 147: 233–244
 92. Nakano M, Kumagai H (2005) Waveform inversion of volcano-seismic signals assuming possible source geometries. *Geophys Res Lett* 32:L12302. doi:10.1029/2005GL022666
 93. Nakano M, Kumagai H, Kumazawa M, Yamaoka K, Chouet BA (1998) The excitation and characteristic frequency of the long-period volcanic event: An approach based on an inhomogeneous autoregressive model of a linear dynamic system. *J Geophys Res* 103:10031–10046
 94. Nakano M, Kumagai H, Chouet BA (2003) Source mechanism of long-period events at Kusatsu-Shirane Volcano, Japan, inferred from waveform inversion of the effective excitation functions. *J Volcanol Geotherm Res* 122:149–164
 95. Nakano M, Kumagai H, Chouet BA, Dawson PB (2007) Waveform inversion of volcano-seismic signals for an extended source. *J Geophys Res* 112:B02306. doi:10.1029/2006JB004490
 96. Neuberg JW (2000) Characteristics and causes of shallow seismicity in andesite volcanoes. *Philos Trans R Soc Lond A* 358:1533–1546
 97. Neuberg JW, Luckett R, Ripepe M, Braun T (1994) Highlights from a seismic broadband array on Stromboli Volcano. *Geophys Res Lett* 21:749–752
 98. Neuberg JW, Luckett R, Baptie B, Olsen K (2000) Models of tremor and low-frequency earthquake swarms on Montserrat. *J Volcanol Geotherm Res* 101:83–104
 99. Neuberg JW, Tuffen H, Collier L, Green D, Powell T, Dingwell D (2006) The trigger mechanism of low frequency earthquakes on Montserrat. *J Volcanol Geotherm Res* 153:37–50
 100. Nishimura T (2004) Pressure recovery in magma due to bubble growth. *Geophys Res Lett* 31:L12613. doi:10.1029/2004GL019810
 101. Nishimura T, Chouet BA (2003) A numerical simulation of magma motion, crustal deformation, and seismic radiation associated with volcanic eruptions. *Geophys J Int* 153: 699–718
 102. Nishimura T, Nakamichi H, Tanaka S, Sato M, Kobayashi T, Ueki S, Hamaguchi H, Ohtake M, Sato H (2000) Source process of very long period seismic events associated with the 1998 activity of Iwate Volcano, northeastern Japan. *J Geophys Res* 105:19135–19417
 103. Nishimura T, Ueki S, Yamawaki T, Tanaka S, Hashino H, Sato M, Nakamichi H, Hamaguchi H (2002) Broadband seismic signals associated with the 2000 volcanic unrest of Mount Bandai, northeastern Japan. *J Volcanol Geotherm Res* 119:51–59
 104. O'Brien GS, Bean CJ (2004) A 3D discrete numerical elastic lattice method for seismic wave propagation in heterogeneous media with topography. *Geophys Res Lett* 31:L14608. doi:10.1029/2004GL020069
 105. Ohminato T (2006) Characteristics and source modeling of broadband seismic signals associated with the hydrothermal system at Satsuma-Iwojima volcano, Japan. *J Volcanol Geotherm Res* 158:467–490
 106. Ohminato T, Chouet BA (1997) A free-surface boundary condition for including 3D topography in the finite difference method. *Bull Seism Soc Am* 87:494–515
 107. Ohminato T, Chouet BA, Dawson PB, Kedar S (1998) Waveform inversion of very long period impulsive signals associated with magmatic injection beneath Kilauea Volcano, Hawaii. *J Geophys Res* 103:23839–23862
 108. Ohminato T, Takeo M, Kumagai H, Yamashina T, Oikawa J, Koyama E, Tsuji H, Urabe T (2006) Vulcanian eruptions with dominant single force components observed during the Asama 2004 volcanic activity in Japan. *Earth Planets Space* 58:583–593
 109. Ripperger J, Igel H, Wasserman J (2003) Seismic wave simulation in the presence of real volcano topography. *J Volcanol Geotherm Res* 128:31–44
 110. Rowe CA, Aster RC, Kyle PR, Schlue JW, Dibble RR (1998) Broadband recording of Strombolian explosions and associated very-long-period seismic signals on Mount Erebus volcano, Ross Island, Antarctica. *Geophys Res Lett* 25: 2297–2300
 111. Rubin AM, Gillard D (1998) Dike-induced seismicity: theoretical considerations. *J Geophys Res* 103:10017–10030
 112. Rubin AM, Gillard D, Got JL (1998) A reinterpretation of seis-

- micity associated with the January 1983 dike intrusion at Kilauea Volcano, Hawaii. *J Geophys Res* 103:10003–10015
113. Saccorotti G, Del Pezzo E (2000) A probabilistic approach to the inversion of data from a seismic array and its application to volcanic signals. *Geophys J Int* 143:249–261
 114. Saccorotti G, Chouet BA, Dawson PB (2001) Wavefield properties of a shallow long-period event and tremor at Kilauea Volcano, Hawaii. *J Volcanol Geotherm Res* 109:163–189
 115. Sakuraba A, Oikawa J, Imanishi Y (2002) Free oscillations of a fluid sphere in an infinite elastic medium and long-period volcanic earthquakes. *Earth Planets Space* 54:91–106
 116. Stump BW, Johnson LR (1977) The determination of source properties by the linear inversion of seismograms. *Bull Seism Soc Am* 67:1489–1502
 117. Sturton S, Neuberg JW (2006) The effects of conduit length and acoustic velocity on conduit resonance: Implications for low-frequency events. *J Volcanol Geotherm Res* 151:319–339
 118. Takei Y, Kumazawa M (1994) Why have the single force and torque been excluded from seismic source models? *Geophys J Int* 118:20–30
 119. Takei Y, Kumazawa M (1995) Phenomenological representation and kinematics of general seismic sources including the seismic vector modes. *Geophys J Int* 121:641–662
 120. Takeo M, Yamasato H, Furuya I, Seino M (1990) Analysis of long-period seismic waves excited by the November 1987 eruption of Izu-Oshima Volcano. *J Geophys Res* 95:19377–19393
 121. Takeuchi H, Saito M (1972) Seismic surface waves. In: Bolt BA (ed) *Methods in Computational Physics*, vol 11. Academic Press, New York, pp 217–295
 122. Tameguri T, Iguchi M, Ishihara K (2002) Mechanism of explosive eruptions from moment tensor analyses of explosion earthquakes at Sakurajima volcano, Japan. *Bull Volcanol Soc Jpn* 47:197–216
 123. Toda S, Stein R, Sagiya T (2002) Evidence from the AD 2000 Izu islands earthquake swarm that stressing rate governs seismicity. *Nature* 419:58–61
 124. Tolstoy I (1954) Dispersive properties of a fluid layer overlying a semi-infinite elastic solid. *Bull Seism Soc Am* 44:493–512
 125. Tuffen H, Dingwell D (2005) Fault textures in volcanic conduits: evidence for seismic trigger mechanisms during silicic eruptions. *Bull Volcanol* 67:370–387
 126. Uhira K, Takeo M (1994) The source of explosive eruptions of Sakurajima volcano, Japan. *J Geophys Res* 99:17775–17789
 127. Ulrych TJ, Clayton RW (1976) Time series modeling and maximum entropy. *Phys Earth Planet Inter* 12:188–200
 128. Ulrych TJ, Sacchi MD (1995) Sompi, Pisarenko and the extended information criterion. *Geophys J Int* 122:719–724
 129. Virieux J (1986) P-SV wave propagation in heterogeneous media: Velocity-stress finite-difference method. *Geophysics* 51:889–901
 130. Wessel P, Smith WHF (1998) New improved version of Generic Mapping Tools released. *Eos trans AGU* 122:149–164
 131. Yamamoto M (2005) Volcanic fluid system inferred from broadband seismic signals. Ph D Thesis, University of Tokyo
 132. Yamamoto M, Kawakatsu H, Kaneshima S, Mori T, Tsutsui T, Sudo Y, Morita Y (1999) Detection of a crack-like conduit beneath active crater at Aso volcano, Japan. *Geophys Res Lett* 26:3677–3680
 133. Yamamoto M, Kawakatsu H, Yomogida K, Koyama J (2002) Long-period (12 sec) volcanic tremor observed at Usu 2000 eruption: Seismological detection of a deep magma plumbing system. *Geophys Res Lett* 29:1329. doi:10.1029/2001GL013996
 134. Yamamura K, Kawakatsu H (1998) Normal-mode solutions for radiation boundary conditions with an impedance contrast. *Geophys J Int* 134:849–855

Books and Reviews

- Dahlen FA, Tromp J (1998) *Theoretical Global Seismology*. Princeton University Press, Princeton
- Kay SM, Marple SL (1981) *Spectrum analysis – A modern perspective*. Proc IEEE 69:1380–1419

Voting

ALVARO SANDRONI, JONATHAN POGACH,
MICHELA TINCANI, ANTONIO PENTA, DENIZ SELMAN
University of Pennsylvania, Philadelphia, USA

Article Outline

Glossary
Definition of the Subject
Introduction
The Collective Choice Problem
Voting Rules
Welfare Economics
Arrow's Impossibility Theorem
Political Ignorance and the Condorcet Jury Theorem
Gibbard–Satterthwaite Theorem
Political Competition and Strategic Voting
The Common Value Setting with Strategic Agents
Future Directions
Bibliography

Glossary

Arrow's impossibility theorem Arrow's Impossibility Theorem states that there does not exist a complete social ranking over alternatives that meets minimum impositions of egalitarianism and efficiency, No Dictatorship and Pareto Optimality, respectively. Consequently, there is no voting mechanism that can simultaneously satisfy basic notions of egalitarianism and efficiency.

Cost of voting Any sacrifice in utility that voting entails, such as cognitive costs, time cost of going to the polls, etc.

Collective or social choice problem A collective or social choice problem is a setting in which a group of individuals must jointly decide on a single alternative from

a set. The outcome of such a problem potentially affects the welfare of all individuals.

Common values A common values problem is one in which agents share preferences over the alternatives, but may differ on their information regarding the attributes of alternatives.

Condorcet jury theorem In a common values setting, the result that under majority voting the correct candidate will (almost always) be elected so long as the following assumptions are satisfied: (1) each voter's belief is correct with a probability higher than half, (2) each voter votes according to her belief and (3) there is a large number of voters. In political science this result is sometimes referred to as *wisdom of crowds*.

Condorcet paradox See voting cycle.

Downsian model of political competition A model in which candidate strategically position themselves on a unidimensional policy space in order to win an election.

Efficiency Efficiency is a broad criterion that may be used to evaluate the social value of alternative outcomes by demanding that society make use of all valuable resources. Examples of efficiency measures are utilitarianism and Pareto Optimality.

Egalitarianism Egalitarianism is a broad criterion used to evaluate the social value of alternative outcomes by demanding that welfare or resources are evenly distributed across the population.

Gibbard–Satterthwaite theorem The Gibbard–Satterthwaite Theorem states that, under some assumptions, every non-dictatorial social choice function is manipulable.

Majority voting Majority voting is a voting rule that stipulates that each agent vote for a single alternative and an alternative that receives more than half of all votes is the collective choice.

Manipulability of a social choice function

A social choice function is said to be manipulable if there is some agent who, given the social choice function, prefers to misreport his true preferences. In a voting context, this translates to voting for an alternative different from that which is most preferred.

Median voter theorem The median voter theorem states that if individuals' preferences are single peaked, then there exists an alternative that beats all others in a pairwise majority vote. Single peaked requires that each individual has a bliss point (most preferred alternative) and alternatives are less preferred the further they are from the bliss point. The selected alternative is then the median bliss point and the voter who has this bliss point is the median voter.

No Dictatorship The No Dictatorship criterion of Arrow's desiderata demands that there is no single individual whose preferences always determine those of society. Any egalitarian arrangement must satisfy the no dictatorship criterion, though arrangements that satisfy no dictatorship need not be egalitarian.

Pairwise majority voting rule A pairwise majority voting rule compares each pair of alternatives in a majority vote. Depending on agents preferences and votes, this rule may lead to a voting cycle.

Paradox of voting the puzzle of why there is high voter turnout in large elections, when the probability of any single vote to be determinant for the outcome is extremely small.

Pareto optimality or pareto efficiency An outcome is Pareto Optimal or Pareto Efficient if it is not possible to increase the welfare of one individual without lessening the welfare of another.

Political ignorance A state in which voters are not well informed about the issues and/or candidates they must vote on.

Social choice function A social choice function is a mapping of all individuals' preferences into an alternative, the social choice.

Strategic abstention The tactical decision of an uninformed citizen to abstain in order to allow informed citizens with the same preferences determine the outcome.

Strategic voting Voting by agents who aim to maximize their utility and might do so by misreporting their true preferences over electoral outcomes.

Utilitarianism Utilitarianism is a conception of efficiency that evaluates outcomes on aggregate utility.

Utility of voting Benefit to citizens from voting, usually divided into two components: a **non instrumental** component which includes utility derived from the mere act of voting and not related to the actual outcome of the election, and an **instrumental** component given by the utility of the outcome a voter would induce if determining the outcome, weighted by the probability that his vote determines the outcome.

Voting cycle or Condorcet's paradox A voting cycle or Condorcet's Paradox results when every feasible alternative is beaten by another in a pairwise majority vote. As such, any collective choice is less preferred to some other alternative by more than half of the population.

Voting rule A voting rule is a mapping of votes into a collective choice. Examples of different voting rules include majority voting and plurality voting. The collective choice may vary under alternative voting rules.

Definition of the Subject

Voting is a fundamental mechanism that individuals use to reach an agreement on which one of many alternatives to implement. The individuals might all be affected by the outcome of such a process and might have conflicting preferences and/or information over alternatives. In a voting mechanism, preferences and information are aggregated as individuals submit votes and a voting rule maps the compilation of votes into the alternative that is to be selected. The use of voting as a means of making a group decision dates back at least to ancient Greece, though French Revolutionary contemporaries Condorcet's and Borda's works are among the pioneers of voting theory. Meanwhile, welfare economists such as Bentham suggested formal definitions of socially desirable outcomes. As voting theory and welfare economics evolved, Arrow's result in the middle twentieth century showed that no mechanism, voting or otherwise, can produce outcomes consistent with some of welfare economists' definitions of socially desirable states. Moreover, results in the early 1970s suggested that voters have incentives to misrepresent their true preferences in elections. Contemporary voting theory has developed new models of strategic behavior to address questions on how political agents behave and which outcomes voting might produce.

Introduction

Voting is one of the most commonly used ways of making collective decisions. Two issues arise when a group of people must find an agreement on a choice that will potentially affect the welfare of all. First, individuals might have conflicting preferences over the set of alternatives they are choosing from. An interesting question is what is the best way to aggregate individual's preferences in order to reach a common decision when preferences conflict. Second, even if agents share the same preferences, they might possess different information about the alternatives. In this situation, an interesting question is what is the best way to aggregate people's conflicting information so as to make the right choice.

The optimal ways to aggregate preferences and information are among the most important questions that the literature on voting has tried to answer. Since voting concerns societies, as opposed to single individuals, this literature relies on works in the field of welfare economics. This branch of economics is primarily concerned with the analysis and the definition of the welfare of a society. There is no agreement among social scientists on a single definition of welfare of a society. However, two concepts are prominent: efficiency, which concerns the minimal waste

scarce resources, and egalitarianism, which concerns the equal distribution of those resources. Using these concepts to define the welfare of a society, social scientists have attempted to answer questions on preference and information aggregation in making a collective choice.

Early works on different voting techniques date back to at least the late eighteenth century, with the works of French mathematicians such as Borda [6] and Condorcet [9]. Their works were among the first to analyze voting procedures with formal mathematical tools, which have since been prominently used in the literature on voting. Continuing in this tradition, a fundamental result in voting theory is Arrow's Impossibility Theorem. This is a formal treatment of the problem of aggregation of preferences that reached a striking result: there is no way, under some assumptions, to aggregate individuals' preferences that is minimally egalitarian and minimally efficient.

Unlike the problem of aggregation of conflicting preferences, studies on the aggregation of conflicting information obtain positive results. In particular, the Condorcet Jury Theorem finds a mathematical justification for the phenomenon that is known in Political Science as the *wisdom of the crowds*, that is, the observation that democracies seem to be better at making decisions than single individuals. However Condorcet's result relies on the assumption that people vote sincerely and subsequent works on voters' behavior suggest that this is not always the case. A fundamental theoretical result, known as Gibbard–Satterthwaite theorem, shows formally that, under some assumptions, in every election at least one individual has an incentive to vote non sincerely, i. e. to vote strategically.

Gibbard and Satterthwaite's result is a starting point for a branch of the voting literature that deals with strategic voting. Numerous works analyze strategic voting though the use of mathematical tools such as Game Theory. The latter has been used not only to explain voters' behavior, but also to describe competing candidates' behaviors in an election. The research in this game theoretic literature focuses on the outcome of political competition and on the development of a theory of turnout. The former is analyzed through the use of a model of political competition. A main result is that in a two party election, both parties choose the same political platform in order to maximize the probability of winning an election. The latter is motivated by the paradox of voting, which refers to the empirical observation that citizens vote even when the probability that their vote determines the outcome of the election is negligible, such as in large elections. At present, there is no widely accepted theory to explain this phenomenon.

As with the paradox of voting, the voting literature has still many unanswered interesting questions. As will be mentioned in the section on future directions, the voter's behavior is still only partially understood and much needs to be explained. On a broader level, the study of the historical evolution of democracies needs further developments. Much has been written on the subject of voting, and some interesting results have been obtained, but much still needs to be explained.

The Collective Choice Problem

The basic framework for understanding voting is a *collective* or *social choice problem*: a group of agents must reach an agreement on which alternative to select, and this decision potentially affects the welfare of everyone. Such problems could range from “what should be taught in public schools?” to “who should be president?” Consider two possible alternatives, A and B, and a group of individuals who must jointly choose one of the two. It might be the case that some individuals in society prefer A and some prefer B. These conflicting preferences pose a challenge in determining the appropriate social choice. Alternatively, consider a scenario where A and B are different characteristics that two candidates running for a public office may possess. Suppose that all individuals agree that A is more desirable than B, i. e. this a *common values* setting. However, individuals differ in their information; some think that candidate 1 possesses trait A, while others think candidate 2 does. In this case, the challenge is finding the best way to balance the conflicting information in arriving to a collective choice.

There are several ways to resolve the problems of conflicting preferences and information. For example, people can bargain to reach an agreement, or they can fight. A collective choice problem might also be solved through a dictatorship, or even through the toss of a coin. A fundamental mechanism used to resolve these conflicts is an election in which people submit votes on the feasible alternatives and a *voting rule* maps the collection of votes into a social choice. As can be seen in the next section, there exists a multitude of voting rules.

Before discussing voting rules, one should note the following distinction between elections: those in which the alternatives are policy and those in which the alternatives are candidates. The former is known as *direct democracy*, a common example of which is a *referendum*. In a referendum, citizens vote on a particular proposal, such as the adoption of a new law. The outcome of such an election is then to implement or not implement the proposal. This is in contrast to the case, known as *representative democracy*,

where the election is over candidates. The collective choice in such a system is an agent or group of agents with the responsibility of choosing policy. The following voting rules apply to both situations.

Voting Rules

Majority voting is one of the most commonly used voting rules. The rule prescribes that each citizen vote for a single alternative and an alternative becomes the social choice if it receives more than half of all votes. Clearly, when there are more than two alternatives, majority voting does not necessarily produce a social choice.

To ensure a comparison between alternatives, one can resort to *pairwise majority voting rule*, in which alternatives are voted over pair by pair with a majority vote. That is, a majority vote is held between every pair of feasible alternatives and for each majority vote, the winner is deemed socially preferable to the loser. However, this voting rule might generate an intransitive social preference in which society chooses x to y , y to z , but z to x . Consider a three-individual committee comprised of voters 1, 2 and 3 who must choose one of three alternatives, x , y and z . Individual preferences are such that voter 1 prefers x to y to z , voter 2 prefers z to x to y , and voter 3 preferences y to z to x . By pairwise majority voting x beats y , which in turn beats z , which in turn beats x . This intransitivity over alternatives is known as a *voting cycle* or *Condorcet's Paradox*.

In the presence of a voting cycle, pairwise majority voting might not produce an overall winner, as each alternative might be beaten by another. So, an agenda setter could end a cycle by specifying the order in which the alternatives are to be compared in a pairwise vote. However, pairwise majority voting then places all the decision power in the hands of the agenda setter. Returning to the previous example, suppose the agenda prescribes that voting be carried out between alternatives x and y first and the winner is then to be compared with z . In the first round of voting x beats y and z then beats x , so z becomes collective choice. However, the agenda setter could instead choose an initial comparison between y and z . Since y beats z in the first round and x beats y in the second, x would then be the collective choice. Hence, the agenda setter decides the outcome of the election by choosing the order of the pairwise voting.

A *plurality voting rule* is an alternative way to make a collective choice: agents each vote for one alternative and the alternative with the most votes is chosen.

Other voting rules require agents to submit scores or rankings of all available alternatives, rather than just vot-

ing for a single one. In a *Borda Count*, agents rank all alternatives assigning the larger numbers to those that are more preferred. The voting rule sums the scores for each alternative across individuals and the alternative with the highest sum is the social choice.

A *supramajority* voting rule stipulates that the ‘status quo’ alternative is chosen unless another alternative receives at least some specified percentage of the vote larger than fifty percent. In the limit, there might be a *unanimity rule* that mandates one hundred percent of the electorate vote for an alternative for it to be chosen against the status quo. Examples of supramajority rules include the passing of constitutional amendments in the United States, where the current constitution is the status quo. Unanimity rules are commonly found in the judicial system in which all jurors must agree on the guilt of the defendant to override the status quo, the presumption of innocence.

Voting rules might also grant veto power to one or more agents. For example, each of the five permanent members of the fifteen member United Nations Security Council has the power to veto resolutions on particular matters. Any collective choice must therefore have the approval of all five permanent members.

The different voting rules are not simply different methods of arriving at the same social choice. Rather, the result of an election depends critically on the voting rule that is used. In fact, an alternative that is the social choice according to one voting rule might be the least preferred under another. For instance, consider alternatives x , y , and z and seven voters, three who prefer x to y to z , two who prefer y to z to x , and two who prefer z to y to x . By pairwise majority voting, x loses to both y and z . In contrast, x beats both y and z in a plurality vote. This suggests that in order to determine which voting rule to use, one must carefully analyze the various resulting outcomes.

To this end, it is useful to identify criteria that allow one to discriminate among the different outcomes produced under various voting rules. There are two main methods of doing this: efficiency and egalitarianism.

Welfare Economics

The analysis of efficiency and egalitarianism of a social state is among the objectives of a discipline called welfare economics. The first criterion for efficiency used by welfare economists dates back at least to Jeremy Bentham [2] and is known as utilitarianism. According to utilitarianism, the social interest is judged in terms of the total utility of a community. For example, if by moving from arrangement A to arrangement B Mr 1 benefits more than Ms 2 suffers, then the movement from A to B is judged as a so-

cial welfare improvement. Notice that in order to implement this criterion, the satisfaction intensities of different individuals must be comparable. In the 1930s this criterion was criticized by Lionel Robbins [35] and other welfare economists who claimed that the comparison of utilities across individuals has no scientific basis. In the 1940s a new criterion was developed which required no comparison of individual utilities: the Pareto criterion. A social outcome is said to be Pareto Optimal (Pareto Efficient) if there is no other outcome that would benefit at least one individual without hurting anyone else. Consider a scenario where ten dollars must be split among two individuals who value money and there are two alternatives: either person 1 receives five dollars, person 2 four and the remaining dollar is thrown away, or both receive five dollars. Clearly, the first alternative is not Pareto Optimal because person 2 can be made better off and person 1 would remain as well off if 2 is given the dollar that is being thrown away. Notice that the first alternative is also non utilitarian; in fact, the sum total of utilities can not be maximized when valuable resources are thrown away. However, a drawback of this efficiency criterion is that there exist multiple non comparable Pareto Optimal outcomes: any division of the ten dollars among the two individuals is Pareto Optimal as long as no money is thrown away, since to make one person better off one would have to take resources away from the other person. Hence, the Pareto Optimality criterion does not allow one to distinguish among multiple outcomes. Finally, notice that Pareto Optimal outcomes can be extremely non egalitarian: person 1 receiving ten dollars and person 2 zero is an unequal but Pareto Efficient division.

An alternative criterion often used to discriminate among social outcomes is egalitarianism, which focuses on the distribution of welfare across members of a society. One of the abstract principles behind egalitarianism is *the veil of ignorance* [18,19,33]. Consider a situation in which two persons must share a cake. Pareto Optimality does not help in selecting a division: as in the ten dollars example, any division of the cake is Pareto Optimal. Suppose that one of the two persons sharing the cake is asked to cut it in two without knowing a priori which piece she will receive. Her ignorance about which piece she will receive makes her cut the cake in two equal shares, an egalitarian division. Notice that there are a number of ways to define egalitarian outcomes. For example, Rawls’s [33] *maximin rule* suggests that the social objective should be to maximize the welfare of the worst-off individual. Finally, notice that an egalitarian outcome might be extremely inefficient. Returning to the ten dollar example, an arrangement where person 1 is given nine dollars and person 2 one dollar is

not as egalitarian as one where both are given two dollars, though the latter does not make use of more than half of the available resources.

Arrow's Impossibility Theorem

Ideally, one would like to use the normative criteria of social efficiency and egalitarianism to discriminate between different voting rules and select the best one. However a general result known as *Arrow's Impossibility Theorem* [1] shows mathematically that this is impossible. In his seminal work, Arrow shows that there is no voting mechanism that generates a social consensus on the ordering of the different alternatives while satisfying a number of axioms, among which are the weakest forms of efficiency and egalitarianism: Pareto Optimality and No Dictatorship. The latter, which states that no individual always determines preferences of society, is a weak form of egalitarianism. While a non-dictatorial society can be quite unequal, any egalitarian society must be non-dictatorial.

A number of possibility results have been obtained by the relaxation of some of Arrow's axioms. For example, pairwise majority voting with a particular restriction on individual tastes, which violates what Arrow called Unrestricted Domain, satisfies Pareto Optimality and No Dictatorship, while generating an ordering of the social alternatives.

Black [4] noticed that pairwise majority voting produces an outcome that is not subject to Condorcet's paradox when individual preferences are single-peaked: every individual must have a most preferred alternative (*bliss point*) and between any two alternatives he prefers the one that is closer to his bliss point. An important result in voting theory, called the median voter theorem, shows that when individuals' preferences satisfy this condition, the bliss point of the *median voter* beats any other alternative by pairwise majority voting. The median voter is found by ordering voters according to their bliss points. The importance of this theorem derives from its ability to describe how democracies work in practice. It is commonly observed that candidates try to appeal to voters who are politically moderate, or "in the middle": this is consistent with the theory, which suggests that these are the preferences that will eventually prevail in a democratic system.

Political Ignorance and the Condorcet Jury Theorem

As mentioned earlier, voting is not only a way to aggregate conflicting preferences but it is also a way to aggregate individual, possibly conflicting, information when preferences are partially or totally aligned. This is the case in *common value* settings. When people would agree on the

best choice if given the same information on alternatives, but differ in the information they actually receive, a natural question is which is the voting mechanism that aggregates information in a way that maximizes the probability of the right decision being made. A result called *Condorcet Jury Theorem* [9] shows that among all the possible voting rules, simple majority rule guarantees that the right decision is made under three crucial assumptions: that each voter has a correct belief with a probability higher than 50%, the voter votes according to his belief, and that the electorate is very large. Before going into the details of the theorem, it must be mentioned that this result has a practical importance. A number of works document that voters are ignorant over both policy and candidate alternatives over which they are to vote. [7] claim that "many people know the existence of few if any of the major issues of policy", while [12] discusses "mass political ignorance" and "mass political apathy" as playing key roles throughout the history of American politics. More recently, the 2004 *American National Election Study* found that Americans performed extremely poorly when asked simple questions about the political system and the leaders in charge of it. This evidence is in favor of what is called *political ignorance*. In a setting where voters are politically ignorant, the Condorcet Jury Theorem provides a valuable insight as to how much political information matters in determining the outcome.

Consider a committee who has to elect an administrator out of two candidates, one "good" and one "bad." Assume that all the members of the committee share the same preferences: they all prefer the good administrator to be selected. Individuals differ, however, in the information they have about which candidate is the good one. Suppose that each voter has a belief about which is the good candidate and votes according to his belief. If each voter has a correct belief with probability higher than 50%, then by the Law of Large Numbers as the number of voters becomes very large the probability that more than half of the electorate votes for the right candidate goes to one. Hence, under simple majority the probability that the right choice is made goes to one. Condorcet's conclusion is that in a common value setting a democratic decision is superior to an individual decision, because each voter makes the wrong decision with a non-negligible positive probability, whereas the population as a whole makes the right decision almost always. As far as political ignorance is concerned, this result shows that it is not necessary for an electorate to be well informed for it to make the right decision. So long as each voter has a correct belief with a probability higher than a half, the electoral outcome will almost always be identical to one in which the electorate

was perfectly informed. Therefore, Condorcet's result implies that the ignorance of individual voters is overcome by the aggregation of information in an election.

Gibbard–Satterthwaite Theorem

Thus far, citizens have been treated as if they disregard any tactical considerations when faced with a voting decision. However, a citizen might find it worthwhile to misrepresent his true preferences in order to achieve a social outcome more preferred than the one that would result if he voted naively. Consider an election in which a status quo will be replaced if a simple majority agrees on one of three candidates. Suppose the status quo is a conservative government, and the three alternative candidates to be voted for are a conservative, a moderate and a liberal. Imagine that there are only three voters, and two votes have already been cast: one is for the moderate candidate, one is for the conservative one. Suppose that the last individual who is called to vote is politically liberal. He knows that if he votes for his truly most preferred candidate, the liberal one, there would be a tie and the status quo conservative government would not be replaced. However, by voting for his second most preferred alternative, the moderate candidate, he would break a tie and the status quo government would be replaced with a moderate one. A liberal voter prefers this outcome to the one where conservatives win. Therefore he has an incentive to misrepresent his true preferences and vote tactically for his second-best alternative.

A powerful result in voting theory called Gibbard–Satterthwaite theorem [17,36] shows formally that in most electoral settings at least one citizen has an incentive to vote tactically. Define a *social choice function* as a mapping of all individuals' preferences into a collective choice. The theorem states that there is no social choice function that is Non Dictatorial and Non Manipulable, i. e. such that no agent has an incentive to vote tactically. Consequently, for every voting rule there is at least one agent with an incentive to misrepresent her preferences.

It should be mentioned that the Gibbard–Satterthwaite theorem places also other technical restrictions. Furthermore, in a setting such as a majority vote, a misrepresentation of one's true preferences coincides with voting for an alternative which the voter does not rank top. In the original formulation of their theorem, however, Gibbard and Satterthwaite dealt with mechanisms where agents are required to submit a ranking over all alternatives, and a misrepresentation of tastes in their framework does not coincide necessarily with a misrepresentation of only the most preferred alternative (see [26]).

This result suggests that for a deep understanding of voting one should not focus only on the assumption that citizens vote sincerely. Tactical voting is not only an abstract possibility, it is also an actual behavior that must be considered in any voting analysis. The following sections explore how the literature on voting has dealt with strategic voting.

Political Competition and Strategic Voting

The early works of Downs [10] and Tullock [39] initiated the analysis of political issues within a strategic framework, where voters and/or candidates are assumed to be rational decision makers. *Political competition* describes a situation in which candidates strategically position themselves in order to win an election, whereas *strategic voting* refers to individuals' decision to vote so to maximize utility by sometimes misreporting true preferences. This game theoretical framework developed due to positive arguments such as Gibbard–Satterthwaite theorem, which suggests that voters have an incentive to behave strategically, and is also due to spread of game theory as a dominant tool in economic analysis.

Political Competition

The classic model analyzing the candidates' choice of positioning on the political spectrum is that of Downs [10], who adapted the classical *Hotelling model* [21] to the analysis of the choice of political platforms by candidates. In the *Downsian model of political competition*, there is a unidimensional policy space, representing the political spectrum. There are two candidates who position themselves on this policy space. Each voter has a most preferred point on this space and prefers points closer to this point than those further away, i. e. each voter has single-peaked preferences. Downs argues that strategic candidates concerned only with winning position themselves at the point that is most preferred by the median voter. If candidate *A* were positioned anywhere else, say to the left of the median voter, candidate *B* could get the majority of votes by positioning himself between candidate *A* and the median voter; all the agents to the right of *B*, constituting more than half of the voters, would prefer *B* to *A*. Given this scenario, candidate *A* (for the same reason) would then have an incentive to position himself between *B* and the median voter, and so on. Hence, the result is that both candidates position themselves at the policy platform most preferred by the median voter. An interesting implication of this result is that under a democracy with two parties, both parties act identically, and therefore there are only as many positions (just one) taken by political parties as there

would be in a dictatorship. However, it is crucial that two parties exist so that the competition between them can allow the chosen policy point to represent the preferences of the voters. This is in contrast to a dictatorship in which the ruling party can implement its own preferred policy without voter approval.

Notice that the example above assumes a two-party system (for models that allow for more than two parties see [3,29]). [11] posits that in a representative democracy with a plurality voting rule, only two parties compete in the elections. This theory, known as *Duverger's Law*, states that a *proportional representation system*, in which parties gain seats proportional to the number of votes received, fosters elections with numerous parties. In contrast, a plurality system marginalizes smaller parties and results in only two parties entering into political competition.

The Decision to Vote: the Paradox of Voting

Another issue raised by Downs, one which focuses on voters' behavior rather than candidates', is known as *the paradox of voting*. It refers to the fact that in a large election, the probability that any single vote determines the outcome is vanishingly small. If every person only votes for the purpose of influencing the outcome of the election, even a small cost of voting would be sufficient to dissuade anyone from voting. Yet, it is commonly observed that turnout is very high, even in large elections. From the large empirical literature on turnout in elections, some facts seem to be acquired knowledge: (1) turnout is higher in more important elections (e. g. Presidential election in the US have a significantly higher turnout than Gubernatorial elections), (2) turnout is generally higher in close elections (i. e. with smaller margins of victory), and (3) turnout rates are different among groups with different demographic characteristics. For instance, from the thorough work by [41], it emerges that education has a substantial effect on the probability that one will vote. Income has less of an effect once it has been controlled for the impact of other variables. After education, the second most important variable is age, which appears to have a strong positive relationship with turnout. Other socio-economic variables are also important; in particular, racial minorities appear to be less likely to vote. Finally, turnout seems to be significantly influenced by factors such as the weather conditions on the day of the election and voters' distance from the polls (see [8]).

Such comparative statics suggest that it is appropriate to model voters' behavior as a rational choice problem within a standard utility maximization framework. The modern theory of voting applies the classic utilitarian

framework to the voting problem, positing that agents decide whether or not to vote by comparing the *cost of voting* with the *utility of voting*. The traditional starting point for the modern theory of voting is [34], who formalize the insights of [10] and [39] in a simple utilitarian model of voting. The *cost of voting* comprises any sacrifice in utility that voting entails. The *utility of voting* is usually divided into two components: a *non-instrumental* component and an *instrumental* component. The *non-instrumental* component includes utility derived from the mere act of voting and not related to the actual outcome of the election. It may include, for instance, the sense of civic duty. There is considerable evidence that voters are motivated by a sense of civic duty (see, for example, [5]). The *instrumental* component is the utility of the outcome a voter induces if her vote determines the outcome, weighted by the probability that her vote actually determines the outcome.

The instrumental component of the utility of voting has attracted most of the attention in the literature. It is typically analyzed through the rational theory of voting, which is motivated by an empirical observation: there exists a strong positive correlation between turnout rate and closeness of the election. This fact suggests that, *ceteris paribus*, voters are more likely to vote if their vote is more likely to make a difference. The main theoretical problem is to endogenize the probability that each voter is pivotal, i. e. that his vote is determinant for the outcome of the election.

Ledyard [23,24] are among the early works in the literature on game theoretical models of the pivotal-voter. In these models, voters infer the probability of being pivotal from the equilibrium strategies of other voters. Subsequently, they decide whether or not to vote, trading off the cost of voting with the expected (instrumental) utility of voting. Although Ledyard did not focus on the magnitude of turnout in a strategic model, this question is addressed by Palfrey and Rosenthal ([30,31]) who model elections with uncertainty about the total number of voters. Voters strategically choose whether or not to vote for their favorite alternative amongst two candidates. However, Palfrey and Rosenthal's theories do not explain high turnout in large elections, when the cost of voting is not very (and unrealistically) low.

Ultimately, the game-theoretic approach to costly voting could not escape the *paradox of voting*. Since the probability of being pivotal is very small in large elections, the individual incentives to vote cannot justify high turnouts unless the cost of voting is sufficiently small. Conversely, regardless of how small the cost of voting is, the theory posits that there should be low turnout as the election becomes arbitrarily large, which is in contrast to empirical

evidence. The puzzle that remains open is how to reconcile the evidence of high turnout in large elections with the responsiveness of turnout levels to the closeness of the election.

Mobilization and Group-Based Notion of Welfare

Two strands of the literature try to overcome the paradox of voting by focusing on groups of like-minded people rather than on individual agents. These are models of *mobilization* and models incorporating a *group based* notion of welfare.

In models of mobilization, the population of voters is assumed to be divided into groups, each of which has a leader who has the same preferences as all agents in the group and coordinates their behavior. The turnout decision within each group is determined by how the leaders allocate costly resources to voters. It is as if leaders buy the votes of the agents in their group, compensating for the agents' costs of voting. Since leaders influence a large number of voters, their decisions have a non-negligible impact on the probability of affecting the electoral outcome and consequently, on the individual instrumental benefit from voting. [37,38] test group based models and provide some empirical support for the mobilization thesis. (see also [27,28,40]). The problem for models of mobilization is that it is not clear how leaders affect the individual behavior of voters.

Models of *group based welfare* consider groups of like-minded individuals whose actions are intended not to maximize their individual utilities, but rather that of the group (see [22,25]). In this case, there is no leader who prescribes behavior as in mobilization models, but instead there is an implicit understanding among agents in the group on appropriate behavior. This idea is developed by [16], who appeal to [20] *Group Rule-Utilitarian Theory* to endogenize the *non-instrumental component* of the utility from voting in a way that preserves the positive relation between closeness of the election and incentive to vote typical of the classic *pivotal-voter models*. In this model, agents derive utility from "doing their part": in the spirit of [20], this is understood to mean following the rule that, when followed by all the agents in a given group, would maximize some measure of the group's utility. The outcome is a set of rules for each group, which are mutually optimal (from the point of view of the group) given that individuals follow the rules within their group. Abstention still occurs because for some agents (those with higher costs of voting) the rule prescribes not to vote, since their contribution to increase the group's utility from the election's outcome does not compensate the increase in the

group's total cost of voting. [8] provide some empirical support to the group rule.

The Common Value Setting with Strategic Agents

Feddersen and Pesendorfer [13,14] consider the Condorcet Jury Theorem in a strategic setting and reach a different conclusion than Condorcet. They model a voting problem in an almost common value setting as a game, that is, as a situation where agents interact strategically. The following simple example provides the basic insights of their model: suppose that there are three voters, 1, 2 and 3, and two candidates, *A* and *B*. Suppose that voter 1 is an *A-partisan*, meaning he prefers candidate *A* in all states of the world. Agents 2 and 3 instead prefer candidate *A* in state s_A and candidate *B* in state s_B . Let p be the probability of state s_A and $1 - p$ the probability of s_B . Now, suppose that agent 2 is informed, i. e. he knows the state of the world before voting, while agent 3 is not. Finally, suppose that there is no cost of voting and that the election is decided by simple majority rule. In this situation, agent 1 votes for *A*, agent 3 for *B*, and agent 2 for *A* if he observes s_A and for *B* if he observes s_B . To understand why the uninformed agent 3 votes for *B*, notice that by doing so the outcome is that *A* is always selected in state s_A , while *B* is always selected in state s_B . This is clearly the best outcome for agent 3, and in all states this is also the best outcome for the majority of the population. In fact, if the true state is s_A , *A* is selected, which is preferred to *B* by all voters; if the true state is s_B , *B* is selected, which is preferred to *B* by two voters out of three.

The uninformed agent in the example votes for *B* no matter what the prior probability p is, even if p is close to one, that is, even if he is almost sure that *A* is the right candidate. By voting for *B* individual 3 counterbalances the *A-partisan's* vote, thereby allowing the informed voter (2) to induce the "right" outcome with probability one. In Condorcet's argument, if voters vote according to their belief about the state of the world, information is aggregated in a way that induces the right social choice to be made. In this setting, where preferences are only partially aligned, information is aggregated so as to always generate the decision that is preferred by the majority of the population only if uninformed voters vote strategically. In this setting, if voters vote sincerely, as is assumed by Condorcet, the result that the aggregation of information taking place during an election delivers the "right" social choice does not hold. In Feddersen and Pesendorfer's framework it is strategic voting that induces the "correct" social choice. This is the major difference with Condorcet's result, which was driven by the assumption of sincere voting.

Recognizing the strategic incentives that voters may have in an election, Feddersen and Pesendorfer [15] apply a similar analysis to the unanimity rule in juries. They find that in the context of a common value setting, unanimity voting might result in convicting the innocent more often than other rules because strategic jurors consider the probability of being pivotal (like voter 3 in the example) and make their decisions conditional on being pivotal.

Now suppose there is another voter, 4, who is uninformed and shares the same preferences as 2 and 3. In this setup, even with a zero cost of voting agent 4 would abstain, so that the informed voter is pivotal with probability one. Voter 4's behavior is known as *strategic abstention*: the act of abstaining by uninformed voters not because voting is costly, but because by doing so they allow the informed voters to be pivotal. By abstaining, uninformed voters in effect delegate the decision to the informed voters. In the example, voter 4's strategic abstention allows for information equivalence to arise: making voter 4 informed would not change the outcome of the election, as long as 4 strategically abstains so that the informed voter determines the outcome. Notice that this result is in the same spirit as Condorcet's Jury Theorem's result: there, having each voter's belief accurate with a probability slightly higher than 50% or substantially higher than 50% does not make a difference. As long as voters vote according to their belief, the outcome is the same no matter what the underlying belief accuracy is (as long as it is greater than a half). Although for different reasons, in both Condorcet's setting and Feddersen and Pesendorfer's model (under some circumstances) the aggregation of information that takes place during an election ensures that the outcome of the election does not vary if the electorate is made more informed.

Future Directions

There are a number of open questions in the literature on voting. As mentioned in earlier sections, at the time of writing there is no universally accepted theory of turnout. In particular, no theory delivers all of the relevant comparative statics observed empirically, that is, the variability of turnout across elections of difference size, importance, and closeness. Broadly speaking, one may say that the behavior of voters is still only partially understood. Whether voters vote based on strategic considerations or vote without regard to how other citizens might be voting is an unsettled issue. Furthermore, individuals' choices in hypothetical and real situations might differ. The act of voting in large elections is almost a hypothetical choice, in that the likelihood that a vote determines the outcome is negli-

ble. An open question then is whether voters choose candidates as they would in a real situation or as they would in a hypothetical situation. As far as empirical work is concerned, little seems to be known of the empirical impact of political ignorance on the outcome of elections. Also, an issue that is both empirical and theoretical and has not been satisfactorily addressed is what types of election rules are best suited for different decisions. Finally, although much has been written on the origins and evolution of democracies, there is no general consensus as to what are the possible reasons of democracies historical evolution. As is clear from this section, many interesting questions in politics have not yet been satisfactorily answered, leaving space for future research.

Bibliography

Primary Literature

1. Arrow KJ (1950) A difficulty in the concept of social welfare. *J Political Econ* 58(4):328–46
2. Bentham J (1789) An introduction to the principles of morals and legislation. Payne, London
3. Besley T, Coate S (1997) An economic model of representative democracy. *Quart J Econ* 112(1):85–114
4. Black D (1948) The decisions of a committee using a special majority. *Econometrica* 16(3):245–61
5. Blais A (2000) To vote or not to vote: The merits and limits of rational choice theory. University of Pittsburgh Press, Pittsburgh
6. Borda J (1781) Mathematical derivation of an election system. *Isis* 44(1–2):42–51
7. Campbell A, Converse PE, Miller WE, Stokes DE (1960) The American voter. Wiley, New York
8. Coate S, Conlin M (2004) A group-rule utilitarian approach to voter turnout: Theory and evidence. *Am Econ Rev* 95(5):1476–1504
9. Condorcet M (1785) Essai sur l'application de l'analyse a la probabilité des décisions rendues a la pluralité des voix. L'Imprimerie Royale, Paris. English translation by Baker (1976) Chelsea, New York
10. Downs A (1957) An economic theory of democracy. Harper, New York
11. Duverger M (1972) Factors in a two-party and multiparty system. In: *Party Politics and Pressure Groups*. Crowell Company, New York, pp 23–32
12. Dye TR, Zeigler TH (1970) The irony of democracy, an uncommon introduction to american politics. Duxbury, Belmont
13. Feddersen T, Pesendorfer W (1996) The swing voter's curse. *Am Econ Rev* 86(3):408–424
14. Feddersen T, Pesendorfer W (1997) Voting behavior and information aggregation in elections with private information. *Econometrica* 65(3):408–424
15. Feddersen T, Pesendorfer W (1998) Convicting the innocent: The inferiority of unanimous jury verdicts. *Am Political Sci Rev* 92:23–35
16. Feddersen T, Sandroni A (2006) Theory A of participation in elections. *Am Econ Rev* 96(4):1271–1282

17. Gibbard A (1973) Manipulation of voting schemes. *Econometrica* 41:587–601
18. Harsanyi JC (1953) Cardinal utility in welfare economics and the theory of risk-taking. *J Political Econ* 61:434–435
19. Harsanyi JC (1977) Rational behavior and bargaining equilibrium in games and social situations. Cambridge University Press, New York
20. Harsanyi JC (1980) Rule utilitarianism, rights, obligations and the theory of rational behavior. *Theory Decis* 12(1):115–33
21. Hotelling H (1929) Stability and competition. *Econ J* 39(1): 41–57
22. Kinder DR, Kiewiet DR (1979) Economic discontent and political behavior: The role of personal grievances and collective economic judgements in congressional voting. *Am J Political Sci* 23(3):495–527
23. Ledyard J (1981) The paradox of voting and candidate competition: A general equilibrium analysis. In: Hoorwich G, Quick JP (eds) *Essays in Contemporary Fields of Economics*. Purdue University Press, Lafayette, pp 54–80
24. Ledyard J (1984) The pure theory of two candidate elections. *Public Choice* 44(1):7–41
25. Markus G (1988) The impact of personal and national economic conditions on the presidential vote: A pooled cross-sectional analysis. *Am J Political Sci* 32(1):137–54
26. Mas-Colell A, Whinston M, Green J (1995) *Microeconomic theory*. Oxford University Press, Oxford
27. Morton R (1987) Group majority a model of voting. *Social Choice and Welfare* 4(2):117–31
28. Morton R (1991) Groups in rational turnout models. *Am J Political Sci* 35:758–76
29. Osborne MJ, Slivinski A (1996) Model a of political competition with citizen-candidates. *Quart J Econ* 111(1):65–96
30. Palfrey T, Rosenthal H (1983) A strategic calculus of voting. *Public Choice* 41(1):7–53
31. Palfrey T, Rosenthal H (1985) Voter participation and strategic uncertainty. *Am Political Sci Rev* 79(1):62–78
32. Persson T, Tabellini G (2001) *Political economics*. Press MIT, Boston
33. Rawls J (1971) *A theory of justice*. Harvard University Press, Cambridge
34. Riker W, Ordeshook P (1968) A theory of the calculus of voting. *Am Political Sci Rev* 62:25–42
35. Robbins L (1938) Interpersonal comparisons of utility: A comment. *Econ J* 48(192):635–41
36. Satterthwaite M (1975) Strategy-proofness and Arrow's conditions: Existence and correspondence theorems for voting procedures and social welfare functions. *J Econ Theory* 10: 187–217
37. Schram A (1991) *Voter behavior in economic perspective*. Springer, Heidelberg
38. Shachar R, Nalebuff B (1999) Follow the leader: Theory and evidence on political participation. *Am Econ Rev* 89(3):525–47
39. Tullock G (1967) *Towards a mathematics of politics*. The University of Michigan Press, Ann Arbor
40. Uhlaner C (1989) Rational turnout: The neglected role of groups. *Am J Political Sci* 33(2):390–422
41. Wolfinger, Rosenstone (1980) *Who votes?* Yale University Press, New Haven

Books and Reviews

- Arrow KJ (1951) *Social choice and individual values*. Wiley, New York
- Arrow KJ, Sen AK, Suzumura K (eds) (2002) *Handbook of social choice and welfare*, vol 1. Elsevier, Amsterdam
- Austen-Smith D, Banks JS (1999) *Positive political theory I: collective preference*. The University of Michigan Press, Ann Arbor
- Cox GW (1997) *Making votes count: strategic coordination in the world's electoral systems*. Cambridge University Press, Cambridge
- Dummett M (1984) *Voting procedures*. Clarendon Press, Oxford
- Duverger M (1959) *Political parties: their organization and activity in the modern state*. Methuen and Co. Ltd, London
- Dworkin R (1981) What is equality? Part 2: Equality of resources. *Phil and Public Affairs* 10:283–345
- Feddersen T (2004) Rational choice theory and the paradox of not voting. *J Econ Perspect* 18(1):99–112
- Katz RS (1997) *Democracy and elections*. Oxford University Press, Oxford
- McLean I (1987) *Public choice: An introduction*. Basil Blackwell Inc., New York
- Milnor AJ (1969) *Elections and political stability*. Little, Brown, Boston
- Myerson R (2000) Large poisson games. *J Econ Theory* 94(1):7–45
- Mueller DC: *Public choice II* (1989) A revised edition of *Public Choice*. Cambridge University Press, Cambridge
- Niemi RG, Weisberg HF (eds) (1972) *Probability models of collective decision making*. Charles Merrill Publishing E company, Columbus
- Ordeshook PC (1986) *Game theory and political theory: An introduction*. Cambridge University Press, Cambridge
- Ordeshook PC (ed) (1989) *Models of strategic choice in politics*. The University of Michigan Press, Ann Arbor
- Rawls J (1958) Justice as fairness. *Phil Rev* 67(2):164–194
- Riker WH (ed) (1993) *Agenda formation*. The University of Michigan Press, Ann Arbor
- Sen AK (1973) *On economic inequality*. Oxford University Press, Oxford
- Sen AK (2002) *Rationality and freedom*. The Belknap Press of Harvard University Press, Cambridge
- Tidean N (2006) *Collective decisions and voting: The potential for public choice*. Ashgate, Burlington
- Tullock G (1998) *On voting*. Edward Elgar Publishing, Northampton

Voting Procedures, Complexity of

OLIVIER HUDRY

École Nationale Supérieure des Télécommunications,
Paris, France

Article Outline

[Glossary](#)

[Definition of the Subject](#)

[Introduction](#)

[Common Voting Procedures](#)

[Complexity Results](#)

Further Directions
Acknowledgments
Bibliography

Glossary

Condorcet winner A candidate is a Condorcet winner if he or she defeats any other candidate in a one-to-one matchup. Such a candidate may not exist; at most, there is only one. Though it could seem reasonable to adopt a Condorcet winner (if any) as the winner of an election, many common voting procedures bypass the Condorcet winner in favor of a winner chosen by other criteria.

Majority relation, strict majority relation In a pairwise comparison method, each candidate is compared to all others, one at a time. If a candidate x is preferred to a candidate y by at least $m/2$ voters (a majority), where m denotes the number of voters, x is said to be preferred to y according to the majority relation. The strict majority relation is defined in a similar way, but with $(m + 1)/2$ instead of $m/2$. If there is no tie, the strict majority relation is a tournament, i.e., a complete asymmetric binary relation, called the majority tournament.

Preference, preference aggregation A voter's preference is some relational structure defined over the set of candidates. Such a structure depends on the chosen voting procedure, and usually ranges between a binary relation on one extreme and a linear order on the other. Given a collection, called a profile, of individual preferences defined on a set of candidates, the aggregation problem consists in computing a collective preference summarizing the profile as well as possible (for a given criterion).

Profile A profile $\Pi = (R_1, R_2, \dots, R_m)$ is an ordered collection (or a multiset) of m relations R_i ($1 \leq i \leq m$) for a given integer m . As the relations R_i can be the same, another representation of a profile Π consists in specifying only the q relations R_i which are different, for an appropriate integer q , and the number m_i of occurrences of each relation R_i ($1 \leq i \leq q$): $\Pi = (R_1, m_1; R_2, m_2; \dots; R_q, m_q)$.

Social choice function, social choice correspondence

A social choice function maps a collection of individual preferences specified on a set of candidates onto a unique candidate, while a social choice correspondence maps it onto a nonempty set of candidates. This provides a way to formalize what constitutes the most preferred choice for a group of agents.

Voting procedure, voting theory A voting procedure is a rule defining how to elect a winner (single-winner election) or several winners (multiple-winner election) or to rank the candidates from the individual preferences of the voters. Voting theory studies the (axiomatic, algorithmic, combinatorial, and so on) properties of the voting procedures designed in order to reach collective decisions.

Definition of the Subject

One main concern of voting theory is to determine a procedure (also called, according to the context or the authors, *rule, method, social choice function, social choice correspondence, system, scheme, count, rank aggregation, principle, solution* and so on), for choosing a winner from among a set of candidates, based on the preferences of the voters. Each voter's preference may be expressed as the choice of a single individual candidate or, more ambitiously, a ranked list including all or some of the candidates. Such a situation occurs, obviously, in the field of social choice and welfare (for a broader presentation of the field of social choice and welfare, see for instance [4,7,8,9,14,17,67,75,97,101,136,143,154]) and especially of elections (for more about voting theory, see [27,63,107,109,110,125,141,156,167,168,169]), but also in many other fields: games, sports, artificial intelligence, spam detection, Web search engines, Internet applications, statistics, and so on.

For a long time, much attention has been paid to the axiomatic properties fulfilled by different procedures that have been proposed. These properties are important in choosing a procedure, since there is no "ideal" procedure (see next section). More recently, in the late 1980s and the early 1990s, the question has arisen regarding the relative difficulty of computing winners according to a given procedure. (The first to study the question may have been J. Orlin in 1981 [142]; for a recent introduction to computational social choice, see [38].) From a practical point of view, it is crucial to be able to announce the winner in a "reasonable" time. This raises the question of the complexity of voting procedures, which should be taken into account to the same extent as their axiomatic characteristics.

Below, we will detail the complexity results of several procedures: plurality rule (one-round procedure), plurality rule with run-off (two-round procedure), preferential voting procedure (STV), Borda's procedure, Nanson's procedure, Baldwin's procedure, Condorcet's procedure, Condorcet–Kemeny problem, Slater problem, prudent orders (G. Köhler, K.J. Arrow and H. Raynaud), maximin procedure (P.B. Simpson), minimax procedure

(K.J. Arrow and H. Raynaud), ranked pairs procedure (T.N. Tideman), Copeland's procedure, the top cycle solution (J.H. Smith), the uncovered set solution (P.C. Fishburn, N. Miller), the minimal covering set solution (B. Dutta), Banks's solution, the tournament equilibrium set solution (T. Schwartz), Dodgson's procedure, Young's procedure, approval voting procedure, majority-choice approval procedure (F. Simmons), and Bucklin's procedure. Sect. "[Introduction](#)" is devoted to a historic overview and to basic definitions and notation. The common voting procedures are depicted in Sect. "[Common Voting Procedures](#)". Sect. "[Complexity Results](#)" specifies the complexity of these procedures. Other considerations linked to complexity in the field of voting theory can be found in Sect. "[Further Directions](#)".

Introduction

The Search for a "Good" Voting Procedure, from Borda to Arrow

It is customarily agreed that the search for a "good" voting procedure goes back at least to the end of the eighteenth century, to the works of the chevalier Jean-Charles de Borda (1733–1799) [24], and of Marie Jean Antoine Nicolas Caritat, marquis de Condorcet (1743–1794) [31] (for references upon the historical context, see [7,17,23,80,81,119,120,121,122,123,124] and references below).

In the 1770s in the 1780s, J.-C. de Borda [24], a member of the French Academy of Sciences, showed that the plurality rule used at that time by the academy was not satisfactory. Indeed, with such a voting procedure, the winner could be contested by a majority of voters who would all agree to choose another candidate over the elected winner. (We may notice that the plurality rule with run-off used in many countries has the same defect.) Borda then suggested another procedure (see below). But, as pointed out by Condorcet in 1784 [31], the procedure advocated by Borda had the same defect as the one depicted by Borda himself for the plurality rule: a majority of dissatisfied voters could agree to constitute a majority coalition against the candidate elected by Borda's procedure in favor of another candidate. Condorcet then designed a method based on pairwise comparisons. By nature, this method cannot elect a winner who will give rise to a majority coalition against him or her. But, unfortunately, Condorcet's method does not always succeed in finding a winner. If such a winner does exist, i.e., if there exists a candidate who defeats any other candidate in such a pairwise comparison, then this candidate is said to be a *Condorcet winner*; if he or she exists, a Condorcet winner is unique. Actually, the Academy of Sciences decided to adopt Borda's

method (until 1803). By the way, notice that, according to I. McLean, H. Lorrey and J. Colomer [124], "both Ramon Llull (ca 1232–1316) and Nicolaus of Cusa (also known as Cusanus, 1401–1464) made contributions which have been believed to be centuries more recent. Llull promotes the method of pairwise comparison, and proposes the Copeland rule to select a winner. Cusanus proposes the Borda rule, which should properly be renamed the Cusanus rule". Despite these historical discoveries, we shall keep the usual names.

After these seminal works, in spite of some works by the Swiss Simon Lhuillier (1750–1840) [112] (see also [128]), the Spanish Joseph Isidoro Morales [139], the French Pierre Claude François Daunou (1761–1840) [54] and Pierre Simon, marquis de Laplace (1749–1827) [105], who, through a slightly different approach, rediscovered Borda's procedure, it seems that the history of the theory of social choice slowed down and almost disappeared until the 1870s or even the 1950s (see [23]). In the 1870s, the English reverend Charles Lutwidge Dodgson (1832–1898), also (or maybe better) known as Lewis Carroll, proposed a voting system in which the winner is the candidate who becomes a Condorcet winner with the fewest appropriate changes in voters' preferences [58,59,60]. Some years later, another English mathematician, Edward J. Nanson (1850–1936) [140] on the one hand, and the Australian Joseph M. Baldwin (1878–1945) [11] in 1926 on the other hand, slightly modified Borda's method by iteratively eliminating some candidates until only one remains.

None of these methods is utterly satisfactory when we consider the properties which are usually considered desirable. In 1951 and 1963, Kenneth J. Arrow [7] shows that there does not exist a "good" voting method, with respect to some "reasonable" axiomatic properties; this is known as the famous "impossibility theorem". More precisely, assuming that the preferences of the voters are complete preorders (see below; notice that the set of complete preorders includes the one of linear orders, quite often considered to model the preferences of the voters) and that the result of the voting procedure should also be a complete preorder, K.J. Arrow considered the following properties:

- Unrestricted domain or universality: the voting procedure must be able to provide a result whatever the preferences of the voters are.
- Independence of irrelevant candidates: the collective preference between candidates x and y must depend only on the individual preferences between x and y ; in other words, the collective preference between x and y must remain the same as long as the individual preferences between x and y do not change.

- Unanimity (or Pareto property): if a candidate x is preferred to another candidate y by all the voters, then x must be preferred to y in the collective preference, too.

K.J. Arrow showed that, if there are at least three candidates (things are much more comfortable with only two candidates!) and at least two voters, the only procedure which satisfies all these conditions at once is the dictatorship, in which one voter (the dictator) imposes his or her preference. Though this impossibility theorem ruins the hope of designing a voting procedure fulfilling the usual desirable properties, several procedures have been suggested since this date; we shall describe some of them below. Among ways to escape Arrow's impossibility theorem, we find the following:

- The definition of other axiomatic systems that would lead to voting procedures which would not be dictatorship.
- The restriction of individual preferences to more constrained domains.
- Adapting the result, when this one is not satisfactory with respect to the required axiomatic properties, into a result fulfilling these properties and fitting the genuine result as well as possible, for some criterion which must be defined.

The main questions associated with the first possibility are “given some axiomatic properties, what are the voting procedures satisfying these properties?” or, conversely, “given a voting procedure, what is the proper axiomatic system characterizing this procedure?”; we will not consider this direction here. The second possibility will be illustrated below, by the restriction of individual preferences to *single-peaked preferences*. The third direction was followed by J.G. Kemeny in 1959 [102], when he studied the aggregation of orders into a *median order* (see below). Notice that this approach is also attributed to Condorcet; in the sequel, we will refer the search for a median linear order as the Condorcet–Kemeny problem (as other people rediscovered this problem or some of its variants [130], the problem has also been known under other names, see [36]). Another related problem, dealing with the *majority tournament* (see below) is one, stated explicitly by P. Slater in 1961 [160], of fitting a tournament into a linear order at minimum distance. This is one of the so-called *tournament solutions* (see [106] and [138]; for references on tournaments, see also [118,134,149,150]), of which the aim is to determine a winner from a tournament. Besides the Slater solution, we shall describe other tournament solutions, such as the top cycle, the uncovered set, the minimal covering set, Banks's solution, the tournament equilibrium

set. The other common tournament solutions are polynomial or their complexities are not completely known (see [93] for more details).

Definitions, Notation and Partially Ordered Sets Used to Model Preferences

Let us assume that we are dealing with m voters who must choose between n candidates denoted x_1, x_2, \dots, x_n or x, y, z, \dots ; X denotes this set of candidates; in the following, we suppose that n is large enough. A binary relation R defined on X is a subset of $X \times X = \{(x, y) : x \in X \text{ and } y \in X\}$. We use the notation xRy instead of $(x, y) \in R$ and $x \not R y$ instead of $(x, y) \notin R$.

It is customary to represent the preferences R_i ($1 \leq i \leq m$) of m voters as an ordered collection (or a multiset) $\Pi = (R_1, R_2, \dots, R_m)$, called the *profile* of the m binary relations. Another representation of the preferences of the voters exists. Since these preferences may be the same for two different voters, we may consider only the different relations R_1, R_2, \dots, R_q arising from the opinions of the voters, where q denotes this number of different opinions. In this way, we combine all the voters sharing the same opinion. Last, if m_i ($1 \leq i \leq q$) denotes the number of voters sharing R_i ($1 \leq i \leq q$) as their preference (notice the equality $\sum_{i=1}^q m_i = m$), we associate this number m_i of occurrences with each type R_i of relations to describe Π . Then Π can be described as the set of such pairs: $\Pi = \{(R_1, m_1); (R_2, m_2); \dots; (R_q, m_q)\}$. Such a representation does represent the data more compactly when m is large with respect to n . Usually, the complexity results are the same for the two representations, because their proofs stand even if m is bounded by a polynomial in n , and in this case there is no qualitative difference between the two representations. With respect to the results stated in Sect. “Complexity Results”, there would be a difference only for the L^{NP} -completeness results of Theorems 5, 14 and 15 (which then should be replaced only by NP-hardness results). So, in the sequel, we shall consider only the first representation. Moreover, we shall assume that the preference of each voter i ($1 \leq i \leq m$) is given by a binary relation R_i defined on X , and that R_i is described by its characteristic vector (see below), which requires n^2 bits. So the size of the data set is about mn^2 .

We will consider two kinds of elections: we want to elect one candidate, or we want to rank all of them into a partially ordered set (or *poset*). One of the most common posets is the structure of linear order. Other posets can be defined from the following basic properties:

Reflexivity $\forall x \in X, xRx$;

Irreflexivity $\forall x \in X, x \not R x$;

Antisymmetry $\forall(x, y) \in X^2, (xRy \text{ and } x \neq y) \Rightarrow y\bar{R}x$;

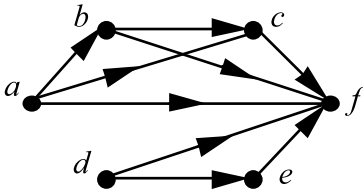
Asymmetry $\forall(x, y) \in X^2, xRy \Rightarrow y\bar{R}x$;

Transitivity $\forall(x, y, z) \in X^3, (xRy \text{ and } yRz) \Rightarrow xRz$;

Completeness $\forall(x, y) \in X^2$, with $x \neq y$, xRy or (inclusively) yRx .

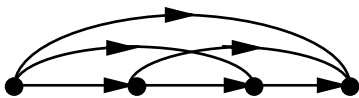
By combining the above properties, we may define different types of binary relations (see for instance [17,32,74,77]). As a binary relation R defined on X is the same as the directed graph $G = (X, R) : (x, y)$ is an arc (i. e., a directed edge; similarly, a directed cycle will be called a circuit in the sequel) of G if and only if we have xRy , we illustrate these types with graph theoretic examples (for basic references on graph theory, see [12] or [22]). It is often possible to define reflexive or irreflexive versions of the following ordered structures. But, as reflexivity and irreflexivity do not matter for complexity results (see [91]), we give below only one version among these two possibilities.

- A *partial order* is an antisymmetric (if reflexive) or asymmetric (if irreflexive) and transitive binary relation (see Fig. 1); \mathcal{O} will denote the set of the partial orders defined on X .
- A *linear order* is a complete partial order (see Fig. 2); \mathcal{L} will denote the set of the linear orders defined on X . If L denotes a linear order defined on X , we will represent L as $x_{\sigma(1)} > x_{\sigma(2)} > \dots > x_{\sigma(n)}$ for some appropriate permutation σ , with the agreement that the notation $x_{\sigma(i)} > x_{\sigma(i+1)}$ (for $1 \leq i < n$) means that $x_{\sigma(i)}$ is preferred to $x_{\sigma(i+1)}$ according to L , the relationship between the other elements of X being involved by transitivity. The element $x_{\sigma(1)}$ will be called *the winner of L*.
- A *tournament* is a complete and asymmetric binary relation (see Fig. 3); \mathcal{T} will denote the set of the tournaments defined on X ; notice that a transitive tournament



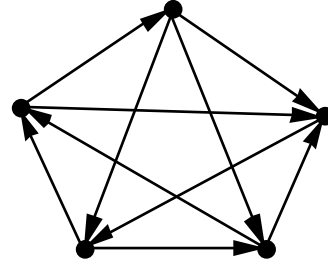
Voting Procedures, Complexity of, Figure 1

A partial order



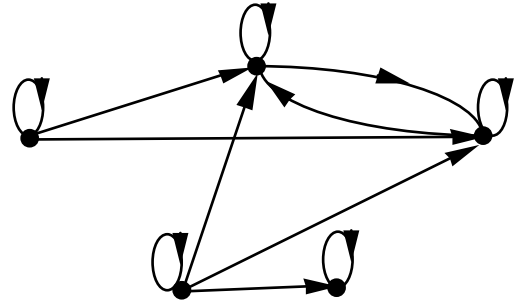
Voting Procedures, Complexity of, Figure 2

A linear order. The partial order of Fig. 1 is not a linear order, for instance because the vertices a and d are not compared



Voting Procedures, Complexity of, Figure 3

A tournament



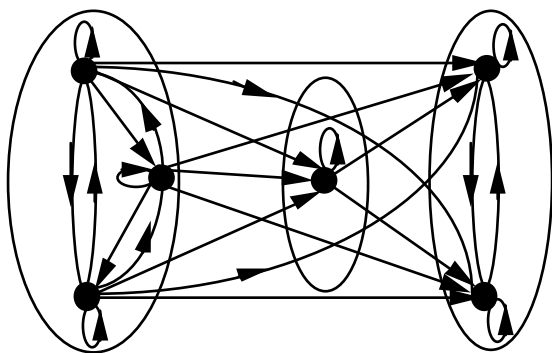
Voting Procedures, Complexity of, Figure 4

A preorder

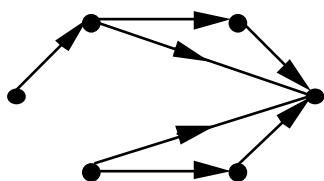
is a linear order and conversely. As a tournament may contain circuits, they are usually not considered as an appropriate structure to represent the collective preference that we seek. Tournaments will be used below to summarize individual preferences in the so-called *majority tournament*.

- A *preorder* is a reflexive and transitive binary relation (see Fig. 4); \mathcal{P} will denote the set of the preorders defined on X .
- A *complete preorder* is a reflexive, transitive and complete binary relation (see Fig. 5); \mathcal{C} will denote the set of the complete preorders defined on X .
- An *acyclic relation* (we should rather say *without circuit*, but *acyclic* is the usual term) is a relation R of which the associated graph G is without any circuit (see Fig. 6); \mathcal{A} will denote the set of the acyclic relations defined on X .

As stated above, it is possible to obtain other structures by adding or removing reflexivity or irreflexivity from the above definitions. In fact, the distinction between reflexive and irreflexive relations is not relevant from the complexity point of view: the results remain the same. Thus, in the following, we do not take reflexivity or irreflexivity into account.



Voting Procedures, Complexity of, Figure 5
A complete preorder



Voting Procedures, Complexity of, Figure 6
An acyclic relation. Its transitive closure is the partial order of Fig. 1

Other types of posets exist, obtained by considering the asymmetric parts of the previous relations (for instance, a *weak order* is sometimes defined as the asymmetric part of a complete preorder) or by adding extra structural properties (for instance to define interval orders or semiorders from partial orders). We will not consider these posets here; the interested reader is referred to [32] for their definitions and to [91] for some complexity results about them. On the contrary, we will pay attention to generic binary relations without any particular property; the set of the binary relations will be noted \mathcal{R} . We may notice several inclusions between these sets, especially the following ones: $\forall Z \in \{\mathcal{A}, \mathcal{C}, \mathcal{L}, \mathcal{O}, \mathcal{P}, \mathcal{R}, \mathcal{T}\}, \mathcal{L} \subseteq \mathcal{Z} \subseteq \mathcal{R}$; in other words, a linear order can be considered as a special case of any one of the other types, and any type is a special case of binary relation.

To conclude this section, we summarize the notation for these sets in Table 1.

Voting Procedures, Complexity of, Table 1
Meaning of the notation $\mathcal{A}, \mathcal{C}, \mathcal{L}, \mathcal{O}, \mathcal{P}, \mathcal{R}, \mathcal{T}$

\mathcal{A} : acyclic relation	\mathcal{L} : linear order	\mathcal{P} : preorder	\mathcal{T} : tournament
\mathcal{C} : complete preorder	\mathcal{O} : partial order	\mathcal{R} : binary relation	

Common Voting Procedures

In this section, we describe the main voting procedures, i.e., plurality rule (one-round procedure), plurality rule with run-off (two-round procedure), preferential voting procedure (STV), Borda's procedure, Nanson's procedure, Baldwin's procedure, Condorcet's procedure, Condorcet–Kemeny problem, Slater problem, prudent orders (G. Köhler, K.J. Arrow and H. Raynaud), maximin procedure (P.B. Simpson), minimax procedure (K.J. Arrow and H. Raynaud), ranked pairs procedure (T.N. Tideman), Copeland's procedure, the top cycle solution (J.H. Smith), the uncovered set solution (P.C. Fishburn, N. Miller), the minimal covering set solution (B. Dutta), Banks's solution, the tournament equilibrium set solution (T. Schwartz), Dodgson's procedure, Young's procedure, approval voting procedure, majority-choice approval procedure (F. Simmons), and Bucklin's procedure (see also [27]). For other tournament solutions, see [106] and [138]).

Plurality Rule, Plurality Rule with Run-Off, Preferential Voting Procedure

One of the easiest voting procedures by which to elect one candidate as a winner is the *plurality rule* (also called *one-round procedure* or *relative majority*, or sometimes *first-past-the-post*, or *winner-takes-all*, or also *majoritarian voting*...; see [95]). In this procedure, each voter gives one point to his or her favorite candidate (so it is not necessary to know the preferences of the voters on the whole set of candidates). The candidate who gains the maximum number of points is the winner.

This procedure belongs to the family of *scoring procedures*. In such a procedure, a *score-vector* (s_1, s_2, \dots, s_n) is fixed independently of the voters, with $s_1 \geq s_2 \geq \dots \geq s_n$. For each voter, a candidate x receives s_i points if x is ranked at the i th position by the considered voter. The *score* of x is the total number of points that x received. The winner is the candidate with the maximum score. If the aim is to rank the candidates, we may also sort them according to decreasing scores and then consider the linear extensions of the complete preorder provided by this sorting. (Another possibility would be to apply the procedure $n - 1$ times, after having removed the winner of the current it-

eration.) For the plurality rule, the score vector is $(1, 0, 0, \dots, 0)$.

There are two rounds in the *plurality rule with run-off*, also called *two-round* (or *two-ballot*) *procedure*. The first round is like the plurality rule described above. At the end of this first step, if a candidate has gained at least $(m + 1)/2$ points (the strict majority), he or she is the winner. Otherwise, the two candidates with the maximum numbers of points remain for a second round and the others are removed from the election. Then the plurality rule is applied again, but only to the remaining two candidates. This method is designed to elect only one winner. If we want to obtain k winners, it is sufficient to apply it k times. Notice that the repetition of a given procedure always makes it possible to elect several winners.

A generalization of these procedures consists in performing a given number of rounds. For each round, each voter gives one point for his or her favorite candidate. If, at the end of a round, there is a candidate who has gained at least $(m + 1)/2$ points, he or she is the winner. Otherwise, the candidates with the lowest numbers of points are eliminated from the competition; the number of candidates eliminated at each round depends on the number of rounds, but is such that only two candidates will remain for the last round. The winner of this last round is the winner of the election. Special cases are the plurality rule with run-off, described above, and the one with at most $n - 1$ rounds. For this latter case, exactly one candidate is removed at each round. This variant, in which the candidate who is the least often ranked at the first position is removed, is also known as *preferential voting* (or *preference voting*) or as *single transferable vote* (STV), or as *instant-runoff voting* (IRV).

Other variants of these voting procedures may be defined by the successive eliminations of the losers. For instance, the candidate who is most often ranked last is removed, and we iterate this process while there remain at least two candidates.

Borda's Procedure and Some Variants (Nanson's and Baldwin's Procedures)

As related above, Borda considered the plurality rule unsatisfactory because the winner can be contested by a majority of voters who would all agree to choose another candidate instead of the elected winner (the same holds for the plurality rule with run-off, see Example 1 below). Borda suggested another procedure in which the voters rank the n candidates according to their preferences. For each voter, the candidate who is ranked first is given $n - 1$ points, a candidate ranked second is given $n - 2$ points,

and so on: more generally, a candidate ranked at the i th position is given $n - i$ points. Then, all these points are summed up for each candidate: this sum is the *Borda score* s_B of the candidate. The candidate with a maximum Borda score is the *Borda winner*. So, Borda's procedure is also a scoring procedure, of which the score-vector is $(n - 1, n - 2, \dots, 1, 0)$.

Using Borda's procedure, one can easily obtain a ranking of all the candidates. A first possibility consists, as for the plurality rule or the plurality rule with run-off, in iterating Borda's procedure $n - 1$ times, after having removed the Borda winner of the current iteration. But we may also apply Borda's procedure only once, and then rank the candidates according to the decreasing values of their Borda scores. This gives a complete preorder. Any linear extension of this complete preorder can be considered as the collective ranking according to Borda's procedure. Notice that these two possibilities do not necessarily provide the same rankings (see Example 1).

Several variants of Borda's procedure have been studied. For instance, we may apply other score-vectors: instead of $n - i$ points given to the candidate ranked at the i th position, we may choose to assign other values. For instance, given an integer k , we may credit k points to the candidate ranked at the first position, $k - 1$ points to the second, and so on, through the candidate ranked at the k th position, who gains 1 point, after which the following candidates gain nothing (the shape of the score-vector is $(k, k - 1, \dots, 1, 0, \dots, 0)$). For $k = 1$, this system is the plurality rule. For $k \geq n - 1$, this system gives the same results as Borda's procedure.

Other systems are based on Borda's procedure, but with the elimination of some candidates. *Nanson's procedure* [140] modifies Borda's procedure by eliminating the candidates whose Borda scores are below the average Borda score and by repeating the computations of the Borda scores with respect to the remaining candidates after these eliminations, until there remains only one candidate. Another variant of Borda's procedure is one suggested by Baldwin in 1926 [11]; as in Nanson's procedure, candidates are iteratively removed from the election. But, in *Baldwin's procedure*, only one candidate is removed at each iteration, the one whose Borda's score is the lowest.

Condorcet's Procedure

Condorcet designed a method based on pairwise comparisons. More precisely, for each candidate x and each candidate y with $x \neq y$, we compute the number m_{xy} , that we will call the *pairwise comparison coefficient* below, of voters who prefer x to y . Then x is considered as better

than y if a majority of voters prefers x to y , i. e., if we have $m_{xy} > m_{yx}$. This defines the (strict) majority relation $T: xTy \Leftrightarrow m_{xy} > m_{yx}$. In some cases, there exists a *Condorcet winner*, i. e., a candidate x defeating any other candidate: $\forall y \neq x, m_{xy} > m_{yx}$. If there exists a Condorcet winner, then he or she is unique. It may even happen that T is a linear order and allows us to rank all the candidates. Such is the case for the following example (due to B. Monjardet [133]), which illustrates the previous voting procedures.

Example 1 Assume that $m = 13$ voters must rank $n = 4$ candidates x, y, z , and t . Suppose the preferences of the voters are given by the following linear orders:

- the preferences of two voters are: $x > y > z > t$;
- the preference of one voter is: $y > z > x > t$;
- the preference of one voter is: $y > z > t > x$;
- the preferences of four voters are: $z > y > x > t$;
- the preferences of five voters are: $t > x > y > z$.

According to the plurality rule, t is the winner with 5 points (2 points for x and for y , 4 points for z). According to the plurality rule with run-off, z is the winner (the four voters who voted for x or y prefer z to t). The Borda scores s_B of the candidates are:

- $s_B(x) = 2 \times 3 + 5 \times 2 + 5 \times 1 + 1 \times 0 = 21$;
- $s_B(y) = 2 \times 3 + 6 \times 2 + 5 \times 1 + 0 \times 0 = 23$;
- $s_B(z) = 4 \times 3 + 2 \times 2 + 2 \times 1 + 5 \times 0 = 18$;
- $s_B(t) = 5 \times 3 + 0 \times 2 + 1 \times 1 + 7 \times 0 = 16$.

So, the winner according to Borda's procedure is y , and the ranking of the four candidates is $y > x > z > t$ (notice that if, while there are at least two candidates, we apply the variant consisting in removing the winner and reapplying Borda's procedure, then we obtain the orders $y > x > z > t$ and $y > z > x > t$ as the possible rankings; the distance to the ranking provided by one application of Borda's procedure may be much more important). In Nanson's procedure, as the Borda scores of z and t are below the average (which is equal to 19.5), z and t are removed and only x and y remain. Then the Borda scores of x and y for the second step become $s_B(x) = 7$ and $s_B(y) = 6$: hence x is the winner according to Nanson's procedure. In Baldwin's procedure, t is first removed. The Borda scores of x, y and z become $s_B(x) = 14, s_B(y) = 15, s_B(z) = 10$. Thus z is removed and the remaining computations are as in Nanson's procedure: here also x is the winner (but it may happen that Nanson's procedure and Baldwin's procedure do not provide the same winners).

Let us now compute the pairwise comparison coefficients m_{xy} necessary to apply Condorcet's procedure:

- $m_{xy} = 2 + 5 = 7$; $m_{yx} = 1 + 1 + 4 = 6$;
- $m_{xz} = 2 + 5 = 7$; $m_{zx} = 1 + 1 + 4 = 6$;
- $m_{xt} = 2 + 1 + 4 = 7$; $m_{tx} = 1 + 5 = 6$;
- $m_{yz} = 2 + 1 + 1 + 5 = 9$; $m_{zy} = 4$;
- $m_{yt} = 2 + 1 + 1 + 4 = 8$; $m_{ty} = 5$;
- $m_{zt} = 2 + 1 + 1 + 4 = 8$; $m_{tz} = 5$.

The bold values are the ones greater than the majority $(m + 1)/2$. These values show that the majority relation, here, is a linear order, namely $x > y > z > t$.

By the way, this example shows the importance of the voting procedure, as already noticed by Borda (see [113]): four procedures, four different winners; so all four of our candidates may claim to be the winners of the election. . . It is often the case that different procedures provide different winners.

Median Orders, Condorcet–Kemeny Problem, Slater Problem

As Condorcet himself discovered, his procedure may lead to a majority relation which is not transitive. The simplest example in this respect is one with $n = 3$ candidates x, y and z , and with $m = 3$ voters whose preferences are respectively $x > y > z, y > z > x, z > x > y$. It is easy to verify that the majority relation T is defined by xTy, yTz, zTx , hence a lack of transitivity. If there is no tie (which is necessarily the case if m is odd, since the individual preferences of the voters are assumed to be linear orders), then T is a tournament, called the *majority tournament*. We may or may not weight T if we want to take the intensity of the preferences into account. If T is not weighted, the search for a winner or for a ranking of the candidates leads to the definition of *tournament solutions* (see [106] for a comprehensive study of these, and [93] for a survey of their complexities, some of which are given below). In the Condorcet–Kemeny problem, T is weighted and the aim is to compute a linear order or, more generally, a poset fitting T “as well as possible”.

To specify what “as well as possible” means, we use the *symmetric difference distance* δ defined, for two binary relations R and S defined on X , by:

$$\delta(R, S) = \left| \left\{ (x, y) \in X^2 : (xRy \text{ and } x\bar{S}y) \text{ or } (x\bar{R}y \text{ and } xSy) \right\} \right|.$$

This quantity $\delta(R, S)$ measures the number of disagreements between R and S . Though it is possible to consider other distances, δ is widely used and is appropriate for many applications. J.-P. Barthélemy [15] shows that δ satisfies a number of naturally desirable properties. J.-P.

Barthélemy and B. Monjardet [17] recall that $\delta(R, S)$ is the Hamming distance between the characteristic vectors (see below) of R and S and point out the links between δ and the L_1 -metric or the square of the Euclidean distance between these vectors (see also [129] and [130]).

So, for a profile $\Pi = (R_1, R_2, \dots, R_m)$ of m relations, we can define the *remoteness* $\Delta(\Pi, R)$ between a relation R and the profile Π by:

$$\Delta(\Pi, R) = \sum_{i=1}^m \delta(R, R_i).$$

The remoteness $\Delta(\Pi, R)$ measures the total number of disagreements between Π and R .

Our aggregation problem can now be seen as a combinatorial optimization problem: given a profile Π , determine a binary relation R^* minimizing Δ over one of the sets $\mathcal{A}, \mathcal{C}, \mathcal{L}, \mathcal{O}, \mathcal{P}, \mathcal{R}, \mathcal{T}$. Such a relation R^* will be called a *median relation* of Π [17]. According to the number m of relations of the profile, and according to the properties assumed for the relations belonging to Π or required from the median relation, we get many combinatorial problems. We note them as follows:

Problems $P_m(\mathcal{Y}, \mathcal{Z})$. For \mathcal{Y} belonging to $\{\mathcal{A}, \mathcal{C}, \mathcal{L}, \mathcal{O}, \mathcal{P}, \mathcal{R}, \mathcal{T}\}$ and \mathcal{Z} also belonging to $\{\mathcal{A}, \mathcal{C}, \mathcal{L}, \mathcal{O}, \mathcal{P}, \mathcal{R}, \mathcal{T}\}$, for a positive integer m , $P_m(\mathcal{Y}, \mathcal{Z})$ denotes the following problem: given a finite set X of n elements, given a profile Π of m binary relations all belonging to \mathcal{Y} , find a relation R^* belonging to \mathcal{Z} minimizing Δ over \mathcal{Z} : $\Delta(\Pi, R^*) = \min\{\Delta(\Pi, R) \text{ for } R \in \mathcal{Z}\}$.

With this notation, the initial problem, possibly considered by Condorcet and then surely by J.G. Kemeny [102], is $P_m(\mathcal{L}, \mathcal{L})$, consisting in aggregating m linear orders into a median linear order. A *Condorcet-Kemeny winner*, or here simply a *Kemeny winner*, is the winner of any median linear order (for references about the Condorcet-Kemeny problem, see for example [36,98,131,132,151] and references therein).

We may easily state the problems $P_m(\mathcal{Y}, \mathcal{Z})$ as 0-1 linear programming problems (see [17,36,89,91,173] for instance) for any profile $\Pi = (R_1, R_2, \dots, R_m)$ of m binary relations R_i ($1 \leq i \leq m$) all belonging to \mathcal{Y} . To this end, consider the characteristic vectors $r^i = (r_{xy}^i)_{(x,y) \in X^2}$ of the relations R_i ($1 \leq i \leq m$) defined by $r_{xy}^i = 1$ if $xR_i y$ and $r_{xy}^i = 0$ otherwise, and similarly the characteristic vector $r = (r_{xy})_{(x,y) \in X^2}$ of any binary relation R . Then, after some computations, we obtain $\Delta(\Pi, R) = C - \sum_{(x,y) \in X^2} \alpha_{xy} r_{xy}$, where $C = \sum_{i=1}^m \sum_{(x,y) \in X^2} r_{xy}^i$ is a constant and with $\alpha_{xy} = 2 \sum_{j=1}^m r_{xy}^j - m$. Notice that, for the problem $P_m(\mathcal{L}, \mathcal{L})$, the sum $\sum_{i=1}^m r_{xy}^i$ is equal for

$x \neq y$ to the pairwise comparison coefficient m_{xy} introduced above. So, because of the equality $m = \sum_{i=1}^m r_{xy}^i + \sum_{i=1}^m r_{yx}^i$, we get $\alpha_{xy} = m_{xy} - m_{yx}$: α_{xy} measures the number of voters who prefer x to y minus the number of voters who prefer y to x . More generally, α_{xy} is equal to twice the gap between the number of voters who prefer x to y and the majority. It is a non-positive or non-negative integer with the same parity as m . To obtain a 0-1 linear programming statement of $P_m(\mathcal{Y}, \mathcal{Z})$, it is then sufficient to express the constraints defining the set \mathcal{Z} , which is easy for the posets described above. For instance, the transitivity of R can be expressed by the following inequalities:

$$\forall (x, y, z) \in X^3, 0 \leq r_{xy} + r_{yz} - r_{xz} \leq 1.$$

As stated above, it is also common to represent a preference R defined on X by a graph. The properties of the graph are the properties of R : it can be antisymmetric, complete, transitive, and so on. Similarly, the profile $\Pi = (R_1, R_2, \dots, R_m)$ can also be represented by a directed, weighted, complete, symmetric graph $G_\Pi = (X, U_X)$: its set of vertices is X , and G_Π contains all the possible arcs except the loops, i.e., $U_X = X \times X - \{(x, x) \text{ for } x \in X\}$. (The loops would be associated with reflexivity; this property, as well as irreflexivity, has no impact on the complexity status of the studied problems, hence this simplification.) The weights of the arcs (x, y) give the intensity of the preference for x over y . The computations above lead us to assign α_{xy} as the weight of any arc (x, y) of G_Π . With this choice, minimizing $\Delta(\Pi, R)$ is the same, from the graph theoretic point of view, as drawing from G_Π a subset of arcs with a maximum total weight and satisfying the structural properties required from R . Notice that characterizations of the graphs that we can associate with profiles Π have been provided by different authors (see [36,55,56,68,91,117,166]); the construction of the profiles can be done in polynomial time, which allows us to study the complexities of the problems $P_m(\mathcal{Y}, \mathcal{Z})$ through their graph theoretic representations G_Π .

Example 2 illustrates these considerations.

Example 2 Assume that $m = 9$ voters must rank $n = 4$ candidates x, y, z , and t . Assume, also, that the preferences of the voters are given by the following linear orders:

- the preferences of three voters are: $x > y > z > t$;
- the preferences of two voters are: $y > t > z > x$;
- the preference of one voter is: $t > z > x > y$;
- the preference of one voter is: $x > z > y > t$;
- the preference of one voter is: $t > y > x > z$;
- the preference of one voter is: $z > t > y > x$.

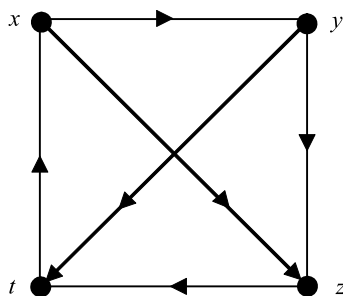
The quantities m_{xy} involved in Condorcet's procedure are the following, where the bold values, again, denote those greater than the majority $(m + 1)/2$:

- $m_{xy} = 5$; $m_{yx} = 4$;
- $m_{xz} = 5$; $m_{zx} = 4$;
- $m_{xt} = 4$; $m_{tx} = 5$;
- $m_{yz} = 6$; $m_{zy} = 3$;
- $m_{yt} = 6$; $m_{ty} = 3$;
- $m_{zt} = 5$; $m_{tz} = 4$.

Here, the majority relation is not a linear order, but the tournament of Fig. 7. Figure 7 also displays the graph G_{Π} summarizing the data. We may observe that the majority tournament is given by the arcs of G_{Π} with a positive weight.

For these data, it is not too difficult to verify that there is only one median linear order, which is $x > y > z > t$, this order keeps all the positive weights except that of the arc (t, x) , of which the weight is the minimum, while the arcs with positive weights do not define a linear order. Hence, x is the only Kemeny winner.

Attention has also been paid to $P_1(\mathcal{T}, \mathcal{L})$, i.e., the approximation of a tournament (which can be the majority tournament of the election) by a linear order at minimum distance. This problem is also known as *Slater problem*, since P. Slater explicitly stated it in 1961 ([160]; see also [36] for a survey of this problem). A linear order L^* at minimum distance (with respect to the symmetric difference distance) from the tournament T constituting the considered instance of $P_1(\mathcal{T}, \mathcal{L})$ is called a *Slater order* of T : $\delta(T, L^*) = \min_L \delta(T, L)$. This minimum distance is usually called the *Slater index* $i(T)$ of T : $\delta(T, L^*) = i(T)$. A *Slater winner* of T is the winner of any Slater order of T .



Prudent Orders, Maximin Procedure, Minimax Procedure, Ranked Pairs Procedure

Other procedures are based on the quantities m_{xy} defined above.

Such is the case for *prudent orders* proposed by G. Köhler [103] and by K.J. Arrow and H. Raynaud [8]. Given the pairwise comparison coefficients m_{xy} , let us define the *cut relation* $R_{>t}$ for any integer t with $-m \leq t \leq m$ by the following:

for $x \in X$ and $y \in X$ with $x \neq y$,

$$xR_{>t}y \Leftrightarrow m_{xy} - m_{yx} > t.$$

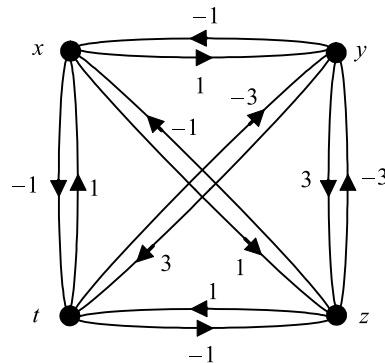
Then define a threshold t_{\min} by:

$$t_{\min} = \min\{t \text{ with } -m \leq t \leq m$$

and such that $R_{>t}$ contains no circuit \}.

A *prudent order* is any linear order which contains $R_{>t_{\min}}$. A winner according to the procedure of the prudent orders is the winner of any prudent order of the profile being considered. For Example 2, we have $t_{\min} = 1$; with respect to the graph G_{Π} of Fig. 7, $R_{>t_{\min}}$ contains only the arcs (y, z) and (y, t) . There are eight prudent orders, including $x > y > z > t$ or $y > t > z > x$, but none of them has z or t as its winner: x and y are the winners according to the prudent order procedure.

The *maximin procedure*, proposed by P.B. Simpson in 1969 [159], is also based on the quantities m_{xy} . In this procedure, for each candidate x , we consider the worst performance $W(x)$ in the pairwise comparisons: $W(x) = \min_{y \neq x} m_{xy}$. The winner is any candidate x^* with a maximum worst performance: $W(x^*) = \max_{x \in X} W(x)$. We may also use these quantities to sort the candidates in decreasing order with respect to the quantities W to obtain



Voting Procedures, Complexity of, Figure 7

The majority tournament (left) and the graph G_{Π} (right) associated with the data of Example 2 and weighted by the quantities $\alpha_{xy} = m_{xy} - m_{yx}$

a collective preference over the whole set of candidates (as usual, another possibility is to remove the winner and to iterate the process). For instance, applied to Example 2, we obtain $W(x) = 4$, $W(y) = 4$, $W(z) = 3$, $W(t) = 3$: x and y are the Simpson winners.

The *minimax procedure*, in which the previous roles of “min” and “max” are switched and in which the candidates are sorted in increasing order with respect to the obtained maxima, has been proposed by K.J. Arrow and H. Raynaud [8]. For Example 2, the winners would be x , z and t .

In 1987, T.N. Tideman introduced the *ranked pairs procedure* [170]. Here, we first sort the quantities m_{xy} decreasingly. Then we scan them in this order to build a linear order L for the collective preference. If m_{xy} is the current quantity that we scan, then we definitely set xLy if such a decision is compatible with the previous ones. We do so until a linear order is completely defined. For instance, for Example 2, we first fix yLz and yLt since m_{yz} and m_{yt} are maxima and z and t cannot be winners. Then we must choose between adding xLy or xLz or tLx or zLt , since m_{xy} , m_{xz} , m_{tx} and m_{zt} are equal. We cannot add all of them simultaneously, because of incompatibilities with yLz or yLt , already fixed. If we choose to add xLy , xLz and zLt , we obtain the linear order $x > y > z > t$, and x is a winner. If we choose to add tLx and zLt , we obtain the linear order $y > z > t > x$, and y is a winner. Here again, x and y are the winners.

Tournament Solutions

The procedures described in this section apply to tournaments, which can function as the majority tournament of an election. They deal with unweighted tournaments, but some of them can be extended to weighted tournaments, as in the case of the solution designed by P. Slater (see above).

Number of Wins: Copeland’s Procedure The procedure designed by A.H. Copeland in 1951 [48] is also based on the m_{xy} ’s. For any two different candidates x and y , we set: $C(x, y) = 1$ if $m_{xy} > m_{yx}$, $C(x, y) = 0.5$ if $m_{xy} = m_{yx}$, $C(x, y) = 0$ if $m_{xy} < m_{yx}$. The Copeland score $C(x)$ of x is $C(x) = \sum_{y \neq x} C(x, y)$. The Copeland winner is any candidate with a maximum Copeland score (here also, we may rank the candidates according to decreasing Copeland scores).

The application of Copeland’s procedure to Example 2 gives: $C(x) = 2$, $C(y) = 2$, $C(z) = 1$, $C(t) = 1$. Here, x and y are the Copeland winners.

The Copeland score has a meaning from a graph theoretic point of view. If we assume that there is no tie, the

majority relation is a tournament (the majority tournament). Then the Copeland score of a candidate x is also the out-degree of the vertex associated with x . Copeland’s procedure is one of the common tournament solutions (see [106]). It can be extended to weighted tournaments by sorting the vertices x according to the sum $\sum_{y \neq x} m_{xy}$ of the pairwise comparison coefficients m_{xy} ; this variant leads to the same ranking as Borda’s procedure.

Top Cycle: Smith’s Solution Another tournament solution is the so-called *top cycle* (also called the *Smith set*) [161]. Any directed graph G can be decomposed into its strongly connected components. We may then define another graph H derived from G . The vertices of H are associated with the strongly connected components of G . Let x (respectively y) be a vertex of G associated with the strongly connected components C_x (respectively C_y) of G . There will exist an arc (x, y) from x to y if there is at least one arc in G from C_x to C_y (notice that, in this case, all the arcs between C_x and C_y are from C_x towards C_y). Then H does not contain any circuits. Moreover, if G is a tournament, H is a linear order and admits a winner (but H contains only one vertex if G is strongly connected). The top cycle of G is the strongly connected component of G associated with the winner of H .

The top cycle solution, when applied to a tournament T , consists of considering all vertices of the top cycle of T as the winners of T . For instance, for the tournament of Fig. 7, which is strongly connected, the top cycle contains the four vertices x , y , z , and t , which are the four winners according to this solution.

Uncovered Set: Fishburn’s and Miller’s Solution A refinement of the top cycle is provided by the set of uncovered vertices. Given a tournament T and two vertices x and y of T , we say that x covers y if (x, y) is an arc of T and if, for any arc (y, z) , (x, z) is also an arc of T . (In other words, considering T as a majority tournament, x beats y and any vertex beaten by y is also beaten by x .) A vertex is said to be *uncovered* if no other vertex covers it. The uncovered set of T is noted $UC(T)$. Adopting the elements of $UC(T)$ as the winners of T has been independently suggested by P. Fishburn in 1977 [76] and by N. Miller in 1980 [126].

For the tournament of Fig. 7, it is easy to see that z is covered by y while x , y and t are uncovered: here, x , y , and t are the three winners according to this solution.

The definition of a covered vertex can easily be extended to weighted tournaments, though the possibility of weights equal to 0 makes the situation more difficult than expected (see [35] for details).

Minimal Covering Set: Dutta's Solution The uncovered set can also be refined, for example by the minimal covering set proposed by B. Dutta [64]. Consider a tournament T defined on X . We say that a subset Y of X is a *covering set* of T if we have the following property: $\forall x \in X - Y, x \notin UC(Y \cup \{x\})$. For instance, $UC(T)$ is a covering set of T . Let $\mathcal{E}(T)$ denote the set of the covering sets of T . Then there exists a minimal element of $\mathcal{E}(T)$ with respect to inclusion; this minimal element is called the *minimal covering set* $MC(T)$ of T .

For the tournament of Fig. 7, the minimal covering set contains x, y , and t , which are the three winners according to this solution, here as for the uncovered set. (But there exist tournaments for which the general inclusion $MC(T) \subseteq UC(T)$ is strict.)

Maximal Transitive Subtournaments: Banks's Solution

Among other tournament solutions, one designed by J. Banks in 1985 [13] is of interest. When the tournament being considered, T , is transitive (i. e., T is a linear order), there exists a unique winner who is selected as the winner of T by the usual tournament solutions. If that is not the case, we may consider the transitive subtournaments of T which are maximal with respect to inclusion, and then select the winner of each of them as the winners of T . This defines the *Banks's solution* [13]: a *Banks winner* of T is the winner of any maximal (with respect to inclusion) transitive subtournament of T .

If we consider the majority tournament of Example 2 (see Fig. 7), three Banks winners exist: x (because of the maximal transitive subtournament $x > y > z$), y (because $y > z > t$) and t (because $t > x$).

Tournament Equilibrium Set: T. Schwartz's Solution

The solution that we deal with in this subsection was designed by T. Schwartz [158] and is called the *tournament equilibrium set*. To define it, we need extra definitions. Let G be a directed graph. The top set $TS(G)$ of G is defined as the union of the strongly connected components of G with no in-coming arcs (if G is a tournament, then $TS(G)$ is equal to $TC(G)$).

Let Sol be a tournament solution and T be a tournament. When Sol is applied to T , we define the *contestatation graph* $G(Sol, T)$ associated with Sol and T as follows: The vertex set of $G(Sol, T)$ is X ; there is an arc (x, y) from x to y in $G(Sol, T)$ if and only if (x, y) is an arc of T and x is a winner according to Sol when Sol is applied to the subtournament of T induced by the predecessors of y in T . In other words, the arcs (x, y) of $G(Sol, T)$ describe the following situation: if y is considered as a possible winner, then x will contest the election of y be-

cause x beats y in T and because x is a winner among the candidates who beat y . We may notice that $G(Sol, T)$ is a subgraph of T . By considering the top set $TS[G(Sol, T)]$ of $G(Sol, T)$, we get a new tournament solution. T. Schwartz proved in [158] that there exists a unique tournament solution, that he called the *tournament equilibrium set* TEQ , which is a fixed point with respect to this process: $\forall T, TEQ(T) = TS[G(TEQ, T)]$.

For the majority tournament of Example 2 (see Fig. 7), the *tournament equilibrium set* contains x, y and t .

Dodgson's Procedure

In the procedure proposed in 1876 by C.L. Dodgson (or Lewis Carroll) [60], each voter ranks all the candidates into a linear order. If a Condorcet winner exists, he or she is also the Dodgson winner. Otherwise, Dodgson's procedure consists of choosing as winners all the candidates who are "closest" to being Condorcet winners: for each candidate $x \in X$, let $D(x)$ be the *Dodgson score* of x , defined as the minimum number of swaps between consecutive candidates in the preferences of the voters such that x becomes a Condorcet winner; a *Dodgson winner* is any candidate x^* minimizing D : $D(x^*) = \min_{x \in X} D(x)$.

Specifically, consider a profile $\Pi = (L_1, L_2, \dots, L_m)$ of m linear orders. Let i be an index between 1 and m and let y and z be two consecutive candidates in L_i : $yL_i z$ and there is no candidate t with $yL_i t$ and $tL_i z$ simultaneously. Then define a linear order L'_i obtained from L_i by swapping y and z in L_i : $zL'_i y$ and, for any other ordered pair of candidates $(t, v) \neq (y, z)$, we have $tL'_i v$ if and only if we had $tL_i v$. By substituting L'_i to L_i , we obtain a new profile. By repeating such swaps as many times as necessary, we may generate all the possible profiles with m linear orders. Among them, some admit x as a Condorcet winner. The Dodgson score $D(x)$ of a candidate x is the minimum number of swaps that must be applied from Π in order to obtain a profile with x as a Condorcet winner.

Let us illustrate these definitions on Example 2. First, let us compute the Dodgson scores of the four candidates. If we want x to become a Condorcet winner, it is necessary that x defeats t , which is not currently the case. Since x is never just after t in the preferences of the voters, one swap is not enough to reach this aim. On the other hand, two swaps are enough, for instance by swapping first y and x in the preference of the last voter, and then by swapping x and t in this new preference. Thus: $D(x) = 2$. One swap is sufficient (and necessary) to make y a Condorcet winner, for instance by swapping y and x in the preference of one of the first three voters: $D(y) = 1$. The computation of $D(z)$ is a little more difficult. To become a Con-

dorcet winner, z must defeat y . Since there are only 3 voters who prefer z to y against 6 who prefer y to z , it is necessary to perform at least 2 swaps so that a new majority of voters will prefer z to y . But, if such swaps exist, they do not help to alleviate the difficulty in helping z to defeat x . For z to defeat x necessitates at least one extra swap. Hence the inequality $D(z) \geq 3$. On the other hand, swapping x and z in the preference of the voter whose preference is $x > z > y > t$ and swapping y and z in the preferences of two of the first three voters makes z a Condorcet winner: $D(z) = 3$. The computation of $D(t)$ is similar to that of $D(z)$, and we also find $D(t) = 3$. These values show that there is only one Dodgson winner (who is not a Kemeny winner): y .

Young's Procedure

Like Dodgson's procedure, H.P. Young's procedure [177] is based on altered profiles. But, instead of performing the fewest possible number of swaps of consecutive candidates in the voters' preferences, we now find the minimum number of voters that must be removed in order for a Condorcet winner to emerge. More precisely, for each candidate x , we define the *Young score* $Y(x)$ of x as the minimum number of voters whose simultaneous removals allow x to become a Condorcet winner. Any candidate with a minimum Young score is a *Young winner*.

For Example 2, we may verify that the Young scores of the four candidates are: $Y(x) = 2$, $Y(y) = 2$, $Y(z) = 4$, $Y(t) = 4$. For instance, for z to defeat x and y requires at least four removals for y . But these removals must keep z defeating t . It is easy to see that removing two of the first three voters, one of the two voters sharing the same preferences and the voter for whom z is in the last position, suffices to make z a Condorcet winner of the new election.

Approval Voting Procedure, Majority-Choice Approval Procedure and Variants

The approval voting procedure was popularized by Steven J. Brams and Peter C. Fishburn in 1978 [25] and 1983 [26]. But, according to [40,52,111], it was already in use in the 13th century in Venice and in papal elections, and then in elections in England during the 19th century, among other places. Its name seems to come from R.J. Weber in 1976 (see [175]; several other persons seem to have found this procedure independently during the late 1960s and early 1970s). The approval voting procedure consists of giving to the voters the possibility of voting for several candidates simultaneously. In other words, instead of appointing their preferred candidate, the voters are invited to answer the question: "who are the candidates for whom you

would like to vote?". Each voter then gives one point to the candidates with whom he or she agrees. The candidate with the greatest number of points is the winner. Notice that, if each voter actually chooses only one candidate, this voting procedure is the same as the plurality rule. In this respect, the approval voting procedure can be seen as a generalization of the plurality rule.

More formally, this procedure assumes that the preferences of the voters are complete preorders with only two classes (one class for the approved candidates and one for the disapproved ones). These preorders must then be aggregated into a collective complete preorder also with two classes, one of them with only one element (the winner), the other class with all the other elements (the losers). Extension for electing several candidates simultaneously is immediate.

Variants (sometimes known as *range voting*, *ratings summation*, *average voting*, *cardinal ratings*, *0–99 voting*, the *score system* or the *point system*) can be based on the same idea. For instance, each voter has a maximum number of points, and he or she can share them out among the candidates as he or she pleases, with or without a constraint on the maximum number of points per candidate. We can also add several rounds, and thus define new procedures. The *majority-choice approval* procedure (MCA) designed by F. Simmons in 2002 can also be seen as a variant of approval voting. In this system, each voter has three possibilities for rating each candidate: "favored", "accepted" or "disapproved". If a candidate is ranked "favored" by an absolute majority of the voters, then any candidate marked "favored" by a maximum number of voters is a winner. Otherwise, the winner is any candidate with the largest number of "favored" or "accepted" marks. It is sometimes required this number to be at least $(m + 1)/2$, otherwise no one will be elected. Ties can be broken using the number of "favored" marks. We may, of course, obtain new variants by increasing the number of levels.

Bucklin's Procedure

The procedure proposed by James W. Bucklin in the early 20th century is also called the *Grand Junction system* (Grand Junction is a city in Colorado, where Bucklin's procedure was applied from 1909 to 1922). In this procedure, we first count, for each candidate x , the number of times that x is ranked first, as in the plurality rule. If a candidate has at least the absolute majority $(m + 1)/2$, he or she is the winner. Otherwise, second choices are added to the first choices. Once again, if a candidate has the absolute majority $(m + 1)/2$, he or she becomes a winner. Otherwise, we consider third choices and so on, until at least

one candidate obtains the absolute majority: then he or she becomes a winner. Since after the first round there are more votes than voters, Bucklin's procedure is sometimes considered as a variant of approval voting procedure, but a main difference is that Bucklin's procedure may require several rounds. It can also be considered as a variant of scoring procedures, since it is the same as iteratively applying a scoring procedure with successively $(1, 0, 0, \dots, 0)$, $(1, 1, 0, 0, \dots, 0)$, $(1, 1, 1, 0, \dots, 0)$, \dots as the score-vectors, until a candidate obtains the majority.

Once again, consider Example 2. In the first round, x gets 4 points; y , 2 points; z , 1 point; t , 2 points. As there is no candidate with at least 5 points, we consider the second choices. Then we obtain: x keeps 4 points; y obtains 6 points; z , 3 points; t , 5 points. As y and t obtain at least 5 points, the process stops here and y and t are the Bucklin winners.

A variant of Bucklin's procedure would be to consider, at the last iteration, the candidates with a maximum number of points as the winners (only y for Example 2).

Complexity Results

After a reminder of the complexity classes that are useful for our purposes, this section examines the complexity of the voting procedures described in the previous section (see also [72]). Among those tournament solutions which can be applied to the majority tournament, we restrict ourselves to the solutions depicted above; the reader interested in the complexity of the other common tournament solutions will find some answers in [93].

Main Complexity Classes

Some complexity classes are well-known: P , NP , $co-NP$, the sets of polynomial problems, of NP -complete problems, of NP -hard problems. . . Let us recall some other notations (for references upon the theory of complexity, see for instance [10,78,82,96]; see also [1] for a list of about 500 complexity classes). Like D.S. Johnson in [96], we will distinguish between decision problems and other types of problems. Let n denote the size of the data. The class L^{NP} , or $P^{NP}[\log]$, $P^{NP}[\log n]$, Θ_2^P , or also $P_{||}^{NP}$, contains those decision problems which can be solved by a deterministic Turing machine with an oracle in the following manner: the oracle can solve an appropriate NP -complete problem in unit time, and the number of consultations of the oracle is upper-bounded by $\log(n)$. The class P^{NP} or Δ_2^P (or sometimes simply Δ_2) or also $P^{NP[n^{O(1)}]} = \bigcup_{k \geq 0} P^{NP[n^k]}$ is defined similarly, but with a polynomial of n instead of $\log(n)$. Notice the inclusions: $NP \cup co-NP \subseteq L^{NP} \subseteq P^{NP}$.

For problems which are not decision problems (i. e., optimization problems in which we look for the optimal value of a given function f , or search problems in which we look for an optimal solution of f , or enumeration problems in which we look for all the optimal solutions of f ; these problems are sometimes called *function problems*), these classes are extended with an "F" in front of their names (see [96]); for instance we thus obtain the classes $FL^{NP}(= F\Theta_2^P \dots)$ or $FP^{NP}(= F\Delta_2^P \dots)$. The usual definition of "completeness" is extended to these classes in a natural way. Though the notation Δ_2^P or Θ_2^P are sometimes more common in complexity theory (especially when dealing with the polynomial hierarchy), we shall keep the pseudonyms P^{NP} and L^{NP} (as well as FP^{NP} and FL^{NP}), as perhaps being more informative.

Similarly, there exist refinements of P . In particular, the class L denotes the subset of P containing the (decision) problems which can be solved by an algorithm using only logarithmic space (in a deterministic Turing machine), the input itself not being counted as part of memory. The classes AC^0 and TC^0 are more technical. The first one, AC^0 , consists of all the problems solvable by uniform constant-depth Boolean circuits with unbounded fan-in and a polynomial number of gates. The second one, TC^0 , consists of all the problems solvable by polynomial-size, bounded-depth, unbounded fan-in Boolean circuits augmented by so-called "threshold" gates, i. e., unbounded fan-in gates that output "1" if and only if more than half their inputs are non-zero (see [96] and the references therein for details). A problem of TC^0 is said to be TC^0 -complete if it is complete under AC^0 Turing reductions. Notice the inclusions $AC^0 \subset TC^0 \subseteq L \subseteq P$.

Complexity Results for the Usual Voting Procedures

We can now examine complexity results of the voting procedures described above. When dealing with linear orders, we assume that we can have direct access to the ordered list of the candidates, especially to their winners (see above). Remember that n denotes the number of candidates and m the number of voters.

Theorem 1 *The following procedures are polynomial.*

- The plurality rule (one-round procedure) is in $O(n + m)$.
- The plurality rule with run-off (two-round procedure) is in $O(n + m)$.
- The preferential voting procedure (STV) is in $O(nm + n^2)$.
- Borda's procedure is in $O(nm)$.

- If the preferences of the voters are known through a profile of complete preorders with two classes, the approval voting procedure (and its variant suggested by F. Simmons) is in $O(nm)$.
- Bucklin's procedure is in $O(nm)$.

More generally, the previous polynomial results can usually be extended to procedures based on score-vectors, often with a complexity of $O(nm)$.

The previous results are rather easy to obtain. For instance, for the plurality rule, an efficient way to determine the winners consists of computing an n -vector V which provides, for each candidate x , the number of voters who prefer x . As the preferred candidate of each voter is assumed to be accessible directly, computing V requires $O(n + m)$ operations (or fewer if we assume that voters sharing similar preferences are gathered, see Subsect. “Definitions, Notation and Partially Ordered Sets Used to Model Preferences”). More precisely, we first initialize V to 0 in $O(n)$. Then, for each voter, we consider his or her preferred candidate x and we increment $V(x)$ by 1 in $O(1)$ for each voter, thus in $O(m)$ for all the voters. By scanning V in $O(n)$, we determine the maximum value contained in V and, once again by scanning V in $O(n)$, the winners: they are the candidates x whose values $V(x)$ are maximum. The whole process requires $O(n + m)$ operations.

When it succeeds in finding an order (or at least a Condorcet winner), Condorcet's procedure is also polynomial. This is also the case for Simpson's procedure, since computing the pairwise comparison coefficients m_{xy} can obviously be done in polynomial time. The same happens for Tideman's ranked pairs procedure, since the detection of a circuit in a graph can be done in a time proportional to the number of arcs of this graph, i. e., here in $O(n^2)$ (see [51]), and for the prudent order procedure or the minmax procedure.

Theorem 2 *When there exists a Condorcet winner, Condorcet's procedure is polynomial, in $O(n^2m)$. The prudent orders procedure, the minimax procedure, Simpson's procedure (maximin procedure), and Tideman's procedure (ranked pairs procedure) are also polynomial.*

When there is no Condorcet winner, the situation is more difficult to manage. In this case, we may pay attention to the problems called $P_m(\mathcal{Y}, \mathcal{Z})$ above. The problems $P_m(\mathcal{Y}, \mathcal{T})$ and $P_m(\mathcal{Y}, \mathcal{R})$, i. e., the aggregation of m preferences into a tournament or into a binary relation in which no special property is required, are polynomial for any m and any set \mathcal{Y} as specified by Theorem 3.

Theorem 3 *Let m be any integer with $m \geq 1$ and let \mathcal{Y} be any subset of \mathcal{R} . Consider a profile $\Pi \in \mathcal{Y}^m$. Then $P_m(\mathcal{Y}, \mathcal{R})$ and $P_m(\mathcal{Y}, \mathcal{T})$ are polynomial.*

For the Condorcet–Kemeny problem, and more generally for the problems $P_m(\mathcal{Y}, \mathcal{Z})$ with \mathcal{Y} belonging to $\{\mathcal{A}, \mathcal{C}, \mathcal{L}, \mathcal{O}, \mathcal{P}, \mathcal{R}, \mathcal{T}\}$ and \mathcal{Z} to $\{\mathcal{A}, \mathcal{C}, \mathcal{L}, \mathcal{O}, \mathcal{P}\}$ and where m is a positive integer, most are NP-hard when m is large enough (see [5,16,19,34,41,65,85,89,91,92,94,173,174]; see also [91] for the NP-hardness of similar problems $P_m(\mathcal{Y}, \mathcal{Z})$ when extended to other posets, including interval orders, interval relations, semiorders, weak orders, quasi-orders).

Theorem 4 *For m large enough, we have:*

- For any set \mathcal{Y} containing \mathcal{L} (this is the case in particular for \mathcal{Y} belonging to $\{\mathcal{A}, \mathcal{C}, \mathcal{L}, \mathcal{O}, \mathcal{P}, \mathcal{R}, \mathcal{T}\}$ or to unions or intersections of such sets), $P_m(\mathcal{Y}, \mathcal{Z})$ is NP-hard and the decision problem associated with $P_m(\mathcal{Y}, \mathcal{Z})$ is NP-complete for $\mathcal{Z} \in \{\mathcal{A}, \mathcal{C}, \mathcal{L}\}$.
- $P_m(\mathcal{R}, \mathcal{Z})$ is also NP-hard and the decision problem associated with $P_m(\mathcal{R}, \mathcal{Z})$ is also NP-complete for $\mathcal{Z} \in \{\mathcal{O}, \mathcal{P}\}$.
- The complexity of $P_m(\mathcal{Y}, \mathcal{Z})$ is unknown for $\mathcal{Y} \in \{\mathcal{A}, \mathcal{C}, \mathcal{L}, \mathcal{O}, \mathcal{P}, \mathcal{T}\}$ and for $\mathcal{Z} \in \{\mathcal{O}, \mathcal{P}\}$, but $P_m(\mathcal{Y}, \mathcal{O})$ and $P_m(\mathcal{Y}, \mathcal{P})$ have the same complexity.

The minimum value of m for which $P_m(\mathcal{Y}, \mathcal{Z})$ is NP-hard in Theorem 4 is usually unknown and, moreover, the parity of m plays a role. Table 2 gives the ranges of lower bounds of m from which $P_m(\mathcal{Y}, \mathcal{Z})$ is known to be NP-hard; for lower values of m , when not trivial, the complexity of $P_m(\mathcal{Y}, \mathcal{Z})$ is usually unknown. (This is the case, for instance, for $P_1(\mathcal{R}, \mathcal{C})$, $P_1(\mathcal{R}, \mathcal{O})$ or $P_1(\mathcal{R}, \mathcal{P})$; notice that $P_2(\mathcal{L}, \mathcal{L})$ is polynomial.) A question mark (?) means that the complexity of the problem is still unknown.

So, the Condorcet–Kemeny problem $P_m(\mathcal{L}, \mathcal{L})$ is NP-hard for m odd and large enough or for m even with $m \geq 4$ (and, as noted above, is polynomial for $m = 2$). More specific results deal with this problem $P_m(\mathcal{L}, \mathcal{L})$ (see [19,85,92]). To state them, let us define, for each element x of X and for any given profile Π , the *Kemeny score* $K(x)$ of x (with respect to Π) as the minimum remoteness $\Delta(\Pi, L_x)$ between Π and the linear orders L_x with x as their winner. The *Kemeny index* of Π , $K(\Pi)$ is the minimum remoteness between Π and any linear order; thus it is the minimum that we look for in $P_m(\mathcal{L}, \mathcal{L})$; it is also the minimum of the Kemeny scores over X .

Theorem 5 *Let Π be a profile of m linear orders with m large enough.*

Voting Procedures, Complexity of, Table 2

Lower bounds of m from which $P_m(\mathcal{Y}, \mathcal{Z})$ is known to be NP-hard

Median relation (\mathcal{Z})	$\mathcal{L} \subseteq \mathcal{Y}$	$\mathcal{L} \subseteq \mathcal{Y}$	$\mathcal{Y} = \mathcal{T}$	$\mathcal{Y} = \mathcal{T}$	$\mathcal{Y} = \mathcal{R}$	$\mathcal{Y} = \mathcal{R}$
	m odd	m even	m odd	m even	m odd	m even
Acyclic relation (\mathcal{A})	$\theta(n^2)$	4	1	2	1	2
Complete preorder (\mathcal{C})	$\theta(n^4)$	$\theta(n^2)$	$\theta(n^3)$	$\theta(n)$	3	2
Linear order (\mathcal{L})	$\theta(n^2)$	4	1	2	1	2
Partial order (\mathcal{O})	?	?	?	?	3	2
Preorder (\mathcal{P})	?	?	?	?	3	2

- The following problems are NP-complete:
 - Given Π , a candidate $x \in X$ and an integer k , is $K(x)$ lower than or equal to k ?
 - Given an integer k , is $K(\Pi)$ lower than or equal to k ?
- The following problems are NP-hard:
 - Given Π and two candidates $x \in X$ and $y \in X$ with $x \neq y$, is $K(x)$ lower than or equal to $K(y)$ (in other words, is x “better” than y)? Moreover, if we assume that the profiles Π are given by the ordered list of the m preferences of the voters (and not by a set of different linear orders with their multiplicities, see Subsect. “Definitions, Notation and Partially Ordered Sets Used to Model Preferences”), this problem is L^{NP} -complete.
 - Given Π and a candidate $x \in X$, is x a Kemeny winner? Moreover, if we assume that the profiles Π are given by the ordered list of the m preferences of the voters, this problem is L^{NP} -complete.
 - Given Π and a candidate $x \in X$, is x the unique Kemeny winner? Moreover, if we assume that the profiles Π are given by the ordered list of the m preferences of the voters, this problem is L^{NP} -complete.
 - Given Π , determine a Kemeny winner of Π . Moreover, this problem belongs to FP^{NP} .
 - Given Π , determine all the Kemeny winners of Π . Moreover, this problem belongs to FP^{NP} .
 - Given Π , determine a Kemeny order of Π . Moreover, this problem belongs to FP^{NP} .
- The following problem belongs to the class co-NP:
 - Given Π and a linear order L defined on X , is L a Kemeny order of Π ?

Attention has also been paid to $P_1(\mathcal{T}, \mathcal{L})$, i. e., the approximation of a tournament (which can be the majority tournament of the election) by a linear order at minimum distance (Slater problem [160]). The complexity of the Slater problem derives from a recent result dealing with the problem called the *feedback arc set problem*, which is known to be NP-complete from work by R. Karp [100] for general graphs. This problem consists of removing a min-

imum number of arcs in a directed graph in order to obtain a graph without any circuits. Recent results [5,34,41] show that this problem remains NP-complete even when restricted to tournaments. For a tournament T , removing a minimum number of arcs to obtain a graph without any circuits is the same as reversing a minimum number of arcs to make T transitive, i. e., a linear order (see [92]). From this, we may prove the following theorem (see [92] for details):

Theorem 6 For any tournament T , we have the following results:

- The computation of the Slater index $i(T)$ of T is NP-hard; this problem belongs to the class FL^{NP} ; the associated decision problem is NP-complete.
- The computation of a Slater winner of T is NP-hard; this problem belongs to the class FP^{NP} .
- Checking that a given vertex is a Slater winner of T is NP-hard; this problem belongs to the class L^{NP} .
- The computation of a Slater order of T is NP-hard; this problem belongs to the class FP^{NP} .
- The computation of all the Slater winners of T is NP-hard; this problem belongs to the class FP^{NP} .
- The computation of all the Slater orders of T is NP-hard.
- Checking that a given order is a Slater order is a problem which belongs to the class co-NP.

Some of the previous results may be generalized to other definitions of remoteness, for instance, if the sum of the symmetric difference distances to the individual preferences is replaced by their maximum, or by the sum of their squares, or by the sum of any of their positive powers, as specified below (see [94]):

Theorem 7 Let Φ denote any remoteness defined for any profile Π such that, when m is equal to 1 with $\Pi = (R_1)$, then the minimization of $\Phi(\Pi, R)$ over the relations R belonging to \mathcal{A} yields to the same optimal solutions as the minimization of $\delta(R_1, R)$ over the same set. Then, for any fixed m with $m \geq 1$, the aggregation of m binary relations

or m tournaments obtained by minimizing Φ (the problems similar to $P_m(\mathcal{R}, \mathcal{Z})$ and $P_m(\mathcal{T}, \mathcal{Z})$ for $\mathcal{Z} \in \{\mathcal{A}, \mathcal{L}\}$ but with respect to Φ) are NP-hard, and the associated decision problems are NP-complete.

An important case exists for which $P_m(\mathcal{L}, \mathcal{L})$ becomes polynomial for any m : it is the one for which the voters' preferences are *single-peaked* linear orders. To define them, assume that we can order the candidates on a line, from left to right, and assume that this linear order Ω does not depend on the voters (from a practical point of view, Ω is not always easy to define, even for political elections). For any voter α , let x_α denote the candidate preferred by α . The preference of α is said to be Ω -*singled-peaked* if, for any candidates y and z with $x \neq y \neq z \neq x$ and located on the same side of Ω from x_α , y is preferred to z by α if and only if y is closer to x_α than z with respect to Ω . Let \mathcal{U}_Ω denote the set of Ω -single-peaked linear orders. D. Black [23] showed that, for any order Ω , the aggregation of Ω -single-peaked linear orders is an Ω -single-peaked linear order (see also [42] for another study dealing with single-peaked preferences). Hence the polynomiality of the aggregation of Ω -single-peaked linear orders into an Ω -single-peaked linear order:

Theorem 8 *For any linear order Ω defined on X and any positive integer m , for any set \mathcal{Z} containing \mathcal{U}_Ω as a subset (this is the case for the sets $\mathcal{A}, \mathcal{C}, \mathcal{L}, \mathcal{O}, \mathcal{P}, \mathcal{R}, \mathcal{T}$), $P_m(\mathcal{U}_\Omega, \mathcal{Z})$ is polynomial. More precisely, $P_m(\mathcal{U}_\Omega, \mathcal{Z})$ can be solved in $O(n^2 m)$.*

The NP-hardness of Slater's problems shows that tournament solutions can be difficult to compute. This obviously depends on the solutions considered. For instance, Copeland's procedure is polynomial, as specified by the next theorem.

Theorem 9 *Copeland's procedure is polynomial, in $O(n^2 m)$.*

If we assume that the tournament related to Copeland's procedure is already computed, and if we do not take the memory-space necessary to code this tournament into account, it is easy to see that the memory-space necessary to compute the maximum of the Copeland scores and then to decide whether a given vertex is a Copeland winner can be bounded by a constant. So, deciding whether a given vertex is a Copeland winner is a problem belonging to class L. In fact, a stronger result is shown by F. Brandt, F. Fischer and P. Harrenstein in [29]:

Theorem 10 *Checking that a given vertex is a Copeland winner is a TC^0 -complete problem.*

Similar results can be stated for Smith's tournament solution (top cycle):

Theorem 11 *Let T be a tournament.*

- *The computation of the Smith winners of T (the elements of the top cycle of T) can be done in $O(n^2)$ (or even in linear time with respect to the cardinality of the top cycle if the sorted scores are known).*
- *Checking that a given vertex is a Smith winner is a TC^0 -complete problem [29].*

For the other tournament solutions depicted above, we have the results stated in Theorem 12 (see [93] for details and for results upon other tournament solutions). This theorem shows that checking whether a given vertex of a given tournament is a Banks winner is NP-complete [176] (and [30] for an alternative proof), while computing a Banks winner is polynomial [90]. Of course, when such a Banks winner is computed, we do not choose the winner that we compute among the set of Banks winners (and so there is no contradiction between the two results if P and NP are different). The polynomiality of the minimal covering set solution (through n resolutions of a linear programming problem, which can be done in polynomial time using L. Khachiyan's algorithm [99]), and the NP-hardness of the tournament equilibrium set solution, are new results respectively due to F. Brandt and F. Fischer [28] and to F. Brandt, F. Fischer, P. Harrenstein and M. Mair [30].

Theorem 12 *Let T be a tournament.*

- *Computing the uncovered elements of T can be done within the same complexity as the multiplication of two $(n \times n)$ -matrices, and so can be done in $O(n^{2.38})$ operations.*
- *Computing the elements of the minimal covering set of T can be done in polynomial time with respect to n .*
- *The following problem is NP-complete: given a tournament T and a vertex x of T , is x a Banks winner of T ?*
- *Computing a Banks winner is polynomial, and more precisely, can be done in $O(n^2)$ operations.*
- *Computing all the Banks winners of T is an NP-hard problem. More precisely, it is a problem belonging to the class FP^{NP} .*
- *The following decision problem is NP-hard (but is not known to be inside NP): given a vertex x of T , does x belong to $TEQ(T)$?*

J.J. Bartholdi III, C.A. Tovey and A. Trick stated in [19] that Dodgson's procedure is NP-hard. More precisely,

they proved the NP-completeness of the problem of Theorem 13 and the NP-hardness of the first two problems of Theorem 14. E. Hemaspaandra, L. Hemaspaandra and J. Rothe [84] sharpened their results (Theorem 14), assuming that Π is given by the ordered list of the m preferences of the voters (and not by a set of different linear orders with their multiplicities).

Theorem 13 *The following problem is NP-complete: given a profile Π of linear orders defined on X , a candidate $x \in X$ and an integer k , is the Dodgson score $D(x)$ of x less than or equal to k ?*

Theorem 14 *The following problems are NP-hard, and more precisely L^{NP} -complete if the considered profiles Π are given by the ordered lists of the m preferences of the voters.*

- Given a profile Π of linear orders defined on X and a candidate $x \in X$, is x a Dodgson winner?
- Given a profile Π of linear orders defined on X and a candidate $x \in X$, is x the unique Dodgson winner?
- Given a profile Π of linear orders defined on X and two candidates $x \in X$ and $y \in X$ with $x \neq y$, is $D(x)$ less than or equal to $D(y)$ (in other words, is x “better” than y)?

Notice that a variant of Dodgson’s procedure, called *homogeneous Dodgson’s procedure* (see [76] and [177]) has been shown to be polynomial by J. Rothe, H. Spakowski and J. Vogel [153]. Consider that each voter is replicated p times, each copy having the same preference. A procedure is said to be *homogeneous* if such a replication does not change the winners. Dodgson’s procedure and Young’s procedure are not homogeneous [76]. Then, instead of the Dodgson score defined above, we may consider, for each candidate x , the limit, when p tends to infinity, of the ratio between, on the one hand, the Dodgson score of x after the replication of each voter p times, and, on the other hand, p . J. Rothe, H. Spakowski and J. Vogel provide in [153] a linear program for computing such a limit for any candidate. Hence the polynomiality of the homogeneous version of Dodgson’s procedure.

They give, in the same paper [153], the complexity of Young’s procedure.

Theorem 15 *The following problems are NP-hard, and more precisely L^{NP} -complete.*

- Given a profile Π of linear orders defined on X and a candidate $x \in X$, is x a Young winner?
- Given a profile Π of linear orders defined on X and two candidates $x \in X$ and $y \in X$ with $x \neq y$, is $Y(x)$ less than or equal to $Y(y)$ (in other words, is x “better” than y)?

Notice that all these problems become obviously polynomial if we assume that the number of candidates is upper-bounded by a constant.

Further Directions

Complexity is a prominent feature of voting procedures. NP-hardness may involve too much important CPU time to solve a given instance if the number of candidates is not small. In this respect, polynomial procedures can be preferable to NP-hard ones. In practice, the number of candidates is not always too large, and the instance considered can be tractable. This also depends on the efficiency of the applied algorithms (see [17,35,36,37,41,88,89,98,108,151,152,173] for references on algorithms designed to solve some of the previous problems). Moreover, complexity is stated here in the worst case. A study about the average complexity (for appropriate probability distributions) remains to be done.

Other directions can be investigated.

For instance, the parameterized complexity (see [62] for a global presentation of this field) of the feedback arc set problem applied to tournaments has also been studied. V. Raman and S. Saurabh [148] (see also [61], where the case of bipartite tournaments is also considered) show that the feedback arc set problem for weighted or unweighted tournaments is fixed-parameter tractable (FPT) by providing appropriate algorithms. (Remember that a problem is said to be FPT if there exist an arbitrary function f and a polynomial function Q such that, for any instance (I, k) where I is an instance of the non-parameterized version of the problem and k is the considered complexity parameter, (I, k) can be solved within a CPU time upper-bounded by $f(k)Q(|I|)$, where $|I|$ denotes the size of I . In particular, if k is upper-bounded by a constant, then the problem becomes polynomial.) V. Raman and S. Saurabh give several algorithms to solve the parameterized version of the feedback arc set problem applied to tournaments. The best complexity of their algorithms for this problem is $O(2.415^k n^\omega)$, where ω denotes the exponent of the running time of the best matrix multiplication algorithm (for instance, in the method designed by D. Coppersmith and S. Winograd [49], ω is about 2.376). Parameterized complexity appears also in [39,115,116] for Kemeny’s, Dodgson’s and Young’s procedures.

Another direction deals with algorithms with approximation guarantees (see [10] or [172] for a presentation of this field). For instance, while the feedback arc set problem is APX-hard in general [69] (remember that, from a practical point of view, this implies that we do not know polynomial-time approximation scheme – PTAS – to solve this

problem), N. Ailon, M. Charikar and A. Newman [3] designed randomized 3-approximation and 2.5-approximation algorithms for the feedback arc set problem when restricted to unweighted tournaments. The 3-approximation algorithm has been derandomized by A. van Zuylen [171], still for unweighted tournaments and with an approximation ratio equal to 3. These methods may be adapted to weighted tournaments with an approximation ratio equal to 5 (see [3] and [50]). N. Alon [5] (see also [2]) shows that, for any fixed $\varepsilon > 0$, it is NP-hard to approximate the minimum size of a feedback arc set for a tournament on n vertices up to an additive error of $n^{2-\varepsilon}$ (but approximating it up to an additive error of εn^2 can be done in polynomial time). Ranking the vertices of a tournament according to their out-degrees (Copeland's procedure) for unweighted tournaments, or according to the sum of the weights of the arcs leaving them minus the sum of the weights of the arcs entering them (Borda's procedure) for weighted tournaments, also provides a method with approximation ratio equal to 5, irrespective of how ties are broken (see [50] and [170]).

Probabilistic algorithms (see [6] for a global presentation of these methods) have also been applied to the feedback arc set problem (or rather to the search for a maximum subdigraph without circuits, which is the same for tournaments), for unweighted [53,57,144,145,163,164,165] or weighted [53] tournaments.

If NP-hardness is usually considered as a drawback (because the CPU time necessary to solve the instances becomes quickly prohibitive, because the algorithms may be difficult to explain to the voters, and so on), it can also be an asset with respect to manipulation, bribery or other attempts to control the election (by adding or deleting candidates or voters, etc.). This is an emerging but already flourishing topic, which becomes a subject on its own (see [18,20,21,33,43,44,45,46,47,66,71,72,73,79,83,86,87,108,114,127,135,137,146,147,155,157,162,169]). A voting procedure is said to be *manipulable* when a voter, who knows how the other voters vote, has the opportunity to benefit by *strategic* or *tactical voting*, i.e., when the voter supports a candidate other than his or her sincerely preferred candidate in order to prevent an undesirable outcome (the main difference between manipulation and bribery is that, for manipulability, the manipulators are known as a part of the instance; for bribery, the number of corrupted voters is bounded but these manipulators are not given). It is known from the theorem by A. Gibbard [79] and M. Satterthwaite [157] that, for at least three candidates, any voting procedure without a dictator is manipulable. Because of this result, manipulation cannot be precluded in any reasonable voting procedure on

at least three candidates. As suggested in [18] and in [20] (see also [72]), the situation is less bad if we adopt a procedure for which manipulation is NP-hard. Some procedures are easy to manipulate: this is the case, for instance, for the plurality rule, Borda's procedure, maximin procedure or Copeland's procedure [20] (see also [72] for variants). Some others are NP-hard: this is the case for some variants of some procedures based on score-vectors [44,47,83], or for other procedures [71,87]. But we must remember that NP-hardness refers to the complexity in the worst case; V. Conitzer and T. Sandholm show in [46] that, under certain assumptions, no voting procedure is hard to manipulate, on average.

Among further related issues, we can still mention complexity issues in voting on combinatorial domains (see for instance [104]), or the complexity of determining if the output of a vote is determined even when some voters have not yet been elicited (see for instance [43]).

Computational complexity has become an important criterion in evaluating voting procedures, even if real elections are not necessarily the most difficult instances (for example because the number of candidates can be limited). Voting methods are increasingly used in multiagent systems. When autonomous software agents are voting over all sorts of issues, then large numbers of candidates may be more likely, and also agents are possibly more likely to manipulate. Thus, complexity is now a property which must be taken into account along with axiomatic properties. In spite of Arrow's impossibility theorem, or maybe because of it, it is still necessary to design new voting procedures, to study them and to compare them to existing procedures. In the mathematical tool box available to do so, there is now a place for computational complexity.

Acknowledgments

I would like to thank Ulle Endriss, Jérôme Lang and Bernard Monjardet for their help. Their comments were very useful to improve the text.

Bibliography

Primary Literature

1. Aaronson S, Kuperberg G (2008) Complexity Zoo. http://qwiki.caltech.edu/wiki/Complexity_Zoo
2. Ailon N, Alon N (2007) Hardness of fully dense problems. Inf Comput 205:117–1129
3. Ailon N, Charikar M, Newman A (2005) Aggregating inconsistent information: ranking and clustering. Proceedings of the 37th annual ACM symposium on Theory of computing (STOC), pp 684–693
4. Aizerman MA, Aleskerov FT (1995) Theory of choice. North Holland, Elsevier, Amsterdam

5. Alon N (2006) Ranking tournaments. *SIAM J Discret Math* 20(1):137–142
6. Alon N, Spencer J (2000) *The probabilistic method*, 2nd edn. Wiley, New York
7. Arrow KJ (1963) *Social choice and individual values*, rev edn. Wiley, New York
8. Arrow KJ, Raynaud H (1986) *Social choice and multicriterion decision-making*. MIT Press, Cambridge
9. Arrow KJ, Sen AK, Suzumura K (eds) (2002) *Handbook of social choice and welfare*, vol 1. North-Holland, Amsterdam
10. Ausiello G, Crescenzi P, Gambosi G, Kann V, Marchetti-Spaccamela A, Protasi M (2003) *Complexity and Approximation*, 2nd edn. Springer, Berlin
11. Baldwin JM (1926) The technique of the Nanson preferential majority system of election. *Proc Royal Soc Victoria* 39:42–52
12. Bang-Jensen J, Gutin G (2001) *Digraphs: theory, algorithms, and applications*. Springer, Berlin
13. Banks J (1985) Sophisticated voting outcomes and agenda control. *Soc Choice Welf* 2:295–306
14. Barnett WA, Moulin H, Salles M, Schofield NJ (eds) (1995) *Social choice, welfare and ethics*. Cambridge University Press, New York
15. Barthélemy J-P (1979) Caractérisations axiomatiques de la distance de la différence symétrique entre des relations binaires. *Math Sci Hum* 67:85–113
16. Barthélemy J-P, Guénoche A, Hudry O (1989) Median linear orders: heuristics and a branch and bound algorithm. *Eur J Oper Res* 41:313–325
17. Barthélemy J-P, Monjardet B (1981) The median procedure in cluster analysis and social choice theory. *Math Soc Sci* 1: 235–267
18. Bartholdi III JJ, Orlin J (1991) Single transferable vote resists strategic voting. *Soc Choice Welf* 8(4):341–354
19. Bartholdi III JJ, Tovey CA, Trick MA (1989) Voting schemes for which it can be difficult to tell who won the election. *Soc Choice Welf* 6:157–165
20. Bartholdi III JJ, Tovey CA, Trick MA (1989) The Computational Difficulty of Manipulating an Election. *Soc Choice Welf* 6: 227–241
21. Bartholdi III JJ, Tovey CA, Trick MA (1992) How hard is it to control an election? *Math Comput Model* 16(8/9):27–40
22. Berge C (1985) *Graphs*. North-Holland, Amsterdam
23. Black D (1958) *The theory of committees and elections*. Cambridge University Press, Cambridge
24. Borda J-C (1784) *Mémoire sur les élections au scrutin*. Histoire de l'Académie Royale des Sciences pour 1781, Paris, pp 657–665. English translation: de Grazia A (1953) *Mathematical Derivation of an Election System*. *Isis* 44:42–51
25. Brams SJ, Fishburn PC (1978) Approval Voting. *Am Political Sci Rev* 72(3):831–857
26. Brams SJ, Fishburn PC (1983) *Approval Voting*. Birkhauser, Boston
27. Brams SJ, Fishburn PC (2002) Voting Procedures. In: Arrow K, Sen A, Suzumura K (eds) *Handbook of Social Choice and Welfare*, vol 1. Elsevier, Amsterdam, pp 175–236
28. Brandt F, Fischer F (2008) Computing the minimal covering set. *Math Soc Sci* 58(2):254–268
29. Brandt F, Fischer F, Harrenstein P (2006) The computational complexity of choice sets. In: Endriss U, Lang J (eds) *Proceedings of the conference Computational Social Choice 2006*. University of Amsterdam, The Netherlands, pp 63–76
30. Brandt F, Fischer F, Harrenstein P, Mair M (2008) A computational analysis of the tournament equilibrium set. In: Fox D, Gomes CP (eds) *Proc. of AAAI*, pp. 38–43
31. Caritat MJAN, marquis de Condorcet (1785) *Essai sur l'application de l'analyse à la probabilité des décisions rendues à la pluralité des voix*. Imprimerie Royale, Paris
32. Caspard N, Monjardet B, Leclerc B (2007) *Ensembles ordonnés finis: concepts, résultats et usages*. Springer, Berlin
33. Chamberlin JR (1985) An investigation into the effective manipulability of four voting systems. *Behav Sci* 30:195–203
34. Charbit P, Thomassé S, Yeo A (2007) The minimum feedback arc set problem is NP-hard for tournaments. *Comb Probab Comput* 16(1):1–4
35. Charon I, Hudry O (2006) A branch and bound algorithm to solve the linear ordering problem for weighted tournaments. *Discret Appl Math* 154:2097–2116
36. Charon I, Hudry O (2007) A survey on the linear ordering problem for weighted or unweighted tournaments. *4OR* 5(1):5–60
37. Charon I, Guénoche A, Hudry O, Woïrgard F (1997) New results on the computation of median orders. *Discret Math* 165–166:139–154
38. Chevalere Y, Endriss U, Lang J, Maudet N (2007) A short introduction to computational social choice. *Proceedings of the 33rd Conference on Current Trends in Theory and Practice of Computer Science (SOFSEM-2007)*. Lecture Notes in Computer Science, vol 4362. Springer, Berlin, pp 51–69
39. Christian R, Fellows M, Rosamond F, Slinko A (2006) On complexity of lobbying in multiple referenda. *Proceedings of the First International Workshop on Computational Social Choice (COMSOC 2006)*. University of Amsterdam, pp 87–96
40. Colomer JM, McLean I (1998) Electing Popes: Approval Balloting and Qualified-Majority Rule. *J Interdisciplinary History* 29(1):1–22
41. Conitzer V (2006) Computing Slater Rankings Using Similarities Among Candidates. In: *Proceedings of the 21st National Conference on Artificial Intelligence, AAAI-06, Boston*, pp. 613–619
42. Conitzer V (2007) Eliciting single-peaked preferences using comparison queries. *Proceedings of the 6th International Joint Conference on Autonomous Agents and Multi Agent Systems (AAMAS-07)*. Honolulu, USA, pp 408–415
43. Conitzer V, Sandholm T (2002) Vote elicitation: complexity and strategy-proofness. *Proceedings of the National Conference on Artificial Intelligence (AAAI)*, pp 392–397
44. Conitzer V, Sandholm T (2002) Complexity of manipulating elections with few candidates. *Proceedings of the 18th National Conference on Artificial Intelligence (AAAI)*, pp 314–319
45. Conitzer V, Sandholm T (2003) Universal voting protocol tweaks to make manipulation hard. In: *Proceedings of the 18th International Joint Conference on Artificial Intelligence (IJCAI-03)*, Acapulco, Mexico, pp 781–788
46. Conitzer V, Sandholm T (2006) Nonexistence of voting rules that are usually hard to manipulate. *Proceedings of the 21st National Conference on Artificial Intelligence (AAAI-06)*, Boston, pp 627–634
47. Conitzer V, Lang J, Sandholm T (2003) How many candidates are needed to make elections hard to manipulate? *Theoretical Aspects of Rationality and Knowledge (TARK)*, pp 201–214
48. Copeland AH (1951) A “reasonable” social welfare function.

- Seminar on applications of mathematics to the social sciences. University of Michigan
49. Coppersmith T, Winograd S (1987) Matrix multiplication via arithmetic progression. In: Proc 19th Ann ACM Symp Theor Comput, pp 1–6
 50. Coppersmith D, Fleischer L, Rudra A (2006) Ordering by weighted number of wins gives a good ranking for weighted tournaments. Proceedings of the 17th annual ACM-SIAM symposium on discrete algorithms (SODA'06), pp 776–782
 51. Cormen T, Leiserson C, Rivest R (1990) Introduction to algorithms, 2nd edn 2001. MIT Press, Cambridge
 52. Cox GW (1987) The Cabinet and the Development of Political Parties in Victorian England. Cambridge University Press, New York
 53. Czygrinow A, Poljak S, Rödl V (1999) Constructive quasi-Ramsey numbers and tournament ranking. SIAM J Discret Math 12(1):48–63
 54. Daunou PCF (1803) Mémoire sur les élections au scrutin. Baudouin, Paris, an XI
 55. Debord B (1987) Caractérisation des matrices de préférences nettes et méthodes d'agrégation associées. Math Sci Hum 97:5–17
 56. Debord B (1987) Axiomatisation de procédures d'agrégation de préférences. PhD thesis, Université scientifique technologique et médicale de Grenoble
 57. de la Vega WF (1983) On the maximal cardinality of a consistent set of arcs in a random tournament. J Comb Theor B 35:328–332
 58. Dodgson CL (1873) A Discussion of the Various Methods of Procedure in Conducting Elections. Imprint by Gardner EB, Hall EP, Stacy JH. Printers to the University, Oxford. Reprinted In: Black D (1958) The Theory of Committees and Elections. Cambridge University Press, Cambridge, pp 214–222
 59. Dodgson CL (1874) Suggestions as to the Best Method of Taking Votes, Where More than Two Issues are to be Voted on. Imprint by Hall EP, Stacy JH. Printers to the University, Oxford. Reprinted In: Black D (1958) The Theory of Committees and Elections. Cambridge University Press, Cambridge, pp 222–224
 60. Dodgson CL (1876) A method of taking votes on more than two issues, Clarendon Press, Oxford. Reprint In: Black D (1958) The theory of committees and elections, Cambridge University Press, Cambridge, pp 224–234; and In: McLean I, Urken A (1995) Classics of social choice. University of Michigan Press, Ann Arbor
 61. Dom M, Guo J, Hüffner F, Niedermeier R, Truß A (2006) Fixed-Parameter Tractability Results for Feedback Set Problems in Tournaments. Lecture Notes in Computer Science, vol 3998. Springer, Berlin, pp 320–331
 62. Downey RG, Fellows MR (1999) Parameterized complexity. Springer, Berlin
 63. Dummett M (1984) Voting Procedures. Clarendon Press, Oxford
 64. Dutta B (1988) Covering sets and a new Condorcet choice correspondence. J Economic Theory 44:63–80
 65. Dwork C, Kumar R, Naor M, Sivakumar D (2001) Rank aggregation methods for the Web. Proceedings of the 10th international conference on World Wide Web (WWW10), Hong Kong, pp 613–622
 66. Elkin E, Lipmaa H (2006) Hybrid voting protocols and hardness of manipulation. In: Endriss U, Lang J (eds) Proceedings of the First International Workshop on Computational Social Choice (COMSOC 2006). University of Amsterdam, pp 178–191
 67. Elster J, Hylland A (eds) (1986) Foundations of Social Choice Theory. Cambridge University Press, New York
 68. Erdős P, Moser L (1964) On the representation of directed graphs as unions of orderings. Magyar Tud Akad Mat Kutató Int Közl 9:125–132
 69. Even G, Naor JS, Sudan M, Schieber B (1998) Approximating minimum feedback sets and multicuts in directed graphs. Algorithmica 20(2):151–174
 70. Fagin R, Kumar R, Mahdian M, Sivakumar D, Vee E (2005) Rank Aggregation: An Algorithmic Perspective. unpublished manuscript
 71. Faliszewski P, Hemaspaandra E, Hemaspaandra L (2006) The complexity of bribery in elections. In: Endriss U, Lang J (eds) Proceedings of the First International Workshop on Computational Social Choice (COMSOC 2006). University of Amsterdam, pp 178–191
 72. Faliszewski P, Hemaspaandra E, Hemaspaandra L, Rothe J (2006) A richer understanding of the complexity of election systems. Technical report TR-2006-903, University of Rochester. To appear in: Ravi S, Shukla S (eds) (2008) Fundamental Problems in Computing: Essays in honor of Professor Daniel J. Rosenkrantz. Springer, Berlin
 73. Faliszewski P, Hemaspaandra E, Hemaspaandra L, Rothe J (2007) Llull and Copeland Voting Broadly Resist Bribery and Control. Technical report TR-2006-903. University of Rochester, NY
 74. Fishburn PC (1973) Interval representations for interval orders and semiorders. J Math Psychol 10:91–105
 75. Fishburn PC (1973) The theory of social choice. Princeton University Press, Princeton
 76. Fishburn PC (1977) Condorcet social choice functions. SIAM J Appl Math 33:469–489
 77. Fishburn PC (1985) Interval orders and interval graphs, a study of partially ordered sets. Wiley, New York
 78. Garey MR, Johnson DS (1979) Computers and intractability, a guide to the theory of NP-completeness. Freeman, New York
 79. Gibbard A (1973) Manipulation of voting schemes. Econometrica 41:587–602
 80. Guilbaud GT (1952) Les théories de l'intérêt général et le problème logique de l'agrégation. Économie Appl 5(4):501–584; Éléments de la théorie des jeux, 1968. Dunod, Paris
 81. Hägele G, Pukelsheim F (2001) Llull's writings on electoral systems. Studia Lulliana 3:3–38
 82. Hemaspaandra L (2000) Complexity classes. In: Rosen KH (ed) Handbook of discrete and combinatorial mathematics. CRC Press, Boca Raton, pp 1085–1090
 83. Hemaspaandra E, Hemaspaandra L (2007) Dichotomy for voting systems. J Comput Syst Sci 73(1):73–83
 84. Hemaspaandra E, Hemaspaandra L, Rothe J (1997) Exact analysis of Dodgson elections: Lewis Carroll's 1876 voting system is complete for parallel access to NP. J ACM 44(6):806–825
 85. Hemaspaandra E, Spakowski H, Vogel J (2005) The complexity of Kemeny elections. Theor Comput Sci 349:382–391
 86. Hemaspaandra E, Hemaspaandra L, Rothe J (2006) Hybrid elections broaden complexity-theoretic resistance to control. Proceedings of the First International Workshop on Computational Social Choice (COMSOC 2006), University of Amsterdam

- dam, pp 234–247; (2007) Proceedings of the 20th International Joint Conference on Artificial Intelligence (IJCAI 2007). AAAI Press, pp 1308–1314
87. Hemaspaandra E, Hemaspaandra L, Rothe J (2007) Anyone but him: the complexity of precluding an alternative. *Artif Intell* 171(5–6):255–285
 88. Homan C, Hemaspaandra L (2006) Guarantees for the success frequency of an algorithm for finding Dodgson-election winners. Proceedings of the 31st International Symposium on Mathematical Foundations of Computer Science. Lecture Notes in Computer Science, vol 4162. Springer, Berlin, pp 528–539
 89. Hudry O (1989) Recherche d'ordres médians: complexité, algorithmique et problèmes combinatoires. Ph D thesis, ENST, Paris
 90. Hudry O (2004) A note on Banks winners. In: Woeginger GJ (ed) tournaments are difficult to recognize. *Soc Choice Welf* 23:1–2
 91. Hudry O (2008) NP-hardness results on the aggregation of linear orders into median orders. *Ann Oper Res* 163(1):63–88
 92. Hudry O (2008) NP-hardness of Slater and Kemeny problems. (submitted)
 93. Hudry O (2008) A survey on the complexity of tournament solutions. *Math Soc Sci* (to appear)
 94. Hudry O (2008) Complexity of the aggregation of binary relations. (submitted)
 95. Inada K (1969) The Simple Majority Decision Rule. *Econometrica* 37:490–506
 96. Johnson DS (1990) A catalog of complexity classes. In: van Leeuwen J (ed) Handbook of Theoretical Computer Science Vol. A: Algorithms and Complexity. Elsevier, Amsterdam, pp 67–161
 97. Johnson PE (1998) Social Choice Theory and Research, CA (Quantitative Applications in the Social Sciences Series, vol 123). Sage Publications, Thousand Oaks
 98. Jünger M (1985) Polyhedral combinatorics and the acyclic subdigraph problem. Heldermann, Berlin
 99. Khachiyan L (1979) A polynomial algorithm in linear programming. *Sov Math Dokl* 20:191–194
 100. Karp RM (1972) Reducibility among combinatorial problems. In: Miller RE, Thatcher JW (eds) Complexity of computer computations. Plenum Press, New York, pp 85–103
 101. Kelly JS (1987) Social Choice Theory: an Introduction. Springer, Berlin
 102. Kemeny JG (1959) Mathematics without Numbers. *Daedalus* 88:571–591
 103. Köhler G (1978) Choix multicritère et analyse algébrique de données ordinales. Ph D thesis, université scientifique et médicale de Grenoble
 104. Lang J (2004) Logical preference representation and combinatorial vote. *Ann Math Artif Intell* 42:37–71
 105. Laplace (marquis de) PS (1795) Journal de l'École Polytechnique, tome II vol. 7–8; Théorie analytique des probabilités. Essai philosophique sur les probabilités. Œuvres de Laplace, tome VII, Paris, 1847
 106. Laslier J-F (1997) Tournament Solutions and Majority Voting. Springer, Berlin
 107. Laslier J-F (2004) Le vote et la règle majoritaire. Analyse mathématique de la politique éditions du CNRS
 108. LeGrand R, Markakis E, Mehta A (2006) Approval voting: local search heuristics and approximation algorithms for the minimax solution. Proceedings of the First International Workshop on Computational Social Choice (COMSOC 2006), University of Amsterdam, pp 234–247
 109. Levenglick A (1975) Fair and reasonable election systems. *Behav Sci* 20:34–46
 110. Levin J, Nalebuff B (1995) An introduction to vote-counting schemes. *J Economic Perspectives* 9(1):3–26
 111. Lines M (1986) Approval Voting and Strategy Analysis: A Venetian. *Ex Theor Decis* 20:155–172
 112. Lhuillier S (1794) Examen du mode d'élection proposé à la Convention nationale de France en février 1793 et adopté à Genève, Genève. Reprint In: (1976) *Math Sci Hum* 54:7–24
 113. Mascart J (1919) La vie et les travaux du chevalier Jean-Charles de Borda (1733–1799): épisodes de la vie scientifique au XVIIIe siècle. Annales de l'université de Lyon vol. II (33). New edition, Presses de l'université de Paris-Sorbonne, 2000
 114. Maus S, Peters H, Storcken T (2006) Anonymous voting and minimal manipulability. Proceedings of the First International Workshop on Computational Social Choice (COMSOC 2006), University of Amsterdam, pp 317–330
 115. McCabe-Dansted J (2006) Feasibility and approximability of Dodgson's rule. Master's thesis, University of Auckland
 116. McCabe-Dansted J, Pritchard G, Slinko A (2006) Approximability of Dodgson's rule. Proceedings of the First International Workshop on Computational Social Choice (COMSOC 2006), University of Amsterdam, pp 234–247
 117. Mc Garvey D (1953) A theorem on the construction of voting paradoxes. *Econometrica* 21:608–610
 118. McKey B (2006) <http://cs.anu.edu.au/pp-bdm/data/digraphs.html>
 119. McLean I (1995) The first golden age of social choice, 1784–1803. In: Barnett WA, Moulin H, Salles M, Schofield NJ (eds) Social choice welfare, and ethics: proceedings of the eighth international symposium in economic theory and econometrics. Cambridge University Press, Cambridge, pp 13–33
 120. McLean I, Hewitt F (1994) Condorcet: Foundations of Social choice and Political Theory. Edward Elgar, Hants
 121. McLean I, Urken A (1995) Classics of social choice. University of Michigan Press, Ann Arbor
 122. McLean I, Urken A (1997) La réception des œuvres de Condorcet sur le choix social (1794–1803): Lhuillier, Morales et Daunou, in Condorcet, Homme des Lumières et de la Révolution, Chouillet A-M, Pierre Crépel (eds) ENS éditions, Fontenay-aux-roses, pp 147–160
 123. McLean I, McMillan A, Monroe BL (1995) Duncan Black and Lewis Carroll. *J Theor Politics* 7:107–124
 124. McLean I, Lorrey H, Colomer JM (2007) Social Choice in Medieval Europe. workshop Histoire des Mathématiques Sociales, Paris
 125. Merrill III S, Grofman B (1999) A Unified Theory of Voting. Cambridge University Press, Cambridge
 126. Miller N (1980) A new solution set for tournaments and majority voting: Further graph-theoretical approaches to the theory of voting. *Am J Political Sci* 24(1):68–96
 127. Mitlöhner J, Eckert D, Klamler C (2006) Simulating the effects of misperception on the manipulability of voting rules. Proceedings of the First International Workshop on Computational Social Choice (COMSOC 2006), University of Amsterdam, pp 234–247
 128. Monjardet B (1976) Lhuillier contre Condorcet au pays des paradoxes. *Math Sci Hum* 54:33–43

129. Monjardet B (1979) Relations à éloignement minimum de relations binaires, note bibliographique. *Math Sci Hum* 67:115–122
130. Monjardet B (1990) Sur diverses formes de la "règle de Condorcet" d'agrégation des préférences. *Math Inf Sci Hum* 111:61–71
131. Monjardet B (2008) Acyclic domains of linear orders: a survey. (to appear)
132. Monjardet B (2008) Mathématique Sociale and Mathematics. A case study: Condorcet's effect and medians. *Electron J Hist Probab Stat* 4(1):1–26
133. Monjardet B Private communication
134. Moon JW (1968) Topics on tournaments. Holt, Rinehart and Winston, New York
135. Moulin H (1980) On strategy-proofness and single peakedness. *Public Choice* 35:437–455
136. Moulin H (1983) The Strategy of Social Choice. North Holland, Amsterdam
137. Moulin H (1985) Fairness and strategy in voting. In: Young HP (ed) Fair Allocation, American Mathematical Society. *Proc Symp Appl Math* 33:109–142
138. Moulin H (1986) Choosing from a tournament. *Soc Choice Welf* 3:272–291
139. Morales JI (1977) Memoria matemática sobre el cálculo de la opinión en las elecciones. Imprenta Real, Madrid. Translated in: McLean I, Urken A (1995) Classics of social choice. University of Michigan Press, Ann Arbor
140. Nanson EJ (1882) Methods of Election. *Trans Proc Royal Soc Victoria* 18:197–240
141. Nurmi H (1987) Comparing Voting Systems. D. Reidel Publishing Company, Dordrecht
142. Orlin J (1981) unpublished
143. Pattanaik PK, Salles M (eds) (1983) Social Choice and Welfare. North-Holland, Amsterdam
144. Poljak S, Turzík D (1986) A polynomial time heuristic for certain subgraph optimization problems with guaranteed lower bound. *Discret Math* 58:99–104
145. Poljak S, Rödl V, Spencer J (1988) Tournament ranking with expected profit in polynomial time. *SIAM J Discret Math* 1(3):372–376
146. Procaccia A, Rosenschein J (2006) Junta distribution and the average-case complexity of manipulating elections. Proceedings of the 5th International Joint Autonomous Agents and Multiagent Systems, ACM Press, pp 497–504
147. Procaccia A, Rosenschein J, Zohar A (2006) Multi-winner elections: complexity of manipulation, control, and winner-determination. Proceedings of the 8th Trading Agent Design and Analysis and Agent Mediated Electronic Commerce Joint International Workshop (TADA/AMEC 2006), pp 15–28
148. Raman V, Saurabh S (2006) Parameterized algorithms for feedback set problems and their duals in tournaments. *Theor Comput Sci* 351:446–458
149. Reid KB (2004) Tournaments. In: Gross JL, Yellen J (eds) Handbook of Graph Theory. CRC Press, Boca Raton, pp 156–184
150. Reid KB, Beineke LW (1978) Tournaments. In: Beineke LW, Wilson RJ (eds) Selected topics in graph theory. Academic Press, London, pp 169–204
151. Reinelt G (1985) The linear ordering problem: algorithms and applications. Research and Exposition in Mathematics 8. Heldermann, Berlin
152. Rothe J, Spakowski H (2006) On determining Dodgson winners by frequently self-knowingly correct algorithms and in average-case polynomial time. Proceedings of the First International Workshop on Computational Social Choice (COMSOC 2006), University of Amsterdam, pp 234–247
153. Rothe J, Spakowski H, Vogel J (2003) Exact complexity of the winner problem for Young elections. *Theor Comput Syst* 36(4):375–386
154. Rowley CK (ed) (1993) Social Choice Theory, vol 1: The Aggregation of Preferences. Edward Elgar Publishing Company, London
155. Saari D (1990) Susceptibility to manipulation. *Public Choice* 64:21–41
156. Saari D (2001) Decisions and Elections, Explaining the Unexpected. Cambridge University Press, Cambridge
157. Satterthwaite M (1975) Strategy-proofness and Arrow's conditions: existence and correspondence theorems for voting procedures and social welfare functions. *J Econ Theor* 10:187–217
158. Schwartz T (1990) Cyclic tournaments and cooperative majority voting: A solution. *Soc Choice Welf* 7:19–29
159. Simpson PB (1969) On Defining Areas of Voter Choice. *Q J Econ* 83(3):478–490
160. Slater P (1961) Inconsistencies in a schedule of paired comparisons. *Biometrika* 48:303–312
161. Smith JH (1973) Aggregation of preferences with variable electorate. *Econometrica* 41(6):1027–1041
162. Smith D (1999) Manipulability measures of common social choice functions. *Soc Choice Welf* 16:639–661
163. Spencer J (1971) Optimal ranking of tournaments. *Networks* 1:135–138
164. Spencer J (1978) Nonconstructive methods in discrete mathematics. In: Studies in Combinatorics, Rota GC (ed) Mathematical Association of America, Washington, pp 142–178
165. Spencer J (1987) Ten lectures on the probabilistic method. CBMS-NSF Regional Conference Series in Applied Mathematics N 52, SIAM, Philadelphia
166. Stearns R (1959) The voting problem. *Am Math Monthly* 66:761–763
167. Straffin PD Jr. (1980) Topics in the Theory of Voting. Birkhäuser, Boston
168. Taylor AD (1995) Mathematics and Politics Strategy, Voting, Power, and Proof. Springer, Berlin
169. Taylor AD (2005) Social Choice and the Mathematics of Manipulation. Cambridge University Press, Cambridge
170. Tideman TN (1987) Independence of clones as criterion for voting rules. *Soc Choice Welf* 4:185–206
171. van Zuylen A (2005) Deterministic approximation algorithms for ranking and clusterings. Cornell ORIE Tech Report No. 1431
172. Vazirani VV (2003) Approximation Algorithms. Springer, Berlin
173. Wakabayashi Y (1986) Aggregation of binary relations: algorithmic and polyhedral investigations. Ph D thesis, Augsburg
174. Wakabayashi Y (1998) The Complexity of Computing Medians of Relations. *Resenhas* 3(3):323–349
175. Weber RJ (1995) Approval voting. *J Econ Perspectives* 9(1):39–49
176. Woeginger GJ (2003) Banks winner in tournaments are difficult to recognize. *Soc Choice Welf* 20:523–528
177. Young HP (1977) Extending Condorcet's rule. *J Economic Theor* 16(2):335–353

Books and Reviews

- Aleskerov FT (1999) *Arrovian Aggregation Models*, Mathematical and statistical methods. Theory and decision library, vol 39. Kluwer, Boston
- Aleskerov FT, Monjardet B (2002) *Utility Maximisation, Choice and preference*. Springer, Berlin
- Baker KM (1975) *Condorcet from Natural Philosophy to Social Mathematics*. The University of Chicago Press, Chicago. Reissued 1982
- Balinski M, Young HP (1982) *Fair Representation*. Yale University Press, New Haven
- Barthélemy J-P, Monjardet B (1988) The median procedure in data analysis: new results and open problems. In: Bock HH (ed) *Classification and related methods of data analysis*. North Holland, Amsterdam
- Batteau P, Jacquet-Lagréze É, Monjardet B (eds) (1981) *Analyse et agrégation des préférences dans les sciences économiques et de gestion*. Economica, Paris
- Black D (1996) Formal contributions to the theory of public choice. In: Brady GL, Tullock G (eds) *The unpublished works of Duncan Black*. Kluwer, Boston
- Bouyssou D, Marchant T, Pirlot M, Tsoukias A, Vincke P (2006) *Evaluation and decision models with multiple criteria*. Springer, Berlin
- Campbell DE (1992) *Equity, Efficiency, and Social Choice*. Clarendon Press, Oxford
- Coughlin P (1992) *Probabilistic Voting Theory*. Cambridge University Press, Cambridge
- Danilov V, Sotskov A (2002) *Social Choice Mechanisms*. Springer, Berlin
- Dubois D, Pirlot M, Bouyssou D, Prade H (eds) (2006) *Concepts et méthodes pour l'aide à la décision*. Hermès, Paris
- Endriss U, Lang J (eds) (2006) *Proceedings of the First International Workshop on Computational Social Choice, COMSOC 2006*, University of Amsterdam
- Enelow J, Hinich M (eds) (1990) *Advances in the Spatial Theory of Voting*. Cambridge University Press, Cambridge
- Farquharson R (1969) *Theory of Voting*. Yale University Press, New Haven
- Feldman AM (1980) *Welfare Economics and Social Choice Theory*. Martinus Nijhoff, Boston
- Felsenthal DS, Machover M (1998) *The Measurement of Voting Power: Theory and Practice, Problems and Paradoxes*. Edward Elgar, Cheltenham
- Gaertner W (2001) *Domains Conditions in Social Choice Theory*. Cambridge University Press, Cambridge
- Greenberg J (1990) *The Theory of Social Situations*. Cambridge University Press, Cambridge
- Grofman B (1981) *When is the Condorcet Winner the Condorcet Winner?* University of California, Irvine
- Grofman B, Owen G (eds) (1986) *Information Pooling and Group Decision Making*. JAI Press, Greenwich
- Heal G (ed) (1997) *Topological Social Choice*. Springer, Berlin
- Hillinger C (2004) *Voting and the cardinal aggregation cardinal of judgments*. Discussion papers in economics 353, University of Munich
- Holler MJ (ed) (1978) *Power Voting and Voting Power*. Physica, Wurtsburg-Wien
- Holler MJ, Owen G (eds) (2001) *Indices and Coalition Formation*. Kluwer, Boston
- Kemeny J, Snell L (1960) *Mathematical models in the social sciences*. Ginn, Boston
- Laslier J-F (2006) *Spatial Approval Voting*. *Political Analysis* 14(2):160–185
- Laslier J-F, Van Der Straeten K (2008) A live experiment on approval voting. *Exp Econ* 11:97–105
- Lieberman B (ed) (1971) *Social Choice*. Gordon and Breach, New York
- Mirkin BG (1979) *Group Choice*. Winston, Washington
- Moulin H (2003) *Fair Division and Collective Welfare*. Institute of Technology Press, Boston
- Nurmi H (1999) *Voting Paradoxes and how to Deal with Them*. Springer, Berlin
- Nurmi H (2002) *Voting Procedures under Uncertainty*. Springer, Berlin
- Pattanaik PK (1971) *Voting and Collective Choice*. Harvard University Press, Cambridge
- Pattanaik PK (1978) *Strategy and Group Choice*. North Holland, Amsterdam
- Peleg B (1984) *Game Theoretic Analysis of Voting in Committees*. Cambridge University Press, Cambridge
- Rothschild E (2001) *Economic Sentiments: Adam Smith, Condorcet, and the Enlightenment*. Harvard University Press, Cambridge
- Saari DG (1994) *Geometry of Voting*. Springer, Berlin
- Saari DG (1995) *Basic Geometry of Voting*. Springer, Berlin
- Saari DG (2000) *Chaotic Elections!* American Mathematical Society, Providence
- Schofield N (1984) *Social Choice and Democracy*. Springer, Berlin
- Schofield N (ed) (1996) *Collective Decision Making: Social Choice and Political Economy*. Kluwer, Boston
- Schwartz T (1986) *The Logic of Collective Choice*. Columbia University Press, New York
- Sen AK (1979) *Collective Choice and Social Welfare*. North Holland, Amsterdam
- Sen AK (1982) *Choice, Welfare and Measurement*. Basil Blackwell, Oxford
- Suzumura K (1984) *Rational Choice, Collective Decisions and Social Welfare*. Cambridge University Press, Cambridge
- Tanguiane AS (1991) *Aggregation and Representation of Preferences, Introduction to Mathematical Theory of Democracy*. Springer, Berlin
- Tideman N (2006) *Collective Decisions and Voting: The Potential for Public Choice*. Ashgate, Burlington
- Woodall DR (1997) Monotonicity of single-seat preferential election rules. *Discret Appl Math* 77:81–98
- Young HP (1974) An Axiomatization of Borda's Rule. *J Econ Theor* 9:43–52
- Young HP (1986) Optimal ranking and choice from pairwise comparisons. In: Grofman B, Owen G (eds) *Information pooling and group decision making*. JAI Press, Greenwich, pp 113–122
- Young HP (1988) Condorcet Theory of Voting. *Am Political Sci Rev* 82:1231–1244
- Young HP (1995) Optimal voting rules. *J Econ Perspect* 9(1): 51–64
- Young HP, Levenglick A (1978) A Consistent Extension of Condorcet's Election Principle. *SIAM J Appl Math* 35:285–300